frontiers | Research Topics

Remote sensing of volcanic gas emissions from the ground, air, and space

Edited by
Christoph Kern, Santiago Arellano, Robin Campion, Silvana Hidalgo and Ryunosuke Kazahaya

Published in
Frontiers in Earth Science

ISSN 1664-8714
ISBN 978-2-8325-4103-6
DOI 10.3389/978-2-8325-4103-6

About Frontiers

Frontiers is more than just an open access publisher of scholarly articles: it is a pioneering approach to the world of academia, radically improving the way scholarly research is managed. The grand vision of Frontiers is a world where all people have an equal opportunity to seek, share and generate knowledge. Frontiers provides immediate and permanent online open access to all its publications, but this alone is not enough to realize our grand goals.

Frontiers journal series

The Frontiers journal series is a multi-tier and interdisciplinary set of open-access, online journals, promising a paradigm shift from the current review, selection and dissemination processes in academic publishing. All Frontiers journals are driven by researchers for researchers; therefore, they constitute a service to the scholarly community. At the same time, the *Frontiers journal series* operates on a revolutionary invention, the tiered publishing system, initially addressing specific communities of scholars, and gradually climbing up to broader public understanding, thus serving the interests of the lay society, too.

Dedication to quality

Each Frontiers article is a landmark of the highest quality, thanks to genuinely collaborative interactions between authors and review editors, who include some of the world's best academicians. Research must be certified by peers before entering a stream of knowledge that may eventually reach the public - and shape society; therefore, Frontiers only applies the most rigorous and unbiased reviews. Frontiers revolutionizes research publishing by freely delivering the most outstanding research, evaluated with no bias from both the academic and social point of view. By applying the most advanced information technologies, Frontiers is catapulting scholarly publishing into a new generation.

What are Frontiers Research Topics?

Frontiers Research Topics are very popular trademarks of the *Frontiers journals series*: they are collections of at least ten articles, all centered on a particular subject. With their unique mix of varied contributions from Original Research to Review Articles, Frontiers Research Topics unify the most influential researchers, the latest key findings and historical advances in a hot research area.

Find out more on how to host your own Frontiers Research Topic or contribute to one as an author by contacting the Frontiers editorial office: frontiersin.org/about/contact

Remote sensing of volcanic gas emissions from the ground, air, and space

Topic editors

Christoph Kern — Cascades Volcano Observatory, United States Geological Survey (USGS), United States

Santiago Arellano — Chalmers University of Technology, Sweden

Robin Campion — National Autonomous University of Mexico, Mexico

Silvana Hidalgo — Instituto Geofísico, Escuela Politécnice Nacional, Ecuador

Ryunosuke Kazahaya — Geological Survey of Japan, National Institute of Advanced Industrial Science and Technology (AIST), Japan

Citation

Kern, C., Arellano, S., Campion, R., Hidalgo, S., Kazahaya, R., eds. (2023). *Remote sensing of volcanic gas emissions from the ground, air, and space*. Lausanne: Frontiers Media SA. doi: 10.3389/978-2-8325-4103-6

Table of contents

frontiers | Frontiers in Earth Science

TYPE Editorial
PUBLISHED 28 November 2023
DOI 10.3389/feart.2023.1340395

OPEN ACCESS

EDITED AND REVIEWED BY
Valerio Acocella,
Roma Tre University, Italy

*CORRESPONDENCE
Christoph Kern,
ckern@usgs.gov

RECEIVED 17 November 2023
ACCEPTED 20 November 2023
PUBLISHED 28 November 2023

CITATION
Kern C, Arellano S, Campion R, Hidalgo S and Kazahaya R (2023), Editorial: Remote sensing of volcanic gas emissions from the ground, air, and space.
Front. Earth Sci. 11:1340395.
doi: 10.3389/feart.2023.1340395

Editorial: Remote sensing of volcanic gas emissions from the ground, air, and space

Christoph Kern[1]*, Santiago Arellano[2], Robin Campion[3], Silvana Hidalgo[4] and Ryunosuke Kazahaya[5]

[1]United States Geological Survey, Volcano Science Center, Vancouver, WA, United States, [2]Department of Space, Earth and Environment, Chalmers University of Technology, Göteborg, Sweden, [3]Universidad Nacional Autónoma de México, México City, Mexico, [4]Instituto Geofísico, Escuela Politécnica Nacional, Quito, Ecuador, [5]Geological Survey of Japan, National Institute of Advanced Industrial Science and Technology (AIST), Tsukuba, Japan

KEYWORDS

volcanic gas emissions, remote sensing, volcanic processes, volcano monitoring, spectroscopy, volcanology

Editorial on the Research Topic
Remote sensing of volcanic gas emissions from the ground, air, and space

When magma rises in volcanic systems, volatile species exsolve from the melt and are outgassed to the atmosphere. The melt composition and temperature, depth at which degassing occurs, extent of gas-water-rock interactions, and volume of ascending magma are all factors that determine the composition and rate of gas emissions at the surface. Interpreted in a petrological framework, gas measurements thus provide information on these fundamental parameters of volcanic systems. Volcanic gases have traditionally been sampled in the field and later analyzed with standard laboratory methods (Giggenbach, 1975; Symonds et al., 1994), but remote sensing measurements are playing an increasingly central role in characterizing emissions and the volcanoes from which they originate. The 17 contributions in this Research Topic summarize the state-of-the-art in volcanic gas remote sensing and identify key areas in which the field could further improve our understanding of global volcanism and its impact on Earth's environment in the next decade.

First introduced approximately 20 years ago as a successor to the popular correlation spectrometer (COSPEC, Moffat and Millan, 1971), miniature differential optical absorption spectrometers (DOAS, Galle et al., 2002; Edmonds et al., 2003) today represent the most established form of ground-based volcanic gas remote sensing. DOAS instruments have been installed at > 50 volcanoes worldwide, many as part of the Network for Observation of Volcanic and Atmospheric Change (NOVAC, Galle et al., 2010; Arellano et al., 2021). These instruments allow for collection and analysis of continuous daytime observations of SO_2 emission rates which have shown to be of great value in characterizing volcanic systems. Gutiérrez et al. review the known record of gas emissions from Santa Ana and San Miguel volcanoes, El Salvador. The DOAS data are supplemented with *in situ* measurements of the volcanic gas composition, resulting in a detailed record of baseline activity to which future measurements can be compared. Kunrat et al. perform a statistical analysis of emission rates leading up to explosive episodes at Sinabung volcano (Indonesia) in 2016–2021. The authors find that SO_2 emissions were usually lower during the 3 days preceding explosions than was

typical during periods of quiescence. They attribute this behavior to the blockage of degassing pathways by a solidifying lava dome at the volcano's summit and finally outline a methodology for forecasting explosions based on continuous SO_2 emissions data.

Next to DOAS instruments, SO_2 camera systems have become increasingly widely used to measure volcanic gases from the ground (Mori and Burton, 2006; Bluth et al., 2007; Kern et al., 2010a). Continuous observations from SO_2 cameras installed in the field are becoming increasingly feasible as technology matures and becomes more affordable. Wilkes et al. present the design of a filter-based SO_2 camera which uses Raspberry Pi components to implement an affordable system capable of continuous acquisition and data processing. They demonstrate this system at Kīlauea (Hawai'i, United States) and Láscar (Chile) volcanoes, and show how such instruments could help proliferate continuous SO_2 emission rate observations at volcanoes.

With robust technology now available, Delle Donne et al. installed two SO_2 cameras on opposite sides of Stromboli volcano's active summit, both of which acquired imagery during daytime for a full year (June 2017 to June 2018). The authors find that explosions were more likely during periods of high passive emission rates as magma supply to the shallow system increased, but that ~90% of SO_2 emissions occur passively rather than during explosive events. Layana et al. characterize the evolution of the magmatic-hydrothermal system beneath Lastarria volcano (Chile) from 1998 to 2019 by combining observations from scanning DOAS instruments, SO_2 cameras, and direct sampling campaigns. They find evidence for pressurization of a deep magma chamber and volatiles interacting with a shallow hydrothermal system on their way to the surface.

The recent introduction of a Fabry-Pérot interferometer (FPI) as a dispersive element in place of the simple bandpass filters used in the original design have also allowed the development of cameras with higher sensitivity and selectivity to SO_2 (Kuhn et al., 2014; Fuchs et al., 2021). Nies et al. have now adapted this design to enable high spatio-temporal resolution measurements of BrO for the first time. Using their prototype at Mount Etna, the authors were able to record BrO imagery at ~10s time resolution and, by comparison to imagery from a second FPI camera tuned to SO_2, derive BrO/SO_2 ratios from the data. Kuhn et al. take the FPI technology in a slightly different direction. Instead of collecting spatially resolved imagery, the authors' design focuses on a single viewing direction but achieves a spectral resolution that is 1–3 orders of magnitude superior to grating spectrometers. This allows them to target hitherto inaccessible gas species, for example, achieving a ~20 ppb detection limit for the hydroxyl radical (OH) over an active lava flow at Nyiragongo volcano, Democratic Republic of the Congo.

Passive DOAS and SO_2/BrO camera observations use scattered sunlight as a light source. The required ultraviolet (UV)/visible wavelengths limit the gas species that are observable with these techniques. Fourier transform infrared spectrometers (FTIR, Francis et al., 1998; Oppenheimer et al., 1998), on the other hand, can measure many more species contained in volcanic gases if a source of infrared (IR) radiation is available. Using the lava lake at Masaya volcano (Nicaragua) as a light source, Kazahaya et al. combined FTIR measurements of gases with *in situ* measurements. The authors find that the CO/CO_2 ratio of 10^{-3} agreed with values predicted by high-temperature thermodynamic magma-gas equilibrium models, but that the H_2/H_2O ratio was orders of magnitude lower than expected values. They attribute this discrepancy to ongoing oxidation of H_2 as magmatic gas is mixed with air at high temperature inside Masaya's Santiago crater.

Rather than using hot lava as a source of IR radiation, Stremme et al. aimed a stationary FTIR spectrometer directly at the Sun to make measurements of the plume emitted from Popocatépetl volcano, Mexico, between 2012 and 2016. The authors were able to derive CO_2/HCl ratios as well as CO_2 and HCl emission rates, which averaged 11.4 ± 4.4, (41.2 ± 16.7) kg/s and (30 ± 0.3) kg/s during the measurement period. Taquet et al. later collocated two UV spectrometers with the FTIR instrument to retrieve SO_2 and BrO column densities during 2017–2019. This setup allowed them to measure BrO/HCl for the first time at Popocatépetl. They postulate an upper bound for the Br/Cl ratio of $\sim 1.1 \times 10^{-3}$ and note an apparent correlation of HCl/SO_2 ratios with lava dome extrusion rates. Smekens et al. explore a novel use of FTIR spectroscopy. Rather than measuring the absorption of IR radiation by gases in the light path, the authors report on experiments seeking to estimate SO_2 and aerosol abundances from measurements of their IR emission.

Remote sensing measurements from satellite platforms provide an opportunity to track degassing at volcanoes in remote locations. Carn et al. apply a suite of satellite instruments to characterize gas and aerosol emissions from the 2021–2022 submarine eruption of Hunga Tonga-Hunga Ha'apai volcano, Tonga. The authors demonstrate how volumetric flow rates can be derived from bi-hourly imagery of gas and aerosol clouds captured by the Earth Polychromatic Imaging Camera (EPIC) aboard the Deep Space Climate Observatory (DSCOVR). The relatively modest SO_2 release of ~0.6–0.7 Tg measured for the entire eruptive episode is ~2 orders of magnitude lower than expected from petrological considerations, a circumstance that the authors hypothesize may be attributed to the rapid reaction of SO_2 with water in the plume.

In another study only made possible by the availability of satellite remote sensing data, Campion and Coppola examine the long-term relationship between volcanic radiative power (VRP) and SO_2 emission rates at volcanoes hosting lava lakes. The authors find that VRP and SO_2 emission rates are anti-correlated at volcanoes with large lava lakes and attribute this observation to the limitation of thermal energy flux through magmatic foams that commonly form in shallow magma reservoirs during the early stages of lava lake formation.

The TROPOMI instrument onboard ESA's Sentinel 5 Precursor satellite has become an extremely valuable resource for the volcanology community, as its ~3.5 × 5 km spatial resolution allows detection of smaller plumes than previously possible (Theys et al., 2019). As the quality and quantity of satellite remote sensing data products continues to increase, the sheer data volume makes manual analysis impossible and advanced algorithms for retrieving gas abundances, plume detection, source identification, and emission rate determination are gaining in importance. Markus et al. test a variety of plume identification algorithms on the operational TROPOMI SO_2 product and identify the DBSCAN multi-class classification algorithms (Ester et al., 1996) as the most promising category for plume classification and segmentation in operational environments. In situations where even greater resolution or sensitivity are needed, airborne Imaging DOAS techniques offer a solution (Louban et al., 2009; General et al., 2014a). Kern and Kelly describe the implementation of an airborne Imaging DOAS system

specifically for remote sensing of volcanic emissions and demonstrate its capabilities in an airborne gas survey of volcanoes in Alaska. The authors use the imagery, combined with the results of *in situ* measurements from a suite of on-board trace gas sensors, to characterize background activity at Iliamna Volcano, Mount Douglas, Mount Martin and Mount Mageik.

The general improvement of accuracy and precision of existing techniques is also of high priority, as improved data quality will allow for more detailed studies of volcanic processes. For techniques that use scattered solar radiation as a light source, a large source of error typically stems from uncertainties in radiative transfer, i.e., the path that measured photons have taken between the Sun and an observing instrument (Millan, 1980; Kern et al., 2010b; Galle et al., 2010). Galle et al. present an algorithm for correction of light dilution in DOAS volcanic plume measurements. They model each measured spectrum as the sum of contributions from two different light paths, one passing through the volcanic plume along the line-of-sight of the instrument, and the other passing around the plume. The relative intensity of the two contributions is then retrieved from DOAS analyses in two separate wavelength bands yielding a dilution-corrected SO_2 column density. Uncertainties in radiative transfer also affect satellite measurements. Yamaguchi et al. use TROPOMI data to investigate the time series of SO_2 emission rates from Mount Tokachi (Hokkaido, Japan). The availability of >100 high-quality images from 2019 to 2022 greatly improved emission estimates from this remote volcano. The authors note, however, that increased ground albedos from seasonal snow cover potentially cause overestimations of SO_2 emission rates.

Remote sensing already plays an important role in volcano monitoring and research today. But the contributions in this volume show how technological advances, innovative applications, improved retrieval techniques, and multi-disciplinary studies can be further improved to help answer additional fundamental questions about volcanism and the emission of volatiles to the atmosphere, as well as provide diagnostic information for use by observatories in eruption forecasts.

Author contributions

CK: Conceptualization, Writing–original draft, Writing–review and editing. SA: Conceptualization, Writing–review and editing. RC: Conceptualization, Writing–review and editing. SH: Conceptualization, Writing–review and editing. RK: Conceptualization, Writing–review and editing.

Funding

The author(s) declare that no financial support was received for the research, authorship, and/or publication of this article.

Conflict of interest

The authors declare that the research was conducted in the absence of any commercial or financial relationships that could be construed as a potential conflict of interest.

Publisher's note

All claims expressed in this article are solely those of the authors and do not necessarily represent those of their affiliated organizations, or those of the publisher, the editors and the reviewers. Any product that may be evaluated in this article, or claim that may be made by its manufacturer, is not guaranteed or endorsed by the publisher.

Author Disclaimer

Any use of trade, firm, or product names is for descriptive purposes only and does not imply endorsement by the U.S. Government.

References

Arellano, S., Galle, B., Apaza, F., Avard, G., Barrington, C., Bobrowski, N., et al. (2021). Synoptic analysis of a decade of daily measurements of SO_2 emission in the troposphere from volcanoes of the global ground-based network for observation of volcanic and atmospheric Change. *Earth Syst. Sci. Data* 13, 1167–1188. doi:10.5194/essd-13-1167-2021

Bluth, G. J. S., Shannon, J. M., Watson, I. M., Prata, A. J., and Realmuto, V. J. (2007). Development of an ultra-violet digital camera for volcanic SO_2 imaging. *J. Volcanol. Geotherm. Res.* 161, 47–56. doi:10.1016/j.jvolgeores.2006.11.004

Edmonds, M., Herd, R. A., Galle, B., and Oppenheimer, C. M. (2003). Automated, high time-resolution measurements of SO_2 flux at Soufriere Hills Volcano, Montserrat. *Bull. Volcanol.* 65, 578–586. doi:10.1007/s00445-003-0286-x

Ester, M., Kriegel, H.-P., Sander, J., and Xu, X. (1996). A density-based algorithm for discovering clusters in large spatial databases with noise. *Proc. Second Int. Conf. Knowl. Discov. Data Min.*, 226. doi:10.5555/3001460.3001507

Francis, P., Burton, M. R., and Oppenheimer, C. (1998). Remote measurements of volcanic gas compositions by solar occultation spectroscopy. *Nature* 396, 567–570. doi:10.1038/25115

Fuchs, C., Kuhn, J., Bobrowski, N., and Platt, U. (2021). Quantitative imaging of volcanic SO_2 plumes using Fabry-Pérot interferometer correlation spectroscopy. *Atmos. Meas. Tech.* 14, 295–307. doi:10.5194/amt-14-295-2021

Galle, B., Johansson, M., Rivera, C., Zhang, Y., Kihlman, M., Kern, C., et al. (2010). Network for Observation of Volcanic and Atmospheric Change (NOVAC)—a global network for volcanic gas monitoring: Network layout and instrument description. *J. Geophys. Res.* 115, D05304. doi:10.1029/2009JD011823

Galle, B., Oppenheimer, C., Geyer, A., Mcgonigle, A. J. S., Edmonds, M., and Horrocks, L. (2002). A miniaturised ultraviolet spectrometer for remote sensing of SO_2 fluxes: a new tool for volcano surveillance. *J. Volcanol. Geotherm. Res.* 119, 241–254. doi:10.1016/S0377-0273(02)00356-6

General, S., Bobrowski, N., Pöhler, D., Weber, K., Fischer, C., and Platt, U. (2014b). Airborne I-DOAS measurements at Mt. Etna: BrO and OClO evolution in the plume. *J. Volcanol. Geotherm. Res.* 300, 175–186. doi:10.1016/j.jvolgeores.2014.05.012

General, S., Pöhler, D., Sihler, H., Bobrowski, N., Frieß, U., Zielcke, J., et al. (2014a). The Heidelberg Airborne Imaging DOAS Instrument (HAIDI) – a novel Imaging DOAS device for 2-D and 3-D imaging of trace gases and aerosols. *Atmos. Meas. Tech.* 7, 3459–3485. doi:10.5194/amt-7-3459-2014

Giggenbach, W. F. (1975). A simple method for the collection and analysis of volcanic gas samples. *Bull. Volcanol.* 39, 132–145. doi:10.1007/BF02596953

Kern, C., Deutschmann, T., Vogel, L., Wöhrbach, M., Wagner, T., and Platt, U. (2010b). Radiative transfer corrections for accurate spectroscopic measurements of volcanic gas emissions. *Bull. Volcanol.* 72, 233–247. doi:10.1007/s00445-009-0313-7

Kern, C., Kick, F., Lübcke, P., Vogel, L., Wöhrbach, M., and Platt, U. (2010a). Theoretical description of functionality, applications, and limitations of SO_2 cameras for the remote sensing of volcanic plumes. *Atmos. Meas. Tech.* 3, 733–749. doi:10.5194/amt-3-733-2010

Kuhn, J., Bobrowski, N., Lübcke, P., Vogel, L., and Platt, U. (2014). A Fabry-Perot interferometer-based camera for two-dimensional mapping of SO_2 distributions. *Atmos. Meas. Tech.* 7, 3705–3715. doi:10.5194/amt-7-3705-2014

Louban, I., Bobrowski, N., Rouwet, D., Inguaggiato, S., and Platt, U. (2009). Imaging DOAS for volcanological applications. *Bull. Volcanol.* 71, 753–765. doi:10.1007/s00445-008-0262-6

Millan, M. (1980). Remote sensing of air pollutants. A study of some atmospheric scattering effects. *Atmos. Environ.* 14, 1241–1253. doi:10.1016/0004-6981(80)90226-7

Moffat, A. J., and Millan, M. M. (1971). The applications of optical correlation techniques to the remote sensing of SO_2 plumes using sky light. *Atmos. Environ.* 5, 677–690. doi:10.1016/0004-6981(71)90125-9

Mori, T., and Burton, M. (2006). The SO_2 camera: a simple, fast and cheap method for ground-based imaging of SO2 in volcanic plumes. *Geophys Res. Lett.* 33, 1–5. doi:10.1029/2006GL027916

Oppenheimer, C., Francis, P., Burton, M., Maciejewski, A. J. H., and Boardman, L. (1998). Remote measurement of volcanic gases by Fourier transform infrared spectroscopy. *Appl. Phys. B* 67, 505–515. doi:10.1007/s003400050536

Symonds, R. B., Rose, W. I., Bluth, G. J. S., and Gerlach, T. M. (1994). "Volcanic-gas studies: methods, results, and applications," in *Volatiles in magmas*. Editors M. R. Carroll and J. R. Hollaway China, (Mineralogical Society of America), 30, 1–66.

Theys, N., Hedelt, P., De Smedt, I., Lerot, C., Yu, H., Vlietinck, J., et al. (2019). Global monitoring of volcanic SO_2 degassing from space with unprecedented resolution. *Sci. Rep.* 9, 1–10. doi:10.1038/s41598-019-39279-y

frontiers | Frontiers in Earth Science

ORIGINAL RESEARCH
published: 14 July 2022
doi: 10.3389/feart.2022.867562

Behaviors of Redox-Sensitive Components in the Volcanic Plume at Masaya Volcano, Nicaragua: H_2 Oxidation and CO Preservation in Air

Ryunosuke Kazahaya[1,2]*, *Matthew Varnam*[2,3], *Ben Esse*[2], *Mike Burton*[2], *Hiroshi Shinohara*[1] *and Martha Ibarra*[4]

[1]Geological Survey of Japan, National Institute of Advanced Industrial Science and Technology, Tsukuba, Japan, [2]Department of Earth and Environmental Sciences, The University of Manchester, Manchester, United Kingdom, [3]Lunar and Planetary Laboratory, University of Arizona, Tucson, AZ, United States, [4]Instituto Nicaragüense de Estudios Territoriales, Frente a Policlínica Oriental, Managua, Nicaragua

Multi-disciplinary volcanic gas observations, including FTIR, Multi-GAS, and Alkali filter pack, were made at Masaya Volcano, Nicaragua, in January 2018. During the observation period, a lava lake was present, and the majority of the volcanic gases were likely emitted directly from the lava without any hydrothermal alterations. It is expected that the volcanic gas composition reflects the conditions of the magma, exhibiting a high equilibrium temperature. The fractions of the major components showed good consistency with previous studies; however, we found the fraction of the combustible components (such as H_2) were lower than expected. The R_H [log(H_2/H_2O)] value was measured to be less than –6, compared to the equilibrium R_H value calculated to be around –3 from the iron speciation. The equilibrium calculations suggest oxidation of the volcanic gases by high-temperature mixing with the air once they are emitted from the lava lake, lowering the H_2 content of the plume. In contrast to H_2, a small amount of CO, another combustible species, was detected and the derived CO_2/CO ratio of ca. 1,000 is consistent with the equilibrium magmatic value. This indicates that CO is kinetically inert compared to H_2. Our findings suggest that volcanic gases in the Masaya plume do not preserve information from when the gases were originally in equilibrium with the high-temperature surrounding magma.

Keywords: volcanic gas composition, Fourier transform infrared spectroscopy, Multi-GAS, plume chemistry, masaya volcano (Nicaragua)

OPEN ACCESS

Edited by:
Yosuke Aoki,
The University of Tokyo, Japan

Reviewed by:
Tjarda Roberts,
UMR7328 Laboratoire de physique et chimie de l'environnement et de l'Espace (LPC2E), France
Peter Kelly,
United States Geological Survey (USGS), United States

***Correspondence:**
Ryunosuke Kazahaya
von.kazahaya@aist.go.jp

Specialty section:
This article was submitted to Volcanology, a section of the journal Frontiers in Earth Science

Received: *01 February 2022*
Accepted: *14 June 2022*
Published: *14 July 2022*

Citation:
Kazahaya R, Varnam M, Esse B, Burton M, Shinohara H and Ibarra M (2022) Behaviors of Redox-Sensitive Components in the Volcanic Plume at Masaya Volcano, Nicaragua: H_2 Oxidation and CO Preservation in Air. Front. Earth Sci. 10:867562. doi: 10.3389/feart.2022.867562

HIGHLIGHTS

1) The plume from the lava lake at Masaya Volcano is depleted in H_2 relative to the theoretical values from equilibrium calculations. However, CO is in good agreement.
2) Depletion in volcanic H_2 indicates oxidization upon mixing of the plume with air.
3) The chemistry of the gas plumes emitted by basaltic lava lakes may not reflect the original high temperature equilibrium at which they were emitted.

INTRODUCTION

Hydrogen (H_2) and carbon monoxide (CO) are minor components of high-temperature magmatic gases, but provide crucial clues on redox states and temperature of the magma (Giggenbach, 1987;

Moussallam et al., 2012; Oppenheimer et al., 2012). Equilibrium concentrations of these gases decrease with decreasing temperature in the gas phase after degassing from the magma via the following redox reactions with T-dependent equilibrium constants, K_1, K_2, and K_3. Further details are given in **Section 4**:

$$H_2 + \frac{1}{2}O_2 = H_2O, \quad (1)$$

$$CO + \frac{1}{2}O_2 = CO_2, \quad (2)$$

$$SO_2 + 3H_2 = H_2S + 2\,H_2O. \quad (3)$$

If the volcanic gas is cooled slowly enough to remain in equilibrium (and without adding oxidant-rich air, i.e., closed system cooling), H_2 and CO will decrease as the equilibrium temperature is lowered. However, at lava lakes, the volcanic gases degas directly into cold ambient air, which is expected to quench the high-temperature equilibrium, preserving the concentrations of H_2 and CO. As a volcano with a lava lake, some previous studies have confirmed this at Erebus volcano in Antarctica (Table 1 in Moussallam et al., 2012). However, other volcanoes with lava lakes have suggested the possibility of oxidization of volcanic H_2, CO, and H_2S in the air for high-temperature volcanic gas at Erta Ale in Ethiopia and Masaya Volcano in Nicaragua (deMoor et al., 2013). Moreover, at Kilauea in Hawaii, H_2 burning has been reported (Cruikshank et al., 1973), supporting the idea that full quenching may not always occur, especially for H_2, which is more rapidly oxidized than other combustible components such as CO (Roberts et al., 2019). It is therefore important to consider if equilibrium model assumptions apply to these hot near-source plumes or not.

Masaya Volcano in Nicaragua is an open vent, basaltic volcano that has four pit craters, with recent volcanic activity centralized within the Santiago crater (**Figure 1**). In late 2015, a lava lake appeared with a very high lava flow speed (Pering et al., 2019), providing opportunities for direct observations of the active convecting magma system. Aiuppa *et al.* (2018) provide a detailed dataset of the volcanic gas composition from the formation of the lava lake (2014–2017). However, combustible components such as H_2 and CO have not been reported yet. In this study, we made multi-disciplinary volcanic gas measurements at Masaya Volcano to reveal the behaviors of the redox-sensitive components such as H_2 and CO in the high-temperature plume emitted from the lava lake.

TABLE 1 | Table to summarize the gas composition collected using Multi-GAS, AF pack, and FTIR. Details of all datasets can be found in **Supplementary Material S1**.

Date	Method	H_2O/SO_2	CO_2/SO_2	H_2/SO_2	SO_2/HCl	HCl/HF
2018/01/09	Multi-GAS	100	3.5	*6.7 × 10^{-4}	–	–
2018/01/09	AF pack	–	–	–	0.9	5.3
2018/01/10	FTIR	210	3.7		2.2	4.6
2018/01/11	Multi-GAS	150	3.9	*9.2 × 10^{-4}	–	–
2018/01/13	Multi-GAS	120	3.8	*8.2 × 10^{-4}	–	–
2018/01/13	AF pack	–	–	–	0.5	5.2
2018/01/13	FTIR	210	–	–	1.6	3.2
2018/01/15	AF pack	–		–	0.9	5.3
2018/01/15	FTIR	150	3.6	–	1.7	4.1

Values are for reference because of the weak signals and the huge background errors. For details, see text.

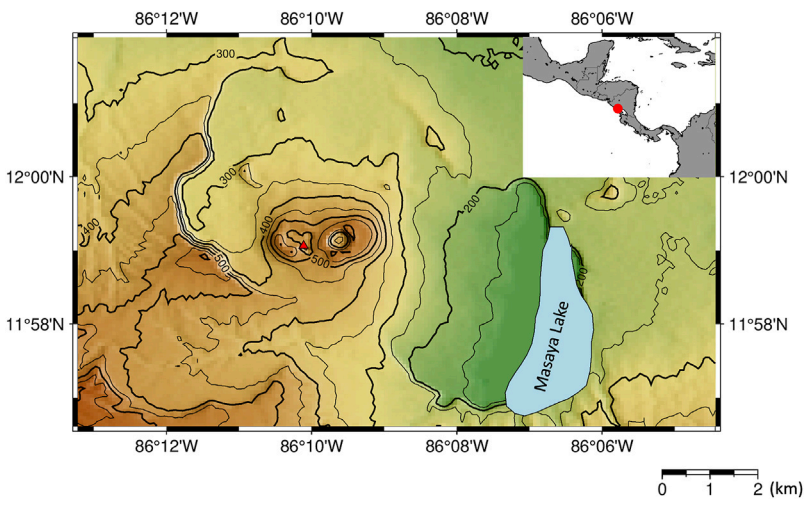

FIGURE 1 | Map of Masaya Volcano. The red triangle represents the location of a lava lake. Inset shows the location of Masaya Volcano (red circle) within Nicaragua.

OBSERVATION AND ANALYTICAL METHODS

FTIR

Open-Path Fourier-transform infrared spectroscopy (OP-FTIR) measures infrared-active gas species such as H_2O, CO_2, SO_2, H_2S, HF, HCl, and CO (e.g., Oppenheimer et al., 1998). Our spectrometer was a MIDAC M4410 equipped with a ZnSe beam splitter and a Stirling pump-cooled MCT detector. We used a 10 millirad, 3" Φ Newtonian telescope. The measurements were made on 10, 13, and 15 January 2018 at the south crater rim using an incandescent lamp as a source of artificial infrared radiation such that the plume flowed between the light source and the detector. The path lengths between the lamp and spectrometer were 30 m on 10 January 2018 and 40 m on 13 and 15 January 2018. An OP-FTIR measurement using a lava lake as a light source was also attempted on 12 January 2018 at a distance of a few hundred meters.

For FTIR data, the gas column amounts were calculated using simulated spectra with a forward model using spectral line parameters from the HITRAN database (Rothman et al., 2008), and finding the best fit to the field data using an optimal estimation non-linear least-squares algorithm (Burton et al., 2000). We analyzed the column amounts of SO_2 (2450–2550 cm^{-1}), H_2O (2100–2240 cm^{-1}), CO_2 (2100–2240 cm^{-1}), HF (4050–4200 cm^{-1}), and HCl (2690–2840 cm^{-1}). Analyses of CO (2070–2130 cm^{-1}) were also attempted using the data of the measurement on 12 January 2018.

Multi-GAS

Multi-GAS (Aiuppa et al., 2005; Shinohara, 2005) is a sensor-based instrument allowing us to have *in situ* measurements of gas species such as H_2O, CO_2, SO_2, H_2S, and H_2. We conducted Multi-GAS measurements on the edge of the crater rim on 9, 11, 12, and 13 January 2018. The observation points were windward relative to the FTIR. The gas sensor system consists of a non-dispersive infrared CO_2–H_2O analyzer (LI-840, LI-COR, Inc., Lincoln, United States), SO_2 and H_2S electrochemical sensors (KTS-512 and KHS-5TA, respectively, Komyo Rikagaku K. K., Kawasaki, Japan), and a H_2 semi-conductor sensor (GM12s, Sensor Tech K. K., Rittou, Japan). A SO_2 scrubber was placed in front of the H_2S sensor to reduce cross-sensitivity of the sensor (Shinohara et al., 2011). The results were recorded with a frequency of 1 Hz using a data logger (NR-1000, Keyence Co. Japan). Ambient air was pumped with a flux of 1 L/min from an inlet. The sensors were calibrated before (1 September 2017) and after (30 January 2018) the observations. The calibrations were made using gas canisters of CO_2 (ca. 400 ppm), SO_2 (ca. 50 ppm), H_2S (ca. 10 ppm), and Ar (pure gas for the zero points of the sensors). H_2O calibration was made using a dew point generator (LI610, LI-COR, INC., Lincoln, United States). The H_2 sensor was calibrated for 0.5, 1, 2, 5, 10, and 20 ppm using a gas chamber; H_2 pure gas was injected into the gas chamber using a syringe into a gas chamber to control the H_2 concentration within the gas chamber.

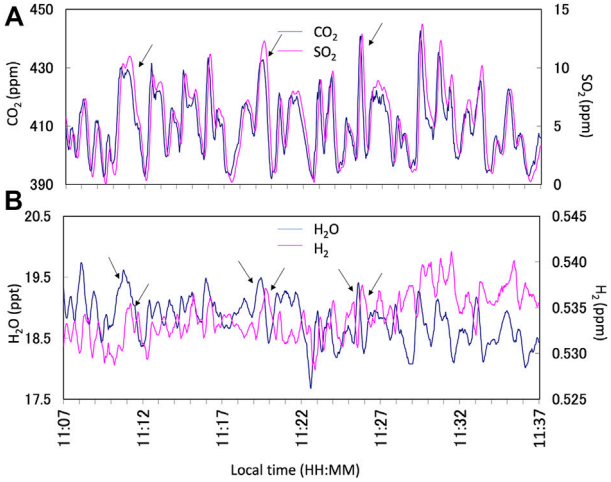

FIGURE 2 | Example of the Multi-GAS observation results on 13 January 2018. **(A)** Time series of CO_2 (blue line) and SO_2 (pink line) concentrations in parts per millions (ppm). **(B)** Time series of H_2O (blue line) and H_2 (pink line) concentrations in parts per thousands (ppt) and ppm, respectively. The arrows indicate the corresponding plume signals for the analyses. Note that the response of the H_2 signal is slow because the sensor is semi-conductor based. All data are filtered by a 15-s running average to reduce the instrumental noises. Notice that the correlation analyses were made using Ratiocalc independently.

Alkali Filter Pack

Alkali filter pack techniques (AF pack) (Shinohara and Witter, 2005; Shinohara et al., 2011) were applied to measure S, Cl, and F in the volcanic plume. The measurements were made on 9, 13, and 15 January 2018 on the edge of the crater rim alongside the Multi-GAS instrument. The filter pack includes a 0.2 μm particle filter followed by two filter holders each with two filters impregnated with 1N NaOH + 20% Glycerol. After field observations, the filters were rinsed with pure water and the solution from the filters was oxidized using hydrogen peroxide solution at GSJ, Japan. The pH was adjusted to near neutral using OnGuard-H (Thermo Fisher Scientific Inc.) before measuring the concentrations of F, Cl, and SO_4^{2-} by ion-chromatography. The first and second holders with the alkaline filters were analyzed separately. Along with the AF pack measurements, the SO_2 exposure level was monitored using a passive dosimeter tube (5D; Gastec Corporation) to ensure that the acid gases are not saturated on the filters.

RESULTS

We made parallel observations using Multi-GAS, FTIR, and AF filter at Masaya Volcano, Nicaragua from 9 to 15 January 2018. Notice that all the gas concentrations and ratios presented here are by mole. Examples of the observation results of the Multi-GAS are shown in **Figure 2**. Detection limits of the measurements depend on the observation conditions. We used signals of SO_2 as a volcanic plume indicator for Multi-GAS because ambient air contains very low concentrations of SO_2, typically 0.1–70 ppb, compared to typical dilute plume concentrations of 1–2 ppm

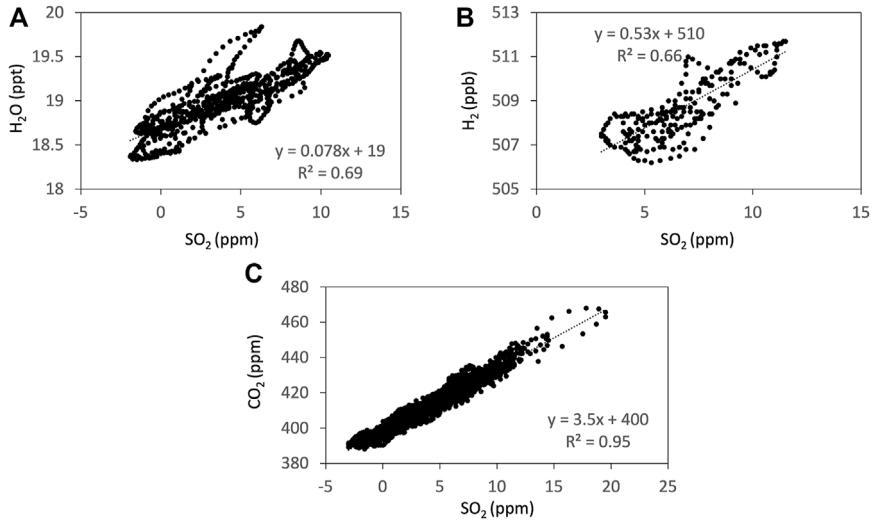

FIGURE 3 | Examples of the correlations from the Ratiocalc analyses (Tamburello, 2015) of SO_2 to H_2O **(A)**, H_2 **(B)**, and CO_2 **(C)** measured using Mutli-GAS on 13 January 2018. The time series are filtered and shifted to take the sensor response into account using Ratiocalc. H_2 concentration is shown in parts per billions (ppb) to avoid rounding errors during the Ratiocalc analyses.

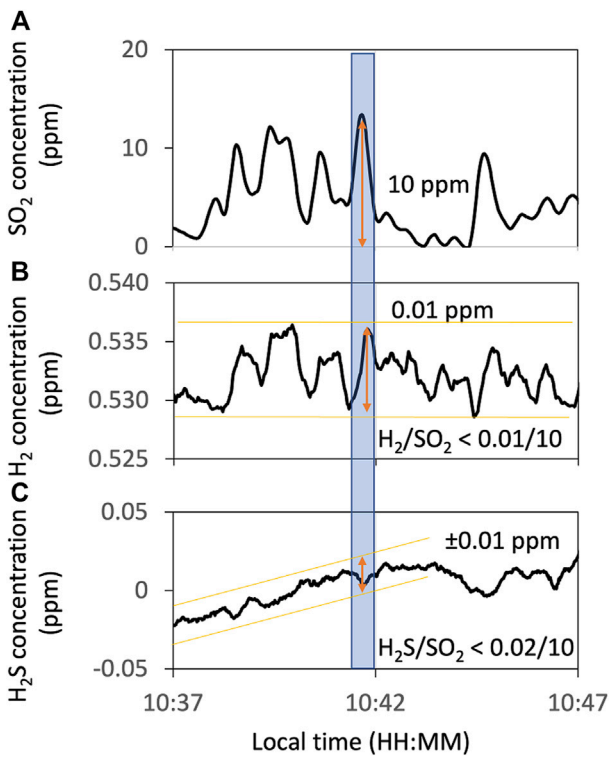

FIGURE 4 | Example of the Multi-GAS observation of H_2S concentration. Concentration timelines of SO_2 **(A)** as an indicator of the volcanic plume and H_2 **(B)** and H_2S **(C)** measured using Multi-GAS on 13 January 2018. Orange lines and arrows show the range of variations of these timelines. The blue-filled area corresponds to the periods used to estimate the maximum H_2/SO_2 and H_2S/SO_2 ratios. All data are filtered by a 15-s running average to reduce instrumental noises.

(Symonds et al., 1994). The gas ratios are derived using Ratiocalc software (Tamburello, 2015). The differences in the response times of IR-based, chemical, and semi-conductor sensors are corrected (Shinohara et al., 2011). For the correlation analysis, only data with the coefficient of determination (R^2 value) of more than 0.6 are accepted. All data analyzed with data processing information including correlation results, determination coefficients, analytical errors, and the parameters of shift and numerical filters, can be found in **Supplementary Material S1**. Examples of the correlation analyses are shown in **Figure 3**.

In Multi-GAS measurements, the concentrations of H_2S recorded are under the detection limit (**Figure 4C**). From the SO_2 signals of ca. 10 ppm and the H_2S signals of less than 0.01 ppm, we concluded that the SO_2/H_2S ratios are more than one thousand.

The H_2 signals are weak and noisy. We tried to extract the H_2 signals based on the objective criteria as follows. Using the SO_2 as an indicator of the plume, only the data where an H_2 peak appears after an SO_2 peak and the R_2 value of more than 0.6 are accepted. The correlation analysis was made using Ratiocalc software (Tamburello, 2015). The H_2/SO_2 ratio was roughly estimated to be less than ca. 10^{-3} (**Table 1**). Because this value could be artifact, we also examined if the H_2 is under the detection limit. From the SO_2 signals of ca. 10 ppm and the H_2 signals of less than 0.1 ppm (**Figure 4B**), the H_2/SO_2 ratio was estimated to be less than ca. 10^{-3}. This estimation is consistent with the H_2/SO_2 ratio derived using Ratiocalc analysis. We concluded that the H_2/SO_2 ratio is less than this value. The H_2/H_2O ratio is estimated to be less than ca. 10^{-6} using the H_2/SO_2 and H_2O/SO_2 ratios (**Table 1**).

To confirm a low H_2 concentration in the plume, Multi-GAS data acquired on 19 January 2009 using the same instruments as this study were also analyzed to estimate the H_2 fraction in the

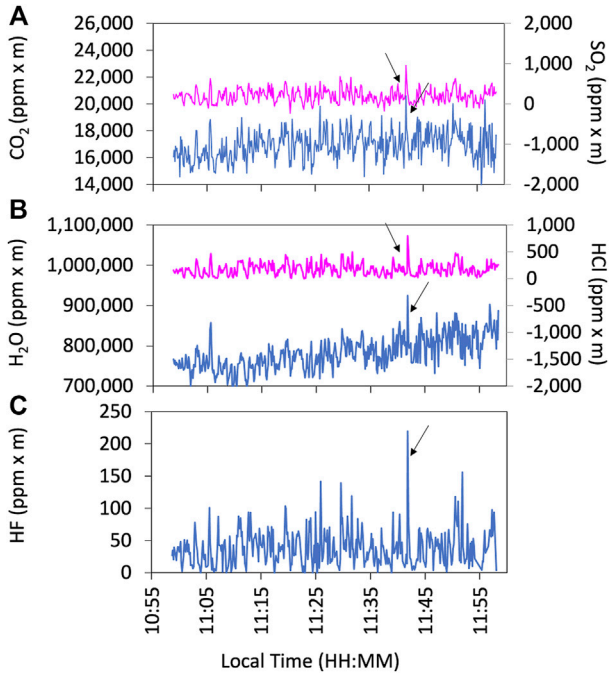

FIGURE 5 | Example of the FTIR observation results on 13 January 2018. Time series of CO_2 (blue line) and SO_2 (pink line) **(A)**, H_2O (blue line) and HCl (pink line) **(B)**, and HF (blue line) **(C)** in column amount (ppm x m). The arrows indicate the corresponding plume signals for the analyses. Because all species are measured based on IR, there are no variations in the response time.

volcanic plume (**Supplementary Figure S1** in **Supplementary Material S2**). In 2009, the magma surface was within ca. 20 m of the crater floor (Martin et al., 2010). During these observations, the SO_2 sensor was broken, so, from the signal peak heights in the time series we estimated the H_2/H_2O ratios directly. Estimated H_2/H_2O ratios of 4.9×10^{-6} were found with errors of ca. 60%, corresponding to the maximum estimation, consistent with our observation results (**Supplementary Material S1**).

Examples of the observation results of the FTIR are shown in **Figure 5**. We used HCl signals as a plume indicator for FTIR as ambient air is mostly HCl-free. The gas ratios are derived using Ratiocalc software and, as with the Multi-GAS analysis, only the data with R^2 values of more than 0.6 are accepted. All data analyzed with errors can be found in the **Supplementary Material S1**. Examples of correlation analyses are shown in **Figure 6**. We attempted to retrieve the column amounts of CO from the FTIR measurements, but the signals were very low as the light path was only 30–40 m. On 12 January, we made the FTIR measurements using the lava lake as the light source with a longer light path of a few hundred meters to detect volcanic CO emission. The column amounts of CO were several thousand ppm × m (**Figure 7**); the CO_2/CO ratio was calculated to be c.a. 1000 using Ratiocalc software. To confirm a low CO concentration, previous FTIR data obtained in 1998 (Burton et al., 2000) were re-analyzed. As shown by comparison to Burton et al. (2000), the composition of the main gas species such as H_2O, CO_2, and SO_2 was stable. During that period, the FTIR measurements were made using incandescence from the magma pond at the crater bottom. The CO signal is very weak, with the CO_2/CO ratio roughly estimated to be 6,000 but with low correlation of the R^2 value of ca. 0.3 (**Supplementary Figure S2** in **Supplementary Material S2**). We concluded that the CO_2/CO ratio is as low as ca. 1,000 and more than several thousands in 2018 and 2009, respectively. This difference could be due to a change in the magmatic activity from 2009 to 2018, as discussed in **Section 4**. The CO_2/CO ratio in Masaya Volcano is significantly larger than that of 13.33 at Erebus volcano in Antarctica (Table 1 in Moussallam et al., 2012) and those of 30–180 at Kīlauea in Hawaii (**Supplementary Figure**

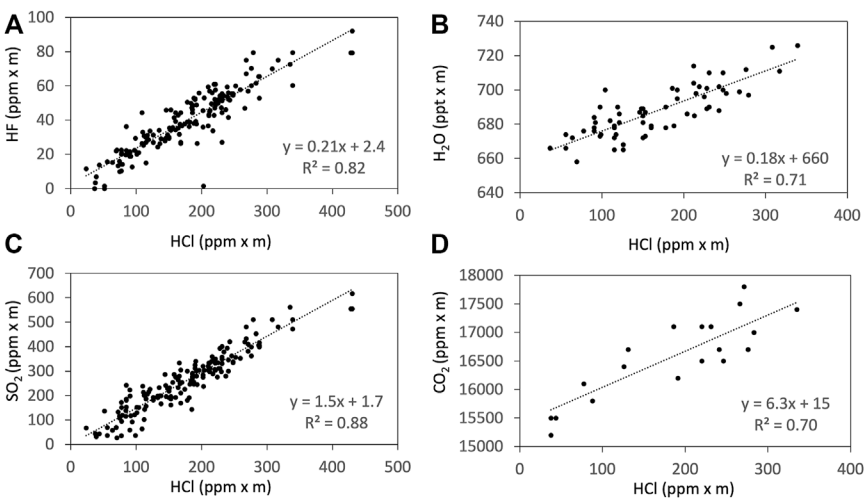

FIGURE 6 | Examples of the correlations from the Ratiocalc analyses (Tamburello, 2015) of HCl to HF **(A)**, H_2O **(B)**, SO_2 **(C)**, and CO_2 **(D)** measured using FTIR on 15 January 2018. The H_2O column amount is shown in ppt x m to avoid rounding errors during the Ratiocalc analyses.

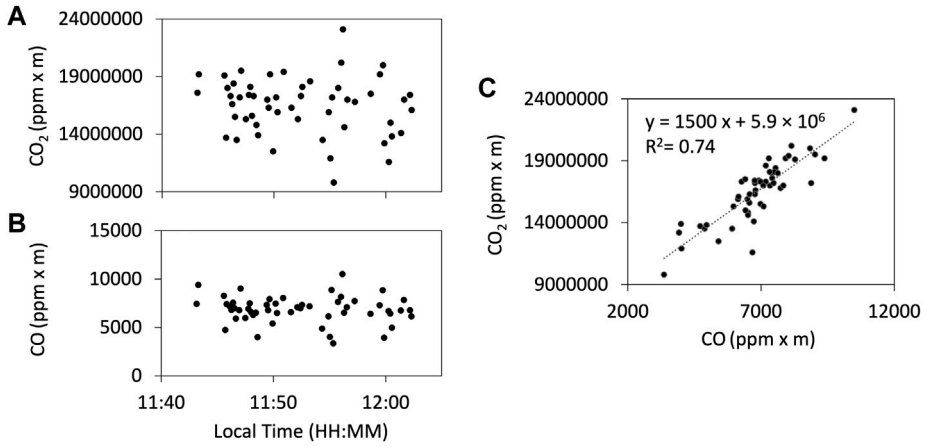

FIGURE 7 | Results of the FTIR observation of CO using the lava lake as the light source on 12 January 2018. Column amount timelines of CO_2 **(A)** and CO **(B)**. **(C)** The correlation plot of the CO_2 and CO column amounts. The CO_2/CO ratio is estimated to be ca. 1,000.

S2 in Oppenheimer et al., 2018), implying the differences in the oxidation state of the parental magmas.

The ratios of CO_2/SO_2 derived by FTIR and Multi-GAS are consistent (**Table 1**). The CO_2/SO_2 and H_2O/SO_2 ratios observed of ca. 4 (3.5–3.9) and ca. 150 (102–206) in this study are within the range of those reported by Aiuppa *et al.* (2018). The ratios of SO_2/HCl and HCl/HF observed are also comparable to those reported by Martin *et al.* (2010). There are disagreements between the FTIR and AF packs, as the SO_2/HCl ratios measured by the FTIR are higher (up to 4.4 times) than those of the AF packs; and the HCl/HF ratios from the FTIR are slightly lower (up to 1.7 times) than those of the AF packs. These trends are similar to the previous studies (Martin et al., 2010; Sawyer et al., 2011). The results imply that the collection of weakly acidic SO_2 may be less efficient than that of strongly acidic HCl; the same argument could be applied for weakly acidic HF and strongly acidic HCl as argued by Sawyer *et al.* (2011).

DISCUSSION

During the observation period at Masaya Volcano, a lava lake could be seen from the crater rim. The temperature of the lava lake is estimated to be 900–1200°C (Pering et al., 2019; INETER, 2021). The volcanic gases emitted are likely to be dominated by those degassed from the lava lake, that is, no secondary interactions with a hydrothermal system after degassing would be expected. Shallow (low-pressure) degassing is presumed (Aiuppa et al., 2018) as the CO_2/SO_2 ratios were as low as ca. 3 (**Table 1**). Before outgassing, the volcanic gases and magma are likely to be in equilibrium at the magmatic temperature of more than 900°C (Pering et al., 2019). After outgassing, the internal redox of the volcanic gases is thought to be quenched close to magmatic temperatures and an atmospheric pressure of 1 bar, as high-temperature volcanic gases (more than 800°C) reach equilibrium rapidly (Martin et al., 2006; Oppenheimer et al., 2018).

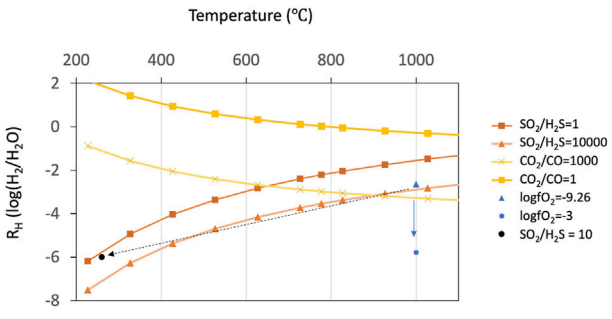

FIGURE 8 | Stability (predominance) diagram in the system C-O-H-S in terms of R_H and equilibrium temperature. Variations of R_H as a function of temperature at a fixed fO_2, SO_2/H_2S ratio, and CO_2/CO ratio are shown. The two orange lines represent Giggenbach's gas buffer lines where SO_2/H_2S ratios are 1 and 10,000 (Giggenbach, 1987). The two yellow lines represent stability lines where CO_2/CO ratios are 1 and 1,000. Two blue dots represent stability points where log fO_2 values are –9.26 and –3 at 1,000°C. The former corresponds to the calculation value from iron speciation (deMoor *et al.* (2013)). The latter corresponds to several percent mixing with the atmospheric air (Martin et al., 2006) that could explain the R_H value of –6 at 1,000°C. Notice that the fO_2 value of parental magma alters with the change in temperature.

High H_2 concentrations are observed in high temperature magmatic gases at other volcanoes (e.g., Giggenbach, 1987; Ohba et al., 1994; Giggenbach, 1996; Henley and Fischer, 2021). The value of $\log(H_2/H_2O)$ (hereafter described as R_H) has been used as an indicator of the redox state in the gas phase (Giggenbach, 1987). The R_H values of high-temperature magmatic gases are typically from –4 to –2 (**Figure 3** in Henley and Fischer, 2021). We estimate a lower R_H value at Masaya Volcano of ca. –6 using the ratios of H_2/SO_2 and H_2O/SO_2 in **Table 1**.

A theoretical R_H value for volcanic gas can be calculated from the oxygen fugacity (fO_2). The fO_2 value of the magma is estimated to be of the order of magnitude of 10^{-9} at ca.

1,000°C (i.e., condition of the lava lake surface from Pering *et al.* (2019)) using the literature iron speciation measurements (Table 1 in deMoor et al., 2013). The R_H value of volcanic gases with magma of this fO_2 value is calculated using the equilibrium constant of the chemical reaction 1) in the gas phase as follows (Table 1 in Ohba et al., 1994):

$$\log K_1(T) = -2.076 + \frac{1576.6}{T^2} - \frac{12448}{T} - 1.6964 \times 10^{-4} T + 0.67067 \ln T \quad (4)$$

$$R_H = \frac{1}{2}\log fO_2 - \log K_1(T). \quad (5)$$

Assuming the magma temperature of 1,000 °C at an atmospheric pressure of 1 bar, the R_H value when volcanic gases and magma are in equilibrium (i.e., log fO_2 of −9) is estimated to be ca. −3 (**Figure 8**). This value should correspond to the original R_H value before outgassing from the lava lake. However, the observed R_H value of ca. −6 is significantly lower.

At the same conditions described previously, the CO_2/CO ratio when the volcanic gases and magma are in equilibrium is estimated using the following reaction (Table 1 in Ohba et al., 1994):

$$CO_2 + H_2 = CO + H_2O, \quad (6)$$

$$\log K_6(T) = 8.6753 + \frac{41163}{T^2} - \frac{2665.2}{T} + 2 \times 10^{-4} \times T - 0.92134 \ln T, \quad (7)$$

$$R_H = -\log K_6(T) - log\frac{X_{CO_2}}{X_{CO}}, \quad (8)$$

where XCO_2 and XCO represent the mole fractions of CO_2 and CO, respectively. When the R_H value is ca. −3 (i.e., fO_2 of 10^{-9}), at 1,000°C, the CO_2/CO ratio is estimated to be ca. 1,000 (**Figure 8**). This value is consistent with the observation in 2018, indicating that the chemical reaction (6) reaches the equilibrium

The observed R_H value of −6 at 1,000°C corresponds to the fO_2 value of more than ca. 10^{-3}, which is higher than the magmatic fO_2 value (**Figure 8**). To explain this discrepancy, we examine three possible processes: 1) additional meteoric or hydrothermal water after outgassing from the lava lake increases the H_2O content, 2) chemical reaction of the volcanic gas within the closed system (i.e., equilibrium) at low temperature, and 3) oxidization of the volcanic gas in the air to lower the H_2 content.

The process of 1) is not plausible. During the observation period a lava lake was present, so the major contribution of volcanic gases is likely to be volatiles degassed directly from the lava without any interactions with geothermal systems. Additional meteoric or non-magmatic H_2O could be emitted by low-temperature hydrothermal fumaroles along the inner crater's wall (Aiuppa et al., 2018). However, the H_2O/SO_2 ratios observed are about 100 and the SO_2 emission rate from this volcano during the observation period is approximately one or two thousand tons per day (*e.g.*, Varnam et al., 2021). To lower the R_H value from -3 to -6 by adding non-magmatic H_2O, the original H_2O/SO_2 ratios equilibrated with the magma would need to be of the order magnitude of 0.1, and non-magmatic H_2O flux of more than several tens of thousands tons/day is required. Because this is not realistic, we reject this possibility.

We examined if cooling with chemical equilibrium in a closed system in the gas phase could explain this discrepancy (i.e., the possibility (b)). Within a closed system in the gas phase, the gas composition (SO_2-H_2-H_2S-H_2O) is thought to be controlled by the chemical reaction 3) (Giggenbach, 1987). The equilibrium constant and its temperature dependence are compiled by Ohba *et al.* (1994) as follows:

$$\log K_3(T) = 8.5667 - \frac{29743}{T^2} + \frac{10449}{T} + 4.7814 \times 10^{-4} \times T - 1.7784 \ln T, \quad (9)$$

$$R_H = -\frac{1}{3}\left(log\frac{X_{SO_2}}{X_{H_2S}} + \log fH_2O + log K_3(T)\right), \quad (10)$$

where XSO_2 and XH_2S represent the mole fraction of SO_2 and H_2S, respectively.

A line on R_H versus temperature plot where SO_2/H_2S ratio is a constant value is called (**Figure 8**) (Giggenbach, 1987). The SO_2/H_2S ratio of volcanic gases in equilibrium with the magma at 1,000 °C and fO_2 of 10^{-9} is estimated to be in the order of magnitude of 10^4 (**Figure 8**). This is consistent with the observation results that H_2S is below the detection limit (i.e., SO_2/H_2S ratio is more than one thousand) (**Figure 4**).

The simple cooling in the gas phase within the closed system (the possibility b) changes the temperature, R_H value, and SO_2/H_2S ratio simultaneously. The reaction 3) consumes 3 H_2 molecules and produces one H_2S molecule with a shift from the left-hand side to the right-hand side by cooling. If the R_H value decreases from −3 to −6 by reaction (3), H_2S is produced by one-third times the H_2 consumption. We examined the amount of H_2S production by reaction (3). Assuming that the initial R_H value is −3 (i.e., $H_2/H_2O = 10^{-3}$) and the SO_2/H_2S ratio is 10^4 at the magmatic temperature, when reaction 3) proceeds to lower the R_H value to −6, the expected SO_2/H_2S ratio is estimated to be ca. 10 at the temperature of ca. 260°C. This value contradicts the observation results as H_2S was under the detection limit (SO_2/H_2S ratio is more than several hundred). Consequently, the simple cooling in the gas phase within the closed system cannot explain the discrepancy.

If chemical reactions occur even after mixing with the air (i.e., not quenched rapidly after outgassing), the R_H value will decrease by oxidation with atmospheric oxygen. The possibility of (c), that is, reaction 1) in the air to increase the fO_2 value to 10^{-3} (**Figure 8**) could oxidize H_2 and reduce the R_H value. Assuming an O_2 volume fraction of the ambient air of 0.21, only ca. 5 percent mixing with ambient air is needed to alter the fO_2 value to 10^{-3}. In this regard, Martin *et al.* (2006) calculated a thermodynamic equilibrium model optimized for volcanic gas chemistry and showed that the fractions of combustible components such as H_2, CO, and H_2S decrease drastically when mixing with the air. Two clear compositional regimes divided by a compositional discontinuity were found (Martin et al., 2006). They concluded that this compositional discontinuity is attributable to the amount of oxygen needed to oxidize the combustible components.

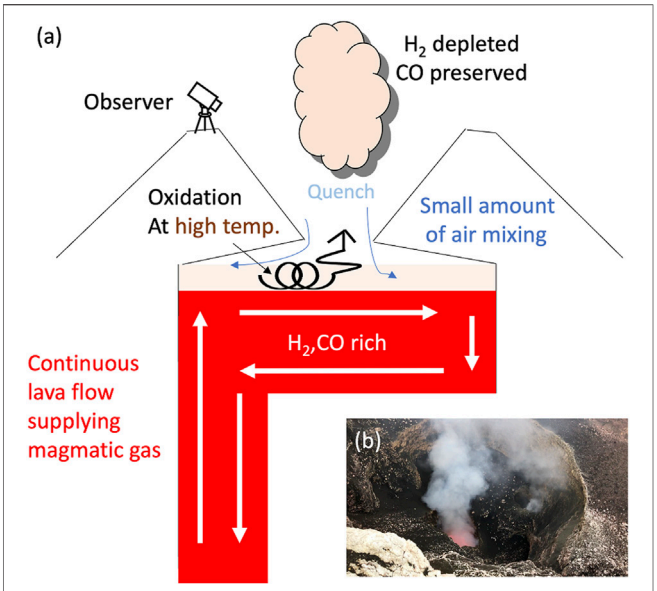

FIGURE 9 | Schematic diagram to show the oxidization of H_2 in the air at Masaya Volcano. **(A)** Cartoon to show the lava lake and the oxidization of the volcanic gases. Initially, when the volcanic gases are in equilibrium with the surrounding magma (red filled area; white arrows show the lava flow direction inferred from Pering *et al.* (2019)), the gases are rich in H_2 and CO. Mixing with the air (blue arrows) at a high temperature oxidizes H_2 (transparent orange area with coil-shaped arrows), then, the volcanic gases are quenched at the outlet of the vent, resulting in a poor H_2 composition as observed. In contrast, CO is preserved because CO is likely to be kinetically inert compared to H_2 (Roberts et al., 2019). **(B)** Photo taken at the rim of the Santiago crater, Masaya Volcano, Nicaragua. Observers could see only a portion of the lava lake through the window (i.e., the outlet of the vent).

The drastic decrease in the fraction of the combustible components (H_2 and CO) occurs within the range of the mixing ratio with the air between 0 and 0.1 and at a temperature of more than 800°C. For instance, at 1,000°C, they exhibited that the R_H value of the "Arc Mean" volcanic gas (Gerlach, 2004) drastically decreases from −2 to −6 with ca. 6 percent mixing with the air (Figure 12 in Martin et al., 2006). This model result is fairly consistent with our findings of an initial magmatic R_H value of −3 but an observed R_H value of −6. However, this thermodynamic model result is inconsistent with the observation of CO not being depleted whilst H_2 is depleted; recent kinetics-based models have shown that H_2 is more readily oxidized than CO (Roberts et al., 2019).

We now propose possible mechanisms that could promote the reaction of volcanic H_2 in air at Masaya Volcano and suggest directions for future research. Hydrogen has been measured using Multi-GAS at the crater rim of Erebus volcano in Antarctica, which also has a lava lake (Moussallam et al., 2012). Measurements suggest that H_2 is preserved in the volcanic plume by quenching in the Antarctic cold air and it is possible that the timescale of cooling is faster than Masaya Volcano. Using this direct comparison, a simple ascent of the plume from the surface of the lava lake to the crater rim alone is not sufficient to cause oxidization attributed to mixing with the air resulting in the huge loss in H_2. To explain the H_2-depleted volcanic plume observed at Masaya Volcano, an additional condition is necessary to oxidize the H_2 after mixing with the air.

At Masaya Volcano, the flow speed of the lava lake was estimated to be as high as 13.7–16.4 m/s (Pering et al., 2019). This speed is significantly higher than other lava lake systems such as Erebus volcano (0.1 m/s) in Antarctica (Peters et al., 2014). Pering *et al.* (2019) concluded that they observed only a window into lava motion processes such as the deflection of ascending magma into a surface chamber. One possible factor to cause efficient oxidization is stagnated volcanic gases at the space above the lava lake that mixes with the air driven by rapid lava flow at high temperature without quenching. A kettle-like shape of the lava lake and the upper space (i.e., the window we observe corresponds to a spout) is presumed to keep volcanic gases at a high temperature (**Figure 9**). Residence time of volcanic gases at the high temperature space above the lava flow for oxidation is difficult to estimate. Roberts *et al.* (2019) argued that the oxidization of volcanic gases could proceed within a time scale of seconds, but this work was for dynamics in much larger plumes. It is not clear if this time scale is applicable for the plume that we observed at Masaya Volcano. However, qualitatively, if the reaction 1) is equilibrated at a high temperature inside of the kettle-like-shaped space above the lava lake, the low observed R_H value of −6 might be explained.

If this speculation is correct, the periodicity of observed signals such as SO_2 flux could not preserve information such as bubble-burst dynamics, which would be masked by the atmospheric transportation in the kettle-shaped space above the lava lake (**Figure 9**). In this regard, Pering *et al.* (2019) reported periodicity of 200–300 s oscillations in SO_2 flux which could also not be seen in the volume of the gas in bubble bursts. They similarly concluded that the periodicity may not be attributed to the volcanic/magmatic process, but to atmospheric mechanisms such as atmospheric transport and turbulence.

These observations imply that volcanic gases are oxidized in the kettle-shaped space above the lava lake, depleting them in H_2 by mixing with the air at a high temperature (**Figure 9**). The observed gas composition is likely to be superimposed by oxidation in air and would not preserve the magmatic information. On the other hand, the high H_2 concentration at Erebus volcano in Antarctica (Moussallam et al., 2012) might be attributable to the quenching of the volcanic gas immediately after outgassing as there are no spaces above the lava lake to keep the volcanic gas at a high temperature and/or due to rapid cooling in the cold Antarctic atmosphere.

In contrast, the CO_2/CO ratio of ca. 1,000 in 2018 corresponds to the equilibrium temperature of 1,000°C and magmatic fO_2 of 10^{-9} (Oppenheimer et al., 2019), indicating that CO is not lost by the oxidization in the air. This result is consistent with the simulation results from Roberts *et al.* (2019), showing a relatively inert characteristic of CO comparing to H_2. The difference in the CO_2/CO ratio between 1998 and 2018 could simply be explained by a cooler, less active surface lava lake in 1998, causing equilibrium at a slightly lower temperature (900°C corresponding to the CO_2/CO ratio of 6,000 rather than 1,000°C). Considering the more active degassing in 2018 (Aiuppa et al., 2018) compared to 1998, we consider this a likely explanation of the difference.

At volcanoes without lava lakes (e.g., Giggenbach, 1987; Aiuppa et al., 2011; Shinohara et al., 2018; Kazahaya et al., 2019; Ohba et al., 1994; Henley and Fischer, 2021) H_2 and CO are detected, and the chemical equilibrium has been discussed to get insights into undermined magmatic/hydrothermal processes. It is also important to elucidate if the heat supply from the lava lake to volcanic gases is required for the oxidization after outgassing.

The high-speed lava flow (13.7–16.4 m/s at Masaya Volcano; Pering *et al.* (2019)) may be the key for the effective oxidization of the volcanic gas in the air. Similar atmospheric oxidations could take place at other volcanoes such as Ambrym, Vanuatu, which have a lava lake with a lava flow speed of 5 m/s (Radebaugh et al., 2016) or volcanoes where the H_2 of the volcanic plume is under the detection limit such as Villarica, Chile (Sawyer et al., 2011; Moussallam et al., 2016).

In this study, we argue that the possibility of the oxidization of the volcanic gases attributed to mixing with the air at a high temperature by a simple predominance examination in the system C-O-H-S (**Figure 8**). However, detailed conditions such as the temperature, mixing ratio of the air, and residence time required to oxidize the volcanic gases are difficult to quantify. One future direction could be given by a plume chemistry model to handle the reaction rates controlling the composition of the volcanic gases in the air (Roberts et al., 2019) combined with a physical model of atmospheric turbulence and heat supply for ash-free plumes. The details of the oxidization processes may need to be examined extensively, not only using volcanic plumes with detectable H_2, but also those depleted in H_2 such as our study site, Masaya Volcano.

CONCLUDING REMARKS

We conducted volcanic gas observations at Masaya Volcano, Nicaragua, in January 2018 with a lava lake present. H_2S was under the detection limit and the observed H_2/H_2O was surprisingly low, with an R_H value of less than −6. This low R_H value is significantly lower than the expected R_H value of −3 calculated from petrological insights (temperature and fO_2). To explain this discrepancy, we proposed that the oxidization in air at a high temperature would play a role controlling the H_2 fraction. These results suggest that H_2 is oxidized by several percent mixing with the air to increase the fO_2 value from the magmatic value (10^{-9}) to the order of magnitude of 10^{-3}.

One key feature of the lava lake in Masaya Volcano is a very rapid lava flow with speeds of 13.7–16.4 m/s (Pering et al., 2019). It is possible that this rapid lava flow encourages effective mixing with the air, oxidizing the volcanic gas. A kettle-like shape around the vent is considered so that the volcanic gases can be stagnated above the lava lake with the air and oxidize at a high temperature.

Martin *et al.* (2006) and Roberts *et al.* (2019) proposed the plume chemistry model to discuss the oxidization of volcanic components such as H_2, CO, and H_2S. At Masaya Volcano, the possibility of combustion of H_2 has been argued by deMoor *et al.* (2013). Our results support their ideas. The observed volcanic gas composition, depleted in H_2, is likely the result of masking by atmospheric oxidization processes, so the gas composition observed does not reflect the original magmatic H_2.

On the other hand, the CO_2/CO ratio of ca. 1,000 observed in 2018 is consistent with the magmatic value with an equilibrium temperature of 1000°C. This implies that CO is not likely to be lost by the oxidization in the air. This hypothesis is consistent with the insight from the simulation results of Roberts et al. (2019) that pointed out that CO is kinetically less reactive comparing to H_2.

Our results show that care must be taken to consider the effect of oxidization in the air, especially when quantifying the composition of high-temperature volcanic gases, when measuring the resulting mixture of volcanic gases and ambient air (e.g., Multi-GAS and FTIR). Lava lakes might traditionally be thought of as unlikely to be affected by secondary alterations such as hydrothermal processes. However, we show that even gas compositions emitted from lava lakes could be superimposed by atmospheric oxidation. Such gases therefore do not necessarily preserve magmatic information. At Masaya Volcano, the results from physical observations (i.e., the speed of lava flow and structure of the upper space above the lava lake) complement the puzzling volcanic gas composition observed to elucidate the processes of oxidization. Multi-disciplinary assessments and model calculations are crucial in solving these puzzles, especially in the interpretation of the complex datasets.

DATA AVAILABILITY STATEMENT

The original contributions presented in the study are included in the article/**Supplementary Material**; further inquiries can be directed to the corresponding author.

AUTHOR CONTRIBUTIONS

RK drafted the manuscript. RK, MV, BE, and MI collected the data in the field and analyzed them. MB and HS analyzed the volcanic gas data. All authors read and approved the final manuscript.

ACKNOWLEDGMENTS

The authors would like to thank the staff of INETER, whose invaluable help and expertise made our fieldwork possible. RK thanks Marco Liuzzo and other INGV staff for their help in calibrating the Multi-GAS instrument. MV and BE acknowledge the support of the Natural Environment Research Council (NERC) EAO Doctoral Training Partnership (grant number NE/L002469/1). RK acknowledges Tjarda Roberts, Peter Kelly, and Valerio Acocella for their thoughtful reviews and comments, improving the manuscript.

SUPPLEMENTARY MATERIAL

The Supplementary Material for this article can be found online at: https://www.frontiersin.org/articles/10.3389/feart.2022.867562/full#supplementary-material

REFERENCES

Aiuppa, A., de Moor, J. M., Arellano, S., Coppola, D., Francofonte, V., Galle, B., et al. (2018). Tracking Formation of a Lava Lake from Ground and Space: Masaya Volcano (Nicaragua), 2014-2017. *Geochem. Geophys. Geosyst.* 19, 496–515. doi:10.1002/2017gc007227

Aiuppa, A., Federico, C., Giudice, G., and Gurrieri, S. (2005). Chemical mapping of a fumarolic field: la Fossa Crater, Vulcano Island (Aeolian Islands, Italy). *Geophys. Res. Lett.* 32, L13309. doi:10.1029/2005gl023207

Aiuppa, A., Shinohara, H., Tamburello, G., Giudice, G., Liuzzo, M., and Moretti, R. (2011). Hydrogen in the Gas Plume of an Open-Vent Volcano, Mount Etna, Italy. *J. Geophys. Res.* 116, B10204. doi:10.1029/2011JB008461

Burton, M. R., Oppenheimer, C., Horrocks, L. A., and Francis, P. W. (2000). Remote Sensing of CO_2 and H_2O Emission Rates from Masaya Volcano, Nicaragua. *Nicar. Geol.* 28 (10), 915–918. doi:10.1130/0091-7613(2000)028<0915:rsocah>2.3.co;2

Cruikshank, D. P., Morrison, D., and Lennon, K. (1973). Volcanic Gases: Hydrogen Burning at Kilauea Volcano, Hawaii. *Science* 1824109, 277–279. doi:10.1126/science.182.4109.277

de Moor, J. M., Fischer, T. P., Sharp, Z. D., King, P. L., Wilke, M., Botcharnikov, R. E., et al. (2013). Sulfur Degassing at Erta Ale (Ethiopia) and Masaya (Nicaragua) Volcanoes: Implications for Degassing Processes and Oxygen Fugacities of Basaltic Systems. *Geochem. Geophys. Geosyst.* 14, 4076–4108. doi:10.1002/ggge.20255

Gerlach, T. M. (2004). Volcanic Sources of Tropospheric Ozone Depleting Trace Gases. *Geochem. Geophys. Geosyst.* 5, Q09007. doi:10.1029/2004gc000747

Giggenbach, W. F. (1996). "Chemical Composition of Volcanic Gases," in *Monitoring and Mitigation of Volcanic Hazards*. Editors R. Scarpa and R. I. Tilling (Berlin: Springer), 221–256. doi:10.1007/978-3-642-80087-0_7

Giggenbach, W. F. (1987). Redox Processes Governing the Chemistry of Fumarolic Gas Discharges from White Island, New Zealand. *Appl. Geochem.* 2, 143–161. doi:10.1016/0883-2927(87)90030-8

Henley, R. W., and Fischer, T. P. (2021). Sulfur Sequestration and Redox Equilibria in Volcanic Gases. *J. Volcanol. Geotherm. Res.* 414, 107181. doi:10.1016/j.jvolgeores.2021.107181

INETER (2021). Boletín mensual Sismos y Volcanes de Nicaragua Mayo, 2021, Dirección General de Geología y Geofísica. Available at: https://webserver2.ineter.gob.ni/boletin/2021/05/boletin-0521.pdf.

Kazahaya, R., Shinohara, H., Ohminato, T., and Kaneko, T. (2019). Airborne Measurements of Volcanic Gas Composition during Unrest at Kuchinoerabujima Volcano, Japan. *Bull. Volcanol.* 81, 7. doi:10.1007/s00445-018-1262-9

Martin, R. S., Mather, T. A., and Pyle, D. M. (2006). High-temperature Mixtures of Magmatic and Atmospheric Gases. *Geochem. Geophys. Geosyst.* 7, 4. doi:10.1029/2005GC001186

Martin, R. S., Sawyer, G. M., Spampinato, L., Salerno, G. G., Ramirez, C., Ilyinskaya, E., et al. (2010). A Total Volatile Inventory for Masaya Volcano, Nicaragua. *J. Geophys. Res.* 115, B09215. doi:10.1029/2010jb007480

Moussallam, Y., Bani, P., Curtis, A., Barnie, T., Moussallam, M., Peters, N., et al. (2016). Sustaining Persistent Lava Lakes: Observations from High-Resolution Gas Measurements at Villarrica Volcano, Chile. *Earth Planet. Sci. Lett.* 454, 237–247. doi:10.1016/j.epsl.2016.09.012

Moussallam, Y., Oppenheimer, C., Aiuppa, A., Giudice, G., Moussallam, M., and Kyle, P. (2012). Hydrogen Emissions from Erebus Volcano, Antarctica. *Bull. Volcanol.* 74, 2109–2120. doi:10.1007/s00445-012-0649-2

Ohba, T., Hirabayashi, J.-i., and Yoshida, M. (1994). Equilibrium Temperature and Redox State of Volcanic Gas at Unzen Volcano, Japan. *J. Volcanol. Geotherm. Res.* 60, 263–272. doi:10.1016/0377-0273(94)90055-8

Oppenheimer, C., Francis, P., Burton, M., Maciejewski, A. J. H., and Boardman, L. (1998). Remote Measurement of Volcanic Gases by Fourier Transform Infrared Spectroscopy. *Appl. Phys. B Lasers Opt.* 67, 505–515. doi:10.1007/s003400050536

Oppenheimer, C., Scaillet, B., Woods, A., Sutton, A. J., Elias, T., and Moussallam, Y. (2018). Influence of Eruptive Style on Volcanic Gas Emission Chemistry and Temperature. *Nat. Geosci.* 11, 678–681. doi:10.1038/s41561-018-0194-5

Pering, T. D., Wilkes, T. C., England, R. A., Silcock, S. R., Stanger, L. R., Willmott, J. R., et al. (2019). A Rapidly Convecting Lava Lake at Masaya Volcano, Nicaragua. *Front. Earth Sci.* 6, 241. doi:10.3389/feart.2018.00241

Peters, N., Oppenheimer, C., Kyle, P., and Kingsbury, N. 2014 Decadal Persistence of Cycles in Lava Lake Motion at Erebus Volcano, Antarctica. *Earth Planet. Sci. Lett.* 395, 1. doi:10.1016/j.epsl.2014.03.032

Radebaugh, J., Lopes, R. M., Howell, R. R., Lorenz, R. D., and Turtle, E. P. (2016). Eruptive Behavior of the Marum/Mbwelesu Lava Lake, Vanuatu and Comparisons with Lava Lakes on Earth and Io. *J. Volcanol. Geotherm. Res.* 322, 105–118. doi:10.1016/j.jvolgeores.2016.03.019

Roberts, T., Dayma, G., and Oppenheimer, C. (2019). Reaction Rates Control High-Temperature Chemistry of Volcanic Gases in Air. *Front. Earth Sci.* 7, 154. doi:10.3389/feart.2019.00154

Rothman, L. S., et al. (2008). The HITRAN 2008 Molecular Spectroscopic Database. *J. Quint. Spectrosc. Ra.* 110, 533. doi:10.1016/j.jqsrt.2009.02.013

Sawyer, G. M., Salerno, G. G., Le Blond, J. S., Martin, R. S., Spampinato, L., Roberts, T. J., et al. (2011). Gas and Aerosol Emissions from Villarrica Volcano, Chile. *J. Volcanol. Geotherm. Res.* 203, 62–75. doi:10.1016/j.jvolgeores.2011.04.003

Shinohara, H. (2005). A New Technique to Estimate Volcanic Gas Composition: Plume Measurements with a Portable Multi-Sensor System. *J. Volcanol. Geotherm. Res.* 143, 319–333. doi:10.1016/j.jvolgeores.2004.12.004

Shinohara, H., and Witter, J. B. (2005). Volcanic Gases Emitted during Mild Strombolian Activity of Villarrica Volcano, Chile. *Geophys. Res. Lett.* 32, L20308. doi:10.1029/2005gl024131

Shinohara, H., Yokoo, A., and Kazahaya, R. (2018). Variation of Volcanic Gas Composition during the Eruptive Period in 2014-2015 at Nakadake Crater, Aso Volcano, Japan. *Earth Planets Space* 70, 151. doi:10.1186/s40623-018-0919-0

Shinohara, H., Matsushima, N., Kazahaya, K., and Ohwada, M. (2011). Magma-hydrothermal System Interaction Inferred from Volcanic Gas Measurements Obtained during 2003-2008 at Meakandake Volcano, Hokkaido, Japan. *Bull. Volcanol.* 73, 409–421. doi:10.1007/s00445-011-0463-2

Symonds, B. R., Rose, W. I., Bluth, G. J. S., and Gerlach, T. M. (1994). "Volatiles in Magmas," in. *Volatiles in Magmas*. Editors M. R. Carroll, Mineralogical Society of America, 30. 1–66. doi:10.1515/9781501509674

Tamburello, G. (2015). Ratiocalc: Software for Processing Data from Multicomponent Volcanic Gas Analyzers. *Comput. Geosciences* 82, 63–67. doi:10.1016/j.cageo.2015.05.004

Varnam, M., Burton, M., Esse, B., Salerno, G., Kazahaya, R., and Ibarra, M. (2021). Two Independent Light Dilution Corrections for the SO_2 Camera Retrieve Comparable Emission Rates at Masaya Volcano, Nicaragua. *Remote Sens.* 13 (5), 935. doi:10.3390/rs13050935

Conflict of Interest: The authors declare that the research was conducted in the absence of any commercial or financial relationships that could be construed as a potential conflict of interest.

frontiers | Frontiers in Earth Science

TYPE Original Research
PUBLISHED 12 September 2022
DOI 10.3389/feart.2022.976928

OPEN ACCESS

EDITED BY
Yosuke Aoki,
The University of Tokyo, Japan

REVIEWED BY
Karoly Nemeth,
Massey University, New Zealand
Dmitri Rouwet,
Istituto Nazionale di Geofisica e Vulcanologia, Italy

*CORRESPONDENCE
Syegi Kunrat,
syegikunrat@gmail.com

SPECIALTY SECTION
This article was submitted to Volcanology, a section of the journal Frontiers in Earth Science

RECEIVED 23 June 2022
ACCEPTED 05 August 2022
PUBLISHED 12 September 2022

CITATION
Kunrat S, Kern C, Alfianti H and Lerner AH (2022), Forecasting explosions at Sinabung Volcano, Indonesia, based on SO_2 emission rates. *Front. Earth Sci.* 10:976928. doi: 10.3389/feart.2022.976928

Forecasting explosions at Sinabung Volcano, Indonesia, based on SO_2 emission rates

Syegi Kunrat[1]*, Christoph Kern[2], Hilma Alfianti[1] and Allan H. Lerner[2]

[1]Center for Volcanology and Geological Hazard Mitigation, Geological Agency of the Ministry of Energy and Mineral Resources, Bandung, Indonesia, [2]U.S. Geological Survey, Volcano Disaster Assistance Program, Vancouver, WA, United States

Dome-building volcanic eruptions are often associated with frequent Vulcanian explosions, which constitute a substantial threat to proximal communities. One proposed mechanism driving such explosions is the sealing of the shallow volcanic system followed by pressurization due to gas accumulation beneath the seal. We investigate this hypothesis at Sinabung Volcano (Sumatra, Indonesia), which has been in a state of eruption since August 2010. In 2013, the volcano began erupting a lava dome and lava flow, and frequent explosions produced eruptive columns that rose many kilometers into the atmosphere and at times sent pyroclastic density currents down the southeast flanks. A network of scanning Differential Optical Absorption Spectrometers (DOAS) was installed on the volcano's eastern flank in 2016 to continuously monitor SO_2 emission rates during daytime hours. Analysis of the DOAS data from October 2016 to September 2017 revealed that passive SO_2 emissions were generally lower in the 5 days leading up to explosive events (~100 t/d) than was common in 5-day periods leading up to days on which no explosions occurred (~200 t/d). The variability of passive SO_2 emissions, expressed as the standard deviation, also took on a slightly wider range of values before days with explosions (0–103 t/d at 1-sigma) than before days without explosions (43–117 t/d). These observations are consistent with the aforementioned seal-failure model, where the sealing of the volcanic conduit blocks gas emissions and leads to pressurization and potential Vulcanian explosions. We develop a forecasting methodology that allows calculation of a relative daily explosion probability based solely on measurements of the SO_2 emission rate in the preceding days. We then calculate forecast explosion probabilities for the remaining SO_2 emissions dataset (October 2017—September 2021). While the absolute accuracy of forecast explosion probabilities is variable, the method can inform the probability of an explosion occurring relative to that on other days in each test period. This information can be used operationally by volcano observatories to assess relative risk. The SO_2 emissions-based forecasting method is likely applicable to other open vent volcanoes experiencing dome-forming eruptions.

KEYWORDS

Sinabung Volcano, Vulcanian explosions, volcanic gases, DOAS, eruption forecasting, sulfur dioxide, volcanic eruptions, remote sensing

1 Introduction

1.1 Forecasting volcanic events

Providing accurate forecasts of volcanic events is at the very core of operational volcanology (Sparks, 2003). Pallister et al., 2019a define a forecast as "the communication passed from an observatory to governmental authorities and the public regarding the probability of future volcanic events" and further state that "a principal goal for a volcano observatory is to accurately communicate results of scientific evaluations and forecasts together with the associated uncertainties". Agencies around the world tasked with volcano monitoring strive to develop forecasting capabilities that allow them to warn at-risk populations of potentially dangerous volcanic phenomena with the goal of protecting lives and property.

When producing forecasts, one key consideration is the time scale for which the forecast is intended (Marzocchi and Bebbington, 2012). Long-term forecasts address relevant hazards over time frames of years or decades and provide a basis for land use and emergency planning. Short-term forecasts address possible events in the coming hours to weeks or months. Short-term forecasts are perhaps the most critical type of forecasts, as their outcome may require immediate action by emergency managers and civil defense (Pallister et al., 2019b). However, even at short time scales, volcanic activity forecasts are generally not certain. Intrinsic uncertainties in model input parameters and the non-linearity of complex volcanic processes lead to uncertain outcomes (Sparks, 2003). Volcanologists therefore increasingly rely on probabilistic rather than deterministic forecasting methods, as these provide not only a range of possible outcomes but also an estimated probability for each (Marzocchi and Bebbington, 2012).

Probabilistic methods to forecast volcanic events largely fall into two categories. One class of techniques relies solely on stochastic analysis of the volcanic event time series itself (i.e., explosions, collapses). For example, Sandri et al. (2021) apply stochastic modelling of explosions at Galeras Volcano (Colombia) to analyze parameters such as the typical inter-event time and the tendency for events to temporally cluster into "eruptive cycles". Derived from the past observational record, the statistical properties of the time series of explosive events can then be used to assign probabilities for future events (see Wickman (1976) for a general overview).

Another class of forecasting methods goes one step further and attempts to identify patterns in volcano monitoring parameters indicative of future behavior. In some cases, the input monitoring data can be relatively general. For example, a progression of seismic activity (event locations, changes in earthquake types and magnitudes) consistent with a conceptual model of magma ascending in a volcanic conduit was used to forecast increased risk of eruption at Sinabung Volcano in 2010 and 2013–2014 (McCausland et al., 2019). Alternatively, forecasts can be based on very specific patterns in monitoring parameters, with these patterns being identified (manually or automatically) in past datasets leading up to volcanic events (e.g., de Moor et al., 2016; Rouwet et al., 2019; Dempsey et al., 2020). This method is most applicable when the volcanic events in question occur frequently at a given volcano, as past time series of monitoring data then provide sufficient test data to allow identification of patterns indicative of a certain behavior.

In this study, we follow this second, monitoring-based approach to develop short-term forecasts of explosions at Sinabung Volcano, Indonesia. Specifically, we examine the volcano's SO_2 degassing behavior in days leading up to explosions and periods of explosive quiescence (i.e., when no explosions occurred but lava effusion may have continued). We develop a simple conceptual model for the relation between degassing and Vulcanian explosions and investigate the ability to derive explosion probabilities based on the volcano's past SO_2 emission rates. Relying exclusively on the magnitude and variability of SO_2 emission rates, we aim to demonstrate the diagnostic power of these monitoring parameters but note that continuous geochemical monitoring can also be used as input data to more comprehensive forecasting tools (e.g., Marzocchi et al., 2008, and references therein).

1.2 Sinabung Volcano, Indonesia

Sinabung Volcano is a stratovolcano located in North Sumatra, Indonesia (Figure 1). Rising to approximately 2,460 m above sea level (ASL) and composed of lava flows and pyroclastic density-current deposits, Sinabung's edifice is perched upon ignimbrite deposits from the Toba caldera and Permian basement rocks (Indrastuti et al., 2019). Prior to 2010, the last dated eruption at Sinabung was ~1,100 years ago (Iguchi et al., 2012), and subsequent activity was limited to minor fumarolic activity near the summit for at least the last 400 years (Iguchi et al., 2011). In August 2010, however, Sinabung experienced a series of phreatic explosions. In 2013, these were followed by additional explosions, with activity quickly transitioning from phreatic to magmatic. In September of that year, pyroclastic density currents reached up to 5 km from the vent and entire villages had to be evacuated, then permanently relocated, affecting over 30,000 citizens (Otneil Ketaren et al., 2016). Formation of a

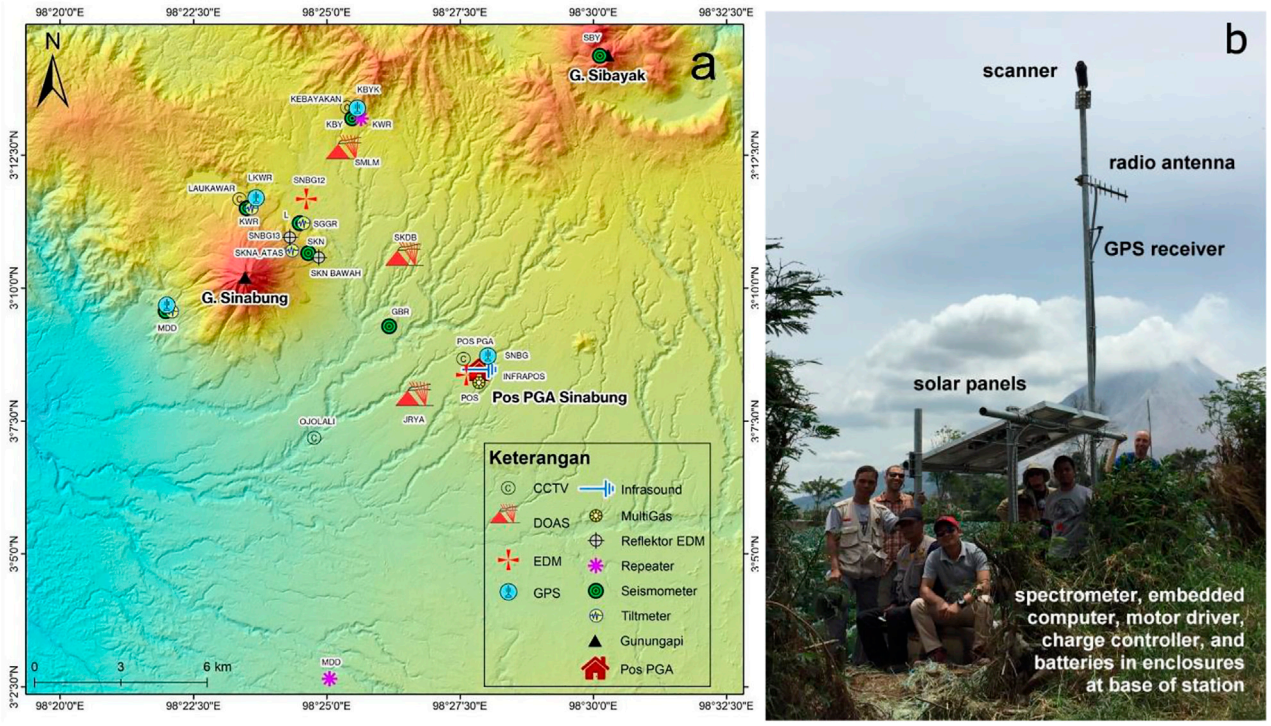

FIGURE 1
(A) Volcano monitoring network maintained by CVGHM at Sinabung. The red symbols labeled SMLM (site 'Simalem'), SKDB (site 'Sukandebi'), and JRYA (site 'Jeraya') indicate the locations of the NOVAC scanning DOAS instruments installed in 2016. Data from these instruments are telemetered to the radio repeater KWR and then on to the pos (observatory; house symbol) in real time. Explosion column height observations are also made from the pos. **(B)** Photograph of the DOAS station installed at JRYA in 2016. Photo by Syegi Kunrat, CVGHM.

lava dome at the summit of the volcano began in December 2013. Subsequent collapses of this dome and of the flow front of a connected lava flow on the southeast portion of the edifice led to pyroclastic density currents that have repeatedly reached up to 5 km from the summit (Pallister et al., 2019a). The eruption is classified by the Global Volcanism Program as having a maximum Volcanic Explosivity Index (VEI) of 4. (Global Volcanism Program, 2013). The eruption at Sinabung continues at the time of writing (June 2022) despite a deflationary trend identified in 2014 that has continued through at least 2016 (Hotta et al., 2019), though the eruption has recently transitioned to predominantly effusive in nature. Based on sulfur dioxide (SO_2) emissions, Sinabung ranked among the three most active degassing volcanoes in Indonesia in the 2010–2019 period (Bani et al., 2022).

With the onset of phreatic eruptions in 2010, the Indonesian Center for Volcanology and Geological Hazard Mitigation (CVGHM) moved quickly to facilitate monitoring. A network of seismometers, tiltmeters, Global Positioning System (GPS) receivers and Electronic Distance Measurement (EDM) lines was installed, with all data sent back to a newly established observatory approximately 8 km southeast of the volcano (Gunawan et al., 2019). At the local observatory (referred to as "pos" in Bahasa Indonesia), CVGHM observers carefully documented activity, both by visual observation and from the incoming geophysical data streams. Together with international partners, the recorded data were used to investigate the geology and eruptive processes occurring at Sinabung, and at times provide forecasts of evolving eruptive styles (Hotta et al., 2019; Indrastuti et al., 2019; McCausland et al., 2019; Wright et al., 2019). One particularly important dataset recorded by observers at the observatory was a time series of explosive events occurring at the volcano's summit. Explosions occurred frequently, particularly after the volcano entered a phase of cyclic Vulcanian events in August 2015 (Gunawan et al., 2019; Nakada et al., 2019). In 2016, the Sinabung monitoring network was expanded to include three scanning Differential Optical Absorption Spectrometers (DOAS) (Primulyana et al., 2019). As described in more detail in the Methods section, these instruments measure the volcanic SO_2 emission rate and were telemetered to the local observatory to provide data in near-real time. This, for the first time, provided the Sinabung observers and research volcanologists with continuous information on volcanic gas emissions at high temporal resolution (5–20 min during the day).

With these detailed time series of explosion occurrences and SO_2 emission rates at Sinabung, we sought to determine whether

the SO_2 emission record could be used to gain insights into the processes leading to the explosive events at the volcano's summit. And if so, might explosive events be probabilistically forecast based on the volcano's SO_2 emission rates?

2 Methods

2.1 Scanning Differential Optical Absorption Spectroscopy

The CVGHM installed a network of three scanning DOAS instruments at Sinabung in August 2016 (Primulyana et al., 2019). The instruments were positioned east of the volcano's edifice (Figure 1) to best detect gas plumes that are transported towards the scanners during the prevailing westerly wind conditions. During daytime hours, each instrument scans the sky from horizon to horizon along a conical geometry surrounding the volcano, recording ultraviolet light scattered in the atmosphere (Galle et al., 2010). Each scan takes ~5–20 min to complete, depending on lighting conditions, so approximately 70 scans per day are obtained from each of the three scanners. When SO_2 gas is present in overhead volcanic plumes, the characteristic absorption of SO_2 is quantified in the recorded spectra. The abundance of SO_2 in the plume can be retrieved from the depth of absorption features using standard DOAS techniques (Galle et al., 2002; Platt and Stutz, 2008).

The DOAS instruments are part of the global Network for Observation of Volcanic and Atmospheric Change (NOVAC), and the data analysis is performed using the NOVAC community's software and general methodology (Arellano et al., 2021; Galle et al., 2010, www.novac-community.org): First, a standard DOAS analysis determines whether any SO_2 absorption is present in the scan. In this step, spectra recorded along all viewing directions within the scan are evaluated relative to the spectrum recorded closest to the zenith. In the next step, the average of the lowest 20% SO_2 column densities retrieved within the scan is subtracted from all columns retrieved within the scan. This so-called 'baseline correction' assumes that plume-free sky is visible somewhere within the scan. In situations where the plume is located overhead, this correction converts relative column densities to absolute column densities and ensures that the lowest columns within the scan are approximately equal to 0 (Galle et al., 2010).

Scans without SO_2 are excluded from further consideration, as the plume is assumed to have traveled away from the scanner at the time of measurement. The software determines whether a scan captured a full or partial SO_2 plume by calculating a "plume completeness" parameter C (Johansson, 2009)

$$C = 1 - \frac{\max\left(\overline{S_L}, \overline{S_R}\right)}{\max\left(S_i\right)} \quad (1)$$

where S_i is the SO_2 slant column density measured along an individual direction within the scan. $\overline{S_L}$ and $\overline{S_R}$ represent the average of the five column densities measured closest to the left and right edges of the scan, respectively. Only scans with $C \geq 0.8$ were included for further analysis.

Whenever multiple scanners detected the gas plume, the plume height was triangulated, thus allowing calculation of the SO_2 burden in the plumes' cross-sections (Galle et al., 2010). Multiplication of this SO_2 burden with the wind speed at plume height yields the volcanic SO_2 emission rate, typically reported in metric tons per day (t/d). In this study, we used wind information from the National Oceanic and Atmospheric Administration (NOAA) National Center for Environmental Predictions (NCEP) Global Forecast System (GFS) at 0.5° resolution, interpolated to the volcano's geographic location and summit altitude, as an estimate of plume speed (see de Moor et al., 2017 for a comparison of GFS data with anemometer measurements).

As is described in the next section, explosive events at the volcano's summit were very common during our 2016–2021 observation period. Explosions varied greatly in size, with some emitting gas and ash to almost 10 km ASL, and others so small they had no noticeable effect on plume height. During large explosions, significant volcanic ash loads were entrained into the eruption clouds, making them appear dark in color and at times leading to ash fallout downwind. The scanning DOAS instruments are not well-suited for quantifying gas emissions associated with large, ash-rich eruption clouds. The problems are two-fold: for one, large explosions often fill much of the visible sky with gas and ash, making it impossible for the scanners to measure a clear-sky spectrum relative to which the other measurements can be evaluated. Also, significant ash concentrations in the large eruptive clouds block solar radiation at all wavelengths, preventing it from penetrating the plume core. If left unmitigated, these conditions will lead to severe underestimation of the gas emission rates (often referred to as 'light dilution'), as the majority of light collected by the instruments has not passed through the plume at all (Kern et al., 2010, 2013). Acknowledging these problems, our analyses excluded SO_2 emission rates recorded on calendar days with explosion columns that reached >4,000 m ASL, or about 1,500 m above the volcano's summit, as the SO_2 amounts within these significant explosion plumes were likely underestimated. Days on which explosions with unknown column heights occurred (189 days over 5 years) were also removed from the SO_2 record. Filtered in this way, we obtained a robust measure of the volcano's "passive" SO_2 emissions. However, we note that the record is missing all emissions associated with large explosive events (see Primulyana et al., 2019 for some examples) and thus represents a minimum constraint on the cumulative SO_2 output over time.

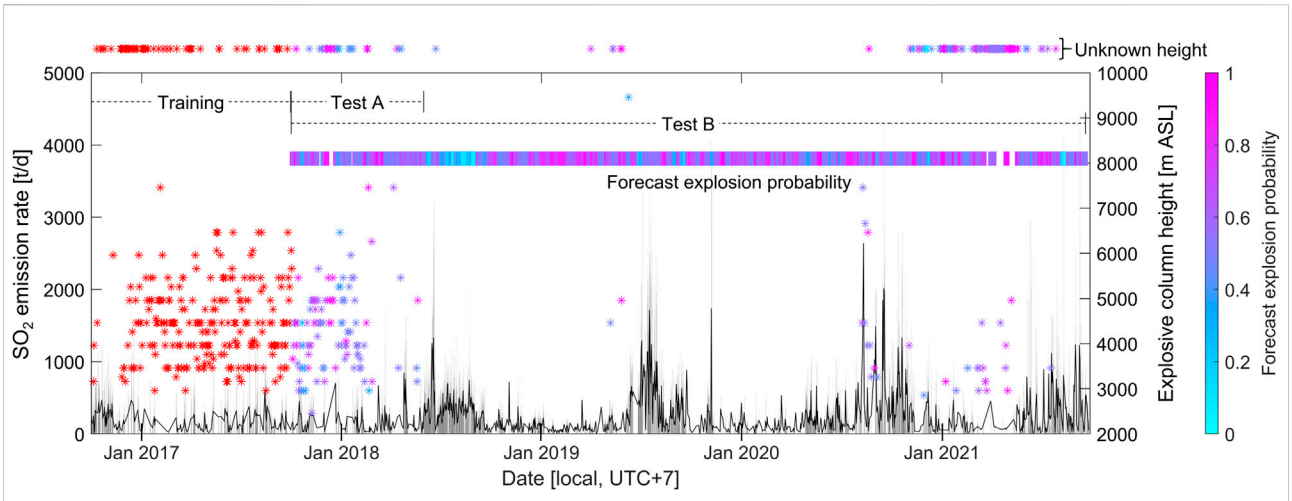

FIGURE 2
SO_2 emission rates and explosive events measured at Sinabung Volcano from 1 October 2016 to 30 September 2021. Vertical grey bars depict the range of instantaneous SO_2 emission rates measured by the scanners in the DOAS network, while the solid black line represents the daily average passive emission rate (see text for details). The timing and column height of explosions is indicated by the position of the stars. Explosive events with unquantified column heights are indicated by stars at the top of the plot. The time windows used for training and testing explosion forecasts are also indicated at the top and labeled 'Training', 'Test A', and 'Test B'. Starting on 1 October 2017, the forecast daily explosion probabilities are represented by the horizontal bar in varying colors, with the color scale given at right; stars indicating column heights are color-coded according to the last valid forecast explosion probability before the corresponding explosion occurred (compare Figure 5C); red stars indicate explosions that occurred during the training period when no forecast was available.

2.2 Identifying explosions and determining column heights

Explosive events occurring at Sinabung produce characteristic seismic signals that are recorded by the volcano's seismic network. These signals typically start as low-frequency events (LFs) but transition to broadband tremor within the first minute after onset. The CVGHM classifies these as 'Emission'-type events (Kushendratno et al., 2012; McCausland et al., 2019) immediately preceded by impulsive low-frequency shaking. These signals are thought to be caused by magmatic gas and steam breaking through the upper conduit and dome on their way to the surface (McCausland et al., 2019).

Data from the seismic network is telemetered to the Sinabung observatory in Kabanjahe, North Sumatra, and sent to the CVGHM headquarters building in Bandung in real time. Based on the seismicity, an audible alarm at the Kabanjahe observatory alerts the observers each time an explosion occurs, and explosions occurring during the daytime are visually confirmed whenever the weather allows. When possible, the observers also note the color (dark/light), opacity, and estimated height of gas and ash plumes stemming from explosions.

The eruptive column heights reported in this study were determined by aiming a set of binoculars with an integrated inclinometer at the top of the column. The inclination was noted and, together with the known distance to the volcanic vent, the approximate column altitude was triangulated. In each case, the column height was determined immediately after the first explosive pulse. At times, the eruption clouds may have lofted further as they dispersed and drifted downwind, but this additional lofting could not be quantitatively captured using the methods at hand, so only the initial height was reported.

3 Measurement results

Running continuously since September 2016, the scanning DOAS network at Sinabung has been able to record the passive SO_2 emission rates from Sinabung for the last 5 years (Figure 2). The instruments were able to record at least one valid emission rate (i.e., $C \geq 0.8$) on approximately 80% of the days in the observation period. On the remaining 20% of days, the plume was either blown to the west where the instruments couldn't capture the emissions, clouds between the plume and the scanners prevented reliable measurements, or a large explosion occurred, and the gas data were discarded due to concerns about ash emission adversely affecting data accuracy (see Section 2.1). Instantaneous passive SO_2 emission rates derived from individual scans ranged from 0 to ~4,800 t/d (maximum rate measured on 9 September 2021), while the maximum daily average emission rate was ~2,600 t/d (measured on 11 August 2020). The mean passive daily average emission rate for the entire 2016–2021 reporting period was ~240 t/d (N = 1,145 days).

Also shown in Figure 2, explosions were detected at Sinabung on a total of 567 days between 1 October 2016 and 30 September 2021. Of these, 432 occurred between 1 September 2016 and

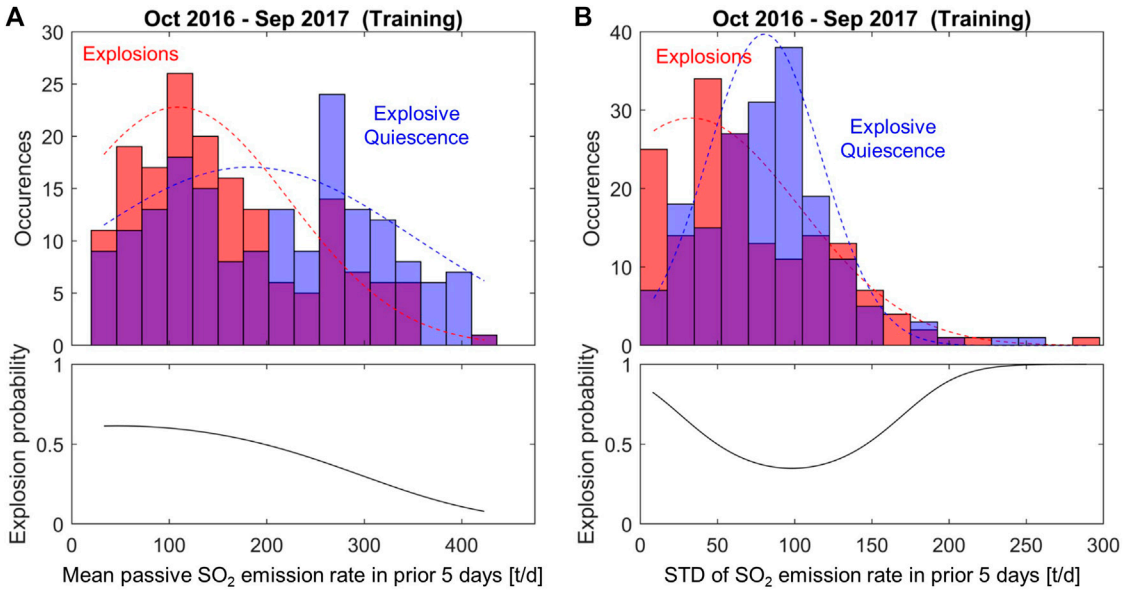

FIGURE 3
Results of a statistical analysis of SO_2 emission rates from Sinabung Volcano during October 2016 to September 2017. The mean **(A)** and standard deviation **(B)** of the passive SO_2 emission rate in the 5 days leading up to each day in this 1-year period were calculated. Histograms of these parameters have been separated into days on which explosions occurred (red, N = 167) and days without explosions (blue, N = 177). Areas where the histograms overlap appear purple. Note that days with explosions were more likely preceded by lower SO_2 emissions than days of explosive quiescence. Days without explosions were also typically preceded by standard deviations (STD) of SO_2 emission rates between 50 and 150 t/d, while days with explosions were preceded by a somewhat wider range of variability in emissions. Fitting normal distributions to the histograms (dotted lines) and requiring that the sum of the two probabilities equals 1, an explosion probability was calculated for each mean and STD value. Shown below each histogram, these probabilities are only valid for the period assessed here (October 2016–September 2017).

20 May 2018, while 135 occurred in the remainder of the observation period. Observations of column heights associated with explosions ranged from 2,500 m (the volcano's summit elevation) to 9,500 m ASL. At least 30% of observed explosions generated plume heights <4,000 m ASL, but the exact percentage is unknown due to some explosions having unquantified column heights. Of the known column heights, the mean height was ~4,400 m and only 5% of explosive columns reached >6,000 m ASL. Indeed, the majority of explosions were relatively small; the warm, tropical environment likely aided associated columns in rising to altitudes that would not have been achieved in mid or high latitudes (Sparks, 1986).

4 Discussion

4.1 Statistical analysis of data collected in the first year (2016–2017)

With the comprehensive record of SO_2 emissions and the large number of explosive events at Sinabung, we sought to determine whether the degassing signals can be used to improve the understanding of Sinabung's activity and/or aid in forecasting explosive events. Initially focusing on the first year of measurements (1 October 2016 to 30 September 2017), we calculated the mean passive SO_2 emission rates during the five preceding days on which explosions occurred. A histogram of these 5-day mean emission rates is shown in red in Figure 3A. Although the distribution encompasses occurrences of SO_2 emission rates as high as 425 t/d, most days with explosions were preceded by relatively low mean emissions ranging from 0 to 200 t/d, with a mode of about 100 t/d.

These observations can be compared to 5-day mean passive SO_2 emissions leading up to days on which no explosions occurred (shown in blue in Figure 3A). Here, the probability distribution has two separate peaks, one coinciding with the peak in pre-explosive SO_2 emissions and one towards higher gas emission rates. Regardless of whether the bi-modal nature of the distribution is truly significant, it appears that days of quiescence (no explosions) tend to be preceded by higher 5-day mean passive SO_2 emission rates than days with explosions. Fitting a normal distribution to the histogram of emissions preceding quiescence, we find that the mode is closer to 200 t/d SO_2, and 5-day periods with SO_2 emission rates averaging >350 t/d were only once followed by an explosion.

Besides the magnitude of SO_2 emissions, we also examined the inter-daily variability of SO_2 emission rates leading up to explosions by calculating the standard deviation (STD) of daily

averaged SO_2 emission rates for the same 5-day windows. We found that periods preceding days with explosions generally have SO_2 emission rate STDs around 40 t/d, while the periods preceding days of quiescence were more likely to be preceded by STDs twice as high, around 80 t/d (Figure 3B). Fitting normal distributions to the histograms, we also find that STDs greater than about 150 t/d are more likely during periods leading up to explosions than those leading to quiescence. In other words, the range of realized STDs preceding days with explosions is higher than that preceding quiescence. Collectively, we observe that SO_2 emission rates are generally lower but exhibit a greater range of variability in the 5-day periods preceding explosive events, whereas SO_2 emission rates in the 5-day period preceding quiescent days are generally higher and vary over a narrower range. We note that the 5-day timespan used here was chosen after manually inspecting a range of other spans. The 5-day window appeared to maximize the notable differences in emissions before explosive vs. quiescent days while at the same time encompassing sufficient data to allow means and STDs to be calculated for most days.

These observations can now be used to calculate daily explosion probabilities for the reference period. Since each observation day falls either into the category of days with explosions or days without explosions, the cumulative probability at each position in the histograms in Figure 3 must equal 1. Using the fitted normal distributions rather than the noise-prone data themselves, we calculate the probability of an explosion occurring for observed mean SO_2 emission rates and STDs in the preceding 5-day period. The resulting probability curves are shown in the bottom panes of Figure 3. The daily explosion probability increases for 5-day periods of low SO_2 emissions and for STDs either significantly lower or higher than the 80 t/d typically associated with quiescence.

4.2 A degassing model for Sinabung

Based on the multi-year SO_2 emission record at Sinabung and the statistical analysis of SO_2 emissions preceding explosions during October 2016—September 2017, we can develop a conceptual model to explain our observations. First, the mean SO_2 emission rate of 240 t/d sustained over a 4-year interval requires a steady supply of magma to relatively shallow depths. In fact, similar emissions have been sustained for over a decade at Sinabung (Primulyana et al., 2019), indicating a relatively constant magma supply rate. The petrologic degassing behavior of sulfur is complex and has not been explicitly studied for Sinabung's andesitic (Nakada et al., 2019) magmas. However, research from other andesitic arc magmas (hydrous, relatively oxidized) suggests that sulfur degassing occurs throughout the mid- and upper-crust, where many magmas are saturated in a H_2O- and CO_2-rich multicomponent vapor phase (Métrich and Wallace, 2008; Fiege et al., 2014). At depths shallower than ~4–6 km, the decreasing pressure causes sulfur to increasingly partition into the vapor phase (Scaillet and Pichavant, 2005; Burgisser et al., 2008; Lesne et al., 2011; Wallace and Edmonds, 2011; Webster and Botcharnikov, 2011; Werner et al., 2020). Sulfur degassing at Sinabung is therefore likely sourced from magmas ascending at various levels within the crustal plumbing system (Christopher et al., 2015; Iacovino, 2015), but particularly from relatively shallow magmas.

A steady magma supply is also consistent with visual observations of generally sustained lava extrusion from Sinabung's summit during 2016–2021. Photographs of the summit (Figure 4A) show steam emissions, mostly focused around the edges of the lava dome where degassing pathways presumably follow stress fractures caused by dome extrusion and growth. This combination of steady magma supply and fairly open degassing pathways around the slowly extruding lava dome allows for moderate gas emissions (100–400 t/d SO_2) in a quasi-steady state (Figure 4B). As the lava dome itself is likely composed of material that previously degassed during slow ascent up the conduit, it is likely to be a highly viscous, crystalline lava (Nakada et al., 2019 measure crystallinities of ~40 volume % in juvenile lava fragments from 2014), and we assume it is not very permeable to gas, consistent with the lack of visible gas or steam plumes emanating from the dome itself (Figure 4A).

Secondly, the decrease in SO_2 emission rates in the days preceding explosive events (Figure 3A) suggests that the established degassing pathways can become sealed by the viscous, degassed dome material, which causes pressurization and eventual explosive rupture. The potential for a protracted phase of repeating explosive events at Sinabung caused by magma densification through degassing and vesicle collapse of the lava dome and upper conduit was already recognized by Primulyana et al. (2019) and Nakada et al. (2019), and this prediction appears to hold true based on recent years of observations. One possible trigger for sealing of the system is a short-term reduction in magma supply rate from depth, which could lead to a slight cooling and reduction in gas streaming through the peripheral lava dome cracks, thus allowing ductile dome material to seal the pathways. When this occurs, the SO_2 emission rate measured downwind decreases, consistent with our observations. Concomitantly, pressure will begin to build beneath the seal as exsolved volatiles accumulate (Figure 4C).

Depending on the strength of the seal, the pressure building beneath the dome may overwhelm it rather quickly. In this case, gas which had begun to accumulate may be released in a non-explosive manner, leading to a brief period of anomalously high SO_2 emissions. For example, in their detailed 2-week record of SO_2 emissions from 2016, Primulyana et al. (2019) discovered gas emission events occurring at Sinabung that appeared to occur contemporaneously with hybrid seismic events. Hybrid

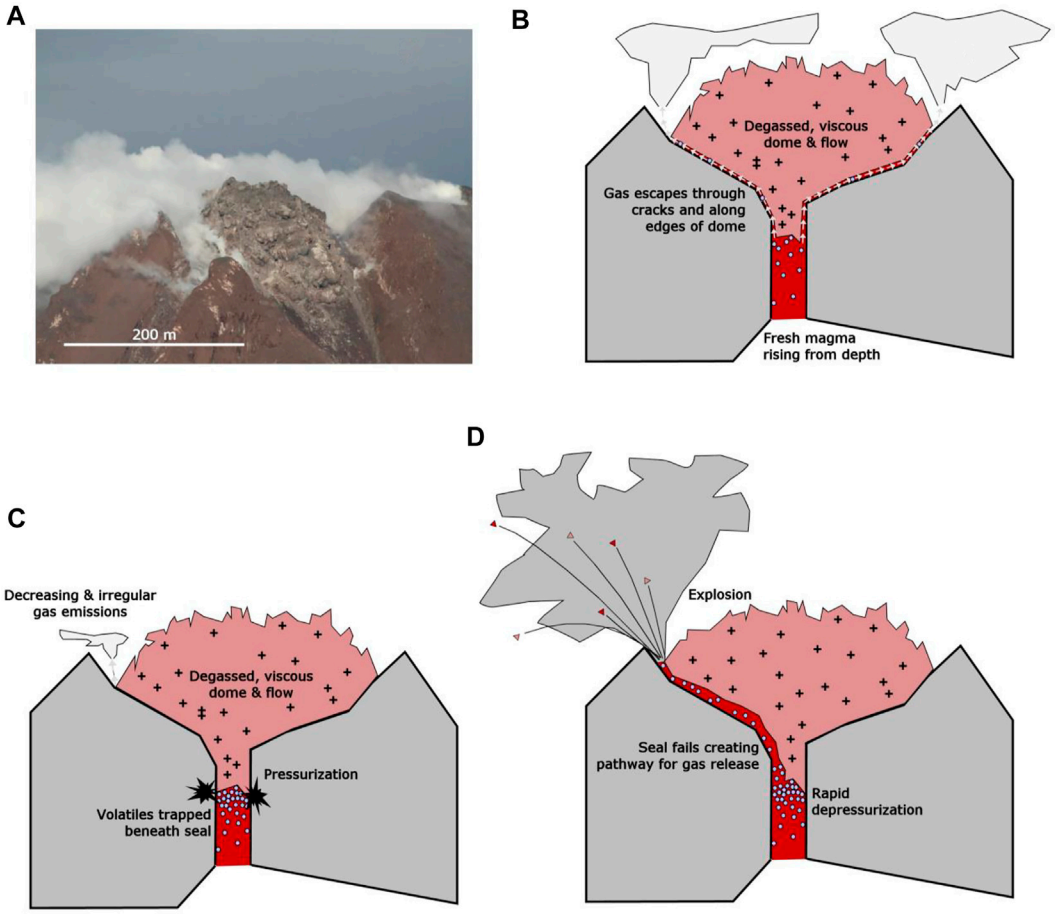

FIGURE 4
Schematic of our conceptual seal-failure model for magmatic degassing and explosions at Sinabung. **(A)** Photograph by CVGHM scientists of the lava dome perched in Sinabung Volcano's summit crater on 25 November 2020. Degassing dominantly occurs from the margins of the dome. **(B)** During periods of explosive quiescence, gases exsolving from magma rising in the conduit escape through cracks in and pathways around the highly viscous and relatively impermeable lava dome. **(C)** If the degassing pathways become sealed, SO_2 emissions decrease and gas accumulating beneath the dome begins to pressurize. Highly variable gas emissions may result if the seal is broken intermittently in a non-explosive manner before a critical pressure is achieved. **(D)** Explosions occur if the pressure builds beyond the threshold for generating new or re-establishing preexisting degassing pathways. Explosions are caused by the rapid depressurization of the shallow conduit. The magnitude of the resulting explosions will depend on the strength of the seal, which determines the accumulated pressure beneath it.

seismicity is often ascribed to brittle failure and resonance in fluid filled cracks (Chouet, 1996; Chouet and Matoza, 2013; McCausland et al., 2019), so these may well be manifestations of the non-explosive gas release events which we postulate here. When the volcanic system is in an unstable state of intermittent or partial sealing of degassing pathways (Figure 4C), gas emissions could well be more variable than during times when steady-state degassing is occurring, which might explain the greater range of standard deviations apparent in the October 2016—September 2017 SO_2 emission rate data (Figure 3B).

However, if the degassing pathways become more robustly sealed, pressurization will continue and eventually lead to an explosion. In this process, the accumulated pressure may break open an existing pathway for gas escape or create a new one. In either case, the accumulated volatiles are rapidly released to the atmosphere, and the top of the conduit is suddenly exposed to near-atmospheric pressure causing additional degassing and expansion of the volatile phase. Gas and magma fragments are jetted from the conduit and form the observed explosive eruption columns (Figure 4D). The magnitude of the explosion and the height to which the resulting gas and ash plume ascends depends on the pressure that was attained beneath the plug at the volcano's summit.

While we believe this simplistic seal-failure model explains the observations of SO_2 degassing and Vulcanian explosive events at Sinabung, we acknowledge that other, more complex models could also be valid. For example, in addition to exsolved volatiles being trapped below a shallow seal, the exsolution of

volatiles from rapid microlite crystallization within the lava dome itself and/or the rapid heating of groundwater could also play a role in producing overpressure that ultimately leads to Vulcanian explosions (Morrissey and Mastin, 2000). The information at our disposal does not allow for definitive conclusions to be drawn regarding the explosive processes. The model is also based only on observations from October 2016 to September 2017 and is therefore not necessarily valid outside this period. For example, if the magma supply rate from depth changed drastically over time, this would lead to significant changes in activity at the volcano's summit that would not necessarily be represented in our model.

On the other hand, if parameters such as magma supply, magma chemistry, and lava effusion rates remained approximately constant over time, we could expect future activity to follow the same patterns as in the past. In this case, the statistical results discussed above might be used to provide forecasts of future behavior, regardless of whether the conceptual model is correct or not.

4.3 A simple framework for forecasting explosions based on SO_2 emissions

As defined in our statistical analysis above, the daily explosion probabilities are strictly accurate only for the evaluated period (October 2016 to September 2017). However, we can consider this a "training" period for a forecasting method which aims to forecast future events. If the system behaved exactly as it did during the training period, future explosions would be expected to follow the same pattern. To produce a forecast, the two separate diagnostics (i.e., mean SO_2 emission rate and standard deviation in the preceding 5 days) must first be combined in some way, as they will typically produce different results. For example, if a 5-day mean SO_2 emission rate of 300 t/d is accompanied by a STD of 200 t/d, the emission rate would indicate an explosion probability of approximately 0.3 while the STD of emissions would indicate a probability of 0.8 (see Figure 3). In the absence of additional information, we choose to weight the 5-day mean and 5-day STD metrics equally (in this example yielding a combined explosion probability of 0.55).

Following this procedure, we can forecast explosion probabilities for most days in our record. Ranging from 0.20 to 0.75, these daily forecasts are shown in a colored horizontal bar spanning 1 October 2017–30 September 2021 in Figure 2. The forecast record contains gaps because gas emissions could not be constrained every day (e.g., when the plume was blown to the west), and days on which large explosions may have occurred are removed from the passive SO_2 emission dataset (see Methods section). Furthermore, in order to calculate meaningful STD values, we only present forecasts for days where SO_2 emissions data are available on at least two of the five preceding days. In the end, we were able to calculate forecasts on approximately 70% of days during 1 October 2017–30 September 2021.

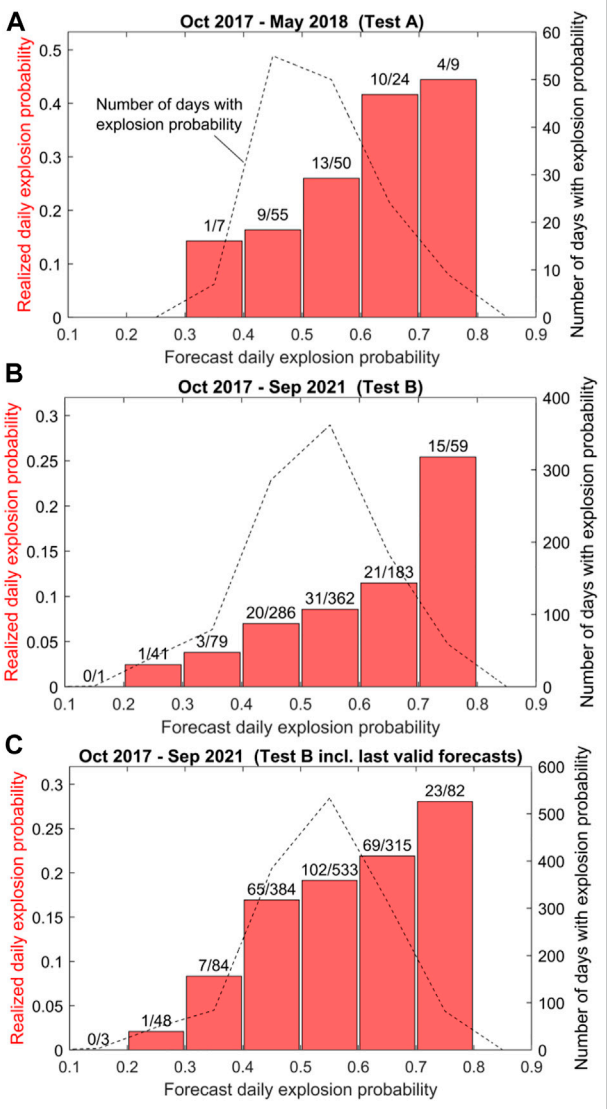

FIGURE 5
Results of several tests of the explosion forecast methodology based on SO_2 emission characteristics. **(A)** In Test A, we applied the explosion forecast framework to data between October 2017 and May 2018, a period that exhibited a similar explosion frequency as the training period (October 2016—September 2017). **(B)** In Test B, the forecast was applied to all available data collected between October 2017 and September 2021. A forecast explosion probability between 0 and 1 was calculated for each day in the respective study, and these were then binned in intervals of 0.1. The dotted line and right axis indicate the number of forecast values in each bin. Dividing the number of explosions that occurred on the days in each bin by the total number of days in the bin yields the realized daily explosion probability, which is indicated by the red bars (left axis). The numbers above the bars give the number of days with observed explosions per number of days in each forecast bin. In **(C)**, we plot the results of Test B, this time including all days in the test period, not just those with a valid forecast. Days without a forecast were assigned the last valid forecast that could be calculated. Note that in all cases, the absolute forecast explosion probabilities were higher than the realized probabilities, but in a relative sense, the probability of an explosion occurring always increased with increasing forecast probability.

4.4 Evaluating forecast accuracy (2017–2021)

We first focus on the period from 1 October 2017 to 31 May 2018 (marked "Test A" in Figure 2). This 8-month period directly follows the 1-year training period and ends just before explosions at Sinabung stopped for about a year in 2018–2019. The rationale for choosing this test period is that the frequency of explosions was similar to that of the training period, and thus the processes driving explosions are likely to be similar to those occurring during the training period.

Based on SO_2 emission characteristics, a total of 145 daily explosion probability forecasts were calculated during this 242-day period, so a forecast could be provided on roughly 60% of days. Forecast daily explosion probabilities ranged from 0.32 to 0.73. A histogram of forecast probabilities is given in Figure 5A. Explosion probabilities between 0.4 and 0.5 were forecast for 55 days, and an additional 50 days had explosion probability forecasts between 0.5 and 0.6. Thus, approximately 75% of all forecast days fell into these two categories. Only 7 days yielded explosion probabilities of less than 0.4, while explosion probabilities >0.6 were forecast for 33 days.

Since this test period lies in the past, the accuracy of the forecasts can be assessed by examining the realized daily explosion probability, which is simply the number of days with explosions divided by the total number of days in the observation period. The bars in Figure 5A show the realized explosion probability disaggregated by forecast explosion probability, with the numbers above each bar indicating the number of explosions per total number of days in the respective bin. For all bins, realized explosion probabilities were lower than the forecast values. For example, only nine explosions occurred during the 55 days that had explosion probability forecasts between 0.4 and 0.5, corresponding to a realized explosion probability of 0.16, or less than half the forecast value. The same holds true for all other bins, with the forecasts exceeding the realized explosion probabilities by about a factor of 2. This observation indicates that the absolute accuracy of the explosion probability forecasts is rather poor, as our method was not able to accurately forecast the total number of explosions that occurred during the test period.

On the other hand, the forecasting method was quite successful in discriminating days with a higher likelihood of explosions from days with a relatively lower probability of an explosion occurring. This is evidenced by the monotonic increase of realized explosion probabilities with increasing forecast values. Explosions were three times more likely on days in the 0.7–0.8 explosion probability forecast category (p = 4/9 = 0.44) than on days with forecasts <0.4 (p = 0.14). Therefore, though the absolute daily explosion probability was overestimated in all bins, the method still provided a means for determining the relative likelihood of an explosion occurring on a given day.

In a second test, we considered the entire available dataset following the training period (labeled "Test B" in Figure 2). Running from 1 October 2017 to 20 September 2021, this 4-year period contains phases of frequent explosive activity, but also phases of explosive quiescence that last for many months at a time. Given the far lower average frequency of explosions in this period and the results of the first test, we do not expect our method to accurately forecast the total number of explosions or absolute daily explosion probability in this test period. However, if the processes that cause explosions remained the same as in the training period, the forecast might again provide a relative indication of daily explosion probability when compared with other days in the period.

The test results appear to confirm this supposition. As shown in Figure 5B, we were able to calculate explosion probability forecasts on 1,011 of 1,450 days, or about 70% of days in the period. Explosion probability forecasts ranged from 0.20 to 0.75, with most days again falling in the range of 0.4–0.6. The realized explosion probabilities were far lower than the forecast values. However, the monotonic increase of realized explosion probabilities with increasing forecast values remained, thus again allowing for discrimination of days with relatively low explosion probability from those with relatively high risk. In fact, the realized likelihood of an explosion occurring on a day in the 0.7–0.8 bin (0.25) was now more than seven times greater than that of one occurring on a day with forecast probability <0.4 (0.033).

Despite the relatively high number of days with valid forecasts available, gaps in our ability to provide a forecast tend to disproportionately occur during phases of frequent explosions as SO_2 emission rates are deemed unreliable (see Methods). In a final test, we assigned the last valid forecast probability to any day on which the probability could not be calculated, thus filling the gaps in our forecast record. The results of this procedure (Figure 5C) are generally consistent with what we found previously. The absolute forecast explosion probabilities were similarly low, but the monotonic increase of realized probabilities with increasing forecast values remained. Relying on the last valid forecast therefore seems to be an acceptable method for dealing with forecast gaps due to unmeasured SO_2 emissions.

We envision the methodology described here could prove useful not just at Sinabung, but also at other volcanoes with dome-building eruptive activity. Notable examples include Santiaguito Volcano, Guatemala, where observations of degassing along the edges of a lava dome are strikingly similar to activity at Sinabung's summit (see Figure 1 in Bluth and Rose, 2004); Popocatépetl Volcano, Mexico, where SO_2 camera data revealed that a subset of explosions were preceded by low emission rates attributed to the accumulation of gas beneath a rapidly compacting dome (Campion et al., 2018); Colima Volcano, Mexico, where measurements of gas flux appeared to track the failure of a crystalized obstruction in the volcano's

shallow system prior to ash-rich explosions (Varley et al., 2010; Cassidy et al., 2015); and Sakurajima Volcano, Japan, where SO_2 emission rates were observed to decrease contemporaneously with increased inflation of the edifice prior to explosions from Showa crater (Yokoo et al., 2013; Kazahaya et al., 2016).

4.5 Future work

Although promising in its ability to provide a relative risk metric, the utilized explosion forecasting approach clearly has limitations. As the forecast output is based on a single training period, the methodology will surely fail if the processes governing explosions and volcanic activity overall at Sinabung Volcano change. For example, if magma supply from depth decreases and the years-long eruption trends towards its end, the forecast will incorrectly predict high explosion probability levels as the mean SO_2 emission rate decreases. Similarly, the methodology fails to forecast the long-term changes in explosion frequency exhibited in our 5-year record. As long-term mean SO_2 emissions did not drop noticeably during periods of explosive quiescence, we hypothesize that magma supply from depth likely continued during these times, but other processes made for efficient degassing and lack of pressurization and explosions. These differences are not captured in our training data, and thus the forecast is unable to predict them.

Also, some of the explosions included in our record were caused by dome-collapse events during which portions of the lava dome and flow broke off or collapsed, instantly decreasing the lavastatic pressure on the upper conduit and leading to rapid decompression, degassing, and explosion (Pallister et al., 2019a). These types of explosions are unlikely to be preceded by changes in degassing caused by variable permeability of the dome, but instead depend on the structural integrity of the dome/lava flow complex and the degree of oversteepening. A notable example of an unforeseen explosion occurred on 9 June 2019 at 16:28 local time. In what was one of the largest eruptive events in the last 5 years, a large explosion at Sinabung produced a thick, black column of gas and ash which ascended to approximately 9,500 m ASL. The explosion produced pyroclastic flows that traveled more than 3 km down the south and southeast flanks of the volcano. This paroxysmal event occurred on a day with a SO_2-emissions-derived explosion probability of only 0.4 according to our forecast method. We attribute the failure to forecast this event to a high likelihood that this explosion was caused by a mechanism not described by our seal-failure model, possibly a dome-collapse as mentioned above.

Although some of our method's limitations are intrinsic to forecasting itself, it may be possible to improve the forecast accuracy in the future by providing additional information upon which to base the projections. Examination of the explosion record at Sinabung reveals that explosions tend to be temporally clustered in phases of frequent activity, interspersed by periods of relative explosive quiescence. If we assume that these phases are significantly longer than our forecasting window, the absolute probability of an explosion occurring on a given day likely depends on which phase of activity the volcano is in and the observed frequency of explosions in that phase. Considering the history of explosions in recent weeks, months, or even years along with the short-term (5-day) degassing behavior might then improve the forecast accuracy. This could be implemented in an approach similar to the Short-Term Average/Long-Term Average (STA/LTA) algorithms which are commonly used in event-detection applications based on geophysical data (Withers et al., 1998; Trnkoczy, 2012; Brill et al., 2018; Power et al., 2021; Viccaro et al., 2021). Alternatively, it may be beneficial to repeat the training process intermittently, either at preset time intervals or whenever volcanic activity is deemed to have entered a new phase. Even a sliding window approach that constantly re-trains the algorithm on a period of time immediately preceding the current day could be implemented, though care must be taken to include a sufficient number of events to avoid imbalanced training data. Such improvements could be particularly valuable when the magma supply rate at a given volcano changes. The current transition towards a more effusive eruption with fewer Vulcanian events at Sinabung may be caused by a decrease in magma supply, which would in turn negatively affect the absolute accuracy of the forecasting method over time (as shown in Section 4.4) unless some sort of re-calibration is performed.

Further improvements might come from a more rigorous analysis of the optimal input features that lead to accurate forecasts. In this study, we chose to base forecasts only on the simple mean and standard deviation of emission rates over the last 5 days after manually inspecting a variety of other properties. Prior maximum and minimum emission rates, short-term and long-term trends in emissions, and the elapsed time since the last explosion all did not appear to exhibit systematic differences leading up to explosions when compared to explosive quiescence during October 2016—September 2017. However, a more rigorous investigation of these and other parameters, possibly even employing machine learning algorithms to select optimal features and produce forecasts, may yield improved results. The drawback of such an approach is that the forecast model becomes less transparent to the users, thus making it more difficult to link the observations to a conceptual model for the explosions. Assessing whether the forecasts remain valid in the face of a potential long-term change in activity at Sinabung thus also becomes more complicated. For these reasons, we have elected not to use machine learning approaches here, instead favoring a simple statistical approach.

Perhaps the greatest improvement could come from combining our forecasting method with others, particularly with methods based on other monitoring parameters. As discussed above, explosions at Sinabung may be caused by a number of different processes, and not all are likely to be preceded by significant changes in gas emissions. Therefore, a

forecasting method based solely on degassing observations will necessarily miss certain events. Pallister et al., 2019b show how information from satellite remote sensing platforms was instrumental in monitoring lava dome stability and forecast dome/lava flow collapse events and pyroclastic flows at Sinabung during 2013–2016. Tracking lava dome changes on timescales comparable with the SO_2-based forecasts (i.e., ~5-day periods) could help determine whether our proposed conduit sealing and gas accumulation model was accompanied by observable lava dome inflation. Low lava dome extrusion rates might also make the system more prone to sealing, and high extrusion rates likely increase the chance of lava dome or flow front collapse. Seismic and geodetic data also provide valuable information about processes occurring at depth that can presage changes in eruptive activity and inform forecasts (Hotta et al., 2019; McCausland et al., 2019). For example, the processes that cause 'Emission'- or 'Hembusan'-type (Caudron et al., 2015; McCausland et al., 2019) and 'Hybrid'-type (Primulyana et al., 2019) seismic events are not yet fully understood. Coupling our gas-based forecasts with those from other automated or process-based forecasts would therefore provide complimentary information and likely result in the most accurate forecasts, particularly when compiled and discussed by a multi-disciplinary team of analysists.

5 Conclusion

Using a relatively simple statistical analysis of passive SO_2 emission rates recorded at Sinabung Volcano during a 1-year period in 2016–2017, we found that explosions were often preceded by below-average emission rates over the prior 5 days (Figure 3A). The absolute standard deviation of the SO_2 emission rate, while typically also lower than average, took on a slightly greater range of values in the 5 days leading up to explosions than before days without explosions (Figure 3B). These findings could be explained by a simple conceptual model in which degassing pathways from the volcano's conduit to the atmosphere are intermittently blocked, allowing pressure to build and sometimes lead to explosions. Based solely on the measurements of SO_2 emissions and timing of explosions, the model is not unique and other, more complex models might also explain the observations. However, the diagnostic nature of the statistical observations appears robust. Derived from the observations of the 2016–2017 training period, a simple method for forecasting explosion probabilities was tested on the remainder of the available gas emission and explosion dataset (2017–2021). Although the method failed to accurately forecast the absolute probability of explosions, it succeeded in providing a relative measure of the daily explosion probability when compared to other days in each test period. Based on these findings, we suggest that the explosion probability forecasts be interpreted as relative rather than absolute probabilities. These forecasts can then be used operationally: days on which a high relative probability is forecast are more likely than others in the same general time window to have explosions occurring.

Forecast explosion probabilities can be obtained daily in a fully automatic process. Interpretation of the relative probabilities requires knowledge of the limitations of the methods used in their calculation. For example, explosions caused by dome-collapse events cannot be forecast with this technique as they are generally not associated with precursory changes in gas emission rates. Time will tell whether the forecasts of future activity at Sinabung will remain accurate, or whether the volcano will transition to a new phase of significantly different activity. Regardless, we envision the described forecasting methodology could well be applied to other volcanoes experiencing dome-building eruptions.

Finally, this study adds to the growing body of research demonstrating that important, actionable information on volcanic activity and processes can be obtained from continuous gas measurements and emphasizes the value of establishing and maintaining continuous gas monitoring at more active volcanoes worldwide (Aiuppa et al., 2007; Werner et al., 2013; de Moor et al., 2016; Kern et al., 2017, 2022; Stix and de Moor, 2018).

Data availability statement

The original contributions presented in the study are included in the Supplementary Material, further inquiries can be directed to the corresponding author and the Indonesian Center for Volcanology and Geological Hazard Mitigation.

Author contributions

SK, CK, and AL led the installation of the gas monitoring instruments on Sinabung Volcano in 2016. SK oversaw data collection and analysis for the observation period. CK developed the presented approach for statistical data analysis and forecasting and wrote the first draft of the manuscript. SK, HA, and AL wrote sections of the manuscript. All authors contributed to manuscript revision and approved the submitted version.

Acknowledgments

Theauthors would like to thank the observers at the Sinabung Observatory (Moh. Nurul Asrori, Armen Putra, Deri Al Hidayat), Sulus Setiono, Ugan B. Saing, and Sofyan Primulyana for assistance with the installation and

maintenance of the monitoring network and reporting explosions at Sinabung. The Indonesian Geological Agency and its Center for Volcanology and Geologic Hazard Mitigation (CVGHM) and the USGS-USAID Volcano Disaster Assistance Program (VDAP) are gratefully acknowledged for providing support for this study. Finally, we would like to acknowledge the Network for Observation of Volcanic and Atmospheric Change (NOVAC) community for providing hardware and software support without which the reported gas measurements would not have been possible. Any use of trade, firm, or product names is for descriptive purposes only and does not imply endorsement by the U.S. Government.

Conflict of interest

The authors declare that the research was conducted in the absence of any commercial or financial relationships that could be construed as a potential conflict of interest.

Publisher's note

Supplementary material

The Supplementary Material for this article can be found online at: https://www.frontiersin.org/articles/10.3389/feart.2022.976928/full#supplementary-material

SUPPLEMENTARY TABLE S1
Table of sulfur dioxide emission rates and the number of observed explosions and notable seismic events from Sinabung Volcano, 2016–2021.

References

Aiuppa, A., Moretti, R., Federico, C., Giudice, G., Gurrieri, S., Liuzzo, M., et al. (2007). Forecasting Etna eruptions by real-time observation of volcanic gas composition. *Geol.* 35, 1115. doi:10.1130/G24149A.1

Arellano, S., Galle, B., Apaza, F., Avard, G., Barrington, C., Bobrowski, N., et al. (2021). Synoptic analysis of a decade of daily measurements of SO_2 emission in the troposphere from volcanoes of the global ground-based Network for Observation of Volcanic and Atmospheric Change. *Earth Syst. Sci. Data* 13, 1167–1188. doi:10.5194/essd-13-1167-2021

Bani, P., Oppenheimer, C., Tsanev, V., Scaillet, B., Primulyana, S., Saing, U. B., et al. (2022). Modest volcanic SO_2 emissions from the Indonesian archipelago. *J. Volcanol. Geotherm. Res.* 13, 1–15. doi:10.1038/s41467-022-31043-7

Bluth, G. J. S., and Rose, W. I. (2004). Observations of eruptive activity at Santiaguito Volcano, Guatemala. *J. Volcanol. Geotherm. Res.* 136, 297–302. doi:10.1016/j.jvolgeores.2004.06.001

Brill, K. A., Waite, G. P., and Chigna, G. (2018). Foundations for forecasting: Defining baseline seismicity at Fuego Volcano, Guatemala. *J. Geophys. Res.* 6, B12204–B12218. doi:10.3389/feart.2018.00087

Burgisser, A., Scaillet, B., and Harshavardhan (2008). Chemical patterns of erupting silicic magmas and their influence on the amount of degassing during ascent. *J. Geophys. Res. Solid Earth* 113, 1–14. doi:10.1029/2008JB005680

Campion, R., Delgado-Granados, H., Legrand, D., Taquet, N., Boulesteix, T., Pedraza-Espitía, S., et al. (2018). Breathing and coughing: The extraordinarily high degassing of Popocatépetl Volcano investigated with an SO_2 camera. *Front. Earth Sci.* 6, 163. doi:10.3389/feart.2018.00163

Cassidy, M., Cole, P. D., Hicks, K. E., Varley, N. R., Peters, N., and Lerner, A. H. (2015). Rapid and slow: Varying magma ascent rates as a mechanism for Vulcanian explosions. *Earth Planet. Sci. Lett.* 420, 73–84. doi:10.1016/j.epsl.2015.03.025

Caudron, C., Syahbana, D. K., Lecocq, T., Van Hinsberg, V., McCausland, W., Triantafyllou, A., et al. (2015). Kawah ijen volcanic activity: A review. *Bull. Volcanol.* 77, 16. doi:10.1007/s00445-014-0885-8

Chouet, B. A. (1996). Long-period volcano seismicity: Its source and use in eruption forecasting. *Nature* 380, 309–316. doi:10.1038/380309a0

Chouet, B. A., and Matoza, R. S. (2013). A multi-decadal view of seismic methods for detecting precursors of magma movement and eruption. *J. Volcanol. Geotherm. Res.* 252, 108–175. doi:10.1016/j.jvolgeores.2012.11.013

Christopher, T., Blundy, J., Cashman, K., Cole, P., Edmonds, M., Smith, P., et al. (2015). Crustal-scale degassing due to magma system destabilization and magma-gas decoupling at Soufrière Hills Volcano, Montserrat. *Geochem. Geophys. Geosyst.* 16, 2797–2811. doi:10.1002/2015GC005791

de Moor, J. M., Aiuppa, A., Pacheco, J., Avard, G., Kern, C., Liuzzo, M., et al. (2016). Short-period volcanic gas precursors to phreatic eruptions: Insights from Poás Volcano, Costa Rica. *Earth Planet. Sci. Lett.* 442, 218–227. doi:10.1016/j.epsl.2016.02.056

de Moor, J. M., Kern, C., Avard, G., Muller, C., Aiuppa, A., Saballos, A., et al. (2017). A new sulfur and carbon degassing inventory for the Southern Central American Volcanic Arc: The importance of accurate time-series datasets and possible tectonic processes responsible for temporal variations in arc-scale volatile emissions. *Geochem. Geophys. Geosyst.* 18, 4437–4468. doi:10.1002/2017GC007141

Dempsey, D. E., Cronin, S. J., Mei, S., and Kempa-Liehr, A. W. (2020). Automatic precursor recognition and real-time forecasting of sudden explosive volcanic eruptions at Whakaari, New Zealand. *Nat. Commun.* 11, 3562–3568. doi:10.1038/s41467-020-17375-2

Fiege, A., Behrens, H., Holtz, F., and Adams, F. (2014). Kinetic vs. thermodynamic control of degassing of H2O-S±Cl-bearing andesitic melts. *Geochim. Cosmochim. Acta* 125, 241–264. doi:10.1016/j.gca.2013.10.012

Galle, B., Johansson, M., Rivera, C., Zhang, Y., Kihlman, M., Kern, C., et al. (2010). Network for observation of volcanic and atmospheric change (NOVAC)—a global network for volcanic gas monitoring: Network layout and instrument description. *J. Geophys. Res.* 115, D05304. doi:10.1029/2009JD011823

Galle, B., Oppenheimer, C., Geyer, A., Mcgonigle, A. J. S., Edmonds, M., and Horrocks, L. (2002). A miniaturised ultraviolet spectrometer for remote sensing of SO_2 fluxes: A new tool for volcano surveillance. *J. Volcanol. Geotherm. Res.* 119, 241–254. doi:10.1016/S0377-0273(02)00356-6

Global Volcanism Program (2013). Sinabung (261080) in Volcanoes of the World. Available at: https://volcano.si.edu/volcano.cfm?vn=261080 (Accessed April 25, 2022).

Gunawan, H., Surono, Budianto, A., Kristianto, Prambada, O., McCausland, W., et al. (2019). Overview of the eruptions of Sinabung Volcano, 2010 and 2013 – present and details of the 2013 phreatomagmatic phase. *J. Volcanol. Geotherm. Res.* 382, 103–119. doi:10.1016/j.jvolgeores.2017.08.005

Hotta, K., Iguchi, M., Ohkura, T., Hendrasto, M., Gunawan, H., Rosadi, U., et al. (2019). Magma intrusion and effusion at Sinabung volcano, Indonesia, from 2013 to 2016, as revealed by continuous GPS observation. *J. Volcanol. Geotherm. Res.* 382, 173–183. doi:10.1016/j.jvolgeores.2017.12.015

Iacovino, K. (2015). Linking subsurface to surface degassing at active volcanoes: A thermodynamic model with applications to Erebus Volcano. *Earth Planet. Sci. Lett.* 431, 59–74. doi:10.1016/j.epsl.2015.09.016

Iguchi, M., Ishihara, K., Surono, and Hendrasto, M., (2011). Learn from 2010 eruptions at Merapi and Sinabung Volcanoes in Indonesia. *Annu. Disas. Prev. Res. Inst.* 54B, 185–194.

Iguchi, M., Surono, Nishimura, T., Hendrast, M., Rosadi, U., Ohkura, T., Triastuty, H., et al. (2012). Methods for eruption prediction and hazard evaluation at Indonesian volcanoes. *J. Disaster Res.* 7, 26–36. doi:10.20965/jdr.2012.p0026

Indrastuti, N., Nugraha, A. D., McCausland, W. A., Hendrasto, M., Gunawan, H., Kusnandar, R., et al. (2019). 3-D seismic tomographic study of Sinabung Volcano, northern Sumatra, Indonesia, during the inter-eruptive period october 2010–july 2013. *J. Volcanol. Geotherm. Res.* 382, 197–209. doi:10.1016/j.jvolgeores.2019.03.001

Johansson, M. (2009). *Application of passive DOAS for studies of megacity air pollution and volcanic gas emissions. PhD thesis*. Gothenburg, Sweden: Chalmers University of Technology. Available at: https://research.chalmers.se/en/publication/88868.

Kazahaya, R., Shinohara, H., Mori, T., Iguchi, M., and Yokoo, A. (2016). Pre-eruptive inflation caused by gas accumulation: Insight from detailed gas flux variation at Sakurajima volcano, Japan. *Geophys. Res. Lett.* 43, 11219–11225. doi:10.1002/2016GL070727

Kern, C., Aiuppa, A., and de Moor, J. M. (2022). A golden era for volcanic gas geochemistry. *Bull. Volcanol.* 84, 43–11. doi:10.1007/s00445-022-01556-6

Kern, C., Deutschmann, T., Vogel, L., Wöhrbach, M., Wagner, T., and Platt, U. (2010). Radiative transfer corrections for accurate spectroscopic measurements of volcanic gas emissions. *Bull. Volcanol.* 72, 233–247. doi:10.1007/s00445-009-0313-7

Kern, C., Masias, P., Apaza, F., Reath, K. A., and Platt, U. (2017). Remote measurement of high preeruptive water vapor emissions at Sabancaya volcano by passive differential optical absorption spectroscopy. *J. Geophys. Res. Solid Earth* 122, 3540–3564. doi:10.1002/2017JB014020

Kern, C., Werner, C., Elias, T., Sutton, A. J., and Lübcke, P. (2013). Applying UV cameras for SO_2 detection to distant or optically thick volcanic plumes. *J. Volcanol. Geotherm. Res.* 262, 80–89. doi:10.1016/j.jvolgeores.2013.06.009

KushendratnoPallister, J. S., Kristianto, Bina, F. R., McCausland, W., Carn, S., et al. (2012). Recent explosive eruptions and volcano hazards at Soputan volcano-a basalt stratovolcano in north Sulawesi, Indonesia. *Bull. Volcanol.* 74, 1581–1609. doi:10.1007/s00445-012-0620-2

Lesne, P., Kohn, S. C., Blundy, J., Witham, F., Botcharnikov, R. E., and Behrens, H. (2011). Experimental simulation of closed-system degassing in the system basalt-H2O-CO2-S-Cl. *J. Pet.* 52, 1737–1762. doi:10.1093/petrology/egr027

Marzocchi, W., and Bebbington, M. S. (2012). Probabilistic eruption forecasting at short and long time scales. *Bull. Volcanol.* 74, 1777–1805. doi:10.1007/s00445-012-0633-x

Marzocchi, W., Sandri, L., and Selva, J. (2008). BET_EF: A probabilistic tool for long- and short-term eruption forecasting. *Bull. Volcanol.* 70, 623–632. doi:10.1007/s00445-007-0157-y

McCausland, W. A., Gunawan, H., White, R. A., Indrastuti, N., Patria, C., Suparman, Y., et al. (2019). Using a process-based model of pre-eruptive seismic patterns to forecast evolving eruptive styles at Sinabung Volcano, Indonesia. *J. Volcanol. Geotherm. Res.* 382, 253–266. doi:10.1016/j.jvolgeores.2017.04.004

Métrich, N., and Wallace, P. J. (2008). Volatile abundances in basaltic magmas and their degassing paths tracked by melt inclusions. *Rev. Mineral. Geochem.* 69, 363–402. doi:10.2138/rmg.2008.69.10

Morrissey, M. M., and Mastin, L. G. (2000). "Vulcanian eruptions," in *Encyclopedia of volcanoes*. Editors H. Sigurdsson, B. F. Houghton, S. R. McNutt, H. Rymer, and J. Stix (San Diego, San Francisco, New York, Boston, London, Syndey, Toronto: Academic Press), 463–475.

Nakada, S., Zaennudin, A., Yoshimoto, M., Maeno, F., Suzuki, Y., Hokanishi, N., et al. (2019). Growth process of the lava dome/flow complex at Sinabung Volcano during 2013–2016. *J. Volcanol. Geotherm. Res.* 382, 120–136. doi:10.1016/j.jvolgeores.2017.06.012

Otneil Ketaren, S., Sudibyato, H. A., Hasan, W., and Purba, A. (2016). Environmental health aspect in health emergency management (a case study : Sinabung vulcanous eruption). *Int. J. Appl. Nat. Sci.* 5, 47–56.

Pallister, J., Papale, P., Eichelberger, J., Newhall, C., Mandeville, C., Nakada, S., et al. (2019b). Volcano observatory best practices (VOBP) workshops - a summary of findings and best-practice recommendations. *J. Appl. Volcanol.* 8, 2. doi:10.1186/s13617-019-0082-8

Pallister, J., Wessels, R., Griswold, J., McCausland, W., Kartadinata, N., Gunawan, H., et al. (2019a). Monitoring, forecasting collapse events, and mapping pyroclastic deposits at Sinabung volcano with satellite imagery. *J. Volcanol. Geotherm. Res.* 382, 149–163. doi:10.1016/j.jvolgeores.2018.05.012

Platt, U., and Stutz, J. (2008). *Differential optical absorption spectroscopy - principles and applications*. Berlin, Heidelberg: Springer. doi:10.1007/978-3-540-75776-4

Power, J. A., Roman, D. C., Lyons, J. J., Haney, M. M., Rasmussen, D. J., Plank, T., et al. (2021). Volcanic seismicity beneath Chuginadak Island, Alaska (Cleveland and Tana volcanoes): Implications for magma dynamics and eruption forecasting. *J. Volcanol. Geotherm. Res.* 412, 107182. doi:10.1016/j.jvolgeores.2021.107182

Primulyana, S., Kern, C., Lerner, A. H., Saing, U. B., Kunrat, S. L., Alfianti, H., et al. (2019). Gas and ash emissions associated with the 2010-present activity of Sinabung Volcano, Indonesia. *J. Volcanol. Geotherm. Res.* 382, 184–196. doi:10.1016/j.jvolgeores.2017.11.018

Rouwet, D., Mora Amador, R. A., Sandri, L., Ramírez-Umaña, C., González, G., Pecoraino, G., et al. (2019). "39 years of geochemical monitoring of laguna caliente crater lake, Poás: Patterns from the past as keys for the future," in *Poás volcano. Active volcanoes of the world*. Editors F. Tassi, O. Vaselli, and R. Mora Amador (Springer), 213–233. doi:10.1007/978-3-319-02156-0_9

Sandri, L., Garcia, A., Costa, A., Guerrero Lopez, A., and Cordoba, G. (2021). Stochastic modeling of explosive eruptive events at Galeras Volcano, Colombia. *Front. Earth Sci.* 8, 1–19. doi:10.3389/feart.2020.583703

Scaillet, B., and Pichavant, M. (2005). A model of sulphur solubility for hydrous mafic melts: Application to the determination of magmatic fluid compositions of Italian volcanoes. *Ann. Geophys.* 48, 671–698. doi:10.4401/ag-3226

Sparks, R. S. J. (2003). Forecasting volcanic eruptions. *Earth Planet. Sci. Lett.* 210, 1–15. doi:10.1016/S0012-821X(03)00124-9

Sparks, R. S. J. (1986). The dimensions and dynamics of volcanic eruption columns. *Bull. Volcanol.* 48, 3–15. doi:10.1007/BF01073509

Stix, J., and de Moor, J. M. (2018). Understanding and forecasting phreatic eruptions driven by magmatic degassing. *Earth Planets Space* 70, 83. doi:10.1186/s40623-018-0855-z

Trnkoczy, A. (2012). "Understanding and parameter setting of STA/LTA trigger algorithm," in *New manual of seismological observatory practice 2. Potsdam: Deutsches Geoforschungszentrum)*. Editor P. Bormann, 1–20. doi:10.2312/GFZ.NMSOP-2_IS_8.1

Varley, N., Arámbula-Mendoza, R., Reyes-Dávila, G., Sanderson, R., and Stevenson, J. (2010). Generation of Vulcanian activity and long-period seismicity at Volcán de Colima, Mexico. *J. Volcanol. Geotherm. Res.* 198, 45–56. doi:10.1016/j.jvolgeores.2010.08.009

Viccaro, M., Cannata, A., Cannavò, F., De Rosa, R., Giuffrida, M., Nicotra, E., et al. (2021). Shallow conduit dynamics fuel the unexpected paroxysms of Stromboli volcano during the summer 2019. *Sci. Rep.* 11, 266–315. doi:10.1038/s41598-020-79558-7

Wallace, P. J., and Edmonds, M. (2011). The sulfur budget in magmas: Evidence from melt inclusions, submarine glasses, and volcanic gas emissions. *Rev. Mineral. Geochem.* 73, 215–246. doi:10.2138/rmg.2011.73.8

Webster, J. D., and Botcharnikov, R. E. (2011). Distribution of sulfur between melt and fluid in S-O-H-C-Cl-bearing magmatic systems at shallow crustal pressures and temperatures. *Rev. Mineral. Geochem.* 73, 247–283. doi:10.2138/rmg.2011.73.9

Werner, C., Kelly, P. J., Doukas, M., Lopez, T., Pfeffer, M., McGimsey, R., et al. (2013). Degassing of CO_2, SO_2, and H_2S associated with the 2009 eruption of Redoubt Volcano, Alaska. *J. Volcanol. Geotherm. Res.* 259, 270–284. doi:10.1016/j.jvolgeores.2012.04.012

Werner, C., Rasmussen, D. J., Plank, T., Kelly, P. J., Kern, C., Lopez, T., et al. (2020). Linking subsurface to surface using gas emission and melt inclusion data at Mount Cleveland

Volcano, Alaska. *Geochem. Geophys. Geosyst.* 21, 1–33. doi:10.1029/2019GC008882

Wickman, F. E. (1976). "Markov models of repose-period patterns of volcanoes," in *Random processes in geology*. Editor D. F. Merriam (Berlin, Heidelberg, New York: Springer), 135–161. Available at: https://link.springer.com/chapter/10.1007/978-3-642-66146-4_11.

Withers, M., Aster, R., Young, C., Beiriger, J., Harris, M., Moore, S., et al. (1998). A comparison of select trigger algorithms for automated global seismic phase and event detection. *Bull. Seismol. Soc. Am.* 88, 95–106. doi:10.1785/bssa0880010095

Wright, H. M. N., Pallister, J. S., McCausland, W. A., Griswold, J. P., Andreastuti, S., Budianto, A., et al. (2019). Construction of probabilistic event trees for eruption forecasting at Sinabung volcano, Indonesia 2013–14. *J. Volcanol. Geotherm. Res.* 382, 233–252. doi:10.1016/j.jvolgeores.2018.02.003

Yokoo, A., Iguchi, M., Tameguri, T., and Yamamoto, A. (2013). Processes prior to outbursts of vulcanian eruption at Show Crater of Sakurajima. *Bull. Volcanol. Soc. Jpn.* 58, 163–181. doi:10.18940/kazan.58.1_163

frontiers | Frontiers in Earth Science

TYPE Original Research
PUBLISHED 13 September 2022
DOI 10.3389/feart.2022.976962

OPEN ACCESS

EDITED BY
Silvana Hidalgo,
Escuela Politécnice Nacional, Ecuador

REVIEWED BY
Jonathan Dehn,
University of Alaska Fairbanks,
United States
Tushar Mittal,
Massachusetts Institute of Technology,
United States

*CORRESPONDENCE
S. A. Carn,
scarn@mtu.edu

SPECIALTY SECTION
This article was submitted to Volcanology, a section of the journal Frontiers in Earth Science

RECEIVED 23 June 2022
ACCEPTED 19 August 2022
PUBLISHED 13 September 2022

CITATION
Carn SA, Krotkov NA, Fisher BL and Li C (2022), Out of the blue: Volcanic SO_2 emissions during the 2021–2022 eruptions of Hunga Tonga—Hunga Ha'apai (Tonga). *Front. Earth Sci.* 10:976962. doi: 10.3389/feart.2022.976962

Out of the blue: Volcanic SO_2 emissions during the 2021–2022 eruptions of Hunga Tonga—Hunga Ha'apai (Tonga)

S. A. Carn[1]*, N. A. Krotkov[2], B. L. Fisher[3] and C. Li[2,4]

[1]Department of Geological and Mining Engineering and Sciences, Michigan Technological University, Houghton, MI, United States, [2]Atmospheric Chemistry and Dynamics Laboratory, NASA Goddard Space Flight Center, Greenbelt, MD, United States, [3]Science Systems and Applications, Inc (SSAI), Lanham, MD, United States, [4]Earth System Science Interdisciplinary Center, University of Maryland, College Park, MD, United States

Most volcanism on Earth is submarine, but volcanic gas emissions by submarine eruptions are rarely observed and hence largely unquantified. On 15 January 2022 a submarine eruption of Hunga Tonga-Hunga Ha'apai (HTHH) volcano (Tonga) generated an explosion of historic magnitude, and was preceded by ~1 month of Surtseyan eruptive activity and two precursory explosive eruptions. We present an analysis of ultraviolet (UV) satellite measurements of volcanic sulfur dioxide (SO_2) between December 2021 and the climactic 15 January 2022 eruption, comprising an unprecedented record of Surtseyan eruptive emissions. UV measurements from the Ozone Monitoring Instrument (OMI) on NASA's Aura satellite, the Ozone Mapping and Profiler Suite (OMPS) on Suomi-NPP, the Tropospheric Monitoring Instrument (TROPOMI) on ESA's Sentinel-5P, and the Earth Polychromatic Imaging Camera (EPIC) aboard the Deep Space Climate Observatory (DSCOVR) are combined to yield a consistent multi-sensor record of eruptive degassing. We estimate SO_2 emissions during the eruption's key phases: the initial 19 December 2021 eruption (~0.01 Tg SO_2); continuous SO_2 emissions from 20 December 2021—early January 2022 (~0.12 Tg SO_2); the 13 January 2022 stratospheric eruption (0.06 Tg SO_2); and the paroxysmal 15 January 2022 eruption (~0.4–0.5 Tg SO_2); yielding a total SO_2 emission of ~0.6–0.7 Tg SO_2 for the eruptive episode. We interpret the vigorous SO_2 emissions observed prior to the January 2022 eruptions, which were significantly higher than measured in the 2009 and 2014 HTHH eruptions, as strong evidence for a rejuvenated magmatic system. High cadence DSCOVR/EPIC SO_2 imagery permits the first UV-based analysis of umbrella cloud spreading and volume flux in the 13 January 2022 eruption, and also tracks early dispersion of the stratospheric SO_2 cloud injected on January 15. The ~0.4–0.5 Tg SO_2 discharged by the paroxysmal 15 January 2022 HTHH eruption is low relative to other eruptions of similar magnitude, and a review of other submarine eruptions in the satellite era indicates that modest SO_2 yields may be characteristic of submarine volcanism, with the emissions and atmospheric impacts likely dominated by water vapor. The origin of the low SO_2 loading awaits further investigation but scrubbing of SO_2 in the water-rich eruption plumes and rapid conversion to sulfate aerosol are plausible, given the exceptional water emission by the 15 January 2022 HTHH eruption.

KEYWORDS

volcanic emissions, submarine eruptions, satellite remote sensing, sulfur dioxide, volcanic eruption chronology

1 Introduction

The majority of active volcanism on Earth (~70%) is submarine; a realm where the eruption products are inaccessible to remote sensing techniques that use electromagnetic radiation (Schmincke, 2006). Submarine volcanic emissions thus remain largely undetected or unquantified, except in the relatively rare cases when submarine eruptions generate surface manifestations of activity such as pumice rafts or volcanic plumes that breach the ocean surface and rise into the atmosphere (e.g., Martí et al., 2013; Green et al., 2013; Jutzeler et al., 2014, 2020; Carey et al., 2018). The latter occurred in dramatic fashion during the 15 January 2022 eruption of Hunga Tonga—Hunga Ha'apai (HTHH), a submarine volcano in Tonga. The 15 January 2022 HTHH eruption, which was the culmination of an eruptive sequence that began in December 2021, produced an eruption column with overshooting tops that rose to lower mesospheric altitudes (~55 km) (Carr et al., 2022), an umbrella cloud that rivalled the 1991 Pinatubo eruption in horizontal extent (Gupta et al., 2022), a plethora of atmospheric waves that propagated globally (Matoza et al., 2022; Wright et al., 2022), vigorous lightning, and local and distal tsunamis (Kubota et al., 2022). The highly explosive nature of the 2022 HTHH eruption was driven by violent magma-seawater interaction, and the event drew comparisons with the 1883 eruption of Krakatau (Indonesia), which produced some analogous atmospheric wave phenomena (Symons, 1888). However, the extent of magma-seawater interaction in the 1883 Krakatau eruption is still debated and may have been limited during most of the eruption sequence (e.g., Self, 1992; Madden-Nadeau et al., 2022), whereas the 2022 HTHH eruption vent was clearly submarine at the onset of the eruption on 15 January 2022. Analysis of the 2022 HTHH eruption therefore provides an unprecedented opportunity to gain insight into violent, shallow submarine eruptions, and into the potential hazards and atmospheric impacts of explosive submarine volcanism.

Here, we present an analysis of sulfur dioxide (SO_2) measurements collected by ultraviolet (UV) satellite instruments during the 2021–2022 eruptive sequence at HTHH, culminating in the paroxysmal 15 January 2022 event. Our goals are to analyze SO_2 emissions prior to the paroxysmal January 15 eruption, to estimate total SO_2 emissions during the HTHH eruptions and aid assessment of potential impacts on the atmosphere and climate, and to gain insight into the fate of volcanic SO_2 emissions during water-rich, explosive submarine eruptions. Whilst the potential for scavenging of volcanic SO_2 by hydrometeors (derived from water of magmatic and atmospheric origin) and volcanic ash particles in subaerial volcanic eruption plumes is well known (e.g., Rose et al., 1995; Textor et al., 2003; Zhu et al., 2020), recent modeling work suggests that such scavenging is enhanced in submarine eruptions involving external surface water (Rowell et al., 2022). As the largest submarine explosive eruption to date in the era of UV satellite observations (since 1978), the 2022 HTHH eruption provides some unique observational constraints on these processes. We also provide a new analysis of SO_2 emissions associated with other submarine volcanic eruptions in the UV satellite era to place the HTHH eruption in context.

2 2021–2022 HTHH eruption

The islands of Hunga Tonga and Hunga Ha'apai (20.536°S, 175.382°W; elevation 114 m) are the subaerial fragments of the massive, submarine Hunga volcano that rises more than 2000 m from the surrounding seafloor in the Tofua volcanic arc (Cronin et al., 2017). Prior to 2021–22, confirmed eruptions of HTHH occurred in June 1988 March 2009, and December 2014–15 (Global Volcanism Program, 2013), with the latter two eruptions including periods of island growth and erosion (Vaughan and Webley, 2010; Garvin et al., 2018). The typical eruption style of HTHH is the rarely observed Surtseyan style of activity, involving magma-seawater interaction, ephemeral island growth, and emission of volcanic plumes rich in water vapor, condensed water and fine volcanic ash, with the potential for significant scrubbing of SO_2 emissions via chemical scavenging and ash sedimentation (e.g., Rowell et al., 2022).

In the intervening years between the 2014–2015 and 2021–2022 HTHH eruptions, high-resolution satellite imagery (e.g., Planet Labs, https://www.planet.com/; Planet Team, 2017) shows persistent seawater discoloration around HTHH, indicative of ongoing submarine hydrothermal activity or degassing as observed at other active submarine volcanoes (e.g., Yeo et al., 2022). However, we have not attempted to track or quantify this inter-eruptive activity here. The 2021–2022 HTHH eruption sequence began abruptly on 20 December 2021 at 09:35 local time in Tonga (20:35 UTC on December 19) with what was (at the time) a significant explosive eruption for HTHH, though this event was much smaller than the subsequent explosive eruptions in January 2022. As we document below, the December 2021 eruption was followed by a period of near-continuous Surtseyan eruptive activity and SO_2 emissions that continued until early January 2022. After a 7–10 days lull in significant subaerial activity, another major explosive eruption occurred on 13 January 2022 at 15:20 UTC, followed by the paroxysmal event at 04:00 UTC on January 15.

TABLE 1 UV satellite instruments.

Sensor	Satellite	Spatial resolution (nadir, km)	Temporal resolution	SO_2 algorithm
OMI	Aura	13 × 24	1 day	*Li et al.* (2017)
OMPS	Suomi-NPP	50 × 50	1 day	*Li et al.* (2017)
EPIC	DSCOVR	18 × 18	~110 min (daytime)	*Fisher et al.* (2019)
TROPOMI	S5P	5.5 × 3.5	1 day	*Theys et al.* (2017)

3 Satellite data

The satellite SO_2 data used here are derived from four operational UV satellite sensors: the Ozone Monitoring Instrument (OMI), operating on NASA's Aura satellite since 2004 (Levelt et al., 2018); the Ozone Mapping and Profiler Suite (OMPS), operating on the NASA/NOAA Suomi-NPP satellite since 2012 (Carn et al., 2015); the Earth Polychromatic Imaging Camera (EPIC), observing Earth from the Deep Space Climate Observatory (DSCOVR) at the L1 Earth-Sun Lagrange point (1,000,000 miles from Earth) since 2015 (Marshak et al., 2018); and the Tropospheric Monitoring Instrument (TROPOMI), operating on ESA's Sentinel-5 Precursor (S5P) satellite since 2017 (Veefkind et al., 2012). Some key characteristics of these instruments are given in Table 1. OMI, OMPS and TROPOMI are aboard polar-orbiting satellites and hence have daily temporal resolution at the tropical latitudes of Tonga, whereas DSCOVR/EPIC collects high cadence UV imagery and, as we demonstrate here, provides novel insight into the HTHH eruptions. During the 2021–2022 HTHH eruptions, DSCOVR was in 'winter cadence' mode, providing UV images every ~110 min (Herman et al., 2018).

Whilst all the UV instruments used here use backscattered UV radiation to retrieve vertical column densities (VCDs) of volcanic SO_2, differences in SO_2 sensitivity arise from variable spectral and spatial resolution and retrieval algorithms (Table 1). OMI, OMPS and TROPOMI are hyperspectral UV sensors capable of detecting VCDs of less than one Dobson Unit (DU; 1 DU = 2.69×10^{16} molecules cm^{-2}) in a single pixel (Li et al., 2017; Theys et al., 2017); hence the relative sensitivity of these sensors to SO_2 mass is governed mainly by pixel size. TROPOMI provides the highest spatial resolution (5.5 km × 3.5 km), followed by OMI (13 km × 24 km) and OMPS (50 km × 50 km; Table 1). DSCOVR/EPIC is a multi-spectral instrument with lower sensitivity to SO_2 (~5–10 DU per pixel; Fisher et al., 2019) but with the advantage of higher temporal resolution (Table 1). All UV SO_2 retrievals require an assumption of SO_2 plume altitude; current operational Level 2 (L2) SO_2 products from OMI, OMPS and TROPOMI provide volcanic SO_2 VCDs assuming center of mass altitudes (CMAs) of 8 km (mid-troposphere) and 18 km (lower stratosphere), the latter being most applicable to the explosive HTHH eruptions on 19 December 2021 and January 13–15, 2022 (Table 2). OMI and OMPS SO_2 data also include a lower tropospheric SO_2 product (CMA = 3 km), which we have used in conjunction with the mid-tropospheric products as an additional constraint on SO_2 emissions from the HTHH activity in December 2021—early January 2022, which produced lower tropospheric plumes (Table 2). All DSCOVR/EPIC SO_2 retrievals assume an upper tropospheric SO_2 CMA of 13 km (Fisher et al., 2019). In addition to the SO_2 products, we also use the EPIC UV Aerosol Index (UVAI; Carn et al., 2018) to map volcanic aerosols in the HTHH eruption clouds, where a positive UVAI indicates the presence of absorbing aerosols (e.g., volcanic ash) and a near-zero or negative UVAI indicates non-absorbing aerosols (e.g., sulfate aerosol or water/ice clouds).

The error budget for OMPS satellite SO_2 measurements in the stratospheric HTHH volcanic plumes includes contributions from spectral fitting uncertainty (~15%), differences between the assumed SO_2 CMA and the actual SO_2 vertical profile (~15%), and errors associated with the omission of aerosols from the SO_2 retrieval schemes (~30%). Here, we assume a relatively large contribution from the latter based on the water-rich plume and large stratospheric aerosol loading observed soon after the 15 January 2022 HTHH eruption (e.g., Sellitto et al., 2022). Despite the significant difference between the a priori lower stratospheric CMA (18 km) and the ~30–55 km plume height reported for the January 15 HTHH eruption (Carr et al., 2022; Gupta et al., 2022), the uncertainty related to plume height is relatively small for stratospheric SO_2 clouds regardless of altitude. Based on this error budget, combining the errors in quadrature yields a total uncertainty of ~35% on the OMPS stratospheric SO_2 measurements and we assume similar errors for OMI and TROPOMI. The EPIC SO_2 measurement uncertainty is larger due to the upper tropospheric CMA used in the retrievals; assuming a ~30% error related to plume height yields a total uncertainty of ~45%. Errors on lower tropospheric OMPS SO_2 retrievals also differ due to a larger contribution from plume height uncertainty at these altitudes (potentially ~50%), but smaller errors related to aerosols (~15%) due to lower aerosol loading. Assuming the same contributions from spectral fitting errors (~15%), the total uncertainty on lower tropospheric OMPS SO_2 measurements is ~54%. Finally, as mentioned earlier, we stress that all SO_2 data

TABLE 2 Satellite measurements of SO_2 emissions from HTHH during the December 2021—January 2022 eruption sequence.

Date (UT)	Time (UT)	Satellite/sensor	SO_2 (Tg)	Plume height (km)[a]	Notes
19 December 2021	**20:35**	**HTHH eruption**		**17**	
	20:53	DSCOVR/EPIC	0.0003		Low sensitivity
	22:41	DSCOVR/EPIC	0.002		Low sensitivity
December 20	01:25	Aura/OMI	0.01		
	02:00	SNPP/OMPS	0.01		
	02:03	S5P/TROPOMI	0.01		Figure 2
December 21	01:41	SNPP/OMPS	0.002	6–12	Surtseyan activity
December 22	01:22	SNPP/OMPS	0.013	8–14	Surtseyan activity
December 23	01:03	SNPP/OMPS	0.015	6–11	Surtseyan activity
December 24	00:44	SNPP/OMPS	0.015	3–12	Surtseyan activity
December 25	02:06	SNPP/OMPS	0.013		Surtseyan activity
December 26	01:47	SNPP/OMPS	0.011		Surtseyan activity
December 27	01:28	SNPP/OMPS	0.011	3–16	Surtseyan activity
December 28	01:09	SNPP/OMPS	0.015	<12	Surtseyan activity
December 29	00:50	SNPP/OMPS	0.011	<12	Surtseyan activity
December 30	02:12	SNPP/OMPS	0.005	<12	Surtseyan activity
December 31	01:53	SNPP/OMPS	0.006	3–18	Surtseyan activity
1 January 2022	01:34	SNPP/OMPS	0.006		Surtseyan activity
January 2	01:14	SNPP/OMPS	0.0001		Surtseyan activity
January 3–6					*No SO_2 detected*
January 7	01:21	SNPP/OMPS	0.00001		SO_2 degassing
January 8	01:06	S5P/TROPOMI	0.0005		SO_2 puff
January 9	00:47	S5P/TROPOMI	0.0001		SO_2 puff
January 10–12					*No SO_2 detected*
13 January 2022	**15:20**	**HTHH Eruption**		**18–19**	
	19:56	DSCOVR/EPIC	0.019		Figure 3A
	21:44	DSCOVR/EPIC	0.011		Figure 3B
January 14	00:27	DSCOVR/EPIC	0.010		Figure 3C
	00:50	SNPP/OMPS	0.056		Figure 5A
	00:54	S5P/TROPOMI	0.053		Figure 3D
	01:18	Aura/OMI	0.058		
	02:15	DSCOVR/EPIC	0.009		Low sensitivity
	04:03	DSCOVR/EPIC	0.032		High SZA/VZA[b]
	20:15	DSCOVR/EPIC	0.005		Partial coverage
January 15	02:12	SNPP/OMPS	0.059		Figure 5B
	02:16	S5P/TROPOMI	0.058		
January 15	**04:00**	**HTHH Eruption**		**30–55**	
	18:46	DSCOVR/EPIC	0.026		Partial coverage; Figure 6A
	20:34	DSCOVR/EPIC	0.22		Figure 6B
	22:22	DSCOVR/EPIC	0.09		Partial coverage
January 16	01:53	SNPP/OMPS	0.42		Figure 5C
	01:57	S5P/TROPOMI	0.40		Partial coverage

[a]Plume heights reported in *Global Volcanism Program* [2021a, 2021b, 2021c, 2022] and *Gupta et al.* (2022).
[b]SZA, solar zenith angle; VZA, viewing zenith angle.

for the HTHH eruption plumes must be evaluated in the context of potentially significant SO_2 removal by hydrometeors and volcanic ash (Rowell et al., 2022), and rapid conversion of volcanic SO_2 to sulfate aerosol in the water-rich plumes (Sellitto et al., 2022). A complete appraisal of the sulfur budget of the HTHH eruptions will require

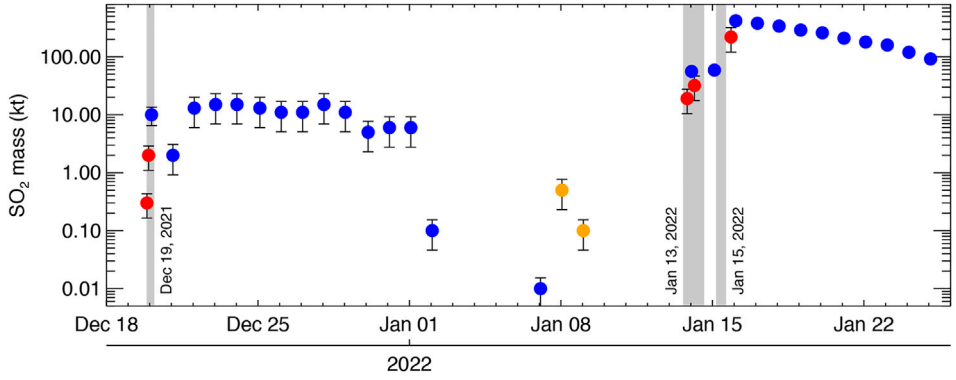

FIGURE 1
Time-series of SO_2 mass [in kilotons (kt) where 1 kt = 1,000 metric tons] measured by DSCOVR/EPIC (*red symbols*), SNPP/OMPS (*blue symbols*) and S5P/TROPOMI (*orange symbols*) during the December 2021—January 2022 HTHH eruption sequence. For clarity, only selected data from Table 2 are plotted here. SNPP/OMPS SO_2 data for January 16–26, 2022 are also included, showing the initial dispersion of the stratospheric SO_2 cloud emitted by HTHH on January 15. Error bars (see Section 3) are only shown where they are larger than the symbol size. *Gray shading* shows the approximate durations of the HTHH eruptions on 19 December 2021, 13 January 2022, and 15 January 2022, as reported by Gupta et al. (2022).

consideration of the sulfate aerosol component not measured by the UV satellite instruments.

All SO_2 products used here are publicly available via the NASA Earthdata portal (https://search.earthdata.nasa.gov/search). We use the Version 003 OMI L2 SO_2 product (OMSO2_003), the Version two OMPS Principal Component Analysis (PCA) SO_2 product (OMPS_NPP_NMSO2_PCA_L2_2) and the Version two DSCOVR/EPIC SO_2 product (DSCOVR_EPIC_L2_SO2_02). TROPOMI SO_2 data are derived from the Offline L2 SO_2 product (S5P_OFFL_L2__SO2), available from NASA Earthdata or the Sentinel-5P Pre-Operations Data Hub (https://s5phub.copernicus.eu/dhus/#/home). Measurements of SO_2 emissions for other volcanic eruptions of the satellite era are derived from Version four of the NASA MEaSUREs Multi-Satellite Volcanic SO_2 Level 4 Long-Term Global database (MSVOLSO2L4; Carn, 2022).

4 Results

Here, we summarize the UV satellite SO_2 measurements in chronological order of the 2021–2022 HTHH eruption sequence (local time in Tonga is 13 h ahead of UTC). The SO_2 measurements from OMI, OMPS, TROPOMI, and DSCOVR/EPIC analyzed here are provided in Table 2, and a subset of these SO_2 data are plotted as a time-series in Figure 1.

4.1 The 20 December 2021 eruption

At the time, the eruption of HTHH at 20:35 UTC on 19 December 2021 (09:35 local time on December 20), was a significant event for the volcano, generating a steam-rich eruption plume that rose to the tropopause or lower stratosphere (~17 km altitude; Gupta et al., 2022), accompanied by lightning, ash emissions and audible explosions (Global Volcanism Program, 2021a). Due to its high temporal resolution, DSCOVR/EPIC detected SO_2 in the eruption plume as early as 20:53 UT on December 19 (~20 min after the eruption onset; Figure 1 and Table 2), although SO_2 columns were close to the detection limit. Later OMI, OMPS and TROPOMI overpasses at 01:25–02:03 UTC measured ~0.01 Tg SO_2 in the volcanic plume (Figure 2; Table 2), and the SO_2 emitted by this eruption continued to be detected for several days. This confirms the upper tropospheric or lower stratospheric injection height, since SO_2 lifetimes longer than ~3 days in the tropics are characteristic of volcanic plumes at these altitudes (e.g., Carn et al., 2016).

4.2 Continuous emissions: December 2021—January 2022

Following the December 19 eruption, HTHH began a phase of continuous Surtseyan eruptive activity (Global Volcanism Program, 2021b; 2021c), accompanied by SO_2 emissions, that continued until 2 January 2022 (Figure 1; Table 2). In Table 2, we report daily SO_2 loadings measured in the HTHH eruption plumes by SNPP/OMPS, though similar SO_2 amounts were also measured by OMI and TROPOMI. Reported plume heights during this period of activity were highly variable, ranging from lower-to upper-tropospheric altitudes (Table 2; Gupta et al., 2022). To constrain SO_2 emissions during this period, we have used the lower- and mid-tropospheric OMPS

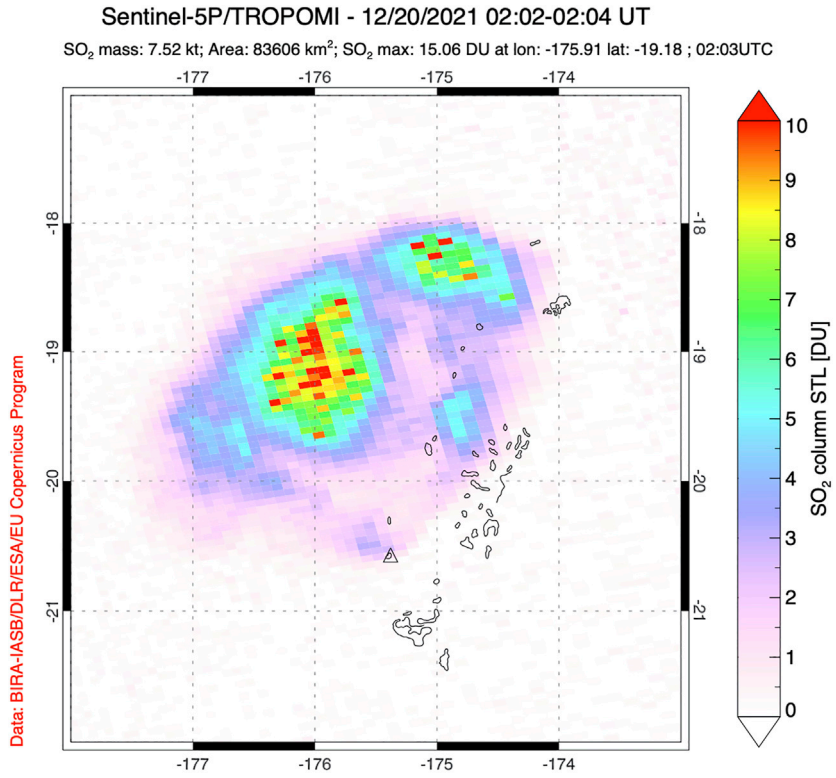

FIGURE 2
Lower stratospheric (STL) SO_2 columns measured by S5P/TROPOMI in the volcanic cloud produced by the eruption of HTHH at 20:35 UTC on 19 December 2021. The S5P/TROPOMI overpass was ~5.5 h after the eruption at 02:03 UTC on December 20. The retrieved SO_2 columns (<10 DU) and the total SO_2 mass (8 kilotons; ~0.01 Tg) are both relatively low for a fresh, upper tropospheric volcanic cloud. Scale: 1° in latitude/longitude corresponds to a distance of ~100 km.

SO_2 products to calculate SO_2 amounts, based on an assessment of bulk SO_2 plume altitude derived from inspection of SO_2 plume maps and winds from regional radiosondes (e.g., from Pago, American Samoa; available from http://weather.uwyo.edu/upperair/sounding.html). This analysis suggests that the peak plume altitudes reported in Table 2 were produced by transient explosions, with most of the SO_2 residing at lower altitudes in the lower-to mid-troposphere.

The cumulative SO_2 mass measured by OMPS in this period (21 December 2021—2 January 2022) is ~0.12 Tg SO_2, and given the water-rich, Surtseyan style of activity (with substantial scrubbing of SO_2 likely) we consider this a minimum estimate of actual SO_2 emissions. No SO_2 emissions were detected by OMI, OMPS or TROPOMI from January 3–6, 2022, though it is possible that heavy cloud cover over Tonga at this time obscured any plumes. Weak emissions of SO_2 resumed temporarily on January 7, and a few discrete 'puffs' of SO_2 were detected by TROPOMI on January 8–9 (Figure 1; Table 2). Although the latter contribute negligible amounts to the total SO_2 measured in this period, we interpret them as evidence of an at least partly 'open' volcanic system at this time, which may be significant in the context of the subsequent major explosive eruptions. After January 9, no further SO_2 emissions were detected until the major explosive eruption on January 13. Our observations are consistent with those of Gupta et al. (2022), who found no evidence for eruption plumes rising above the meteorological cloud deck from January 1–12, 2022.

We note that the satellite SO_2 observations (Figure 1) are broadly consistent with infrasound and hydrophone data reported by Matoza et al. (2022). Infrasound generated by the HTHH activity was recorded continuously from December 19–31, 2021, coincident with the strongest SO_2 emissions (Figure 1; Table 2), and regular hydrophone detections of activity show a lull from January 4–13, 2022, which is also consistent with the observed decline in SO_2 discharge (Figure 1), suggesting that this is genuine. Overall, we find the SO_2 emissions measured in the 21 December 2021—9 January 2022 period, which were significantly higher than emissions measured at HTHH during prior eruptions in 2009 and 2014–2015 (see Section 5.1 for discussion), to be strong evidence for a significant rejuvenation of the magmatic system at HTHH prior to the January 13–15 eruptions. This period of

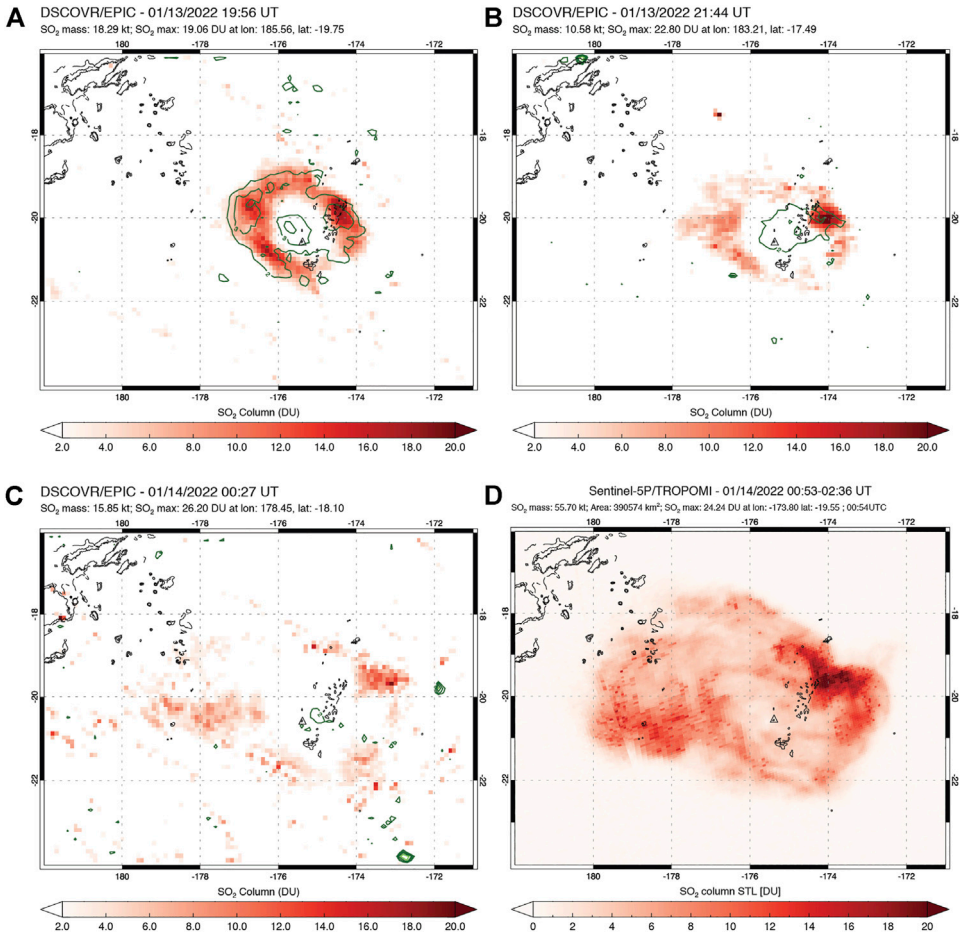

FIGURE 3
UV satellite observations of the 13 January 2022 HTHH volcanic SO_2 cloud by DSCOVR/EPIC and TROPOMI. *Green contours* in **(A–C)** show the EPIC UV Aerosol Index (UVAI), where positive values indicate absorbing aerosols such as volcanic ash (note the low UVAI values in this case; UVAI ≤3). **(A)** DSCOVR/EPIC SO_2 data at 19:56 UTC; **(B)** DSCOVR/EPIC SO_2 data at 21:44 UTC; **(C)** DSCOVR/EPIC SO_2 data at 00:27 UTC on January 14; **(D)** S5P/TROPOMI SO_2 data at 00:53 UTC on January 14. Scale: 1° in latitude/longitude corresponds to a distance of ~100 km.

activity also involved substantial subaerial growth of the HTHH edifice, as seen in high resolution satellite imagery (e.g., Harrison, 2022).

4.3 The 13 January 2022 eruption

The HTHH eruption at 15:20 UTC on 13 January 2022 (04:20 local time in Tonga on January 14) was larger than the 19 December 2021 event. It produced a lower stratospheric, water/ice-rich umbrella cloud that expanded to 240 km in diameter at 20 km altitude (Global Volcanism Program, 2022; Gupta et al., 2022). Geostationary satellite observations of the umbrella cloud from Himawari-8 suggest that the eruption continued for nearly 24 h (Gupta et al., 2022). Based on umbrella cloud radius alone (~120 km), this eruption would rank as a Volcanic Explosivity Index (VEI) of 4 (Newhall and Self, 1982), and it exceeds the cloud radii observed in many VEI four magmatic eruptions of recent years (Constantinescu et al., 2021). SO_2 emitted by the eruption was detected by all the UV satellite instruments, with a consistent peak total SO_2 mass of ~0.06 Tg measured by OMI, OMPS and TROPOMI (Table 2; Figure 3). Due to its lower SO_2 sensitivity, DSCOVR/EPIC measured a lower total SO_2 mass (~0.03 Tg; Figure 1), but we focus here on the unique high cadence UV EPIC observations of the umbrella cloud.

DSCOVR/EPIC first detected SO_2 in the January 13 eruption cloud at 19:56 UTC on January 13 (06:56 local time on January 14), ~4.3 h after the eruption onset (Figure 3A). This first EPIC SO_2 image (the first UV satellite measurement of the eruption by any sensor) shows a distinctive ring-shaped feature with SO_2 only detected towards the margins of the expanding umbrella cloud,

TABLE 3 Growth of the 13 January 2022 HTHH volcanic SO_2 cloud observed by DSCOVR/EPIC and TROPOMI.

Date (UT)	Time (UT)	Time since eruption onset (min)	Plume area (km^2)	Equivalent radius (km)	Satellite/Sensor
January 13	19:56	264	104,500	182	DSCOVR/EPIC
January 13	21:44	372	126,000	200	DSCOVR/EPIC
January 14	00:27	535	261,100	288	DSCOVR/EPIC
January 14	00:54	562	366,600	341	S5P/TROPOMI

and SO_2 absent or below the EPIC detection limits (~5 DU) in the cloud core. Such an observation is highly unusual for a fresh eruption cloud, in which UV satellite measurements usually show high SO_2 columns, even in prior submarine eruptions such as at Bogoslof (Alaska, United States) in 2016–2017 (Carn et al., 2018). Furthermore, the retrieved EPIC UVAI values in the volcanic cloud are relatively low (maximum UVAI = ~3; Figure 3), suggesting that UV-absorbing volcanic ash was not dominant in the umbrella cloud. SO_2 amounts in explosive eruption clouds may be underestimated in the presence of high volcanic ash loading (e.g., UVAI >10), but we reject this as a cause of the low EPIC SO_2 columns in this case due to the low observed UVAI.

There are at least two plausible interpretations of the EPIC SO_2 data (Figure 3). The observed SO_2 distribution may be diagnostic of the water-rich, phreatomagmatic HTHH eruption in which SO_2 in the plume core was significantly scrubbed or entirely stripped from the plume by co-emitted water (derived from the magma, seawater and/or entrained atmosphere), as modeled by Rowell et al. (2022). Alternatively, the EPIC SO_2 observations may reflect temporally variable magmatic SO_2 emissions during the eruption, e.g., due to pre-eruptive accumulation of magmatic gases (including SO_2) at the top of the magma reservoir supplying the eruption. Either of these processes could also explain the spatial variation in SO_2 in the umbrella cloud, with higher SO_2 columns observed north-east of HTHH (Figure 3); e.g., if SO_2 scrubbing was spatially variable, or if the eruption involved multiple discrete explosions releasing variable amounts of SO_2. We are not able to distinguish these hypotheses with the available observations. The novel contribution of the EPIC SO_2 measurements, which show radial spreading of the SO_2 signal, is to confirm the presence of SO_2 in the umbrella cloud (Figures 3B,C). At the time of the eruption, the closest available radiosonde soundings, from Pago (American Samoa), show easterly winds in the lower stratosphere at 20 km altitude (Supplementary Figure S1); hence the EPIC SO_2 observation of SO_2 spreading east (i.e., upwind) is key. The EPIC measurements of umbrella cloud expansion with no concomitant increase in SO_2 mass loading (Table 2; Figure 3) strongly suggests that most of the mass added to the umbrella during the eruption was highly water-rich (and/or SO_2-poor). However, the early

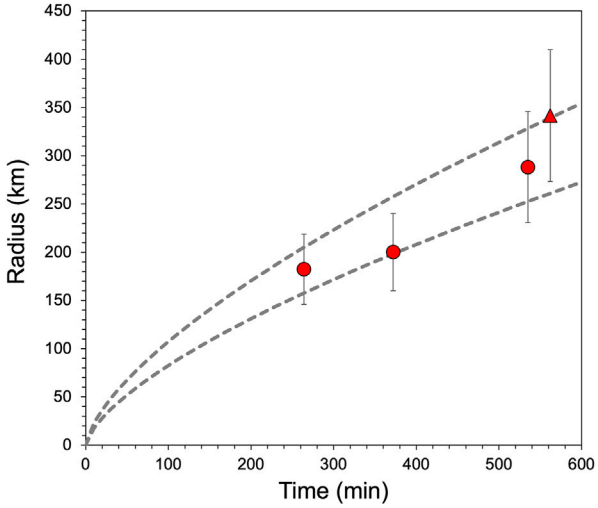

FIGURE 4
Equivalent radius of the January 13–14, 2022 HTHH umbrella cloud as observed in DSCOVR/EPIC (*circles*) and S5P/TROPOMI (*triangle*) SO_2 data between 19:56 UT on January 13 and 00:54 UT on January 14. Error bars denote 20% uncertainty on the cloud radii. *Gray lines* show the evolution of umbrella cloud radius predicted by the *Woods and Kienle* [1994] model for two volumetric flow rates (VFR) that bracket the satellite observations, assuming an eruption onset at 15:32 UT on January 13. The lower and upper bounds correspond to VFRs of 6.3 and 13.8 $km^3\ s^{-1}$, respectively.

detection of SO_2 by EPIC also confirms some magmatic gas input, perhaps concentrated in the first few hours of the ~24-h eruption via the emission of a volatile-rich cap.

Using the EPIC SO_2 measurements (Table 3) it is possible to estimate the bulk volumetric flow rate (VFR) of gas, ash and entrained atmosphere (V; $m^3\ s^{-1}$) into the eruption plume using the Woods and Kienle (1994) gravity current model of an expanding umbrella cloud at the neutral buoyancy height:

$$R = \left[\frac{3\lambda NV}{2\pi}\right]^{1/3} t^{2/3}$$

where R is the radius of the plume (estimated here as an equivalent radius $R = \sqrt{(A/\pi)}$, where A is the non-circular

SO_2 cloud area measured from the EPIC and TROPOMI SO_2 images in Figure 3 and Table 3), λ is an empirical constant related to the Froude number of the gravity current [(where 0.2 is an appropriate value for tropical atmospheres (Suzuki and Koyaguchi, 2009)], N is the Brunt-Väisälä frequency or buoyancy frequency of the ambient atmosphere (s^{-1}), and t is the time since the onset of plume spreading (assumed to be 15:32 UTC on 13 January 2022). Using a Pago radiosonde sounding at 12:00 UTC on January 13, we calculate a Brunt-Väisälä frequency of 0.026 s^{-1} at 20 km altitude for this case using the MetPy package (May et al., 2022). Based on these values, a fit of the Woods and Kienle (1994) model to the EPIC and TROPOMI observations (Table 3; Figure 4) yields VFRs of ~6–14 km^3 s^{-1}. Notably, our VFR estimates for the January 13 eruption are higher than that of Gupta et al. (2022), who report a VFR of ~5 km^3 s^{-1} for the first ~2 h of the eruption based on infrared (IR) geostationary Himawari-8 satellite data. Since our data cover a later phase of the eruption (~4–9 h after the eruption onset; Figure 4), this could reflect variable eruption dynamics, as alluded to above. This conclusion is also supported by the minimum Himawari-8 cloud-top brightness temperatures reported by Gupta et al. (2022), which show some significant variations during the eruption (related to variable cloud-top altitude and hence eruption intensity), especially after 00:00 UTC on January 14. As a further comparison, Prata et al. (2020) report a volume flux of ~5 km^3 s^{-1} for the explosive phase of the 2018 Anak Krakatau eruption (Indonesia), which was also phreatomagmatic.

Prior analysis of umbrella cloud growth during volcanic eruptions has been based on geostationary satellite imagery with higher temporal resolution than EPIC (e.g., Van Eaton et al., 2016; Prata et al., 2020; Gupta et al., 2022). Our study is the first attempt to use high-cadence UV imagery to analyze umbrella cloud growth, one key difference with prior work being that EPIC is sensitive to volcanic SO_2, whereas IR geostationary measurements of volcanic cloud spread are based on the cloud-top brightness temperature of the bulk, opaque plume (i.e., a mixture of volcanic gas, ash, hydrometeors, etc.). We acknowledge that our analysis is limited by temporal resolution (i.e., the first EPIC SO_2 observation is >4 h after the eruption onset (Figure 4), and hence missed any earlier umbrella growth phase, and EPIC's hourly cadence is lower than geostationary sensors) and EPIC's sensitivity (i.e., the volcanic cloud could be larger in extent than shown in the EPIC SO_2 data). However, although we might expect differences between VFRs calculated using the UV and IR satellite data (as shown here) the availability of DSCOVR/EPIC SO_2 data offers the potential for wider application of this technique and may provide better sensitivity to volcanic clouds under certain conditions (e.g., gas-rich and ash-poor eruptions).

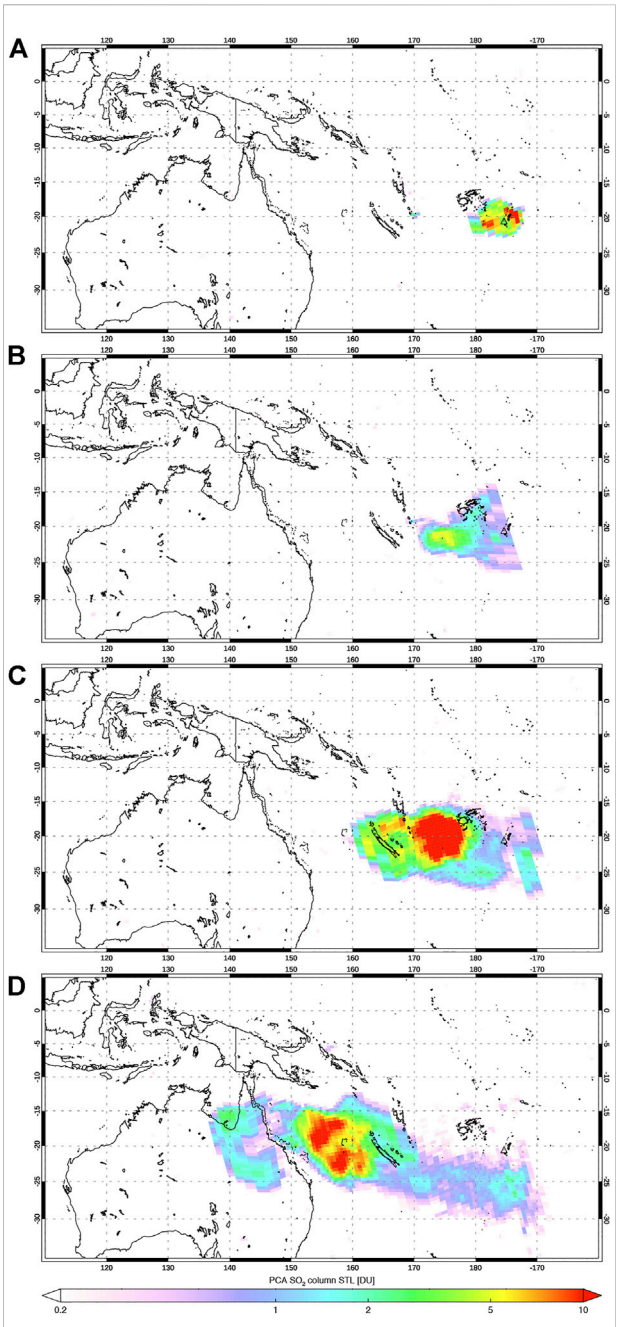

FIGURE 5
Daily SNPP/OMPS observations of HTHH SO_2 emissions from January 14–17, 2022. **(A)** 00:50 UTC on January 14 (0.06 Tg SO_2); **(B)** 02:12 UTC on January 15 (0.06 Tg SO_2); **(C)** 01:53 UTC on January 16 (0.4 Tg SO_2); **(D)** 03:16 UTC on January 17 (0.38 Tg SO_2). Scale: 1° in latitude/longitude corresponds to a distance of ~100 km.

4.4 The 15 January 2022 eruption

Following the January 13 eruption, the bulk of the emitted SO_2 drifted west from Tonga under the influence of the easterly

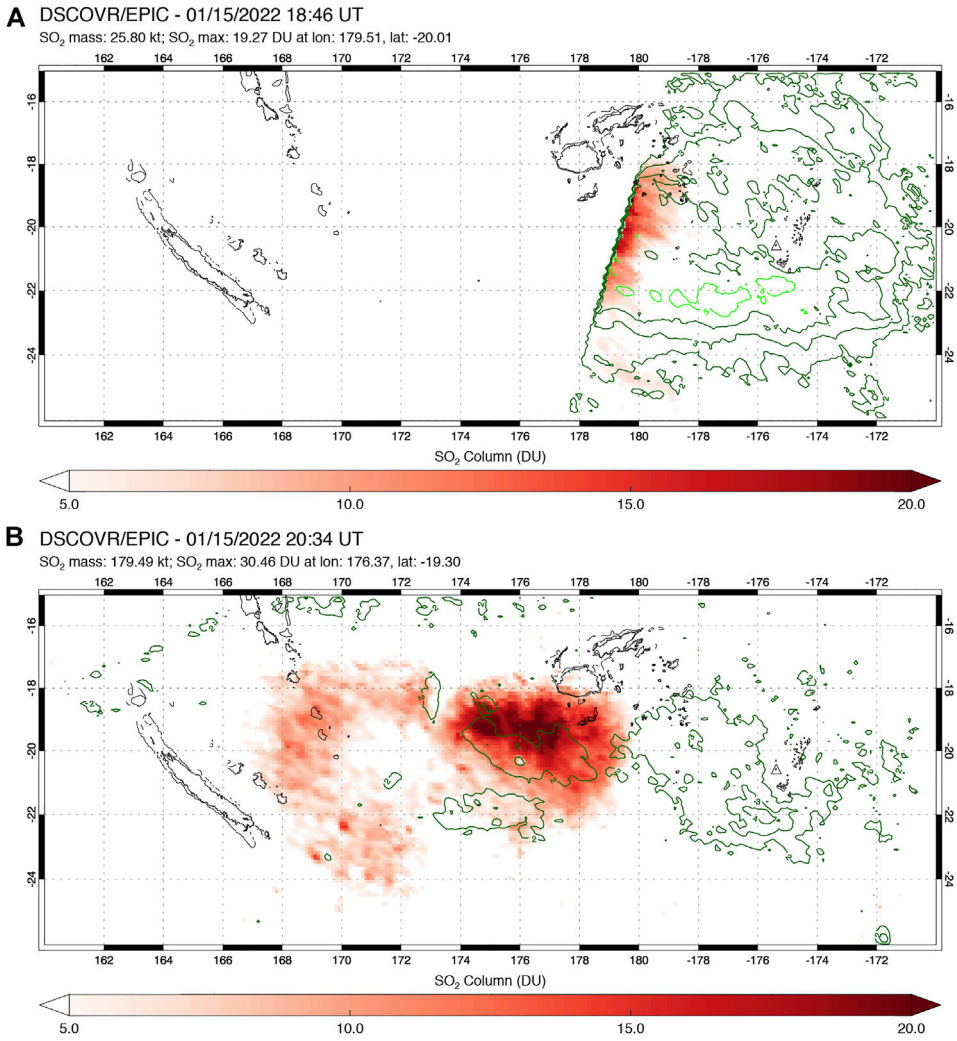

FIGURE 6
DSCOVR/EPIC observations of the 15 January 2022, HTHH eruption cloud. *Green contours* show the EPIC UV Aerosol Index (UVAI), where positive values indicate absorbing aerosols such as volcanic ash (but note the low UVAI values in this case). **(A)** Detection of the eastern edge of the plume at 18:46 UTC on January 15. The sharp boundary in the image is the terminator where the solar zenith angle becomes too high for UV measurements further west; **(B)** Full coverage of the volcanic SO_2 cloud at 20:34 UTC on January 15. Note the ~200 km westward drift of the SO_2 cloud in the 108 min between the two EPIC exposures. Scale: 1° in latitude/longitude corresponds to a distance of ~100 km.

lower stratospheric winds (Figure 5). The presence of the January 13 SO_2 cloud precludes detection of any SO_2 emissions between January 13 and 15 in UV satellite imagery, but inspection of geostationary GOES-West Advanced Baseline Imager (ABI) imagery (available in NASA Worldview; https://worldview.earthdata.nasa.gov/) reveals several 'puffs' from HTHH, on January 14 at 18:00 UTC and 21:10 UTC, and at 02:50 UTC on January 15, shortly before the major eruption (Supplementary Video S1). Hence sporadic emissions were clearly ongoing.

The paroxysmal HTHH eruption occurred at ~04:00 UTC on January 15, which is close to nightfall in Tonga (17:00 local time) and hence precluded early UV SO_2 observations of the nascent eruption cloud. A DSCOVR/EPIC exposure at 04:21 UTC, just ~20 min after the eruption, failed to detect any SO_2 due to the high solar zenith angle (SZA) or simply because the cloud was too small. Hence, in contrast to the January 13 eruption, analysis of umbrella cloud spread using the EPIC SO_2 data was not possible in this case. The first EPIC SO_2 observation on the following day (18:46 UTC on January 15; 09:46 local time on January 16 in Tonga) captured the eastern edge of the SO_2 cloud emitted by the January 15 eruption (Figure 6). The next EPIC exposure at 20:34 UTC shows a ~200 km westward drift of the SO_2 cloud in the 108 min elapsed between the measurements (Figure 6), indicating a wind speed of ~31 m/s. Such high wind speeds were only measured at altitudes above 30 km in the Pago sounding (Supplementary Figure S2), consistent with other

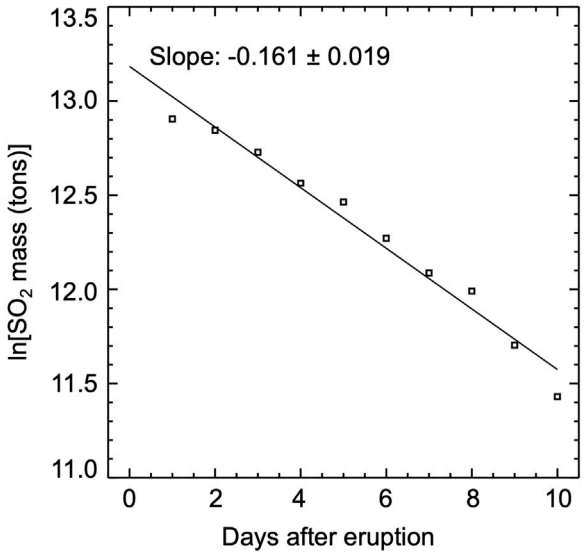

FIGURE 7
Trend in SO_2 mass measured by SNPP/OMPS in the 15 January 2022 HTHH eruption cloud during 10 days of atmospheric residence. The SO_2 mass e-folding time is ~6 days, and extrapolation of the SO_2 mass decay back to the eruption time yields an estimated initial SO_2 mass of 0.54 Tg.

constraints on the injection altitude of the January 15 HTHH SO_2 cloud (e.g., Carr et al., 2022; Gupta et al., 2022; Millán et al., 2022).

Whilst the DSCOVR/EPIC data provide information on SO_2 cloud transport, the total SO_2 mass of ~0.2 Tg measured by EPIC at 20:34 UTC on January 15 is an underestimate of the actual SO_2 loading due to the lower SO_2 VCDs than typically expected in a fresh volcanic cloud. More sensitive SNPP/OMPS observations at 01:53 UTC on January 16 measured ~0.4 Tg SO_2 in the volcanic cloud (Table 2; Figures 1, 5), though this also includes the ~0.06 Tg SO_2 emitted by the January 13 eruption, which is merged with the January 15 emissions. Very similar SO_2 amounts were measured by TROPOMI (Table 2).

SNPP/OMPS tracked the stratospheric volcanic SO_2 cloud produced by the January 13–15 HTHH eruptions for at least 10 days as it drifted west over Australia, the Indian Ocean and southern Africa (Figure 5; Supplementary Movie 2). Figure 7 shows the trend in SO_2 mass retrieved using the OMPS data, which indicate an e-folding time of ~6 days. This is short relative to other tropical stratospheric eruptions observed in the satellite era (e.g., Carn et al., 2016; Zhu et al., 2020). The January 15 HTHH eruption injected SO_2 to altitudes of over 30 km, where we would expect SO_2 lifetimes of ~30–40 days based on the 1982 El Chichón and 1991 Pinatubo eruptions. However, the submarine, phreatomagmatic HTHH eruption differs notably from these other, magmatic, eruptions in that it also injected a huge mass of water vapor into the mid-stratosphere, estimated at ~150 Tg H_2O by Millán et al. (2022) using Aura/Microwave Limb Sounder (MLS) data. As also proposed by other studies (e.g., Zhu et al., 2022), we suspect that the relatively short lifetime of the HTHH SO_2 is due to this co-emitted water vapor, which acts as a source of OH that in turn catalyzes the oxidation of SO_2 to H_2SO_4 (sulfate) aerosol (Glaze et al., 1997).

Using the observed SO_2 mass decay (Figure 7) we can also estimate the initial erupted SO_2 mass by extrapolating the trend back to the time of the January 15 eruption, assuming a constant decay rate. This yields an initial SO_2 mass loading of ~0.49–0.54 Tg, and subtracting the 0.06 Tg SO_2 emitted on January 13 leaves 0.43–0.48 Tg SO_2 produced by the January 15 eruption. This is in very good agreement with the 0.41 ± 0.02 Tg stratospheric SO_2 mass measured by Aura/MLS (Millán et al., 2022) and confirms that most or all the emitted SO_2 was injected into the stratosphere.

5 Discussion

5.1 Submarine volcanic eruptions of the satellite era

Here, we review available satellite measurements of SO_2 emissions for reported submarine eruptions in the satellite era (since 1978) to provide context for the 2021–2022 HTHH eruptions. As of April 2022, the Smithsonian Institution's Global Volcanism Program (GVP) reports 120 active Holocene submarine volcanoes, of which 80 have reported eruption dates and 40 last erupted since 1978 (Global Volcanism Program, 2013). Volcano elevations for the 40 submarine volcanoes that have erupted since 1978 range from −4,100 m [i.e., 4.1 km below sea level (bsl)] to 1.4 km above sea level with an average of ~0.9 km bsl. Note that elevations above sea level refer to the small, emergent portions of some submarine volcanic edifices, whereas the eruption vents are always below sea level. Some of the submarine volcanoes [e.g., HTHH, Home Reef and Lateiki (Tonga), Fukutoku-Oka-no-Ba (Japan)] have multiple reported eruptions since 1978, and it is perhaps not surprising that these are among the shallowest and hence more likely to produce plumes that breach the surface, although modeling of condensable submarine volcanic gas jets by Cahalan and Dufek (2021) suggests that surface breaching is possible from vents as deep as 500 m below sea level.

A review of global ultraviolet (UV) satellite SO_2 measurements since 1978 (Carn, 2022) reveals that ~13 submarine eruptions (not including the 2021–2022 HTHH eruptions) were sufficiently energetic to generate plumes that breached the ocean surface and produce potentially detectable SO_2 emissions (Table 4). Note that eruptions prior to 2004 were measured by the Total Ozone Mapping Spectrometer (TOMS) instruments, which had much lower sensitivity than OMI, OMPS, and TROPOMI (Carn et al.,

TABLE 4 Submarine volcanic eruptions in the satellite era (since 1978) with potential or confirmed subaerial plumes.

Volcano	Elevation (m)[a]	Eruption date(s)	SO_2 (kt)[b]	Plume height (km)[c]
Lateiki (Tonga)[d]	43	May-July 1979	nd	Pumice rafts
Home Reef (Tonga)	−10	1 March 1984	nd	12
Fukutoku-Oka-no-Ba (Japan)	−29	20 January 1986	5?	4?
Bogoslof (United States)	150	6 July 1992	nd	6
Fukutoku-Oka-no-Ba (Japan)	−29	1 July 2005	5?	1?
Home Reef (Tonga)	−10	August 8–15, 2006	~50	>5
HTHH (Tonga)	114	13 March 2009	0.5	4–7.6[e]
South Sarigan (CNMI)	−184	29 May 2010	1.1	12
HTHH (Tonga)	114	24 December 2014	14	3
Bogoslof (United States)	150	December 2016-August 2017	0.1–22[e]	12[e]
"Volcano F" (Tonga)	−200	August 6–8, 2019	nd	<1[e]
Lateiki (Tonga)	43	13 October 2019	0.2	3–5
Fukutoku-Oka-no-Ba (Japan)	−29	12 August 2021	20	17
HTHH (Tonga)	114	20 December 2021	10	17[e]
HTHH (Tonga)	114	13 January 2022	60	18–19[e]
HTHH (Tonga)	114	15 January 2022	400–500	30–55[e]

[a]Denotes the maximum elevation of each volcanic edifice above sea level. Although some volcanoes are partly emergent, all eruptions listed here are assumed to originate from submarine vents. Eruption vent depths are often unknown, as is the case for the 15 January 2022 HTHH eruption.
[b]From Carn [2022]; nd: none detected above sensor detection limits (~5–10 kt for eruptions in 1978–2003; ~0.05 kt for eruptions since 2004).
[c]Maximum reported volcanic plume height above sea level, as reported in the Smithsonian Institution Global Volcanism Program Volcanoes of the World database [Global Volcanism Program, 2013], unless otherwise noted. For some submarine eruptions (e.g., 1979 Lateiki), the only evidence of eruption is pumice rafts.
[d]Lateiki was previously known as Metis Shoal.
[e]2009 HTHH plume heights from Vaughan and Webley [2010]; 2016–2017 Bogoslof plume heights and SO^2 emissions from Lopez et al., 2020; 2019 "Volcano F" plume height from Jutzeler et al., 2020; 2021–2022 HTHH plume heights from Gupta et al., 2022 and Carr et al., 2022.

2016). Also, no TOMS instrument was operating in June 1995, when another submarine eruption occurred at Lateiki (Tonga) (Global Volcanism Program, 2013). Table 4 includes two prior eruptions of HTHH in 2009 and 2014–15, which produced lower tropospheric plumes. One of the more remarkable events in Table 4 was the May 2010 eruption of South Sarigan seamount (CNMI), which produced a subaerial eruption column that rose to ~12 km from an eruption vent at ~200 m water depth (Green et al., 2013; Searcy, 2013; Embley et al., 2014). To date, this appears to be the deepest submarine eruption to have produced SO_2 emissions detectable from space, although the measured SO_2 mass was low [~1 kiloton (kt)]. Indeed, in a review of subaqueous eruptions, Mastin and Witter (2000) list only two other submarine volcanoes reported to have produced surface breaching from depths of >100 m: at Kick'em Jenny (West Indies) in 1939, 1974 and 1988; and Ritter Island (Papua New Guinea) in 1972 and 1974. In these cases, the subaerial eruption columns extended only a few hundred meters above the ocean surface (Mastin and Witter, 2000). Nevertheless, the 2010 South Sarigan eruption showed that unpredictable, upper tropospheric plumes are a potential hazard of submarine eruptions, and the January 2022 HTHH eruptions demonstrate that in rare cases such plumes can penetrate deep into the stratosphere.

The data in Table 4 suggest that, despite the potential for upper tropospheric or stratospheric plumes, SO_2 emissions from submarine eruptions are typically lower than subaerial eruptions of comparable magnitude (i.e., generating similar plume heights). This is likely due to the significant scrubbing of SO_2 expected in water-rich, submarine eruption plumes. The 15 January 2022 HTHH eruption produced the highest SO_2 emissions measured during a submarine eruption to date (~0.4–0.5 Tg), and yet the SO_2 mass is relatively modest given the inferred magnitude of the event (VEI 5–6). The mean SO_2 yield for subaerial magmatic eruptions with VEI five is ~2.3 Tg (Carn et al., 2016), although there have been only five eruptions of this magnitude in the satellite era to date. Based on the data in Table 4, reduced SO_2 yield may be a consistent feature of submarine eruptions, with implications for their climate impacts, and making it difficult to assess the magnitude of such events based on SO_2 emissions alone.

As alluded to earlier, it is also apparent from Table 4 that the SO_2 emissions from HTHH in 2021–2022 were at least an order of magnitude higher than those measured during its previous eruptions in 2009 (0.0005 Tg SO_2) and 2014–2015 (0.014 Tg SO_2). This may be due in part to increasingly emergent (i.e., subaerial) activity since 2009, with higher SO_2 fluxes due to reduced scrubbing of SO_2. The abrupt onset, high altitude plume, and SO_2 loading associated with the 19 December 2021 HTHH eruption, coupled with the subsequent SO_2 emissions (Figure 1; Table 2), suggests that the onset of the

2021–2022 eruption sequence may have been driven by an injection of fresh magma into the volcano at shallow depths, promoting a phreatomagmatic eruption. Abrupt eruptions may also be triggered by second boiling of resident, cooling magma but are perhaps unlikely to be followed by increased SO_2 emissions without fresh magma recharge. The period of continuous eruptive activity at HTHH between December 2021 and early January 2022 (emitting ~0.12 Tg SO_2; Figure 1) is particularly significant, and in retrospect is a strong indication of a rejuvenated magmatic system prior to the January 13 and 15 eruptions. Although this may not represent a true eruption 'precursor', it was a much clearer manifestation of increased unrest than typically seen prior to submarine eruptions; e.g., before the 2019 Lateiki submarine eruption the only precursor was an 8-months non-unique increase in hydrothermal discharge (Yeo et al., 2022).

5.2 Modest SO_2 emissions in the 15 January 2022 eruption

Although the precise eruption magnitude and erupted volume remain uncertain, the 15 January 2022 HTHH eruption undoubtedly rivals the largest eruptions of the past Century or more. The maximum plume height of ~55 km for the overshooting tops (Carr et al., 2022) is unprecedented in the satellite era, Wright et al. (2022) estimate an eruption energy yield of 10–28 Exajoules (EJ; 1 EJ $=10^{18}$ J), and Matoza et al. (2022) report exceptional atmospheric Lamb wave amplitudes. Based on these metrics, the climactic 15 January 2022 HTHH explosion was likely larger than the 1991 Pinatubo eruption and comparable to the 1883 Krakatau eruption. However, the HTHH SO_2 discharge (~0.4–0.5 Tg) is ~2 orders of magnitude lower than those eruptions, which produced ~15–30 Tg SO_2.

Although a detailed analysis is beyond the scope of this paper, there are several plausible reasons for the modest measured SO_2 emission. The January 15 HTHH eruption emitted at least ~150 Tg of water vapor (Millán et al., 2022), likely dominated by evaporated seawater but potentially also including water vapor exsolved from magma and entrained from the atmosphere. Potentially significant amounts of SO_2 (and other soluble volcanic gases such as HCl) could have been scavenged by liquid water and ice particles in the water-rich HTHH plume (e.g., Textor et al., 2003; Rowell et al., 2022). The DSCOVR/EPIC observations of the January 13 eruption (Section 4.3) are potentially consistent with SO_2 scavenging by water, and this was perhaps even more efficient in the January 15 plume. Aura/MLS measured only a weak enhancement in stratospheric HCl on January 16–18 (Millán et al., 2022), which is also consistent with scavenging by water. Other satellite observations of the January 15 HTHH eruption show large stratospheric aerosol optical depths (AODs) soon after the event, attributed to rapid sulfate aerosol formation (Sellitto et al., 2022), which is another sink for SO_2. It is also possible that the magma driving the eruption was relatively sulfur-poor, or that sulfur outgassing was hindered by high hydrostatic pressures and premature quenching of fragmented magma before complete vesiculation, or complete suppression of magma fragmentation, which are expected in Surtseyan and other submarine eruptions (e.g., Lackschewitz et al., 1994; Colombier et al., 2018; Rowell et al., 2022). Finally, it is well-known that magma-water interaction in phreatomagmatic eruptions can generate one to two orders of magnitude greater explosion energy than magmatic eruptions (e.g., Sato and Taniguchi, 1997). Hence the magma mass supplying the HTHH eruption (i.e., the source of the emitted sulfur) could have been smaller than that erupted at Pinatubo or Krakatau, and yet could still have produced an explosion of comparable or larger size if magma-water interaction was highly efficient.

5.3 Water vapor emissions

Regardless of the origin of the modest SO_2 emissions, by far the most significant atmospheric impact of the January 15 HTHH eruption is likely to be the resulting stratospheric water vapor (H_2O) injection (Millán et al., 2022), which is also the probable cause of the short SO_2 lifetime (Figure 7; Supplementary Video S2) (Glaze et al., 1997; Zhu et al., 2022), and will likely impact the stratospheric aerosol evolution in significant ways, e.g., by increasing aerosol size and AOD (LeGrande et al., 2016). Millán et al. (2022) estimate a stratospheric H_2O loading of 146 ± 5 Tg using Aura/MLS data (~10% of the typical stratospheric water vapor burden), but the initial water vapor injection during the January 15 eruption could have been significantly higher due to early water loss to ice in the eruption plume (Guo et al., 2004; Zhu et al., 2022). It is worth noting that the emission of ~150 Tg H_2O by a volcanic eruption would not be unprecedented; using petrological arguments, Gerlach et al. (1996) estimated that the 1991 Pinatubo eruption emitted ~500 Tg H_2O (derived from magmatic degassing and an accumulated vapor phase), although no stratospheric H_2O anomaly was measured after the eruption. Guo et al. (2004) also measured an additional ~80 Tg of ice in the young Pinatubo volcanic cloud. However, the HTHH H_2O anomaly is unprecedented in its altitude (~25–30 km), and MLS H_2O measurements are the most effective way of tracking the zonal and meridional dispersion of the volcanic H_2O as it disperses in the stratosphere (Figure 8).

Volcanic eruptions can hydrate the stratosphere either by direct injection of H_2O (as at HTHH), or by heating of the cold-point tropopause by volcanic aerosols, which increases the flux of tropospheric water into the stratosphere (Kroll et al., 2021). Work by Glaze et al. (1997) on volcanic H_2O injection into the stratosphere found that larger eruption columns are dominated by magmatic water (not entrained atmospheric

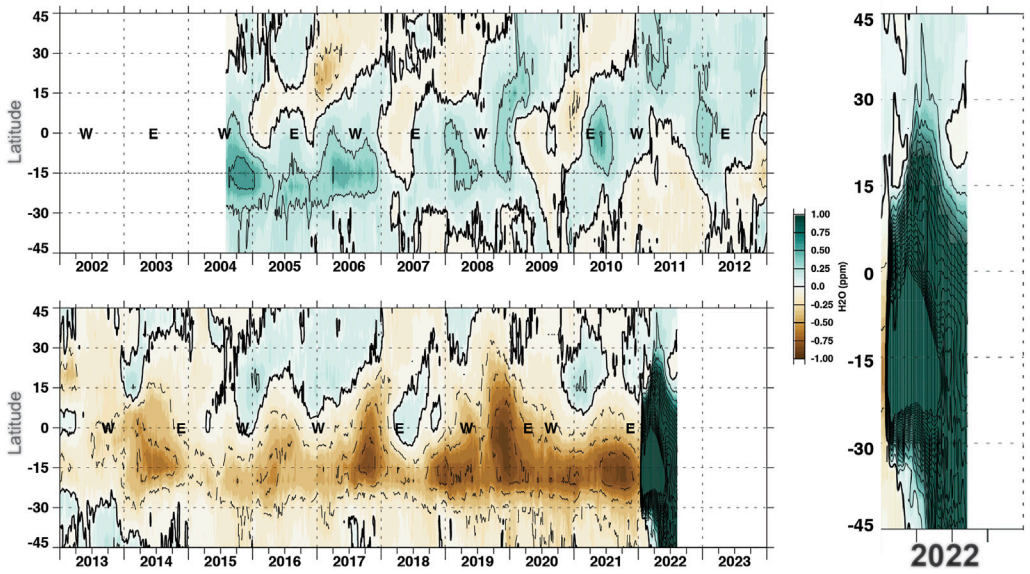

FIGURE 8
Zonal mean stratospheric water vapor at 26.1 hPa (in ppmv) vs. latitude from Aura/MLS (2004-present) showing the unprecedented stratospheric H_2O anomaly due to the January 2022 HTHH eruption. The *left* plot shows MLS water vapor gridded into 5° latitude bins, with the annual cycle removed, missing data filled with linear interpolation, data detrended, and Gaussian smoothing applied (1/2 amplitude = 10 days) to remove higher frequency structure. The easterly (E) and westerly (W) points are as shown in the Singapore zonal winds and indicate the prevailing phase of the Quasi-biennial Oscillation (QBO) of stratospheric winds, which was easterly in January 2022. Zoom-in showing 2022 only is shown on the *right*. The HTHH water vapor has spread into the northern hemisphere (below ~30°N) but most resides in the southern hemisphere. Source: NASA Goddard QBO website (P.A. Newman & N. Kramarova), https://acd-ext.gsfc.nasa.gov/Data_services/met/qbo/.

water), but they did not consider submarine eruptions. Based on modeling by Glaze et al. (1997), a large explosive eruption column in a wet atmosphere could inject ~4 × 10^9 kg H_2O per hour (4 Tg/h); hence ~24 h of continuous activity could deposit ~100 Tg H_2O into the stratosphere (equivalent to ~100 midlatitude thunderstorms or 7% of the total stratospheric H_2O). The January 2022 HTHH eruption injected at least as much H_2O in a shorter timespan (~11 h).

Actual measurements of stratospheric volcanic H_2O injections are rare, and upper tropospheric volcanic H_2O injections are challenging to detect due to swamping by ambient tropospheric water. Using Aura/MLS data, Sioris et al. (2016) estimated a stratospheric H_2O injection of ~2 Tg by the 2015 Calbuco (Chile) eruption (VEI 4), which was similar to short-lived (~1 week), local stratospheric H_2O perturbations observed after the 1980 Mount St. Helens (MSH) and 2008 Kasatochi eruptions. Murcray et al. (1981) measured up to ~40 ppm H_2O in the 1980 MSH eruption plume on 22 May 1980 at ~19–20 km altitude, against a background of 20–30 ppm. There are no *in-situ* H_2O observations for the largest eruptions of recent decades (1982 El Chichón, 1991 Pinatubo, 1991 Cerro Hudson) although, as noted by Glaze et al. (1997), Burnett and Burnett (1984) reported elevated OH radicals after the 1982 El Chichón eruption, possibly sourced from the volcanic H_2O injection. Based on petrological estimates, the 1815 Tambora eruption (VEI 7) could have injected up to 2000–3,000 Tg H_2O into the stratosphere, which would double the stratospheric H_2O load (Glaze et al., 1997). For the ~75 ka Toba eruption, the H_2O injection could have been on the order of 27 Pg (27,000 Tg) (LeGrande et al., 2016). However, the ~150 Tg stratospheric H_2O injection by the 2022 HTHH eruption is clearly the largest such perturbation measured in the instrumental era, revealing that shallow submarine volcanic eruptions may be a previously unrecognized, yet effective (though perhaps rare) mechanism for stratospheric hydration.

5.4 Optical effects of the stratospheric volcanic cloud

Another measure of eruption magnitude and atmospheric impact is the geographical extent of the resulting atmospheric optical effects. The 15 January 2022 HTHH eruption is perhaps the largest volcanic explosion since the 1883 Krakatau eruption, and the vivid volcanic twilights, 'blue suns and moons' and other atmospheric phenomena observed in the months after August 1883 are well known (Symons, 1888). However, given the modest HTHH SO_2 emission (~one to two orders of magnitude less than Krakatau and Pinatubo) and the high stratospheric H_2O loading, we might expect different effects in 2022 due to the distinctive

stratospheric aerosol composition (fewer primary sulfate particles) and probable larger 'hydrated' aerosol particle size (e.g., Zhu et al., 2022; Sellitto et al., 2022). To date, this appears consistent with limited atmospheric observations from the southern hemisphere (e.g., public photos from Australia, Zimbabwe and Chile posted on the Space Weather image gallery: https://spaceweathergallery.com/index.php).

There have been no reports of blue (or otherwise unusually colored) suns or moons since the HTHH eruption, but these were observed soon (a few days to weeks) after the August 1883 Krakatau eruption (Symons, 1888). Since 'blueing' of the Sun or moon requires a specific stratospheric aerosol particle size of ~0.5 μm (e.g., Garrison et al., 2021), this may tentatively be attributed to the larger size of the HTHH aerosol particles. Another atmospheric phenomenon first reported after the 1883 Krakatau eruption was the 'Bishop's Ring' halo around the Sun, observed from Honolulu (Hawai'i) by the Reverend Sereno Bishop (Hamilton, 2012). A similar solar halo was observed from Zimbabwe (at a similar latitude to Tonga) throughout the day on 12 February 2022 (https://spaceweathergallery.com/indiv_upload.php?upload_id=182436). Aerosols or ice crystals at very high altitudes near the mesopause can also form noctilucent clouds, and such clouds have been observed in the aftermath of the HTHH eruption, such as this example from Chile on 30 January 2022: https://spaceweathergallery.com/indiv_upload.php?upload_id=182031. As indicated by the stratospheric H_2O distribution in Figure 8, the HTHH stratospheric aerosol and H_2O veil has not penetrated deep into the northern hemisphere to date, but in the coming months we might expect more atmospheric optical effects to be reported from further north as the aerosols are dispersed meridionally by the Brewer-Dobson Circulation.

The initial dispersion of the January 15 HTHH eruption cloud also bore a strong resemblance to the 1883 Krakatau eruption. After the 1883 eruption, the Krakatau volcanic aerosol cloud (and associated twilight phenomena) spread rapidly westwards from Indonesia and completed a global circuit in ~2 weeks (Hamilton, 2012). The 1883 eruption provided the first observation of tropical stratospheric winds (the 'Krakatoa Easterlies') and was key to the later discovery of the phased variability in stratospheric wind direction now known as the Quasi-biennial Oscillation (QBO) (Hamilton, 2012; Figure 8). Similarly, after the 15 January 2022 HTHH eruption, the high-level stratospheric H_2O anomaly at 2.1 hPa (~45 km altitude) dispersed rapidly west under the prevailing easterly phase of the QBO, and had almost entirely circled the globe by January 22, whilst H_2O at lower altitudes (26 hPa) traveled more slowly (Millán et al., 2022).

5.5 Challenges for eruption response, volcanic cloud sampling and tracking

NASA has a major volcanic eruption response plan to activate in the event of a major explosive eruption that could potentially impact climate (e.g., Carn et al., 2021). However, the 2022 HTHH eruption was unexpected in its magnitude and plume altitude (~30–55 km) and posed unanticipated challenges for volcanic cloud sampling and eruption response (e.g., *in-situ* sampling). The ~30 km altitude of the January 15 HTHH umbrella cloud, at which most volatile emissions (H_2O, SO_2) were emplaced, is too high for direct sampling by NASA's high-altitude aircraft (e.g., NASA's ER-2 has a ceiling of ~21 km altitude), and hence direct sampling of the stratospheric volcanic gas and aerosol cloud must rely on balloon-borne campaigns (e.g., Kloss et al., 2022). Furthermore, the modest HTHH SO_2 loading (but high H_2O loading) defies conventional views of climate-forcing eruptions, since the NASA eruption response is primarily contingent on high SO_2 loading measured by satellites (where >5 Tg SO_2 indicates a potentially significant event), whereas in the HTHH case the stratospheric H_2O anomaly is the more significant effect, and could lead to surface warming rather than the surface cooling expected after SO_2-rich stratospheric eruptions (e.g., Joshi and Jones, 2009; Sellitto et al., 2022; Millán et al., 2022).

The 2022 HTHH eruption also comes at a turning point in NASA's satellite observation-strategy. The agency plans to terminate its Earth Observing System flagship Terra (1999—present), Aqua (2002—present) and Aura (2004—present) missions in summer 2023 to prepare for the next generation Earth System Observatory (https://science.nasa.gov/earth-science/earth-system-observatory), although the Aura mission has sufficient fuel and solar power generation to continue operating until 2025. Termination of Aura would mean the loss of OMI SO_2 and MLS H_2O measurements, which would preclude monitoring of the unprecedented HTHH stratospheric H_2O anomaly (Figure 8), which could persist for several years and have significant impacts on stratospheric chemistry (e.g., ozone depletion) and climate. The historic HTHH eruption therefore constitutes strong motivation for extending the Aura mission for as long as spacecraft resources permit.

6 Summary

The 15 January 2022 HTHH eruption ranks among the largest volcanic eruptions since 1883, but UV satellite observations from OMI, OMPS, TROPOMI and EPIC indicate a modest stratospheric SO_2 injection of ~0.4–0.5 Tg, consistent with other satellite measurements. A month of Surtseyan eruptive activity and precursory explosive eruptions (December 2021—January 2022) emitted an additional ~0.2 Tg SO_2, significantly exceeding SO_2 emissions from prior HTHH eruptions and providing strong evidence for rejuvenation of the HTHH volcanic system prior to the paroxysmal event. The relatively low SO_2 loading and short stratospheric SO_2 lifetime observed after the 2022 HTHH eruptions are most likely attributed to abundant water in the volcanic plumes, which also has implications for the evolution and impacts of the stratospheric aerosols and the related optical effects.

Data availability statement

Publicly available datasets were analyzed in this study. OMI, OMPS and EPIC data can be found here: https://search.earthdata.nasa.gov/search. TROPOMI data can be found here: https://s5phub.copernicus.eu/dhus/#/home.

Author contributions

SC performed the bulk of the data analysis, created the figures and wrote the first draft of the manuscript. NK provided computing resources and data. BF generated the EPIC data products. CL provided the OMI and OMPS data and analyzed the data for Figure 7. All authors provided comments and input on the final version of the manuscript.

Funding

We acknowledge funding from the NASA Earth Science Division through the Science of Terra, Aqua and SNPP (grant 80NSSC18K0688 to CL), Aura Science Team (grant 80NSSC20K0983 to SC), DSCOVR Science Team (grant 80NSSC19K0771 to SC) and Interdisciplinary Research in Earth Science (grant 80NSSC20K1773 to SC) programs.

Acknowledgments

We also thank the two reviewers for comments that significantly improved the paper.

Conflicts of interest

Author BF is employed by the company Science Systems and Applications, Inc (SSAI).

The remaining authors declare that the research was conducted in the absence of any commercial or financial relationships that could be construed as a potential conflict of interest.

Publisher's note

Supplementary material

The Supplementary Material for this article can be found online at: https://www.frontiersin.org/articles/10.3389/feart.2022.976962/full#supplementary-material

SUPPLEMENTARY FIGURE S1
Radiosonde sounding from Pago Pago (American Samoa) at 12:00 UTC on January 13, 2022. The y-axis units are atmospheric pressure in millibars (in blue) and equivalent altitude above sea level in meters (in black); the x-axis units are temperature (°C). Horizontal blue lines are isobars (lines of equal pressure), and vertical blue lines are isotherms (lines of equal temperature). Thick black lines on the sounding indicate the atmospheric temperature profile (right-hand line) and the dew point profile (left-hand line); when the air is saturated (100% relative humidity) the temperature equals the dew point. Inclined green, blue and purple lines show dry adiabatic lapse rates, saturated adiabatic lapse rates, and saturation mixing ratio lapse rates, respectively. Wind barbs to the right of the plot show the profile of wind speed and direction, where short barbs, long barbs and flag symbols denote wind speed increments of 5, 10 and 50 knots, respectively. Source: http://weather.uwyo.edu/upperair/sounding.html.

SUPPLEMENTARY FIGURE S2
Radiosonde sounding from Pago Pago (American Samoa) at 00:00 UTC on January 15, 2022. The y-axis units are atmospheric pressure in millibars (in blue) and equivalent altitude above sea level in meters (in black); the x-axis units are temperature (°C). Horizontal blue lines are isobars (lines of equal pressure), and vertical blue lines are isotherms (lines of equal temperature). Thick black lines on the sounding indicate the atmospheric temperature profile (right-hand line) and the dew point profile (left-hand line); when the air is saturated (100% relative humidity) the temperature equals the dew point. Inclined green, blue and purple lines show dry adiabatic lapse rates, saturated adiabatic lapse rates, and saturation mixing ratio lapse rates, respectively. Wind barbs to the right of the plot show the profile of wind speed and direction, where short barbs, long barbs and flag symbols denote wind speed increments of 5, 10 and 50 knots, respectively. The sounding plot terminates at ~31 km altitude but the raw data show wind speeds of up to 75 knots (39 m/s) at higher altitudes (32 km). Source: http://weather.uwyo.edu/upperair/sounding.html.

SUPPLEMENTARY MOVIE S1
Animation of GOES-West Advanced Baseline Imager (ABI) GeoColor imagery (with 10-min temporal resolution) between 17:00 UTC on January 14 and 04:20 UTC on January 15, showing puffing from HTHH (at image center) prior to the January 15 eruption (the beginning of which is shown in the final frame). Imagery was visualized using NASA Worldview (https://worldview.earthdata.nasa.gov/).

SUPPLEMENTARY MOVIE S2
Animation of SNPP/OMPS SO2 measurements from January 12–27, 2022, showing SO_2 emissions from the January 13 and January 15 HTHH eruptions, and westerly transport of the stratospheric SO_2 cloud.

References

Burnett, C. R., and Burnett, E. B. (1984). Observational results on the vertical column abundance of atmospheric hydroxyl: Description of its seasonal behavior 1977–1982 and of the 1982 El Chichon Perturbation. *J. Geophys. Res.* 89, 9603–9611. doi:10.1029/jd089id06p09603

Cahalan, R. C., and Dufek, J. (2021). Explosive submarine eruptions: The role of condensable gas jets in underwater eruptions. *J. Geophys. Res. Solid Earth* 126, e2020JB020969. doi:10.1029/2020JB020969

Carey, R., Adam Soule, S., Manga, M., White, J. D. L., McPhie, J., Wysoczanski, R., et al. (2018). The largest deep-ocean silicic volcanic eruption of the past century. *Sci. Adv.* 4, e1701121. doi:10.1126/sciadv.1701121

Carn, S. A., Clarisse, L., and Prata, A. J. (2016). Multi-decadal satellite measurements of global volcanic degassing. *J. Volcanol. Geotherm. Res.* 311, 99–134. doi:10.1016/j.jvolgeores.2016.01.002

Carn, S. A., Krotkov, N. A., Fisher, B. A., Li, C., and Prata, A. J. (2018). First observations of volcanic eruption clouds from the L1 Earth-Sun Lagrange point by DSCOVR/EPIC. *Geophys. Res. Lett.* 45, 11456–11464. doi:10.1029/2018GL079808

Carn, S. A. (2022). *Multi-satellite volcanic sulfur dioxide L4 long-term global database V4*. Greenbelt, MD, USA: Goddard Earth Science Data and Information Services Center GES DISC doi:10.5067/MEASURES/SO2/DATA405 (Accessed April 14 2022)

Carn, S. A., Newman, P. A., Aquila, V., Gonnermann, H., and Dufek, J. (2021). Anticipating climate impacts of major volcanic eruptions. *Eos* 102. doi:10.1029/2021EO162730

Carn, S. A., Yang, K., Prata, A. J., and Krotkov, N. A. (2015). Extending the long-term record of volcanic SO_2 emissions with the Ozone Mapping and Profiler Suite (OMPS) nadir mapper. *Geophys. Res. Lett.* 42, 925–932. doi:10.1002/2014GL062437

Carr, J. L., Horváth, Á., Wu, D. L., and Friberg, M. D. (2022), Stereo plume height and motion retrievals for the record-setting Hunga Tonga- Hunga Ha'apai eruption of 15 January 2022. *Geophys. Res. Lett.*, 49, e2022GL098131. https://doi. org/doi:10.1029/2022GL098131

Colombier, M., Scheu, B., Wadsworth, F. B., Cronin, S., Vasseur, J., Dobson, K. J., et al. (2018). Vesiculation and quenching during Surtseyan eruptions at Hunga Tonga-Hunga Ha'apai volcano, Tonga. *J. Geophys. Res. Solid Earth* 123, 3762–3779. doi:10.1029/2017JB015357

Constantinescu, R., Hopulele-Gligor, A., Connor, C. B., Bonadonna, C., Connor, L. J., Lindsay, J. M., et al. (2021). The radius of the umbrella cloud helps characterize large explosive volcanic eruptions. *Commun. Earth Environ.* 2, 3. doi:10.1038/s43247-020-00078-3

Cronin, S. J., Brenna, M., Smith, I. E. M., Barker, S. J., Tost, M., Ford, M., et al. (2017). New volcanic island unveils explosive past. *Eos* 98. doi:10.1029/2017EO076589

Embley, R. W., Tamura, Y., Merle, S. G., Sato, T., Ishizuka, O., Chadwick, W. W., Jr., et al. (2014). Eruption of South Sarigan seamount, Northern Mariana Islands: Insights into hazards from submarine volcanic eruptions. *Oceanogr. Wash. D. C.* 27 (2), 24–31. doi:10.5670/oceanog.2014.37

Fisher, B. L., Krotkov, N. A., Bhartia, P. K., Li, C., Carn, S. A., Hughes, E., et al. (2019). A new discrete wavelength backscattered ultraviolet algorithm for consistent volcanic SO_2 retrievals from multiple satellite missions. *Atmos. Meas. Tech.* 12, 5137–5153. doi:10.5194/amt-12-5137-2019

Garrison, C., Kilburn, C., Smart, D., and Edwards, S. (2021). The blue suns of 1831: Was the eruption of Ferdinandea, near Sicily, one of the largest volcanic climate forcing events of the nineteenth century? *Clim. Past.* 17, 2607–2632. doi:10.5194/cp-17-2607-2021

Garvin, J. B., Slayback, D. A., Ferrini, V., Frawley, J., Giguere, C., Asrar, G. R., et al. (2018). Monitoring and modeling the rapid evolution of Earth's newest volcanic island: Hunga Tonga Hunga Ha'apai (Tonga) using high spatial resolution satellite observations. *Geophys. Res. Lett.* 45, 3445–3452. doi:10.1002/2017GL076621

Gerlach, T. M., Westrich, H. R., and Symonds, R. B. (1996). "Preeruption vapor in magma of the cli- mactic mount Pinatubo eruption: Source of the giant stratospheric sulfur dioxide cloud," in *Fire and mud: Eruptions and lahars of mount Pinatubo, Philippines*. Editors C. G. Newhall and R. S. Punongbayan (Seattle, USA: University of Washington Press), 415–434. Available at: https://pubs.usgs.gov/pinatubo/index.html.

Glaze, L. S., Baloga, S. M., and Wilson, L. (1997). Transport of atmospheric water vapor by volcanic eruption columns. *J. Geophys. Res.* 102 (D5), 6099–6108. doi:10.1029/96jd03125

Green, D. N., Evers, L. G., Fee, D., Matoza, R. S., Snellen, M., Smets, P., et al. (2013). Hydroacoustic, infrasonic and seismic monitoring of the submarine eruptive activity and sub-aerial plume generation at South Sarigan, May 2010. *J. Volcanol. Geotherm. Res.* 257, 31–43. doi:10.1016/j.jvolgeores.2013.03.006

Guo, S., Rose, W. I., Bluth, G. J. S., and Watson, I. M. (2004). Particles in the great Pinatubo volcanic cloud of June 1991: The role of ice. *Geochem. Geophys. Geosyst.* 5, Q05003. doi:10.1029/2003GC000655

Gupta, A. K., Bennartz, R., Fauria, K. E., and Mittal, T. (2022). Timelines of plume characteristics of the Hunga Tonga-Hunga Ha'apai eruption sequence from 19 December 2021 to 16 January 2022: Himawari-8 observations. *Earth Space Sci. Open 'rchive*. doi:10.1002/essoar.10510853.2

Hamilton, K. (2012). Sereno Bishop, Rollo Russell, Bishop's Ring and the discovery of the "Krakatoa Easterlies". *Atmosphere-Ocean* 50 (2), 169–175. doi:10.1080/07055900.2011.639736

Harrison, T. (2022). *Expanding islands in the south pacific*. San Francisco, California, United States: Planet Labs Stories. Available at: https://www.planet.com/pulse/expanding-islands-in-the-south-pacific/.

Herman, J., Huang, L., McPeters, R., Ziemke, J., Cede, A., and Blank, K. (2018). Synoptic ozone, cloud reflectivity, and erythemal irradiance from sunrise to sunset for the whole Earth as viewed by the DSCOVR spacecraft from the Earth-Sun Lagrange 1 orbit. *Atmos. Meas. Tech.* 11 (1), 177–194. doi:10.5194/amt-11-177-2018

Joshi, M. M., and Jones, G. S. (2009). The climatic effects of the direct injection of water vapour into the stratosphere by large volcanic eruptions. *Atmos. Chem. Phys.* 9 (16), 6109–6118. doi:10.5194/acp-9-6109-2009

Jutzeler, M., Marsh, R., Carey, R. J., White, J. D. L., Talling, P. J., and Karlstrom, L. (2014). On the fate of pumice rafts formed during the 2012 Havre submarine eruption. *Nat. Commun.* 5, 3660. doi:10.1038/ncomms4660

Jutzeler, M., Marsh, R., van Sebille, E., Mittal, T., Carey, R. J., Fauria, K. E., et al. (2020), Ongoing dispersal of the 7 August 2019 pumice raft from the Tonga arc in the southwestern Pacific Ocean. *Geophys. Res. Lett.*, 47(5), e1701121, https://doi.org/doi:10.1029/2019GL086768

Kloss, C., Sellitto, P., Renard, J.-B., Baron, A., Begue, N., Legras, B., et al. (2022). Aerosol characterization of the stratospheric plume from the volcanic eruption at Hunga Tonga January 15th 2022. *Earth Space Sci. Open Archive*. doi:10.1002/essoar.10511312.1

Kroll, C. A., Dacie, S., Azoulay, A., Schmidt, H., and Timmreck, C. (2021). The impact of volcanic eruptions of different magnitude on stratospheric water vapor in the tropics. *Atmos. Chem. Phys.* 21, 6565–6591. doi:10.5194/acp-21-6565-2021

Kubota, T., Saito, T., and Nishida, K. (2022). Global fast-traveling tsunamis driven by atmospheric Lamb waves on the 2022 Tonga eruption. *Science* 377, 91–94. doi:10.1126/science.abo4364

Lackschewitz, K. S., Dehn, J., and Wallrabe-Adams, H.-J. (1994). Volcaniclastic sediments from mid-oceanic Kolbeinsey Ridge, north of Iceland: Evidence for submarine volcanic fragmentation processes. *Geol.* 22 (11), 975–978. doi:10.1130/0091-7613(1994)022<0975:vsfmok>2.3.co;2

LeGrande, A. N., Tsigaridis, K., and Bauer, S. E. (2016). Role of atmospheric chemistry in the climate impacts of stratospheric volcanic injections. *Nat. Geosci.* 9, 652–655. doi:10.1038/ngeo2771

Levelt, P., Joiner, J., Tamminen, J., Veefkind, J. P., Bhartia, P. K., Stein Zweers, D. C., et al. (2018). The Ozone Monitoring Instrument: Overview of 14 years in space. *Atmos. Chem. Phys.* 18, 5699–5745. doi:10.5194/acp-18-5699-2018

Li, C., Krotkov, N. A., Carn, S. A., Zhang, Y., Spurr, R. J. D., and Joiner, J. (2017). New-generation NASA Aura Ozone Monitoring Instrument volcanic SO_2 dataset: Algorithm description, initial results, and continuation with the Suomi-NPP Ozone Mapping and Profiler Suite. *Atmos. Meas. Tech.* 10, 445–458. doi:10.5194/amt-10-445-2017

Lopez, T., Clarisse, L., Schwaiger, H., Van Eaton, A., Loewen, M., Fee, D., et al. (2020). Constraints on eruption processes and event masses for the 2016–2017 eruption of Bogoslof volcano, Alaska, through evaluation of IASI satellite SO_2 masses and complementary datasets. *Bull. Volcanol.* 82, 17. doi:10.1007/s00445-019-1348-z

Madden-Nadeau, A. L., Cassidy, M., Pyle, D., Mather, T., Watt, S., Engwell, S., et al. (2022). The magmatic and eruptive evolution of the 1883 caldera-forming eruption of Krakatau: Integrating field- to crystal-scale observations. *J. Volcanol. Geotherm. Res.* 411, 107176. doi:10.1016/j.jvolgeores.2021.107176

Marshak, A., Herman, J., Szabo, A., Blank, K., Cede, A., Carn, S., et al. (2018). Earth observations from DSCOVR/EPIC instrument. *Bull. Am. Meteorol. Soc.* 99 (9), 1829–1850. doi:10.1175/BAMS-D-17-0223.1

Martí, J., Pinel, V., Lõpez, C., Geyer, A., Abella, R., Tárraga, M., et al. (2013). Causes and mechanisms of the 2011–2012 El Hierro (Canary Islands) submarine eruption. *J. Geophys. Res. Solid Earth* 118 (3), 823–839. doi:10.1002/jgrb.50087

Mastin, L. G., and Witter, J. B. (2000). The hazards of eruptions through lakes and seawater. *J. Volcanol. Geotherm. Res.* 97, 195–214. doi:10.1016/S03770273(99)00174-2

Matoza, R. S., Fee, D., Assink, J. D., Iezzi, A. M., Green, D. N., Kim, K., et al. (2022). Atmospheric waves and global seismoacoustic observations of the January 2022 Hunga eruption, Tonga. *Science* 377, 95–100. doi:10.1126/science.abo7063

May, R. M., Arms, S. C., Marsh, P., Bruning, E., Leeman, J. R., Goebbert, K., et al. (2022). MetPy: A Python package for meteorological data, unidata. Available at: https'//github.com/Unidata/MetPy. doi:10.5065/D6WW7G29

Millán, L., Santee, M. L., Lambert, A., Livesey, N. J., Werner, F., Schwartz, M. J., et al. (2022), The Hunga Tonga-Hunga Ha'apai hydration of the stratosphere.

Geophys. Res. Lett., 49, e2022GL099381, https://doi. org/doi:10.1029/2022GL099381

Murcray, D. G., Murcray, F. J., Barker, D. B., and Mastenbrook, H. J. (1981). Changes in stratospheric water vapor associated with the Mount St. Helens eruption. *Science* 211, 823–824. doi:10.1126/science.211.4484.823

Newhall, C. G., and Self, S. (1982). The volcanic explosivity index (VEI): An estimate of explosive magnitude for historical volcanism. *J. Geophys. Res.* 87, 1231–1238. doi:10.1029/jc087ic02p01231

Planet Team (2017). "*Planet application program interface: In space for life on Earth*. San Francisco, CA: Planet Labs. Available at: https://api.planet.com.

Prata, A. T., Folch, A., Prata, A. J., Biondi, R., Brenot, H., Cimarelli, C., et al. (2020). Anak Krakatau triggers volcanic freezer in the upper troposphere. *Sci. Rep.* 10, 3584. doi:10.1038/s41598-020-60465-w

Rose, W. I., Delene, D. J., Schneider, D. J., Bluth, G. J. S., Krueger, A. J., Sprod, I., et al. (1995). Ice in the 1994 Rabaul eruption cloud: Implications for volcano hazard and atmospheric effects. *Nature* 375, 477–479. doi:10.1038/375477a0

Rowell, C. R., Jellinek, A. M., Hajimirza, S., and Aubry, T. J. (2022). External surface water influence on explosive eruption dynamics, with implications for stratospheric sulfur delivery and volcano-climate feedback. *Front. Earth Sci.* 10, 788294. doi:10.3389/feart.2022.788294

Sato, H., and Taniguchi, H. (1997). Relationship between crater size and ejecta volume of recent magmatic and phreato-magmatic eruptions: Implications for energy partitioning. *Geophys. Res. Lett.* 24 (3), 205–208.

Schmincke, H.-U. (2006), *Volcanism*. Berlin, Germany: Springer-Verlag, 324 pp. ISBN: 3-540-43650-2.

Searcy, C. (2013). Seismicity associated with the May 2010 eruption of South Sarigan seamount, Northern Mariana Islands. *Seismol. Res. Lett.* 84 (6), 1055–1061. doi:10.1785/0220120168

Self, S. (1992). Krakatau revisited: The course of events and interpretation of the 1883 eruption. *GeoJournal* 28, 109–121. doi:10.1007/BF00177223

Sellitto, P., Podglajen, A., and Belhadji, R. (2022), The unexpected radiative impact of the Hunga Tonga eruption of January 15th, 2022, 18 April 2022, PREPRINT (Version 1) available at Research Square, doi:10.21203/rs.3.rs-1562573/v1

Global Volcanism Program (2021a). "Report on Hunga Tonga-Hunga Ha'apai (Tonga)," in *Weekly volcanic activity report, 15 December-21 December 2021*. Editor S. K. Sennert (Washington, DC, United States: Smithsonian Institution and US Geological Survey). https://volcano.si.edu/showreport.cfm?wvar=GVP.WVAR20211215-243040.

Global Volcanism Program (2021b). "Report on Hunga Tonga-Hunga Ha'apai (Tonga)," in *Weekly volcanic activity report, 22 December-28 December 2021*. Editor S. K. Sennert (Washington, DC, United States: Smithsonian Institution and US Geological Survey). https://volcano.si.edu/showreport.cfm?wvar=GVP.WVAR20211222-243040.

Global Volcanism Program (2021c). "Report on Hunga Tonga-Hunga Ha'apai (Tonga)," in *Weekly volcanic activity report, 29 December-4 January 2022*. Editor S. K. Sennert (Washington, DC, United States: Smithsonian Institution and US Geological Survey). https://volcano.si.edu/showreport.cfm?wvar=GVP.WVAR20211229-243040.

Global Volcanism Program (2022). "Report on Hunga Tonga-Hunga Ha'apai (Tonga)," in *Weekly volcanic activity report, 12 January-18 January 2022*. Editor S. K. Sennert (Washington, DC, United States: Smithsonian Institution and US Geological Survey). https://volcano.si.edu/showreport.cfm?wvar=GVP.WVAR20220112-243040.

Sioris, C. E., Malo, A., McLinden, C. A., and D'Amours, R. (2016). Direct injection of water vapor into the stratosphere by volcanic eruptions. *Geophys. Res. Lett.* 43, 7694–7700. doi:10.1002/2016GL069918

Suzuki, Y. J., and Koyaguchi, T. (2009). A three-dimensional numerical simulation of spreading umbrella clouds. *J. Geophys. Res.* 114, B03209. doi:10.1029/2007JB005369

G. J. Symons (Editor) (1888). (London, U.K: Report of the Krakatoa Committee of the Royal Society. Royal Society).*The Eruption of Krakatoa, and subsequent phenomena.*

Textor, C., Graf, H.-F., Herzog, M., and Oberhuber, J. M. (2003). Injection of gases into the stratosphere by explosive volcanic eruptions. *J. Geophys. Res.* 108 (D19), 4606. doi:10.1029/2002JD002987

Theys, N., De Smedt, I., Yu, H., Danckaert, T., van Gent, J., Hormann, C., et al. (2017). Sulfur dioxide retrievals from TROPOMI onboard Sentinel-5 Precursor: Algorithm theoretical basis. *Atmos. Meas. Tech.* 10, 119–153. doi:10.5194/amt-10-119-2017

Van Eaton, A. R., Amigo, Á., Bertin, D., Mastin, L. G., Giacosa, R. E., González, J., et al. (2016). Volcanic lightning and plume behavior reveal evolving hazards during the April 2015 eruption of Calbuco volcano, Chile. *Geophys. Res. Lett.* 43, 3563–3571. doi:10.1002/2016GL068076

Vaughan, R. G., and Webley, P. (2010). Satellite observations of a surtseyan eruption: Hunga Ha'apai, Tonga. *J. Volcanol. Geotherm. Res.* 198 (1–2), 177–186. doi:10.1016/j.jvolgeores.2010.08.017

Veefkind, J. P., Aben, I., McMullan, K., Forster, H., de Vries, J., Otter, G., et al. (2012). TROPOMI on the ESA Sentinel-5 Precursor: A GMES mission for global observations of the atmospheric composition for climate, air quality and ozone layer applications. *Remote Sens. Environ.* 120, 70–83. doi:10.1016/j.rse.2011.09.027

Global Volcanism Program (2013). "Volcanoes of the World,". Editor E. Venzke (Smithsonian Institution), 4.10.6. Downloaded 05 Apr 2022. doi:10.5479/si.GVP.VOTW4-2013

Woods, A. W., and Kienle, J. (1994). The dynamics and thermodynamics of volcanic clouds: Theory and observations from the April 15 and April 21, 1990 eruptions of Redoubt volcano, Alaska. *J. Volcanol. Geotherm. Res.* 62, 273–299. doi:10.1016/0377-0273(94)90037-X

Wright, C., Hindley, N. P., Alexander, M. J., Barlow, M., Hoffmann, L., Mitchell, C. N., et al. (2022). Surface-to-space atmospheric waves from Hunga Tonga-Hunga Ha'apai eruption. *Nature*. doi:10.1038/s41586-022-05012-5

Yeo, I. A., McIntosh, I. M., Bryan, S. E., Tani, K., Dunbabin, M., Metz, D., et al. (2022). The 2019–2020 volcanic eruption of Late'iki (Metis Shoal), Tonga. *Sci. Rep.* 12, 7468. doi:10.1038/s41598-022-11133-8

Zhu, Y., Bardeen, C., and Tilmes, S. (2022), 2022 Hunga-Tonga eruption: Stratospheric aerosol evolution in a water-rich plume, Preprint (Version 1) available at Research Square doi:10.21203/rs.3.rs-1647643/v1

Zhu, Y., Toon, O. B., Jensen, E. J., Bardeen, C. G., Mills, M. J., Tolbert, M. A., et al. (2020). Persisting volcanic ash particles impact stratospheric SO_2 lifetime and aerosol optical properties. *Nat. Commun.* 11, 4526. doi:10.1038/s41467-020-18352-5

frontiers | Frontiers in Earth Science

TYPE Original Research
PUBLISHED 28 October 2022
DOI 10.3389/feart.2022.972071

OPEN ACCESS

EDITED BY
Silvana Hidalgo,
Instituto Geofísico-Escuela Politécnice Nacional, Ecuador

REVIEWED BY
Tom D. Pering,
The University of Sheffield, United Kingdom
Ryunosuke Kazahaya,
National Institute of Advanced Industrial Science and Technology (AIST), Japan

*CORRESPONDENCE
Dario Delle Donne,
dario.delledonne@ingv.it

SPECIALTY SECTION
This article was submitted to Volcanology, a section of the journal Frontiers in Earth Science

RECEIVED 17 June 2022
ACCEPTED 05 October 2022
PUBLISHED 28 October 2022

CITATION
Delle Donne D, Lo Coco E, Bitetto M, La Monica FP, Lacanna G, Lages J, Ripepe M, Tamburello G and Aiuppa A (2022), Spatio-temporal changes in degassing behavior at Stromboli volcano derived from two co-exposed SO_2 camera stations.
Front. Earth Sci. 10:972071.
doi: 10.3389/feart.2022.972071

Spatio-temporal changes in degassing behavior at Stromboli volcano derived from two co-exposed SO_2 camera stations

Dario Delle Donne[1,2]*, Eleonora Lo Coco[1], Marcello Bitetto[1], Francesco Paolo La Monica[1], Giorgio Lacanna[3], Joao Lages[1], Maurizio Ripepe[3], Giancarlo Tamburello[4] and Alessandro Aiuppa[1]

[1]DiSTeM, Università di Palermo, Palermo, Italy, [2]Istituto Nazionale di Geofisica e Vulcanologia, Napoli, Italy, [3]Dipartimento di Scienze della Terra, Università di Firenze, Firenze, Italy, [4]Istituto Nazionale di Geofisica e Vulcanologia, Bologna, Italy

Improving volcanic gas monitoring techniques is central to better understanding open-vent, persistently degassing volcanoes. SO_2 cameras are increasingly used in volcanic gas studies, but observations are commonly limited to one single camera alone viewing the volcanic plume from a specific viewing direction. Here, we report on high frequency (0.5 Hz) systematic measurements of the SO_2 flux at Stromboli, covering a 1-year long observation period (June 2017-June 2018), obtained from two permanent SO_2 cameras using the same automated algorithm, but imaging the plume from two different viewing directions. Our aim is to experimentally validate the robustness of automatic SO_2 camera for volcano monitoring and to demonstrate the advantage of using two co-exposed SO_2 camera stations to better capturing degassing dynamics at open-vent volcanoes. The SO_2 flux time-series derived from the two SO_2 camera stations exhibit good match, demonstrating the robustness of the automatic SO_2 camera method. Our high-temporal resolution SO_2 records resolve individual Strombolian explosions as transient, repetitive gas bursts produced by the sudden release of over pressurized gas pockets and scoriae. Calculations show that explosive degassing activity accounts for ~10% of the total SO_2 emission budget (dominated by passive degassing) during mild regular open-vent activity. We show that the temporal variations of the explosive SO_2 flux go in tandem with changes in total SO_2 flux and VLP seismicity, implicating some commonality in the source processes controlling passive degassing and explosive activity. We exploited the spatial resolution of SO_2 camera to discriminate degassing at two distinct regions of the crater area, and to minimize biases due by the station position respect to the target plume. We find that the SO_2 fluxes from southwest-central (SWCC) and northeast (NEC) crater areas oscillate coherently but those from the NEC are more sensitive to the changes in the volcanic intensity. We interpret this as due to preferential gas/magma channeling into the structurally weaker north-eastern portion of the crater terrace in response to increasing supply rate of buoyant, bubble-rich magma in the shallow plumbing system.

10.3389/feart.2022.972071

KEYWORDS

volcanic degassing, Stromboli (Italy), Strombolian activity, UV camera, SO_2 flux, volcano monitoring

Introduction

Magmatic gases are the drivers for explosive volcanic eruptions, making their sensing and quantification of prime importance for characterizing volcano behavior (Oppenheimer et al., 2014; Vergniolle and Métrich, 2022). The advent of the SO_2 camera technique (see reviews in Kern et al., 2010a, Burton et al., 2015; McGonigle et al., 2017) has paved the way to monitoring SO_2 flux emissions at Stromboli (and elsewhere) with finer temporal and spatial resolution (Tamburello et al., 2012; Delle Donne et al., 2017; Aiuppa et al., 2021) than before (Allard et al., 2008). More broadly at open-vent volcanoes, SO_2 cameras have led to enormous progresses in understanding the link between SO_2 degassing, seismicity (McGonigle et al., 2009; Kazahaya et al., 2011; Tamburello et al., 2012; Waite et al., 2013; Nadeau et al., 2015), infrasound (Dalton et al., 2010; Delle Donne et al., 2016; Delle Donne et al., 2017), and deformation (Watson et al., 2000; Saballos et al., 2014). These studies have exploited the advantage of SO_2 cameras of enabling high temporal resolution measurements of the total SO_2 flux (Mori and Burton, 2006; Bluth et al., 2007), and their ability to resolve (and contribute to characterize) the variety of volcanic degassing forms and modes (Mori and Burton, 2009; Tamburello et al., 2012; Delle Donne et al., 2017).

SO_2 Camera observations are normally operated by using one single SO_2 camera station observing the plume from a specific viewing direction. However, the SO_2 camera method, as other spectroscopic techniques used in volcanology (Oppenheimer et al., 2011), is strongly dependent on geometrical constraints (position of the observation point relative to the volcanic plume) that determine—among others—the conditions of sunlight illumination of the volcanic plume, and the presence of clear sky conditions (required to identify a correct background light intensity) (Kern et al., 2010b). The uncertainties related to these effects are difficult to quantify with one SO_2 camera system alone. In addition, using one single SO_2 camera station often prevents from resolving SO_2 emissions from different degassing vents in the volcanic crater area—a condition commonly encountered at worldwide active volcanoes.

Here, we report on SO_2 flux observations obtained at Stromboli volcano (in the period June 2017–June 2018) by using two independent, fully autonomous SO_2 camera stations (Figure 1) imaging the volcanic plume from two different viewing directions. One aim of the work is to empirically test the extent to which SO_2 camera measurements depend on specific observation site conditions, in the attempt to validate the robustness of automatic SO_2 camera for volcano monitoring and surveillance. We also use such two differently positioned, simultaneously acquiring SO_2 camera stations to spatially resolve and characterize the SO_2 flux emissions from the two persistent Stromboli's gas sources that we have recognized from data: the northern (NEC) and central-southwestern (SWCC) areas of the summit crater terrace (Figure 1, 2). We additionally exploit the high temporal resolution of the cameras to derive independent records of explosive (during Strombolian explosions) and passive (in between the explosions) SO_2 emissions, integrating SO_2 observations with other independent geophysical parameters such as the volcanic tremor and the Very Long Period (VLP) seismicity. The integration of these independent datasets helps us better interpreting the shallow conduit gas-magma dynamics that feed the Stromboli's persistent Strombolian activity. Our results are also relevant for understanding use conditions and limitations of the automatic SO_2 camera method in detecting changes in intensity of mild persistent open-vent volcanic activity.

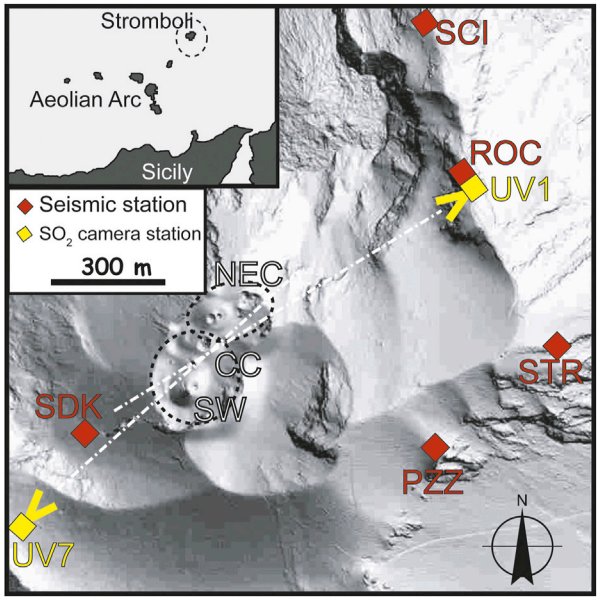

FIGURE 1
Map of the Stromboli's summit crater area, showing the position of the two SO_2 camera stations (UV1 and UV7), the locations of the LGS-UNIFI seismo-acoustic and thermal stations (ROC, SCI, STR, PZZ, SDK) used for the daily evaluation of volcanic activity index, for the detection of seismic VLP events and evaluation volcanic tremor amplitude. The positions of the three summit craters (NEC, north-eastern crater; SW, southwest, and CC, central craters) are also shown. White dashed lines represent the limit separating the two degassing sources (SWCC and NEC) within the two station's field of views, as also indicated in Figures 5A,B.

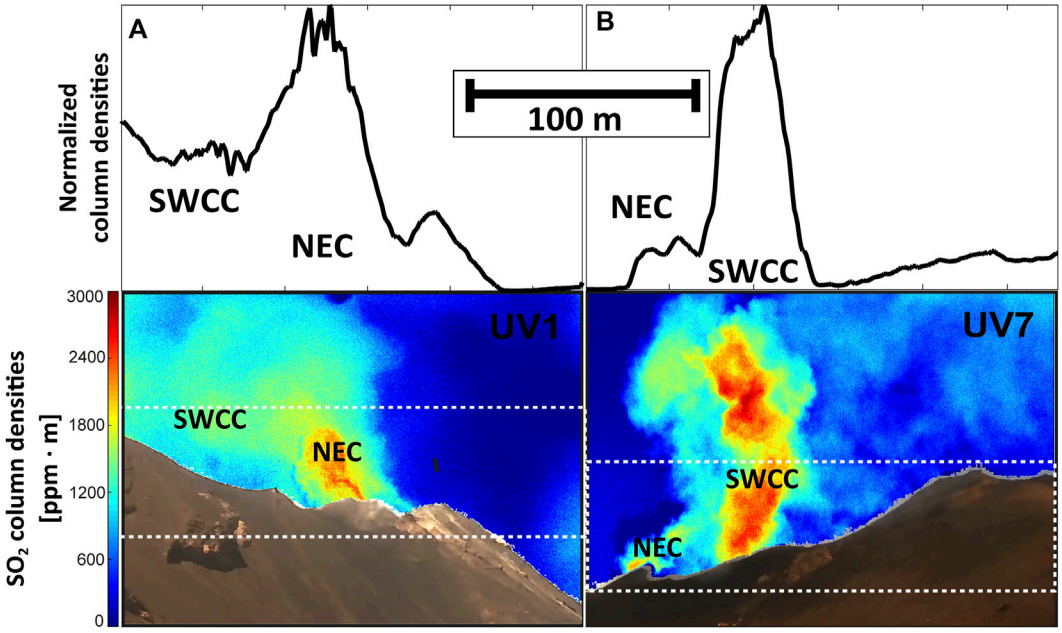

FIGURE 2
SO_2 column density images derived from processing of UV1 **(A)** and UV7 **(B)** SO_2 camera stations. The top panels represent the normalized SO_2 column amount profiles obtained along transects (one per camera) intersecting the crater terrace (see dashed white areas in the pseudo-color images). These profiles allow spatially locating the NEC and SWCC emission sources, and separately resolving their SO_2 contributions.

Open questions on degassing mechanisms at Stromboli

Stromboli is a worldwide known open-vent volcano characterized by persistent mild explosive activity that consists of about 8–17 mild, discrete explosions per hour (Ripepe et al., 2008). Such mild explosive activity is sustained by continuous magma overturning in the shallow conduits (Allard et al., 1994; Laiolo et al., 2022) and is thought to result from outbursting of large over-pressurized gas slugs at the top of the magma column (Harris and Ripepe, 2007b). Stromboli's volcanic activity takes place within a NE–SW elongated crater terrace composed of three main vent areas, named northeast (NEC), southwest (SW) and central craters (CC) (Figure 1). The terrace is located at an elevation of ~750 m a.s.l. on the upper margin of the Sciara del Fuoco, a deep horse-shoe depression resulting from several lateral collapses (Rosi et al., 2013). Stromboli's gas emissions are sustained by distinct forms of degassing that are related to distinct volcanic processes: passive degassing, puffing and explosions (Harris and Ripepe, 2007b). Tamburello et al. (2012) studied a dataset of 130 explosions and 50 gas puffs acquired during brief campaign-style surveys, from which they discriminated the relative contributions of passive (~77%), puffing (~16%) and explosive (~7%) degassing to the total gas output. However, such estimates are made based upon a limited dataset taken over short temporal intervals, leaving the question open of if, and to what extent, these proportions fluctuate in time and with changing volcanic activity. Our longer term observations here, covering 12 months, are aimed also at specifically answer this question.

Another aspect that has received scarce attention is if (and to what extent) degassing activity varies spatially over Stromboli's crater terrace (Figure 1), and what the spatial distribution of degassing activity can tell us on the geometry of the shallow plumbing system, and on the modes/rates of gas and magma ascent in the feeding conduit(s). It is well known that degassing occurs simultaneously from several vents hosted in the crater terrace (North-East crater, NEC; South-West crater, SW; Central crater, CC; Figure 1), but the relative gas contributions from these sources have only occasionally been characterized (Pering et al., 2020). The three craters are characterized by distinct degassing and explosive regimes (Ripepe and Braun, 1994; Harris and Ripepe, 2007b; Ripepe et al., 2008), and are therefore likely to contribute differently to the degassing budget (Pering et al., 2020). Moreover, recent effusive eruptions on Stromboli have systematically been preceded by clustering of puffing and explosive activity on the gravitationally unstable NEC (Calvari et al., 2005; Neri and Lanzafame, 2009; Ripepe et al., 2009; Calvari et al., 2010; Calvari et al., 2011; Valade et al., 2016). This shift can be tracked by automatic infrasonic locations (Ripepe and Marchetti, 2002), anticipated by weeks the 2007 flank eruption (Ripepe et al., 2009) and by hours most of the small lava

overflows occurring from the summit craters (Valade et al., 2016). Therefore, it is vital to demonstrate the ability of Stromboli's SO_2 cameras to capture this activity shift toward the NEC in the SO_2 flux record.

Materials and methods

We use two stand-alone, permanent SO_2 camera stations, located at respectively Roccette (38°47′53″ N, 15°13′0.1″ E; NE upper flank of Stromboli, at 750 m a.s.l.; UV1 in Figure 1) and Valle della Luna (38°47′ 28″ N, 15°12′ 26″ E; SW upper flank of Stromboli, at 750 m above sea level; UV7 in Figure 1). The two SO_2 camera stations are both located ~500 m away from the center of the summit crater (range: 400–600 m) allowing us to image the crater plume(s) from two different viewing directions (Figure 1).

The SO_2 camera stations are designed to output high-rate (0.5 Hz) long-term SO_2 flux observations in continuous mode for 6 h per day. Both stations are equipped with two JAI CM-140GE-UV cameras sensitive to UV-radiation fitting two distinct band-pass optical filters (both of 10 nm Full Width at Half Maximum) with central wavelengths of 310 (SO_2 absorption) and 330 nm (no SO_2 absorption) (Kern et al., 2010a; Kantzas et al., 2010; Burton et al., 2015). Data from a collocated UV spectrometer (Ocean-Optic USB 2000+), along with periodic field calibration campaigns using gas cells of known SO_2 concentration, allow calibration the SO_2 camera images (Delle Donne et al., 2017). Measurement principles of the SO_2 camera station are detailed in Mori and Burton (2006), Kantzas et al. (2010) and Kern et al. (2010b), whilst hardware, software and acquisition/processing routines used in this work are described in Delle Donne et al. (2017) and Delle Donne et al. (2019). SO_2 column densities are measured on a restricted image portion, capturing a sub-region located just above the crater rim where the SO_2 absorption signal is maximized and atmospheric effects, such as air entertainment in the plume and complexities in the local wind field, are minimized. Plume speed is calculated by applying the Lucas and Kanade (1981) optical flow algorithm included in the OpenCV open source library (Bradski and Kaehler, 2008) (https://opencv.org/) to sets of consecutive images. This involves an automatic selection of plume fronts (i.e., high SO_2 column density) showing high spatial coherence and being characterized by consistent velocity vectors. The SO_2 flux is then obtained from combination of plume speed and SO_2 column density profiles along an ideal section encompassing the entire crater area (Figure 2). The use of an optimal viewing condition algorithm that determines, for each acquired image, the presence of clear sky and the degree of reliability in the SO_2 signal within the image, allows us to discard image sequences with a low signal to noise ratio (Delle Donne et al., 2017; Delle Donne et al., 2019). SO_2 flux measurements that fulfil the quality requirements are then averaged on a daily basis in order to obtain a long-term trend of degassing. This is obtained by averaging the 6 h long (acquisition time is fixed for both SO_2 camera stations from 6.30 to 12.30 UTC) daily image datasets.

Uncertainties in automatic SO_2 camera retrievals for volcanic SO_2 flux

The advent of passive spectroscopic techniques to measure gas emissions from volcanoes, such as the SO_2 camera method, has made a step forward in volcano monitoring, allowing us to quantify volcanic gas plume emissions from remote and safe locations, thus increasing significantly the robustness and continuity of observations. Besides, passive spectroscopic gas measurements are characterized by intrinsic uncertainties that are often difficult to constrain in real time and which may lead to significant biases in the results (Platt and Stuts, 2008; Kern et al., 2010a; Klein et al., 2017). In general, a main source of bias in spectroscopic techniques for volcanic plume SO_2 detection is the presence of ash and aerosol in the plume and in the atmosphere, which can mask the SO_2 signal of a certain quantity. Moreover, the evaluation of volcanic plume velocity vectors from UV images is not straightforward, as UV images allow to detect only the velocity component that is parallel to the focal plane of the image. An additional source of error resides in the assumption that every pixels in the image correspond to the same plume-SO_2 camera distance, that is not valid if the plume is moving toward, or away from, the SO_2 camera. Among all the sources of uncertainty, light dilution can also affect the SO_2 camera measurements, determining a significant bias in interpretation of the results (Kern et al., 2010b; Campion et al., 2015; Varnam et al., 2021). Light dilution is mainly controlled by the distance of the observation point from the target plume: Campion et al. (2015) estimated for Stromboli a degree of underestimation due to light dilution of 25% for a target plume at a distance of 2.2 km. Therefore, given our much shorter distances of the SO_2 camera sites to the target plume (~500 m), light dilution would play a minor role in our measurements. However, to better constrain uncertainty related to light dilution effects, we used the formula of Campion et al. (2015) to correct for light dilution pixel intensities measured from each camera:

$$I_c = \frac{I - I_A\left(1 - e^{-\sigma d}\right)}{e^{-\sigma d}} \quad (1)$$

where $\boldsymbol{I_C}$ is pixel intensity corrected for light dilution, $\boldsymbol{I}$ is the uncorrected pixel intensity, and $\boldsymbol{I_A}$ is the pixel intensity produced by light dilution. σ and $\boldsymbol{d}$ are the atmosphere scattering coefficient in dry air (=1.326E-4 m^{-1} at STP condition for a wavelength of 310 nm, Penndorf, 1957) and the distance to the target plume (in our case is ~500 m for both SO_2 cameras) respectively. Then, applying Eq. 1 to our data, we obtain that the term $e^{-\sigma d}$ = 0.953, and then very close to 1 (i.e., light dilution effects weight less than one order of magnitude on the measured

pixel intensities). In this condition, the corrected pixel intensity for light dilution $\boldsymbol{I_C}$ can be approximated by the measured pixel intensity $\boldsymbol{I}$ retrieved by the cameras without introducing significant errors. However, such conclusions may be not valid when aerosol concentration within the plume becomes significant, determining a change in scattering coefficient. However such condition is avoided since our automatic algorithm discards images associated with cloudy conditions and/or periods with extremely low SO_2 signal to noise ratio (see Delle Donne et al., 2019 for further details on the automatic algorithm). We conclude that light dilution has only a marginal role on our measurements mainly because of the short proximity of the stations from the target plumes. Rather, other factors can be far more important to introduce errors in measurements. In particular, instrumental set-up (e.g., position of the measurement sites relative to the plume) may cause uncertainties in SO_2 flux estimations, considering that observing the plume from different viewing directions implies different sunlight position relative to the target. The use of two SO_2 camera stations to measure the same gas emissions from different viewing angles will give us an empirical evidence on how significant this effect can be. Moreover, in our case, the morphological complexity of the volcano can also play a role, since the proximity between SO_2 cameras and the target plumes could prevent a full capture of the whole plume within our restricted field of view, especially during period of strong winds, during which the plume is not developing vertically but rather spreading horizontally along the rough topography of the summit crater area. In this work we demonstrate that the use of two SO_2 camera stations at different locations can minimize of less than 30% the errors in quantification of the SO_2 fluxes due to topographic effects.

SO_2 degassing source location

The positions of the two SO_2 camera stations relative to the multiple gas emissions sources allow us to spatially distinguish two main degassing areas which are displaced in a rough SW-NE striking direction (Figure 1). The northernmost degassing source is associated with the NEC crater, while the southernmost source corresponds to degassing from both SW and Central craters (SWCC), being the latter in the same line of sight of the two SO_2 camera stations (Figure 1). Figure 2 shows examples of two pseudo-color images of plume SO_2 column densities derived from processing of UV images taken (in the same measurement day) from respectively UV1 (Figure 2A) and UV7 (Figure 2B). Visual inspection of the images shows that, for geometrical reasons related to the configuration of the network and to the topography of the summit crater area, images taken from UV1 capture well gas emissions arising from the NEC, while they may underestimate emissions from the SWCC, these being (at least partially) hidden by the NEC ridge (see also Delle Donne et al., 2017). On the other hand, gas emissions seen by UV7 fully enclose the gas plume(s) issuing from the SWCC region, while gas emissions from NEC emissions could be underestimated due to the same geometrical reasons. Then, in order to obtain a more robust estimate of the total SO_2 flux, and of the distinct gas emission sources, we combined the flux measurements retrieved from the two SO_2 camera stations (see Figures 1, 2), as described below.

Images taken from the SO_2 cameras open the possibility to spatially resolving the SO_2 flux associated with degassing at distinct crater sources (Figure 2). To this aim, we adopt a procedure to evaluate the spatial distribution of degassing from UV absorbance images (Delle Donne et al., 2017). The individual vent contributions to the bulk plume can be resolved by tracing an ideal profile on sets of absorbance images of the near-vent plume (Figure 2). Then, the profile's segment with highest absorbance corresponds to the source crater area where gas exits from the vents. Long-term analysis conducted on the same image profiles allows evaluating the fluctuations through time of the two main (NEC and SWCC) degassing sources, and to separate spatially their distinct contributions to the total flux. Since the proximity of the SO_2 camera stations respect to the emission sources, we are confident the complex wind patterns produce little biases in the location of degassing source within the image, particularly for the long term period of analysis.

Explosive vs. passive degassing

High-rate SO_2 flux time-series at Stromboli typically exhibit sudden and short-lived gas flux pulses over-imposed on a rather constant background signal (Figure 3A) (McGonigle et al., 2009; Tamburello et al., 2012; Pering et al., 2016). These pulses correspond to the rapid ascent, within the camera field of view, of over-pressured gas jets released by Strombolian explosions (Mori and Burton, 2006; Tamburello et al., 2012). Stromboli's SO_2 total flux can thus be interpreted as the summation of two independent degassing processes: a nearly constant gas emission originating from persistent degassing, which comprises of puffing and passive degassing, and a sequence of short-lived gas transients related to gas outburst during Strombolian explosions (Figure 3A). To fully characterize these distinct degassing behaviors, we use an automatic peak-finder algorithm (developed upon the built-in Matlab *findpeaks* function; https://it.mathworks.com/help/signal/ref/findpeaks.html) to detect (and count) the transient SO_2 pulses in the SO_2 flux time-series, and to quantify duration and amplitude of every single pulse. Typically, these active SO_2 emissions are characterized by an abrupt onset with a relatively fast increase in flux, followed by a slower decreasing phase down to the average flux (Figure 3A, see also Pering et al., 2016). The SO_2 mass associated with each pulse is derived by integrating the SO_2 flux over the pulse duration (Delle Donne et al., 2017). Very long

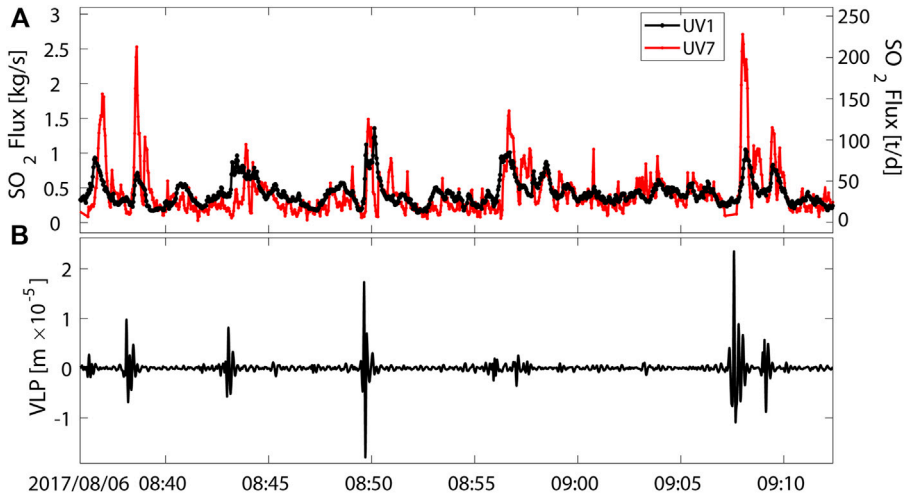

FIGURE 3
(A) Example of a simultaneous high-frequency SO_2 flux records derived from the two SO_2 camera stations (using the same automatic algorithm). The temporal plot highlights the transient gas pulses produced by the mild Strombolian explosive activity. These are superimposed over a continuous background SO_2 emission sustained by passive degassing. **(B)** VLP seismic displacement (bandpass filter: 0.05–0.2 Hz), derived from the EW component of ground motion recorded a STR station (Figure 1), highlighting the temporal match between VLP seismic events and gas pulses detected by the two SO_2 camera stations.

period (VLP) seismicity records (Figure 3B) are also used to detect independently the explosive activity at craters (Ripepe et al., 2021), and to validate the explosion-related nature of SO_2 pulses detected by automatic peak-find algorithm (McGonigle et al., 2009; Tamburello et al., 2012; Delle Donne et al., 2017).

Volcanic activity, tremor and VLP seismicity

During the time interval covered by our observations (June 2017–June 2018), volcanic activity remained within the "ordinary" Strombolian activity levels (Ripepe et al., 2008; Laiolo et al., 2022) that had persisted since the August-November 2014 effusive crisis (Rizzo et al., 2015; Zakšek et al., 2015; Valade et al., 2016; Delle Donne et al., 2017; Di Traglia et al., 2018). More specifically, the 2017–2018 period marked a phase of progressive Strombolian activity rejuvenation that interrupted a two-year long phase of very low activity following the 2014 effusive eruption. In our analyzed temporal interval, this activity rejuvenation manifests in regular mild (Strombolian) explosive activity being interrupted by eight major explosions, and by a short-lived lava summit overflows that took place on 15 December 2017 from the northern rim of the NEC crater (Giudicepietro et al., 2019).

To better interpret the degassing trends seen by the SO_2 cameras, we complement the gas results with other independent geophysical observations taken by the Laboratorio di Geofisica Sperimentale (LGS) of the University of Firenze (LGS, 2022 available at http://lgs.geo.unifi.it/index.php/monitoring/volcanoes/stromboli2). In particular, we here compare the observed gas results with volcanic tremor, Very Long Period (VLP) seismic rate, and the Volcanic Activity Index (Ripepe et al., 2009) reported by LGS. In particular the Volcano Activity Index is performed by weighting information from infrasonic amplitude of explosions/puffing activity (Ripepe et al., 2007), and thermal radiance detected either from fixed thermal cameras and from satellite images (Valade et al., 2016). This index can vary from low to very high depending on fluctuations of regular Strombolian activity, is calibrated over the last 20 years of continuous observations covering the three last main eruptive phases of 2007, 2014, and 2019, and thus constitutes a reliable proxy for volcanic intensity on Stromboli. During the period of investigation, the Volcanic Activity Index ranged from low to medium levels for ~80% of the period, with short-lived phases of "high" (≤20%).

Results

Vent-resolved SO_2 fluxes

The apparent total SO_2 fluxes (daily averages along with their associated weekly-long moving averages), independently evaluated from the two UV1 and UV7 SO_2 camera stations, are illustrated in Figure 4A, and show similar trends (Pearson correlation coefficient R=0.5). The SO_2 flux time-averaged means and standard deviations (for the period June 2017-June 2018) are 61 ± 32 t/d (range: 12–180 t/d) and 68 ± 45 t/d (range: 10–202 t/d) for UV1 and UV7, respectively, and fall at the lower bound of

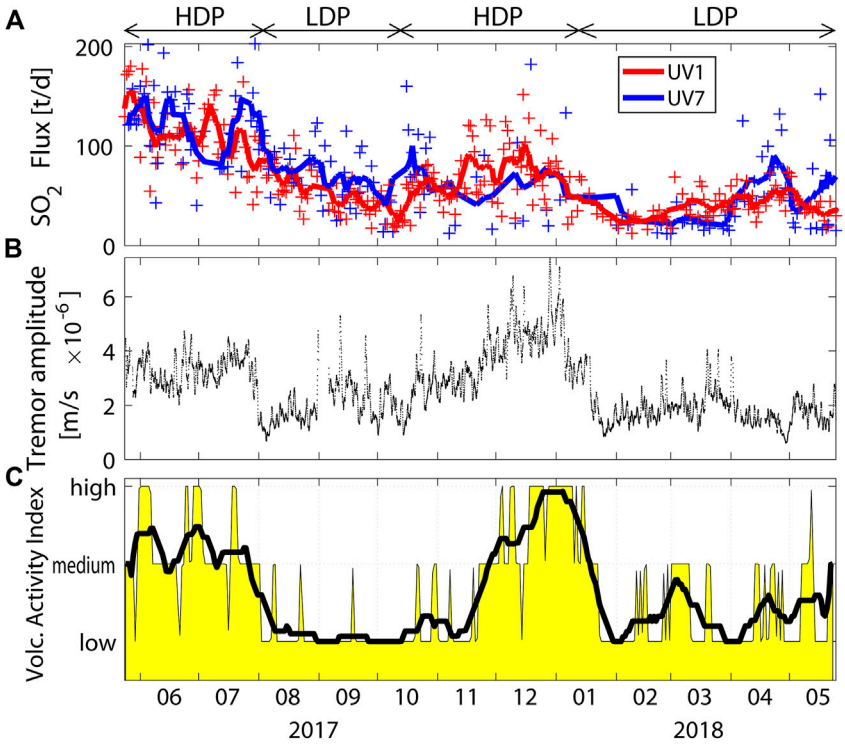

FIGURE 4
(A) Daily averaged SO_2 fluxes derived from the two SO_2 camera stations (crosses) with their 7-day long moving averages (solid lines), identifying the alternation of high (HDP) and low (LDP) degassing phases. The SO_2 temporal records obtained from the two SO_2 camera stations generally agree well in their long-term weekly averaged trends (that differ one each other by 28 ± 20%). Larger discrepancies are observed in individual measurement days, that spread around their weekly means by 44 ± 34%. **(B)** Volcanic tremor amplitude, and the **(C)** Volcanic Activity Index delivered daily by LGS-UNIFI (black line represents the associated 7-day moving average).

estimates obtained at Stromboli during regular persistent Strombolian activity (Allard et al., 2008; Burton et al., 2009; Delle Donne et al., 2017; Laiolo et al., 2022; LGS, 2022). The SO_2 temporal records obtained from the two camera stations generally agree well in their long-term weekly averaged trends, differing between each other by 28 ± 20%, up to a maximum of 79%. Larger discrepancies are observed in distinct daily measurements, which show a variability around their weekly mean of 44 ± 34% and a maximum difference of 143%. Besides such uncertainties, the long-term weekly averaged degassing trends inferred from the two camera stations show coherent fluctuations through time. We identify two main phases of relatively more sustained degassing activity (higher degassing phases, HDP) in June-August 2017 and October 2017-mid January 2018, when both SO_2 cameras exhibit higher-than-average SO_2 fluxes, and peak emissions of up to ~200 t/d. These two more energetic phases are separated by periods of lower degassing (lower degassing phases, LDP), during which the SO_2 fluxes average at ~50 t/d (Figure 4A). These SO_2 flux temporal variations are coherent with fluctuations detected by independent geophysical parameters, such as volcanic tremor amplitude (Figure 4B) and Volcanic Activity Index, as reported by LGS daily bulletins (Figure 4C).

Moreover, the close proximity of the SO_2 camera stations to the emission sources, together with their high spatial resolution (pixel size is less than 1 m), allows us to capture the gas at the vent exit before it spreads in the atmosphere. Figures 5A,B are temporal records of the normalized (daily averaged) spatial distribution of SO_2 column densities along the crater terrace, as separately imaged by the UV1 and UV7 SO_2 camera stations. In these temporal plots, the blue to red color tones are proportional to SO_2 column amounts. SO_2 column density peaks, marked by red areas, therefore convey information on the position(s) along the crater terrace where degassing activity concentrates (at any given time). These dominant gas-venting sources correspond to positions, within the crater terrace, of either one of the two main active vent sectors that can be resolved in the SO_2 cameras' field of view: the SWCC and the NEC. The limit (see white dashed lines in Figures 5A,B) between these two emission sources has been set at a fixed position along the transect based on visual inspection of the images, and corresponds to the area where the long-term averaged SO_2 density is the lowest. The figures demonstrate coherent (for the two SO_2 camera stations) temporal changes in the spatial distribution of SO_2 degassing: the SO_2 column density peaks (red

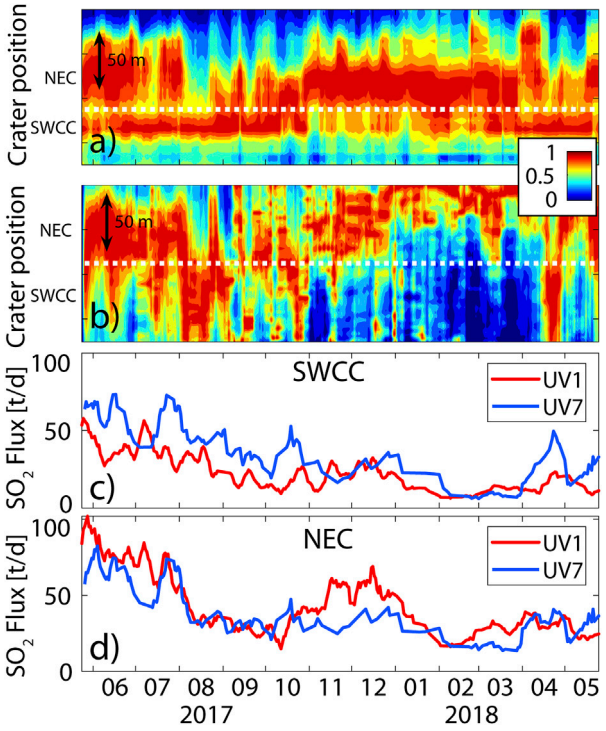

FIGURE 5
Temporal records of time-averaged normalized column densities along the a transect through the crater terrace (y-axis), as derived for UV1 **(A)** and UV7 **(B)** (from Figure 2). These plots highlight the presence of two main degassing sources in the crater terrace. White dashed lines in **(A,B)** represent the limit between SWCC and NEC areas, as identified from visual inspection of images (see also Figure 1). These plots are used to time resolving the flux contributions from the two identified sources in **(C)** and **(D)**.

tones) switch from one vent area to another multiple times during 2017–2018, implying large temporal fluctuations in the *NEC* vs. *SWCC* relative gas contributions.

By processing images from the two SO_2 camera stations, we derive two independent records of the vent-resolved contributions from NEC and SWCC, as illustrated in Figures 5C,D. This operation is accomplished by calculating the relative contribution of degassing between the two sources, and therefore by integrating, over the two segment portions of the profile associated with NEC and SWCC respectively, the normalized column densities (of Figures 5A,B). The two so-derived quantities are used to partition the total daily averaged SO_2 flux. Then, we obtain two different estimates for the same degassing source from the two independent SO_2 cameras (Figures 5C,D). The vent-resolved SO_2 fluxes obtained from the two cameras exhibit coherent temporal oscillations. However, as expected from the geometry of the network (the position of the two cameras relative to the SWCC and NEC; Figure 1, 2), a generally higher NEC SO_2 flux is derived from UV1 than from UV7 (Figure 5D); likewise, the SWCC SO_2 flux is generally largest as measured from UV7 (Figure 5C). In order to minimize these biases induced by the different positions of the SO_2 cameras, we therefore extract, for each measurement day, the maximum of the two independently estimated (one from UV1 and one from UV7) NEC and SWCC time-series, and take them as representative of the NEC and SWCC fluxes. The use of the maxima is justified by the fact that all source of uncertainties (cfr. 2.1), especially the incomplete plume coverage due to its frequent partial hiding behind the summit volcano's slopes (Figure 2), lead to SO_2 flux under-estimation. These maxima-based NEC and SWCC fluxes are graphically shown in Figure 6. Based on these results, we estimate time-averaged SO_2 fluxes and associated standard deviations for the entire period of investigations of 43 ± 22 t/d (range 9–116 t/d) for NEC and of 35 ± 22 t/d (range 4–99 t/d) for SWCC (Figure 6A).

Then, we calculate the total SO_2 flux (shown in Figure 6A) as the algebraic summation of the NEC and SWCC fluxes of Figure 6A. These total fluxes, integrating together results of the two SO_2 camera stations, are higher than the SO_2 flux records obtained by any single SO_2 camera (data in Figure 4A) for the reasons explained above. We infer a mean total (NEC+SWCC) SO_2 flux of 81 ± 40 t/d. During the LDPs, the daily total SO_2 flux averages at 54 ± 24 t/d (range, 17–123 t/d), the NEC SO_2 flux ranges between 13 and 55 t/d (mean, 31 t/d), and the SWCC SO_2 flux ranges between 4 and 72 t/d (mean, 23 t/d) (Figure 6A). During the HDPs, SO_2 degassing increases at both craters, with the NEC fluxes ranging between 15 and 116 t/d (mean, 57 t/d) and the SWCC fluxes between 8 and 97 t/d (mean 40 t/d); the total (NEC+SWCC) flux therefore averages at 97 ± 40 t/d (Figure 6A). Interestingly, during HDPs, the NEC SO_2 flux is roughly 43% as much as higher as the SWCC flux, while we observe a more similar SO_2 flux contributions from NEC and SWCC during LDPs, with NEC 30% higher than SWCC (Figure 6A).

We illustrate the relative contributions of NEC and SWCC to the SO_2 budget using the differential flux Φ_D (Figure 6B):

$$\Phi_D = \Phi_{NEC} - \Phi_{SWCC} \quad (2)$$

where Φ_{NEC} is the daily averaged SO_2 flux from NEC, and Φ_{SWCC} is daily averaged SO_2 flux from SWCC. Eq. 2 implies that Φ_D approaches ~0 when the two vent areas contribute same amounts of gas, Φ_D is >0 if NEC emits more SO_2 than SWCC, and <0 when/if SWCC is the dominant gas source. We find that Φ_D averages at 13 t/d, indicating that degassing is generally more intense at NEC than at SWCC, and shows significant fluctuations between -13 t/d and 44 t/d, up to three times respect than the long-term average. We also find that the fluctuations observed volcanic tremor amplitude mimic those observed in Φ_D (Figure 6B) and in the total SO_2 flux, with a correlation of R~0.53 and R~0.48 (Pearson coefficient)

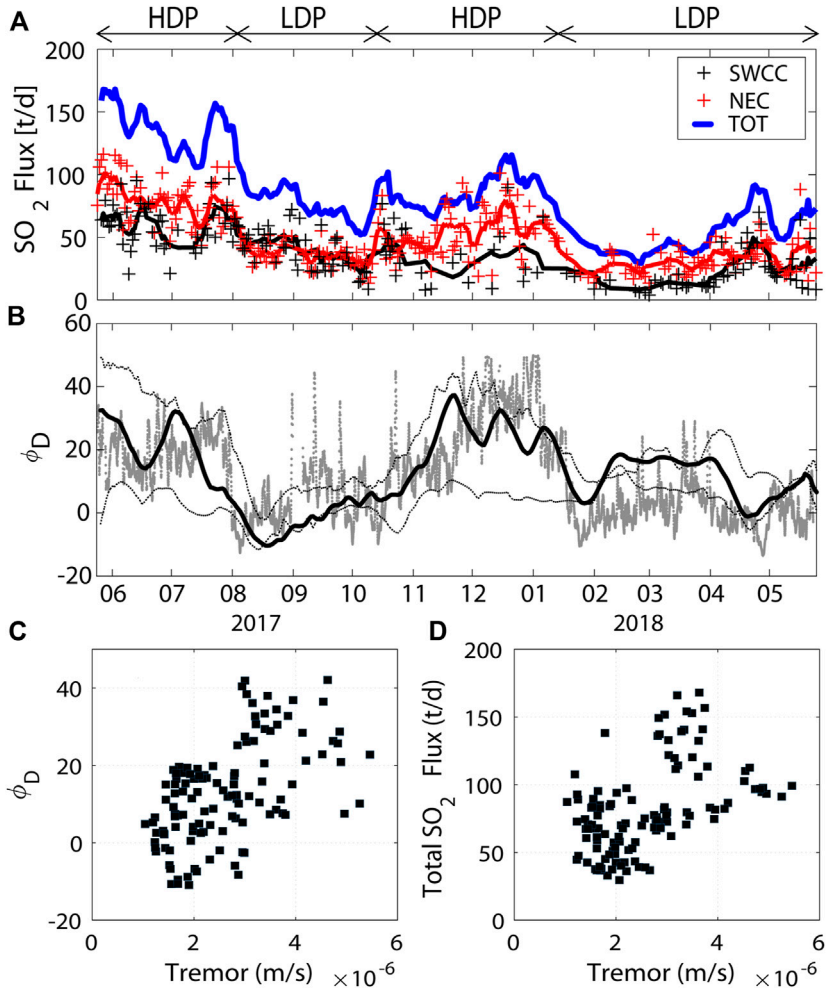

FIGURE 6
(A) SWCC (black) and NEC (red) SO_2 daily averaged fluxes (crosses) and their associated 7-day long moving averages (lines) are shown together with the total SO_2 fluxes (blue line, derived by summation of the two components). **(B)** The differential flux trend (Φ_D), calculated as the net difference between the two emission sources (the black bold line represents Φ_D calculated combining data from the two camera stations, while the two thin black lines represent Φ_D calculated using separately the data from UV1 and UV7 camera stations respectively), agrees well with the volcanic tremor temporal amplitude (gray). This suggests that escalating volcanic activity, as traced by HDPs, are accompanied by escalating SO_2 degassing clustering at the NEC. **(C)** and **(D)** represent the scatter plots relating tremor amplitude with Φ_D and total SO_2 fluxes respectively, which highlight how the increase in volcanic activity is always accompanied with an increase in bulk degassing with the NEC source contribution becoming dominant.

respectively (Figures 6B,C). Specifically, we find Φ_D to be much greater than its average (e.g., NEC dominates the total SO_2 budget) during phases of heightened activity (HDPs), when tremor amplitude (and volcanic activity, Figure 4C) is also high. In contrast, the low degassing regime (LDPs), during which tremor amplitude is consistently low, is associated with more similar contributions from the two crater regions, with Φ_D oscillating near its long-term average. In summary, our data show that degassing fluctuations nicely follow the fluctuations in the tremor amplitude (Figure 6D), and that the higher is the tremor amplitude and the more the degassing concentrates at the NEC (Figure 6C).

SO_2 degassing produced by the mild strombolian explosive activity

The high sampling rate of SO_2 cameras can be exploited to resolve the transient sin-explosive SO_2 pulses (that, as demonstrated by synchronous VLP seismic signals, are related to Strombolian explosions; Ripepe et al., 2021; Figure 3) from the passive (not associated with a VLP seismic signal) gas emissions (Mori and Burton, 2006; Tamburello et al., 2012; Delle Donne et al., 2017). Our aim here is to test if explosive degassing scales with passive degassing and with volcanic activity level. We caution that, due to the relatively slow acquisition rate used (0.5 Hz), our SO_2 camera stations cannot resolve the repetitive

(every 1–2 s) but short-lived (~0.5 s) degassing pulses produced by puffing (Harris and Ripepe, 2007a). In other words, the puffing contribution to degassing (accounting for ~16% of the total flux, according to Tamburello et al., 2012) is seen by the SO_2 cameras as a (unresolved) component of the background degassing signal. While in this study (for simplicity) we refer to the term "passive" to account for such non-explosive gas release, we are aware puffing involves, by definition, the release of over-pressured gas pockets (and, therefore, is ultimately an active degassing mode). We analyze the derived SO_2 flux time series with a peak finder routine (Delle Donne et al., 2017) to derive degassing exclusively associated with the explosions; this is possible thanks to their typical transient short-lived waveform that render them easily extractable from the gas flux time series (Figure 3A). In total, we identify ~7,000 explosive pulses throughout the study period (~1 year) associated with mild Strombolian explosions at the NEC and SWCC craters.

The SO_2-derived explosion rate varies widely during June 2017-June 2018, between 1 and 20 events/hour (Figure 7B). These variations parallel those of the passive SO_2 flux (Figure 7A) and of the seismic VLP rate (Figure 7B). The HDPs/LDPs are associated with parallel increase/decrease in the SO_2-derived explosion rate, from 5–20 events/hour during HDPs to 1-5 events/hour during LDPs. However, Figure 7B shows that the SO_2-derived explosive rate is always lower than VLP rate, confirming that SO_2 camera is not able to resolve the totality of the explosive events occurring at the summit craters. This is particularly true for the ash-rich explosions, which are typically difficult to detect spectroscopically (Kern et al., 2010a).

The automatic detection of explosive transients also allows quantifying the total SO_2 mass produced by each Strombolian explosion. This is obtained by time integration of a SO_2 flux time series after subtracting the stationary trend associated with passive degassing (Delle Donne et al., 2017). Then, we derive explosive SO_2 average masses and associated standard deviations of 30 ± 22 kg (range, 1–385 kg); these are released during temporal intervals of 24 ± 12 s on average, and up to 140 s (Figures 8A,B). Considering a typical 4 wt.% SO_2 concentration in Stromboli's explosive gas outbursts (Burton et al., 2007), the so-derived sin-explosive SO_2 masses convert into total explosion gas masses of 750 ± 550 kg, in agreement with previous observations (Mori and Burton, 2006; Tamburello et al., 2012; Delle Donne et al., 2016; Delle Donne et al., 2017). If we consider a temperature of ~625 K (Harris and Ripepe, 2007a) for a typical gas mixture, we can infer a ~0.35 kg/m^{3}gas density at ambient pressure, from which we estimate the total gas volume released by an explosion of 2,100 ± 1,600 m^3. This is consistent with previous estimates made with SO_2 cameras (1,500–4,100 m^3, Mori and Burton, 2006) and thermal records (300–3,000 m^3, Delle Donne and Ripepe, 2012). The summation of all explosive masses for each measurement day allows quantifying a record of the SO_2 flux (in tons/day) solely contributed by explosive activity (Figure 7B; see also Delle Donne et al., 2017). The passive SO_2 flux (Figure 7A; 8A) is then derived by subtracting the explosive flux from the total flux. Within the investigated period of analysis (June 2017-June 2018), the explosive SO_2 flux averages at 6 t/d (range, 0.3–20 t/d), on average contributing ~10% of the total SO_2 budget, confirming that explosive activity plays a minor role in the total magma degassing at Stromboli (see also Tamburello et al., 2012; Delle Donne et al., 2017). Notably, we find that the explosive and passive fluxes are well correlated (R=0.5; Figures 8C,D), showing coherent fluctuations during the analyzed temporal interval (Figure 7).

Discussion

Empirical constraints on potentials and limitations of automatically generated SO_2 camera-based fluxes

The automatic SO_2 flux retrievals using the UV camera method, although technically challenging, promise a step-change in our ability to capture the spatio-temporal evolution of volcanic degassing at open-vent volcanoes, with implications for volcano surveillance. However, the multiple sources of uncertainty related to this un-supervised method make it very difficult to apply it in real-time and in different volcanic environments worldwide.

SO_2 camera fluxes at volcanoes are typically quantified using a single camera pointing at the volcanic plume from one single viewing direction. This operation can be complicated by optical/geometrical constraints (complexities in the summit crater topography, and position of the Sun relative to the SO_2 camera station, among others), and can hamper a proper resolution of distinct gas emissions from multiple vents/craters (where they exist). Our SO_2 flux records here, based on applying the same automated algorithm to two independently acquired image datasets, demonstrate the advantage of using two SO_2 camera stations simultaneously, gathering plume images from two different viewing directions. Using two SO_2 camera stations, degassing from distinct sources can be more reliably quantified (Figure 5) and, by summation, a more robust estimate of the total SO_2 flux can be derived (Figures 4, 6, 7).

One important aspect is that, despite the use of a single SO_2 camera station can introduce greater uncertainties, we show (at least for Stromboli) that the two individual SO_2 camera records from UV1 and UV7 stations (Figure 4A) exhibit coherent temporal SO_2 fluctuations, and well record the alternation of high/low degassing regimes as well as the changes in degassing partitioning between the two individuated degassing sources (Figure 5). This demonstrates that the numerous uncertainties associated with the automatic method effectively play a minor role in producing biases which may affect significantly the reliability of the gas measurement. This observation corroborates the effectiveness of the single UV camera

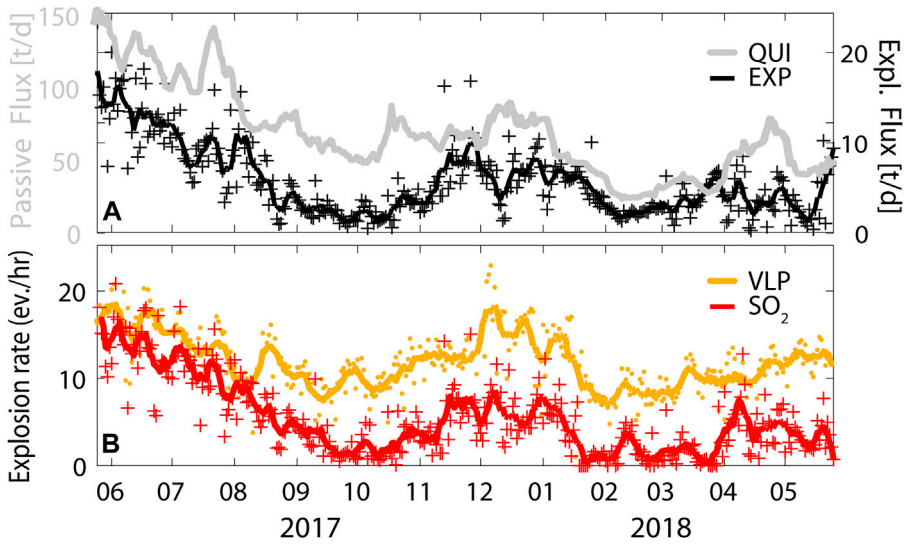

FIGURE 7
(A) Daily averaged (red crosses) SO_2 explosive fluxes and associated 7-day long moving averages (black line) range 1–20 t/d. These are plotted together with the passive fluxes (gray line), derived by removing the explosive flux component from the total fluxes of Figure 6A. Explosive and passive trends match well, as seen by the explosive flux increasing when the passive flux increases. **(B)** Explosion rates evaluated at a daily basis from SO_2 flux and VLP records show good similarities and the same fluctuations.

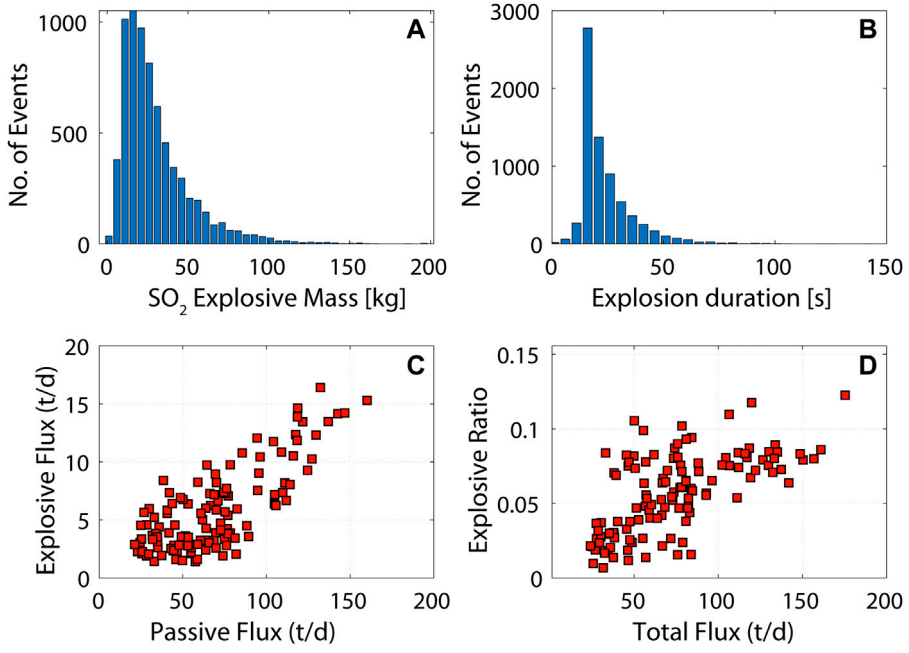

FIGURE 8
Histograms showing the frequency distributions of SO_2 masses **(A)** and SO_2 pulse durations **(B)** associated with the mild Strombolian explosions, obtained from a database of ~7,000 events. We estimate an average SO_2 mass released by individual Strombolian explosions of 30 ± 22 kg during temporal intervals of 24 ± 12 s and which can reach a maximum of 140 s; **(C)** Passive and explosive SO_2 fluxes show a positive correlation with R=0.5 that suggests a commonality in their source processes; **(D)** SO_2 total flux and the explosive to total degassing ratio are also positively correlated (i.e., the higher is the total gas flux, the more gas is released explosively).

approach to continuously monitor volcanic degassing in time, as already empirically demonstrated in occasion of the Stromboli's 2014 (Delle Donne et al., 2017) and 2019 (Aiuppa et al., 2021; Laiolo et al., 2022) crises. Notably, as the two cameras image the plume from two very distinct viewing directions (Figure 1), their generally coherent records (Figure 4A) suggest that uncertainties in UV camera-based gas quantification, arising from the different position of the SO_2 camera station relative to the plume, are relatively modest. We give an estimation of these uncertainties from the SO_2 flux difference between the two camera records in Figure 4A. This difference is 28 ± 20% (maximum difference of 79%) if calculated from the weekly averaged SO_2 fluxes measured at the two instruments, while it rises to 44 ± 34% (maximum difference of 143%) if daily average values are considered instead. We conclude our automatic SO_2 camera method can resolve well degassing intensity variations occurring over timescales of weeks to months, while accurately resolving faster (daily) variations is more complicated by instrumental and environmental noise due to intrinsic uncertainties of the method.

Evidence for magma channeling toward the NEC during enhanced volcanic activity

At the numerous volcanoes worldwide that comprise more than one simultaneously active crater/vent, degassing/eruptive activity is not uniformly distributed, but rather typically concentrated at one particular vent at any given time (Fee and Matoza, 2013; D'Aleo et al., 2016; D'Aleo et al., 2019). At Stromboli, for example, temporal shifts in infrasonic source location are frequently observed during periods of regular, mild Strombolian activity (Ripepe et al., 2007; Landi et al., 2011). These are interpreted as due to shifts in magmatic gas bubble flow into, and surface bursting from, the shallow conduits that feed the different active vents/craters (Ripepe et al., 2007, 2009). Our fully automatic SO_2 camera stations allow to systematically (and continuously) resolve the distinct emission sources over the crater terrace (Figures 1, 2). These results reveal, over temporal timescales of months, that the two degassing sources are active at the same time, although multiple swings in degassing partitioning along the crater terrace (red tones in Figures 5C,D), from one crater to another, are observed. While NEC and SWCC contribute ~60% and ~40% of the total SO_2 emissions on a yearly average (June 2017-June 2018), there exist large temporal fluctuations in their relative SO_2 contributions, as indicated by our Φ_D parameter ranging from −13 to +44 t/d, and averaging at 13 t/d (Φ_{AVG}). Notably, we find that such temporal changes are well consistent with oscillations in the intensity of regular Strombolian activity, as indicated by the geophysical proxies (Figures 4, 6, 7). We show, in particular, that periods of heightened degassing (HDP) and seismicity are systematically marked by degassing accelerating at the NEC over the SWCC ($\Phi_D > \Phi_{AVG}$); while periods of relatively reduced degassing (LDP) and milder Strombolian activity are systematically characterized by roughly similar SO_2 contributions ($\Phi_D \sim \Phi_{AVG}$) from the two sources (or even by the SWCC dominating over the NEC; $\Phi_D < 0$). These observations suggest that any increase in shallow magma transport (as indicated by increasing total SO_2 flux and seismicity; Allard et al., 2008; Ripepe et al., 2008) leads to preferential magma channeling toward the NEC (Figure 6B). This clustering of SO_2 degassing at NEC with heightened Strombolian activity is fully consistent with observed shifts in infrasound location before Stromboli's effusive eruptions (Ripepe et al., 2009; Valade et al., 2016).

The northeastern portion of Stromboli's crater terrace corresponds to a prime structural weakness zone of the volcano, as testified by geological information (Francalanci et al., 2013), geo-structural constraints (i.e., Tibaldi, 2001; Acocella et al., 2006; Corazzato et al., 2008), slope failure, ground deformation data (Tarchi et al., 2008; Tommasi et al., 2008), and geophysical evidence (Chouet et al., 2003; Ripepe et al., 2005; Marchetti et al., 2008). Magma accumulation (Ripepe et al., 2015; Ripepe et al., 2017) and cone growth in the gravitationally unstable NEC sector is known to trigger flank instability (Valade et al., 2016), opening of lateral vents, and onset of tsunamigenic lava effusion in the Sciara del Fuoco (Bonaccorso et al., 2003; Rosi et al., 2013; Di Traglia et al., 2014). As such, the ability of our SO_2 camera stations to spatially (vent-to-vent) resolve any magma input rate increase (Figure 6B) adds to existing geophysical knowledge (Ripepe et al., 2008; Ripepe et al., 2009; Ripepe et al., 2015) that helps forecasting transition from ordinary to effusive activity, with obvious implications for volcanic risk mitigation.

Explosive activity goes with passive degassing

One major advantage of UV cameras is that, because of their high temporal resolution, they allow identifying the rapid, transient SO_2 bursts produced by Strombolian explosions (Figure 3). We estimate an average SO_2 mass released by individual Strombolian explosions of 30 ± 22 kg. Our results, that use of a dataset of more than 7,000 explosions, strengthen previous conclusions (Mori and Burton, 2009; Tamburello et al., 2012; Delle Donne et al., 2017) of a minor (~10% on average) contribution of explosive degassing to the total (explosive + passive) SO_2 budget, at least during regular activity on Stromboli (Figures 7B, 8A).

Results indicate that gas is released during explosions in temporal intervals of 24 ± 12 s (up to 140 s), in the same order of magnitude as previously observed (Pering et al., 2016). The explosion-related SO_2 burst therefore last longer than thermal gas thrusts (5–15s; Ripepe et al., 2008), implicating a post-explosion degassing mechanism (Pering et al., 2016) in which daughter bubbles are delivered post-explosion from the de-compressing upper portion of the magma column (Ripepe et al., 2021).

One important novel aspect we bring here to light is the statistically significant (R ~0.5, Figure 8C) correlation between passive and explosive SO_2 fluxes during the observational period. This correlation suggests that passive and explosive degassing are commonly modulated, and are therefore likely to be driven by a common source process. One additional key (and novel) observation is that the explosive/total SO_2 flux ratio scales with the total SO_2 flux (Figure 8D), suggesting that more gas is released explosively as the total SO_2 flux (and volcanic activity) increases.

The total (explosive + passive) SO_2 flux on Stromboli (Allard et al., 1994; Allard et al., 2008), as well as at other open-vent volcanoes (Shinohara, 2008), is thought to be controlled by the rate of convective magma transport in the shallow (<3 km) plumbing system (Harris and Stevenson, 1997; Bonaccorso et al., 2008). This degassing-driven shallow magma convection process is operated by fresh (gas-rich) magma ascent continuously replacing viscous and degassed magma sinking back into the conduit (Shinohara, 2008). This mechanism helps to explain the observed excess SO_2 degassing (Allard et al., 2008), the longevity of Strombolian activity (Rosi et al., 2013), and the overall homogeneity of magma chemistry (Bertagnini et al., 2008). In a constant geometry (conduit radius) scenario (likely in the "stable" Stromboli 2017 conditions), any change in magma input (convection) rate would mainly be controlled by changing magma rheology, and especially by the density difference between non-degassed (ascending) and degassed (sinking) magmas (Stevenson and Blake, 1998; Shinohara, 2008). The latter in turn mostly depends on magma vesicularity (gas bubble volumetric fraction) of the ascending magma. Notably, ascent of a more "bubbly" magma in the conduits leads to both faster convection and escalating explosivity (Gonnermann and Manga, 2013), offering a simple explanation for the relationship between passive and explosive fluxes, observed here (Figure 8A). In this interpretation, Stromboli swings in between high and low degassing regime periods would depend on the bubble-rich vs. bubble-poor nature of the ascending magma (Ripepe et al., 2002). Following the methodology of Allard et al. (1994), Allard et al. (2008) we can convert the measured SO_2 fluxes into a magma input rate, and assuming an initial sulfur content of 0.18 wt%, a magma density of 2,700 kg/m^3, and a crystallinity of 30%. In line with previous estimations, we find a magma input rate ~0.15 m^3/s as threshold between HDP and LDP phases. Therefore, we propose that, as the magma supply rate in the conduit approaches or reaches this threshold, regular Strombolian activity intensifies, heighted tremor and VLP seismicity are observed, and degassing activity escalates to concentrate at the NEC (Figure 4-7). In the most extreme cases, this acceleration can lead to an effusive eruption (Ripepe et al., 2009).

A common source for explosive and passive degassing: Volcanological implications

Our results are also relevant to testing the role played by the viscous cap on-top of the conduit in driving the mild persistent and paroxysmal Strombolian explosive activity (Gurioli et al., 2014; Del Bello et al., 2015; Caracciolo et al., 2021; Mattia et al., 2021; Viccaro et al., 2021). There is a growing evidence supporting the presence of a crystal mush as a stable feature of the Stromboli's shallow conduit (Suckale et al., 2016; Barth et al., 2019; Ripepe et al., 2021), acting as a viscous cap.

The presence of a viscous cap would represent a permeability barrier for volcanic gases, thus promoting gas accumulation and the pressure buildup to trigger the explosive activity (Barth et al., 2019; Woitischek et al., 2020). An open question is if (and to what extent) Strombolian explosive activity can change with time in response to rheological (and geometrical) changes of the viscous cap. A permeability change in the viscous cap is, at least in principle, expected to modulate the partitioning between passive (bubbles) and explosive (slugs) degassing, ultimately determining a condition of enhanced explosivity at surface due by a permeability decrease (more bubbles accumulate deep instead to degas at surface, and forming more gas slugs) (Gurioli et al., 2014; Del Bello et al., 2015). This should be reflected in a drop of passive degassing in response to increased explosivity (Thivet et al., 2021). However, the observation evidence we bring to light in this study is that persistent vs. explosive gas emissions are instead commonly modulated (Figure 7, 8), indicating that fluctuations in explosive activity are also accompanied by coherent fluctuations of the passive (and total) degassing. These observations suggest a marginal (if any) role played by a potential rheologic stiffening of the viscous cap in controlling the observed week to monthly long trends in volcanic activity. The model we propose instead is one in which faster magma circulation of bubbly magma (Laiolo et al., 2022) leads to both more sustained passive degassing and larger sin-explosive gas release (Ripepe et al., 2002; Ripepe et al., 2009) (Figure 8D). Our results therefore suggest that viscous cap, although a stable element of the Stromboli's feeding conduit, plays no (or marginal) role in controlling degassing and activity regimes, at least over the first-order degassing fluctuations at a timescale of weeks-months.

Our coherent fluctuations between explosive and passive degassing (Figures 7, 8) suggest a common and unique degassing source, whose fluctuations through time are explained in term of changes in the rate of magma ascent (that, in turn, control the rate of bubble nucleation, expansion, and separate rise in the silicate melt). To reconcile this unique source of degassing with the widely accepted paradigm that passive and explosive gases at Stromboli are compositionally different (Burton et al.,

2007; Aiuppa et al., 2010; Pering et al., 2020; Woitischek et al., 2020), we invoke a role played by different re-equilibrium kinetics of small and large bubbles (slugs) in the conduit. Bubble ascent velocities are dependent on bubble size, so that large bubbles (that evolve into slugs by coalescence and expansion in the conduit, or at the base of the viscous plug) rise faster through silicate melts (Gonnermann and Manga, 2013). Because of their faster ascent, large bubbles, as the slugs feeding Strombolian explosions (Burton et al., 2007), are therefore more prone to preserve molar ratios (e.g., high CO_2/SO_2 and SO_2/HCl) characteristic of gas-melt equilibrium at deeper magmastatic depths than smaller bubbles. We caution that during gas bubble ascent, the temperature drop due to adiabatic expansion has been shown to promote bubble compositional change (Oppenheimer et al., 2018). However, such re-equilibration upon bubble adiabatic expansion and cooling, while affecting to some extent ratios between redox couples (e.g., SO_2/H_2S and CO_2/CO ratios), is unlikely to alter bulk gas chemistry (Oppenheimer et al., 2018). Ultimately, the high C, low-Cl signature of deeply sourced bubbles will be preserved if slugs rise fast. In contrast, the smaller bubbles sustaining passive degassing would travel slower within the conduit, therefore chemically re-equilibrating with the surrounding melt upon ascent in the shallow conduit, and ultimately acquiring their low CO_2/SO_2 and SO_2/HCl signature (Burton et al., 2007; Woitischek et al., 2020).

Conclusive remarks

Our automatic SO_2 flux measurements at Stromboli, derived from two simultaneously operating cameras observing the plume from two different viewing directions, support the robustness of SO_2 camera monitoring at volcanoes. Using two co-exposed SO_2 camera stations provides insights into temporal swings in degassing activity between the NEC and SWCC that can only partially be detected using one single SO_2 camera station (Delle Donne et al., 2017). When interpreted in tandem with seismic parameters (volcanic tremor and VLP seismicity), our vent-resolved SO_2 flux data contribute to better understanding degassing mechanisms operating in the shallow plumbing system during Stromboli's regular activity.

Our results indicate that regular degassing activity fluctuates significantly in terms of intensity and spatial distribution along the crater terrace, and concentrates at the NEC during the phases of escalating Strombolian activity. During phases of heightened regular Strombolian activity, as indicated by increasing volcanic tremor and VLP seismic rate, the total (passive + explosive) and explosive SO_2 fluxes increase in parallel. We propose these fluctuations reflect temporal changes in the gas bubble cargo of the feeding magma in the shallow conduits. Temporal records of SO_2 fluxes, captured at high spatial and temporal resolution by automated UV cameras, allows to "live" monitoring degassing activity, thus contributing to understanding (and potentially forecasting) changes in volcanic activity style.

Data availability statement

The raw data supporting the conclusion of this article will be made available by the authors, upon reasonable request.

Author contributions

DD conceived the manuscript and drafted the figures. DD and AA, and wrote the manuscript; EC analyzed and validated the results of the automatic processing; DD, MB, FM, JL, and GT designed, install, and maintained the permanent SO_2 camera stations; GL and MR analyzed the seismic VLP and tremor data. AA and MR supervised the work. All the authors have contributed to the realization of the final version of the manuscript.

Funding

The research leading to these results has received funding from the European Research Council under the European Union's Seventh Framework Programme (FP7/2007/2013)/ ERC grant agreement no. 305377 (Principal Investigator: AA). The authors also acknowledge funding from the Italian Civil Protection (DPC) through sub-contract with Università of Firenze (n. 2089/2019), from the Italian Ministero Istruzione Università e Ricerca (Miur, Grant No. 2017LMNLAW), and from Istituto Nazionale Geofisica e Vulcanologia (INGV, Grant Number 9999.815 VOLC-GAS).

Acknowledgments

We acknowledge RK and TP for their constructive comments, which improved the manuscript.

Conflict of interest

The authors declare that the research was conducted in the absence of any commercial or financial relationships that could be construed as a potential conflict of interest.

The handling editor SH declared a past co-authorship with the author AA.

Publisher's note

References

Acocella, V., Neri, M., and Scarlato, P. (2006). Understanding shallow magma emplacement at volcanoes: Orthogonal feeder dikes during the 2002–2003 Stromboli (Italy) eruption. *Geophys. Res. Lett.* 33, L17310. doi:10.1029/2006GL026862

Aiuppa, A., Bertagnini, A., Métrich, N., Moretti, R., Di Muro, A., Liuzzo, M., et al. (2010). A model of degassing for Stromboli volcano. *Earth Planet. Sci. Lett.* 295, 195–204. doi:10.1016/j.epsl.2010.03.040

Aiuppa, A., Bitetto, M., Delle Donne, D., La Monica, F. P., Tamburello, G., Coppola, D., et al. (2021). Volcanic CO2 tracks the incubation period of basaltic paroxysms. *Sci. Adv.* 7 (38), eabh0191. doi:10.1126/sciadv.abh0191

Allard, P. A., Carbonelle, J., Métrich, N., Loyer, H., and Zettwoog, P. (1994). Sulphur output and magma degassing budget of Stromboli volcano. *Nature* 368, 326–330. doi:10.1038/368326a0

Allard, P., Aiuppa, A., Burton, M., Caltabiano, T., Federico, C., Salerno, G., et al. (2008). "Crater gas emissions and the magma feeding system of Stromboli volcano," in *The Stromboli volcano: An integrated study of the 2002–2003 eruption*. Editors S. Calvari, S. Inguaggiato, G. Puglisi, M. Ripepe, and M. Rosi (Washington, DC: AGU), 182, 65–80. Geophys. Monogr. Ser.

Barth, A., Edmonds, M., and Woods, A. (2019). Valve-like dynamics of gas flow through a packed crystal mush and cyclic strombolian explosions. *Sci. Rep.* 9, 821. doi:10.1038/s41598-018-37013-8

Bertagnini, A., Métrich, N., Francalanci, L., Landi, P., Tommasini, S., and Conticelli, S. (2008). "Volcanology and magma geochemistry of the present-day activity: Constraints on the feeding system," in *Learning from Stromboli*. Editors S. Calvari, S. Inguaggiato, G. Puglisi, M. Ripepe, and M. Rosi (Washington, DC: Am Geophys Union), 182, 19–38. Geophys. Mon.

Bluth, G. S. J., Shannon, J. M., Watson, I. M., Prata, A. J., and Realmuto, V. J. (2007). Development of an ultra-violet digital camera for volcanic SO_2 imaging. *J. Volcanol. Geotherm. Res.* 161, 47–56. doi:10.1016/j.jvolgeores.2006.11.004

Bonaccorso, A., Calvari, S., Garfì, G., Lodato, L., and Patanè, D. (2003). Dynamics of the December 2002 flank failure and tsunami at Stromboli volcano inferred by volcanological and geophysical observations. *Geophys. Res. Lett.* 30 (18), 1941. doi:10.1029/2003GL017702

Bonaccorso, A., Gambino, S., Guglielmino, F., Mattia, M., Puglisi, G., and Boschi, E. (2008). Stromboli 2007 eruption: Deflation modeling to infer shallow-intermediate plumbing system. *Geophys. Res. Lett.* 35, L06311. doi:10.1029/2007gl032921

Bradski, G., and Kaehler, A. (2008). *Learning OpenCV: Computer vision with the OpenCV library*. Newton, MA, USA: O'Reilly Media.

Burton, M. R., Allard, P., Murè, F., and La Spina, A. (2007). Magmatic gas composition reveals the source depth of slug-driven Strombolian explosive activity. *Science* 317, 227–230. doi:10.1126/science.1141900

Burton, M. R., Caltabiano, T., Murè, F., Salerno, G., and Randazzo, D. (2009). SO_2 flux from Stromboli during the 2007 eruption: Results from the FLAME network and traverse measurements. *J. Volcanol. Geotherm. Res.* 182 (3), 214–220. doi:10.1016/j.jvolgeores.2008.11.025

Burton, M. R., Prata, F., and Platt, U. (2015). Volcanological applications of SO_2 cameras. *J. Volcanol. Geotherm. Res.* 300, 2–6. doi:10.1016/j.jvolgeores.2014.09.008

Calvari, S., Lodato, L., Steffke, A., Cristaldi, A., L Harris, A. J., Spampinato, L., et al. (2010). The 2007 Stromboli eruption: Event chronology and effusion rates using thermal infrared data. *J. Geophys. Res.* 115 (B04201), B04201. doi:10.1029/2009JB006478

Calvari, S., Spampinato, L., Bonaccorso, A., Oppenheimer, C., Rivalta, E., and Boschi, E. (2011). Lava effusion—A slow fuse for paroxysms at Stromboli volcano? *Earth Planet. Sci. Lett.* 301 (1–2), 317–323. doi:10.1016/j.epsl.2010.11.015

Calvari, S., Spampinato, L., Lodato, L., Harris, A. J. L., Patrick, M. R., Dehn, J., et al. (2005). Chronology and complex volcanic processes during the 2002–2003 flank eruption at Stromboli Volcano (Italy) reconstructed from direct observations and surveys with a hand-held thermal camera. *J. Geophys. Res.* 110, B02201. doi:10.1029/2004JB003129

Campion, R., Delgado-Granados, H., and Mori, T. (2015). Image-based correction of the light dilution effect for SO2 camera measurements. *J. Volcanol. Geotherm. Res.* 300, 48–57. doi:10.1016/j.jvolgeores.2015.01.004

Caracciolo, A., Gurioli, L., Marianelli, P., Bernard, J., and Harris, A. (2021). Textural and chemical features of a "soft" plug emitted during strombolian explosions: A case study from Stromboli volcano. *Earth Planet. Sci. Lett.* 559, 116761. doi:10.1016/j.epsl.2021.116761

Chouet, B., Dawson, P., Ohminato, T., Martini, M., Saccorotti, G., Giudicepietro, F., et al. (2003). Source mechanisms of explosions at Stromboli volcano, Italy, determined from moment-tensor inversions of very-long-period data. *J. Geophys. Res.* 108 (B1), ESE 7-1–ESE 7-25. doi:10.1029/2002JB001919

Corazzato, C., Francalanci, L., Menna, M., Petrone, C. M., Renzulli, A., Tibaldi, A., et al. (2008). What controls sheet intrusion in volcanoes? Structure and petrology of the Stromboli sheet complex, Italy. *J. Volcanol. Geotherm. Res.* 173, 26–54. doi:10.1016/j.jvolgeores.2008.01.006

D'Aleo, R., Bitetto, M., Delle Donne, D., Coltelli, M., Coppola, D., McCormick Kilbride, B., et al. (2019). Understanding the SO2 degassing budget of Mt etna's paroxysms: First clues from the december 2015 sequence. *Front. Earth Sci.* 6, 239. doi:10.3389/feart.2018.00239

D'Aleo, R., Bitetto, M., Delle Donne, D., Tamburello, G., Battaglia, A., Coltelli, M., et al. (2016). Spatially resolved SO2 flux emissions from Mt Etna. *Geophys. Res. Lett.* 43, 7511–7519. doi:10.1002/2016GL069938

Dalton, M. P., Waite, G. P., Watson, I. M., and Nadeau, P. A. (2010). Multiparameter quantification of gas release during weak strombolian eruptions at Pacaya volcano, Guatemala. *Geophys. Res. Lett.* 37, L09303. doi:10.1029/2010GL042617

Del Bello, E., Lane, S. J., R James, M., Llewellin, E. W., Taddeucci, J., Scarlato, P., et al. (2015). Viscous plugging can enhance and modulate explosivity of strombolian eruptions. *Earth Planet. Sci. Lett.* 423, 210–218. doi:10.1016/j.epsl.2015.04.034

Delle Donne, D., and Ripepe, M. (2012). High-frame rate thermal imagery of Strombolian explosions: Implications for explosive and infrasonic source dynamics. *J. Geophys. Res. Solid Earth* 117 (B9), 9206. doi:10.1029/2011JB008987

Delle Donne, D., Aiuppa, A., Bitetto, M., D'Aleo, R., Coltelli, M., Coppola, D., et al. (2019). Changes in SO_2 flux regime at Mt. Etna captured by automatically processed ultraviolet camera data. *Remote Sens. (Basel).* 11, 1201. doi:10.3390/rs11101201

Delle Donne, D., Ripepe, M., Lacanna, G., Tamburello, G., Bitetto, M., and Aiuppa, A. (2016). Gas mass derived by infrasound and UV cameras: Implications for mass flow rate. *J. Volcanol. Geotherm. Res.* 325, 169–178. doi:10.1016/j.jvolgeores.2016.06.015

Delle Donne, D., Tamburello, G., Aiuppa, A., Bitetto, M., Lacanna, G., D'Aleo, R., et al. (2017). Exploring the explosive-effusive transition using permanent ultraviolet cameras. *J. Geophys. Res. Solid Earth* 122, 4377–4394. doi:10.1002/2017jb014027

Di Traglia, F., Calvari, S., D'Auria, L., Nolesini, T., Bonaccorso, A., Fornaciai, A., et al. (2018). The 2014 effusive eruption at Stromboli: New insights from *in situ* and remote-sensing measurements. *Remote Sens. (Basel).* 10, 2035. doi:10.3390/rs10122035

Di Traglia, F., Nolesini, T., Intrieri, E., Mugnai, F., Leva, D., Rosi, M., et al. (2014). The ground-based InSAR monitoring system at Stromboli volcano: Linking changes in displacement rate and intensity of persistent volcanic activity. *Bull. Volcanol.* 139, 786–335. doi:10.1007/s00445-013-0786-2

Fee, D., and Matoza, R. S. (2013). An overview of volcano infrasound: From Hawaiian to plinian, local to global. *J. Volcanol. Geotherm. Res.* 249, 123–139. doi:10.1016/j.jvolgeores.2012.09.002

Francalanci, L., Lucchi, F., Keller, J., De Astis, G., and Tranne, C. A. (2013). "The aeolian islands volcanoes," in *Geol. Soc. Lond. Mem.* Editors F. Lucchi, A. Peccerillo, J. Keller, C. A. Tranne, and P. L. Rossi (London: Geological Society), 3737, p397–p471. Memoirs. doi:10.1144/M37.13

Giudicepietro, F., Calvari, S., Alparone, S., Bianco, F., Bonaccorso, A., Bruno, V., et al. (2019). Integration of ground-based remote-sensing and *in situ*

multidisciplinary monitoring data to analyze the eruptive activity of Stromboli volcano in 2017–2018. *Remote Sens. (Basel).* 11, 1813. doi:10.3390/rs11151813

Gonnermann, H. M., and Manga, M. (2013). "Dynamics of magma ascent in the volcanic conduit," in *Modeling volcanic processes: The physics and mathematics of volcanism* (Cambridge: Cambridge University Press), 55.

Gurioli, L., Colo', L., Bollasina, A. J., Harris, A. J., Whittington, A., and Ripepe, M. (2014). Dynamics of strombolian explosions: Inferences from field and laboratory studies of erupted bombs from Stromboli volcano. *J. Geophys. Res. Solid Earth* 119 (1), 319–345. doi:10.1002/2013jb010355

Harris, A. J. L., and Stevenson, D. S. (1997). Thermal observations of degassing open conduits and fumaroles at Stromboli and Vulcano using remotely sensed data. *J. Volcanol. Geotherm. Res.* 76, 175–198. doi:10.1016/s0377-0273(96)00097-2

Harris, A., and Ripepe, M. (2007b). Synergy of multiple geophysical approaches to unravel explosive eruption conduit and source dynamics—a case study from Stromboli. *Geochemistry* 67 (1), 1–35. doi:10.1016/j.chemer.2007.01.003

Harris, A., and Ripepe, M. (2007a). Temperature and dynamics of degassing at Stromboli. *J. Geophys. Res.* 112, B03205. doi:10.1029/2006JB004393

Kantzas, E. P., McGonigle, A. J., Tamburello, G., Aiuppa, A., and Bryant, R. G. (2010). Protocols for UV camera volcanic SO2 measurements. *J. Volcanol. Geotherm. Res.* 194 (1-3), 55–60. doi:10.1016/j.jvolgeores.2010.05.003

Kazahaya, R., Mori, T., Takeo, M., Ohminato, T., Urabe, T., and Maeda, Y. (2011). Relation between single very long period pulses and volcanic gas emissions at Mt. Asama, Japan. *Geophys. Res. Lett.* 38, L11307. doi:10.1029/2011GL047555

Kern, C., Deutschmann, T., Vogel, L., Wöhrbach, M., Wagner, T., and Platt, U. (2010a). Radiative transfer corrections for accurate spectroscopic measurements of volcanic gas emissions. *Bull. Volcanol.* 72 (2), 233–247. doi:10.1007/s00445-009-0313-7

Kern, C., Kick, F., Lübcke, P., Vogel, L., Wöhrbach, M., and Platt, U. (2010b). Theoretical description of functionality, applications, and limitations of SO₂ cameras for the remote sensing of volcanic plumes. *Atmos. Meas. Tech.* 3 (3), 733–749. doi:10.5194/amt-3-733-2010

Klein, A., Lübcke, P., Bobrowski, N., Kuhn, J., and Platt, U. (2017). Plume propagation direction determination with SO_2 cameras. *Atmos. Meas. Tech.* 10 (3), 979–987. doi:10.5194/amt-10-979-2017

Laiolo, M., Delle Donne, D., Coppola, D., Bitetto, M., Cigolini, C., Della Schiava, M., et al. (2022). Shallow magma dynamics at open-vent volcanoes tracked by coupled thermal and SO2 observations. *Earth Planet. Sci. Lett.* 594, 117726. doi:10.1016/j.epsl.2022.117726

Landi, P., Marchetti, E., La Felice, S., Ripepe, M., and Rosi, M. (2011). Integrated petrochemical and geophysical data reveals thermal distribution of the feeding conduits at Stromboli volcano, Italy. *Geophys. Res. Lett.* 38 (8). doi:10.1029/2010gl046296

LGS (2022). LGS bulletins. Available at: http://lgs.geo.unifi.it/index.php/reports/stromboli-daily (Accessed 11 October, 2022).

Lucas, B. D., and Kanade, T. (1981). An iterative image registration technique with an application to stereo vision. *IJCAI* 81, 674–679.

Marchetti, E., Ripepe, M., Ulivieri, G., Burton, M. R., Caltabiano, T., and Salerno, G. (2008). "Gas flux rate and migration of the magma column," in *The Stromboli volcano: An integrated study of the 2002–2003 eruption*. Editors S. Calvari, S. Inguaggiato, G. Puglisi, M. Ripepe, and M. Rosi (Washington, DC: AGU), 182, 259–267. Geophys. Monogr. Ser. doi:10.1029/182GM21

Mattia, M., Di Lieto, B., Ganci, G., Bruno, V., Romano, P., Ciancitto, F., et al. (2021). The 2019 eruptive activity at Stromboli volcano: A multidisciplinary approach to reveal hidden features of the "unexpected" 3 july paroxysm. *Remote Sens.* 13 (20), 4064. doi:10.3390/rs13204064

McGonigle, A. J. S., Aiuppa, A., Ripepe, M., Kantzas, E. P., and Tamburello, G. (2009). Spectroscopic capture of 1 Hz volcanic SO2 fluxes and integration with volcano geophysical data. *Geophys. Res. Lett.* 36 (21), L21309. doi:10.1029/2009gl040494

McGonigle, A. J. S., Pering, T. D., Wilkes, T. C., Tamburello, G., D'Aleo, R., Bitetto, M., et al. (2017). Ultraviolet imaging of volcanic plumes: A new paradigm in volcanology. *Geosciences* 7, 68. doi:10.3390/geosciences7030068

Mori, T., and Burton, M. (2009). Quantification of the gas mass emitted during single explosions on Stromboli with the SO_2 imaging camera. *J. Volcanol. Geotherm. Res.* 188 (4), 395–400. doi:10.1016/j.jvolgeores.2009.10.005

Mori, T., and Burton, M. (2006). The SO_2 camera: A simple, fast and cheap method for ground-based imaging of SO_2 in volcanic plumes. *Geophys. Res. Lett.* 33, L24804. doi:10.1029/2006GL027916

Nadeau, P. A., Werner, C. A., Waite, G. P., Carn, S. A., Brewer, I. D., Elias, T., et al. (2015). Using SO2 camera imagery and seismicity to examine degassing and gas accumulation at Kilauea volcano, May 2010. *J. Volcanol. Geotherm. Res.* 300, 70–80. doi:10.1016/j.jvolgeores.2014.12.005

Neri, M., and Lanzafame, G. (2009). Structural features of the 2007 Stromboli eruption. *J. Volcanol. Geotherm. Res.* 182, 137–144. doi:10.1016/j.jvolgeores.2008.07.021

Oppenheimer, C., Fischer, T. P., and Scaillet, B. (2014). "Volcanic degassing: Process and impact," in *Treatise on geochemistry*. Second Edition (Elsevier), 4, 111–179.

Oppenheimer, C., Scaillet, B., and Martin, R. S. (2011). Sulfur degassing from volcanoes: Source conditions, surveillance, plume chemistry and Earth system impacts. *Rev. Mineralogy Geochem.* 73 (1), 363–421. doi:10.2138/rmg.2011.73.13

Oppenheimer, C., Scaillet, B., Woods, A., Sutton, A. J., Elias, T., and Moussallam, Y. (2018). Influence of eruptive style on volcanic gas emission chemistry and temperature. *Nat. Geosci.* 11 (9), 678–681. doi:10.1038/s41561-018-0194-5

Penndorf (1957). Tables of the refractive index for standard air and the Rayleigh scattering coefficient for the spectral region between 02 and 200 μ and their application to atmospheric optics. *J. Opt. Soc. Am.* 47, 176–182. doi:10.1364/josa.47.000176

Pering, T. D., Liu, E. J., Wood, K., Wilkes, T. C., Aiuppa, A., Tamburello, G., et al. (2020). Combined ground and aerial measurements resolve vent-specific gas fluxes from a multi-vent volcano. *Nat. Commun.* 11 (1), 3039. doi:10.1038/s41467-020-16862-w

Pering, T. D., McGonigle, A. J. S., James, M. R., Tamburello, G., Aiuppa, A., Delle Donne, D., et al. (2016). Conduit dynamics and post explosion degassing on Stromboli: A combined UV camera and numerical modeling treatment. *Geophys. Res. Lett.* 43 (10), 5009–5016. doi:10.1002/2016gl069001

Platt, U., and Stutz, J. (2008). "Differential absorption spectroscopy," in *Differential optical absorption spectroscopy* (Berlin, Heidelberg: Springer), 135–174.

Ripepe, M., and Braun, T. (1994). Air-wave phases in strombolian explosion-quakes seismograms: A possible indicator for the magma level? *Acta vulcanol.* 5, 201–206.

Ripepe, M., Delle Donne, D., Genco, R., Maggio, G., Pistolesi, M., Marchetti, E., et al. (2015). Volcano seismicity and ground deformation unveil the gravity-driven magma discharge dynamics of a volcanic eruption. *Nat. Commun.* 6, 6998. doi:10.1038/ncomms7998

Ripepe, M., Delle Donne, D., Harris, A. J. L., Marchetti, E., and Ulivieri, G. (2008). "Dynamics of strombolian activity," in *The Stromboli volcano: An integrated study of the 2002–2003 eruption*. Editors S. Calvari, S. Inguaggiato, G. Puglisi, M. Ripepe, and M. Rosi (Washington, DC: AGU publication), 182, 39–48. doi:10.1029/182GM05

Ripepe, M., Delle Donne, D., Lacanna, G., Marchetti, E., and Ulivieri, G. (2009). The onset of the 2007 Stromboli effusive eruption recorded by an integrated geophysical network. *J. Volcanol. Geotherm. Res.* 182, 131–136. doi:10.1016/j.jvolgeores.2009.02.011

Ripepe, M., Delle Donne, D., Legrand, D., Valade, S., and Lacanna, G. (2021). Magma pressure discharge induces very long period seismicity. *Sci. Rep.* 11 (1), 20065. doi:10.1038/s41598-021-99513-4

Ripepe, M., Harris, A. J., and Carniel, R. (2002). Thermal, seismic and infrasonic evidences of variable degassing rates at Stromboli volcano. *J. Volcanol. Geotherm. Res.* 118 (3-4), 285–297. doi:10.1016/s0377-0273(02)00298-6

Ripepe, M., and Marchetti, E. (2002). Array tracking of infrasonic sources at Stromboli volcano. *Geophys. Res. Lett.* 29 (22), 33-1–33–4. doi:10.1029/2002GL015452

Ripepe, M., Marchetti, E., Ulivieri, G., Harris, A., Dehn, J., Burton, M. R., et al. (2005). Effusive to explosive transition during the 2003 eruption of Stromboli Volcano. *Geol.* 33 (5), 341–344. doi:10.1130/G21173.1

Ripepe, M., Marchetti, E., and Ulivieri, G. (2007). Infrasonic monitoring at Stromboli volcano during the 2003 effusive eruption: Insights on the explosive and degassing process of an open conduit system. *J. Geophys. Res.* 112, B09207. doi:10.1029/2006JB004613

Ripepe, M., Pistolesi, M., Coppola, D., Delle Donne, D., Genco, R., Lacanna, G., et al. (2017). Forecasting effusive dynamics and decompression rates by magmastatic model at open-vent volcanoes. *Sci. Rep.* 7, 3885. doi:10.1038/s41598-017-03833-3

Rizzo, A. L., Federico, C., Inguaggiato, S., Sollami, A., Tantillo, M., Vita, F., et al. (2015). The 2014 effusive eruption at Stromboli volcano (Italy): Inferences from soil CO_2 flux and $^3He/^4He$ ratio in thermal waters. *Geophys. Res. Lett.* 42, 2235–2243. doi:10.1002/2014gl062955

Rosi, M., Pistolesi, M., Bertagnini, A., Landi, P., Pompilio, M., and Di Roberto, A. (2013). "Stromboli volcano, aeolian islands (Italy): Present eruptive activity and hazards," in *The aeolian islands volcanoes*. Editors F. Lucchi, PeccerilloA, J. Keller, C. A. Tranne, and P. L. Rossi (Lyell Collection), 37, 473–490. doi:10.1144/M37.14

Saballos, J. A., Conde, V., Malservisi, R., Connor, C. B., Alvarez, J., and Munoz, A. (2014). Relatively short-term correlation among deformation, degassing, and

seismicity: A case study from concepción volcano, Nicaragua. *Bull. Volcanol.* 76, 843. doi:10.1007/s00445-014-0843-5

Shinohara, H. (2008). Excess degassing from volcanoes and its role on eruptive and intrusive activity. *Rev. Geophys.* 46, RG4005. doi:10.1029/2007RG000244

Stevenson, D. S., and Blake, S. (1998). Modelling the dynamics and thermodynamics of volcanic degassing. *Bull. Volcanol.* 60, 307–317. doi:10.1007/s004450050234

Suckale, J., Keller, T., Cashman, K., and Persson, P. O. (2016). Flow to fracture transition in a volcanic mush plug may govern normal eruptions at Stromboli. *Geophys. Res. Lett.* 43. doi:10.1002/2016gl071501

Tamburello, G., Aiuppa, A., Kantzas, E. P., McGonigle, A. J. S., and Ripepe, M. (2012). Passive vs. active degassing modes at an open-vent volcano (Stromboli, Italy). *Earth Planet. Sci. Lett.* 359–360, 106–116. doi:10.1016/j.epsl.2012.09.050

Tarchi, D., Casagli, N., Fortuny-Guasch, J., Guerri, L., Antonello, G., and Leva, D. (2008). Ground deformation from ground-based SAR interferometry. The Stromboli Volcano, an integrated study of the 2002–2003 eruption. *AGU Geophys. Monogr.* 182, 359–372.

Thivet, S., Harris, A. J., Gurioli, L., Bani, P., Barnie, T., Bombrun, M., et al. (2021). Multi-parametric field experiment links explosive activity and persistent degassing at Stromboli. *Front. Earth Sci. (Lausanne).* 9, 431. doi:10.3389/feart.2021.669661

Tibaldi, A. (2001). Multiple sector collapses at Stromboli volcano, Italy: How they work. *Bull. Volcanol.* 63, 112–125. doi:10.1007/s004450100129

Tommasi, P., Baldi, P., Chiocci, F. L., Coltelli, M., Marsella, M., and Romagnoli, C. (2008). "Slope failures induced by the December 2002 eruption at Stromboli volcano," in *The Stromboli volcano: An integrated study of the 2002–2003 eruption*. Editors S. Calvari, S. Inguaggiato, G. Puglisi, M. Ripepe, and M. Rosi (Washington, DC: AGU), 182, 129–145. Geophys. Monogr. Ser.

Valade, S., Lacanna, G., Coppola, D., Laiolo, M., Pistolesi, M., Delle Donne, D., et al. (2016). Tracking dynamics of magma migration in open-conduit systems. *Bull. Volcanol.* 78 (11), 78. doi:10.1007/s00445-016-1072-x

Varnam, M., Burton, M., Esse, B., Salerno, G., Kazahaya, R., and Ibarra, M. (2021). Two independent light dilution corrections for the SO2 camera retrieve comparable emission rates at masaya volcano, Nicaragua. *Remote Sens.* 13 (5), 935. doi:10.3390/rs13050935

Vergniolle, S., and Métrich, N. (2022). An interpretative view of open-vent volcanoes. *Bull. Volcanol.* 84 (9), 83–45. doi:10.1007/s00445-022-01581-5

Viccaro, M., Cannata, A., Cannavò, F., De Rosa, R., Giuffrida, M., Nicotra, E., et al. (2021). Shallow conduit dynamics fuel the unexpected paroxysms of Stromboli volcano during the summer 2019. *Sci. Rep.* 11 (1), 266. doi:10.1038/s41598-020-79558-7

Waite, G. P., Nadeau, P. A., and Lyons, J. J. (2013). Variability in eruption style and associated very long period events at Fuego volcano, Guatemala. *JGR. Solid Earth* 118, 1526–1533. doi:10.1002/jgrb.50075

Watson, I. M., Oppenheimer, C., Voight, B., Francis, P. W., Clarke, A., Stix, J., et al. (2000). The relationship between degassing and ground deformation at Soufriere Hills Volcano, Montserrat. *J. Volcanol. Geotherm. Res.* 98117, 117–126. doi:10.1016/S0377-0273(99)00187-0

Woitischek, J., Woods, A. W., Edmonds, M., Oppenheimer, C., Aiuppa, A., Pering, T. D., et al. (2020). Strombolian eruptions and dynamics of magma degassing at Yasur Volcano (Vanuatu). *J. Volcanol. Geotherm. Res.* 398, 106869. doi:10.1016/j.jvolgeores.2020.106869

Zakšek, K., Hort, M., and Lorenz, E. (2015). Satellite and ground based thermal observation of the 2014 effusive eruption at Stromboli Volcano. *Remote Sens. (Basel).* 7, 17190–17211. doi:10.3390/rs71215876

frontiers | Frontiers in Earth Science

TYPE Original Research
PUBLISHED 05 January 2023
DOI 10.3389/feart.2022.1064171

OPEN ACCESS

EDITED BY
Christoph Kern,
United States Geological Survey (USGS), United States

REVIEWED BY
Taryn Lopez,
University of Alaska Fairbanks, United States
Ben Esse,
The University of Manchester, United Kingdom

*CORRESPONDENCE
Manuel Wöllhaf,
woellhaf@tu-berlin.de

SPECIALTY SECTION
This article was submitted to Volcanology, a section of the journal Frontiers in Earth Science

RECEIVED 07 October 2022
ACCEPTED 29 November 2022
PUBLISHED 05 January 2023

CITATION
Markus B, Valade S, Wöllhaf M and Hellwich O (2023), Automatic retrieval of volcanic SO_2 emission source from TROPOMI products.
Front. Earth Sci. 10:1064171.
doi: 10.3389/feart.2022.1064171

Automatic retrieval of volcanic SO_2 emission source from TROPOMI products

Balazs Markus[1], Sébastien Valade[2], Manuel Wöllhaf[1]* and Olaf Hellwich[1]

[1]Fachgebiet Computer Vision & Remote Sensing, Technische Universität Berlin, Berlin, Germany, [2]Instituto de Geofísica, Universidad Nacional Autónoma de México (UNAM), Mexico City, Mexico

Volcanic sulfur dioxide (SO_2) satellite observations are key for monitoring volcanic activity, and for mitigation of the associated risks on both human health and aviation safety. Automatic analysis of this data source, including robust source emission retrieval, is in turn essential for near real-time monitoring applications. We have developed fast and accurate SO_2 plume classifier and segmentation algorithms using classic clustering, segmentation and image processing techniques. These algorithms, applied to measurements from the TROPOMI instrument onboard the Sentinel-5 Precursor platform, can help in the accurate source estimation of volcanic SO_2 plumes originating from various volcanoes. In this paper, we demonstrate the ability of different pixel classification methodologies to retrieve SO_2 source emission with a good accuracy. We compare the algorithms, their strengths and shortcomings, and present plume classification results for various active volcanoes throughout the year 2021, including examples from Etna (Italy), Sangay and Reventador (Ecuador), Sabancaya and Ubinas (Peru), Scheveluch and Klyuchevskoy (Russia), as well as Ibu and Dukono (Indonesia). The developed algorithms, shared as open-source code, contribute to improving analysis and monitoring of volcanic emissions from space.

KEYWORDS

clustering, satellite remote sensing, semantic segmentation, SO_2 volcanic plumes, volcano monitoring

1 Introduction

The accurate retrieval of the source location and mass loading of volcanic plumes is essential to study volcanic processes and mitigate the associated hazards. In particular, Sulfur Dioxide (SO_2) gas emissions are a key parameter informing on the eruptive activity of volcanoes (Oppenheimer et al., 2014). An increase in SO_2 flux is for instance often considered as a precursor to volcanic eruptions. Likewise, decrease in SO_2 emissions can indicate changes in the volcanic conduit permeability (Edmonds et al., 2003), which can lead to violent explosions (Matthews et al., 1997; Campion et al., 2018). Moreover, these volcanic gases can have severe impact on human health (Sierra-Vargas et al., 2018; Carlsen et al., 2021; Heaviside et al., 2021 and air traffic safety Bernard and Rose, 1990;

Prata, 2009; Schmidt et al., 2014). In particular, injection of sulfur dioxide in the atmosphere receives considerable attention due to its subsequent conversion into aerosols and potentially strong effects on global climate (Robock, 2000).

Space-based measurements of the atmospheric composition have blossomed over the past 2 decades, from relatively crude, prototype products, to refined products suitable for operational monitoring and assimilation. These products include tropospheric vertical column density of different gases, including SO_2 (Carn et al., 2017). In 2017, the Tropospheric Monitoring Instrument (TROPOMI) was launched onboard the Sentinel-5 Precursor satellite. Thanks to an improved spatial resolution at nadir (i.e., 3.5 km × 7 to 5.5 km footprint) and a better SO_2 detection limit (by a factor of 4 with respect to previous sensors), it significantly improved the possibility of detecting small SO_2 volcanic emissions previously undetectable (Theys et al., 2017; Theys et al., 2019). In turn, TROPOMI has been extensively used to accurately measure SO_2 masses and fluxes emitted from both passive volcanic degassing and large explosive eruptions (Corradini et al., 2021; Queißer et al., 2019; Pardini et al., 2020).

Nonetheless, the SO_2-contaminated pixels have no data regarding their origin nor source emission, meaning that only manual inspection and interpretation by the user can determine this. Yet it is of primordial importance to be able to discriminate gas plumes originating from neighboring volcanoes, especially in locations where multiple volcanoes are located in a relatively small area. Various attempts have been made to automatically obtain mass of SO_2 emitted from active volcanoes. The MOUNTS operational volcano monitoring system (Valade et al., 2019) for example, which automatically processes TROPOMI products over several tens of active volcanoes worldwide, was using in its initial version a radius-based approach to obtain SO_2 mass values per volcano, whereby SO_2 contaminated pixels were classified based on their distance to the source volcano. This method however presents pitfalls as gas emissions coming from neighboring volcanoes cannot be discriminated in a robust manner.

In general, SO_2 source emission estimation is most often performed manually, which is a tedious process involving human work. Automating this process can make analysis of eruptions significantly faster and more accurate, with the ultimate goal to provide the derived information in near real-time. Automatic plume detection algorithms for TROPOMI products have been actively researched in the recent years, not just for SO_2 (Cofano et al., 2021), but also for other gas species recorded by TROPOMI such as NO_2 (Finch et al., 2022). This work focuses on the retrieval of the gas source emission, rather than on its detection in the TROPOMI product.

We present different algorithms that were developed to retrieve the source of volcanic SO_2-contaminated pixels. The efficiency of these algorithms is tested at various active volcanoes worldwide. The article is organized as follows: in Section 2, the used materials and data are presented. In Section 3, the methods developed to classify the source of SO_2-contaminated pixels are summarized. The shortcomings, strengths and the overall results are presented in Section 4 while in Section 5 a discussion of the results and areas of improvement are presented. Final conclusions are then drawn in Section 6.

2 Materials and data

2.1 Sentinel-5P TROPOMI products of case-study volcanoes

In this work, Sentinel-5P Near-Real-Time (NRTI) L2 SO_2 products were used. NRTI products are suited for near-real-time applications and are only available during 15-days after sensing, after which they are merged and replaced by Offline (OFFL) products. For an arbitrary pixel in the product, several relevant data is available, including: vertical column density (VCD), which correspond to SO_2 gas density computed over vertical slices (1 km thick slices at three different altitudes of the atmosphere), the latitude and longitude of the pixel center point, and a SO_2 detection flag, provided in the TROPOMI SO_2 L2 product as "sulfurdioxide_detection_flag". This flag identifies pixels with a high SO_2 concentration (Romahn et al., 2022), by marking them with either 0 for no detection, 1 for SO_2 detection, 2 for clear volcanic detection, 3 for detection close to a known anthropogenic source, or 4 for detection at high SZA (potential false-positive). We hereafter use the term "detection mask" to refer to the matrix of all SO_2-contaminated pixels (all the pixels marked with flag ≥1), which is used as input to the algorithms presented here. Summing up the pixels volcanic SO_2 detection mask, using the vertical column density (VCD), the total mass of volcanic SO_2 plumes on the image can be calculated (Valade et al., 2019). This total SO_2 mass can then be assigned to one or multiple source volcanoes.

The algorithms were evaluated on non-cropped L2 SO_2 NRTI products collected by the monitoring system MOUNTS (http://www.mounts-project.com, Valade et al., 2019) over seven active volcanoes. These include: Sangay, Sabancaya, Nevado del Ruiz, Etna, Popocatépetl, Dukono, and Yasur, as shown in Table 3. These volcanoes were chosen based on their sustained SO_2 degassing activity, and based on the fact that several are located in regions where other nearby volcanoes are emitting contemporaneously. This allowed us to test the algorithms capability to discriminate plumes originating from different neighboring volcanoes. It is worth specifying that these volcanoes are those used for the quantitative evaluation of the algorithms, which implied generating hand-labeled ground truth (see Section 2.2). The algorithms were then applied to a larger list of volcanoes for qualitative evaluation, some of which are presented in the paper (e.g., Scheveluch, Klyuchevskoy, Ibu, Ubinas, Reventador). The products used for evaluation were acquired during the year 2021. In order to decrease the overall dataset, we selected 1 TROPOMI acquisition per day and per

TABLE 1 Overview of all the tested methods.

Binary classification						Multi-class classification	
Pixel-based			Cluster-based				
No wind	No wind	With wind	No wind	With wind	With wind	No wind	With wind
Radius search classifier (BC-1)	Flood-fill classifier (BC-2)	Flood-fill classifier with wind data (BC-3)	DBSCAN classifier (BC-4)	DBSCAN classifier with wind data (BC-5)	Reverse Trajectory DBSCAN classifier (BC-6)	Multi-class DBSCAN classifier (MC-1)	Multi-class Reverse Trajectory DBSCAN classifier (MC-2)

volcano, with 10-day interval between the products, resulting in a total of 231 non-cropped TROPOMI products used for evaluation. Given that the satellite orbit cycle repeat time is 16 days, this 10-day sampling allowed to sample various swath positions for each volcano, while reducing the overall dataset size.

2.2 Ground truth

In order to evaluate the performances of the algorithms, the entire set of volcanic SO_2 detection masks was hand-labeled with a unique label according to the source volcano, which was manually determined based on available meteorological data and volcano eruption records. These manual labels form the "ground truth", which is compared with the automated classification results to obtain metrics of their efficiency. The ground truth has the same size as the SO_2 detection mask, but instead of detection flags it contains either the source volcano ID for each flagged pixel, or a label of false volcanic SO_2 detection (which may occur when SO_2 pixels from anthropological sources get detected by the sensor as a volcanic SO_2 pixel–in this case the pixel should not be assigned to any volcano).

2.3 List of volcanoes

The algorithms use a list of volcano-specific data, which consists of the latitude, longitude, elevation, and a unique identification number for several volcanoes. In this list, all the volcanoes from the MOUNTS monitoring system (Valade et al., 2019) are included, even those that are not present in our case study, as they play a role in the way how some of the presented algorithms work.

2.4 Predicted plume trajectories

In order to obtain estimated trajectories of SO_2 plumes, the Hybrid Single-Particle Lagrangian Integrated Trajectory model (HYSPLIT) is used. HYSPLIT is a numerical model that is used to compute air parcel trajectories to determine how far and in what direction a parcel of air, and subsequently air pollutants, will travel. Lagrangian particle models compute trajectories of a large number of so-called particles to describe the transport and diffusion of tracers in the atmosphere (Stein et al., 2015). Combined with the archived reprocessed GDAS meteorological models (NCEP, NWS, NOAA, U.S. DOC, 2009), which are publicly available on NOAA's FTP servers, the estimated latitude and longitude of an air parcel can be obtained along a specified time range with great temporal resolution (Warner, 2018). Although reprocessed GDAS models are less suited to near real-time applications than the forecast GDAS models, these are expected to perform significantly better. The presented plume trajectories used by the algorithms were computed on a 12-h time range before/after sensing with 1-h temporal resolution. When generating forward trajectories, the start time of the trajectory is set to 1 h before the image acquisition time, and the backwards trajectories are started exactly at the image acquisition time.

3 Methods

The goal is, using the input of non-classified pixels of the volcanic SO_2 detection map (as non-geocoded matrices), and the additional wind and volcano information, to obtain an output of classified pixels, which can provide information about which volcano each pixel originates from. One volcano represents a class, meaning that a pixel being classified to a volcano can be interpreted as saying that the pixel originates from that specific volcano.

To reach this goal, eight algorithms are presented, as depicted in Table 1, in ascending order of complexity. Two approaches are tested, as shown in Figure 1: the first corresponds to binary classification methods (BC), which can decide whether a pixel is originating from a selected volcano (the queried volcano is required as an input) or not, and the second corresponds to multi-class classification methods (MC), which provide an estimate for each pixel about which volcano it originates from (no input volcano required). In the final subsection, the metrics used for the evaluation of these algorithms are presented.

3.1 Binary-class classification algorithms

An intuitive approach is to select a volcano, and iterate through the pixels with a binary decision algorithm that either associates the pixel with the selected volcano, or leaves it unassociated. Six binary-class classification algorithms are tested, which we describe hereafter.

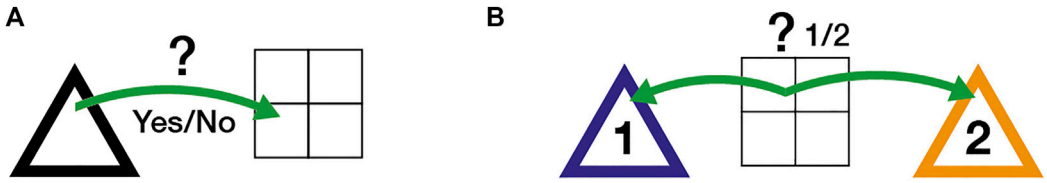

FIGURE 1
Difference between binary and multi-class classification approaches. **(A)** Binary approach. **(B)** Multi-class approach.

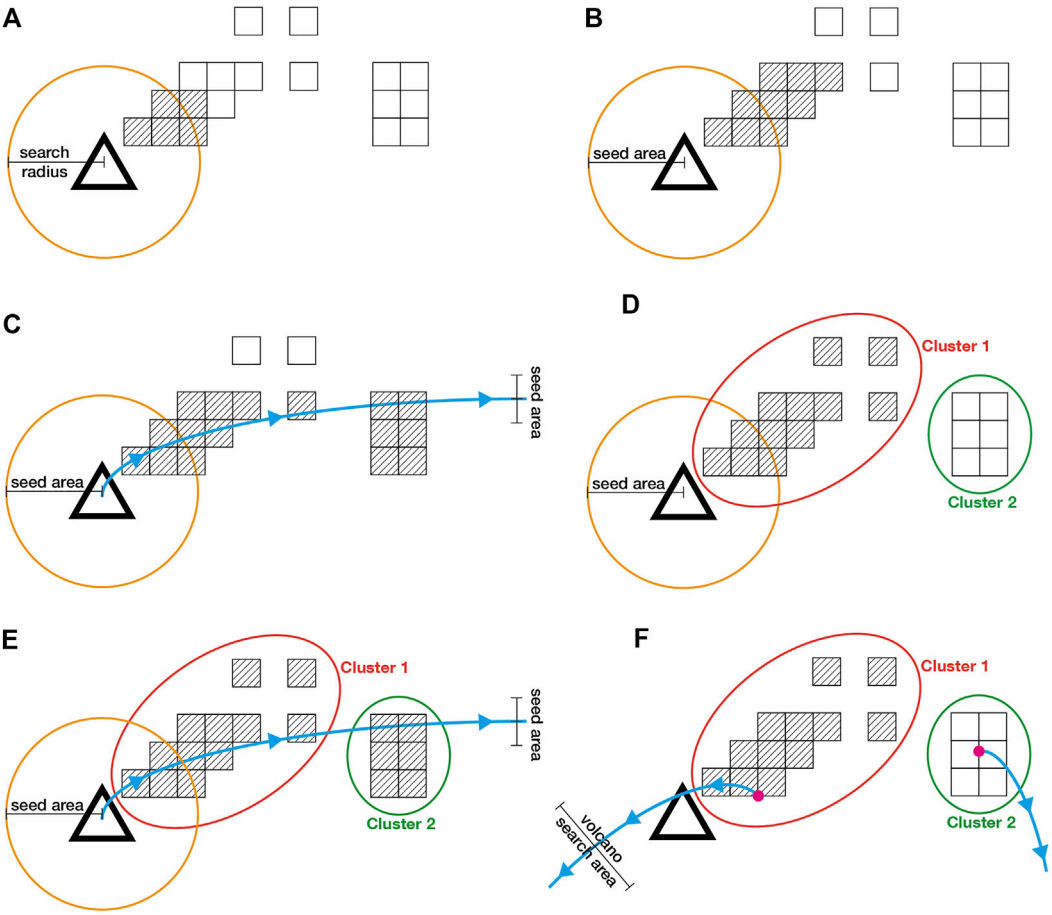

FIGURE 2
Demonstration of the binary classifier algorithms. **(A)** Radius search classifier. **(B)** Flood-fill classifier. **(C)** Flood-fill classifier with wind data. **(D)** DBSCAN classifier. **(E)** DBSCAN classifier with wind data. **(F)** Reverse Trajectory DBSCAN classifier.

3.1.1 Radius search classifier (BC-1)

The radius search classifier automatically associates every SO_2 detection within a specified arbitrary radius (100 km by default in this paper). The algorithm starts from the pixel at volcano center, then it iteratively jumps onto the next nearest unassociated pixel, as shown in Figure 2A. The distance of the pixel is then calculated with Vincenty's formulae using the ellipsoidal model WGS-84, which provides better accuracy than a plain spherical model (Vincenty, 1975). This process continues until the calculated distance of the new pixel is above the specified radius.

3.1.2 Flood-fill classifier (BC-2)

Flood-fill is a standard algorithm used to identify and change adjacent values in a multidimensional array, based on their similarity to an initial seed point. The conceptual analogy is the "paint bucket" tool in many graphic editors. The Flood-fill algorithm can be simply modeled as a graph traversal problem, representing the given area as a matrix and considering every cell of that matrix as a vertex that is connected to points around it. The seed point for the algorithm is set by default to the pixel where the volcano of interest is located. As the goal of the algorithm is to classify pixels that are flagged with detected SO_2-contamination, the seed point has to be an SO_2-flagged one on the detection mask (then, pixels marked with flag ≥1 that are touching the seed point are classified, and the filling continues until there are no additional touching points). If the seed point above the volcano is zero (meaning that there is no flagged SO_2 contamination), the algorithm searches for the nearest non-zero element within the seed area (20 km chosen by default in this paper), and if it finds one, it becomes the seed point, as shown in Figure 2B.

3.1.3 Flood-fill classifier with wind data (BC-3)

With the Flood-fill classifier (BC-2), the algorithm could only have one seed point. This case further increases the number of seed points *via* an extension where a predicted plume trajectory is generated, starting from the top of the queried volcano. Every point on this trajectory acts as a seed point, and if the trajectory point on the SO_2 detection mask is zero, the algorithm searches for the nearest non-zero element in a seed area the same way as with the original seed point, as shown in Figure 2C.

3.1.4 DBSCAN classifier (BC-4)

In the three previous algorithms, classification is done on a pixel level, using only information that is available for that individual pixel (i.e., values of pixels within the locality of another pixel are ignored). With object-based classification, the algorithms are working on a localized group of pixels, taking the spatial properties of each pixel and their relationship to each other into account. In this sense, an example for a classification algorithm acts on of a group of pixels, and the classification algorithm would accordingly output a class prediction for pixels on a group basis.

In order to acquire clusters, the DBSCAN (Density-based spatial clustering of applications with noise) algorithm is used. Based on a set of points, DBSCAN can group together points that are close to each other based on a (usually Euclidean) distance measurement and a minimum number of points (Ester et al., 1996). Furthermore, it is also capable of marking points in low-density regions as outliers.

Similarly to the Flood-fill classifier (BC-2), the DBSCAN classifier (BC-4) starts from a seed point and assigns new pixels to the cluster in an iterative way, with the difference that it is not filling pixels one-by-one, but rather whole clusters of pixels, as shown in Figure 2D. The seed area, similarly to the Flood-fill algorithms, is the pixel at the center of the volcano and its near area (20 km chosen by default in this paper).

The algorithm generally requires two parameters. The first is the parameter ε, which specifies how close points should be to each other on a pixel grid to be considered a part of a cluster. If the grid distance between two points is lower or equal to this value, those two points are considered neighbors. The second parameter is called *minPoints*, and it represents the minimum number of points to form a dense region. For example, setting the *minPoints* parameter as 4 means that at least 4 points are needed to form a dense region. Setting the ε parameter low generally produces more clusters, but it also results in an increased number of outliers, as shown in Figure 3. We chose a value $\varepsilon = 4.0$ and *minPoints* = 3 for our use case, which gave best results when applied to the TROPOMI data set. These values were chosen manually by testing several products, where noise points and outliers were minimized while preserving as many clusters as possible. In addition, DBSCAN makes it possible to assign weights to each pixel. We used the SO_2 column density value of each pixel as weights when creating clusters. This improves clustering in cases when multiple plumes originating from neighboring volcanoes come to overlap. In such a case they are forming a common plume, but as the SO_2 density generally tends to be higher around the center of the source volcanoes, the distinct high-density areas (which are thus highly weighted) can induce a separation of the unique plume into smaller clusters.

3.1.5 DBSCAN classifier with wind data (BC-5)

Similarly to the Flood-fill classifier with wind data (BC-3), this case is an extension of the DBSCAN classifier where a predicted plume trajectory is generated, starting from the top of the queried volcano, as shown in Figure 2E. Every point of this trajectory acts as a seed point, and if the trajectory point on the SO_2 detection mask is zero, the algorithm searches for the nearest non-zero element in a seed area the same way as with the original seed point.

3.1.6 Reverse trajectory DBSCAN classifier (BC-6)

A reverse plume trajectory is started from the center of mass of each cluster using the wind models, as shown in Figure 2F. The position of the center of mass is computed in grid space (i.e., in the non-geocoded matrix), weighted by the VCD values (raised to the power of 4 to make the dense parts more dominant in the positioning of the reference point in long plumes, as opposed to the simple DBSCAN classifier, where the weights only serve the cluster generation), and the latitude and longitude of the corresponding pixel is then used to define the cluster position, from which the trajectory is started. On the other hand, the altitude from which the trajectory is computed is defined as the summit altitude of the queried volcano. If a trajectory that was started from a plume is within a specified distance of the queried volcano (50 km by default in this paper), the cluster is associated

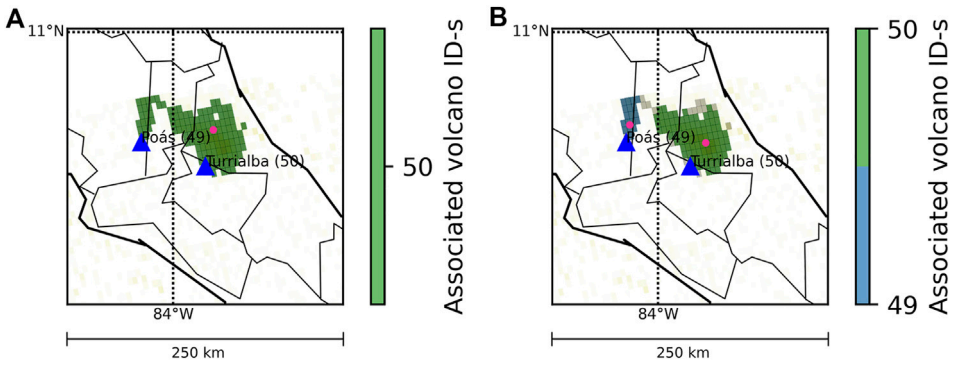

FIGURE 3
Difference in the created DBSCAN clusters with touching plumes (Turrialba and Poás volcanoes, on 23.03.2021), depending on the ε value. **(A)** ε = 4.0 **(B)** ε = 1.0.

with it. In the ideal case, the trajectory that starts from a cluster that is actually originating from the queried volcano should go right over the volcano.

3.2 Multi-class classification algorithms

The aforementioned algorithms have a common shortcoming: when applied to a TROPOMI product that covers an area that contains multiple volcanoes (which happens frequently in areas with high volcano density), the iterative use of binary classifiers can result in ambiguous, overlapping classifications, as shown in Figure 4. For example, if the predicted plume trajectories of two different volcanoes intersect, i.e. contain the same pixels, those pixels are going to be associated with both volcanoes. This happens frequently with nearby volcanoes (e.g., Ibu and Dukono volcanoes, only 35 km apart from one another). To prevent that, the algorithms should be retrofitted based on the fundamental concept that a pixel can only be associated with one volcano.

3.2.1 Multi-class DBSCAN classifier (MC-1)

The binary DBSCAN classifier algorithm could only associate one cluster to a volcano, even though it is possible for multiple clusters to originate from one source. To eliminate this problem, first we build the clusters the same way as we did in the binary DBSCAN case (BC-4), then we decide whether a cluster is going to be associated or not. This algorithm does not use any wind models, it only relies on the location of the volcanoes and the generated clusters (see Algorithm 1 pseudo-code). The latitude and longitude position of a cluster are equal to its calculated center of mass (computed in grid space, as described in BC-6), and the distance to the volcano is computed as the geodetic distance to the volcano summit. The plume height does not play a role in this case.

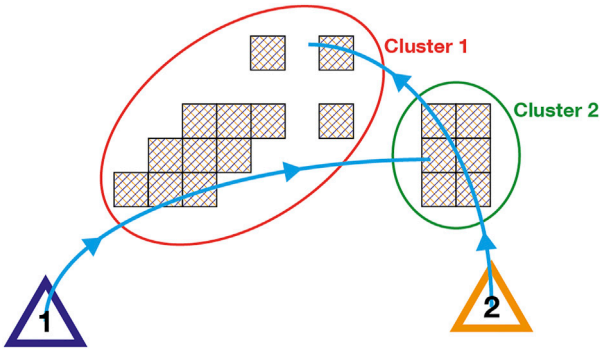

FIGURE 4
Iterative use of binary classifiers on the same image can result in overlapping classifications.

Input: SO_2 detection mask, list of volcanoes with coordinates (cannot be empty)
Output: List of cluster label - volcano ID pairs **associations**
clusters ← DBSCAN(SO_2 detection mask) ▷ labels and positions of clusters
current cluster ← Cluster that is nearest to any volcano
source volcano ← nearest volcano of current cluster
$n \leftarrow 1$
associations ← []
while len(associations) ≠ len(clusters) **do**
  if nearest volcano of current cluster = source volcano **then**
    if current cluster **not in** associations **then**
      append (current cluster, source volcano) to associations
    else
      current cluster ← current cluster's nearest unassociated cluster
    end if
  else
    if nearest volcano distance ≥ tolerance **and** jump distance ≤ nearest volcano distance **then**
      append (current cluster, source volcano) to associations
    else
      $n \leftarrow n + 1$
      current cluster ← cluster with the n-th smallest volcano-cluster distance
      source volcano ← nearest volcano of current cluster
    end if
  end if
end while

ALGORITHM 1. Multi-class DBSCAN classifier algorithm (MC-1).

First, the cluster that is the nearest to any volcano on the image is selected as a starting cluster, and its nearest volcano

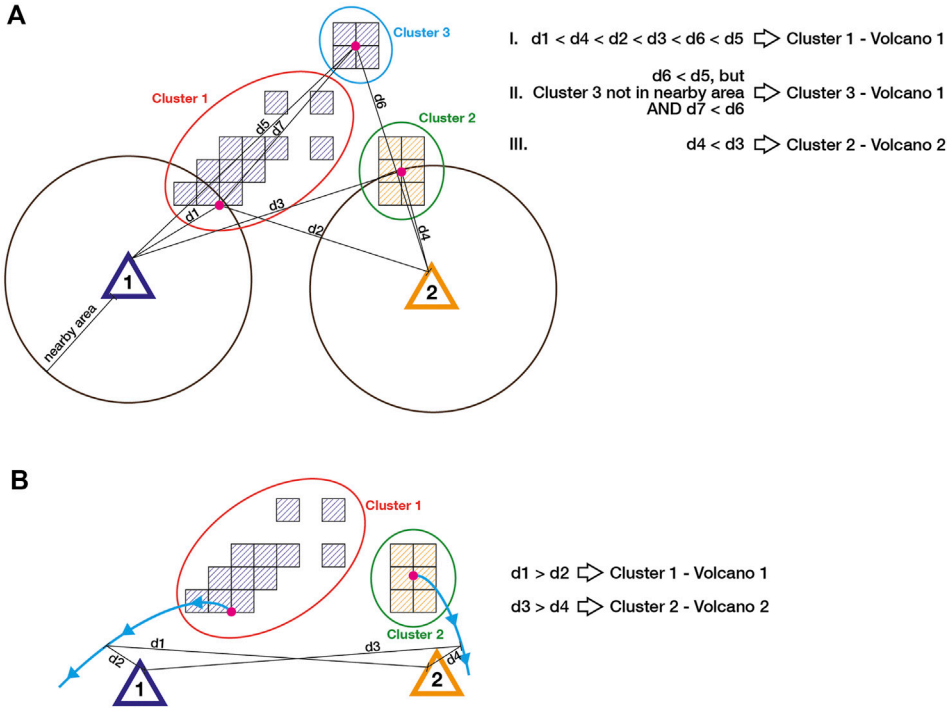

FIGURE 5
Demonstration of the multi-class algorithms. The magenta dot represents the plume center of mass, and the colored ovals show the generated clusters. **(A)** Multi-class DBSCAN classifier. **(B)** Multi-class Reverse Trajectory DBSCAN classifier.

becomes the "source volcano". The algorithm associates the nearest unassociated clusters until the new cluster's nearest volcano is not the source volcano anymore - in that case, it checks how far the new cluster is from the nearest volcano. If it's above a specified tolerance (200 km by default in this paper), and the new cluster is closer to the previous cluster than to the nearest volcano, it keeps assigning it to the original source volcano. This is to prevent another volcano of "hijacking" a plume in long stretched plume groups, when the plume is already closer to another cluster than to the original source volcano. Without this addition, the algorithm would associate every cluster automatically to the closest volcano. The procedure is depicted in Figure 5A.

If the aforementioned conditions do not apply, meaning that the next nearest cluster is farther than the specified tolerance (200 km), or if it is closer to its nearest volcano than to the previous cluster, the algorithm stops assigning clusters to the original source volcano, and it selects a new source volcano to start from. This is the volcano that is the nearest to any unassociated cluster (similarly, at the beginning we started at the smallest volcano-unassociated cluster distance, but at that time all the clusters were unassociated). The clusters are then being assigned the same way as with the original source volcano. To keep track of the jumps (and to be able to select the new source volcano), the number of source volcano changes is stored. Optionally, clusters that are further away from volcanoes and other clusters than a specified tolerance can be left unclassified. This is to ignore occasional false positives in the volcanic SO_2 detection mask in the TROPOMI product.

3.2.2 Multi-class reverse trajectory DBSCAN classifier (MC-2)

This algorithm follows the same logic as the binary Reverse Trajectory DBSCAN classifier (BC-6), with the additional rule that every cluster has to be associated with only one volcano (see Algorithm 2 pseudo-code). A reverse plume trajectory is started from the center of mass of every cluster using the wind models, as shown in Figure 5B. The latitude and longitude position of a cluster are equal to its center of mass, and the height of the plume, where the trajectory is started from, is equal to the elevation of its nearest volcano. As the TROPOMI L2 SO_2 product does not include plume height, using an input volcano's elevation as a plume height would make the algorithm volcano-dependent, and with this solution we can overcome that problem. The cluster is associated with the volcano that is nearest to any point of the reverse trajectory. In the ideal case, the trajectory goes right over the source volcano, which makes this distance zero.

TABLE 2 The performance metrics used in the evaluation.

Measure	Equation	Domain	Ideal value
F1-score	$F1 = \frac{2*Precision*Recall}{Precision+Recall} = \frac{2*TP}{2*TP+FP+FN}$	[0,1]	1
Precision	$Precision = \frac{TP}{TP+FP}$	[0,1]	1
Recall	$Recall = \frac{TP}{TP+FN}$	[0,1]	1
Accuracy	$Accuracy = \frac{TP+TN}{TP+TN+FP+FN}$	[0,1]	1

Input: SO_2 detection mask, list of volcanoes with coordinates (cannot be empty)
Output: List of cluster label - volcano ID pairs **associations**
clusters ← DBSCAN(SO_2 detection mask) ▷ labels and positions of clusters
associations ← []
for all cluster **in** clusters **do**
trajectory ← reverse trajectory starting from cluster center of mass
associated volcano ← first volcano in the volcano list
for all point **in** trajectory **do**
if nearest volcano to point ≥ distance to associated volcano **then**
associated volcano ← nearest volcano to point
end if
end for
append (cluster, associated volcano) to associations
end for

ALGORITHM 2. Multi-class Reverse Trajectory DBSCAN classifier algorithm (MC-2).

3.3 Metrics for the evaluation

Evaluation of classification methods can be quite complex because it is required to measure classification accuracy as well as localization correctness. The aim is to score the similarity between the predicted and annotated volcanoes (prediction vs. ground truth). Over the years, a large variety of evaluation metrics has been introduced. The presented metrics in this work are common, widespread scores for performance measurement in computer vision and remote sensing fields. The main goal in metric selection was to minimize statistical bias in evaluation.

All presented metrics are based on the computation of a confusion matrix for a binary segmentation task, which contains the number of true positive (TP), false positive (FP), true negative (TN), and false negative (FN) predictions. In this context, a true positive pixel is a detected SO_2-contaminated pixel which was correctly classified to the queried volcano, and a false positive pixel is one that was incorrectly classified to the queried volcano. Similarly, a true negative pixel is one that is correctly not classified to the queried volcano, and a false negative pixel is one that is incorrectly not classified to the queried volcano. Generally, the value ranges of all presented metrics span from zero (worst) to one (best). The selected metrics are Accuracy, Precision, Recall, and the F1-Score, as presented in Table 2.

- **Accuracy** represents *the fraction of predictions that the evaluated model got right.*
- **Precision** shows *the proportion of positive identifications that were actually correct.*
- **Recall** shows *the proportion of actual positives that were identified correctly.*
- The **F1-score** is an overall measure of a model's effectiveness that *combines precision and recall, by calculating the harmonic mean.* We use the harmonic mean instead of a simple average because it punishes extreme values. A classifier with a precision of 1.0 and a recall of 0.0 has a simple average of 0.5 but an F1-score of 0. That is, a good F1-score means that we have low false positives and low false negatives, so we are correctly identifying real threats and we are not disturbed by false alarms. The aforementioned features make this metric well suited for measuring the performance of the tested algorithms.

4 Results

In this section, the performances of the proposed algorithms are compared using the presented metrics. The algorithms were all implemented in a Python environment. The source code of the

TABLE 3 Contents of the evaluating dataset.

Name	Latitude [dec. deg.]	Longitude [dec. deg.]	Elevation [m]	Country	Time range	Temporal resolution
Sangay	−2.005	−78.341	5,286	Ecuador	01 Jan 2021–30 Nov 2021	10 days
Sabancaya	−15.787	−71.857	5,960	Peru	01 Jan 2021–30 Nov 2021	10 days
Nevado del Ruiz	4.892	−75.324	5,279	Colombia	01 Jan 2021–30 Nov 2021	10 days
Etna	37.748	14.999	3,295	Italy	01 Jan 2021–30 Nov 2021	10 days
Popocatépetl	19.023	−98.622	5,426	Mexico	01 Jan 2021–30 Nov 2021	10 days
Dukono	1.693	127.894	1,229	Indonesia	01 Jan 2021–30 Nov 2021	10 days
Yasur	−19.532	169.447	361	Vanuatu	01 Jan 2021–30 Nov 2021	10 days

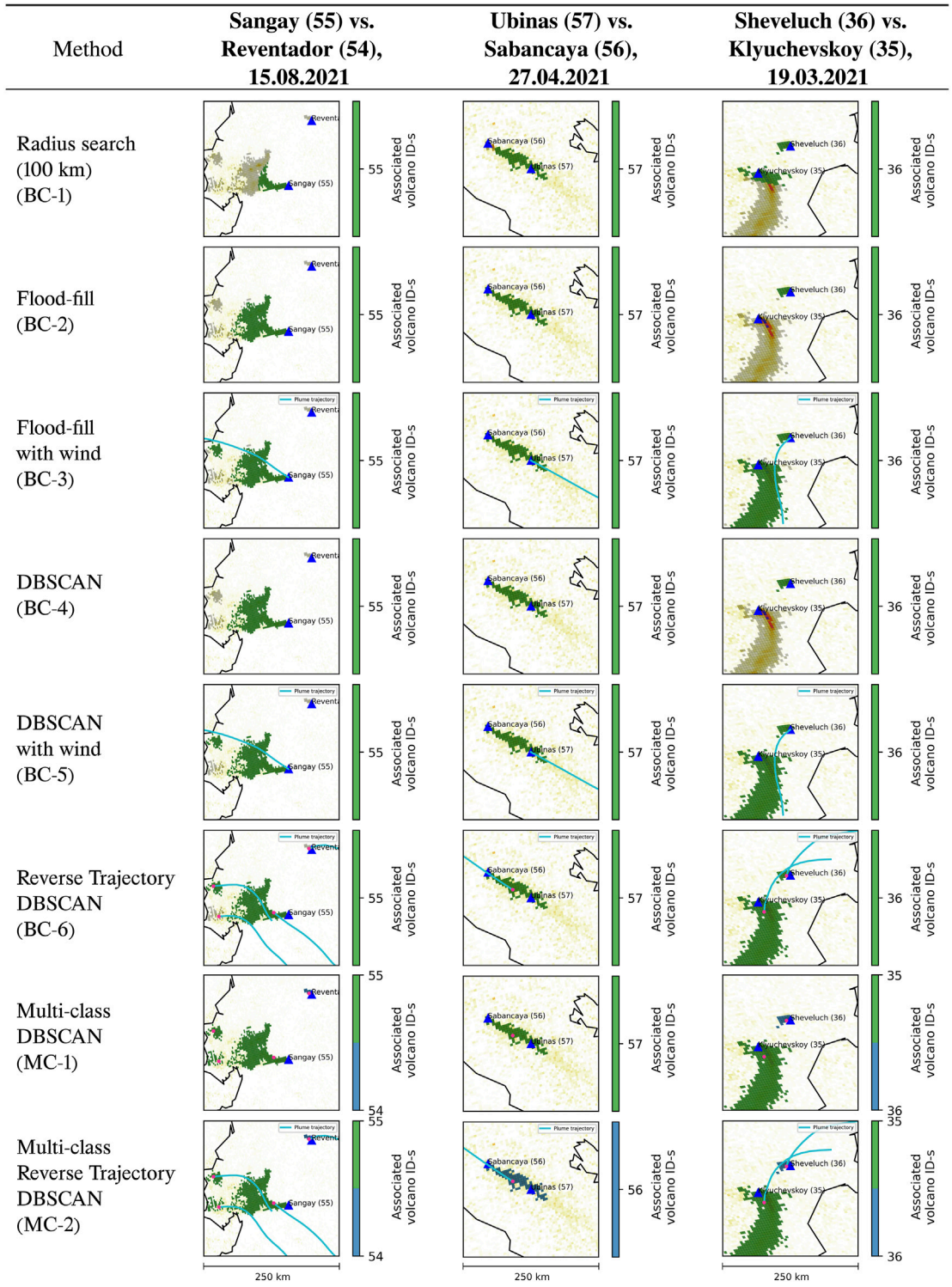

FIGURE 6
Plots of evaluation runs with different classifier algorithms on three volcanic scenarios. The plots represent 250 × 250 km regions. Magenta dots represent cluster center of mass, and cyan lines are computed plume trajectories.

TABLE 4 The mean values of performance metrics across the evaluating dataset.

	Binary classification								Multi-class classification	
	Pixel-based				Cluster-based					
	No wind		With wind		No wind		With wind		No wind	With wind
	Radius search (100 km) (BC-1)	No wind Flood-fill (BC-2)	Flood-fill with wind (BC-3)		DBSCAN (BC-4)		DBSCAN with wind (BC-5)	Reverse Trajectory DBSCAN (BC-6)	Multi-class DBSCAN (MC-1)	Multi-class Reverse Trajectory DBSCAN (MC-2)
F1-score	**0.6655**	**0.8365**	**0.8817**		**0.9030**		**0.9309**	**0.9054**	**0.9451**	**0.9313**
Precision	0.9725	0.9748	0.9650		0.9718		0.9636	0.9414	0.9478	0.9594
Recall	0.5594	0.6576	0.8061		0.7383		0.8778	0.7277	0.8664	0.8498
Accuracy	0.6328	0.7209	0.8313		0.7804		0.8823	0.7430	0.8532	0.8432

algorithms is publicly available from a GitHub repository (Markus, 2022a).

To verify that the accuracy improvement provided by the proposed methods is significant, and to systematically evaluate the performance of the proposed methods we conduct an averaging of the results for different products. We select TROPOMI SO_2 products of seven volcanoes, with a 10-day temporal resolution across the year of 2021, as shown in Table 3. The labeled ground truth and the configuration files are publicly available (Markus, 2022b). We compute the accuracy, precision, recall and F1-score for the presented algorithms using the selected products within the specified time range. The values are then averaged for the cases where classification is possible (empty cases without detection are not taken into account). The initial hypothesis is that the multi-class methods reach a higher overall mean accuracy.

4.1 Evaluation

Figure 6 shows a series of TROPOMI SO_2 images, overlaid with the classification results of the 8 algorithms described previously. Three cases were considered: Sangay (queried volcano) *vs.* Reventador 2021-08-15 acquisition, Ubinas (queried volcano) *vs.* Sabancaya 2021-04-27 acquisition where a plume originating from Sabancaya traveled over the Ubinas volcano, and Sheveluch (queried volcano) *vs.* Kluchevskoy 2021-03-19 acquisition. Each row in Figure 6 shows the result of a given algorithm for all three cases. The shades of white to yellow/red represent the SO_2 gas concentration, the gray pixels are the flagged SO_2 detections in the TROPOMI product, and the green/blue filled pixels are the pixels that were associated with a volcano label according to the color bar. The cyan lines are the wind trajectories, and the magenta points represent the center of mass of a generated cluster.

The results for each metric respective to the algorithms are presented in Table 4. Results show that on average, the radius search algorithm (BC-1) under-performs compared to other methods. The precision of the algorithm is high, but the recall value is comparatively low. The small value of recall indicates that this algorithm is prone to under-segmentation (which means it ignores pixels that should have been associated with the volcano), while also not providing any prevention from falsely associating SO_2 pixels of nearby volcanoes. This algorithm performs best in areas where the spatial density of volcanoes is low, and/or where winds are low (i.e., plume stays close to the volcano).

The second proposed method, Flood-fill (BC-2) shows a higher degree of robustness with respect to the accuracy, and is able to classify entire plumes, which the radius search algorithm failed to achieve (see Figure 7). Still, it fails to provide fully satisfactory classification as it is only able to fill

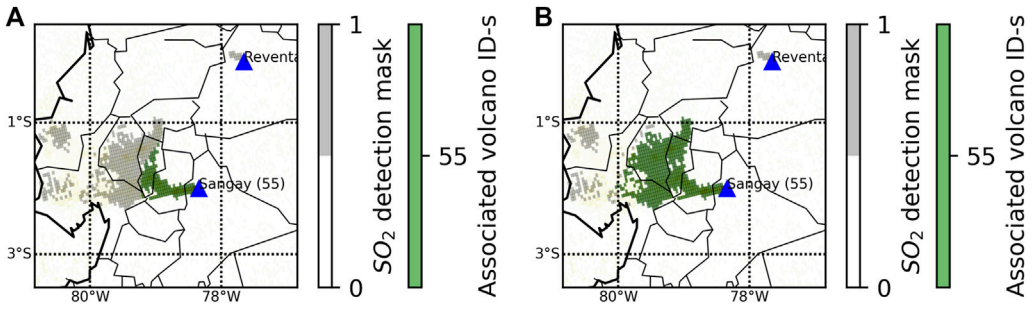

FIGURE 7
Comparison of two basic binary classifications (Sangay volcano, on 15.08.2021). **(A)** Radius search classifier. **(B)** Flood-fill classifier.

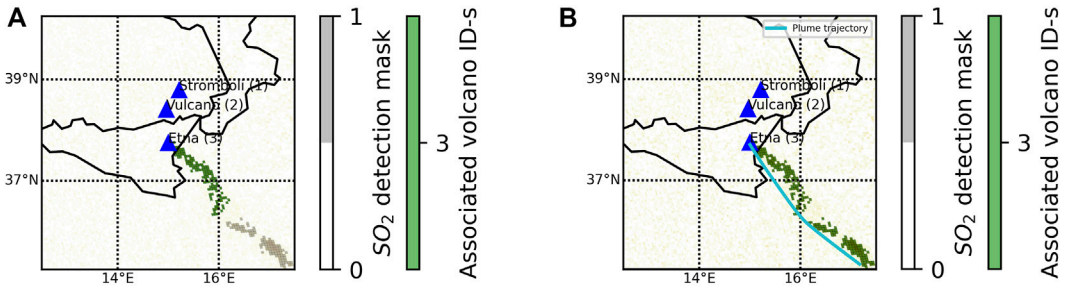

FIGURE 8
Difference in binary DBSCAN classifications (Etna volcano, on 17.06.2021). **(A)** Without wind. **(B)** With wind.

interconnected plumes. Indeed, SO_2 plumes often appear discontinuous in TROPOMI imagery, thus making the filling approach incapable of classifying the gas plume as a whole. Small isolated SO_2-contaminated pixels near the plume are also left unfilled, as there is no direct connection to the plume. The extension of the Flood-fill algorithm with the air parcel trajectory (BC-3) starting from the volcano achieves a better accuracy, because it is able to fill disconnected plumes, thanks to the wind trajectory which acts as an extended seed area. Although it still leaves isolated SO_2 pixels near the main plume unfilled, the bulk of the plume can be successfully filled. Extension of the seed area induces a significant increase in recall, but a small decrease in precision can be observed. Informally, besides reducing under-segmentation, the larger seed area caused the algorithm to incorrectly associate pixels that were originating from a different source, especially in areas of multiple SO_2 sources.

The cluster-based DBSCAN filling method (BC-4) demonstrates higher accuracy and recall value with respect to the pixel-based Flood-fill, as besides incorporating small isolated SO_2 pixels near the edges a plume, fragmented but cohesive plumes are considered as one entity. Extending this with the air parcel trajectory starting from the volcano (BC-5) eliminates the under-segmentation problem when multiple plumes are originating from one volcano, as shown in Figure 8, increasing the recall value even higher than the "Flood-fill with wind" algorithm. This method performs well in most cases, i.e., when the plumes from a volcano are not traveling over other volcanoes (in which case the plume can be associated with multiple volcanoes). Compared to the one-trajectory DBSCAN algorithm, the binary reverse trajectory classification (BC-6) generally under-performed in all metrics. Possible causes for this include: the fixed time ranges of the trajectories (which makes the trajectories fall out of the volcano search area, causing under-segmentation), and/or the fact that the trajectory is arbitrarily computed starting from the volcano summit altitude. Addressing this problem would require prior knowledge of SO_2 layer height, which is currently not provided in the product.

The multi-class DBSCAN algorithm (MC-1) achieves the best overall metrics, with the highest F1-score and a better accuracy. The main reference points of this algorithm are the

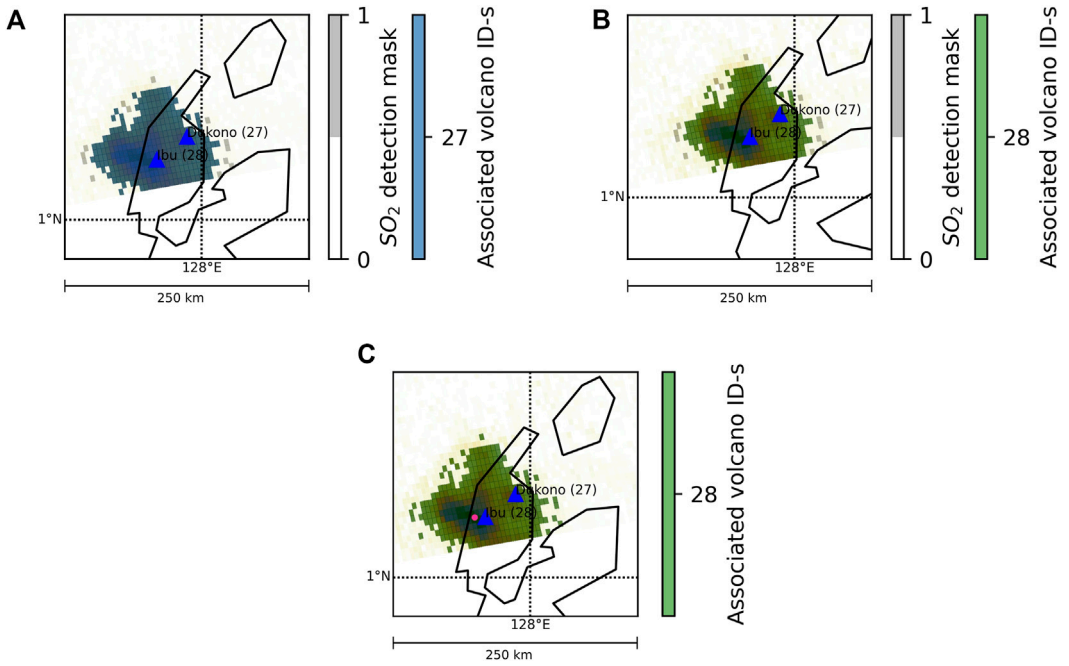

FIGURE 9
Difference in binary floodfill **(A,B)** vs. multi-class DBSCAN **(C)** classifications in an ambiguous case (Ibu volcano, on 19.03.2021). **(A)** Binary flood-fill with Dukono (27) as source volcano. **(B)** Binary flood-fill with Ibu (28) as source volcano. **(C)** Multi DBSCAN with Dukono (27) as source volcano.

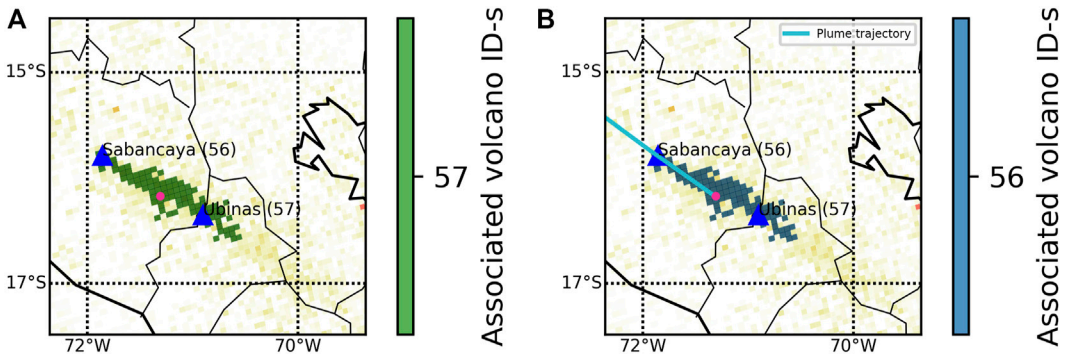

FIGURE 10
Difference in multi-class classifications in an ambiguous case (Plume from Sabancaya traveling over Ubinas volcano, on 27.04.2021). **(A)** Without wind data. **(B)** With the predicted trajectory.

volcano center points, making this algorithm vulnerable to areas where the spatial density of volcanoes is high, but performing well in general cases. The multi-class nature eliminates false associations that are caused by the binary classification, as shown on Figure 9C: no matter which volcano we are starting from, the plume is always going to be associated with one volcano. This is more robust than the binary classifications (Figure 9A for Dukono and Figure 9B for Ibu), where depending on the selected source volcano the plume is being associated with the currently selected one. Basically the multi-class algorithm answers the question "Which volcano does this plume originate from?", while the binary algorithms are based on the question "Is this plume coming from the selected source volcano?".

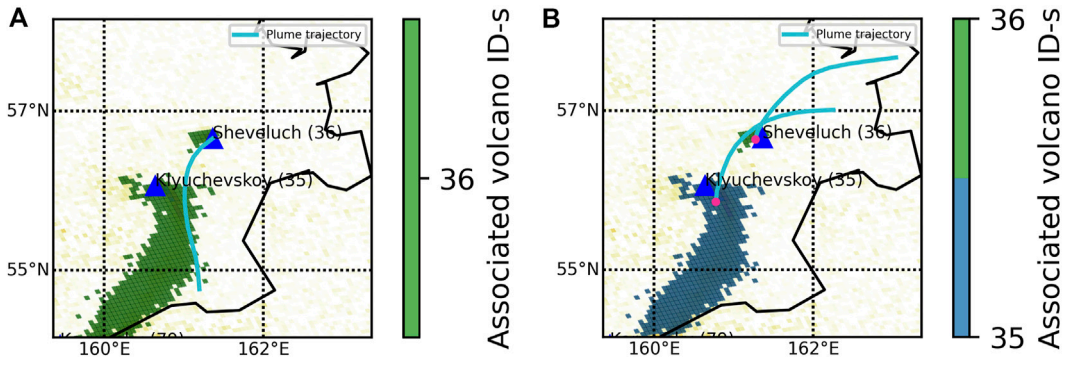

FIGURE 11
Difference in binary vs. multi-class DBSCAN classifications in an ambiguous case (Sheveluch volcano, on 19.03.2021). **(A)** Binary (DBSCAN with wind, with forward wind trajectory). **(B)** Multi-class (Multi Reverse Trajectory DBSCAN, with reverse wind trajectory).

The wind-based multi-class algorithm (MC-2) performs generally well in dense areas where plumes can travel over other volcanoes, as shown on Figure 10. However it is prone to errors in the wind models and the trajectories, which are started from the height of the nearest volcano, instead of using the actual SO_2 plume height. Utilizing the multi-class approach, the plume is always associated with the volcano that is nearest to the trajectory starting from it, avoiding overlapping classifications, as shown on Figure 11B, where the small pixel cluster originating from the volcano Sheveluch is classified correctly with the multi-class method, while the binary approach fails (Figure 11A). The method generally reaches good metric values, with the F1-score being the second best in comparison, as the precision and recall values are similarly high. These results demonstrate that the multi-class method is capable of segmenting remote sensing volcanic SO_2 products to multiple sources, based on both their physical features and external meteorological information.

5 Discussion

Overall, the results follow intuitive expectations. Contrary to expectations however, the multi-class classification without wind performed slightly better than the one which uses reverse trajectories. One possible cause for this are the limitations of the meteorological models used. GDAS has a 1-degree resolution, compared to GFS, which has 0.25. Using GFS models might improve trajectory prediction, but with more data, the file size of the meteorological models increases dramatically, reducing the portability of the wind-based algorithms by a substantial amount (NCEP, NWS, NOAA, U.S. DOC, 2009). For computational reasons, only one trajectory is started from each cluster, dividing the clusters and starting multiple trajectories has the potential of improving the results, but it also greatly increases computation time. The environmental characteristics of tested volcanoes also play a role in the overall outcome. As an example, the algorithms tend to perform better with volcanoes where the plumes are generally less fragmented due to stable, continuous degassing and less wind influence. Furthermore, because the plume height is not retrieved from the TROPOMI product but rather assumed to be equal to the volcano summit altitude, the generated trajectories can suffer errors, as the strength and direction of the wind changes with the elevation.

5.1 Operational SO_2 plume monitoring

The presented algorithms are relatively small and require limited computing time, ranging from a few milliseconds to a few seconds, with the wind-based algorithms having longer computing times as the ones without wind data. As such, they could be suited for near real-time operational volcano monitoring tasks. As the multi-class classification algorithms provides the best effectiveness/implementation complexity ratio, they are recommended for implementation in operational frameworks. Future work will focus on testing the algorithms on a larger number and variety of eruptive plumes, with the aim to implement them in monitoring systems such as MOUNTS (Valade et al., 2019).

5.2 Areas of improvement

Considering the previously presented strengths and weaknesses, the algorithms still provide room for further research and development. A first aspect to improve in the

multi-class classification algorithms is the way pixel clusters are assigned to volcanoes. As of now, the assignment is based on the distance between a cluster's center of mass (in grid space), and the volcano summit coordinates. Although this is efficient in a large majority of cases (i.e., small gas plumes, and/or plumes where the highest gas concentration is located nearby the volcano summit), it can fail in the case of strong eruption plumes, where high gas concentrations can extend several tens-hundreds of kilometers away form the emitting volcano. Indeed, this can result in the plume center of mass being off-centered with respect to the volcano, which can potentially result in erroneous associations of the SO_2 plume to another non-emitting volcano closer to the plume center. An alternative to the center of mass could be using the cluster skeleton (Zhang and Suen, 1984), or the cluster shape to determine the source emission point.

Secondly, the results can be possibly improved for strong eruption plumes by incorporating near-real-time SO_2 layer height retrieval, which would make the reverse trajectory calculation more deterministic and exact. As mentioned before, because the plume height is not retrieved from the TROPOMI product but rather assumed to be equal to the volcano summit altitude, the generated trajectories can suffer errors. This could be improved in the future *via* the SO_2 Layer Height product (Hedelt et al., 2019), which provides accurate information about the height of the plumes, making reverse trajectory based algorithms more accurate (Theys et al., 2022). There are promising developments underway for that, as for major eruptions the TROPOMI SO_2 Layer Height product is available. Because these products are a separate entity distinct from the actual SO_2 product, and because they are only available for major eruptions, the algorithms have to query for their presence to make sure that the layer height can be retrieved. It should be stressed that using layer heights would be very useful for explosive eruption plumes having high gas concentrations and high altitudes; however they are likely to be much less useful for passive degassing plumes having have lower gas content and altitudes, as the layer height retrieval is more complicated in these cases.

As the TROPOMI L2 SO_2 product is being continuously developed, the initial segmentation of volcanic SO_2 detection mask is improved as well, which results in easier cluster generation, less outliers, and less false associations. This enables the lowering of ε values without losing outliers, although the increased number of clusters makes the trajectory generation slower and more complicated.

In the compared methods each pixel is associated with exactly one source. A future version should make a weighted attribution to multiple sources per pixel for cases of merging plumes.

6 Concluding remarks

In this work, we have managed to classify volcanic SO_2 plume pixels in satellite imagery using classic clustering, segmentation and image processing techniques. The developed algorithms can be applied to SO_2 L2 products from the Sentinel-5P TROPOMI instrument, to help with the accurate source estimation of SO_2 plumes originating from various volcanoes. Furthermore, besides contributing to improving analysis and monitoring of volcanic processes from space, these algorithms can be useful in other general plume localization tasks. In particular, another potential application of the presented methods is to identify anthropogenic plume sources.

Data availability statement

The TROPOMI SO2 data used in this paper can be downloaded from the Copernicus Open Access Hub. The Global Data Assimilation System (GDAS) meteorological files used in the trajectory generation are publicly available through the NOAA ARL FTP server. HYSPLIT is available on NOAA's website.

Author contributions

BM performed the bulk of the data analysis, design and implementation of the algorithms, created the figures and wrote the first draft of the manuscript. BM, SV, and MW conceptualized the study. SV collected and analyzed the volcanic gas data. MW and OH ensured the fundamental theoretical correctness of the methods. All authors provided comments and input on the results and final version of the manuscript. Work was done as part of a BM's Master's Thesis, supervised by SV and MW.

Funding

We acknowledge support by the German Research Foundation and the Open Access Publication Fund of TU Berlin. SV was supported by DGAPA-PAPIIT grant IA102221.

Acknowledgments

We wish to thank the special editor Christoph Kern, as well as the two anonymous reviewers for their valuable suggestions which helped improve the manuscript. We also acknowledge the European Space Agency for providing open-access TROPOMI data, and the NOAA for providing access to GDAS meteorological models. Lastly, we wish to thank Pascal Hedelt for providing access to SO_2 Layer Height products.

Conflict of interest

The authors declare that the research was conducted in the absence of any commercial or financial relationships that could be construed as a potential conflict of interest.

Publisher's note

References

Bernard, A., and Rose, W. I. (1990). The injection of sulfuric acid aerosols in the stratosphere by the El Chichón volcano and its related hazards to the international air traffic. *Nat. Hazards (Dordr).* 3, 59–67. doi:10.1007/bf00144974

Campion, R., Delgado-Granados, H., Legrand, D., Taquet, N., Boulesteix, T., Pedraza-Espitía, S., et al. (2018). Breathing and coughing: The extraordinarily high degassing of Popocatépetl volcano investigated with an SO2 camera. *Front. Earth Sci. (Lausanne).* 6, 163. doi:10.3389/feart.2018.00163

Carlsen, H. K., Valdimarsdóttir, U., Briem, H., Dominici, F., Finnbjornsdottir, R. G., Jóhannsson, T., et al. (2021). Severe volcanic SO2 exposure and respiratory morbidity in the Icelandic population – A register study. *Environ. Health* 20, 23. doi:10.1186/s12940-021-00698-y

Carn, S. A., Fioletov, V. E., McLinden, C. A., Li, C., and Krotkov, N. A. (2017). A decade of global volcanic SO2 emissions measured from space. *Sci. Rep.* 7, 44095. doi:10.1038/srep44095

Cofano, A., Cigna, F., Amato, L. S., de Cumis, M. S., and Tapete, D. (2021). *Exploiting sentinel-5P TROPOMI and ground sensor data for the detection of volcanic SO2 plumes and activity in 2018–2021 at stromboli*, 21. Basel, Switzerland: Italy. Sensors. doi:10.3390/s21216991

Corradini, S., Guerrieri, L., Brenot, H., Clarisse, L., Merucci, L., Pardini, F., et al. (2021). Tropospheric volcanic SO2 mass and flux retrievals from satellite. The Etna december 2018 eruption. *Remote Sens. (Basel).* 13, 2225. doi:10.3390/rs13112225

Edmonds, M., Oppenheimer, C., Pyle, D., Herd, R., and Thompson, G. (2003). So2 emissions from soufrière hills volcano and their relationship to conduit permeability, hydrothermal interaction and degassing regime. *J. Volcanol. Geotherm. Res.* 124, 23–43. doi:10.1016/S0377-0273(03)00041-6

Ester, M., Kriegel, H.-P., Sander, J., and Xu, X. (1996). A density-based algorithm for discovering clusters in large spatial databases with noise. *KDD*, 226.

Finch, D. P., Palmer, P. I., and Zhang, T. (2022). Automated detection of atmospheric NO_2 plumes from satellite data: A tool to help infer anthropogenic combustion emissions. *Atmos. Meas. Tech.* 15, 721–733. doi:10.5194/amt-15-721-2022

Heaviside, C., Witham, C., and Vardoulakis, S. (2021). Potential health impacts from sulphur dioxide and sulphate exposure in the UK resulting from an Icelandic effusive volcanic eruption. *Sci. Total Environ.* 774, 145549. doi:10.1016/j.scitotenv.2021.145549

Hedelt, P., Efremenko, D. S., Loyola, D. G., Spurr, R. J. D., and Clarisse, L. (2019). Sulfur dioxide layer height retrieval from Sentinel-5 Precursor/TROPOMI using FP_ILM. *Atmos. Meas. Tech.* 12, 5503–5517. doi:10.5194/amt-12-5503-2019

Markus, B. (2022a). *bazsimarkus/tropomi-emission-source: Initial release.* Zenodo. doi:10.5281/zenodo.7311026

Markus, B. (2022b). *bazsimarkus/tropomi-emission-source: Supplementary data.* Zenodo. doi:10.5281/zenodo.7311105

Matthews, S. J., Gardeweg, M. C., and Sparks, R. S. J. (1997). The 1984 to 1996 cyclic activity of lascar volcano, northern Chile: Cycles of dome growth, dome subsidence, degassing and explosive eruptions. *Bull. Volcanol.* 59, 72–82. doi:10.1007/s004450050176

NCEP, NWS, NOAA, U.S. DOC (2009). *NCEP GDAS satellite data 2004-continuing.* Research Data Archive at the National Center for Atmospheric Research, Computational and Information Systems Laboratory. doi:10.5065/DWYZ-Q852

Oppenheimer, C., Fischer, T., and Scaillet, B. (2014). "Volcanic degassing: Process and impact," in *Treatise on geochemistry* (Elsevier), 111–179. doi:10.1016/b978-0-08-095975-7.00304-1

Pardini, F., Corradini, S., Costa, A., Esposti Ongaro, T., Merucci, L., Neri, A., et al. (2020). Ensemble-based data assimilation of volcanic ash clouds from satellite observations: Application to the 24 december 2018 Mt. Etna explosive eruption. *Atmosphere* 11, 359. doi:10.3390/atmos11040359

Prata, A. J. (2009). Satellite detection of hazardous volcanic clouds and the risk to global air traffic. *Nat. Hazards (Dordr).* 51, 303–324. doi:10.1007/S11069-008-9273-Z

Queißer, M., Burton, M. R., Theys, N., Pardini, F., Salerno, G., Caltabiano, T., et al. (2019). TROPOMI enables high resolution SO2 flux observations from Mt. Etna, Italy, and beyond. *Sci. Rep.* 9, 957. doi:10.1038/s41598-018-37807-w

Robock, A. (2000). Volcanic eruptions and climate. *Rev. Geophys.* 38, 191–219. doi:10.1029/1998RG000054

Romahn, F., Pedergnana, M., Loyola, D., Apituley, A., Sneep, M., and Veefkind, J. P. (2022). *S5P/TROPOMI L2 product user manual sulphur dioxide SO2 - S5P-L2-DLR-PUM-400E.* European Space Agency.

Schmidt, A., Witham, C. S., Theys, N., Richards, N. A. D., Thordarson, T., Szpek, K., et al. (2014). Assessing hazards to aviation from sulfur dioxide emitted by explosive Icelandic eruptions. *J. Geophys. Res. Atmos.* 119 (14), 14, 180196–180214, 196. doi:10.1002/2014JD022070

Sierra-Vargas, M. P., Vargas-Domínguez, C., KarenBobadilla-Lozoya, C., and Aztatzi-Aguilar, O. G. (2018). *Health impact of volcanic emissions.* Volcanoes - Geological and geophysical setting, theoretical Aspects and numerical modeling, Applications to Industry and their Impact on the human health. Rijeka: IntechOpen. doi:10.5772/INTECHOPEN.73283

Stein, A. F., Draxler, R. R., Rolph, G., Stunder, B., Cohen, M. D., and Ngan, F. (2015). NOAA's HYSPLIT atmospheric transport and dispersion modeling system. *Bull. Am. Meteorol. Soc.* 96, 2059–2077. doi:10.1175/BAMS-D-14-00110.1

Theys, N., Hedelt, P., de Smedt, I., Lerot, C., Yu, H., Vlietinck, J., et al. (2019). Global monitoring of volcanic SO2 degassing with unprecedented resolution from TROPOMI onboard Sentinel-5 Precursor. *Sci. Rep.* 9, 2643. doi:10.1038/s41598-019-39279-y

Theys, N., Lerot, C., Brenot, H., van Gent, J., de Smedt, I., Clarisse, L., et al. (2022). Improved retrieval of SO2 plume height from TROPOMI using an iterative Covariance-Based Retrieval Algorithm. *Atmos. Meas. Tech.* 15, 4801–4817. doi:10.5194/amt-15-4801-2022

Theys, N., Smedt, I. D., Yu, H., Danckaert, T., van Gent, J., Hörmann, C., et al. (2017). Sulfur dioxide retrievals from TROPOMI onboard sentinel-5 precursor: Algorithm theoretical basis. *Atmos. Meas. Tech.* 10, 119–153. doi:10.5194/AMT-10-119-2017

Valade, S., Ley, A., Massimetti, F., D'Hondt, O., Laiolo, M., Coppola, D., et al. (2019). Towards global volcano monitoring using multisensor Sentinel missions and artificial intelligence: The MOUNTS monitoring system. *Remote Sens. (Basel).* 11, 1528. doi:10.3390/RS11131528

Vincenty, T. (1975). Direct and inverse solutions of geodesics on the ellipsoid with application of nested equations. *Surv. Rev.* 23, 88–93. doi:10.1179/SRE.1975.23.176.88

Warner, M. S. C. (2018). Introduction to PySPLIT: A Python toolkit for NOAA ARL's HYSPLIT model. *Comput. Sci. Eng.* 20, 47–62. doi:10.1109/MCSE.2017.3301549

Zhang, T. Y., and Suen, C. Y. (1984). A fast parallel algorithm for thinning digital patterns. *Commun. ACM* 27, 236–239. doi:10.1145/357994.358023

frontiers | Frontiers in Earth Science

TYPE Original Research
PUBLISHED 06 January 2023
DOI 10.3389/feart.2022.1005738

OPEN ACCESS

EDITED BY
Robin Campion,
National Autonomous University of Mexico, Mexico

REVIEWED BY
Wolfgang Stremme,
National Autonomous University of Mexico, Mexico
Simon Carn,
Michigan Technological University, United States
Pasquale Sellitto,
UMR7583 Laboratoire inter-universitaire des systèmes atmosphèriques (LISA), France

*CORRESPONDENCE
Jean-François Smekens,
Francois.Smekens@earth.ox.ac.uk

SPECIALTY SECTION
This article was submitted to Volcanology, a section of the journal Frontiers in Earth Science

RECEIVED 28 July 2022
ACCEPTED 13 December 2022
PUBLISHED 06 January 2023

CITATION
Smekens J-F, Mather TA, Burton MR, La Spina A, Kabbabe K, Esse B, Varnam M and Grainger RG (2023), Quantification of gas, ash, and sulphate aerosols in volcanic plumes from open path Fourier transform infrared (OP-FTIR) emission measurements at Stromboli volcano, Italy.
Front. Earth Sci. 10:1005738.
doi: 10.3389/feart.2022.1005738

Quantification of gas, ash, and sulphate aerosols in volcanic plumes from open path Fourier transform infrared (OP-FTIR) emission measurements at Stromboli volcano, Italy

Jean-François Smekens[1]*, Tamsin A. Mather[1], Mike R. Burton[2], Alessandro La Spina[3], Khristopher Kabbabe[4], Benjamin Esse[2], Matthew Varnam[2,5] and Roy G. Grainger[6]

[1]Department of Earth Sciences, University of Oxford, Oxford, United Kingdom, [2]Department of Earth and Environmental Sciences, University of Manchester, Manchester, United Kingdom, [3]Istituto Nazionale di Geofisica e Vulcanologia, Osservatorio Etneo, Catania, Italy, [4]Department of Mechanical, Aerospace and Civil Engineering, University of Manchester, Manchester, United Kingdom, [5]Lunar and Planetary Laboratories, University of Arizona, Tucson, AZ, United States, [6]COMET, Atmospheric, Oceanic and Planetary Physics, University of Oxford, Oxford, United Kingdom

Field-portable Open Path Fourier Transform Infrared (OP-FTIR) spectrometers can be used to remotely measure the composition of volcanic plumes using absorption spectroscopy, providing invaluable data on total gas emissions. Quantifying the temporal evolution of gas compositions during an eruption helps develop models of volcanic processes and aids in eruption forecasting. Absorption measurements require a viewing geometry which aligns infrared source, plume, and instrument, which can be challenging. Here, we present a fast retrieval algorithm to estimate quantities of gas, ash and sulphate aerosols from thermal emission OP-FTIR measurements, and the results from two pilot campaigns on Stromboli volcano in Italy in 2019 and 2021. We validate the method by comparing time series of SO_2 slant column densities retrieved using our method with those obtained from a conventional UV spectrometer, demonstrating that the two methods generally agree to within a factor of 2. The algorithm correctly identifies ash-rich plumes and gas bursts associated with explosions and quantifies the mass column densities and particle sizes of ash and sulphate aerosols (SA) in the plume. We compare the ash sizes retrieved using our method with the particle size distribution (PSD) of an ash sample collected during the period of measurements in 2019 by flying a Remotely Piloted Aircraft System into the path of a drifting ash plume and find that both modes of the bimodal PSD (a fine fraction with diameter around 5–10 μm and a coarse fraction around 65 μm) are identified within our datasets at different times. We measure a decrease in the retrieved ash particle size with distance downwind, consistent with settling of larger particles, which we also observed visually. We measure a decrease in the SO_2/SA ratio as the plume travels downwind, coupled with an increase in measured SA particle size (range 2–6 μm), suggesting rapid hygroscopic particle growth and/or SO_2

oxidation. We propose that infrared emission spectroscopy can be used to examine physical and chemical changes during plume transport and opens the possibility of remote night-time monitoring of volcanic plume emissions. These ground-based analyses may also aid the refinement of satellite-based aerosol retrievals.

KEYWORDS

OP-FTIR, volcanic gases, volcanic aerosols, plume chemistry, Stromboli, remotely piloted aircraft system, UAS

1 Introduction

Emissions of gas and particulate matter accompany volcanic activity of all types, from mild effusive eruptions to large explosions. They form volcanic plumes consisting of a mixture of gases and particulates, including sulphate aerosols (SA) and sometimes volcanic ash (Carey and Bursik, 2015), which interact with the atmosphere as they travel away from their source, affecting the environment locally, and sometimes regionally or globally (Delmelle, 2003; Mather, 2015). Depending on the intensity of the emissions, the duration of a particular eruptive episode and the injection height, volcanic emissions can present significant hazards to local populations (Horwell, 2007; Gudmundsson, 2011; Tang et al., 2020; Carlsen et al., 2021), infrastructures (Barsotti et al., 2010; Wilson et al., 2014) and air traffic (Carn et al., 2009; Schmidt et al., 2014). The emergence of automated, continuous monitoring of volcanic plume composition provides valuable insights into the behaviour of volatiles over the course of volcanic crises and technical advances in instrumentation now offer new possibilities to measure plume composition in real-time and in a safe manner (Kern et al., 2022). Here we present a new method to measure gas and particle composition in volcanic plumes using an Open Path Fourier Transform Infrared (OP-FTIR) spectrometer collecting passive emission measurements.

FTIR spectroscopy is a powerful tool to identify and quantify atmospheric composition, as a number of trace gases present distinctive rotational and vibrational features at wavelengths from the near-infrared to the far-infrared. Since the emergence of relatively portable OP-FTIR spectrometers, it has been used extensively by the volcanic gas community over the past 30 years (Notsu et al., 1993; Mori et al., 1995; Mori and Notsu, 1997; Oppenheimer et al., 1998a; Francis et al., 1998; Horrocks et al., 1999; Horrocks et al., 2001). The most common method utilizes hot eruptive material (lava flow, lava dome, lava fountains, etc.) as a source of infrared (IR) radiation to measure the absorption features of the emitted gases directly at the source (Burton et al., 2000; Burton et al., 2007; La Spina et al., 2015; Pfeffer et al., 2018). In order to target passive gas plumes, measurements can also be performed by using the Sun or the Moon as the source of radiation, a method known as solar/lunar occultation (Francis et al., 1998; Burton et al., 2001; Duffell et al., 2001; Butz et al., 2017); or, when the plume travels at or passes through, ground-level, using an artificial IR radiation source placed on the other side of the plume from the observer or combined with a mirror to achieve a longer path length (Burton et al., 2000; Vanderkluysen et al., 2014). These methods all rely on the principle of absorption spectroscopy, whereby the variable of interest (i.e., the quantity of a given gas species) is related to the strength of absorption of radiation by said gas, and the gas quantity is retrieved by fitting a modelled spectrum to the measured spectrum (Burton et al., 2000; Burton et al., 2007). While absorption spectroscopy using a hot radiation source (>~300°C) offers the key advantage of a relatively simple retrieval of the amounts of the most abundant volcanic gases, a specific geometry to align a hot source, the volcanic plume and the instrument is required. This is quite straightforward to achieve when using the Sun as a source of radiation, but the long atmospheric path then precludes quantification of key gases such as CO_2 and H_2O, although near-infrared solar retrievals of volcanic CO_2 have been demonstrated (Butz et al., 2017). OP-FTIR is most useful when there is explosive volcanic activity, as this provides an ample radiation source. In the case of ash-rich eruption columns only the cooler gas on the outside of the plume is measurable, but this is sufficient to produce accurate retrievals of the key gas species. In these conditions *in-situ* sensors are extremely challenging to use, so OP-FTIR provides the best opportunity for gas quantification. This has been successfully applied to plumes from effusive or fire fountaining activity using incandescent vents and flows as a source of radiation (Allard et al., 2005; Edmonds and Gerlach, 2007; La Spina et al., 2010; La Spina et al., 2015; Allard et al., 2016), or passive emissions using artificial sources (Burton et al., 2000; Vanderkluysen et al., 2014; Sellitto et al., 2019). When using solar/lunar occultation (Burton et al., 2001; Duffell et al., 2001; Butz et al., 2017), available time windows for measurements are also constrained by the position of the celestial objects in the sky. OP-FTIR is generally used for short regular measurements, where data are collected for a few minutes, rather than for continuous monitoring. One example of continuous monitoring is the Cerberus instrument on Stromboli volcano in Italy (La Spina et al., 2013), a system using hot rocks from the crater walls as a source of IR radiation and capable of determining gas composition from individual vents, which operated between 2009 and 2019 when it was destroyed by a paroxysm episode. Long-term regular (~weekly) solar FTIR measurements of SO_2, HCl and HF have been conducted on

Mt Etna in Italy, and regular daytime measurements of the plume of Popocatépetl volcano in Mexico have been conducted for 4 years (Taquet et al., 2019) using a solar-tracking OP-FTIR instrument originally meant for long-term atmospheric composition monitoring, and which intersected the passive emissions generated by the nearby volcano when the wind direction was favourable.

In contrast, emission spectroscopy quantifies the radiance produced by volcanic gases when viewed against a cold background (i.e., a clear sky or clouds at higher altitudes). The method was first introduced to volcanology by Love et al. (1998), and used to quantify volcanic gases in the gas plume produced by Popocatépetl volcano in Mexico (Love et al., 1998; Love et al., 2000; Goff et al., 2001). The main assumption of the method is of a thermal contrast between a cold sky and a relatively warmer plume. It is therefore best suited for plumes measured close to their emission source (where they are more likely to be warmer than the background atmosphere) and with a relatively high viewing angle, both of which are factors maximizing the thermal contrast. Following these early efforts, the method had been largely unused until more recent studies, once again at Popocatépetl, demonstrated its use for routine measurements of a passive plume (Stremme et al., 2012; Taquet et al., 2017). These most recent efforts focus exclusively on gases, using individual, relatively narrow retrieval windows dedicated to each target gas. When using absorption spectroscopy, the strength of absorption for various gases is quantified by reproducing the observed unprocessed intensity signal (i.e., without performing radiometric calibration), with a model in which the source intensity is simulated by a polynomial function that represents a series of physical parameters, including the Planck function for the source temperature, the instrument response function and, crucially, the broadband absorption of light by particulate species. Similarly, in previous emission studies (Love et al., 1998; Love et al., 2000; Goff et al., 2001; Stremme et al., 2012; Taquet et al., 2017), particulate species which are likely often present in the volcanic plume are treated as interfering with the retrieval and require a correction during data processing or are dismissed during quality control. However, the radiometric calibration performed during the pre-processing stage of emission measurements provides a way of characterizing most of the physical parameters which form the polynomial function described above, and therefore presents a unique opportunity to isolate and quantify the contribution from species with broader spectral features, such as sulphate aerosols and ash. Sellitto et al. (2019) have shown that the simultaneous retrieval of SO_2 and sulphate aerosols is possible from active absorption measurements where the intensity of the radiative source can be assumed to remain constant. They show that the presence of sulphate aerosols may lead to significant overestimation in SO_2 amounts if not accounted for. Accurate quantification of particulate matter (PM) concentration and size in plumes is also important in its own right when forecasting, for example, the respiratory hazards and environmental consequences associated with volcanic emissions (e.g., Ilyinskaya et al., 2017).

In this study we present a fast retrieval algorithm capable of simultaneously extracting slant column densities (SCDs) of gas and particles from OP-FTIR data collected in emission mode in near real-time, using a broad fitting window.

2 Methods

2.1 Data acquisition strategy

We present data from two separate measurement campaigns at Stromboli volcano in Italy: September 9–11, 2019, and September 23–25, 2021 (Figure 1). Thermal emission measurements were performed using a Bruker EM27 OP-FTIR spectrometer lent by the Osservatorio Etneo dell'Istituto Nazionale di Geofisica e Vulcanologia (INGV). The EM27 consists of a "Rock Solid interferometer" (corner cube mirrors on a pendulum around the beam splitter) directing radiation towards a Stirling-cooled Mercury-Cadmium-Telluride (MCT) detector using entirely reflective optics (i.e., no external telescope was added) with an optical path difference of 1.8 cm and a field-of view (FOV) of 30 mrad. Spectra were acquired in the frequency range 600—2,000 cm^{-1} with a resolution of ~0.5 cm^{-1} (or a ~0.25 cm^{-1} spectral sampling), and averaged with five co-adds, resulting in a sampling interval of 8–10 s. Radiometric calibration was performed using an internal blackbody target with adjustable temperature. Using two blackbody spectra at two different temperatures (typically around 20°C and 40°C), we created an instrument calibration function which can be applied to convert the single beam spectrum to calibrated radiance or brightness temperature. Clear sky spectra were collected by pointing the instrument towards an area of sky outside of the plume while keeping the inclination angle as close to that of the plume measurements as possible. The duration of acquisition periods varied between 30 min and several hours, and calibration and clear sky measurements were performed every hour or so to account for the thermal drift of the instrument and to reflect changing atmospheric conditions. In datasets for which multiple calibration sets were acquired, we account for instrument drift by interpolating the blackbody spectra between the calibration sets, thereby creating a time-dependent calibration function with unique values for each measurement. We also create a similar time-dependent representation of the expected background spectrum by interpolating between clear sky spectra. This is especially important when working with longer datasets or with datasets acquired at the time of local sunrise and sunset, when the thermal profile of the atmosphere changes rapidly.

During the first field campaign in 2019, measurements were performed from the l'Osservatorio restaurant, providing a direct

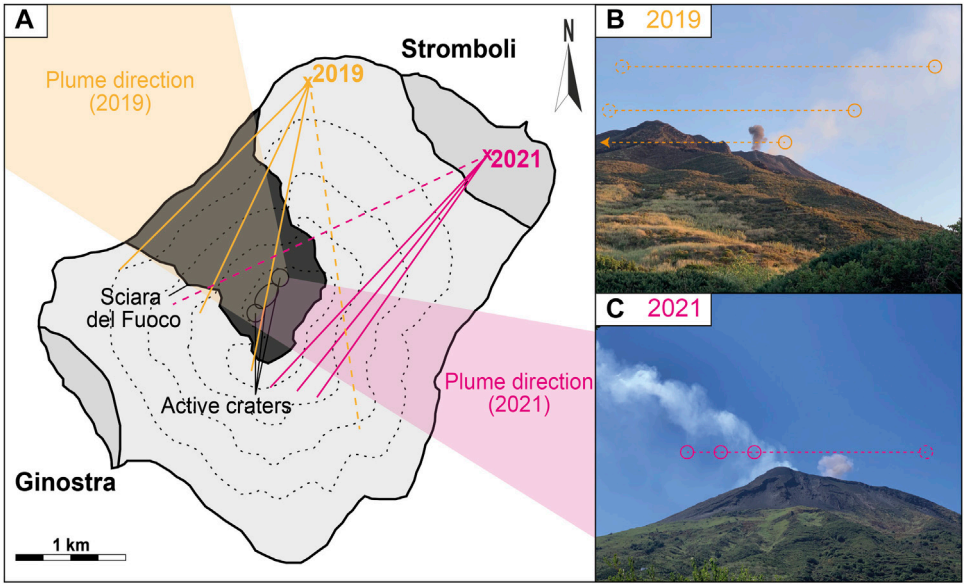

FIGURE 1
(A) Sketch map of the island of Stromboli, depicting the measurement locations and approximate plume geometries during the two measurement campaigns [2019 in yellow, 2021 in magenta]. Grey shaded areas (labeled Stromboli and Ginostra) represent settlements on the island. The black shaded area represents the collapse feature known as the *Sciara del Fuoco*. The approximate location of the three main crater areas (Northeast, Central and Southwest) is indicated by ellipses. Shaded coloured polygons represent the general plume direction during measurements. Coloured lines represent the range of azimuths during plume (solid) and clear sky (dashed) measurements **(B** and **C)** Photographs taken from the measurement location in the 2019 **(B)** and 2021 **(C)** campaigns. Circles represent the approximate location of the instrument field of view during plume (solid) and clear sky (dashed) measurements.

view of the craters (Figure 1). Wind direction was relatively constant during the 3-day period, and the plume drifted over the Sciara del Fuoco in a NE direction. We collected multiple short sets of 30–60 min of measurements, moving the instrument field-of-view to intersect the plume at various distances from the vent. The activity during this campaign was typical for Stromboli, with explosive events occurring every 5 min on average. Events at the crater were logged manually in a notebook, with the observer entering the time, nature of the event and crater of origin as far as it was possible to observe. We also organized a series of flights with a Remotely Piloted Aircraft System (RPAS) developed and built at the University of Manchester, with the aim of sampling ash from the drifting volcanic plume during the measurement period (Figure 2). The RPAS was a quadcopter carrying a hoover-like sampling mechanism. Once the RPAS had reached the desired location within the plume, the sampling mechanism was triggered remotely, turning on a high mass-flow ducted fan to direct airflow and ash into a small vacuum cleaner bag connected to the system. We were able to collect a single sample at 17:02 local time on 11 September 2019 (analysis results in Section 3.1). The particle size distribution (PSD) of the sample collected during the RPAS flight was measured using a Retch Camsizer X2 particle size analyser at the University of Leeds. Further, the sample was mounted onto SEM stubs using clear epoxy, polished and carbon-coated for analysis with an Electron Microprobe Analyser (EMPA) at the University of Oxford, to determine the chemical composition of individual phases.

In 2021, measurements were performed from the roof of the Pedra Residence hotel in Stromboli village. The wind direction was approximately to the East, and the line of sight of the instrument intersected the plume as it passed over the summit of the island. We collected longer datasets (3-4 h) with the specific purpose of evaluating the usefulness of the method as a monitoring tool. A GoPro camera was used to capture time-lapse imagery from the observer's vantage point, and the eruptive events were logged by reviewing the footage. Although the method allows for a continuous record of events over long periods, weaker events and those without an associated ash-rich plume were often not detectable in the footage because we did not have a direct view of the craters. Therefore, we could not assign a specific vent to any given event either. During this second campaign, we also collected simultaneous spectra with a UV spectrometer to validate the infrared SO_2 retrieval. Light was collected using a collimated telescope (diameter = 25.4 mm, f = 100 mm), connected to an Ocean Optics USB 2000+ spectrometer *via* an optical fibre. The spectrometer was controlled and powered by a connected laptop *via* USB cable. SO_2 slant column densities were retrieved using the iFit method (Esse et al., 2020). The wavelength window for the retrieval was 310—320 nm and

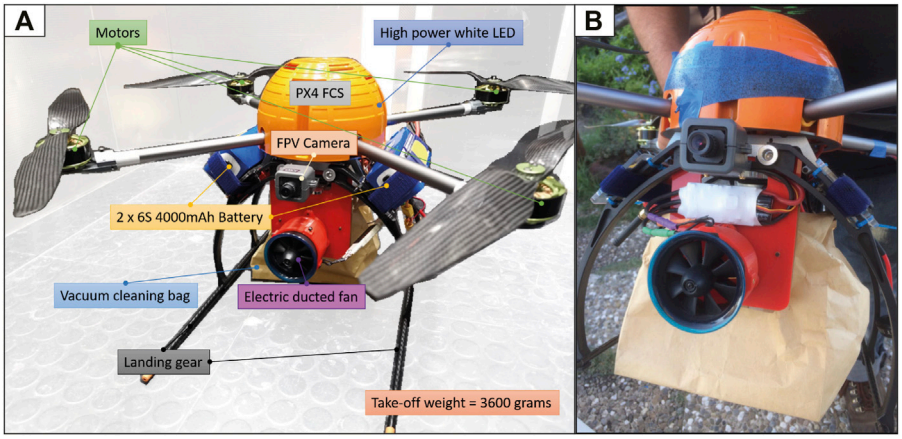

FIGURE 2
(A) Photograph of the Remotely Piloted Aircraft System (RPAS) used during field deployment. The red 3D printed housing seen in the middle of the multirotor houses an electric ducted fan system used to pull air and ash into the sample bag. Acronyms: LED—Light-Emitting Diode; FPV—First-Person View; FCS—Flight Controller System **(B)** Photograph of the RPAS after successful collection at Stromboli on 11 September 2019. Note the ash particles collected on a piece of tape affixed to the FCS housing in order to confirm plume intercept.

the fit included absorption cross-sections for SO_2 at 295 K (Rufus et al., 2003) and O_3 at 223 K (Serdyuchenko et al., 2014), a Ring spectrum, a wavelength shift and stretch and a linear intensity offset. The instrument line shape (ILS) was characterised using a super-Gaussian with the shape parameters also fitted for each spectrum to account for changes with time (e.g., due to changes in temperature).

2.2 Retrieval algorithm

The emission spectrum retrieval algorithm (developed in Python and available at https://www.github.com/jfsmekens/plumeIR) follows the basic principles laid out by Love et al. (1998), where the simplified radiative transfer expression comprises three layers (Figure 3): 1) a lower layer between the observer and the plume, 2) a plume layer, and 3) an upper layer encompassing the atmosphere in the line-of-sight behind the plume. Given a plume height (h) and a vertical plume thickness (z_v), the plume layer is defined between the height $h_1 = h - z_v/2$ and $h_2 = h + z_v/2$. The forward model computes the radiance difference between a clear sky and a plume measurement, which offers the advantage of isolating the spectral features of the volcanic species. The aim is to provide a tool which can be used in the field to quantify target species in real time as the measurements are taken (i.e., with a target processing time of <10 s for each individual spectrum, comparable to the acquisition time between consecutive spectra). The algorithm was developed around an iterative non-linear least-squares fitting method. High-resolution radiative transfer calculations (.04 cm^{-1} spectral sampling) over the entire vertical atmospheric profile are performed in a pre-processing stage to generate reference spectra used in the forward model. In contrast to recent efforts undertaken at Popocatépetl (Stremme et al., 2012; Taquet et al., 2017), where the effects of particulate species are simulated using a polynomial, we use a broad retrieval window (700–1,300 cm^{-1}) and model the radiation and attenuation due to particulate species from Mie theory, allowing us to retrieve SCDs for those species as well. The radiance difference method presents the advantage of emphasizing the spectral features due to the presence of a volcanic layer, thereby minimising the influence of atmospheric variables such as temperature and water vapour volume mixing ratios at higher altitude in the vertical profile.

2.2.1 Reference spectra

The first step in the retrieval is to create a set of reference radiance and optical depth spectra for each layer (Figure 4), which are then scaled in the forward model without having to perform computationally expensive radiative transfer calculations. For this task, we use the Reference Forward Model (RFM version 5), a radiative transfer model developed at the University of Oxford (Dudhia, 2017), capable of simulating atmospheric transmittance and emission at high spectral resolution using line data and reference cross-sections for individual gases extracted from the high-resolution transmission molecular absorption database (HITRAN, Rothman et al., 2009). Firstly, we determine the radiance and transmittance of each layer (L_x and T_x) in the absence of a plume. Starting with a standard mid-latitude summer atmospheric profile evaluated with measurements from the Michelson Interferometer for Passive Atmospheric Sounding (MIPAS)

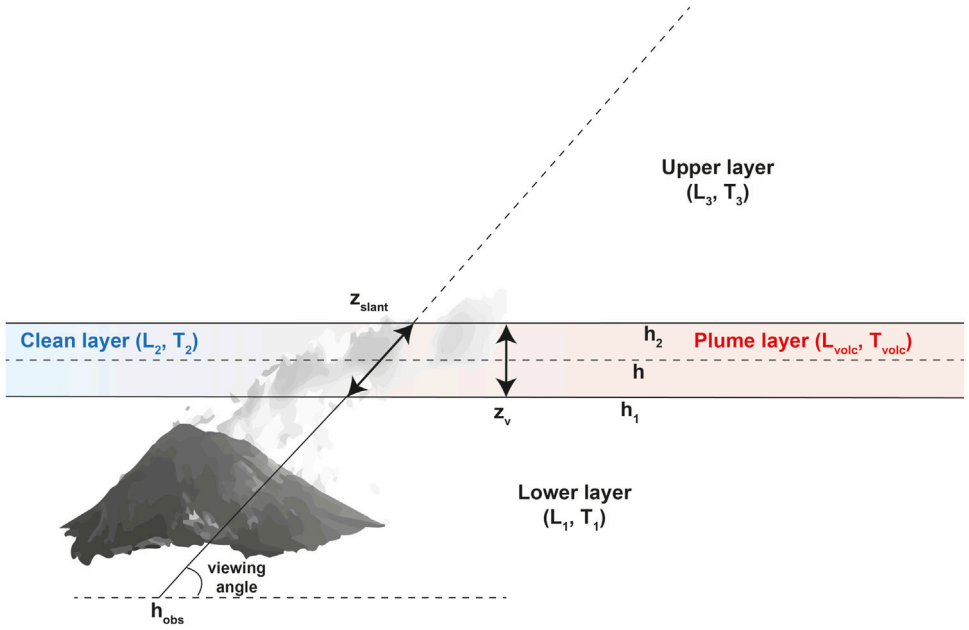

FIGURE 3
Simplified model of the viewing geometry and key parameters defining the measurements. h_{obs}: observer altitude; *viewing angle*: zenith angle determining the slant line-of-sight through the atmosphere; h: plume centre height; h_1: plume bottom height; h_2: plume top height; z_v: plume vertical thickness; z_{slant}: plume thickness along the line-of-sight; L_i: layer radiance; T_i: layer transmittance. In the model, the plume layer contains only the volcanic species, and coexists with the slice of "clean" air in layer 2.

(https://eodg.atm.ox.ac.uk/RFM/atm/) and adjusted to reflect present-day CO_2 concentration (400 ppm), we consider a small number of absorbing gases (H_2O, CO_2, N_2O, CH_4 and O_3) over a broad spectral window of 700–1,300 cm^{-1}. The vertical profile is then modified in the layers below 30 km to match the pressure, temperature and relative humidity from a local meteorological balloon sounding taken at a time closest to data acquisition from the station of Trapani in Sicily (launched twice daily and available at https://weather.uwyo.edu/upperair/sounding.html). It should be noted that Trapani is located >100 km west of Stromboli. The sounding might therefore be less representative than desired, and accuracy could be improved with dedicated local soundings. Finally, we resample the profile over an uneven vertical grid (spacing increases with altitude) with 25 layers. The profile is split into the three layers described above (Section 2.2; Figure 3) and RFM simulations are performed to extract radiance (L), transmittance (T), and optical depth (τ) for each of the three layers. Simulations are run with varying amounts of water vapour (21 steps from zero to two times the original concentrations). This allows the forward model to account for changes in relative humidity over the entire profile.

Next, we generate reference optical depth spectra for each target volcanic species (SO_2, ash and sulphate aerosols), assuming a homogeneous distribution of gas within layer 2 (Figure 4). Temperature and pressure are derived from the atmospheric profile at the plume height, which was set at around 1 km from visual observations placing the plume just above the craters. The optical depth for each species is derived for any given volume concentration by relating it to the reference concentration as follows:

$$\tau_i = \frac{\rho_i}{\rho_{i,ref}} \tau_{i,ref} \quad (1)$$

where τ_i is the optical depth and ρ_i is the volume mixing ratio (VMR in ppmv) for gas i within the layer. Atmospheric gases are also added as "plume" species and allowed to take positive or negative concentrations, which is meant to introduce an *ad hoc* correction in the forward model to account for small variations of the background gases in each plume measurement.

In addition to absorbing gases, we consider two types of volcanic particles: aqueous sulphate aerosols (SA) and silicate ash. For SA, we consider droplets of a binary solution of H_2SO_4 and H_2O. The H_2SO_4 mixing ratio and relevant temperature can be chosen by the user, and the extinction (β_{ext}) and absorption (β_{abs}) coefficients are calculated following Mie theory using complex refractive indices found in Lund Myhre et al. (2003) and the PyMieScatt software package (Sumlin et al., 2018). We follow a similar process for ash particles, and the user can choose between refractive indices for natural samples found in previous studies (Reed et al., 2018; Deguine et al., 2020) or calculated based on bulk chemical composition (SiO_2 wt%) using the

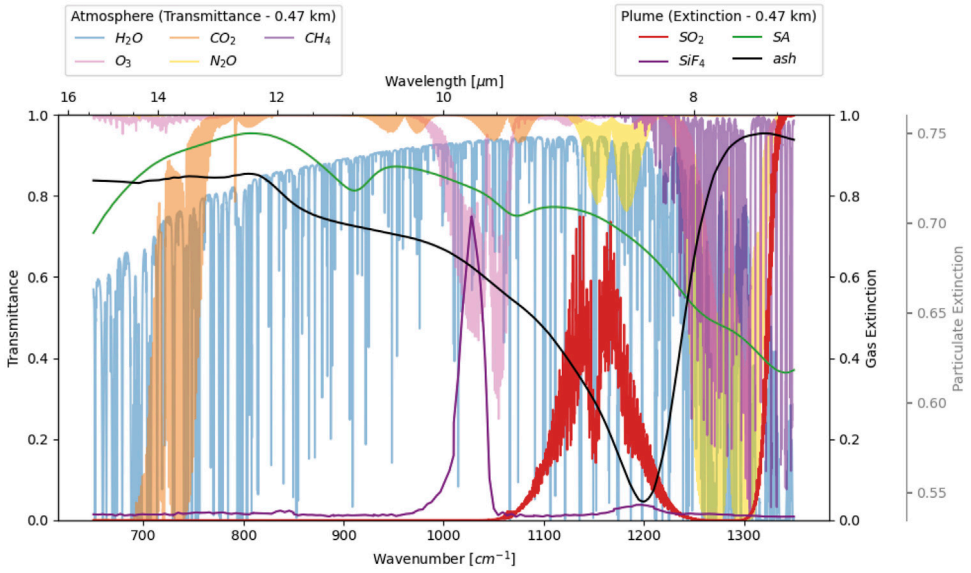

FIGURE 4
Reference spectra for the gases and particles considered in the retrieval. The transmittance of the atmospheric gases in layer two is shown in lighter shades [axis on the left], while the extinction of the plume species is shown in darker shades [axes on the right]. Note that the particulate species are plotted on a separate *y*-axis [offset to the right in grey] to emphasize their spectral features. Volume mixing ratios for each species were chosen to emphasize spectral shapes and are not necessarily representative of the actual quantities encountered during the retrieval process, except in the case of H_2O, where we show the actual transmittance at plume height. Note the strong water vapour continuum absorption.

parameterisation found in Prata et al. (2019). Assuming a reference mass volume concentration of particles (1×10^{-3} g cm^{-3} for ash, 5×10^{-3} g cm^{-3} for SA), the mass is distributed into size bins so that the number fraction follows a log-normal particle size distribution (PSD) around a mean effective diameter (d_{eff}), which can be set by the user or retrieved as a quantitative parameter. Particle shape is not considered in the model and particles are assumed to be spherical. This assumption is reasonable for SA particles but may lead to significant differences due to inhomogeneous scattering in the case of ash particles. Figure 5 shows the expected variations in shape and intensity of the optical depth spectra in the plume layer for a given mass volume concentration as a function of chemical composition and particle size. As documented previously, the H_2SO_4 mixing ratio has a significant effect on the expected shape of spectral extinction for aqueous SA (Biermann et al., 2000; Sellitto and Legras, 2016). However, we observe rather modest variations when considering a given mass concentration and varying the H_2SO_4 mixing ratios (Figure 5B). Variations in particle size also lead to significant changes in the spectral features of SA (Figure 5A). Consistent with previous observations, we observe an increase in maximum extinction on the order of 20%–30% when the effective diameter increases from .1 μm to 1 μm. For larger particles, the volume to surface area ratio increases dramatically, and the scattering coefficient becomes dominant in the spectral shape, leading to a flattening of the spectral features for a given mass concentration. In this study, we have chosen to fix the chemical composition of the particle species and leave particle size as a free parameter in the retrieval.

Volcanic ash can be described according to its bulk chemical composition in terms of the relative mass percentage of silica (SiO_2 wt%), with values ranging from 45 wt% for the more basaltic compositions (e.g., Eyjafjallajökull 2010; Sigmundsson et al., 2010) to 75% for the most silicic (e.g., Chaitén 2008; Alfano et al., 2011). In Figures 5A, D a range of attenuations are shown for ash with bulk composition ranging from 45 to 80 wt% SiO_2 using the parameterization developed by Prata et al. (2019), as well as those for a selection of natural samples from several recent eruptions (Reed et al., 2018). For SA, we consider a composition of 65 wt% H_2SO_4 - a value similar to the one recently measured by absorption FTIR spectroscopy for primary aerosols in the Masaya plume (Sellitto et al., 2019)—and use refractive indices measured for this composition by Lund Myhre et al. (2003). Ash optical depth spectra from natural samples follow a general trend with a shift of the spectral minimum and a deepening of the Si-O bond spectral feature as bulk SiO_2 content increases. This dependency of the position and depth of the Si-O bond absorption feature on bulk SiO_2 composition has been thoroughly documented within the planetary science literature (Lyon, 1965; Ramsey and Christensen, 1998; Michalski, 2004; Rogers and Nekvasil, 2015; Henderson et al., 2021), as well as within datasets using natural ash samples from recent eruptions

TABLE 1 Retrieved parameters for the forward model along with their bounds and a priori guess.

Symbol	Units	Parameter	A priori		Bounds
Gas and particulates parameters					
ρ_{gas}	ppmv	Gas volume mixing ratio (VMR) [CO_2, O_3, N_2O, CH_4, SO_2,]	CO_2	400	[1x10^{-12}—∞]
			O_3	0.01	
			N_2O	0.001	
			CH_4	1.7	
			SO_2	0.5	
ρ_{part}	g·cm^{-3}	Particulate mass volume concentration [ash, SA]	ash	0.001	[1x10^{-12}—∞]
			SA	0.0005	
$d_{eff\ (part)}$	μm	Particle effective diameter [ash, SA]	ash	2.0	[1—100]
			SA	0.5	[0.1–10]
Atmospheric layers parameters					
Δt_{prox}	K	Temperature difference in layer 1	0		[0—50]
Δt_{plume}	K	Temperature difference in layer 2	0		[0—50]
α_{H2O}	n/a	H_2O scaling factor	1		[0—2]
Spectral parameters					
$\tilde{v}_{shift}$	cm^{-1}	Frequency shift	0		[-5—5]
FOV	rad	Field of view	0.030		[0.001—0.5]

(e.g., Reed et al., 2018; Deguine et al., 2020; Piontek et al., 2021), and is accurately captured by the Prata et al. (2019) parameterization (grey shades in Figure 5D). We use a value of 51 wt% SiO_2 (based on the bulk composition of our sample, see Section 3.1) to calculate the reference extinction spectra for ash. A dependency of the spectral shape on particle size like that observed for SA also exists for ash.

Rather than modelling the measured radiance of a plume spectrum, the forward model replicates the radiance difference at the observer height between a plume measurement and a clear sky measurement (ΔL) from the parameters listed in Table 1. This is done to minimize the effects of the total atmospheric column amounts of background gases and instrument calibration and emphasize the spectral signatures of the volcanic components. The SCDs of all gas and particulate species within the plume layer are retrieved (ash, SA and SO_2), along with ad hoc correction factors for O_3, CO_2, N_2O and CH_4 and a scaling factor for H_2O in all three layers. The size of each particulate species can also be retrieved.

Following radiative transfer theory, the radiance measured at the observer position (L_{obs}) in this simplified model can be expressed as:

$$L_{obs} = L_1 + T_1 (L_2 + T_2 L_3) \quad (2)$$

where L_x represents the radiance and T_x the transmittance of layer x. In the presence of a volcanic plume, the slice of "clean" air in layer 2 (see Figure 3) is replaced by a plume layer, which contains the volcanic components in addition to the atmospheric gases; such that the radiance difference between a plume measurement and a clear sky measurement (ΔL) is:

$$\Delta L = T_1\left(L_{plume} - L_2 + L_3\left(T_{plume} - T_2\right)\right) \quad (3)$$

In the forward model, both the volcanic layer and the clean air slice are assigned separate optical depths. Firstly, we calculate the optical depth of the clean air slice (τ_2), adjusted for relative changes in water vapour content. The simple linear relationship expressed in Eq. 1) does not hold for H_2O, due to the existence of a continuum absorption, such that an accurate optical depth spectrum cannot simply be scaled from a reference quantity. Instead, we calculate a series of reference spectra for a range of scaling factors (0–2) applied to the original H_2O VMR at plume height. At each wavenumber $\tilde{v}$, we fit a polynomial to represent the dependency of the optical depth to the adjusted VMR, such that:

$$\tau_{2,\alpha,\tilde{v}} = \sum_{j=0}^{p} c_{j,\tilde{v}}\, \alpha^j \quad (4)$$

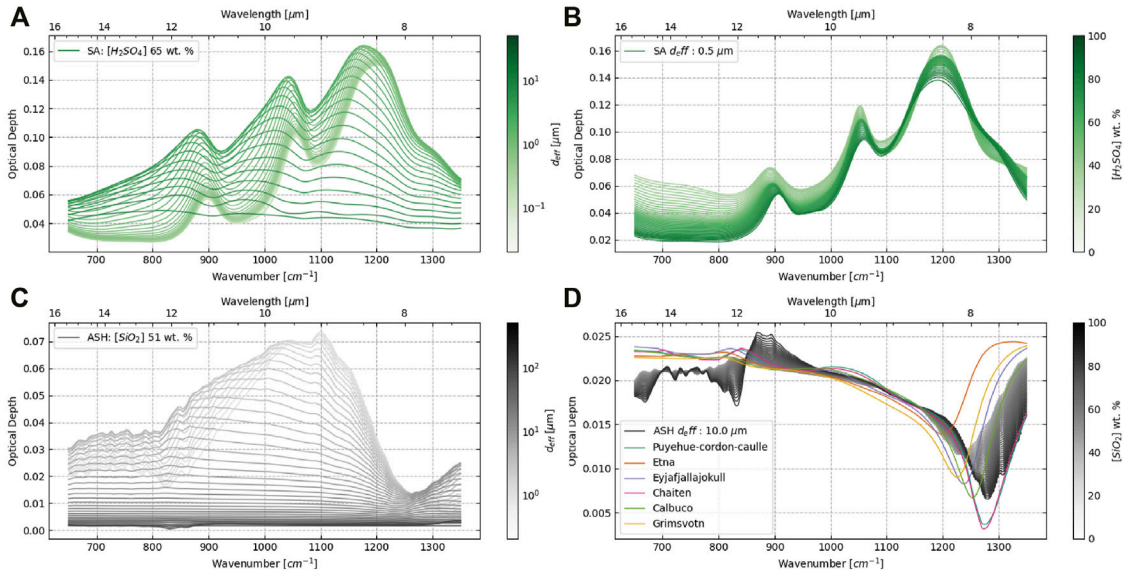

FIGURE 5
Optical depth reference spectra for both particle types considered in the retrieval: sulphate aerosols (SA) ((**A,B**)—green) and ash ((**C**, D—grey) **(A** and **C)** Optical depth cross sections as a function of particle size. All reference spectra are calculated for the same mass volume concentration of 1x10^{-3} g m^{-3}, and only the particle size distribution (PSD) varies. PSDs are log-normal with a mean effective diameter varying according to the colour scale (0.1–10 μm for SA and 0.1–200 μm for ash) and a sigma value of 1.5 **(B** and **D)** Optical depth spectra as a function of chemical composition. The effective particle diameter is kept constant (0.5 μm for SA, 10 μm for ash), and only the composition varies. SA compositions range from 38 to 81 wt% H_2SO_4, and spectra are calculated using refractive indices from (Lund Myhre et al., 2003). Ash bulk compositions range from 45 to 80 wt% SiO_2, and spectra are calculated using the parameterization algorithm for complex refractive indices found in (Prata et al., 2019). The mass volume concentration is again fixed at 1x10^{-3} g m^{-3}. Also shown are some example spectra calculated for natural samples from recent eruptions with refractive indices found in (Deguine et al., 2020) for the same particle size.

where α is the H_2O scaling factor, p is the degree of the polynomial, and c_j is the coefficient in the polynomial expression for the term of degree j. In the forward model, this set of polynomials can be used to accurately calculate optical depth spectra for any continuous value of parameter α as long it is strictly restricted to within the range used in the reference set. This approach avoids having to call RFM to derive H_2O extinction coefficients during the iterative process. We found that this method is computationally much faster than a classical interpolation method and yields accurate results within the bounds of the parameterization. The adjusted transmittance for layer 2 is then simply:

$$T_{2,adj} = e^{-\tau_{2,adj}} \tag{5}$$

Next, we calculate the optical depth of the volcanic species (τ_{volc}) by summing individual optical depth spectra for each volcanic species:

$$\tau_{volc} = \sum_i \tau_i \tag{6}$$

where τ_i is the optical depth for gas i derived from reference spectra calculated at the plume height and temperature using the relationship in Eq. 1). For ash and SA, we use the same polynomial fitting approach expressed in Equation 4 to quantify the relationship between effective particle diameter and optical depth for each wavenumber (see Figure 5):

$$\tau_{i,d_{eff},\tilde{\nu}} = \sum_{j=0}^{n} c_{j,\tilde{\nu}}\, {d_{eff}}^j \tag{7}$$

where d_{eff} is the mean effective diameter of the particles for particulate species i (either ash or SA). This allows the model to accurately calculate optical depth spectra for any continuous value of d_{eff} within the bounds used in the reference set (0.1–10 μm for SA; 1–200 μm for ash). The transmittance of the volcanic layer (T_{volc}) is then given simply by:

$$T_{volc} = e^{-\tau_{volc}} \tag{8}$$

The volcanic and clean layers are treated separately (i.e., each given a separate optical depth) but are geometrically occupying the same location. They have identical height, thickness and pressure, but the temperature of the plume species is allowed to differ from that of the ambient gases by a fixed amount (Δt_{plume}). The radiance for each layer is calculated using the transmittances obtained in equations Eqs. 5, 6, such that the total plume radiance (L_{plume}) is:

$$L_{plume} = B_{t_2}\left(1 - T_{2,adj}\right) + B_{\left(t_2+\Delta t_{plume}\right)}\left(1 - T_{plume}\right) \quad (9)$$

where B_t is the blackbody radiance calculated using the Planck relationship, t_2 is the atmospheric temperature at plume height, and Δt_{plume} is the temperature difference between plume and ambient temperature. This temperature difference only affects the radiance of the volcanic components and is usually set to a fixed value in our retrievals. The transmittance of the plume layer (T_{plume}) is simply the product of the transmittance of both layers:

$$T_{plume} = T_{volc}\, T_{2,adj} \quad (10)$$

Each atmospheric gas is also included as an individual species in the volcanic layer in order to enable *ad hoc* corrections to compensate for small differences in total column that could arise between a clear sky measurement and the plume measurement (due to changes in temperature profiles and/or viewing angles). The VMRs and temperature of those gases is fixed within layers 1 and 3 (foreground and background) in the forward model. Adding them as free parameters within the plume layer offers a way of improving the fits around their spectral features. Large variations of the total column of H_2O should also be expected, even over relatively short time windows. These can arise from changes in relative humidity and temperature over the course of the acquisition period. In contrast with previous studies where these large variations are circumvented by using spectral micro-windows in between water vapour absorption lines (e.g., Clarisse et al., 2012; Carboni et al., 2016; Sellitto and Legras, 2016; Sellitto et al., 2019; Guermazi et al., 2021), here we accounted for them using an ad hoc scaling factor for H_2O applied to all layers. Finally, the temperature in the proximal layer (layer 1) can be modified, allowing for small changes in temperature in the proximal layer over the course of a measurement set, which results in a non-uniform offset in the measured radiance difference ΔL. It should be noted that the mathematical expression of the forward model described above does not consider radiance scattered within the line of sight from other directions or multiple scattering.

Up to this point, all computations are performed using high-resolution RFM reference spectra. The last steps in the forward model are to 1) apply a spectral shift to the model grid (the magnitude of the frequency shift is a retrieved parameter); 2) convolve the spectrum with the ILS function (the width of the FOV is also a retrieved parameter, though the retrieved value is stable at 30 mrad throughout all our measurements); and 3) resample the convolved spectrum to match instrument resolution. The resulting radiance difference is the final processed spectrum used in the fitting algorithm. Optimal parameters are determined using an iterative non-linear least-squares method, and the Root Mean Square Error (RMSE) and coefficient of determination (R^2) are calculated for the best fit model result.

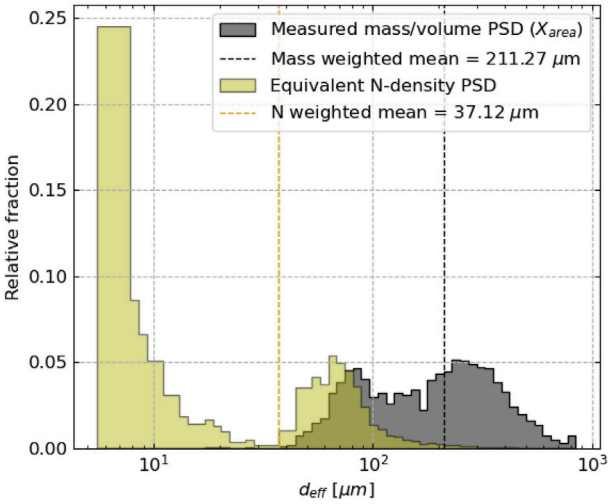

FIGURE 6
Particle size distribution (PSD) measured in the ash sample collected with the RPAS on 11 September 2019. [grey] Original measurement from Camsizer. Volumetric fraction of the particles with regards to their equivalent diameter (X_{area}: diameter of the area equivalent circle of each particle projection), yielding a mass fraction PSD with a mean at 211.17 µm. [yellow] Number density PSD, where the relative fraction is based on the number of particles instead, converted from volumetric fraction assuming spherical particles. N-density PSD is heavily skewed towards smaller particles (mean of 37.12 µm) and is more directly comparable with retrieved sizes in this work.

3 Results

3.1 RPAS ash sample analysis

The ash sample collected during the first measurement campaign in 2019 was analysed for particle size and chemical composition. This section details the results of these analyses, which were used to a) guide the selection of the most appropriate ash refractive indices in the retrieval, and b) compare particle size information between the sample and the values retrieved by the algorithm. The sample's mass-equivalent PSD (Figure 6) is bimodal, with a population of coarser particles (200–400 µm) and a separate population of finer particles (70–100 µm), seemingly lacking very fine particles. This PSD is generally similar to that of fallout samples collected at the summit of Stromboli in 2015 (Freret-Lorgeril et al., 2019). However, this representation can be misleading, as the Camsizer measurement describes the volume fraction of particles based on their equivalent diameter (X_{area}: diameter of the area equivalent circle of each particle projection). In these terms, the larger particles take an outsized representation, as the very fine fraction (<10 µm) represents a negligible volume within the overall sample, despite representing the vast majority of the particles. In order to emphasize this effect, we also show the

TABLE 2 Chemical composition of crystalline phases and glass measured in the ash sample collected with the RPAS on 11 September 2019.

	Glass	Ol	Cpx	Plag	Bulk
n	23	20	13	15	
Phase %	60	5	10	25	
SiO_2	52.29	37.38	50.42	50.4	50.89
TiO_2	1.59	0.02	0.84	0.06	1.05
Al_2O_3	15.42	0.03	3.22	30.12	17.11
FeO(t)	0.2	26.68	8.34	0.8	2.49
MnO	9.99	0.51	0.22	0.0	6.04
MgO	3.37	35.1	14.15	0.12	5.22
CaO	7.37	0.37	21.23	13.91	10.04
Na_2O	2.89	0.01	0.37	3.23	2.58
K_2O	4.04	0.0	0.14	0.59	2.59
P_2O_5	1.05	0.08	0.07	0.04	0.65
Cr_2O_5	0.0	0.0	0.02	0.01	0.0
NiO	0.0	0.04	0.01	0.01	0.01
Total	98.22	100.22	99.03	99.29	98.66

For each phase (Ol=olivine, Cpx=clinopyroxene, Plag=plagioclase), the data presented is the mean oxide composition in units of wt%, derived from *n* analyses. The *Phase %* is the relative areal fraction occupied by the phase, estimated from backscattered SEM, images. The bulk composition is the mean of all measured phases weighted according to their relative areal fraction.

PSD in terms of fractional number density (N-density) of particles by size—calculated based on the measured volume fraction and assuming spherical particles - which is heavily shifted towards smaller particle size bins. The resulting N-density PSD is also bimodal with a large peak around 5–10 μm, and a second one around 65 μm. We argue that the relatively small number of very large particles has a limited effect on the overall optical properties of the ash within the FOV of the OP-FTIR instrument, especially for dilute plumes, and that the comparatively large number of finer particles dictates the shape of the overall extinction profile. Therefore, we believe the N-density PSD is more directly comparable with the sizes retrieved in this work, as the strongest effects on the overall shape of the particle extinction coefficients from Mie scattering largely depend on the number density of particles with diameters close to that of the measured wavelength (i.e., 8–12 μm, see Figure 5).

The chemical composition of several crystalline phases, as well as the glass matrix as determined *via* EMPA analysis are presented in Table. 2. The glass composition represents a basaltic trachyandesite, and the main crystalline phases are olivine (Ol), clinopyroxene (Cpx) and plagioclase (Plag). Using the backscattered images from the EPMA analysis, we estimated the relative surface area fractions for each phase (Glass: 60%; Ol: 5%; Cpx: 10%, Plag: 25%) and used these relative fractions to calculate an approximate bulk composition for the sample. This bulk composition (a trachybasalt with ~51 wt% SiO_2) was used to parameterize the refractive index of the ash during the retrieval (see sect. 2).

3.2 Spectral fits

Figure 7 illustrates typical results of individual fits for selected spectra. Over the broad fitting window, the radiance difference spectra are dominated by a broadband contour representing the water vapour continuum. This contour can be positive or negative in absolute value, representing either an increase or a decrease in total water vapour column between the plume and clear sky measurements. The dashed line in the top panel of each figure emphasises this effect and shows the expected difference before considering the contributions from the plume. It is obtained by computing the radiance difference using best-fit parameters for water vapour scaling and observer temperature only and omitting all plume species. The shape of this baseline spectrum at the start of measurements depends on the respective positions of the line-of-sight between clear sky and plume and should approach zero for a clear sky taken at the plume location. Note that this radiance difference already contains recognisable spectral features for H_2O (continuum and narrow absorption/emission lines), O_3 and CO_2 resulting from the overall change in total atmosphere transmission when simply moving the line-of-sight of the instrument. In Figure 7A, showing a spectrum acquired in 2019, O_3 (1,000–1,080 cm^{-1}) and CO_2

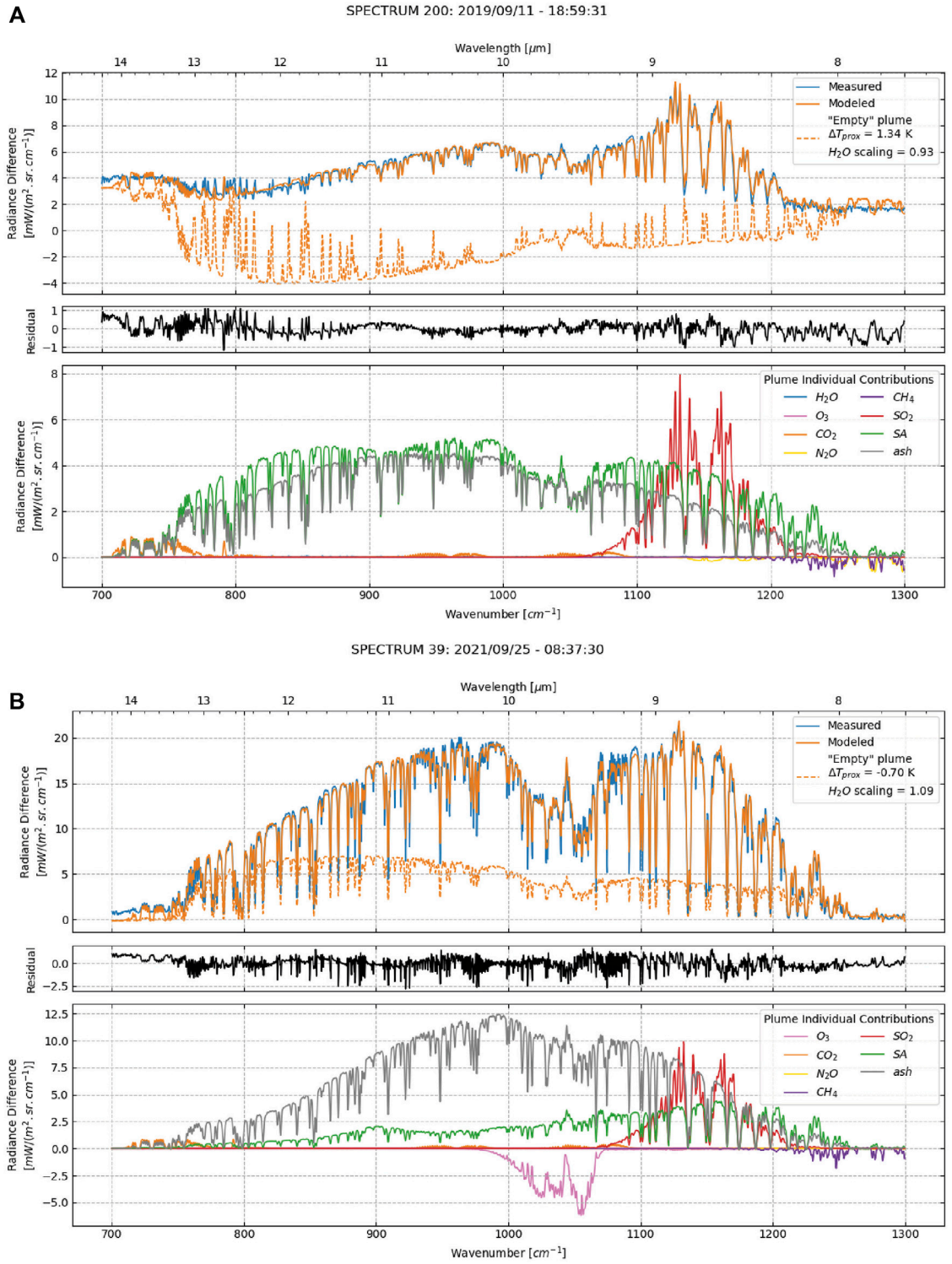

FIGURE 7
Example of fit results for selected individual spectra. In each subpanel: the top plot shows the measured [blue] and modelled [orange] spectra, along with the expected radiance difference without a plume in the line of sight [dotted orange] based on best-fit parameters for water vapour scaling and observer temperature; the middle plot shows the residual between modelled and measured spectra [black]; and the bottom plot shows the individual contribution of each plume species to the modelled spectrum **(A)** Plume spectrum with both ash and sulphate aerosol (SA) particulates, highlighting the differences in spectral shape between the two species, acquired on 11 September 2019 **(B)** Ash-rich plume spectrum acquired on 25 September 2021. Note the large O_3 adjustment needed to fit the depth of the measured absorption feature.

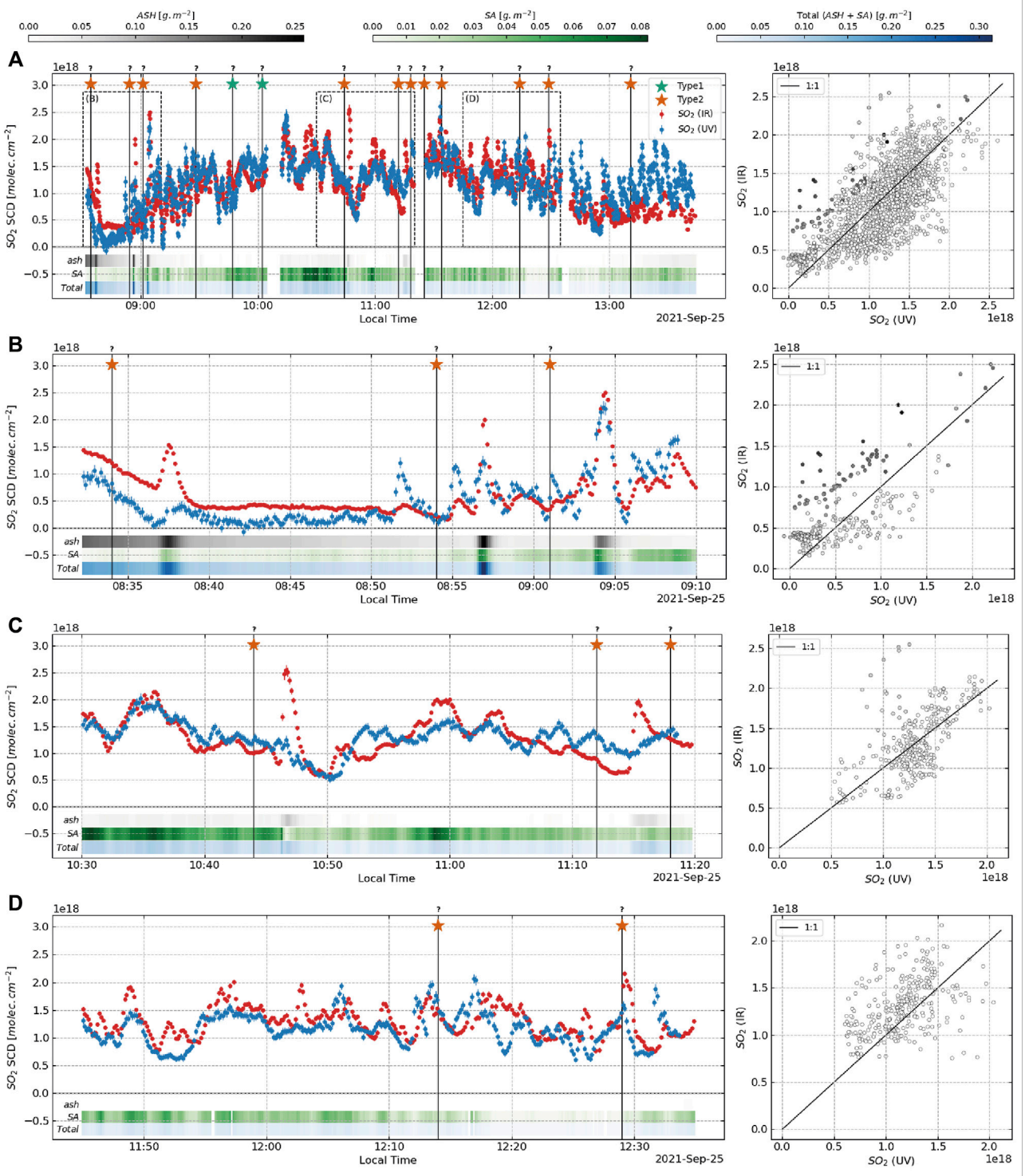

FIGURE 8
Time series of SO_2 SCDs measured on 25 September 2021. SCDs retrieved from the IR dataset are shown in red. SCDs retrieved from UV measurements are shown in blue. The UV time series was resampled after cross-correlation and has been shifted by 71 s to correct for the misalignment between the telescopes. Also shown are the mass SCDs for ash [grey], sulphate aerosols [SA, green] and total particulates [blue]. Stars represent individual events, recorded at the time when a plume is visible over the crater rim in video footage. Inset on the right shows a scatter plot between UV and IR SCDs, and the datapoints are coloured according to the retrieved ash SCD. Time and *y*-axis scales change between panels, but colour scales remain the same **(A)** Full dataset. Zoom windows for subsequent panels are shown as dashed boxes. Note that systematic disagreement between UV and IR retrieval occur towards the beginning and end of the measurement periods **(B)** Zoom window showing three ash-

(*Continued*)

FIGURE 8 (Continued)
bearing events between 08:30 and 09:10. Most data points departing from the 1:1 line on the scatter plot are associated with higher ash burdens. Note the relatively high ash burden during the first 7–8 min leading to the first ash event and the corresponding disagreement between UV and IR retrievals during that period **(C)** Zoom window showing two ash-bearing events between 10:30 and 11:20. Note that relatively high SA SCDs before the first event do not lead to significant disagreement between UV and IR retrievals **(D)** Zoom window with no ash-bearing event between 11:45 and 12:35. Note the change in scale in the ash SCD colour scale.

(925–1,000 cm^{-1}) appear as emission lines (due to the reduced transmission associated with a H_2O scaling factor <1), and the baseline minimum value goes from −1 to −6 $mW/(m^2{\cdot}sr{\cdot}cm^{-1})$ over the course of ~30 min. This value is expected to gradually change over the course of measurements, as the background atmospheric conditions evolve. In contrast, Figure 7B shows a spectrum acquired in 2021, where the baseline is a positive radiance difference (H_2O scaling factor >1) and O_3 and CO_2 appear as absorption features. The fitting window was deliberately chosen to include areas on either side where the atmosphere is virtually opaque (<730 cm^{-1} and >1,270 cm^{-1}). The radiance at those wavelengths represents the blackbody emission at the temperature of the most proximal layer, and we can use the value of the radiance difference to retrieve the temperature of the proximal layer (layer 1).

The bottom panel in each figure shows the contributions of each plume species (including the ad hoc corrections for atmospheric gases) superimposed over the baseline radiance difference. Each individual contribution is computed using the forward model and zeroing all quantities within the plume except for the species of interest. Note that because the background and foreground atmosphere are always an inherent part of the forward model, water vapour absorption lines still appear in the contribution from each individual species. The most instantly recognisable feature is the emission associated with SO_2. In particulate-rich spectra, a strong O_3 absorption is visible, related to the severe decrease in transmission introduced by the heavy particle burden and often requiring an ad hoc correction.

3.3 Side-by-side IR and UV measurements

Figure 8 shows the time series of SO_2 SCDs retrieved from our FTIR measurements for one dataset acquired during our second measurement campaign in 2021. We also present SO_2 SCDs measured using a co-located UV spectrometer. Disagreement in both absolute values of the SCD and timing of individual peaks are to be expected. They may arise as a consequence of differences in a series of factors between the two methods, such as: 1) the size of the respective FOVs (.03 rad for the IR, .1 rad for the UV); 2) the alignment of the telescopes; 3) the integration time (0.2 s in the UV, 8.9 s in the IR); and 4) different random and systematic error sources between the two methods. The UV time series was smoothed using a kernel of length equal to the IR integration time and resampled to match the temporal x-axis in the IR time series. Moreover, we determined the optimal lag using a cross-correlation method and shifted the UV time series accordingly. We would expect this lag to vary over the course of the measurements, as it is tied to the plume velocity, and plumes associated with crater explosions will travel at greater velocities. However, we found that an overall lag of ~71 s resulted in a good match between the timing of the main events. Retrieved SCDs between the IR and UV measurements generally agree within a factor of ~2 (scatter plot in Figure 8A). The main discrepancies occur towards the beginning and end of datasets with the IR method retrieving systematically lower SCDs than the UV method at the beginning of the dataset in Figure 8A, and systematically higher SCDs towards the end of the dataset.

Figure 8 further documents explosive events, as recorded in GoPro time-lapse footage (orange stars). Here we only report ash explosions, defined as type 1 events following the terminology in Patrick et al. (2007), and mark them at the time of their first appearance above the crater rim from our vantage point. Type 2 events (essentially bubble bursts associated with ballistics) were much more difficult to identify from the 2021 vantage point without a direct view of the craters (Figure 1). It is also impossible to assign a specific crater of origin for individual events for the 2021 time series. All documented events are followed by a marked increase in retrieved SO_2, SA and ash contents, after a delay of 1-2 min representing the time needed for the plume to move into the FOV of the instruments.

3.4 Near-vent measurements

During the 2019 campaign, we performed measurements from the l'Osservatorio restaurant, with a direct view of the crater area (Figure 1B). We were able to move the FOV of the instrument to intersect the plume directly above the vent. A time series of the retrieved quantities for a dataset collected in this configuration is shown in Figure 9. During this period, we captured the baseline passive degassing plume, as well as plumes resulting from explosive events. Events were documented through visual observation and logged manually. As we had a direct view of the crater area, the explosive plumes can be separated into two classes with relation to the event types defined by Patrick et al. (2007). Type 1 events (bubble bursts + ballistics) produce plumes with low ash content and elevated concentrations of SO_2 (green

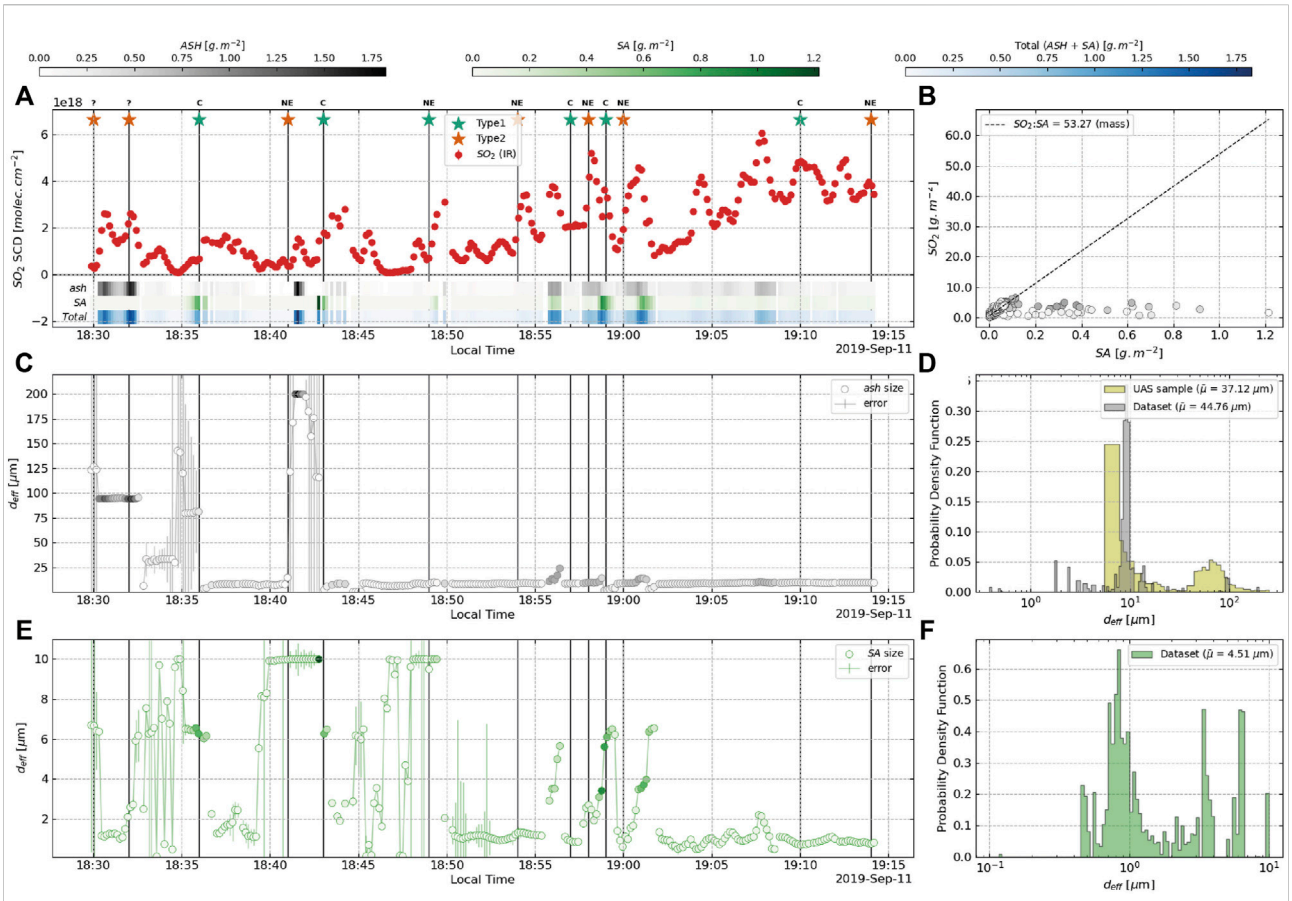

FIGURE 9
Time series of retrieved quantities for a dataset collected directly above the vents on 11 September 2019 **(A)** SO_2 SCDs [red]. Error bars represent the modelling error only (i.e., the covariance estimated during the linear regression). Stars represent individual events visually documented in the crater area (type 1 or 2), labelled according to the vent from which they originated (NE: northeast; C central). The mass SCDs for ash [grey], sulphate aerosols [SA, green], and the total particulates [blue] for each individual measurement are also shown in colour bars located at the bottom of the plot (colour scales at the top) **(B)** Scatter plot between SO_2 and SA SCDs, and the linear fit for this data (SO_2/SA ratio = 53.27). Individual data points are coloured according to the ash SCD **(C)** Retrieved effective diameter for ash particles **(D)** Histogram of the retrieved ash sizes over the entire dataset [light grey] weighted according to the ash SCD to minimise the importance of measurements with very low amounts of ash. For comparison the particle size distribution measured in the ash sample collected with the RPAS is also shown [yellow] **(E)** Retrieved effective diameters for the SA **(F)** Histogram of the retrieved sizes over the entire dataset [light green] weighted according to the SA SCD to minimise the importance of measurements with very low amounts of SA. Note that size distributions for both ash and SA are bimodal.

stars). Type 2 events, on the other hand, are ash-rich with a visibly dark plume (orange stars). The FOV of the instrument was positioned directly above the NE crater area. As a result, this dataset mainly contains events originating from the NE and central vents (which were directly behind the NE vents along the line of sight). Some emissions from the SW crater area may have entered our FOV but, given the wind direction during our measurements, this was challenging to determine visually. Type 1 events originated from both NE and C areas, and type 2 events mainly originated from the NE craters. Absolute retrieved SCDs for SO_2, ash and sulphate aerosols above the vents are relatively high (peak SO_2: 6 × 10^{18} molec·cm^{-2}, peak ash: 1.75 g·m^{-2}, peak SA: 1.2 g·m^{-2}). Peaks in SO_2 within the time series generally occur shortly after the onset of each event. Retrieved SA particle sizes are shown in the bottom plot in Figures 9E, F. The probability density function, where each measurement of particle size is weighed according to the associated SCD, exhibits a mode around .8 μm, representative of the typical size retrieved during low level degassing (mean d_{eff} value of 1.79 ± 3.08 μm). There are also several peaks at higher diameters, representing d_{eff} values retrieved during the explosive events (i.e., type 2 ca 18:56, 18:58 and 19:02 and type 1 ca 18:36 and 18:43, Figure 9E).

In a scatter plot between SO_2 and SA over the entire dataset (Figure 9B), the measurements with lower amounts of particulates (light shades) define a ratio line. We calculate SO_2/SA mass ratios using a robust linear regression (Siegel,

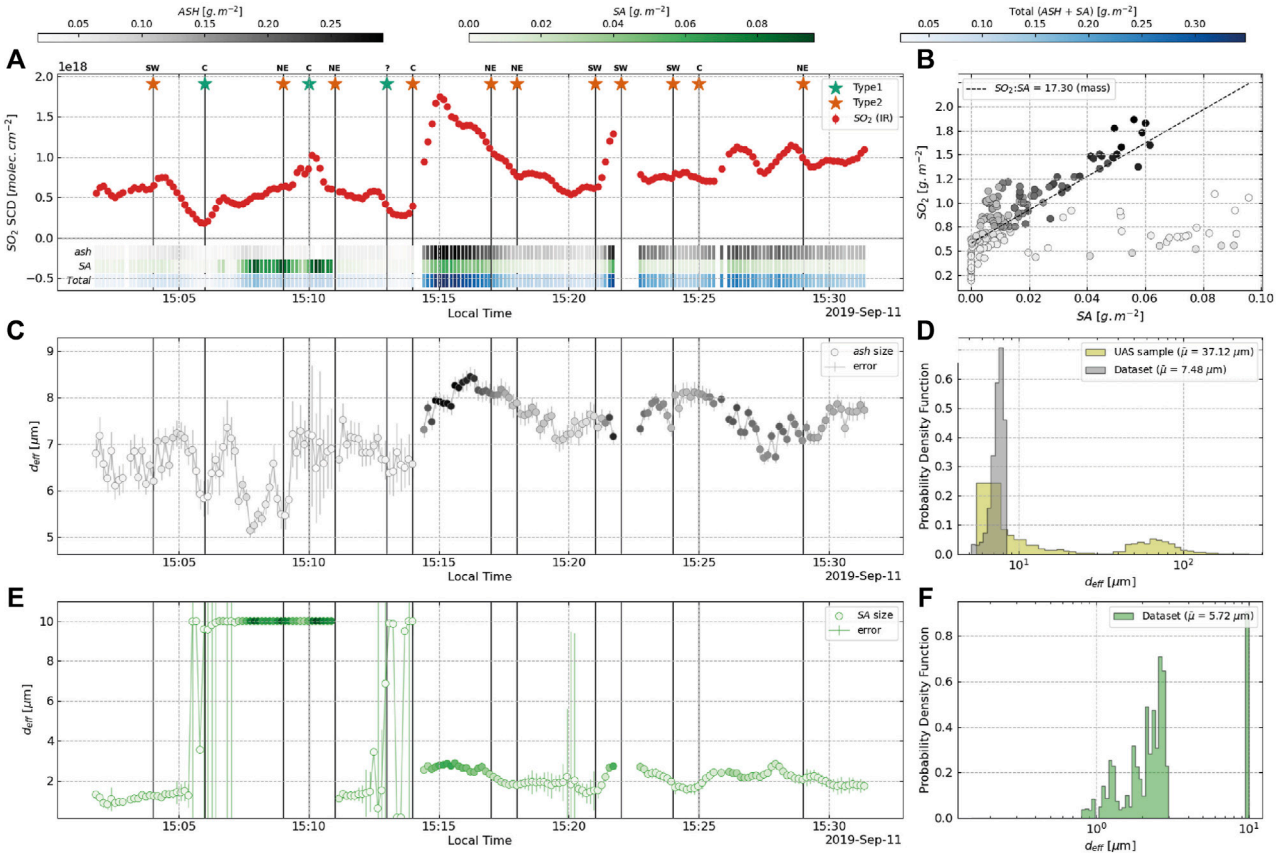

FIGURE 10
Time series of retrieved quantities for a dataset collected downwind on 11 September 2019 **(A)** SO_2 SCDs [red]. Error bars represent the modelling error only (i.e., the covariance estimated during the linear regression). Stars represent individual events visually documented in the crater area (type 1 or 2), labelled according to the vent from which they originated (NE: northeast; C central; SW: southwest; ? unknown). The mass SCDs for ash [grey], sulphate aerosols [SA, green], and the total particulates [blue] for each individual measurement are also shown in colour bars located at the bottom of the plot (colour scales at the top) **(B)** Scatter plot between SO_2 and SA SCDs, and the linear fit for this data (SO_2/SA ratio = 17.3). Individual data points are coloured according to the ash SCD **(C)** Retrieved effective diameter for ash particle **(D)** Histogram (N density) of the retrieved sizes over the entire dataset [light grey] weighted according to the ash SCD so that sizes retrieved during ash bursts are represented more heavily. For comparison the particle size distribution measured in the sample collected with the RPAS is also shown [yellow] **(E)** Retrieved effective diameters for the SA **(F)** Histogram of the retrieved sizes over the entire dataset [light green] weighted according to the SA SCD.

1982) which emphasises the overall trend rather than more extreme data points, in order to minimise the effects of those measurements with high amounts of particulates during the explosive events. This is done so we can quantify the sulphur partitioning in the gas plume during passive degassing periods. We observe a ratio of ~53 by mass in this dataset. Values from similar datasets range between 40 and 80.

Retrieved ash particle sizes are shown in the middle plot in Figures 9C, D. The retrieved size for ash particles increases during explosive events. The probability density function exhibits a clear mode at ~10 μm during non-explosive phases (range between 5 and 15 μm). During the most intense ash-rich type 2 events (e.g., ca 18:30–18:33 and ca 18:42 in Figure 10), ash d_{eff} reaches much higher values, up to 200 μm, the upper bound for ash size set in the algorithm. During type 2 events of lower intensity (e.g., three events in quick succession ca. 18:56, 18:58 and 19:00), particle size also increases during each event, but to lower values of 10–30 μm.

3.5 Downwind measurements

Figure 10 shows a time series of measurements acquired from the same vantage point and on the same day (11 September 2019) as those measurements shown in Figure 9, but where the instrument FOV intersected the plume ~0.8 km downwind (Figure 1B). The measured SCDs for all target species (peak SO_2: 2×10^{18} molec·cm^{-2}, peak ash: .3 g·m^{-2}, peak SA: .1 g·m^{-2}) are lower than in the near-vent measurements, representing the dilution of the plume and loss processes (e.g., SO_2 oxidation and

settling of PM) as it travels. Wind speed on that day was relatively low, and this distance corresponds to a plume age of approximately 3–5 min. Recorded type 1 and type 2 events at the vents appear disassociated with peaks in the SO_2 time series. However, we identify three individual events within the time series: one event with elevated SO_2 and SA, with a slow onset at ca. 15:07, assumed to be a type 2 event), and two events with sharper onsets at ca. 15:14 and 15:21 showing elevated SO_2, SA and ash contents (assumed to be type 2 events). The mean SO_2/SA mass ratio for this particular dataset is ~17, and values for downwind datasets range between 10 and 30.

Retrieved sizes for the SA downwind are 5.21 ± 4.27 μm during low level degassing, and 2.19 ± 0.36 μm on average during explosive events (type 1 and type 2). Sizes retrieved during a type 1 event with a high SA SCD (ca 15:07–15:10 in Figure 10) show elevated values, reaching the upper bound for SA size set in the algorithm (10 μm). Retrieved sizes for ash in the downwind dataset are 6.66 ± 0.57 μm outside of ash-rich events, and 7.68 ± 0.38 during ash-rich events. Both values are in good agreement with the smaller mode of the particle size distribution found in our collected sample (Figure 6).

4 Discussion

4.1 Sensitivity to plume temperature

The principal source of uncertainty in the method comes from the estimation of plume temperature in the FTIR forward model. This is illustrated by systematic disagreements between the UV and IR retrievals of SO_2 SCDs towards the beginning and end of datasets (see Figure 8A). As the measurement period evolves, the actual temperature at plume height increases or decreases (depending on time of day), while the assumed plume temperature in our model remains the same (extracted from the reference atmospheric sounding, which is taken only in 12 h intervals, and at a location >100 km away from the measurement location). If the assumed temperature is colder than the plume actually is, the amount of SO_2 retrieved by our method will be an overestimate of the actual SO_2 in the plume. Conversely, if the assumed temperature is warmer than the actual temperature, our measurements will be an underestimate. UV spectroscopy is not affected by this assumption and thus differences may arise between the retrieved quantities from the FTIR and the UV measurements. A further complication is that both plume height and atmospheric temperature at plume height may vary over the course of the measurements, leading to systematic errors in all quantities retrieved by the method. As the radiance difference is calculated using a clear sky spectrum acquired at the beginning or end of the measurements, exacerbating the differences in measured radiance which result from changing atmospheric conditions in spectra collected further away from the calibration period, using more frequent clear sky measurements will yield more consistent results. In addition, plume temperature might be higher due to the presence of the volcanic plume, i.e., the actual temperature in layer 2 may differ from the one recorded in the atmospheric profile due to the hot volcanic gas and particles.

To quantify the error linked with the plume layer temperature, we introduced a fixed temperature difference (Δt_{plume}) between the temperature in the volcanic layer at the time of measurement and the clean air layer temperature in the clear sky measurement and performed the retrieval on a subset of 1,000 measurements from 25 September 2021, for various values of Δt_{plume} (Figure 11). The temperature of the plume at Stromboli is frequently recorded using a Multi-component Gas Analyser System (Multi-GAS) at the summit (Aiuppa et al., 2009; Aiuppa et al., 2010). Although temperature measurements are not reported in published studies, they are recorded by the instrument and typically fall within 1–3 degrees of the ambient temperature when the plume drifts over the summit (INGV personal communication). Therefore, we vary Δt_{plume} between values of −5 K and + 5 K. In addition, we ran the retrieval on the same data subset leaving the temperature of the volcanic layer as a free parameter. This latter approach yielded unrealistic results, with Δt_{plume} ranging from −30 K to + 30 K within the same dataset, leading to overestimates of up to a factor of four in the retrieved SO_2 SCD in spectra with the highest amounts of particulates. However, these results allow us to quantify the expected errors related to plume temperature. When plotting the ratio between the SO_2 SCD retrieved with a free t_{plume} and the SO_2 SCD retrieved with a fixed t_{plume} against the associated Δt_{plume}, they outline a very clear relationship, which can be approximated using an exponential decay function. We estimate that uncertainties in assumed plume temperature will lead to errors in the retrieved SO_2 SCDs of a factor of ~3.5% per K. When considering a realistic range of assumed plume temperatures, this translates to overestimates of up to 19% (Δt_{plume} = −5 K) and underestimates of up 16% (Δt_{plume} = + 5 K). Measurements with high SCDs of particulates depart from this overall relationship and introduce larger overestimates. Similar values are found when examining other retrieved quantities (summarised in Table 3). These uncertainties are much larger than the typical fitting error of ~2.2% and represent the largest limitation in the method. Local measurements of temperature at plume height and accurate visual determination of the plume height will help mitigate the potential for error.

4.2 Plumes with high optical thickness

Previous measurements have shown the PM-related optical properties of the Stromboli plume to vary with the occurrence of

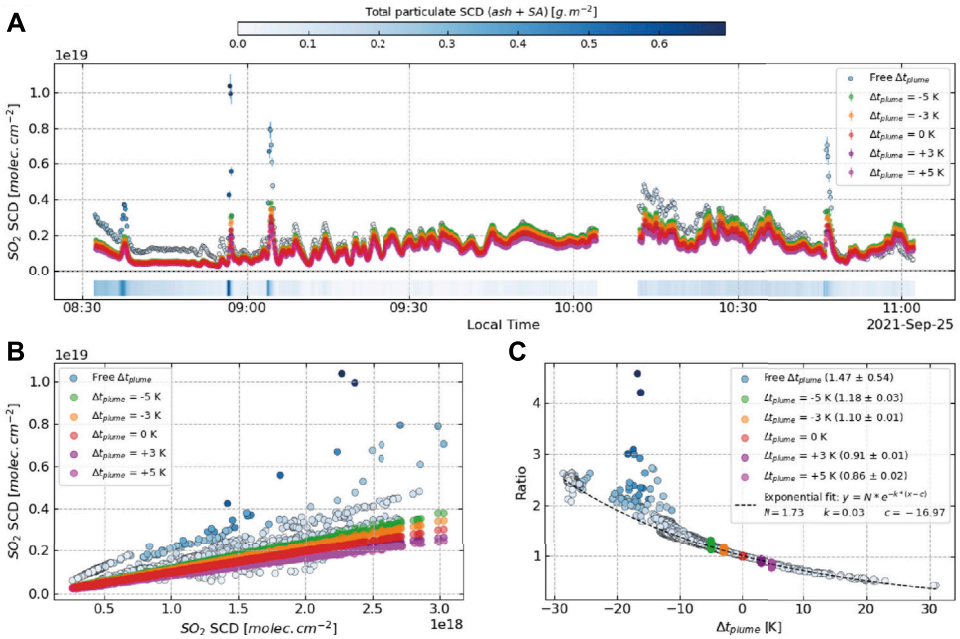

FIGURE 11
Sensitivity analysis of the effect of plume temperature on the retrieved SO_2 SCDs. **(A)** Time series of SO_2 SCDs for a subset of 1,000 spectra measured on 25 September 2021, using various values of Δt_{plume} (green: −5 K; orange: −3 K; red: 0 K; purple: +3 K; magenta: +5 K; blue: free parameter). Bar plot at the bottom shows the total SCD for all particulate species (colour scale at the top), highlighting the eruptive events with high ash or sulphate aerosols (SA). Data points in the free T_{plume} retrieval are also coloured according to the total particulate SCD **(B)** Retrieved SO_2 SCDs for each of the time series mentioned above against the corresponding SO_2 SCD in the reference retrieval (Δt_{plume} = 0 K). Note that measurements with high amounts of particulates produce larger overestimates in the retrieved SO_2 **(C)** Ratio between retrieved SO_2 in each time series against the reference retrieval (Δt_{plume} = 0 K). Measurements with low particulate content outline an exponential relationship, with an expected uncertainty of ~3.5% per K.

TABLE 3 Estimated errors associated with plume temperature. Expressed as the ratio of the retrieved SCD over a reference dataset with Δt_{plume} = 0 K.

Δt_{plume}	SO_2 error	SA error	Ash error
−5 K	1.18 ± 0.03	1.18 ± 0.05	1.04 ± 0.07
−3 K	1.10 ± 0.01	1.11 ± 0.03	1.03 ± 0.04
+3 K	0.91 ± 0.01	0.91 ± 0.02	0.97 ± 0.03
+5 K	0.86 ± 0.02	0.86 ± 0.03	0.915 ± 0.04

individual events (Sellitto et al., 2021). Our results further support these observations, with type 1 events generally associated with a peak in SO_2 SCD, and an increase in SA SCD, whereas type 2 events are associated with increased amounts of both ash and SA SCD (Figure 9). Some type 1 and type 2 events were not accompanied by particle increases and in one case no SO_2 peak was observed. This may reflect the fact that some plumes drifted above the FOV of our instrument, either because the explosion that produced them injected significant momentum into the plumes, or because shifts in wind direction or speed caused the plume to rise more vertically in some cases than others. As the dataset shown in Figure 9 was acquired in the run up to sunset (approximately 19:15 local time), it is also possible that our manual observations are incomplete or inaccurate, particularly towards the end of the dataset as it became darker.

The presence of high amounts of particulates within a plume (e.g., ash-bearing plumes after explosions or those with a high optical thickness due to large amounts of aerosols) can negatively affect UV measurements and lead to large errors in retrieved SO_2 SCDs if realistic radiative transfer is not taken into account (Kern et al., 2010; Kern et al., 2012; Kern et al., 2013; Varnam et al., 2020). Although both over- and underestimations are possible, depending on the specific conditions within a plume (i.e., magnitude of the SO_2 column amounts and nature of the scattering aerosol), underestimates are more likely in plumes with high optical thicknesses, particularly if the particulate species within the plume also exhibit strong absorbing properties, as is the case for ash-laden plumes captured close to the vent (Kern et al., 2013). In such cases, IR retrievals may offer an advantage, as they are less likely to be impacted by multiple scatterings (typical sizes for volcanic particles are often much smaller than the 8–12 μm wavelength range of the method) and by light dilution effects. Our method offers a means of quantifying the aerosol optical thickness and SO_2 SCDs from a

TABLE 4 Sulphur speciation in proximal volcanic plumes from this and previous studies.

Volcano	Study	SO_2/SA (mass)	SO_4^{2-}/SO_2 (molar)
Masaya	Allen et al. (2002)	95–1,200	0.04–0.4[a]
	Mather et al. (2003a)	25[a]	0.01
	Sellitto et al. (2019)	400	0.15[a]
Vulcano	Mather et al. (2004a)	100[a]	0.04
Lascar	Mather et al. (2004b)	25[a]	0.01
Villarica	Mather et al. (2004b)	50[a]	0.02
Etna	Roberts et al. (2018)	38[a]	0.015
Stromboli	This study	53	0.021

[a]Converted from originally reported value assuming SA, acidity of 65 wt. % H_2SO_4.

single measurement. For optically thick plumes containing very large amounts of ash or PM, underestimates in our IR retrievals should still be expected, as the radiance collected at the instrument would originate mainly from the surface of the plume. However, for moderate particle concentrations, our method offers a way to compensate for the expected loss of radiance from within the plume layer. This is apparent at several points in the time series presented in Figure 8 and highlighted in subpanels B-C, where ash-rich plumes are generally associated with higher retrieved SO_2 SCDs in the IR, by factors ranging from 2 to 5. We propose that this represents an underestimate of the true SO_2 burden by the UV method, and that the SCDs retrieved in the IR are closer to the concentrations within the plume at the time of measurement. Alternatively, it is possible that plumes with high amounts of ash retain heat more efficiently, and as a result the assumption of a plume in thermal equilibrium with the atmosphere is no longer valid. In such a case, the retrieved SO_2 SCD with the IR method would constitute an overestimate of the real values, as warmer plumes emit more radiation. These discrepancies merit further investigation within a dedicated, systematic side-by-side experiment in which multiple scattering and light dilution effects are accounted for in both UV and IR retrievals.

4.3 Sulphur speciation during plume transport

Table 4 summarises sulphur speciation values previously reported and measured in proximal plumes (<1 km from source) at Stromboli and elsewhere. Sulphur partitioning between the gas and aerosol phases is generally reported as the molar ratio of SO_4^{2-} ions to SO_2 (SO_4^{2-}/SO_2) when measured with filter packs. Alternatively, when retrieved with spectroscopic techniques, the reported value is often the mass ratio of the gas phase over the aerosol phase, including the water (SO_2/SA). The conversion between the two values depends on the acidity of the aerosols themselves, which is not always reported. For a simple comparison, we assume an acidity of 65 wt% H_2SO_4 (the value used to generate our reference extinction spectra), and present both ratios. The SO_2/SA measured in our near-vent measurements is on the lower side of the range observed in proximal plumes at other volcanoes, suggesting the presence of large amounts of primary sulphate aerosols (i.e., those condensed directly from the high-temperature gas emitted from the magma) in the passive plume and during type 1 events (which typically have lower particulate loads than type 2 events). Alternatively, this could reflect the rapid formation of sulphate *via* oxidation of SO_2 condensing onto the primary particles in the plume or a higher water content of the SA in our measurements. This is supported by the observations that the sizes measured here (Figure 9) are rather large compared to those expected for newly formed particles (<.1 μm for particles within the "nucleation mode") (Whitby, 1978; Mather et al., 2003b).

SO_2/SA ratios in diluted downwind datasets (range 10–30, mean of ~17 in the dataset illustrated in Figure 10) are lower than those found near-vent (range 40–80, mean of ~53 in the dataset illustrated in Figure 9), suggesting either an increase in sulphate aerosol mass and/or a decrease in SO_2 mass as the plume ages. Several mechanisms exist which could explain the observed decrease in SO_2/SA ratio with plume age. SO_2 depletion by oxidation into sulphuric acid is a commonly proposed mechanism (Eatough et al., 1994) and has been documented in volcanic plumes, with SO_2 loss rates in tropospheric plumes ranging between 10^{-7} and 10^{-3} s^{-1} (Oppenheimer et al., 1998b; McGonigle et al., 2004; Rodríguez et al., 2008). As SO_2 is oxidized, the decrease in SO_2/SA ratio then results from both a loss of gaseous SO_2 in the plume, and from condensation of sulphate formed as SO_2 is oxidized, either increasing the size of existing particles, or nucleating new particles, and ultimately causing an increase in aerosol mass. However, even assuming a fast depletion rate at the upper bound of the range documented above (10^{-3} s^{-1}), it is not clear that this oxidation process would be fast enough to explain the changes observed here, which took

place over distances of <1 km and for plume ages of only a few minutes. Alternatively, the mass of SA may also be increased by condensation of water into the aerosol, a process by which the existing sulphate aerosols lower the supersaturation threshold required to grow droplets (Mather et al., 2004a; Mather et al., 2004b), potentially ultimately acting as seeds for the formation of clouds (Pianezze et al., 2019). This process would increase the overall mass of the SA while decreasing their relative acidity. Given the fixed parameter for SA acidity in our retrieval, our model is not able to measure this change in acidity. However, hygroscopic growth is consistent with both the slight increase in retrieved SA size (during periods of passive degassing) and the decrease in SO_2/SA mass ratio in the downwind measurements and is therefore a plausible mechanism to explain our observations. Two recent studies have investigated the evolution of SO_2 and SA in the Stromboli and Etna plume (Pianezze et al., 2019; Sahyoun et al., 2019). Both studies found an increase in the number concentration of SA particles with distance from the vent, combined with an increase in the size of the measured particles. Although the mechanisms investigated by these studies take place over much larger distances and targeting older plumes, their interpretations are broadly consistent with our observations, and suggest the mechanisms of particle growth that ultimately can result in cloud condensation occur even in very young plumes such as those we measured. Further investigation of these mechanisms might elucidate volcanic impacts and interactions with cloud cover in the troposphere (e.g., Ebmeier et al., 2014).

4.4 Ash settling during plume transport

As mentioned previously, the sensitivity of the retrieval to particle sizes above 20 μm is not well established, and it is possible that the retrieved values do not represent the true size within the plume. Nevertheless, our observations of significant increases in optical depth in the long-wave infrared spectrum and rapid shifts in particle size during type 2 events are consistent with the increase in aerosol optical depth and decrease in the Angstrom exponent observed at shorter wavelengths by Sellitto et al. (2021) and are the likely the result of an injection of coarser particles from the explosions. Sizes retrieved over the entirety of the dataset capture the full range of ash particle sizes found in the sample collected with the RPAS, with the fine fraction often found during low-level degassing and the coarser particles during type 2 events.

The size of ash retrieved in diluted plumes (either downwind or above the vent during non-explosive activity) is remarkably consistent, with values of 5–10 μm in both datasets. This value is also consistent with the fine size fraction in our collected sample. Coarser particles (65–200 μm) retrieved from near-vent measurements are not detected in the downwind measurements, even when a high SCD of ash is retrieved, suggesting that they have already been removed by sedimentation at that point. This is consistent with our visual observations during the measurement period of large "fingers" of ash raining from the drifting plumes and depositing the coarser particles on the slopes of the volcano, as documented in Freret-Lorgeril et al. (2020). It is also consistent with the observations of Sellitto et al. (2020) who found a decrease in aerosol size with increasing distance from the vent in the proximal (<20 km) plume at Etna volcano, which they interpreted as due to the sedimentation of ash (and possibly coarser SA). It should be noted that the sensitivity of the IR retrieval to particle size is most pronounced in the range of particle sizes 1–10 μm, where the size of the particles approaches the wavelength of radiation. The spectral shape for ash shows relatively little variation with increasing sizes above 20 μm (see Figure 5), and the detection of coarser particle sizes in this work should be taken as an indication of their presence rather than an accurate determination of their actual size.

5 Conclusion and future work

Here we present a new method for simultaneous quantification of gases and particulates in volcanic plumes using emission OP-FTIR measurements. Using a broad fitting window, the method allows for identification and quantification of ash and sulphate aerosols within a plume, and the determination of particle size. Retrieved SO_2 column densities are in reasonable agreement (within a factor of 2) with those retrieved using UV spectroscopy with the larger discrepancies occurring during ash-rich events. SO_2 SCDs retrieved with the IR method are generally larger than those retrieved with traditional UV methods. The ability to measure particles and gas simultaneously could prove useful in understanding and quantifying the underestimation of SO_2 column densities by UV methods which results from multiple scattering, either in plumes containing large amounts of particulates or when measurements are performed from large distances (e.g., Kern et al., 2013; Campion et al., 2014; Varnam et al., 2020). This invites further investigation of ash- and SA-rich plumes using simultaneous measurements with both methods.

Using this new methodology, we document the plume composition during different types of volcanic activity at Stromboli (passive degassing, type 1 ash-poor and type 2 ash-rich explosions) and its evolution over a short distance downwind of the active vent. Our algorithm consistently identifies a fine ash fraction (5–10 μm) present even during non-explosive phases and in distal plumes, as well as coarser ash particles (30–200 μm, ~65 μm mean) found only in datasets collected near the vent after type 2 events. We collected an *in-situ* sample of ash during an explosive event using a Remotely Piloted Aircraft System (RPAS), allowing us to compare particle sizes measured remotely with those found directly within the plume.

Both size modes detected by our FTIR method were found in the RPAS sample, providing validation for the retrieval algorithm. The measured loss of the coarse ash size at a short distance (~.8 km) from the vent is consistent with visual observations of particle settling below the drifting plume. Measurements of SA size (slightly coarser particles found in downwind datasets) and SO_2/SA mass ratios (from 53 near the vent to 17 downwind) suggest rapid aerosol growth over these short distances as well, which we propose to be dominated by water uptake. Long-term deployment of this method might provide useful additional metrics alongside a baseline of SO_2 data to investigate physical and chemical processes occurring within tropospheric plumes over short (1–10 km) distances. Emission IR measurements also enable measurements during periods when UV methods cannot be used (i.e., at night) and without the need to align the spectrometer with an IR source, opening the possibility for flexible 24 h gas monitoring.

Given the encouraging results reported here, we suggest the method should be further developed to explore its full potential. Future work will focus on longer term deployment at Stromboli and other volcanoes, with the aim of creating time series spanning days or weeks, and to evaluate the usefulness of the method for continuous monitoring. As well, systematic comparison with UV retrievals should be explored, with the aim of improving SO_2 quantification in particulate-rich plumes. Finally, a number of improvements and extensions should be tested and implemented within the source code: 1) fitting of individual absorption lines for gases such as CO_2 following the method outlined in Goff et al. (2001); 2) quantitative retrieval of SiF_4; 3) improved spectral fits focused on the particulate species using spectral micro-windows in order to alleviate the effects of water vapour absorption; and 4) exploring the evolution in aerosol composition by fixing the particle size and targeting SA particle composition, including the possibility of sulphate-coated ash particles.

Data availability statement

The raw data supporting the conclusions of this article will be made available by the authors, without undue reservation.

Author contributions

J-FS designed and supervised the measurement campaigns, developed the algorithm, processed the data and wrote the manuscript first draft. TM and MB supervised all work, participated in field campaigns and assisted in the development of the algorithm. AS provided the OP-FTIR instrument, assisted in data collection and analysis. BE and MV assisted in the collection and analysis of UV measurements, RG advised on the implementation of the quantitative retrieval for particulates. All authors edited the manuscript.

Funding

The work outlined in this manuscript was supported by NERC award NE/S004025/1.

Acknowledgments

The authors would like to thank INGV-Catania, and particularly Giuseppe Salerno, for facilitating access to Stromboli volcano during the field campaigns and for loaning UV equipment. We would also like to thank Evgenia Ilyinskaya for her help in the PSD analysis of the ash sample, Zoltán Taracsák for performing the EMPA measurements, and Anu Dudhia for insightful discussions about the physics behind the method and the use of the RFM software. We also thank Simon Carn, Pasquale Sellitto and Wolfgang Stremme for their insightful comments and suggestions which led to significant improvement of the manuscript. For the purpose of Open Access, the author has applied a CC BY public copyright licence to any Author Accepted Manuscript (AAM) version arising from this submission.

Conflict of interest

The authors declare that the research was conducted in the absence of any commercial or financial relationships that could be construed as a potential conflict of interest.

Publisher's note

References

Aiuppa, A., Federico, C., Giudice, G., Giuffrida, G., Guida, R., Gurrieri, S., et al. (2009). The 2007 eruption of Stromboli volcano: Insights from real-time measurement of the volcanic gas plume CO_2/SO_2 ratio. *J. Volcanol. Geotherm. Res.* 182, 221–230. doi:10.1016/j.jvolgeores.2008.09.013

Aiuppa, A., Bertagnini, A., Métrich, N., Moretti, R., Di Muro, A., Liuzzo, M., et al. (2010). A model of degassing for Stromboli volcano. *Earth Planet. Sci. Lett.* 295, 195–204. doi:10.1016/j.epsl.2010.03.040

Alfano, F., Bonadonna, C., Volentik, A. C. M., Connor, C. B., Watt, S. F. L., Pyle, D. M., et al. (2011). Tephra stratigraphy and eruptive volume of the May, 2008, Chaitén eruption, Chile. *Bull. Volcanol.* 73, 613–630. doi:10.1007/s00445-010-0428-x

Allard, P., Burton, M., and Muré, F. (2005). Spectroscopic evidence for a lava fountain driven by previously accumulated magmatic gas. *Nature* 433, 407–410. doi:10.1038/nature03246

Allard, P., Burton, M., Sawyer, G., and Bani, P. (2016). Degassing dynamics of basaltic lava lake at a top-ranking volatile emitter: Ambrym volcano, Vanuatu arc. *Earth Planet. Sci. Lett.* 448, 69–80. doi:10.1016/j.epsl.2016.05.014

Allen, A. G., Oppenheimer, C., Ferm, M., Baxter, P. J., Horrocks, L. A., Galle, B., et al. (2002). Primary sulfate aerosol and associated emissions from Masaya volcano, Nicaragua: Primary sulfate aerosol from masaya volcano. *J.-Geophys.-Res.* 107, ACH 5-1–ACH 5-8. doi:10.1029/2002JD002120

Barsotti, S., Andronico, D., Neri, A., Del Carlo, P., Baxter, P. J., Aspinall, W. P., et al. (2010). Quantitative assessment of volcanic ash hazards for health and infrastructure at Mt. Etna (Italy) by numerical simulation. *J. Volcanol. Geotherm. Res.* 192, 85–96. doi:10.1016/j.jvolgeores.2010.02.011

Biermann, U. M., Luo, B. P., and Peter, Th. (2000). Absorption spectra and optical constants of binary and ternary solutions of H_2SO_4, HNO_3, and H_2O in the mid infrared at atmospheric temperatures. *J. Phys. Chem. A* 104, 783–793. doi:10.1021/jp992349i

Burton, M. R., Oppenheimer, O., Horrocks, L. A., and Francis, P. W. (2000). Remote sensing of CO_2 and H_2O emission rates from Masaya volcano, Nicaragua. *Geology* 28, 915–918. doi:10.1130/0091-7613(2000)028<0915:rsocah>2.3.co;2

Burton, M. R., Oppenheimer, C., Horrocks, L. A., and Francis, P. W. (2001). Diurnal changes in volcanic plume chemistry observed by lunar and solar occultation spectroscopy. *Geophys. Res. Lett.* 28, 843–846. doi:10.1029/2000GL008499

Burton, M., Allard, P., Mure, F., and La Spina, A. (2007). Magmatic gas composition reveals the source depth of slug-driven strombolian explosive activity. *Science* 317, 227–230. doi:10.1126/science.1141900

Butz, A., Dinger, A. S., Bobrowski, N., Kostinek, J., Fieber, L., Fischerkeller, C., et al. (2017). Remote sensing of volcanic CO_2, HF, HCl, SO_2, and BrO in the downwind plume of Mt. Etna. *Atmos. Meas. Tech.* 10, 1–14. doi:10.5194/amt-10-1-2017

Campion, R., Delgado-Granados, H., and Mori, T. (2014). Image-based correction of the light dilution effect for SO_2 camera measurements. *J. Volcanol. Geotherm. Res.* 300, 48–57. doi:10.1016/j.jvolgeores.2015.01.004

Carboni, E., Grainger, R. G., Mather, T. A., Pyle, D. M., Thomas, G. E., Siddans, R., et al. (2016). The vertical distribution of volcanic SO_2 plumes measured by IASI. *Atmos. Chem. Phys.* 16, 4343–4367. doi:10.5194/acp-16-4343-2016

Carey, S., and Bursik, M. (2015). "Volcanic plumes," in *The encyclopedia of volcanoes* (Elsevier), 571–585. doi:10.1016/B978-0-12-385938-9.00032-8

Carlsen, H. K., Ilyinskaya, E., Baxter, P. J., Schmidt, A., Thorsteinsson, T., Pfeffer, M. A., et al. (2021). Increased respiratory morbidity associated with exposure to a mature volcanic plume from a large Icelandic fissure eruption. *Nat. Commun.* 12, 2161. doi:10.1038/s41467-021-22432-5

Carn, S. A., Krueger, A. J., Krotkov, N. A., Yang, K., and Evans, K. (2009). Tracking volcanic sulfur dioxide clouds for aviation hazard mitigation. *Nat. Hazards* 51, 325–343. doi:10.1007/s11069-008-9228-4

Clarisse, L., Hurtmans, D., Clerbaux, C., Hadji-Lazaro, J., Ngadi, Y., and Coheur, P.-F. (2012). Retrieval of sulphur dioxide from the infrared atmospheric sounding interferometer (IASI). *Atmos. Meas. Tech.* 5, 581–594. doi:10.5194/amt-5-581-2012

Deguine, A., Petitprez, D., Clarisse, L., Guðmundsson, S., Outes, V., Villarosa, G., et al. (2020). Complex refractive index of volcanic ash aerosol in the infrared, visible, and ultraviolet. *Appl. Opt.* 59, 884–895. doi:10.1364/AO.59.000884

Delmelle, P. (2003). Environmental impacts of tropospheric volcanic gas plumes. *Geol. Soc. Lond. Spec. Publ.* 213, 381–399. doi:10.1144/GSL.SP.2003.213.01.23

Dudhia, A. (2017). The reference forward model (RFM). *J. Quantitative Spectrosc. Radiat. Transf.* 186, 243–253. doi:10.1016/j.jqsrt.2016.06.018

Duffell, H., Oppenheimer, C., and Burton, M. (2001). Volcanic gas emission rates measured by solar occultation spectroscopy. *Geophys. Res. Lett.* 28, 3131–3134. doi:10.1029/2000GL012425

Eatough, D. J., Caka, F. M., and Farber, R. J. (1994). The conversion of SO2 to sulfate in the atmosphere. *Israel J. Chem.* 34, 301–314. doi:10.1002/ijch.199400034

Ebmeier, S. K., Sayer, A. M., Grainger, R. G., Mather, T. A., and Carboni, E. (2014). Systematic satellite observations of the impact of aerosols from passive volcanic degassing on local cloud properties. *Atmos. Chem. Phys.* 14, 10601–10618. doi:10.5194/acp-14-10601-2014

Edmonds, M., and Gerlach, T. M. (2007). Vapor segregation and loss in basaltic melts. *Geology* 35, 751–754. doi:10.1130/G23464A.1

Esse, B., Burton, M., Varnam, M., Kazahaya, R., and Salerno, G. (2020). iFit: A simple method for measuring volcanic SO_2 without a measured Fraunhofer reference spectrum. *J. Volcanol. Geotherm. Res.* 163, 107000. doi:10.1016/j.jvolgeores.2020.107000

Francis, P., Burton, M. R., and Oppenheimer, C. (1998). Remote measurements of volcanic gas compositions by solar occultation spectroscopy. *Nature* 396, 567–570. doi:10.1038/25115

Freret-Lorgeril, V., Donnadieu, F., Eychenne, J., Soriaux, C., and Latchimy, T. (2019). *In situ* terminal settling velocity measurements at Stromboli volcano: Input from physical characterization of ash. *J. Volcanol. Geotherm. Res.* 374, 62–79. doi:10.1016/j.jvolgeores.2019.02.005

Freret-Lorgeril, V., Gilchrist, J., Donnadieu, F., Jellinek, A. M., Delanoë, J., Latchimy, T., et al. (2020). Ash sedimentation by fingering and sediment thermals from wind-affected volcanic plumes. *Earth Planet. Sci. Lett.* 534, 116072. doi:10.1016/j.epsl.2020.116072

Goff, F., Love, S. P., Warren, R. G., Counce, D., Obenholzner, J., Siebe, C., et al. (2001). Passive infrared remote sensing evidence for large, intermittent CO2 emissions at Popocatépetl volcano, Mexico. *Chem. Geol.* 177, 133–156. doi:10.1016/S0009-2541(00)00387-9

Gudmundsson, G. (2011). Respiratory health effects of volcanic ash with special reference to Iceland. A review: Respiratory health effects of volcanic ash. *Clin. Respir. J.* 5, 2–9. doi:10.1111/j.1752-699X.2010.00231.x

Guermazi, H., Sellitto, P., Cuesta, J., Eremenko, M., Lachatre, M., Mailler, S., et al. (2021). Quantitative retrieval of volcanic sulphate aerosols from IASI observations. *Remote Sens.* 13, 1808. doi:10.3390/rs13091808

Henderson, M. J. B., Horgan, B. H. N., Rowe, M. C., Wall, K. T., and Scudder, N. A. (2021). Determining the volcanic eruption style of tephra deposits from infrared spectroscopy. *Earth Space Sci.* 8. doi:10.1029/2019EA001013

Horrocks, L., Burton, M., Francis, P., and Oppenheimer, C. (1999). Stable gas plume composition measured by OP-FTIR spectroscopy at Masaya Volcano, Nicaragua, 1998-1999. *Geophys. Res. Lett.* 26, 3497–3500. doi:10.1029/1999GL008383

Horrocks, L. A., Oppenheimer, C., Burton, M. R., Duffell, H. J., Davies, N. M., Martin, N. A., et al. (2001). Open-path Fourier transform infrared spectroscopy of SO_2: An empirical error budget analysis, with implications for volcano monitoring. *J. Geophys. Res.* 106, 27647–27659. doi:10.1029/2001JD000343

Horwell, C. J. (2007). Grain-size analysis of volcanic ash for the rapid assessment of respiratory health hazard. *J. Environ. Monit.* 9, 1107–1115. doi:10.1039/b710583p

Ilyinskaya, E., Schmidt, A., Mather, T. A., Pope, F. D., Witham, C., Baxter, P., et al. (2017). Understanding the environmental impacts of large fissure eruptions: Aerosol and gas emissions from the 2014–2015 Holuhraun eruption (Iceland). *Earth Planet. Sci. Lett.* 472, 309–322. doi:10.1016/j.epsl.2017.05.025

Kern, C., Deutschmann, T., Vogel, L., Wöhrbach, M., Wagner, T., and Platt, U. (2010). Radiative transfer corrections for accurate spectroscopic measurements of volcanic gas emissions. *Bull. Volcanol.* 72, 233–247. doi:10.1007/s00445-009-0313-7

Kern, C., Deutschmann, T., Werner, C., Sutton, A. J., Elias, T., and Kelly, P. J. (2012). Improving the accuracy of SO_2 column densities and emission rates obtained from upward-looking UV-spectroscopic measurements of volcanic plumes by taking realistic radiative transfer into account. *J. Geophys. Res. Atmos.* 117, D20302. doi:10.1029/2012JD017936

Kern, C., Werner, C., Elias, T., Sutton, A. J., and Lübcke, P. (2013). Applying UV cameras for SO_2 detection to distant or optically thick volcanic plumes. *J. Volcanol. Geotherm. Res.* 262, 80–89. doi:10.1016/j.jvolgeores.2013.06.009

Kern, C., Aiuppa, A., and de Moor, J. M. (2022). A golden era for volcanic gas geochemistry? *Bull. Volcanol.* 84, 43. doi:10.1007/s00445-022-01556-6

La Spina, A., Burton, M., and Salerno, G. G. (2010). Unravelling the processes controlling gas emissions from the central and northeast craters of Mt. Etna. *J. Volcanol. Geotherm. Res.* 198, 368–376. doi:10.1016/j.jvolgeores.2010.09.018

La Spina, A., Burton, M. R., Harig, R., Mure, F., Rusch, P., Jordan, M., et al. (2013). New insights into volcanic processes at Stromboli from Cerberus, a remote-controlled open-path FTIR scanner system. *J. Volcanol. Geotherm. Res.* 249, 66–76. doi:10.1016/j.jvolgeores.2012.09.004

La Spina, A., Burton, M., Allard, P., Alparone, S., and Murï¿½, F. (2015). Open-path FTIR spectroscopy of magma degassing processes during eight lava fountains on Mount Etna. *Earth Planet. Sci. Lett.* 413, 123–134. doi:10.1016/j.epsl.2014.12.038

Love, S. P., Goff, F., Counce, D., Siebe, C., and Delgado-Granados, H. (1998). Passive infrared spectroscopy of the eruption plume at Popocatepetl volcano, Mexico. *Nature* 396, 563–567. doi:10.1038/25109

Love, S. P., Goff, F., Schmidt, S. C., Counce, D., Pettit, D., Christenson, B. W., et al. (2000). "Passive infrared spectroscopic remote sensing of volcanic gases: Ground-based studies at White Island and Ruapehu, New Zealand, and Popocatépetl, Mexico," in *Geophysical monograph series*. Editors P. J. Mouginis-Mark, J. A. Crisp, and J. H. Fink (Washington, D. C.: American Geophysical Union), 117–138. doi:10.1029/GM116p0117

Lund Myhre, C. E., Christensen, D. H., Nicolaisen, F. M., and Nielsen, C. J. (2003). Spectroscopic study of aqueous H_2SO_4 at different temperatures and compositions: Variations in dissociation and optical properties. *J. Phys. Chem. A* 107, 1979–1991. doi:10.1021/jp026576n

Lyon, R. J. P. (1965). Analysis of rocks by spectral infrared emission (8 to 25 microns). *Econ. Geol.* 60, 715–736. doi:10.2113/gsecongeo.60.4.715

Mather, T. A., Allen, A. G., Oppenheimer, C., Pyle, D. M., and McGonigle, A. J. S. (2003a). Size-Resolved characterisation of soluble ions in the particles in the tropospheric plume of Masaya volcano, Nicaragua: Origins and plume processing. *J. Atmos. Chem.* 46, 207–237. doi:10.1023/a:1026327502060

Mather, T. A., Pyle, D. M., and Oppenheimer, C. (2003b). "Tropospheric volcanic aerosol," in *Geophysical monograph series*. Editors A. Robock and C. Oppenheimer (Washington, D. C.: American Geophysical Union), 189–212. doi:10.1029/139GM12

Mather, T. A., Oppenheimer, C., Allen, A. G., and McGonigle, A. J. S. (2004a). Aerosol chemistry of emissions from three contrasting volcanoes in Italy. *Atmos. Environ.* 38, 5637–5649. doi:10.1016/j.atmosenv.2004.06.017

Mather, T. A., Tsanev, V. I., Pyle, D. M., McGonigle, A. J. S. S., Oppenheimer, C., and Allen, A. G. (2004b). Characterization and evolution of tropospheric plumes from Lascar and Villarrica volcanoes, Chile. *J. Geophys. Research-Atmospheres* 109. doi:10.1029/2004JD004934

Mather, T. A. (2015). Volcanoes and the environment: Lessons for understanding Earth's past and future from studies of present-day volcanic emissions. *J. Volcanol. Geotherm. Res.* 304, 160–179. doi:10.1016/j.jvolgeores.2015.08.016

McGonigle, A. J. S., Delmelle, P., Oppenheimer, C., Tsanev, V. I., Delfosse, T., Williams-Jones, G., et al. (2004). SO_2 depletion in tropospheric volcanic plumes: Volcanic SO_2 depletion. *Geophys. Res. Lett.* 31. doi:10.1029/2004GL019990

Michalski, J. R. (2004). Thermal infrared analysis of weathered granitic rock compositions in the Sacaton Mountains, Arizona: Implications for petrologic classifications from thermal infrared remote-sensing data. *J. Geophys. Res.* 109, E03007–E03015. doi:10.1029/2003JE002197

Mori, T., and Notsu, K. (1997). Remote CO, COS, CO_2, SO_2, HCl detection and temperature estimation of volcanic gas. *Geophys. Res. Lett.* 24, 2047–2050. doi:10.1029/97GL52058

Mori, T., Notsu, K., Tohjima, Y., Wakita, H., Nuccio, P. M., and Italiano, F. (1995). Remote detection of fumarolic gas chemistry at Vulcano, Italy, using an FT-IR spectral radiometer. *Earth Planet. Sci. Lett.* 134, 219–224. doi:10.1016/0012-821X(95)00119-W

Notsu, K., Mori, T., Igarashi, G., Tohjima, Y., and Wakita, H. (1993). Infrared spectral radiometer: A new tool for remote measurement of SO_2 of volcanic gas. *Geochem. J.* 27, 361–366. doi:10.2343/geochemj.27.361

Oppenheimer, C., Francis, P., Burton, M., Maciejewski, A. J. H., and Boardman, L. (1998a). Remote measurement of volcanic gases by Fourier transform infrared spectroscopy. *Appl. Phys. B Lasers Opt.* 67, 505–515. doi:10.1007/s003400050536

Oppenheimer, C., Francis, P., and Stix, J. (1998b). Depletion rates of sulfur dioxide in tropospheric volcanic plumes. *Geophys. Res. Lett.* 25, 2671–2674. doi:10.1029/98GL01988

Patrick, M. R., Harris, A. J. L., Ripepe, M., Dehn, J., Rothery, D. A., and Calvari, S. (2007). Strombolian explosive styles and source conditions: Insights from thermal (FLIR) video. *Bull. Volcanol.* 69, 769–784. doi:10.1007/s00445-006-0107-0

Pfeffer, M., Bergsson, B., Barsotti, S., Stefánsdóttir, G., Galle, B., Arellano, S., et al. (2018). Ground-based measurements of the 2014–2015 holuhraun volcanic cloud (Iceland). *Geosciences* 8, 29. doi:10.3390/geosciences8010029

Pianezze, J., Tulet, P., Foucart, B., Leriche, M., Liuzzo, M., Salerno, G., et al. (2019). Volcanic plume aging during passive degassing and low eruptive events of Etna and Stromboli volcanoes. *J. Geophys. Res. Atmos.* 124, 11389–11405. doi:10.1029/2019JD031122

Piontek, D., Hornby, A. J., Voigt, C., Bugliaro, L., and Gasteiger, J. (2021). Determination of complex refractive indices and optical properties of volcanic ashes in the thermal infrared based on generic petrological compositions. *J. Volcanol. Geotherm. Res.* 411, 107174. doi:10.1016/j.jvolgeores.2021.107174

Prata, G. S., Ventress, L. J., Carboni, E., Mather, T. A., Grainger, R. G., and Pyle, D. M. (2019). A new parameterization of volcanic ash complex refractive index based on NBO/T and SiO_2 content. *J. Geophys. Res. Atmos.* 124, 1779–1797. doi:10.1029/2018JD028679

Ramsey, M. S., and Christensen, P. R. (1998). Mineral abundance determination Quantitative deconvolution of thermal emission spectra. *J. Geophys. Res.* 103, 577–596. doi:10.1029/97JB02784

Reed, B. E., Peters, D. M., McPheat, R., and Grainger, R. G. (2018). The complex refractive index of volcanic ash aerosol retrieved from spectral mass extinction. *J. Geophys. Res. Atmos.* 123, 1339–1350. doi:10.1002/2017JD027362

Roberts, T. J., Vignelles, D., Liuzzo, M., Giudice, G., Aiuppa, A., Coltelli, M., et al. (2018). The primary volcanic aerosol emission from Mt Etna: Size-resolved particles with SO_2 and role in plume reactive halogen chemistry. *Geochimica Cosmochimica Acta* 222, 74–93. doi:10.1016/j.gca.2017.09.040

Rodríguez, L. A., Watson, I. M., Edmonds, M., Ryan, G., Hards, V., Oppenheimer, C. M. M., et al. (2008). SO_2 loss rates in the plume emitted by Soufrière Hills volcano, Montserrat. *J. Volcanol. Geotherm. Res.* 173, 135–147. doi:10.1016/j.jvolgeores.2008.01.003

Rogers, A. D., and Nekvasil, H. (2015). Feldspathic rocks on mars: Compositional constraints from infrared spectroscopy and possible formation mechanisms: Feldspathic rocks on mars: Constraints. *Geophys. Res. Lett.* 42, 2619–2626. doi:10.1002/2015GL063501

Rothman, L. S., Gordon, I. E., Barbe, A., Benner, D. C., Bernath, P. F., Birk, M., et al. (2009). The HITRAN 2008 molecular spectroscopic database. *J. Quantitative Spectrosc. Radiat. Transf.* 110, 533–572. doi:10.1016/j.jqsrt.2009.02.013

Rufus, J., Stark, G., Smith, P. L., Pickering, J. C., and Thorne, A. P. (2003). High-resolution photoabsorption cross section measurements of SO_2, 2: 220 to 325 nm at 295 K: SO_2 photoabSOrption cross sections. *J. Geophys. Res.* 108. doi:10.1029/2002JE001931

Sahyoun, M., Freney, E., Brito, J., Duplissy, J., Gouhier, M., Colomb, A., et al. (2019). Evidence of new particle formation within Etna and Stromboli volcanic plumes and its parameterization from airborne *in situ* measurements. *J. Geophys. Res. Atmos.* 124, 5650–5668. doi:10.1029/2018JD028882

Schmidt, A., Witham, C. S., Theys, N., Richards, N. A. D., Thordarson, T., Szpek, K., et al. (2014). Assessing hazards to aviation from sulfur dioxide emitted by explosive Icelandic eruptions. *J. Geophys. Res. Atmos.* 119, 14180–14196. doi:10.1002/2014JD022070

Sellitto, P., Guermazi, H., Carboni, E., Siddans, R., and Burton, M. (2019). Unified observation co-existing volcanic sulphur dioxide and sulphate aerosols using ground-based Fourier transform infrared spectroscopy. *Atmos. Meas. Tech. Discuss.*, 1–12. doi:10.5194/amt-2019-186

Sellitto, P., Salerno, G., Spina, A. L., Caltabiano, T., Boselli, A., Leto, G., et al. (2020). Small-scale volcanic aerosols variability, processes and direct radiative impact at Mount Etna during the EPL-RADIO campaigns. *Sci. Rep.* 1, 15224–15313. doi:10.1038/s41598-020-71635-1

Sellitto, P., Salerno, G., Doussin, J.-F., Triquet, S., Dulac, F., and Desboeufs, K. (2021). Photometric observations of aerosol optical properties and emission flux rates of Stromboli volcano plume during the PEACETIME campaign. *Remote Sens.* 13, 4016. doi:10.3390/rs13194016

Sellitto, P., and Legras, B. (2016). Sensitivity of thermal infrared nadir instruments to the chemical and microphysical properties of UTLS secondary sulfate aerosols. *Atmos. Meas. Tech.* 9, 115–132. doi:10.5194/amt-9-115-2016

Serdyuchenko, A., Gorshelev, V., Weber, M., Chehade, W., and Burrows, J. P. (2014). High spectral resolution ozone absorption cross-sections – Part 2: Temperature dependence. *Atmos. Meas. Tech.* 7, 625–636. doi:10.5194/amt-7-625-2014

Siegel, A. F. (1982). Robust regression using repeated medians. *Biometrika* 69, 242–244. doi:10.1093/biomet/69.1.242

Sigmundsson, F., Hreinsdóttir, S., Hooper, A., Árnadóttir, T., Pedersen, R., Roberts, M. J., et al. (2010). Intrusion triggering of the 2010 Eyjafjallajökull explosive eruption. *Nature* 468, 426–430. doi:10.1038/nature09558

Stremme, W., Krueger, A., Harig, R., and Grutter, M. (2012). Volcanic SO_2 and SiF_4 visualization using 2-D thermal emission spectroscopy Part 1: Slant-columns and their ratios. *Atmos. Meas. Tech.* 5, 275–288. doi:10.5194/amt-5-275-2012

Sumlin, B. J., Heinson, W. R., and Chakrabarty, R. K. (2018). Retrieving the aerosol complex refractive index using PyMieScatt: A Mie computational package

with visualization capabilities. *J. Quantitative Spectrosc. Radiat. Transf.* 205, 127–134. doi:10.1016/j.jqsrt.2017.10.012

Tang, Y., Tong, D. Q., Yang, K., Lee, P., Baker, B., Crawford, A., et al. (2020). Air quality impacts of the 2018 Mt. Kilauea volcano eruption in Hawaii: A regional chemical transport model study with satellite-constrained emissions. *Atmos. Environ.* 237, 117648. doi:10.1016/j.atmosenv.2020.117648

Taquet, N., Meza Hernández, I., Stremme, W., Bezanilla, A., Grutter, M., Campion, R., et al. (2017). Continuous measurements of SiF_4 and SO_2 by thermal emission spectroscopy: Insight from a 6-month survey at the Popocatépetl volcano. *J. Volcanol. Geotherm. Res.* 341, 255–268. doi:10.1016/j.jvolgeores.2017.05.009

Taquet, N., Stremme, W., Grutter, M., Baylón, J., Bezanilla, A., Schiavo, B., et al. (2019). Variability in the gas composition of the popocatépetl volcanic plume. *Front. Earth Sci.* 7, 1–14. doi:10.3389/feart.2019.00114

Vanderkluysen, L. L., Burton, M. R., Clarke, A. B., Hartnett, H. E., and Smekens, J. F. F. (2014). Composition and flux of explosive gas release at LUSI mud volcano (East Java, Indonesia). *Geochem. Geophys. Geosystems* 15, 2932–2946. doi:10.1002/2014GC005275

Varnam, M., Burton, M., Esse, B., Kazahaya, R., Salerno, G., Caltabiano, T., et al. (2020). Quantifying light dilution in ultraviolet spectroscopic measurements of volcanic SO_2 using dual-band modeling. *Front. Earth Sci.* 8, 1–11. doi:10.3389/feart.2020.528753

Whitby, K. T. (1978). "The physical characteristics of sulfur aerosols," in *Sulfur in the atmosphere* (Elsevier), 135–159. doi:10.1016/B978-0-08-022932-4.50018-5

Wilson, G., Wilson, T. M., Deligne, N. I., and Cole, J. W. (2014). Volcanic hazard impacts to critical infrastructure: A review. *J. Volcanol. Geotherm. Res.* 286, 148–182. doi:10.1016/j.jvolgeores.2014.08.030

frontiers | Frontiers in Earth Science

TYPE Original Research
PUBLISHED 07 February 2023
DOI 10.3389/feart.2023.1040199

OPEN ACCESS

EDITED BY
Georg Rümpker,
Goethe University Frankfurt, Germany

REVIEWED BY
Karoly Nemeth,
Institute of Earth Physics and Space Sciences, Hungary
Johan Varekamp,
Wesleyan University, United States

*CORRESPONDENCE
Robin Campion,
robin@geofisica.unam.mx

SPECIALTY SECTION
This article was submitted to Volcanology, a section of the journal Frontiers in Earth Science

RECEIVED 09 September 2022
ACCEPTED 20 January 2023
PUBLISHED 07 February 2023

CITATION
Campion R and Coppola D (2023), Classification of lava lakes based on their heat and SO_2 emission: Implications for their formation and feeding processes. *Front. Earth Sci.* 11:1040199. doi: 10.3389/feart.2023.1040199

Classification of lava lakes based on their heat and SO_2 emission: Implications for their formation and feeding processes

Robin Campion[1]* and Diego Coppola[2]

[1]Instituto de Geofísica, Universidad Nacional Autónoma de México, México City, Mexico, [2]Dipartimento di Scienze della Terra, Universitá di Torino, Turin, Italy

Lava lakes are a fascinating but somewhat rare form of volcanic activity. Lava lakes are large free surfaces of hot lava that discharge continuously, and almost quietly, heat and volcanic gases into the atmosphere. They are thought to be fed by convection processes that bring hot gas-rich magma to the surface and back downward, after its cooling and outgassing. A lava lake represents a latent threat for the populations living nearby, as it can drain suddenly through fissures and generate dangerously fast lava flows. We present time series of Volcanic Radiative Power (VRP) and SO_2 flux measured from satellites (MODIS and OMI, respectively) from several lava lakes on Earth (Erta Ale, Nyiragongo, Kilauea, Nyamuragira, Ambrym, and Villarrica). Based on long-term trends plotted in a simple VRP *versus* SO_2 flux diagram, we propose a new classification of lava lakes in three categories: small lakes, large foam-dominated lakes, and large melt-dominated lakes. Small lakes show a long-term correlation between VRP and SO_2 emissions, while large lakes seem to show an anticorrelation between VRP and SO_2 emissions. This at-first-glance surprising anticorrelation probably results from the limited heat transport capacity of the gas-rich foam that initially feeds the convection of these lakes. We also show that the formation of three large lava lakes in the last 2 decades at the rift and hotspot volcanoes followed a similar trend of transitioning, in a few months, from foam-dominated to melt-dominated. We deduce that lava lake formation at these volcanoes follows a common sequence of processes that includes the formation of a large shallow magma reservoir and its outgassing through a newly formed pit crater.

KEYWORDS

lava lake, SO_2 flux, Volcanic Radiative Power, magmatic convection, magmatic foam, satellite remote sensing, OMI, MODIS

1 Introduction

Lava lakes can be defined as large free surfaces of magma in contact with the atmosphere, discharging quietly but continuously considerable amounts of heat and volcanic gases into it. This is rather an uncommon form of volcanic activity on Earth. At the time of writing, only six or seven volcanoes are known to host a lava lake (Figure 1). These are Erta Ale (Ethiopia, Le Guern et al., 1979), Masaya (Nicaragua, Aiuppa et al., 2018), Nyamuragira (Democratic Republic of Congo, Campion, 2014; Coppola et al., 2016a), Mt. Erebus (Antarctica, Sweeney et al., 2008), Villarrica (Chile, Witter et al., 2004; Moussallam et al., 2016), and possibly Mt. Michael (South Sandwich Islands, inferred from satellite data by Gray et al. (2019), but not yet observed directly). In the past, notorious permanent lava lakes have been observed at Kilauea (Hawaii Island) and Mt. Nyiragongo (Democratic Republic of Congo). Although being amongst the quietest forms of volcanic activity, a lava lake represents a latent volcanic hazard. Indeed, historical experience has taught us that they can

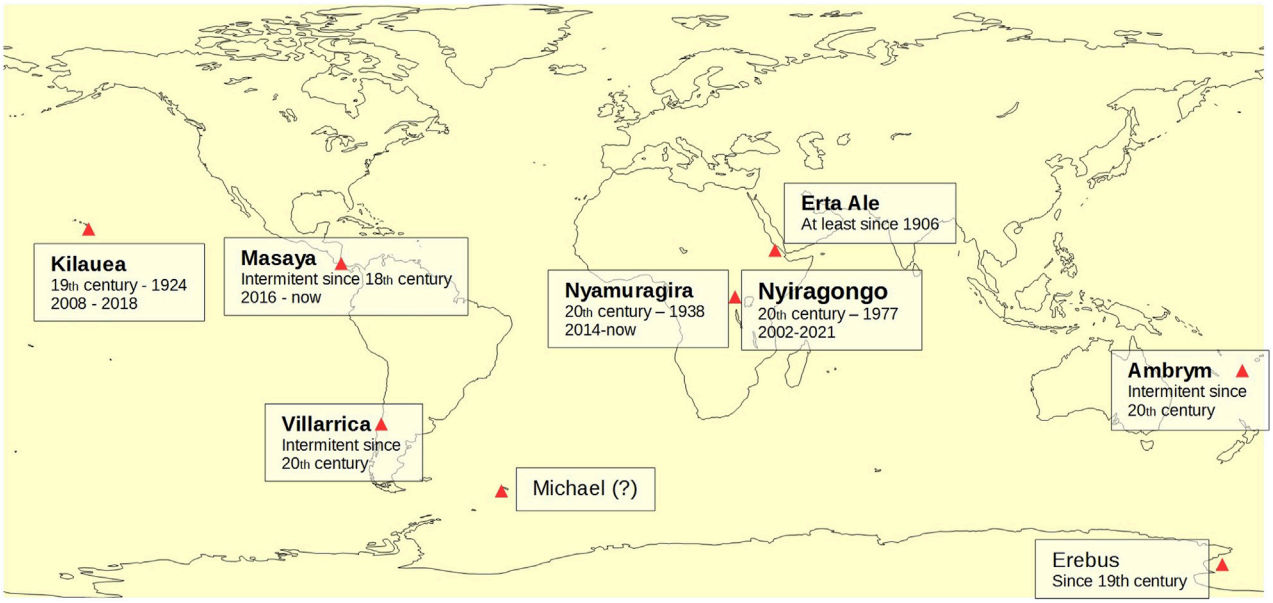

FIGURE 1
Location of the volcanoes that are hosting or have recently hosted a lava lake. Volcanoes in bold are discussed in this study. The periods of existence of each lava lake are mentioned when known.

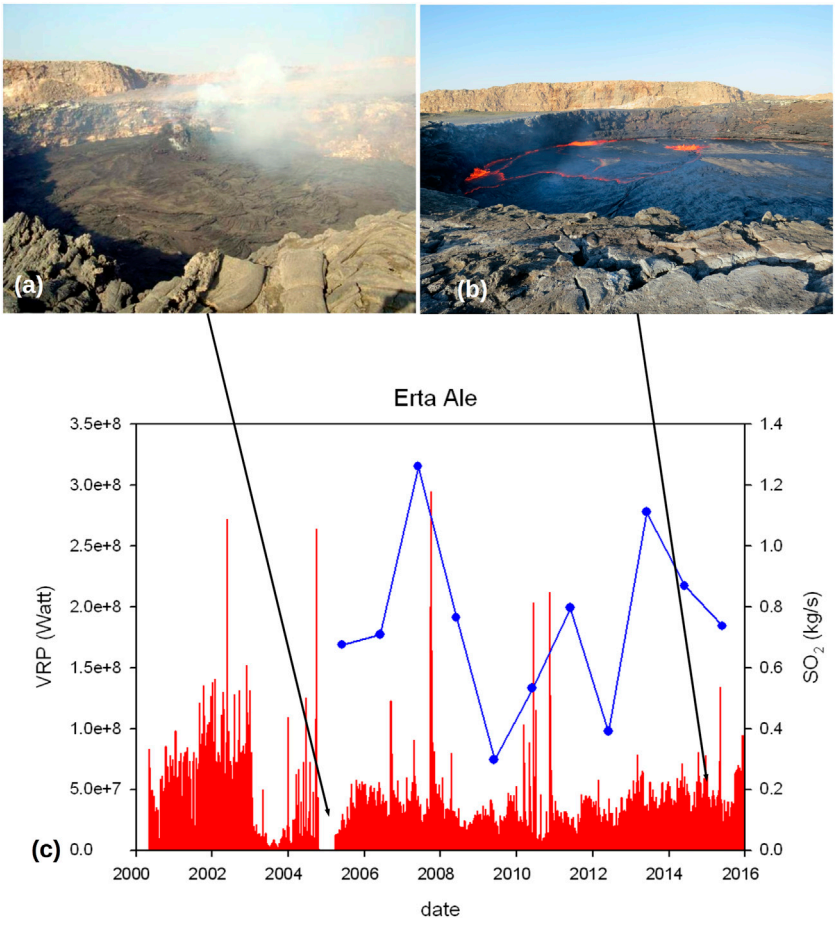

FIGURE 2
(A) Crust-covered lava lake in the south pit of Erta Ale in December 2004. Degassing was focused on a group of hornitos (photo: J.M. Bardintzeff). **(B)** In February 2015, the lava lake had regained its free surface and had a stable size (~diameter 50 m) and level (Photo P. Marcel). **(C)** Time series of the yearly-averaged SO_2 flux from Carn et al. (2017) and daily Volcanic Radiative Power from the lava lake of Erta Ale Volcano.

drain suddenly through fissures cutting the volcanic edifices that host them, unleashing fast-flowing lava flows on their outer slopes. Many long-lived lava lakes have disappeared in this way, after several years to decades of activity, such as those of Nyiragongo in 1977 (Tazieff, 1977) and 2021 (Smittarello et al., 2022), Kilauea in 2018 (Patrick et al., 2020), and Ambrym in 2018 (Shreve et al., 2019).

Lava lakes have also played a historically important role in the development of volcanology because their long-lasting and safely accessible activity allowed the planning and deployment of the first multidisciplinary measurement campaigns on active volcanoes (e.g., Jaggar, 1917; Tazieff, 1966). It soon became evident to these pioneers that the tremendous heat loss by radiation needed to be compensated by a vigorous convection process bringing juvenile hot and volatile-rich magma to the surface and returning it at depth after cooling and degassing. This concept has since then been modeled and refined by various authors (Kazahaya et al., 1994; Stevenson and Blake, 1998; Harris et al., 1999; Witham et al., 2006; Palma et al., 2011). Bouche et al. (2010) proposed an alternative theory to the magmatic convection model that the heat transfer was caused by gas bubbles dragging the magma upward in their wake. Multiparametric observations of the activity of several lava lakes suggest that gas flux, magma viscosity, and lake size exert major controls on its convection dynamics (Moussallam et al., 2016; Lev et al., 2019). In a recent review, Lev et al. (2019) defined two categories of lava lakes based on the velocity field of their surface currents and their percentage of crust-covered surface: *Chaotic lakes* are stirred by fast (>1 m/s) and turbulent currents and incessant bubble bursting, which maintain their surface mostly crust-free and incandescent, while the surface of *organized lakes* is covered by a plastic to semi-rigid cooling crust divided in plates that moves in a slower (a few centimeters per second) and more coherent way. Lev et al. (2019) reported a rather good correlation between the surface velocity of the convection currents and the ratio of gas flux emitted by the lake to its surface area. Although these studies are interesting to characterize the activity of a lava lake at a certain time, they paid little attention to the changes of a given lava lake from one type to another and their significance in how lava lakes form and are fed.

In this work, we present time-resolved data sets of SO_2 flux and thermal power radiated from the lava lakes worldwide. We propose a new classification based on a simple diagram of Volcanic Radiative Power (VRP) *versus* SO_2 flux, which can be obtained purely from the remote sensing data. We identify, based on this diagram, families of lava lakes and a common trend associated with the formation and maturation of the three new lava lakes that have appeared over the last 2 decades. We interpret these trends in terms of the styles of magma supply to the lakes and propose a model of lava lake formation and evolution at the rifts and hotspot volcanoes.

2 Methods

2.1 OMI measurements of SO_2 fluxes

Since we are interested in long-term trends, the SO_2 flux measurements presented here are the monthly average values. Campion (2014) showed that a tight linear correlation exists between the monthly averaged SO_2 mass around the volcano and the monthly average of the SO_2 fluxes calculated on a daily basis over the same month using the traverse method. The R^2 correlation coefficient of these correlations is usually superior to 0.8, and their slope coefficient is specific for each volcano, depending on the plume transport and atmospheric conditions. The SO_2 fluxes presented in this study were calculated from the monthly averaged SO_2 mass after calibrating the mass to flux relation for each volcano over a period of several months of fluctuating SO_2 flux (see calibration details for each volcano in Supplementary Material). When the SO_2 emissions are too small to cause a monthly SO_2 anomaly that stands consistently out of the sensor noise, we average the images over a year and calibrate with the flux data of Carn et al. (2017). We used the literature values in the cases where no OMI data were available (Nyiragongo during 2002 and 2003)

2.2 MODIS measurements of Volcanic Radiative Power

In this work, we used the MODIS data processed by the MIROVA algorithm (Coppola et al., 2016b; https://www.mirovaweb.it/). This system processes the infrared images at 1 km of resolution acquired daily by the two MODIS sensors on board the polar satellites Terra and Aqua (EOS-NASA missions). The algorithm is built to detect and locate sub-pixel thermal anomalies sourced by the various types of high-temperature volcanic activity, including lava lakes (Coppola et al., 2016a). Once a thermal anomaly is detected the associated VRP is calculated by using the "MIR method" (Wooster et al., 2003), an approach based on the analysis of the mid-infrared (MIR) radiance in excess to the background (see Coppola et al., 2016a for details). The VRP is calculated in Watts (W) and represents a combined measurement of the area of the volcanic emitter (i.e., the lava lake area) and its effective radiating temperature. The MODIS MIR band (Band 21 or 22) is centered at 3,959 μm, with a bandwidth ranging from 3,929–3,989 μm. The CO_2 absorption band in the MIR is centered at 4.2 μm and does not produce a significant absorption in the MODIS band 21. H_2O does not absorb in that wavelength range either. SO_2 does have an absorption band (ν1 +ν2, stretching from 3.95 μm to 4.07 μm) that overlaps marginally on Band 21, but this is a weak absorption band (HITRAN database, https://hitran.org/lbl/, Rothman et al., 2013). Our calculations show that a 200 m thick plume with 200 ppm should produce a band-integrated absorbance of less than 5%. Band 21 can therefore be considered quite transparent to volcanic gases and the atmosphere. Aerosols are more of a concern. The plumes emanating from lava lakes have a quite variable optical thickness that depends strongly on the atmospheric humidity and mixing pattern (see Matsushima and Shinohara, 2006). Several volcanoes in this study are located in the tropical regions where meteorological clouds or water droplets condensing in the plume often mask, partially or totally, the thermal radiance emitted by the lake. To cope with this variable underestimation factor, the VRP values that are used in this study are the maximum values recorded each month. This approach is based on the assumption that most of the data variability over a month is due to the partial masking of the IR radiation by the clouds or the condensed plume so that the maximum VRP of each month is recorded when the volcano is observed on the optimal viewing conditions. We checked this hypothesis by comparing the variability of the monthly means, weekly maxima and monthly maxima calculated for a time series of VRP from Nyiragongo volcano during year 2010, where field observations showed a very stable activity and constant lake dimension. However, we acknowledge that each lava lake's activity has its own variability and that the abovementioned approach may lead to a slight overestimation of the "true" mean VRP radiated by the lava lake.

3 Results

In this section, we present the time series of monthly averaged SO_2 flux and monthly maximal VRP for several volcanoes that are or have recently been hosting a lava lake, together with a summary of their activity.

3.1 Erta Ale

Erta Ale (Ethiopia, 13.6°N, 40.67°E) is a broad tholeiitic shield volcano located on the spreading axis of the Danakil Rift. Its 0.7 × 1.6 km, elliptical summit caldera hosts two pit craters. The northern pit crater contained a lava lake until the mid-seventies and has been the seat of permanent fumarolic activity and occasional lava spattering or small intra-crater flows since then (Oppenheimer et al., 2004). The smaller southern pit crater has contained a lava lake discovered in 1969 (Le Guern et al., 1979). The southern lava lake of Erta Ale has shown large variations of activity, size, and level, as shown in Figures 2A, B and sometimes overflowed the rim of its pit, feeding lava flows that have covered the caldera floor (e.g., Field et al., 2012). In January 2017, after a year-long gradual increase in the lake level, with several overflowing events, a dike-fed fissure eruption on the southern flank produced copious lava flows for more than 3 years. The eruption covered ~30×10^6 m^2 with >1×10^8 m^3 of lava but it did not lead to the disappearance of the lava lake (Global Volcanism Program, 2018) and did not cause any major collapse in the caldera. Instead, Xu et al. (2020) reported a very wide deflation, extending well beyond the limits of the volcanic edifice, which they attribute to the extraction of magma from a mid-crustal storage area. The long duration of the eruption, the absence of a caldera collapse and the persistence of the lava lake indicate that it was not a draining event, although the lava level rise prior to it and drop during it, indicate some degree of hydraulic connection with the lava lake.

The VRP time series, in Figure 2C, shows a relatively weak thermal emission which shows strong variations, ranging between 10^7 and 1.5×10^8 W. The stronger VRP spikes that exceed the background values correspond to short-lived lake overflows, either inside the pit crater or on the bottom of the caldera. During a small period in 2005, the thermal emission disappeared completely. The SO_2 flux shows small values, between 0.3 and 1.2 kg/s and evolves grossly in a similar way as the VRP. The relatively low values of VRP and SO_2 flux emitted by Erta Ale are in agreement with the previous field studies (Le Guern et al., 1979; Oppenheimer et al., 2004)

3.2 Nyiragongo

Nyiragongo, (1.52°S, 29.25°E, Democratic Republic of Congo) is a foiditic stratovolcano located in the Western Branch of the East African Rift. It has hosted a permanent lava lake that was discovered in 1948 (Tazieff 1974) and disappeared in a catastrophic drainage event in 1977 (Tazieff 1977). Hundreds of people were killed by the fast-moving lava

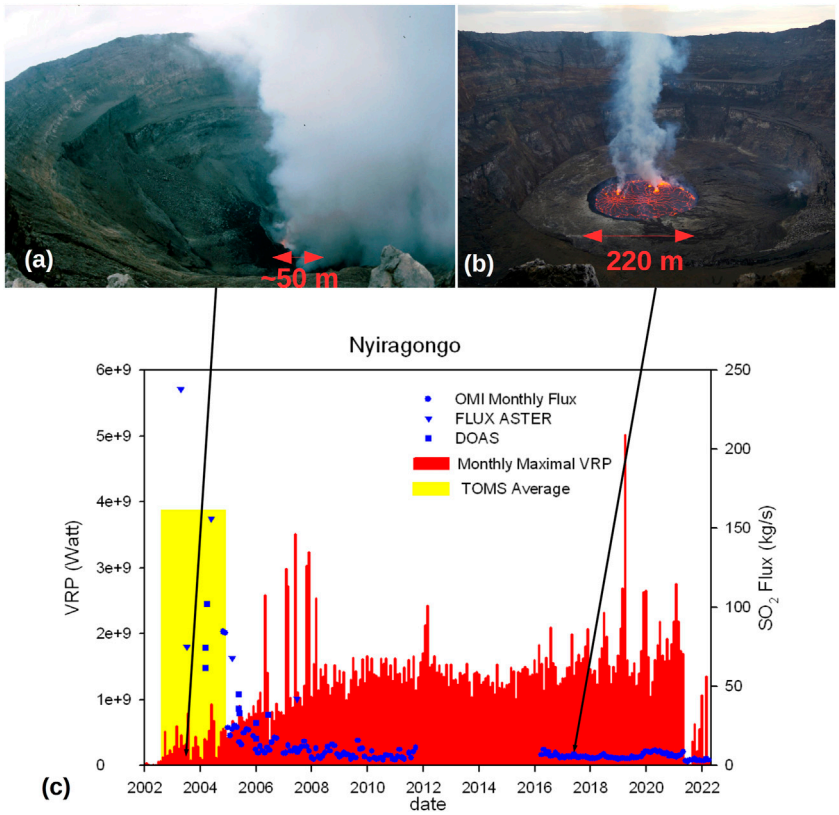

FIGURE 3
(A) Heavily fuming lava lake of Nyiragongo in June 2003 in the early stage of its formation (photo: M. Caillet). **(B)** View of the lava lake from approximately the same point in June 2017. Note the increase in area and level of the lake (photo: P. Marcel). **(C)** Time series of the SO_2 flux from several methods (TOMS data from Carn (2004), monthly averaged OMI data, daily ground-based mobile DOAS, and daily space-based ASTER) and daily Volcanic Radiative Power from the lava lake of Nyiragongo. The data gap in OMI data between 2012 and 2016 correspond to the period where SO_2 emissions from Nyiragongo were dwarfed by those of neighboring Nyamuragira during the formation of its own lava lake.

flows rushing downslope at initial velocities estimated close to 30 m/s. The crater suffered a massive collapse as a result of the drainage of the upper magmatic system. Intra-crater eruptions in 1982 and 1994–1995 gradually refilled the crater but failed to form a permanent lake (Tazieff, 1994). In January 2002, a new lateral eruption triggered by a regional dyking and rifting event drained the upper magmatic system (Komorowski et al., 2002). The fast-flowing lava flows invaded the city of Goma, again killing hundreds of people. In the summer of 2002, a new lava lake gradually formed, and has since then enlarged considerably to a maximum size of ~240 m diameter (Burgi et al., 2014; Valade et al., 2018). Figures 3A, B illustrate the growth and rise of the lava lake between 2003 and 2017. The level of the lake followed a step-wise increasing trend, to reach an altitude comparable to that of 1972–1977, considered as critical for the risk of draining (Burgi et al., 2020). Once again in June 2021, , fissures opened suddenly on the south and southeast flank of the volcano, releasing lava flows that rapidly reached the outskirt of Goma (Global Volcanism Program, 2021; Smittarello et al., 2022). The lava lake drained completely and has not yet reformed at the time of writing. The OMI data, which started in late 2004, do not cover the SO_2 emissions in the first 2 years of the lake existence. In order to fill this gap, the SO_2 flux dataset was completed with the ground-based DOAS measurements of Sawyer et al. (2008), flux measurements from three ASTER (Advanced Spaceborne Thermal Emission and Reflection) images with the band ratio method of Campion et al. (2010), and the data obtained by Carn (2004) with the TOMS (Total Ozone Mapping Spectrometer) spaceborne sensor.

The SO_2 data (Figure 3C) show a 2 year period of extremely high SO_2 emissions (100–250 kg/s) at the beginning of the lava lake's existence, followed by an initially rapid and then slower decrease to reach, by 2009, a relatively stable value of ~10 kg/s that has persisted until the disappearance of the lake. This decrease in the SO_2 flux coincides with a continuous increase of the VRP that materializes the growth of the surface area of the lake and the rise of its level (Burgi et al., 2014). Spikes in the thermal power graph are due to the frequent overflowing events that accompanied the lava lake rise from ~800 m below the crater rim in 2002 to 400 m in 2011 (Burgi et al., 2014). A drastic drop of both SO_2 flux and VRP marks the May 2021 drainage. The activity since then has not completely disappeared but the produced VRP has been weak and discontinuous so far. SO_2 fluxes have stayed much lower than before the lava lake drainage, and two orders of magnitude lower than in 2002 and 2003, when the former lake started to form. We conclude that the activity since 2021 has not yet reformed a permanent lava lake.

3.3 Nyamuragira

Nyamuragira, (Democratic Republic of Congo, 1.408°S, 29.2°E), is a basanitic shield volcano located 15 km northeast from Nyiragongo. It has hosted a lava lake between an uncertain date at the beginning of the 20th century and a massive flank eruption that drained the lake in 1938 (Verhoogen, 1948). From 1948 to 2012, Nyamuragira produced frequent voluminous flank eruptions (e.g., Wadge and Burt, 2011). In 2012, after a major lateral eruption that partially drained the upper magmatic system of the volcano, a new lava lake started to form in a new collapse pit in its summit caldera (Campion 2014; Coppola et al.,

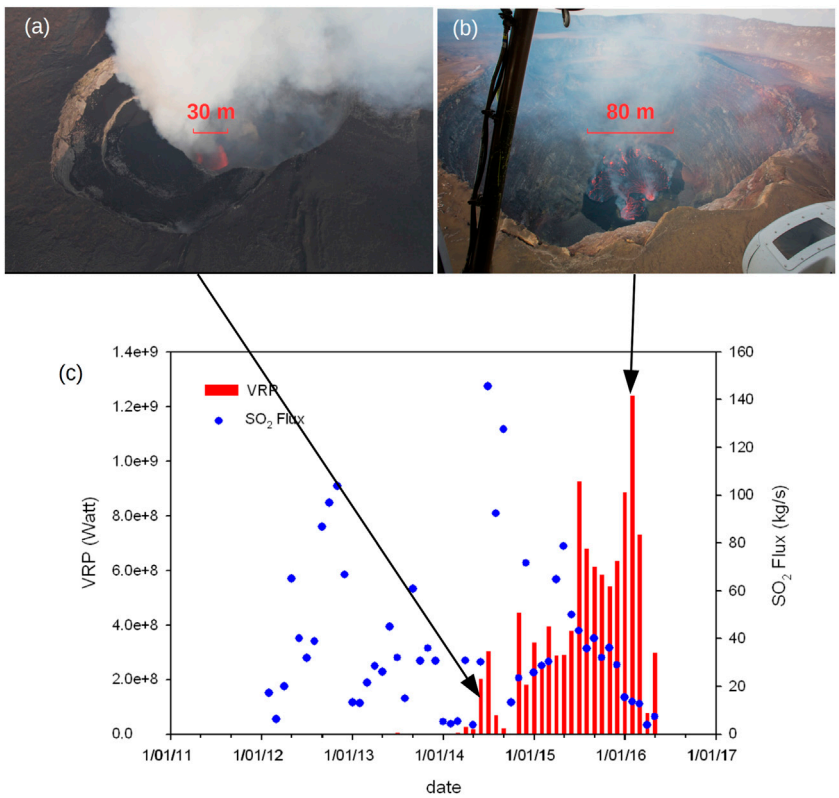

FIGURE 4
(A) Small fountaining lava lake in the newly-formed collapse pit in Nyamuragira's Caldera in June 2014 (photo: D. Tedesco). **(B)** View of the mature lava lake in February 2016. Note the increase in lake size and the notable decrease in plume vigor (photo: G. Kourounis). **(C)** Time series of the SO_2 flux and daily Volcanic Radiative Power from Nyamuragira volcano. Inter-eruptive SO_2 flux before 2012 was close to 0.

2016b). The formation of the lava lake started with a 2.5 years period of intense SO_2 emission during which only very weak radiant heat emissions were infrequently detected (Figure 4C). A fountaining lava lake was observed from the ground for the first time in June 2014 (Figure 4A) and starting in October 2014, the SO_2 flux diminished and the radiant heat emissions increased and became more frequent, as the lava lake had become larger and more stable (Figure 4B). The lava lake has passed through two periods of very reduced activity, from June 2016 to December 2016 and from June 2017 to April 2018, which has shown its surface becoming completely crusted over (Global Volcanism Program, 2017, Global Volcanism Program, 2019), although the emission of SO_2 never stopped. The scarce cloud-free images that ASTER took since the end of these reduced activity periods show weak SO_2 emissions, below or barely above detection limit, which yield an SO_2 flux inferior to 3–5 kg/s, which is dwarfed by the emissions of neighboring Nyiragongo. Burgi et al. (2021) documented a regime of piston-like rising and sinking of the mostly crusted lava lake surface since 2016, possibly differing from the classical convection scheme that is thought to feed lava classical lakes.

3.4 Kilauea

Kilauea (19.421°N, 155.287°W, Big Island of Hawaii, United States of America), is a tholeiitic shield volcano. It hosted a permanent lava lake in the Halemaumau pit crater of its summit caldera until 1924, when it disappeared during a collapse event and explosive eruption, possibly associated with a submarine eruption. Since 1983, Kilauea was in a state of constant effusion of lava through the Puu O'o vent on its East Rift zone. After years of summit inflation, a new lava lake formed gradually, starting in March 2008, in a new pit crater located in the Halemaumau summit caldera (Poland et al., 2010). During its first month of existence, the only surface expressions of the lava lake were the extraordinary degassing and fresh fluidal basaltic glass fragments that were lofted by the gas plume. By the end of 2008, the gas emissions started to decrease and the lake level started to rise, becoming more frequently visible. It often showed rapid filling and draining cycles, or sometimes had the aspect of a cascade. The pit containing the lava lake enlarged over the years by frequent collapses of its rim, resulting in a continuous increase of the lava lake size (Patrick et al., 2013). Figures 5A, B illustrate the spectacular growth of the lake between 2008 and 2017. The large changes of the level of the lava lake were caused by changes in the pressure of the magmatic system of the volcano (Patrick et al., 2015), while the smaller short-term changes were caused by the cycles of foam accumulation below the lake skin and outgassing through spattering (Nadeau et al., 2015). Our measurements with OMI (Figure 5C), confirms extremely high SO_2 flux values during the first year of the existence of the lava lake in Halemaumau, reported by Beirle et al. (2014). The monthly averaged flux peaked at ~300 kg/s, whereas the VRP remained very low. The VRP data show a strong long-term increase that started shortly after the extreme SO_2 emissions of the initial phase had declined, and stabilized around 2016. A short but very prominent spike in VRP appeared in April 2018, without any

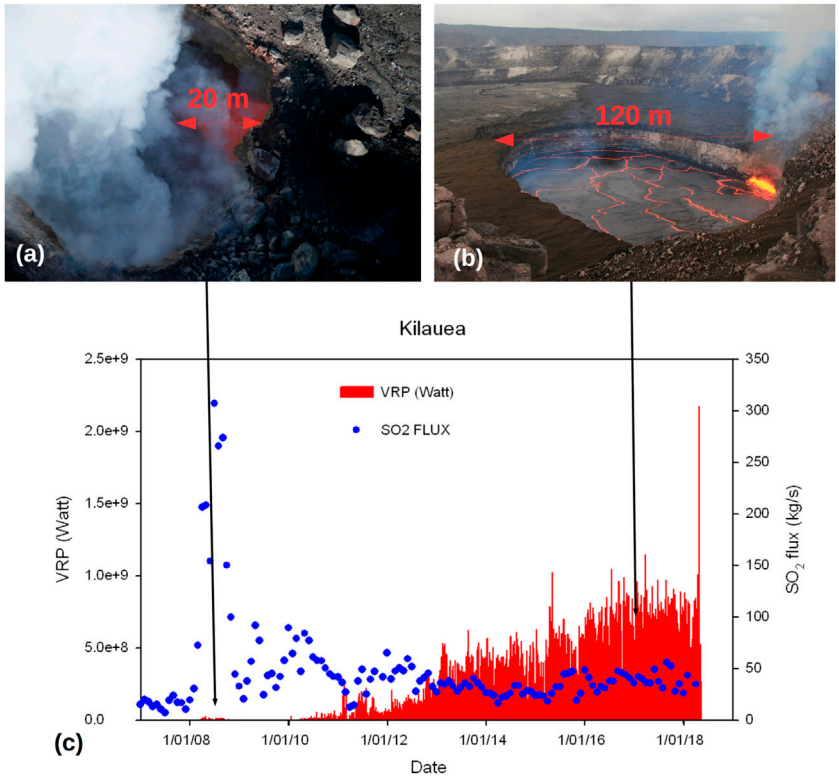

FIGURE 5
(A) Narrow collapse pit in Halemaumau crater containing an embryonic lava lake of Kilauea in May 2008 (photo: USGS). **(B)** View of the mature lava lake in October 2017 (photo: USGS). **(C)** Time series of the SO_2 flux and daily Volcanic Radiative Power from Kilauea volcano. The SO_2 flux of 10–25 kg/s before the formation of the lava lake in Halemaumau crater in 2008 was almost entirely emitted from the long-lasting Pu'u O'o effusive eruption in the East Rift Zone of the volcano.

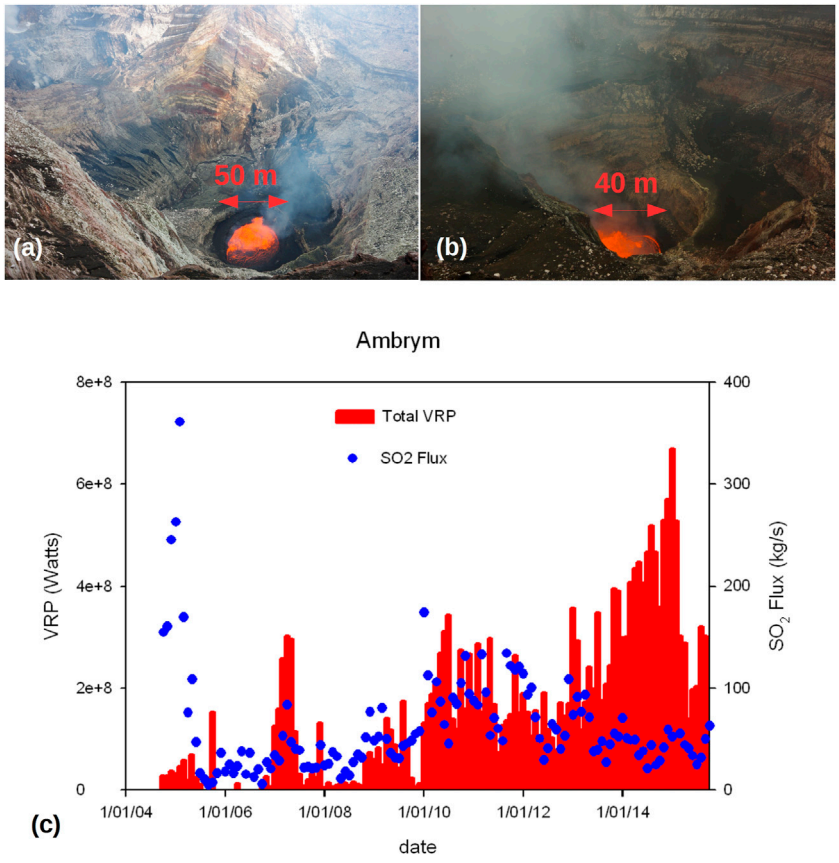

FIGURE 6
Lava lakes of Bembow **(A)** and Marum **(B)** in December 2014. At this time, their areas were approximately identical, but both have suffered large variations of their size and level (photos: C. Normand). **(C)** Time series of the monthly averaged SO_2 flux and monthly maximal Volcanic Radiative Power from the lava lakes of Ambrym Volcano. The generally increasing trend of the VRP that culminated with the partial lake draining event of 2015 was decoupled or even anticorrelated with the SO_2 Flux.

increase in the SO_2 flux. It corresponds to a series of large lake overflows that were later considered as a precursor to the massive May-August 2018 eruption which drained the lava lake and summit magma reservoir into Kilauea's Lower East Rift Zone. Although two effusive eruptions have partly refilled the collapse caldera left by the 2018 draining eruption, they have not reformed a permanent lava lake.

3.5 Ambrym

Ambrym Volcano, (Republic of Vanuatu, 16.25°S, 168.12°E) is a large island arc basaltic to dacitic volcano crowned by a 12 km wide caldera that contains several cones and craters. Two of these cones, Marum and Benbow (Figures 6A, B), have been hosting lava lakes semi-permanently for at least 3 decades (Allard et al., 2016; Coppola et al., 2016c). Short-lived lateral eruptions in the caldera, like those of 1988 and 2015, or in the rift zones, like those of 1914 (Nemeth and Cronin, 2011) and 2018 have partially or completely drained the lava lakes. The degassing of Ambrym's lava lakes was extremely vigorous (e.g., Bani et al., 2009; Allard et al., 2016), maintaining its surface permanently bubbling and agitated, and placing Ambrym as the long-term strongest permanent emitter of Sulfur Dioxide. However, following a major dyking episode and submarine eruption in December 2018, the lava lakes of Ambrym have disappeared (Shreve et al., 2019). The time series of total VRP emitted from Ambrym, combining the heat emission from both Marum and Benbow, shows a waxing and waning trend with a clear increase since 2012, leading to a fissure eruption in February 2015, and a marked decrease immediately after it (Figure 7C). The time series of the SO_2 flux shows very high values, with a prominent peak in 2004–2005, followed by ups and downs usually uncorrelated with the thermal emissions. Interestingly, a general decrease in the SO_2 flux is observed during the 3-year-long period of VRP increase preceding the 2015 eruption (Coppola et al., 2016c).

3.6 Masaya

Masaya volcano (Nicaragua, 11.98°N, 86.16°W), is a large complex of calderas in central Nicaragua formed by powerful basaltic plinian eruptions (Perez and Freundt, 2006). A small shield volcano crowned by a complex of juxtaposed cones and pit-craters has built since the last caldera-forming eruption (Rymer et al., 1998). It has hosted lava lakes episodically since before the Spanish conquest, and also produced several large effusive effusions (Viramonte and Incer-Barquero, 2008). Masaya has been known as a strong permanent emitter of SO_2 and other gases even when no lava lake was visible at the surface (Delmelle et al., 2002). Starting in December 2015, a lava lake appeared in the Santiago crater of Masaya volcano and gradually enlarged until May 2016, when it reached its maximal size

of 40 × 30 m (Figure 6A). Aiuppa et al. (2018) reported the changes in gas flux and composition that accompany its formation, most notably an increase in the SO_2 flux and the CO_2/SO_2 ratio. The low altitude and small size of the Masaya plume make it difficult to measure with OMI on a monthly base. We, therefore, averaged images over 1-year periods to produce the long-term trend of SO_2 fluxes. Figure 7B shows the SO_2 flux and VRP from Masaya. SO_2 emission is permanent but shows a pronounced waxing and waning pattern, a behavior that has characterized the volcanoes since at least the seventies (Delmelle et al., 1999). A strong and rapid increase of both the SO_2 flux and the VRP marked the appearance of the lava lake in 2016, followed by a gradual decrease over the next 4 years. The detection of low thermal anomalies is occasional before the appearance of the lava lake. These anomalies occurred predominantly during the period of moderately high SO_2 flux that prevailed during 2007–2010 and have low VRP values.

3.7 Villarrica

Villarrica volcano (Chile, 39.42°S, 71.93°W), is a medium-sized ice-clad stratovolcano built on two recent calderas associated with the basaltic plinian eruptions and pyroclastic flows (Lohmar et al., 2007). Its narrow summit crater is permanently degassing and is often the seat of mild strombolian and lava lake activity (Palma et al., 2008; Moussallam et al., 2016), but has also produced several stronger eruptions (VEI 2-3, Aiuppa et al., 2019). The daily variability of VRP from Villarrica is the highest among the volcanoes studied in this work. Additionally to the cloud-related variability, it might also result from the frequent bursting of large bubbles at the surface of the lake that eject abundant lava spatters out of the lava lake, and/or rapid cycles of building and collapse of cooled scoria benches that partially covered the lava lake. In the long term, the VRP time series (Figure 8C)

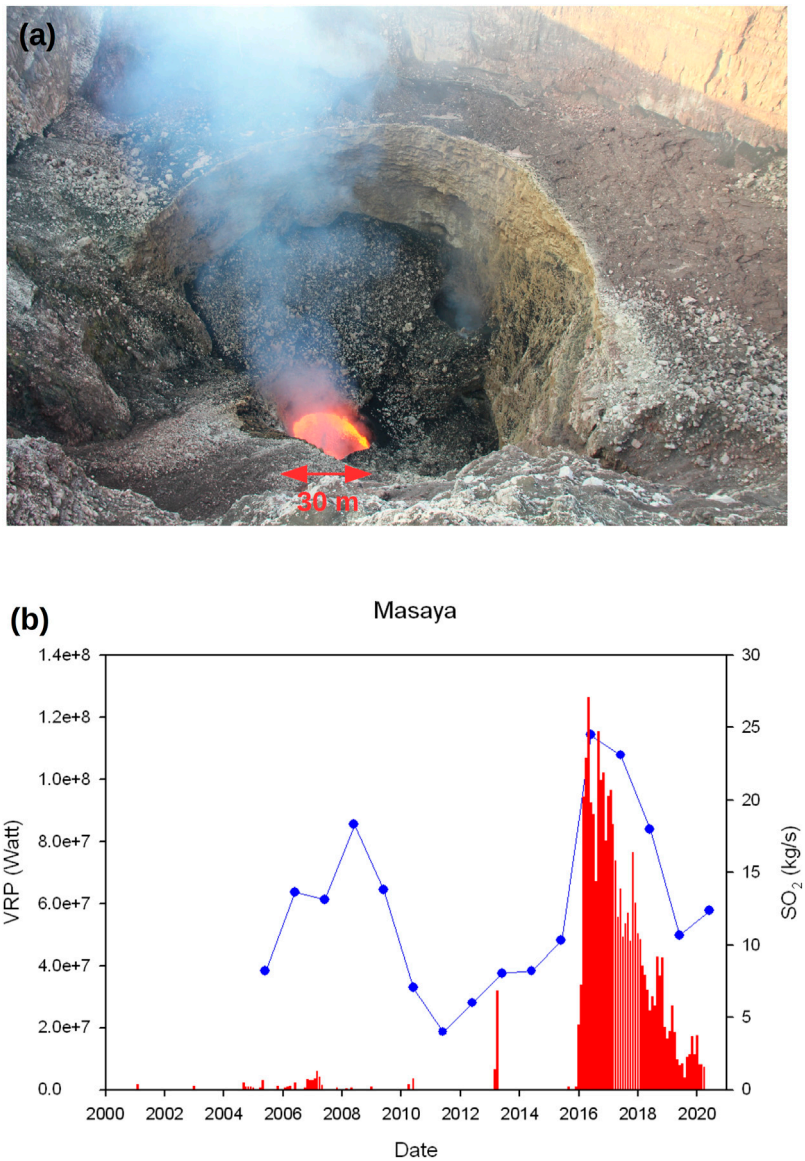

FIGURE 7
(A) Masaya lava lake at its highest level, in May 2016. **(B)** Time series of the yearly-averaged SO_2 flux and daily Volcanic Radiative Power from the Masaya Volcano. Masaya is a permanent SO_2 emitter and showed sporadic weak incandescence in its vent area. The appearance of the lava lake at the surface resulted in a significant increase in the SO_2 flux and VRP.

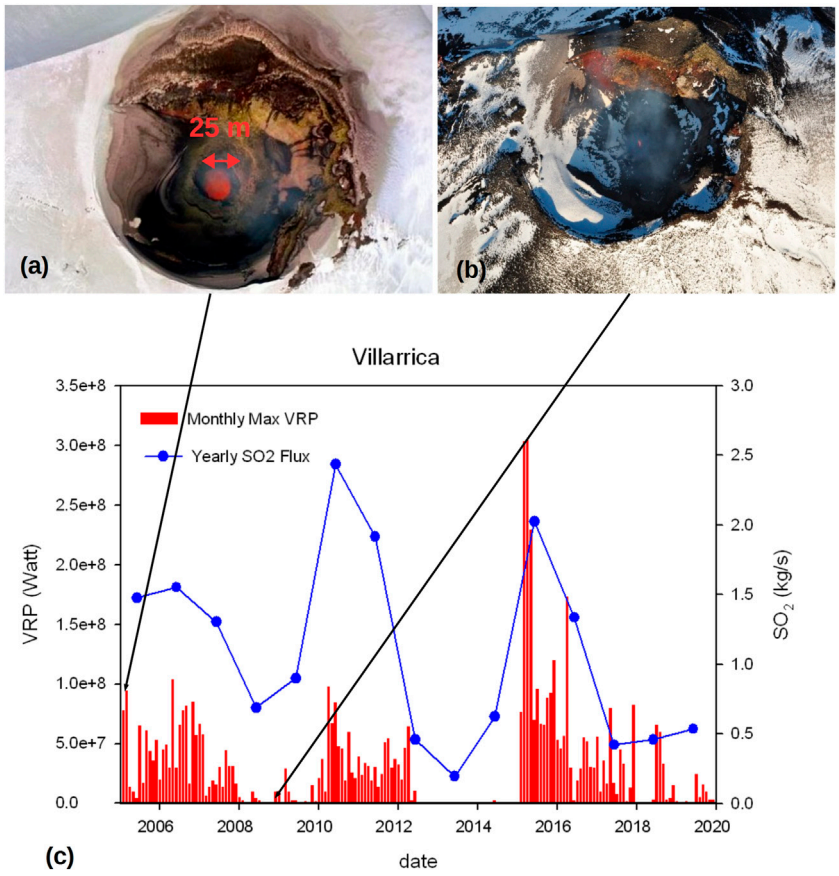

FIGURE 8
Lava lake of Villarrica shows large size and activity variations from a 25 m wide boiling lava lake, as in **(A)** dating from December 2004 (photo: J.C. Tanguy *via* GVP), to a narrow glowing hole as in **(B)** dating from 2009 (photo: T. Dockx). **(C)** Time series of the yearly averaged SO_2 and Monthly Maximal VRP emitted by the lava lake of Villarrica.

highlight the intermittency of Villarrica's lava lake. The periods of heightened activity lasting 2 to 3 years and radiating up to 3×10^8 W are separated by intervals of nearly complete quiescence also lasting 2 to 3 years. The typical SO_2 flux from Villarrica is too low to be measured on a daily or even on a monthly basis by OMI. So, in this work we used the time series from Carn et al. (2017) and extended it until 2020. It follows a temporal trend that is strikingly parallel to the VRP time series. This cyclic behavior of both the VRP and the SO_2 flux corresponds to periods of alternating periods high and low surface, level, and activity of the lava lake (Figures 8A, B).

4 Discussion

4.1 Comparing lava lakes

Comparing quantitatively lava lakes together is not a straightforward task because their heat and gas emissions span more than two orders of magnitudes (see Table 1). One approach is to compare intensive parameters (i.e. that are not dependent on the lake size). One of them is the equivalent radiating temperature T_{AR}, which is calculated using the inverse of the Stefan–Boltzmann law:

$$T_{ER} = \sqrt[4]{VRP/(A.\sigma.\varepsilon)}, \quad (1)$$

where A is the lake area, ε its emissivity (0.95 for basaltic lava), and σ is the Stefan–Boltzmann constant ($5.668\ 10^{-8}$ W/m^{2}K^4). The distinction made by Lev et al. (2019) is particularly apparent in Table 1, which clearly shows two populations of T_{ER}, which correspond to the chaotic lakes (T_{AR} between 1,100 and 1,200 K) and the ordered lakes (T_{ER} between 800 and 900 K). In Figure 9, we plot the apparent radiating temperature against the SO_2 flux per unit area of the lake. This shows an expected positive correlation between these two parameters, demonstrating that the chaotic lakes are not only hotter but also richer in gas. The explanation for this is that the T_{ER} is dominantly dependent on the percentage of the lake that is covered by a cooling skin and not by the absorption of the gas plume overlying the lake. The gas-poor lakes do have such a crust while the permanent bubbling at the surface of gas-rich lakes hampers its formation.

More information can be gained by comparing extensive parameters. The VRP vs. SO_2 flux diagram in Figure 10 shows that two leagues can be distinguished, those with small SO_2 and heat emissions (including Villarrica, Erta Ale, Masaya and likely Erebus although it was not included in our study), and those whose SO_2 or VRP emission are higher than either 25 kg/s or 5×10^8 W

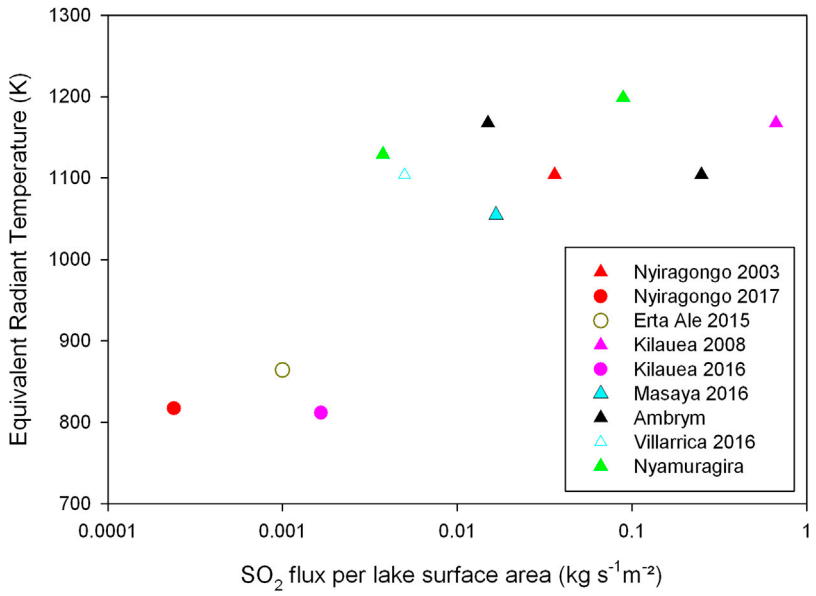

FIGURE 9
Diagram of the apparent radiant temperature *versus* SO_2 flux per area for the data of Table 1. The upper group corresponds to chaotic (hot, gas-rich lakes) while the lower group corresponds to ordered (colder, gas-poor lakes).

(Nyamulagira, Nyiragongo, Halemaumau, and Ambrym). Different behaviors seem to characterize these two leagues.

The group defined as small lakes contains volcanoes that are known for their permanent degassing over very long periods. Their lava lakes, when visible, have surface areas that vary between a few tens and a few thousands of square meters. They show coupled variations of their SO_2 flux and VRP, which maintain a certain linear correlation over time. In all cases, these fluctuations correspond to large changes of the height of the magmatic column, sometimes to the point of disappearing from sight in the case of Masaya and Villarrica, or overflowing in the case of Erta Ale. These lakes do not seem to suffer transitions from the chaotic type (to which Masaya and Villarrica belong) to the organized type (to which Erta Ale belongs). The most likely explanation for the long-term coupling of their VRP and SO_2 flux is that both are linked to the flow rate of the magmatic convection that feeds the lake. If this is the case, the slope of the regression line in the VRP *versus* SO_2 plots should depend on the initial sulfur content of the convecting magma and the efficiency of the convective process to dissipate heat.

Instead, large lava lakes, especially at the early stages of their existence show a strong anti-correlation between their heat and gas emissions. Within large lava lakes, two groups can clearly be distinguished. The first group is characterized by very high gas emissions and small to moderate VRP. It regroups the early-stage

TABLE 1 Main characteristics of the lava lakes at certain stages of their existence. Area is estimated from the photographs shown previously, except for Villarrica taken from Moussallam et al. (2016) and Ambrym in 2004 (T. Dockx, Pers. Com.).

Volcano	Year	SO_2 flux (kg/s)	VRP (watt)	Area (m^2)	SO2 flux per area ($kg/m^2.s$)	Heat flux per area (W/m^2)	T_{ER} (K)
Nyiragongo	2003	180	4.00E+08	5,000	3.60E-02	8.00E+04	1,104
Nyiragongo	2017	10	1.20E+09	50,000	2.00E-04	2.40E+04	817
Erta Ale	2015	1	3.00E+07	1,000	1.00E-03	3.00E+04	864
Kilauea	2008	200	3.00E+07	300	6.67E-01	1.00E+05	1,167
Kilauea	2015	50	7.00E+08	30,000	1.67E-03	2.33E+04	811
Masaya	2016	25	1.00E+08	1,500	1.67E-02	6.67E+04	1,055
Ambrym	2004	250	8.00E+07	1,000	2.50E-01	8.00E+04	1,104
Ambrym	2015	60	4.00E+08	4,000	1.50E-02	1.00E+05	1,167
Villarrica	2015	2.5	4.00E+07	500	5.00E-03	8.00E+04	1,104
Nyamuragira	2014	80	1.00E+08	900	8.89E-02	1.11E+05	1,199
Nyamuragira	2016	30	7.00E+08	10,000	3.00E-03	7.00E+04	1,068

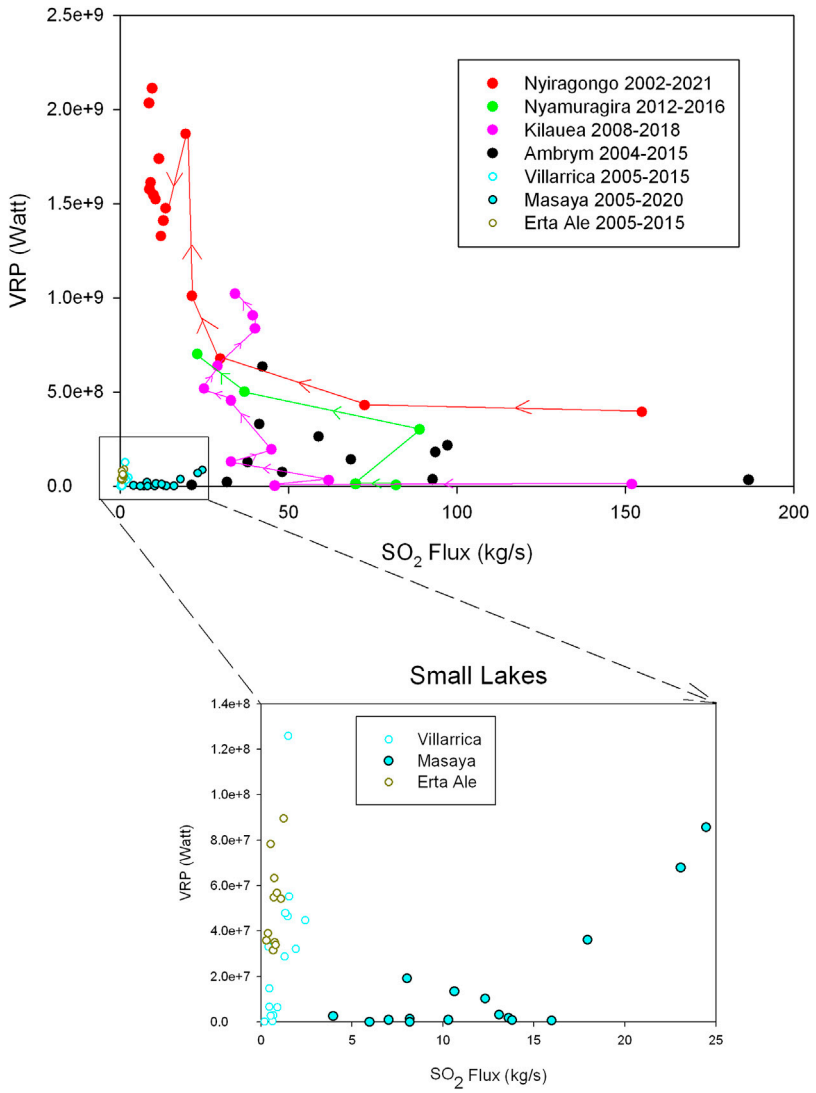

FIGURE 10
Diagram of the SO_2 flux *versus* VRP for lava lakes of the world. For the sake of clarity, each data point represents the average, over a year, of monthly maximum VRP. Arrows between points represent evolutions from year to year.

lava lakes of Kilauea, Nyiragongo, and Nyamuragira and the lava lakes of Ambrym. Visually, these lakes have a small size, brightly incandescent and vigorously bubbling surface, are stirred by very fast currents, or may even look like a small permanent lava fountain (e.g., Smets et al., 2014). They belong to the "Chaotic" category of Lev et al. (2019). The second group is characterized by high heat emissions and comparatively low gas emissions, and contains only mature lava lakes from rifts and hotspot volcanoes ["Organized" category according to Lev et al. (2019)]. The visual observations show that more than 80% of their surface is covered by a cooling skin or crust that is stirred by relatively slow convection currents until it sinks back into the lake.

The strong decoupling of SO_2 flux and radiant flux during the early stage of all three lava lake formations at Nyiragongo, Kilauea, and Nyamuragira is at a first glance surprising result, as most of the previous studies on lava lakes have reported or assumed a correlation between SO_2 emission and lava lake surface (e.g., Oppenheimer et al., 2004; Sweeney et al., 2008). It is, however, easily explained if we consider that the upwelling material feeding the lake is a magmatic foam. We show in the next section that the thermodynamic and phenomenological implications of this hypothesis match all of the observations reported on lava lakes.

4.2 Heat transport capacity of a magmatic foam

A lava lake can be considered, over a large period of time, as a steady state system, where the thermal power brought by the magmatic convection Q is equal to the sum of three following loss terms (Harris et al., 1999).

$$Q = VRP + CLC + CLA + Q_g. \quad (2)$$

The VRP, the radiated thermal power from the lake surface, is the dominant heat loss mechanism at these very high temperatures (Harris et al., 1999). The conductive heat loss through the wall of

the conduit (CLC) can be considered constant and negligible for a well-established steady-state system (Henley and Hughes, 2016). The conductive heat loss to the atmosphere (CLA) amounts to 10 (for hot lakes) to 30% (for colder lakes) of the VRP (Harris et al., 1999) and is also proportional to the lake surface area. Q_g is the heat lost by the transfer of hot gases from the lake to the atmosphere, and its magnitude depends on the total gas flux emitted by the lava lake.

The short-term excursions of the system away from this equilibrium can occur when the magma flux F_m feeding the system at depth varies. When F_m decreases, the heat transported by the magmatic convection is insufficient to balance the heat loss and a portion of the lake's surface solidifies, reducing the exposed radiating surface until the heat loss is again balanced. This leads to the formation of a bank of solidified lava. When F_m increases, the convection gets more vigorous, and the gas flux also increases so that more bubbling and more incandescent surfaces are exposed to the atmosphere. As a result, the heat loss increases until it balances the heat transported by the convection. Lake may enlarge by thermal erosion of its walls, its level tends to rise (because of the increased volume occupied by the rising magma and its gas) possibly until the point of overflowing, as often observed at the lava lakes of Erta Ale, Nyiragongo, Nyamuragira, and Kilauea.

If the material feeding the lava lake is considered as a bubble-rich liquid, or even as foam, composed of a volumetric fraction of magmatic gas X_g and a fraction of silicate melt equal to 1-X_g. The transported thermal energy flux can be calculated as

$$Q = F_m.\Big(\big(1 - X_g\big).\big(\rho_l.Cp_l.(T_u - T_d) + X_S \cdot \Delta HC_S\big) + X_g \cdot \rho_g.Cp_g \cdot (T_u - T_a)\Big), \quad (3)$$

where F_m is the volumetric flux of rising magmatic foam, ρ_l and ρ_g are the densities of the melt and gas, respectively, Cp_l and Cp_g are their specific heat, X_S is the proportion of melt that solidifies before sinking back, ΔHC_S the latent heat of solidification of the melt and T_U, T_D, and T_A are the temperature of the upwelling magma, of the downwelling lava, and of the atmosphere, respectively. Because silicate melts have a much higher density than gases, the thermal energy transported by the melt fraction of the foam is typically one order of magnitude higher than what its gaseous phase can transport. When magmatic gases escape into the atmosphere, they cool rapidly due to their mixing with air. Because of their very low emissivity at the wavelengths used in the MIROVA algorithm (HITRAN database, https://hitran.org/lbl/, Rothman et al., 2013), the gas, once emitted, does not contribute to the radiated power. Additionally, the rise from depth of a bubbly magmatic liquid implies that part of its thermal energy is consumed by the adiabatic expansion of the gas phase during its ascent (Stevenson and Blake 1998). Although the related temperature decrease may be compensated by the latent heat released by the partial crystallization of the foam's liquid phase (La Spina et al., 2016), the total energy available for radiation into the atmosphere is anyway decreased.

The consequence of all this is that the more gas the foam contains at the bottom of the convection cell, the less thermal energy it can transport to the surface and radiate into the atmosphere. This point is the cornerstone to understand the anticorrelation of heat and gas flux during the early stage of lava lake formation. The gas-rich lava lakes are fed by a material that can be considered true foam, which likely contains more than 80% of gas. The consequences of this are as follows:

1) The density contrast between the undegassed upwelling foam and the degassed downwelling lava is extremely high, which results in a very dynamic convection, with fast superficial currents, a lower exposure time to the atmosphere, and less surface cooling for the downwelling lava.
2) The outgassing of the foam produces a considerable volume loss that hampers the lake to reach a surface area that is much larger than the volcanic conduit feeding the lake. This partly explains why gas-rich lava lakes are relatively small.
3) The thermal energy avaliable to sustain the VRP emission from the lake is also limitted by the melt flux, so that the lake must remain small to remain liquid.

4.3 Large or small? The importance of a large shallow storage system

If our hypothesis that the SO_2 *vs.* VRP anticorrelation is due to the changes in the gas/melt ratio of the material feeding the magmatic convection, then why do small lakes show a correlation between their SO_2 and VRP? The answer to this question lies probably in the presence or absence of a large and shallow magma storage system, where SO_2-rich gas can exsolve and separate from the magma to accumulate as foam. We propose that large lava lakes have a large shallow magma storage system and small lava lakes do not. The presence of a relatively large shallow magma storage area beneath large lava lakes is also the reason why they are affected by catastrophic draining events. These events release massive lava flows with colossal effusion rates and empty, totally or partially, the shallow magma storage associated with the lava lake, to the point of generating massive collapse and smothering for the next several years of the volcanic activity, as happened in Kilauea in 2018 (Patrick et al., 2020), Nyiragongo in 1977 (Tazieff, 1977) and 2021 (Smittarello et al., 2022), and Ambrym in 2018 (Shreve et al., 2019). Small lakes may have storage areas underneath them (Stephens and Wauthier, 2018 for Masaya; Xu et al., 2020 for Erta Ale) but they must be either small or located deeper than the exsolution depth of the SO_2 in their magma.

4.4 Formation of large lava lakes at the rift and hotspot volcanoes: A common sequence of events

In this section, we highlight a four-stage sequence of processes leading to the formation of a lava lake at the rift and hotspot volcanoes. This sequence is schematized in Figure 11.

The first stage may start years to months before the first visible signs of lava lake formation appear. This stage is the previous accumulation of magma in the plumbing system of the volcanoes, when the upper conduit system of the volcano is still closed and does not allow the release of high-temperature magmatic gases to the surface. Several seismic and/or deformation studies have suggested that significant magma accumulation had taken place before the formation of a new lava lake at Nyiragongo, Kilauea, and Nyamuragira. Intrusion of a massive dyke occurred, after a year of seismic unrest, in January 2002 at Nyiragongo volcano (Wauthier et al., 2012), and preceded by 6 months the appearance of the new lava lake. A pulse of increased magma supply and accumulation was documented by deformation, seismicity, and gas measurement at Kilauea during 2003–2007 (Poland et al., 2012; Wauthier et al., 2013). Large-scale inflation was detected before the 2011 and 2012 eruption of Nyamuragira volcano (Albino et al., 2013) which marked the beginning of the formation process of Nyamuragira volcano. Simultaneously to this

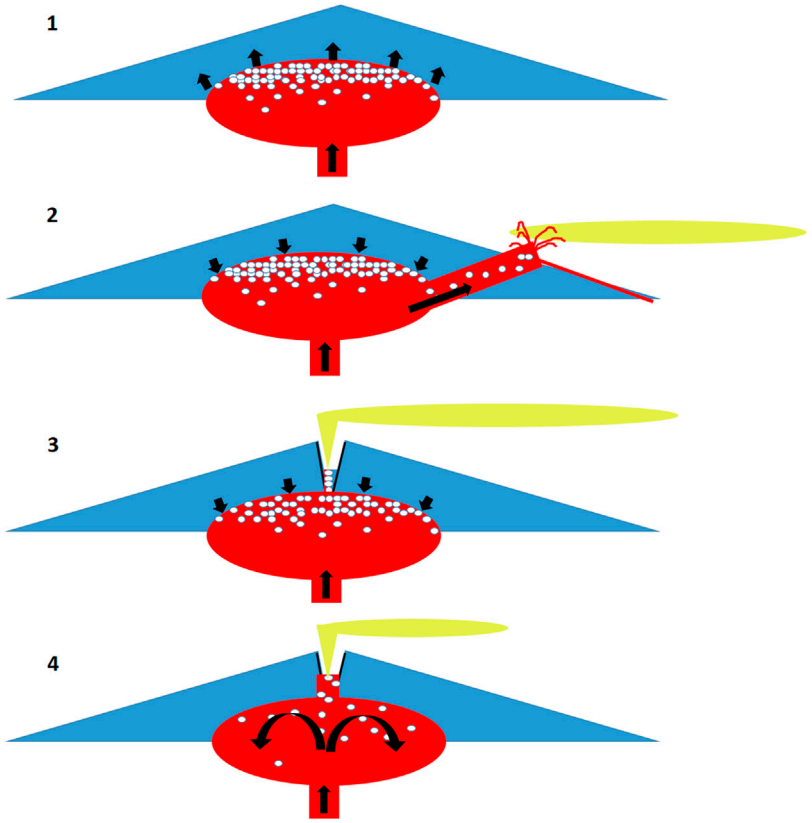

FIGURE 11
Schematic drawings of the four stage common sequence of lava lake formation at rift and hotspot volcanoes (not to scale, the size of the magma reservoir has been exaggerated). 1) Magma accumulation and gas segregation under a closed system condition. 2) Partial drainage of the storage area. 3) Opening of the system through the formation of a pit crater. A small foam-fed lava lake produces an intense degassing but low amounts of VRP. 4) Exhaustion of the foam, establishment of classical magmatic convection, and growth of the lava lake.

magma accumulation, a magmatic foam layer rich in gas is likely to accumulate at the top of the magma storage area (Jaupart and Vergniolle, 1989; Wallace 2001; Allard et al., 2005).

The second stage is the development of an open conduit system that allows magmatic degassing from the summit. In all three cases, the opening of the system was achieved through the migration of magma through laterally propagating dikes, the partial drainage of the upper plumbing system of the volcano, and the formation of a pit crater. At Nyiragongo, this second stage was materialized by the catastrophic eruption of January 2002 and the massive collapse of the caldera floor. At Kilauea, it was much less dramatic, being just materialized by a small fissure eruption in June 2007, generalized deflation (Poland et al., 2012), and the formation of an initially very narrow pit crater. This is probably because magma was already injecting continuously through its rift zone to feed the long-lived Pu'u O'o eruption. At Nyamuragira, this second stage was characterized by the large 2011–2012 eruption, one of the most voluminous in its history, and the collapse of a pit crater in its caldera (Campion, 2014; Coppola et al., 2016b).

The third stage is characterized by a strong degassing with little to no magma yet reaching the surface. This stage may initiate simultaneously to the lateral migration of magma and formation of the collapse pit, as was probably the case at Nyamuragira (Coppola et al., 2016b), or be delayed by a few months as in Nyiragongo and Kilauea. During this stage, the SO_2 emission rate typically reaches values of more than 100 kg/s, whereas the lava lake remains very deep in its newly formed collapse pit. If visible, the proto lava lake may look, at this stage, like a small lava fountain (Smets et al., 2014) or like an endless lava cascade (HVO photo archive, 2010), or be subject to huge level variations. All these phenomena result from the dynamics of the gas-rich magmatic foam that is feeding the lake. The duration of this stage of high gas/low heat emission probably corresponds to the time needed for the accumulated foam to be outgassed by the proto lava lake.

The fourth stage, characterized by a high and stable ratio of radiated heat to emitted gas corresponds to a fully mature lava lake fed by magmatic convection. Although the transition from stage three to four is usually progressive, it seems that the drop in SO_2 flux is more rapid (a few months) than the increase in VRP, which spans several years. This materializes the exhaustion of the pre-accumulated foam, the resulting increase of the melt/gas ratio in the material feeding the lake, and possibly thermal erosion of the conduit feeding the lava lake. The convection speed slows accordingly because the density contrasts between the ascending magma and the descending degassed lava decrease. The bubble bursting at the top of the magma column decreases and a cooling skin can start to form. It is likely that the magma feeding these mature lava lakes has already partly degassed during stage 3 and/or is a mixture between the partly degassed magma from stage 3 and the juvenile magma that is continuing to enter the system.

4.5 Lava lakes at arc volcanoes

The formation sequence described in the previous section applies to the rift and hotspot volcanoes, which are fed by a volatile-poor basaltic magma. Primitive basaltic magmas from arcs are richer in volatiles and more commonly produce explosive basaltic eruptions. However three of the volcanoes studied here, Villarrica, Ambrym, and Masaya, do host most of the time a lava lake. Interestingly, they all share the following three characteristics:

1) They are associated with large calderas (>5 km) that have produced large plinian basaltic eruptions in recent times (<10 ky)
2) They are characterized by a permanent open conduit degassing, whether a lava lake is visible or not
3) The magma that feeds them, known from the most primitive melt inclusions available, contains significantly less volatiles than other primitive arc magmas (see data from Witter et al., 2004 for Villarrica; Sadofsky et al., 2008 for Masaya; Allard et al., 2016 for Ambrym)

We can, thus, reasonably suspect that arc lava lakes, even though they all belong to the gas-rich type, are fed by a previously degassed magma or more likely a mix between a large batch of degassed magma and small repeated injection of juvenile magma, as suggested by the strong variations in our time series of SO_2 flux from Ambrym, Villarrica, and Masaya and by recent gas composition time series at these volcanoes (Allard et al., 2016; Aiuppa et al., 2017; Aiuppa et al., 2018, respectively).

5 Conclusion

Our study presents long-term time series of SO_2 flux and Volcanic Radiative Power for most of the lava lakes of the world. We characterize lava lakes in a simple diagram displaying SO_2 flux *versus* VRP, and demonstrate that they fall into three categories: small lakes, which show a correlation between their gas and heat emissions, large lakes with low gas and high VRP, and large lakes with high gas and low VRP. We show that the anticorrelation of VRP and SO_2 flux in large lakes is most easily explained by considering that these are fed by magmatic foam, whose gas fraction, responsible for the SO_2 emissions is inversely proportional to its liquid fraction, which mostly accounts for the radiated heat emission. We propose that the presence of a large shallow magma storage system beneath large lava lakes allows the accumulation of SO_2-rich foam that accounts for the observed anticorrelation. We unraveled a common sequence of events that has characterized the formation of three large lava lakes at volcanoes in the rift and hotspot environments in the last 20 years (Nyiragongo, Kilauea, and Nyamuragira). This sequence is composed of the following four steps:

1) Magma accumulation and foam accumulation at its upper part.
2) Partial drainage of the magma reservoir through a lateral injection of magma.
3) Formation of a pit crater and intense degassing with low heat emissions.
4) Gradual decrease of the gas emissions and concomitant increase of the lake level, area, and heat emissions. In this last step, a steady convective system is established and the lake is considered as mature.

The formation sequence described in our work could be helpful in the future to detect the formation of a true long-term lava lake and discriminate it from the short-lived eruption that occurs in a crater and just accumulate lava in it without establishing a true convective system, such as the 2020 and 2021 events on Kilauea Volcano or the brief effusions spurts that have occurred in Nyiragongo since its lake drained in 2021.

Probably the most interesting outcome of the present work is the discovery that classes of lava lakes, the large lakes, are likely associated with shallow magma reservoirs and are, therefore, more susceptible to drain catastrophically. Nyamuragira volcano hosts, at the time of writing, the last specimen of this class. We highlight that a catastrophic draining event is a likely scenario at this volcano for the next years or decades, considering the recent rise of the lava lake level, and the historical precedent of the 1938 eruption.

The rarity of lava lakes in the world is likely the result of the numerous conditions they require to form and persist. The present study highlights the importance of magma accumulation and outgassing in a large and shallow magma reservoir as a requisite to its formation. A high and sustained supply of relatively volatile-poor magma is also necessary to keep the lake active. The strain state of the volcano is also playing a role. Many volcanoes alternate periods of stable behavior where activity is mostly constrained to their summit area, and unstable periods where spreading and dyke intrusion dominate. Lava lakes obviously need stable conditions to persist, but our work shows the importance of dyke intrusion and pit crater collapse to gently decompress the magma reservoir that will eventually feed the lava lake. This combination of conditions may be relatively uncommon, so only a restricted number of volcanoes recurrently develop lava lakes.

Data availability statement

The raw data supporting the conclusions of this article will be made available by the authors, without undue reservation.

Author contributions

RC conceived the research idea, processed the OMI data to calculate the SO_2 flux, and wrote most of the manuscript. DC processed the MODIS thermal data, wrote parts of the manuscript, commented on initial versions, and provided additional ideas.

Funding

This project benefited from funding by the SEPCONACYT grant for basic science #CB A1-S-30127.

Acknowledgments

The authors thank Jacques Marie Bardintzeff, Marc Caillet, Thierry Dockx, George Kourounis, Patrick Marcel, Cédric Normand, and Dario Tedesco for sharing their pictures.

Conflict of interest

The authors declare that the research was conducted in the absence of any commercial or financial relationships that could be construed as a potential conflict of interest.

Publisher's note

All claims expressed in this article are solely those of the authors and do not necessarily represent those of their affiliated organizations, or those of the publisher, the editors, and the reviewers. Any product that may be evaluated in this article, or claim that may be made by its manufacturer, is not guaranteed or endorsed by the publisher.

Supplementary material

The Supplementary Material for this article can be found online at: https://www.frontiersin.org/articles/10.3389/feart.2023.1040199/full#supplementary-material

References

Aiuppa, A., Bitetto, M., Francofonte, V., Velasquez, G., Bucarey Parra, C., Guidice, G., et al. (2017). A CO_2-gas precursor to the March 2015 Villarrica volcano eruption. *Geochem. Geophys. Geosystems* 18, 2120–2132. doi:10.1002/2017GC006892

Aiuppa, A., de Moor, J. M., Arellano, S., Coppola, D., Galle, B., Francofonte, V., et al. (2018). Tracking Formation of a lava lake from ground and space: Masaya Volcano (Nicaragua), 2014-2017. *Geosystems* 19, 496–515. doi:10.1002/2017GC007227

Allard, P., Burton, M., and Murè, F. (2005). Spectroscopic evidence for a lava fountain driven by previously accumulated magmatic gas. *Nature* 43 (7024), 407–410. doi:10.1038/nature03246

Albino, F., Kervyn, F., Smets, P., and d'Oreye, N. (2013). "InSAR study on the 2011 eruption at Nyamulagira volcano, D.R.C.: Lava flow emplacement and post-eruption ground deformation," in AGU Fall Meeting Abstracts 2013, G31A-0957

Allard, P., Aiuppa, A., Bani, P., Métrich, N., Bertagnini, A., Gauthier, P-J., et al. (2015). Overview of the precursors and dynamics of the 2012–13 basaltic fissure eruption of Tolbachik Volcano, Kamchatka, Russia. *J. Volcanol. Geotherm. Res.Special issue Vanuatu Volcanoes* 304, 378. doi:10.1016/j.jvolgeores.2015.08.022

Allard, P., Burton, M., Sawyer, G., and Bani, P. (2016). Degassing dynamics of basaltic lava lake at a top-ranking volatile emitter: Ambrym volcano, Vanuatu arc. *Earth Planet Sci. Lett.* 448, 69–80. doi:10.1016/j.epsl.2016.05.014

Bani, P., Oppenheimer, C., Tsanev, V. I., Carn, S. A., Cronin, S. J., Crimp, R., et al. (2009). Surge in sulphur and halogen degassing from Ambrym volcano, Vanuatu. *Vanuatu. Bull. Volcanol.* 71 (10), 1159–1168. doi:10.1007/s00445-009-0293-7

Beirle, S., Hörmann, C., Penning de Vries, M., Dörner, S., Kern, C., and Wagner, T. (2014). Estimating the volcanic emission rate and atmospheric lifetime of SO_2 from space: A case study for kilauea volcano, Hawai`i. *Atmos. Chem. Phys.* 14, 8309–8322. doi:10.5194/acp-14-8309-2014

Bobrowski, N., Giuffrida, G. B., Arellano, S., Yalire, M., Liotta, M., Brusca, L., et al. (2017). Plume composition and volatile flux of Nyamulagira volcano, Democratic Republic of Congo, during birth and evolution of the lava lake, 2014–2015. *Bull. Volcanol.* 79, 90. doi:10.1007/s00445-017-1174-0

Bouche, E., Vergniolle, S., Staudacher, T., Nercessian, A., Delmont, J.-C., Frogneux, M., et al. (2010). The role of large bubbles detected from acoustic measurements on the dynamics of Erta 'Ale lava lake (Ethiopia). *Earth Planet. Sci. Lett.* 295, 37–48. doi:10.1016/j.epsl.2010.03.020

Burgi, P-Y., Darrah, T. H., Tedesco, D., and Eymold, W. K. (2014). Dynamics of the mount Nyiragongo lava lake. *J. Geophys Res. Solid Earth* 119, 4106–4122. doi:10.1002/2013JB010895

Burgi, P-Y., Boudoire, G., Rufino, F., Karume, K., and Tedesco, D. (2020). Recent activity of Nyiragongo (Democratic Republic of Congo): New insights from field observations and numerical modeling. *Geophys. Res. Lett.* 47, e2020GL088484. doi:10.1029/2020GL088484

Burgi, P.-Y., Valade, S., Coppola, D., Boudoire, G., Mavonga, G., Rufino, F., et al. (2021). Unconventional filling dynamics of a pit crater. *Earth Planet. Sci. Lett.* 576, 117230. doi:10.1016/j.epsl.2021.117230

Campion, R. (2014). New lava lake at Nyamuragira volcano revealed by combined ASTER and OMI SO_2 measurements. *Geophys. Res. Lett.* 41, 7485–7492. doi:10.1002/2014GL061808

Campion, R., Salerno, G., Coheur, P., Hurtmans, D., Clarisse, L., Kazahaya, K., et al. (2010). Measuring volcanic degassing of SO_2 in the lower troposphere with ASTER band ratios, Journ. Volcanol. Geotherm. Res. *J. Volcanol. Geotherm. Res.* 194, 42–54. doi:10.1016/j.jvolgeores.2010.04.010

Carbone, D., Poland, M. P., Patrick, M. R., and Orr, T. R. (2013). Continuous gravity measurements reveal a low-density lava lake at Kīlauea Volcano, Hawaii. *Earth Planet. Sci. Lett.* 376, 178–185. doi:10.1016/j.epsl.2013.06.024

Carn, S. A. (2004). Eruptive and passive degassing of sulfur dioxide at Nyiragongo volcano (D.R. Congo): The 17 january 2002 eruption and its aftermath. *Acta Vulcanol.* 14-15, 75–86.

Carn, S. A., Fioletov, V. E., McLinden, C. A., Li, C., and Krotkov, N. A. (2017). A decade of global volcanic SO_2 emissions measured from space. *Sci. Rep.* 7, 44095. doi:10.1038/srep44095

Coppola, D., Laiolo, M., Cigolini, C., Delle Donne, D., and Ripepe, M. (2016a). "Enhanced volcanic hot-spot detection using MODIS IR data: Results from the MIROVA system," in *Detecting, modelling and responding to effusive eruptions*. Editors A. J. L. Harris, T. De Groeve, F. Garel, and S. A. Carn (London: Geological Society), 426, 181–205. Special Publications. doi:10.1144/SP426.5

Coppola, D., Campion, R., Laiolo, M., Cuoco, E., Balagizi, C., Ripepe, M., et al. (2016b). Birth of a lava lake: Nyamulagira volcano 2011–2015. *Bull. Volcanol.* 78 (3), 20–13. doi:10.1007/s00445-016-1014-7

Coppola, D., Laiolo, M., and Cigolini, C. (2016c). Fifteen years of thermal activity at Vanuatu's volcanoes (2000-2015) revealed by MIROVA. *J. Volcanol. Geotherm. Res.* 322, 6–19. doi:10.1016/j.jvolgeores.2015.11.005

de Moor, J. M., Fischer, T. P., Sharp, Z. D., King, P. L., Wilke, M., Botcharnikov, R. E., et al. (2013). Sulfur degassing at Erta Ale (Ethiopia) and Masaya (Nicaragua) volcanoes: Implications for degassing processes and oxygen fugacities of basaltic systems. *Geochem. Geophys. Geosyst.* 14, 4076–4108. doi:10.1002/ggge.20255

Delmelle, P., Baxter, P., Beaulieu, A., Burton, M., Francis, P., Garcia-Alvarez, J., et al. (1999). Origin, effects of Masaya Volcano's continued unrest probed in Nicaragua, Eos Trans. *AGU* 80, 575–581. doi:10.1029/EO080i048p00575

Delmelle, P., Stix, J., Baxter, P. J., Garcia-Alvarez, J., and Barquero, J. (2002). Atmospheric dispersion, environmental effects and potential health hazard associated with the low-altitude gas plume of Masaya volcano, Nicaragua. *Bull. Volcanol.* 64, 423–434. doi:10.1007/s00445-002-0221-6

Field, L., Barnie, T., Blundy, J., Brooker, R. A., Keir, D., Lewi, E., et al. (2012). Integrated field, satellite and petrological observations of the November 2010 eruption of Erta Ale. *Bull. Volcanol.* 74, 2251–2271. doi:10.1007/s00445-012-0660-7

Global Volcanism Program (2018). Report on Erta Ale (Ethiopia). *Bulletin of the global volcanism network*. Editors A. E. Crafford and E. Venzke (Smithsonian Institution), 43, 4. doi:10.5479/si.GVP.BGVN201804-221080

Global Volcanism Program (2017). Report on Nyamulagira (DR Congo). *Bulletin of the Global Volcanism Network*. Editors A. E. Crafford and E. Venzke (Smithsonian Institution), 42, 6. doi:10.5479/si.GVP.BGVN201706-223020

Global Volcanism Program (2019). Report on Nyamulagira (DR Congo). *Bulletin of the Global Volcanism Network*. Editors A. E. Crafford and E. Venzke (Smithsonian Institution), 44, 5. doi:10.5479/si.GVP.BGVN201905-223020

Gray, D. M., Burton-Johnson, A., and Fretwell, P. T. (2019). Evidence for a lava lake on Mt. Michael volcano, saunders island (south Sandwich islands) from landsat, sentinel-2 and ASTER satellite imagery. *J. Volcanol. Geotherm. Res.* 379, 60–71. doi:10.1016/j.jvolgeores.2019.05.002

Harris, A. J. L., Flynn, L. P., Rothery, D. A., Oppenheimer, C., and Sherman, S. B. (1999). Mass flux measurements at active lava lakes: Implications for magma recycling. *J. Geophys. Res.* 104, 7117–7136. doi:10.1029/98JB02731

Head, E. M., Shaw, A. M., Wallace, P. J., Sims, K. W. W., and Carn, S. A. (2011). Insight into volatile behavior at Nyamuragira volcano (D.R. Congo, Africa) through olivine-hosted melt inclusions. *Geochem. Geophys. Geosyst.* 12, Q0AB11. doi:10.1029/2011GC003699

Henley, R. W., and Hughes, G. (2016). SO_2 flux and the thermal power of volcanic eruptions. *J. Volcanol. Geotherm. Res.* 324, 190–199. doi:10.1016/j.jvolgeores.2016.04.024

HVO photo archive (2010). *HVO photo archive*. United States Geological Survey. January-June 2010. Available at: https://volcanoes.usgs.gov/volcanoes/kilauea/archive/multimedia/2010/2010_Jan-Jul.shtml accessed on 22/07/2022.

Jaggar, T. A. (1917). Thermal gradient of Kilauea lava lake. *J. Wash. Acad. Sci.* 7, 397–405.

Jaupart, C., and Vergniolle, S. (1989). The generation and collapse of a foam layer at the roof of a basaltic magma chamber. *J. Fluid Mech.* 203, 347–380. doi:10.1017/S0022112089001497

Kazahaya, G., Shinohara, H., and Saito, G. (1994). Excessive degassing of izu-oshima volcano: Magma convection in a conduit. *Bull. Volcanol.* 56, 207–216. doi:10.1007/bf00279605

Komorowski, J., et al. (2002). The january 2002 flank eruption of Nyiragongo volcano (democratic republic of Congo): Chronology, evidence for a tectonic rift trigger, and impact of lava flows on the city of goma. *Acta Vulcanol.* 14, 27–62.

Kyle, P. R., Sybeldon, L. M., McIntosh, W. C., Meeker, K., and Symonds, R. (1994). "Sulfur dioxide emission rates from Mount Erebus, Antarctica," in *Volcanological and environmental studies of mount Erebus*. Editor P. R. Kyle (Antarctica: American Geophysical Union Geophysical, Monograph), 66, 69–82.

La Spina, G., Burton, M., Vitturi, M. M., and Arzilli, F. (2016). Role of syn-eruptive plagioclase disequilibrium crystallization in basaltic magma ascent dynamics. *Nat. Commun.* 7, 13402. doi:10.1038/ncomms13402

Le Guern, F., Carbonnelle, J., and Tazieff, H. (1979). Erta'Ale lava lake: Heat and gas transfer to the atmosphere. *J. Volcanol. Geotherm. Res.* 6, 27–48. doi:10.1016/0377-0273(79)90045-3

Lev, E., Ruprecht, P., Oppenheimer, C., Peters, N., Patrick, M., Hernández, P. A., et al. (2019). A global synthesis of lava lake dynamics. *J. Volcanol. Geotherm. Res.* 381, 16–31. doi:10.1016/j.jvolgeores.2019.04.010

Lohmar, S., Robin, C., Gourgaud, A., Clavero, J., Parada, M. Á., Moreno, H., et al. (2007). Evidence of magma-water interaction during the 13,800 years BP explosive cycle of the Licán Ignimbrite, Villarrica volcano (southern Chile). *Andean Geol.* 34 (2), 233–247.

Matsushima, N., and Shinohara, H. (2006). Visible and invisible volcanic plumes. *Geophys. Res. Lett.* 33, L24309. doi:10.1029/2006GL026506

Moussallam, Y., Bani, P., Curtis, A., Barnie, T., Moussallam, M., Peters, N., et al. (2016). Sustaining persistent lava lakes: Observations from high-resolution gas measurements at Villarrica volcano, Chile. *Earth Planet. Sci. Lett.* 454, 237–247. doi:10.1016/j.epsl.2016.09.012

Németh, K., and Cronin, S. J. (2011). Drivers of explosivity and elevated hazard in basaltic fissure eruptions: The 1913 eruption of Ambrym volcano, Vanuatu (SW-pacific). *J. Volcanol. Geotherm. Res.* 201, 194–209. doi:10.1016/j.jvolgeores.2010.12.007

Oppenheimer, C., McGonigle, A. J. S., Allard, P., Wooster, M. J., and Tsanev, V. I. (2004). Sulfur heat and magma budget of Erta 'Ale lava lake, Ethiopia. *Geology* 32, 509–512. doi:10.1130/g20281.1

Palma, J. L., Calder, E. S., Basualto, D., Blake, S., and Rothery, D. A. (2008). Correlations between SO_2 flux, seismicity, and outgassing activity at the open vent of Villarrica Volcano, Chile. *J. Geophys. Res.* 113, B10201. doi:10.1029/2008JB005577

Palma, J. L., Blake, S., and Calder, E. S. (2011). Constraints on the rates of degassing and convection in basaltic open-vent volcanoes. *Geochem. Geophys. Geosyst.* 12, Q11006. doi:10.1029/2011GC003715

Patrick, M. R., Orr, T. A., Sutton, J., Elias, T., and Swanson, D. (2013). The first five years of Kīlauea's summit eruption in Halema'uma'u Crater, 2008–2013. *U.S. Geol. Surv. Fact. Sheet* 2013–3116, 4. doi:10.3133/fs20133116

Patrick, M. R., Anderson, K. R., Poland, M. P., Orr, T. R., and Swanson, D. A. (2015). Lava lake level as a gauge of magma reservoir pressure and eruptive hazard. *Geology* 43, 831–834. doi:10.1130/G36896.1

Patrick, M., Johanson, I., Shea, T., and Waite, G. (2020). The historic events at kīlauea volcano in 2018: Summit collapse, rift zone eruption, and mw 6.9 earthquake: Preface to the special issue. *Bull. Volcanol.* 82, 46. doi:10.1007/s00445-020-01377-5

Perez, W., and Freundt, A. (2006). "The youngest highly explosive basaltic eruptions from Masaya caldera (Nicaragua): Stratigraphy and hazard assessment," in *Volcanic hazards in Central America*. Editors W. I. Rose, G. J. S. Bluth, M. J. Carr, J. W. Ewert, L. C. Patino, and J. W. Vallance (Geol Soc Amer Spec Pap), 412, 189–207.

Poland, M., Miklius, A., Jeff Sutton, A., and Thornber, C. R. (2012). A mantle-driven surge in magma supply to Kīlauea Volcano during 2003–2007. *Nat. Geosci.* 5, 295–300. doi:10.1038/ngeo1426

Rothman, L. S., Gordon, I. E., Babikov, Y., Barbe, A., Chris Benner, D., Bernath, P. F., et al. (2013). The HITRAN 2012 molecular spectroscopic database. *J. Quantitative Spectrosc. Radiat. Transf.* 130, 4–50. doi:10.1016/j.jqsrt.2013.07.002

Rymer, H., van Wyk de Vries, B., Stix, J., and Williams-Jones, G. (1998). Pit crater structure and processes governing persistent activity at Masaya Volcano, Nicaragua. *Bull. Volcanol.* 59, 345–355. doi:10.1007/s004450050196

Sadofsky, S. J., Portnyagin, M., Hoernle, K., and van den Bogaard, P. (2008). Subduction cycling of volatiles and trace elements through the central American volcanic arc: Evidence from melt inclusions. *Contrib. Mineral. Pet.* 155, 433–456. doi:10.1007/s00410-007-0251-3

Sawyer, G. M., Carn, S. A., Tsanev, V. I., Oppenheimer, C., and Burton, M. (2008). Investigation into magma degassing at Nyiragongo volcano, democratic republic of the Congo. *Geochem. Geophys. Geosyst.* 9, Q02017. doi:10.1029/2007GC001829

Shreve, T., Grandin, R., Boichu, M., Moussallam, Y., Ballu, V., Delgado, F., et al. (2019). From prodigious volcanic degassing to caldera subsidence and quiescence at Ambrym (Vanuatu): The influence of regional tectonics. *Sci. Rep.* 9, 18868. doi:10.1038/s41598-019-55141-7

Smets, B., D'Oreye, N., and Kervyn, F. (2014). Toward another lava lake in the virunga volcanic field? *Eos Trans. AGU* 95, 377–378. doi:10.1002/2014eo420001

Smittarello, D., Smets, B., Barrière, J., Michellier, C., Oth, A., Shreve, T., et al. (2022). Precursor-free eruption triggered by edifice rupture at Nyiragongo volcano. *Nature* 609, 83–88. doi:10.1038/s41586-022-05047-8

Stephens, K., and Wauthier, C. (2018). Satellite geodesy captures offset magma supply associated with lava lake appearance at Masaya volcano, Nicaragua. *Geophys. Res. Lett.* 45, 2669–2678. doi:10.1002/2017GL076769

Stevenson, D. S., and Blake, S. (1998). Modelling the dynamics and thermodynamics of volcanic degassing. *Bull. Volcanol.* 60, 307–317. doi:10.1007/s004450050234

Sweeney, D., Kyle, P. R., and Oppenheimer, C. (2008). Sulfur dioxide emissions and degassing behavior of Erebus volcano, Antarctica. *J. Volcanol. Geotherm. Res.* 177, 725–733. doi:10.1016/j.jvolgeores.2008.01.024

Tazieff, H. (1966). État actuel des connaissances sur le volcan Niragongo (République Démo. du Congo). *Bull. Soc. Géol. Fr.* t VIII, 176–200.

Tazieff, H. (1974). *Niragongo ou le Volcan interdit, flammarion*. Paris, France.

Tazieff, H. (1977). An exceptional eruption: Mt. Niragongo, jan. 10th, 1977. *Bull. Volcanol.* 30, 189–200. doi:10.1007/bf02596999

Tazieff, H. (1984). Mt. Niragongo: Renewed activity of the lava lake. *J. Volcanol. Geotherm. Res.* 20, 267–280. doi:10.1016/0377-0273(84)90043-x

Tazieff, H. (1994). Permanent lava lakes: Observed facts and induced mechanisms. *J. Volcanol. Geotherm. Res.* 63, 3–11. doi:10.1016/0377-0273(94)90015-9

Valade, S., Ripepe, M., Giuffrida, G., Karume, K., and Tedesco, D. (2018). Dynamics of Mount Nyiragongo lava lake inferred from thermal imaging and infrasound array. *Earth Planet Sci. Lett.* 500, 192–204. doi:10.1016/j.epsl.2018.08.004

Verhoogen, J. (1948). "Les éruptions 1938–1940 du volcan Nyamuragira, Missions Jean Verhoogen," in *Fascicule 1, 1938–1940* (Brussels, Belgium, 187.

Viramonte, J. G., and Incer-Barquero, J. (2008). Masaya, the "mouth of hell", Nicaragua: Volcanological interpretation of the myths, legends and anecdotes. *J. Volcanol. Geotherm. Res.* 176, 419–426. doi:10.1016/j.jvolgeores.2008.01.038

Wadge, G., and Burt, L. (2011). Stress field control of eruption dynamics at a rift volcano: Nyamuragira, D.R. Congo. *J. Volcanol. Geotherm. Res.* 207 (1–2), 1–15. doi:10.1016/j.jvolgeores.2011.06.012

Wallace, P. J. (2001). Volcanic SO_2 emissions and the abundance and distribution of exsolved gas in magma bodies. *J. Volcanol. Geotherm. Res.* 108, 85–106. doi:10.1016/S0377-0273(00)00279-1

Wauthier, C., Cayol, V., Kervyn, F., and d'Oreye, N. (2012). Magma sources involved in the 2002 Nyiragongo eruption, as inferred from an InSAR analysis. *J. Geophys. Res.* 117, B05411. doi:10.1029/2011JB008257

Wauthier, C., Roman, D. C., and Poland, M. P. (2013). Moderate-magnitude earthquakes induced by magma reservoir inflation at Kīlauea Volcano, Hawai'i. *Geophys. Res. Lett.* 40, 5366–5370. doi:10.1002/2013GL058082

Witham, F., Woods, A. W., and Gladstone, C. (2006). An analogue experimental model of depth fluctuations in lava lakes. *Bull. Volcanol.* 69 (1), 51–56. doi:10.1007/s00445-006-0055-8

Witter, J. B., Kress, V. C., Delmelle, P., and Stix, J. (2004). Volatile degassing, petrology, and magma dynamics of the Villarrica lava lake, southern Chile. *J. Volcanol. Geotherm. Res.* 134 (4), 303–337. doi:10.1016/j.jvolgeores.2004.03.002

Xu, W., Xie, L., Aoki, Y., Rivalta, E., and Jónsson, S. (2020). Volcano-wide deformation after the 2017 Erta Ale dike intrusion, Ethiopia, observed with radar interferometry. *J. Geophys. Res. Solid Earth* 125, e2020JB019562. doi:10.1029/2020JB019562

frontiers | Frontiers in Earth Science

TYPE Original Research
PUBLISHED 01 March 2023
DOI 10.3389/feart.2023.1039093

OPEN ACCESS

EDITED BY
Christoph Kern,
United States Geological Survey (USGS), United States

REVIEWED BY
Emmanuel Dekemper,
The Royal Belgian Institute for Space Aeronomy (BIRA-IASB), Belgium
Andrea Gabrieli,
University of Hawaii at Manoa, United States

*CORRESPONDENCE
Jonas Kuhn,
jkuhn@iup.uni-heidelberg.de

SPECIALTY SECTION
This article was submitted to Volcanology, a section of the journal Frontiers in Earth Science

RECEIVED 07 September 2022
ACCEPTED 03 February 2023
PUBLISHED 01 March 2023

CITATION
Kuhn J, Bobrowski N, Boudoire G, Calabrese S, Giuffrida G, Liuzzo M, Karume K, Tedesco D, Wagner T and Platt U (2023), High-spectral-resolution Fabry-Pérot interferometers overcome fundamental limitations of present volcanic gas remote sensing techniques. *Front. Earth Sci.* 11:1039093. doi: 10.3389/feart.2023.1039093

High-spectral-resolution Fabry-Pérot interferometers overcome fundamental limitations of present volcanic gas remote sensing techniques

Jonas Kuhn[1,2]*, Nicole Bobrowski[1,3], Guillaume Boudoire[4,5], Sergio Calabrese[5,6], Giovanni Giuffrida[3], Marco Liuzzo[5], Katcho Karume[7], Dario Tedesco[8,9], Thomas Wagner[2] and Ulrich Platt[1,2]

[1]Institut für Umweltphysik, Universität Heidelberg, Heidelberg, Germany, [2]Max Planck Institut für Chemie, Mainz, Germany, [3]Instituto Nazionale di Geofisica e Vulcanologia—Osservatorio Etneo, Catania, Italy, [4]Laboratoire Magmas et Volcans, OPGC, CNRS, IRD, UCA, Aubière, France, [5]Instituto Nazionale di Geofisica e Vulcanologia, Palermo, Italy, [6]DiSTeM, Università Degli Studi di Palermo, Palermo, Italy, [7]Observatoire Volcanologique de Goma, Goma, Democratic Republic of Congo, [8]DISTABIF, Università Degli Studi Della Campania Luigi Vanvitelli, Caserta, Italy, [9]Instituto Nazionale di Geofisica e Vulcanologia—Osservatorio Vesuviano, Napoli, Italy

Remote sensing (RS) of volcanic gases has become a central tool for studying volcanic activity. For instance, ultraviolet (UV) skylight spectroscopy with grating spectrographs (GS) enables SO_2 (and, under favourable conditions, BrO) quantification in volcanic plumes from autonomous platforms at safe distances. These measurements can serve volcanic monitoring and they cover all stages of volcanic activity in long measurement time series, which substantially contributes to the refinement of theories on volcanic degassing. Infrared (IR) remote sensing techniques are able to measure further volcanic gases (e.g., HF, HCl, CO_2, CO). However, the employed Fourier transform spectrometers (FTSs) are intrinsically intricate and, due to limited resolving power or light throughput, mostly rely on either lamps, direct sun, or hot lava as light source, usually limiting measurements to individual field campaigns. We show that many limitations of grating spectrographs and Fourier transform spectrometer measurements can be overcome by Fabry-Perot interferometer (FPI) based spectrograph implementations. Compared to grating spectrographs and Fourier transform spectrometers, Fabry-Perot interferometer spectrographs reach a 1-3 orders of magnitude higher spectral resolution and superior light throughput with compact and stable set-ups. This leads to 1) enhanced sensitivity and selectivity of the spectral trace gas detection, 2) enables the measurement of so far undetected volcanic plume constituents [e.g., hydroxyl (OH) or sulfanyl (SH)], and 3) extends the range of gases that can be measured continuously using the sky as light source. Here, we present measurements with a shoe-box-size Fabry-Perot interferometer spectrograph

Abbreviations: RS, remote sensing; FPI, Fabry-Pérot interferometer; UV, ultraviolet; GS, grating spectrograph; IR, infrared; FTS, Fourier transform spectroscopy; SWIR, short wave infrared; DOAS, differential optical absorption spectroscopy; LED, light emitting diode; OSM, order sorting mechanism; OSGS, order sorting grating spectrograph; ROI, region of interest.

(resolving power of ca. 150000), performed in the crater of Nyiragongo volcano. By analysing the light of a ultraviolet light emitting diode that is sent through the hot gas emission of an active lava flow, we reach an OH detection limit of about 20 ppb, which is orders of magnitude lower than the mixing ratios predicted by high-temperature chemical models. Furthermore, we introduce example calculations that demonstrate the feasibility of skylight-based remote sensing of HF and HCl in the short-wave infrared with Fabry-Perot interferometer spectrographs, which opens the path to continuous monitoring and data acquisition during all stages of volcanic activity. This is only one among many further potential applications of remote sensing of volcanic gases with high spectral resolution.

KEYWORDS

Fabry-Pérot interferometer, remote sensing, volcanic gases, spectroscopy, hydroxyl radical, halogens

1 Introduction

Volcanic gas geochemistry and studies of the chemical evolution of volcanic plumes have made significant progress in the recent decades, essentially driven by developments in remote sensing (RS) techniques (see, e.g., Platt et al., 2018). However, many studies still rely on few and infrequent observations, which in most cases only poorly constrain degassing models. Present RS techniques remain fundamentally limited by either intricate instrumentation with poor field-applicability or by low spectral resolution.

Several recent RS approaches rely on reduced spectral resolution in order to increase the spatial and/or temporal resolution of passive remote sensing instruments (see e.g., Mori and Burton, 2006; Prata and Bernardo, 2014; Platt et al., 2015; Varon et al., 2021). In principle, this approach mostly represents a matching of the observing geometry of the RS measurement to the temporal and spatial scales of the observed process. Under particular atmospheric conditions enhanced spatio-temporal resolution improves measurements of trace gas fluxes of localized sources (e.g., volcanoes). However, these techniques remain limited to (in most cases extraordinarily) high trace gas fluxes. While the approach has led to substantial achievements, cross interference (with e.g., aerosol extinction or gases absorbing in the same spectral region) eventually preclude the quantification of lower fluxes, weaker absorbers or spectrally overlapping absorption of several gases with similar strength. For this reason, we will not further discuss low-spectral-resolution (i.e., resolving power $R = \frac{\lambda}{\delta\lambda_{\text{meas}}} < 100$, with the operational wavelength λ and the width of the resolved spectral interval $\delta\lambda_{\text{meas}}$) approaches in this work.

Fundamental light throughput advantages of Fabry-Pérot interferometers (FPIs, see Jacquinot, 1954; Jacquinot, 1960) can, on the one hand, be used to increase the spatio-temporal resolution of volcanic gas RS measurements without reducing the spectral resolution[1] (e.g.,Kuhn et al., 2014; Kuhn et al., 2019; Fuchs et al., 2021). On the other hand, FPIs enable the implementation of compact high resolution spectrographs with high light throughput (Kuhn et al., 2021). Here, we advocate the use of high resolution FPI spectrographs by demonstrating that they enable novel and improved volcanic gas measurements to fill substantial gaps in field observations. We frequently refer to the work of Kuhn et al. (2021), which describes the technique in more detail.

Spectroscopic RS measurements of volcanic plume gases in the atmosphere are routinely performed for SO_2 in the ultraviolet (UV) and, for higher SO_2 amounts, also in the thermal infrared (IR) spectral range. Autonomous ground- and satellite-based measurements provide global, long-term, and close-to-real-time data, also during eruptive periods (e.g., Prata and Bernardo, 2007; Galle et al., 2010; Carn et al., 2017; Warnach et al., 2019). So far, except for some studies on bromine monoxide (BrO, e.g., Hörmann et al., 2013; Lübcke et al., 2014), SO_2 remains the only species to be measured with such high spatio-temporal resolution. Contemporary RS techniques of other species, such as IR absorption and emission spectroscopy of e.g., HF, HCl, CO_2, CO, or SiF_4 (Mori et al., 1993; Francis et al., 1998; Sawyer et al., 2008; Notsu and Mori, 2010; Taquet et al., 2017) rely on instrumentation, which is less suited for autonomous operation in volcanic environments (see below). Therefore, similarly to DOAS measurements of water vapour, which require an extremely dry background atmosphere (see Kern et al., 2017), the available data on these gases is almost exclusively based on occasional field campaigns at specific volcanoes.

The resolving power of state-of-the-art volcanic trace gas RS measurements ranges between about 10^3 for measurements in the UV, visible and towards the thermal IR spectral range and about 10^4 for measurements in the short-wave IR (SWIR, at around 1–2 μm). The width of an individual absorption line of a molecule is however on the order of $\frac{\lambda}{\delta\lambda_{\text{line}}} \approx 10^5$.

In the UV-visible spectral range dense vibrational bands—consisting of many individual rotational transitions—cause characteristic absorption structures detectable with lower spectral resolution ($\frac{\lambda}{\delta\lambda} \approx 10^3$, e.g., SO_2 and BrO, see **Figure 1B**). Furthermore, scattered sunlight (skylight) or sunlight reflected from the Earth's surface can be used as light source, which is favorable since it allows flexible adjustments of viewing geometries and straight-forward autonomous measurement operation. For instance,

1 Nies, A., Heimann, J., Fuchs, C., Kuhn, J., Bobrowski, N., and Platt, U. (2022). Volcanic BrO and SO_2 imaging using Fabry-Perot interferometer correlation spectroscopy.

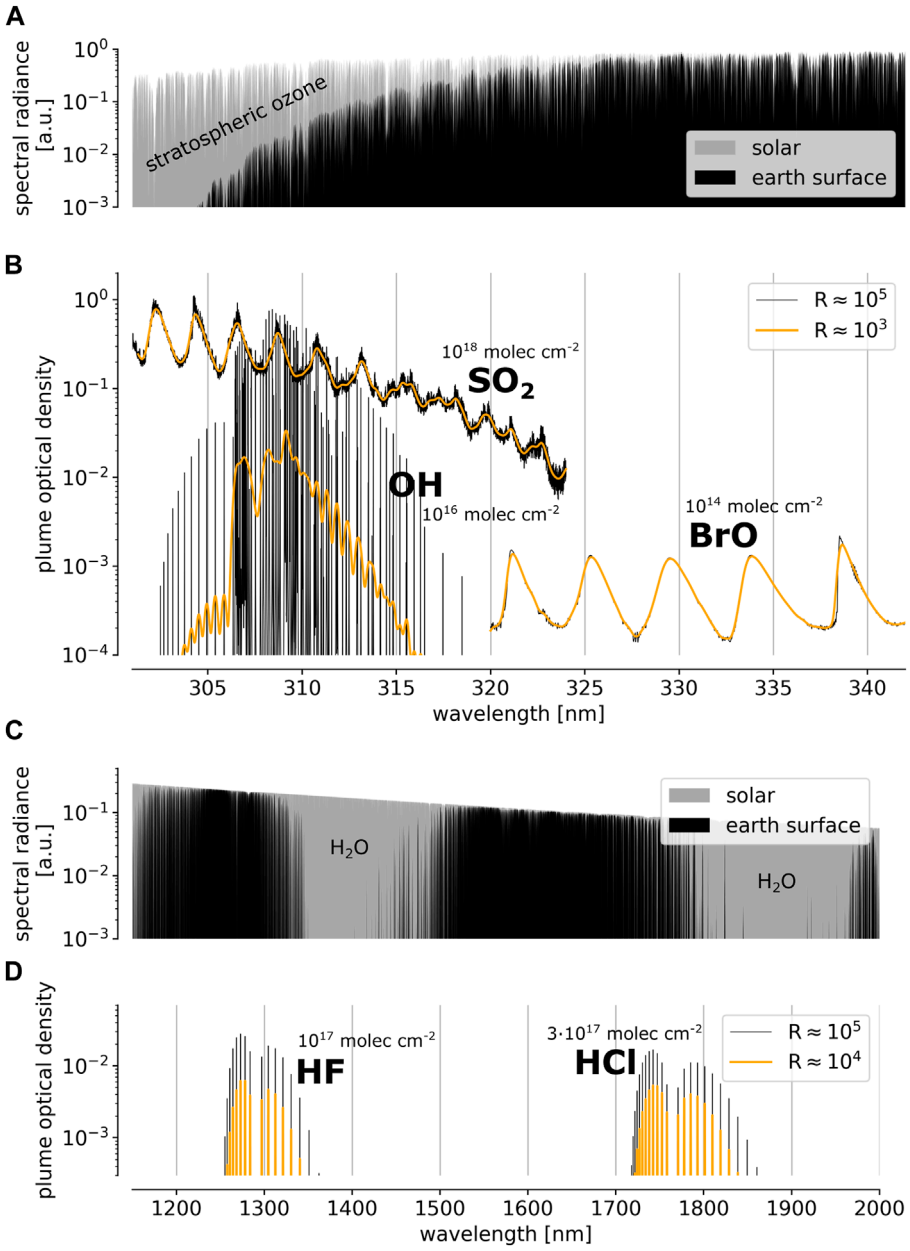

FIGURE 1
(A,C) show the spectral solar radiance arriving at the top of Earth's atmosphere (gray) and at Earth's surface (black) in the near UV and the SWIR spectral range. The corresponding panels **(B,D)** show, for the respective spectral ranges, the contributions of individual gases to the optical density of a typical volcanic plume (OH is only expected in the early and hot part). The black lines show the spectral absorption as observed with a resolving power R of 10^5 (BrO data is only available with R≈$6 \cdot 10^3$). The orange lines indicate the spectral absorption of the gases with the resolving power of conventional volcanic trace gas RS techniques. Data from Rufus et al. (2003); Fleischmann et al. (2004); Rothman et al. (2013).

satellite measurements with daily global coverage in near real-time are possible (e.g., Theys et al., 2019). Moreover, cross sections of volcanic plumes can be scanned by employing zenith-looking instruments on mobile platforms or by scanning a viewing angle sequence containing the plume (e.g., Galle et al., 2010). The limited skylight radiance demands a high light throughput of the employed spectrometers, which is facilitated by grating spectrographs (GS) with moderate resolving power (R ≈10^3). The typically low absorption optical densities of the background atmosphere and of volcanic plumes in the near UV (>300 nm) to visible spectral range (except for high SO_2 amounts at short UV wavelengths) allow the application of differential optical absorption spectroscopy (DOAS, Platt and Stutz, 2008). A reference spectrum recorded with the same instrument is commonly used to simultaneously correct imperfections (e.g., drifts) of the GS's optics and detector and spectral effects due to highly structured solar Fraunhofer lines (see **Figure 1A**). In this way, DOAS measurements can detect differential optical densities of volcanic plume constituents on the

order of 10^{-3}–10^{-4}, which, besides facilitating SO_2 and—under given conditions—H_2O measurements, led to the detection and quantification of secondary plume species like BrO and OClO (see e.g., Platt et al., 2018).

In the IR, a resolving power of up to $R \approx 10^4$ is commonly used to identify the ro-vibrational bands of absorbing molecules, such as HF, HCl or CO_2 in the SWIR (e.g., Butz et al., 2017) or HF, HCl, CO, OCS, SO_2 or CO_2 at longer wavelengths (e.g., Sawyer et al., 2008; Notsu and Mori, 2010). Because the IR background atmosphere is optically thick across large ranges of the spectrum (see e.g., **Figure 1C**), the spectrum is much more variable when for instance changing the measurement's viewing geometry. The evaluation of such data relies on a precise knowledge of the atmospheric state along the entire measurement light path (with increasing importance of temperature towards longer IR wavelength), particularly when the absorption lines are not well-resolved (i.e., $R \ll 10^5$). The commonly employed Fourier transform spectroscopy (FTS) technique is usually based on Michelson interferometers, which are inherently complicated and delicate instruments with moving parts. Although much progress has been made in FTS instrument design, it is unlikely that these instruments will reach the simplicity and stability of stationary spectrographs without moving parts (e.g., GSs). The interferograms are recorded in a time sequence while mechanically tuning the interferometer. This introduces a sensitivity to intensity fluctuations, which can be limiting for the measurements (see e.g., Notholt et al., 1997). Consequently, FTS measurements are basically restricted to solar occultation measurements at clear sky conditions or to using lamps or lava thermal emission as a light source. Recent photo-detector technology enables the implementation of GSs (which are largely insensitive to intensity fluctuations) in the SWIR spectral range (e.g., Crisp et al., 2017). However, GSs with high resolving power ($R \approx 10^4$–10^5) are bulky, heavy, and yield a low light throughput (Kuhn et al., 2021; Platt et al., 2021).

FPIs can yield a much higher light throughput than GSs even for high resolving powers (around 10^5) and allow the implementation of compact spectrograph set-ups without moving parts (Fabry and Buisson, 1908; Jacquinot, 1954; Kuhn et al., 2021). With that advantage they overcome fundamental limitations of present-day volcanic gas RS techniques in both, the UV and IR spectral range. Kuhn et al. (2021) describe and examine possible implementations of high-resolution FPI spectrographs. They find that, depending on the spectrograph implementation and size of the FPI clear aperture (limited by the manufacturing process), FPI spectrographs—based on recent FPI manufacturing technology—can yield a >100 times higher resolving power than GSs, without significantly reducing the light throughput or the compactness and stability.

Higher spectral resolution of RS observations generally leads to a more selective measurement, i.e., a better identification of the target gas. More details of the spectral absorption signal of a target gas are resolved and allow an accurate separation of overlapping absorption bands of different molecule species, drastically reducing interference by other gases. Moreover, in most cases, higher resolution increases the sensitivity of a measurement since the amplitude of the effective differential absorption cross sections is considerably enhanced, when observed with higher resolving power (see **Figures 1B, D**). Thus, for a given light throughput, higher spectral resolution lowers the detection limits of the respective gases, also enabling the detection of gas species that could not be measured so far.

Furthermore, the light throughput advantage of FPI spectrographs over GSs can extend the range of skylight-based RS applications at volcanoes towards the IR. By that, the number of plume constituents quantified continuously by autonomous RS measurements (e.g., from ground-based stations or from satellites; so far only SO_2 and larger BrO amounts) can be increased.

This article consists of two independent parts that demonstrate the feasibility and the benefits of the use of FPI spectrographs for volcanic gas RS: In **Section 2** we present a shoe-box-sized FPI spectrograph prototype reaching a resolving power of $R \approx 150{,}000$ in the UV. Measurements above a lava flow at Nyiragongo volcano (Democratic Republic of Congo) reach a ppb-level detection limit for OH, which is sufficient to detect the high amounts of OH (ppm range) reported in model studies of high-temperature volcanic gas emissions (e.g., Gerlach, 2004). Moreover, the study proves the excellent mobility and stability of high-resolution FPI spectrographs under harsh conditions and introduces evaluation approaches of the obtained high resolution spectra. In **Section 3** we present calculations on the feasibility of HF and HCl RS using skylight at around 1,278 and 1,742 nm and show that FPI spectrographs allow DOAS-type measurements of these gases in volcanic plumes.

2 Experimental proof-of-concept—Active remote sensing of OH radicals in hot volcanic gases

OH radicals are known for their high reactivity (Willbourn and Hinshelwood, 1946) and for driving central processes in atmospheric chemistry, such as the removal of pollutants and greenhouse gases from the atmosphere (e.g., Levy, 1971; Crutzen, 1974). While tropospheric OH levels are in the sub-ppt-range, simulations of the high-temperature emission of magmatic gases into the atmosphere find ppm-levels of OH within the hot and early plume (e.g., Gerlach, 2004; Roberts et al., 2019). Such high amounts of OH are very likely to substantially influence the magmatic gas composition, particularly the redox state it represents, within split-seconds after their emission (Kuhn, 2022; Kuhn et al., 2022), taking into question the results based on common thermodynamic equilibrium assumptions prevailing in volcanic gas geochemistry (see, e.g., Symonds et al., 1994; Moussallam et al., 2019). The development of kinetic emission models paired with measurements of volcanic OH (and other short-lived radicals) is crucial for understanding the chemical evolution of volcanic gas plumes in the atmosphere.

OH absorbs in the UV spectral range at around 309 nm. The absorption spectrum consists of discrete ro-vibronic lines (**Figure 1B**). Their selective detection requires high spectral resolution (around 2 pm), formerly only provided by bulky and intricate laser- and GS-systems (Stone et al., 2012). **Section 2.1** and **Section 2.2** describe a compact FPI-based prototype set-up capable of quantifying volcanic OH.

OH is only expected in gas emissions with high temperature (e.g., Roberts et al., 2019; Kuhn, 2022; Kuhn et al., 2022). Nyiragongo - and the neighboring Nyamulagira—volcano are

located in the Western Branch of the East African Rift in the Democratic Republic of Congo. Nyiragongo is known for its lava lake, which, in the recent decades, often was among the largest on the planet. It is characterized by strong dynamics and frequent changes in activity (e.g., Le Guern, 1987; Bobrowski et al., 2017; Valade et al., 2018), which can lead to disastrous eruptive events (e.g., Tedesco et al., 2007; Smittarello et al., 2022). On the other hand, these dynamic changes can lead to periods (e.g., on the order of months to years), in which the lava lake and active lava flows are relatively easily accessible (e.g., Pouclet and Bram, 2021). These are rare opportunities for sampling the hot gas emissions of lava lakes (e.g., Le Guern, 1987) and to examine the still poorly understood high-temperature interface between magma and the atmosphere, which is likely to significantly influence all open-vent volcanic gas emissions (Kuhn et al., 2022). **Section 2.3** describes measurements with the introduced prototype performed at an active lava flow within the crater of Nyiragongo volcano in February 2020.

2.1 Instrumentation

The set-up has been designed and manufactured at the Institute of Environmental Physics in Heidelberg. **Figure 2** illustrates the instrument set-up and outlines the principle of the FPI spectrograph. The mobility of the set-up able to perform spectroscopic measurements with $R \approx 150,000$ is unprecedented in volcanic and atmospheric RS. Open-path optics, light source, spectrograph, laptop, batteries and casing sum up to about 20 kg and can be carried by one person in a backpack. The total power consumption mainly depends on sensor cooling and is generally well below 20 W, which means a light-weight battery can provide sufficient power for several hours of continuous operation.

2.1.1 Compact open-path optical setup

The compact open-path setup (see **Figures 2A**, **3C, E**) consists of a UV light emitting diode (LED, 305 nm centre wavelength, ca. 10 nm full width at half maximum) within a box (10 cm × 10 cm × 5 cm). The light is coupled into 6 "transmitting" quartz fibers and, after being collimated by a telescope (71 mm clear aperture, 300 mm focal length), is sent across the gas volume to be sampled. A retro reflector reverses the light path and, after traversing the gas volume for a second time, feeds the light back into the telescope, where it is coupled into a single "receiving" quartz fiber leading to the entrance slit of the FPI spectrograph (see, e.g., Merten et al., 2011, for details).

2.1.2 FPI spectrograph prototype

The concept and implementation of FPI spectrographs are described in detail in Kuhn et al. (2021). **Figures 2B–D** illustrate the functioning principle of the prototype (ca. 8 L volume and 5 kg weight) used in this study.

The employed FPI etalon (custom-built by SLS Optics Ltd.) has a free spectral range (spectral separation of transmission orders) of ca. 0.2 nm at 300 nm. Its finesse (ratio between free spectral range and full width at half maximum of a transmission peak) is about 95 across a clear aperture of 5 mm (**Figure 2C**). The individual FPI transmission orders are separated by the superimposed dispersion of a grating (grating order sorting mechanism, OSM, see also Kuhn et al., 2021). First, the light enters the slit of a commercial miniature GS, serving as order sorting GS (OSGS, F-number: 3.9, focal length: 75 mm, slit width: 50 μm, linear dispersion: 5.34 nm mm^{-1}, $R \approx 1,100$). By using a second imaging optics in series, the spectrum of the OSGS (intermediate image) is re-imaged onto a focal plane imaging detector (UV-enhanced charge coupled device, CCD, ca. 60% quantum efficiency at 310 nm, 1,024 × 1,024 pixels of 13.3 μm pitch). Within the second imaging optics the FPI is placed in a collimated beam (**Figure 2B**). The slightly different incidence angles of the light of the collimated beam onto the FPI are then separated in the focal plane in concentric rings of equal spectral FPI transmission. The GS dispersion separates the individual FPI transmission orders (similar to the descriptions by e.g., Fabry and Buisson, 1908; Vaughan, 1989).

Figure 2D shows the spectrum of the UV LED with the absorption lines of OH (dark spots) from a burner flame inside the light path. The OSGS dispersion is aligned along the horizontal detector dimension. For this prototype, the individual FPI transmission orders slightly overlap and cause close-to-vertical stripes of high intensity between the orders. As mentioned above, each order corresponds to ca. 0.2 nm. The radial symmetry of equal FPI transmission is indicated by the shape of the OH absorption lines on the detector plane. As the properties and behavior of the optical components are known, the spectra can be analysed and evaluated using an instrument model (as described in **Section 2.2** below).

2.1.3 Processing of the spectra

Prior to their evaluation, the spectra recorded with the FPI spectrograph prototype are corrected for the CCD detector's dark signal and sensitivity characteristics. The dark signal is approximated by a dark spectrum recorded with unchanged detector settings in temporal proximity to the measurement to be corrected. In this study, the dark spectrum was recorded with the light source turned off in the otherwise unchanged optical setup. Moreover, a flat field image recorded in the laboratory corrects the sensitivity differences of the individual detector pixels. In order to reduce photon shot noise, sequentially recorded spectra are co-added after their individual correction.

2.2 Instrument model

Here we describe a model that allows the evaluation of spectra recorded by the camera in the focal plane of the FPI spectrograph. It refers to the grating OSM implementation of an FPI spectrograph (as used in this study), but it can similarly be used for interferometric OSM approach (Kuhn et al., 2021). The grating OSM implementation of an FPI spectrograph employs an OSGS in line with the FPI imaging unit (see **Section 2.1.2** above).

The spectral characteristics (λ denotes wavelength) of the optical components in use are well-determined and enable accurate modeling of the spectral instrument transfer function $T_{\text{inst}}(\lambda;\ i,j)$, which converts a spectral radiance to measured signals at each detector pixel (i,j). The recorded signal is determined by the superposition of the OSGS's spectral transmission function $H(\lambda;\ i,j)$ and the FPI transmission spectrum $T_{\text{FPI}}(\lambda;\ i,j)$:

$$T_{\text{inst}}(\lambda;i,j) = H(\lambda;i,j) \cdot T_{\text{FPI}}(\lambda;i,j) \quad (1)$$

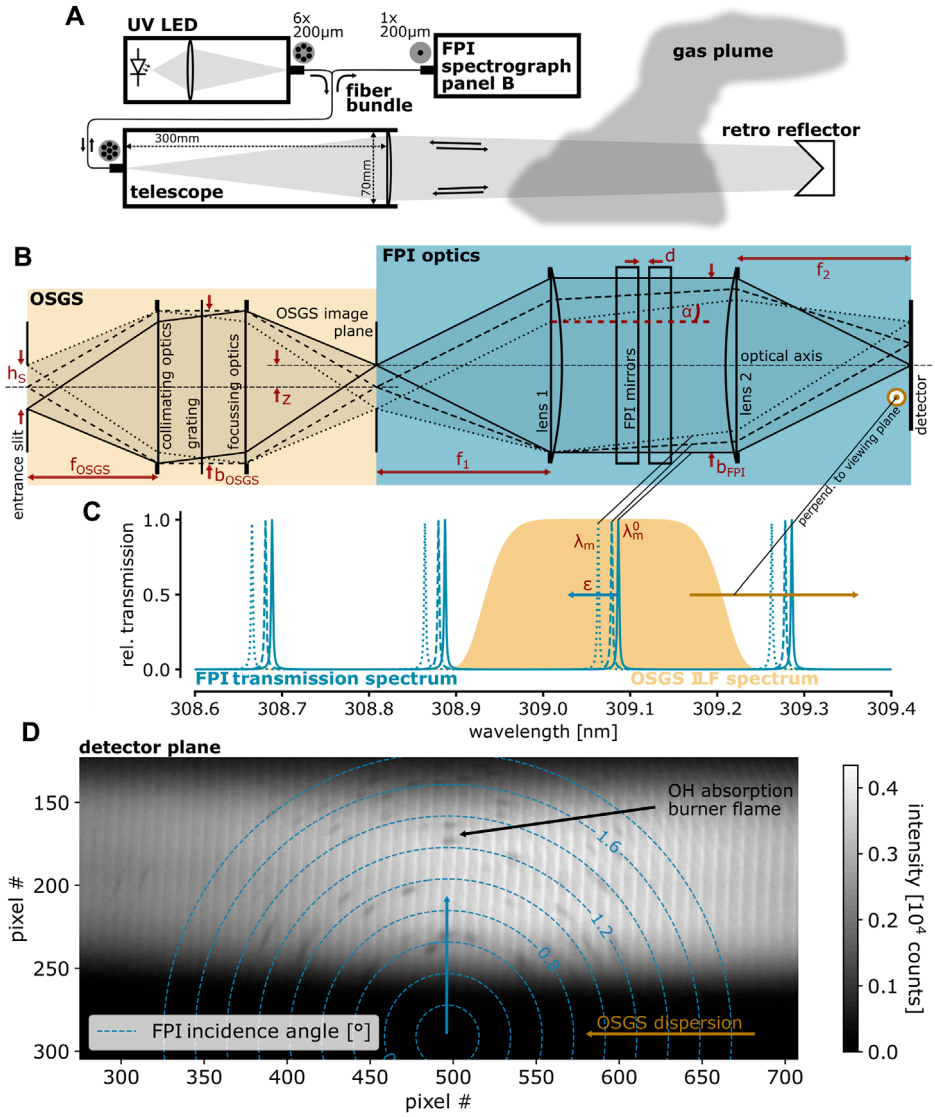

FIGURE 2
(A) Open-path set-up as used for the measurement at Nyiragongo: The light of a UV LED is coupled into 6 "transmitting" optical fibres, collimated by the telescope, sent across the volcanic plume, reflected back by a retro reflector, coupled into a single "receiving"fiber by the same telescope, finally reaching the FPI spectrograph. **(B)** Optical schematic of the FPI spectrograph with grating OSM: The entrance slit of the OSGS is imaged onto the FPI spectrographs detector. The superposition of linear grating dispersion and radially symmetric FPI transmission is indicated in **(C)**, illustrating how the FPI's (blue) and the GS's (brown) spectral transmission change across the detector. **(D)** Spectrum of a UV LED after traversing a burner flame. Absorption lines of OH are visible, aligned along the indicated lines of equal FPI incidence angle. Parts of this figure are adapted from Kuhn et al. (2021).

Broadband spectral contributions (e.g., lens transmission, grating efficiency, etc.) are not considered here since they are negligible on the narrow spectral scales of interest. The OSGS's line function, i.e., its spectral transmission, can be approximated with a higher order Gaussian (e.g., Beirle et al., 2017):

$$H(\lambda;i,j) = \exp\left(\frac{(\lambda_c(i)-\lambda)^2}{2c^2}\right)^p \quad (2)$$

with a full width at half maximum $\delta_H = 2c\sqrt{2(\log 2)^{\frac{1}{p}}}$ for different shapes, determined by the order p and the parameter c. The centre wavelength λ_c of the instrument line function depends on the pixel location i on the detector in grating dispersion (here horizontal) direction and is determined *via* the linear dispersion of the OSGS and a reference wavelength.The FPI transmission spectrum is given for a single light beam (index sb) by the Airy function (e.g., Perot and Fabry, 1899):

$$T_{FPI,sb}(\lambda;i,j) = \left[1 + \frac{4\mathcal{F}^2}{\pi^2}\sin^2\left(\frac{2\,n\,d\,\pi}{\lambda}\cos(\alpha(i,j))\right)\right]^{-1} \quad (3)$$

For the FPI spectrograph the separation of the reflective surfaces d (ca. 240 μm in this study) and the finesse $\mathcal{F}$ (ca. 95 in this study) are fixed. n is the refractive index of the medium between the reflective surfaces and n-1 is assumed proportional to the ambient pressure (as the used air-spaced etalon is not sealed). The incidence angle $\alpha(i,j)$ is dependent on the location on the detector, i.e., on the individual

FIGURE 3
(A) Sketch of the crater area of Nyiragongo volcano (February 2020) with measurement sites I and II. **(B)** Photograph of the crater area. **(C)** The setup of the camping stove calibration measurement in a shelter at the crater rim (site II). **(D)** Retro reflector for the measurement at the active lava flow within the crater [**(E)**, site I]. Parts of this figure are adapted from Kuhn et al. (2022).

pixel (i,j) see Figure 2B:

$$\alpha(i,j) = \sqrt{\arctan^2\left(\frac{(i-i_{oa})\,d_{pix}}{f_2}\right) + \arctan^2\left(\frac{(j-j_{oa})\,d_{pix}}{f_2}\right)} \quad (4)$$

with the pixel size d_{pix}, the focal length f_2 of the imaging lens and the pixel (i_{oa},j_{oa}), where the FPI surface normal (generally the optical axis) intersects the image plane (i.e., the detector surface).

Furthermore, the spatial extent of the detector pixels needs to be accounted for. It imposes a slight divergence of the beams reaching an individual pixel, which can be approximated by a cone geometry delimited by the pixel size and the focal length of the imaging lens. Integrating the individual single beam FPI transmission spectra along the cone's dimensions yields the effective FPI transmission spectrum for each pixel (see also Fuchs et al., 2021):

$$T_{FPI}(\lambda;\alpha(i,j)) \approx 2\pi \int_{\alpha-\tan\frac{d_{pix}}{2f_2}}^{\alpha+\tan\frac{d_{pix}}{2f_2}} T_{FPI,sb}(\lambda;\theta)\,\sin\theta \mathrm{d}\theta \quad (5)$$

The angular range delimited by a pixel is almost independent of the pixel's location. Accounting for finite pixel size leads to a slight blurring of the FPI transmission spectra at pixels that correspond to higher FPI incidence angles α (see Figure 2C).

The instrument transfer function (Eq. 1) can now be used to convert literature spectra to detector images. This simple model is sufficient to fit trace gas absorption spectra to measured optical density distributions on the detector across large fractions of the spectrum (see Section 2.3).

2.3 Measurements at Nyiragongo volcano, DR Congo

We present measurement results from a field campaign at Nyiragongo volcano in the Democratic Republic of Congo during February 2020. Figure 3 shows schematics and photographs of the measurement site. In the following, we describe an instrument characterization measurement at the crater rim (site II in Figures 3A, C) and a measurement made above (ca. 1 m) an active lava flow within the crater region (site I in Figures 3A, E).

2.3.1 Characterization measurement at the crater rim

A characterization measurement of the instrument set-up was made inside a small shelter at the crater rim. The measurement light path (ca. 1 m) of the set-up sketched in Figure 2A traverses the flame of a camping stove, providing a high amount of OH (see, e.g., Cattolica et al., 1982). Figure 4A shows the spectrum of the UV LED on the FPI "spectrograph's" detector plane (the flame radiance is negligible). Bright vertical stripes are due to a remaining overlap of the individual FPI transmission orders (see Section 2.1.2; Figure 2). OH absorption lines induce distinct dark spots within the spectrum, aligned to the circles of equal FPI incidence angle (see Figure 2). The steps of the further evaluation are:

1. A region of interest (ROI) for the spectral evaluation is defined (see Figures 4A, B).

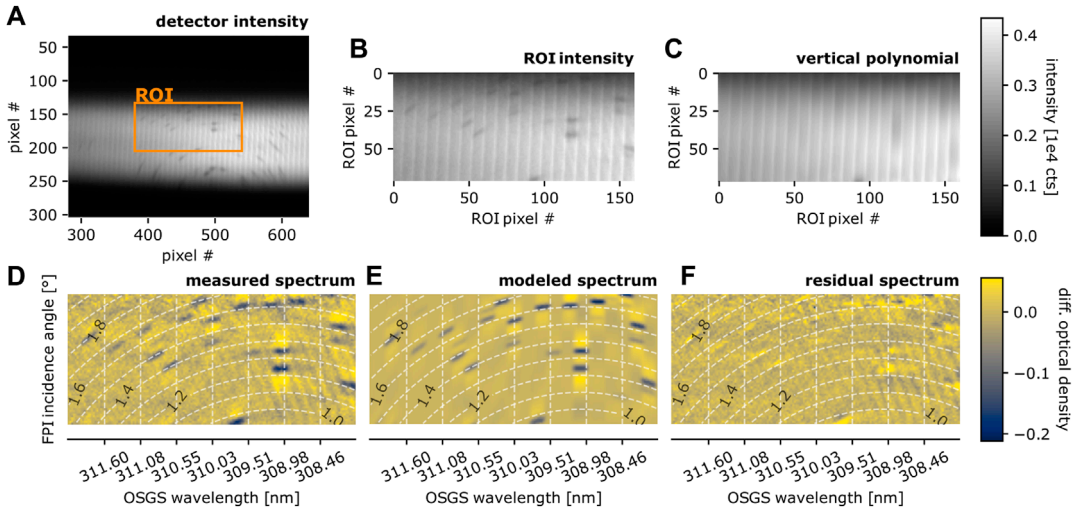

FIGURE 4
Calibration measurement at site II (Figure 3C), absorption spectrum of the flame of a camping stove: **(A)** Intensity distribution on the detector plane with indicated region of interest (ROI) used for the spectral evaluation. **(B)** Individual vibronic OH absorption lines are visible as dark spots within the ROI. **(C)** Column-wise polynomial fit to remove slow intensity gradients and the vertical bright stripes (induced by overlapping orders). **(D)** Differential narrow-band optical density image, i.e., logarithmic ratio of intensity distributions in **(B,C)**. **(E)** Modeled differential optical density, i.e., logarithmic ratio of modeled intensity image (model parameters in Table 1) and a column-wise (vertical) polynomial fit. **(F)** Difference between **(D,E)**. Figure adapted from Kuhn, 2022

2. Within the ROI column-wise (vertical) polynomial fits (here 7th order) approximate the broadband intensity gradients, including the vertical bright striping (see Figure 4C).
3. The intensity distribution obtained from step 2 is used as reference intensity I_0 in order to approximate the differential (narrow-band) optical density τ of the spectrum according to $\tau = \log\frac{I_0}{I}$ with I being the intensity distribution of the spectrum (Figure 4B). Figure 4D shows the result.
4. Figure 4E shows the modeled differential optical density spectrum. It is obtained by modeling the intensity distribution on the detector (according to the procedure described in Section 2.2, above) and, subsequently, performing step 2 and 3.
5. By varying the OH column density and temperature within the model the residual (Figure 4F, difference between measured and modeled differential optical density image) is minimized.

The measured absorption spectrum of OH is well reproduced by the model (parameters in Table 1, OH absorption data from Rothman et al., 2013). The OH mixing ratio in the flame is approximately:

$$X_{OH} = \frac{S_{OH}\, k_B\, T}{L\, p} \tag{6}$$

with the temperature T, pressure p, light path length within the absorber L, and the measured OH column density S_{OH}. The resulting mixing ratio of $X_{OH} = 3.5 \cdot 10^{-4}$ for a light path of L = 6 cm (i.e., 2 cm × 3 cm) is realistic (Cattolica et al., 1982). Remaining uncertainties are introduced by e.g., the unknown distribution of flame temperature along the light path, which could be included in future evaluations.

TABLE 1 Model parameters for measurement at site I and II, see Figures 5E, 4E.

Parameter	Unit	Site I (Lava flow)	Site II (Burner flame)
FPI			
d	μm	239.854	
$\mathcal{F}$		95.2	
n_{air}(1013hPa)		1.0002916	
pressure	hPa	660	645
OSGS			
λ_c	nm	308.96	309.15
δ_H	nm	0.2065	
p		2.42	
D_{GS}	nm pix^{-1}	0.02625	
Optics			
f_2	mm	70.75	
d_{pix}	mm	0.013	
i_{oa}	pix	493.6	
j_{oa}	pix	280.3	
Spectral			
$S_{SO^{\cdot}2}$	molec cm^{-2}	$5.21 \cdot 10^{17}$	-
S_{OH}	molec cm^{-2}	-	$7.8 \cdot 10^{15}$
T_{OH}	K	-	1760

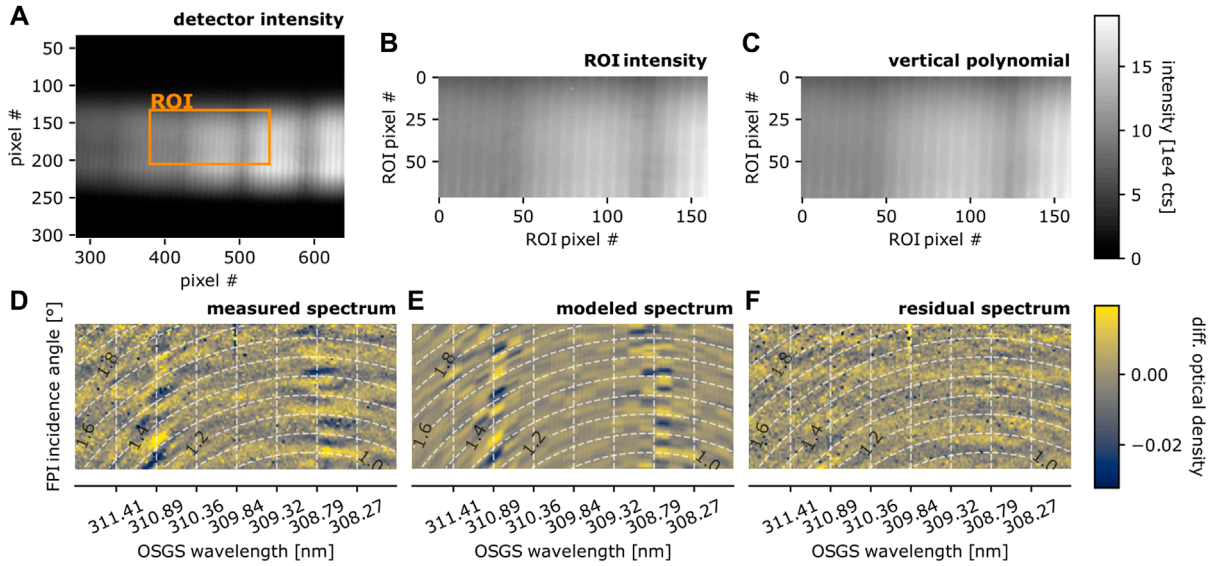

FIGURE 5
Measurement above the active lava flow at site I (**Figure 3E**). Panel designations are equal to **Figure 4**. The broad-band (nanometre-scale) absorption bands of SO_2 (see **Figures 1B**, **6**) are visible in the intensity distributions **(A,B)**. **(D)** Shows the narrow-band (picometre-scale) SO_2 absorption. The model (with adjusted pressure and OSGS wavelength, **Table 1**) shows good agreement with the measurement with a realistic SO_2 column. OH absorption lines, present within the covered spectral range are not observed, which limits maximum OH amounts to about 20 ppb. Figure adapted from Kuhn, 2022.

This simple experiment demonstrates the capability of the FPI spectrograph prototype to resolve the OH absorption and that the instrument model is suited to quantitatively evaluate the recorded spectra.

2.3.2 Measurement above an active lava flow within the crater

We recorded spectra with a measurement light path crossing about 1 m above an active lava flow (velocity of about 20–50 cm·s^{-1}). On one side of the lava flow the retro reflector is placed on the ground. From the other side the telescope and FPI spectrograph are operated (**Figures 3D, E**). **Figure 5** illustrates the result of the measurement. The measurement spectrum is the sum of 100 individual spectra with 10 s integration time each. The evaluation is performed according to the above described procedures (**Section 2.3.1**; **Figure 4**).

The broad vertical dark stripes in the spectrum (**Figures 5A–C**) represent the broad-band (nanometre-scale) absorption structures of SO_2, which are used for conventional SO_2 DOAS measurements. The differential optical density image (**Figure 5D**) shows the narrow-band (picometre-scale) absorption features of SO_2, which are again well reproduced by the model using absorption data from Rufus et al. (2003). Despite uncertainties such as unknown sample gas temperature and behavior of the absorption of SO_2 at higher temperature, the residual spectrum is dominated by a homogeneous noise pattern with a root mean square in the range of 0.01. The noise likely is introduced by inaccuracies in the detector's dark signal correction, as a drift of the detector temperature (from −6° to −1°) during the measurement was observed. The dark signal was therefore approximated in lab measurements retrospectively, which was only possible with an uncertainty due to hysteresis effects in the detector electronics.

Figure 6 indicates the wavelength coverage of the evaluation of the lava flow measurement (**Figure 5**). The gray shaded areas in the spectrum (right panel) show the wavelength range that is covered by the individual FPI transmission orders separated by the grating on the FPI spectrograph's detector plane. The color code indicates the location of each FPI transmission order on the detector plane (left panel). The spectral optical density of SO_2 with the retrieved column density (S_{SO_2} = 5.21 ·10^{17} molec cm^{-2}) is plotted together with the optical density of an OH column of 10^{15} molec cm^{-2}. Strong OH absorption lines appear within the FPI "spectrographs" wavelength coverage and the evaluation ROI, allowing the quantification of an upper limit of the OH amount within the sampled gas.

According to **Figure 6** several strong OH absorption lines are covered by the evaluation ROI, for example, between 308 and 308.5 nm. Their amplitude for a column density of 10^{15} molec cm^{-2} exceeds an optical density of 0.1. Thus, within the noisy residual (root means square of ca. 0.01, **Figure 5F**) it should be possible to detect OH absorption peaks corresponding to a column density of ca. 2 ·10^{14} molec cm^{-2}. For an assumed gas temperature between 800 K and 1,200 K and a light path of 20 m within the hot gas, the OH detection limit would correspond to a mixing ratio of 17–25 ppb. For the same assumptions on the light path, the retrieved SO_2 column corresponds to a mixing ratio of 44–64 ppm.

2.4 Discussion

In this exploratory field study we could not detect volcanic OH. The main reason for that might be a low gas temperature and the low emission of the probed lava flow (indicated by the relatively low SO_2 levels measured). Nevertheless, it demonstrates central aspects of the field-applicability and the substantial added value

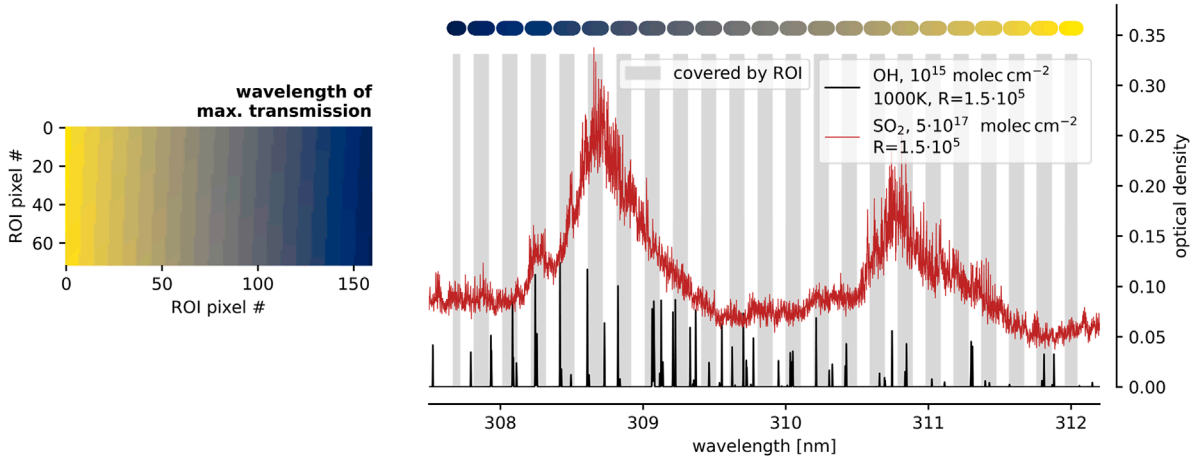

FIGURE 6
The right panel shows the spectral optical density, calculated from literature absorption cross sections, of given amounts of SO_2 (red, as measured above the lava flow) and OH (black, hypothetical value of 10^{15} molec cm^{-2}) observed with R = 1.5 ·10^5. The gray shaded areas indicate the spectral range covered by individual FPI transmission orders within the ROI used for the evaluation of the lava flow measurement (**Figure 5**). The colour above the respective FPI transmission order indicates its location within the ROI (in the left panel). Figure adapted from Kuhn, 2022.

through FPI spectrograph measurements for volcanic gas studies. The presented FPI spectrograph measurements yield high spectral resolution ($R \approx$ 150,000), exceeding that of former volcanic gas RS measurements by at least one order of magnitude. Furthermore, it shows excellent stability under field conditions. The introduced evaluation using high-resolution spectral absorption data enables an accurate calibration of the spectrograph by directly adjusting physical parameters in the instrument model. The burner flame measurement at the crater rim and the measurement at the lava flow within the crater were made on the same day, separated by a few hours and a steep decent of 300 vertical metres into the crater with the instrument set-up in a backpack. Even under the harsh conditions (moist, sunny, hot, dusty, windy) the FPI spectrograph's calibration remained constant, except for a slight shift of the OSGS wavelength axis (see **Table 1**). This slight spectral shift might have been introduced by mechanical impacts during transportation and its effects could readily be accounted for by the instrument model within the SO_2 evaluation (i.e., re-calibration using the high-resolution SO_2 absorption features).

Beyond this proof-of-concept study, the instrument set-up and the spectral evaluation can be significantly improved. Avoiding overlapping orders (e.g., higher OSGS dispersion) and a more appropriate shielding of the detector (to sustain temperature stabilization) would provide photon-shot-noise-limited spectra. Moreover, a FPI spectrograph with interferometric OSM instead of the grating (i.e., using a band-pass filter instead of the OSGS) can increase the light throughput by a factor of 100 (basically by reducing the spectral coverage, see Kuhn et al., 2021, for details). Temperature measurements and high-temperature data of absorption cross sections (e.g., for SO_2) would further improve the spectral evaluation. In combination with an optimized (longest possible) light path inside the plume, all these measures might lower the detection limit for OH by another two orders of magnitude. Infrastructural challenges related to the accessibility of hot volcanic gas emissions (e.g., volcano-related hazards) would remain a limiting aspect for OH radical quantification in high-temperature volcanic gases. The placement of retro reflectors by unoccupied aerial vehicles would significantly increase the number of potential measurement sites.

3 Theoretical proof-of-concept—Remote sensing of HF and HCl in volcanic plumes using skylight

Volcanic halogens play significant roles in many volcanic processes and impact the local to regional volcanic environment and Earth's atmosphere (see, e.g., Aiuppa et al., 2009, and references therein). As halogens tend to degas from the magma at rather shallow depth (e.g., Spilliaert et al., 2006), continuous quantification of volcanic halogen emissions (similar to present-day volcanic SO_2 quantification, e.g., Galle et al., 2010; Kern et al., 2022) would substantially contribute to improving models of magma dynamics and degassing and bear a high potential for volcanic monitoring.

Most RS measurements of HF and HCl were only possible with FTS using lamps, lava thermal emission, or direct sunlight (solar occultation) as light source (e.g., Francis et al., 1998; Sawyer et al., 2008; Butz et al., 2017). The reason for this limitation is in part the limited light throughput of FTS instruments. In addition, they are sensitive to intensity fluctuations in the atmosphere, as interferograms are recorded in a time-sequence while delicate optics are tuned mechanically. Moreover, when using sunlight as light source, limited spectral resolution leads to the requirement of an exact knowledge of the atmospheric background spectrum for the evaluation (e.g., *via* additional O_2 measurements and radiative transfer modeling, see e.g., Butz et al., 2017).

For spectrographs, i.e., spectrometers that record all spectral channels simultaneously (like GSs and FPI spectrographs), the influence of temporal intensity variations is negligible and instruments are implemented without movable parts. The thereby gained simplicity, stability, and lower power consumption is an essential advantage for the (automated) employment in harsh volcanic environments. The implementation of spectrographs in the SWIR has become feasible by the development of appropriate focal plane detectors (e.g., Crisp et al., 2017). However, GS implementations with the resolving power required for accurate trace gas retrievals (typically $R = 10^4$-10^5 in the SWIR) and a high light throughput are large and heavy and thus hardly suited for most volcanic applications.

Here, we investigate the feasibility of passive RS measurements of HF and HCl in volcanic plumes using FPI spectrographs and skylight as a SWIR light source. The photon budget calculations rely on skylight radiance estimates (**Section 3.1.1**) and the quantification of the light throughput of FPI spectrographs relative to that of GSs (based on results of Kuhn et al., 2021; **Section 3.1.2**). We propose suitable wavelength windows and optimized resolution of the FPI spectrograph and demonstrate the feasibility of a DOAS-type detection of HF and HCl in volcanic plumes by using skylight (**Section 3.2**).

3.1 The photon budget of skylight measurement geometry

A trace gas can be detected by spectral RS once its effective differential absorption along the measurement light path $\delta\bar{\tau}$ exceeds the noise of the recorded spectrum. We assume the measured spectra to be photon-shot-noise-limited. Photon-shot-noise is proportional to the square root of the counted photo-electrons N per spectral interval. The photo-electron flux J_{ph} (e^- s^{-1}) at the detector for an individual spectral channel of the spectrograph is given by the incoming radiance I (photons mm^{-2} sr^{-1} nm^{-1} s^{-1}) and the spectrograph's light throughput k (e^- ph^{-1} mm^2 sr nm, including the quantum efficiency of the detector):

$$J_{ph} = k\,I \tag{7}$$

The noise of an optical density measurement $\tau = \log\frac{J_{ph,0}}{J_{ph}}$ for weak absorbers (i.e., $J_{ph,0} \approx J_{ph}$) and an exposure time δt is then:

$$\Delta\tau \approx N^{-\frac{1}{2}} = \left(J_{ph}\,\delta t\right)^{-\frac{1}{2}} = \left(k\,I\,\delta t\right)^{-\frac{1}{2}} \tag{8}$$

The effective differential optical density of an absorber $\delta\bar{\tau}$ and the light throughput k of the spectrograph are dependent on the spectral resolution, which has to be chosen to optimize the signal to noise ratio (SNR) and to provide sufficiently accurate and selective spectroscopic detection. In the following, we approximately quantify the skylight radiance and use light throughput estimates for GSs and FPI spectrographs by Kuhn et al. (2021).

3.1.1 The spectral radiance of skylight

The radiance of the daytime sky (i.e., the scattered sunlight across the sky) can be extremely variable, strongly depending on, e.g., aerosol and cloud conditions. This variability remains rather moderate at UV-visible wavelength (i.e., usually varying by less than one order of magnitude, see, e.g., Wagner et al., 2004; 2014). The strong spectral dependence of Rayleigh scattering and the generally much weaker spectral dependence of light scattering on aerosol and cloud droplets cause a rapidly increasing contrast between the blue sky and aerosol layers or clouds towards IR wavelengths. We use the parametrization by Ångström (1929) to approximate the spectral scattering efficiency ϵ with the Angstrom exponent γ:

$$\epsilon(\lambda) \propto \lambda^{-\gamma} \tag{9}$$

In the coarse assessment of the skylight radiance in this work, we assume:

1. A blackbody spectrum (5,800 K) and a solar line list of Toon (2015) are used to approximate the solar spectrum. The absorption of tropospheric H_2O, CO_2, O_2, CH_4 (atmospheric background values, constant temperature T = 300 K; Rothman et al., 2013), and stratospheric O_3 (vertical column density of ca. 300 Dobson units, 223 K, Serdyuchenko et al., 2014) is included to approximate the atmosphere's transmission. In order to account for common measurement viewing geometries, we assume a single scattering atmospheric light path roughly corresponding to a viewing elevation angle of ca. 20° (corresponding to an about 3-fold extension compared to the vertical path).
2. At 400 nm, the radiance of the blue sky, an aerosol layer, and that of a cloud are the same.
3. The radiance of the blue sky I_{bs} is governed by Rayleigh scattering (i.e., $\gamma = 4$, Strutt, 1871), i.e.,:

$$I_{bs} = I_{400}\left(\frac{400\,\text{nm}}{\lambda}\right)^{-4} \tag{10}$$

4. Angstrom exponents for aerosols in the atmosphere range from about 0.7 to 2 (e.g., Martınez-Lozano et al., 1998), while the radiance of clouds, due to the larger particle size parameter is even less dependent on wavelength (see e.g., Stephens and Platt, 1987). We approximate the scattering efficiency of clouds to be independent of wavelength (i.e., $\gamma = 0$) and that of aerosol particles (I_{ae}) to scale according to $\gamma = 1$:

$$I_{ae} = I_{400}\left(\frac{400\,\text{nm}}{\lambda}\right)^{-1} \tag{11}$$

5. The skylight radiance I_{al} of the sky covered by an aerosol layer with moderate aerosol optical density τ_{al} (AOD, $\tau_{al} < 1$) is approximated by the sum of blue sky radiance and that of aerosol scattering, weighted with the AOD:

$$I_{al} = \left(1 - \tau_{al}\right) I_{bs} + \tau_{al}\, I_{ae} \tag{12}$$

The variability of the radiance between different types of clouds or different types of aerosol layers introduces a large uncertainty to this simplified approximation of skylight radiances. Particularly for optically very thick clouds the radiances can be much lower. Nevertheless, the above assumptions facilitate a rough but reasonable approximation for the assessment of the photon budget of atmospheric and volcanic RS instruments.

Figure 7 summarises the above assumptions and indicates the resulting spectral skylight radiances of 1) the blue sky, 2) an aerosol layer with slant AOD = 0.2, and 3) a white cloud (relative to 400 nm).

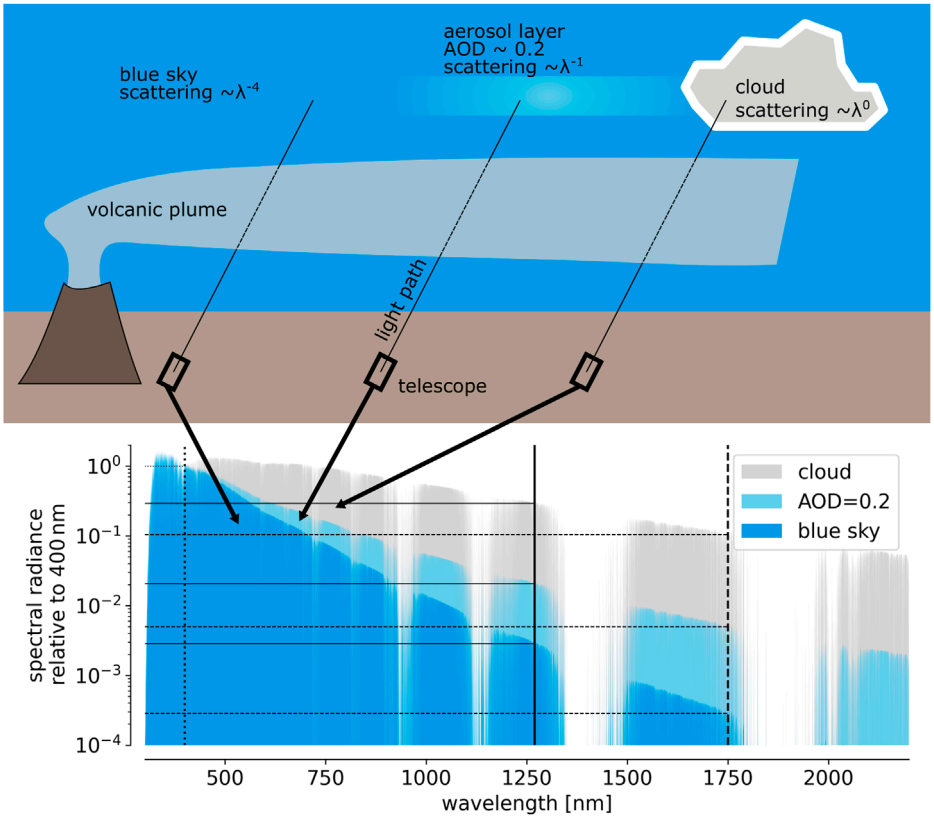

FIGURE 7
Approximation of the relative spectral skylight radiance for different sky conditions. In the blue spectral range (ca. 400 nm) the radiance of the blue sky, an aerosol layer and that of a cloud are similar. Towards IR wavelength the contrast between the different sky conditions increases drastically, which is approximated by representative Angstrom exponents.

3.1.2 The relative light throughput of GS and FPI spectrographs

The light throughput k of a spectrograph determines the flux J_{ph} of photons with wavelength between λ and $\lambda + \delta\lambda$ at the detector for a given incident spectral radiance $I(\lambda)$ (see Eq. 7). The light throughput of a spectrograph is determined by the etendue E, the spectral resolution $\delta\lambda$ and losses μ related to optical components and the detector:

$$k = E\,\delta\lambda\,\mu \tag{13}$$

With the assumption that the losses μ are similar for both, GS and FPI spectrograph, their light throughput for a given resolving power R can be compared based on the etendue. The etendue of a compact GS E_{GS} is essentially determined by the square of its slit width w_S. Furthermore, the ratio of the GS's principal focal length f to the slit width approximates its resolving power (Kuhn et al., 2021):

$$E_{GS} \approx \frac{\pi}{4} w_S^2 = \frac{\pi f^2}{4 R^2} \tag{14}$$

The etendue E_{FPI} that can be reached by high-resolution FPI spectrographs is given by (Jacquinot, 1954; Kuhn et al., 2021):

$$E_{FPI} \approx \frac{\pi^2 b_{FPI}^2}{2 R} \tag{15}$$

It is basically determined by the FPI's clear aperture diameter b_{FPI} and scales, in contrast to GSs, only with the inverse resolving power.

3.2 SWIR DOAS measurements of HF and HCl using skylight

3.2.1 Resolving power

The SWIR spectral range is characterized by many narrow and strong absorption lines of atmospheric gases, mainly H_2O, CO_2, O_2, and CH_4 (see, e.g., **Figures 1C, 7**). Since all of these gases either are present in large amounts or show a more or less uniform distribution in the atmosphere, the strength of their absorption within scattered skylight spectra strongly depends on the atmospheric light path, which is for instance influenced by the viewing geometry and the atmospheric state in terms of aerosol content or clouds. Precise knowledge of the measurement light paths and the atmospheric state along these light paths is required, which, in practice, limits the precision and accuracy of remote detection of for instance CO_2 gradients in the atmosphere (e.g., volcanic plumes, see, e.g., Butz et al., 2017).

While being emitted by volcanoes in large quantities, HF and HCl exhibit very low atmospheric background levels. Thus, similar

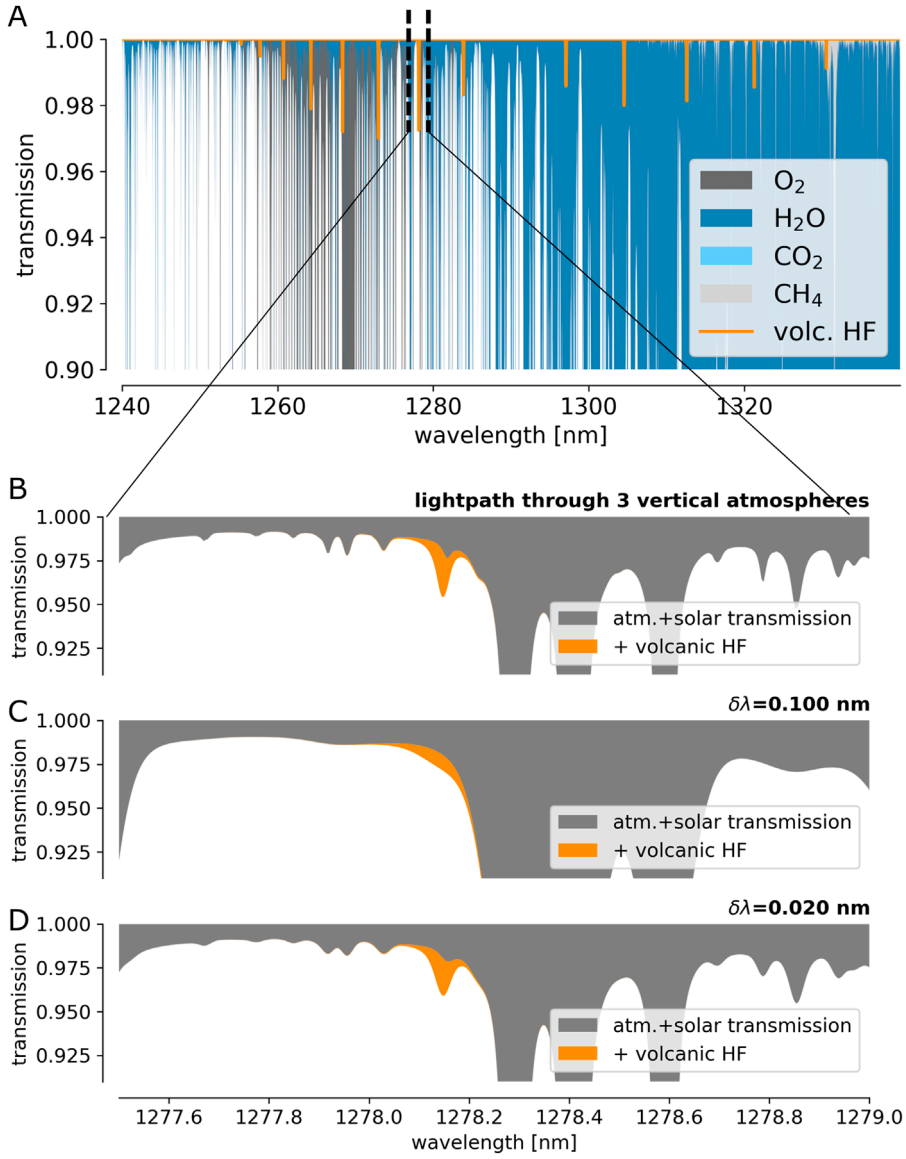

FIGURE 8
(A) High-resolution spectrum of the atmospheric transmission with a typical amount of volcanic HF (10^{17} molec cm^{-2}) at 1,278 nm. **(B)** Extract of **(A)** around an individual HF absorption line. **(C,D)** show the spectrum of **(B)** as seen with instruments with a spectral resolution δλ of 0.1 and 0.02 nm, respectively.

to DOAS measurements of volcanic SO_2 in the UV, the measured absorption introduced by HF and HCl within an atmospheric light path traversing the volcanic plume can be unambiguously assigned to the volcanic emission. Figures 8, 9 show a more detailed view of the atmospheric SWIR spectrum at the spectral windows with strong HF and HCl absorption. The upper panels (A) illustrate the spectral jungle of sharp and strong lines of the background atmosphere. Panels B show the closer vicinity of an individual HF (or HCl) line. Panels C show the same spectral range as observed with a spectral resolution of $\delta\lambda = 0.1$ nm ($R \approx 10^4$), which is typical for volcanic FTS measurements in the SWIR. With that resolving power, the absorption line is poorly defined within the spectrum and its absorption can only be quantified when the atmospheric background is well-determined. When increasing the spectral resolution to $\delta\lambda = 0.02$ nm ($\delta\lambda$ can be optimized depending on the measurement scenario), the HF (or HCl) absorption line is resolved and causes a significantly stronger and more defined absorption pattern, which, in this case, allows the application of common DOAS evaluation procedures.

3.2.2 Photon budget

We calculate the photon budget for FPI spectrograph measurements using skylight in the spectral range of HF and HCl absorption (Figures 8, 9). A skylight DOAS measurement, performed with a GS (f = 100 mm, R = 1,000), reaches a noise level on the order of $\Delta\tau = 10^{-4}$ for an exposure time δt of ca. 30 s. This is in accordance with skylight radiance quantification by Blumthaler et al. (1996), who find a radiance of at least

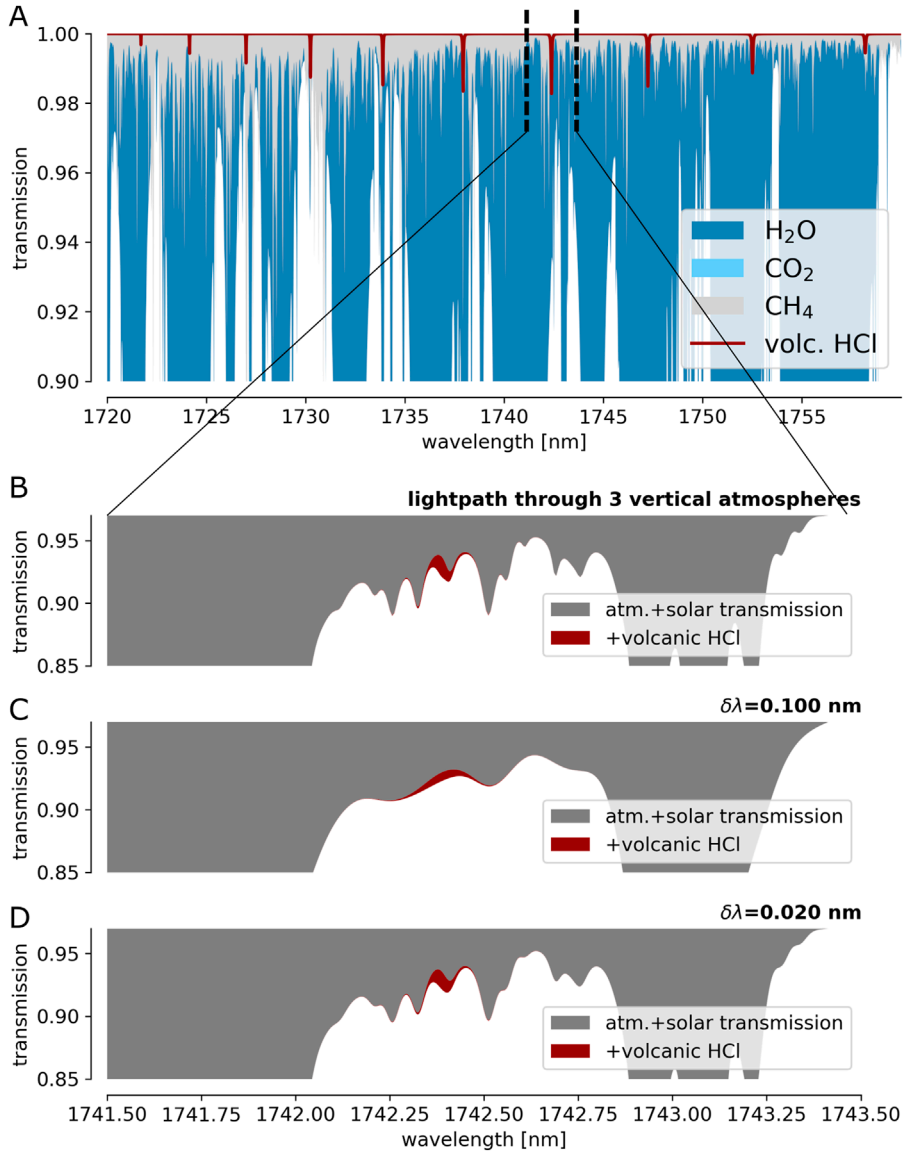

FIGURE 9
Same as **Figure 8** for HCl ($3 \cdot 10^{17}$ molec cm^{-2}) at 1,742 nm.

20 mW·m^{-2}·sr^{-1}·nm^{-1} at 400 nm for clear sky conditions and a solar zenith angle of 68°. This equals $I = 4 \cdot 10^{10}$ photons mm^{-2} sr^{-1} nm^{-1} s^{-1}. With the GS's etendue (Eq. **14**), spectral resolution ($\delta\lambda$ = 400 nm/R = 0.4 nm), and a loss factor of $\mu \approx 0.03$ (accounting for: quantum efficiency of the detector, grating efficiency, transmission/reflectivity of mirrors, fibres, telescopes and stray-light filters), this leads to a number of counted photo-electrons of $N \approx 10^8$ for an exposure time of δt =30 s (see Eqs **8**, **13**).

This number serves as a reference for approximating the SNR of HF and HCl measurements with FPI spectrographs. The above introduced relative skylight radiance quantification (relative to 400 nm) and light throughput quantification of FPI spectrographs (relative to GSs) allows to infer noise limits $\Delta\tau$ and relate them to differential optical densities $\delta\tau_{\mathrm{volc}}$ introduced by typically observed volcanic trace gas columns (HF: 10^{17} molec cm^{-2}, HCl: $3 \cdot 10^{17}$ molec cm^{-2}, e.g., Butz et al., 2017).

Table 2 summarises the result of these calculations. It shows that HF and HCl can be quantified by FPI spectrograph based DOAS measurements using skylight. As expected, the SNR is dependent on the sky conditions with the blue sky scenario representing a lower bound to the skylight radiance as there always is a certain amount of atmospheric aerosol (vertical AOD typically > 0.03 in the UV, see e.g., Wagner et al., 2021).

3.3 Discussion

The above calculations rely on rough skylight radiance approximations. However, the choice of the absolute radiance value is quite conservative. It is based on measurements made at a high solar zenith angle (68°) and, depending on the viewing geometry, it can be by more than an order of magnitude higher

TABLE 2 Photon budget calculations for skylight RS measurements of volcanic HF and HCl.

	DOAS (400 nm)	HF (1,278 nm)			HCl (1,742 nm)		
		10^{17} molec cm^{-2}			$3 \cdot 10^{17}$ molec cm^{-2}		
Instrument	GS	FPI spectrograph			FPI spectrograph		
$\delta\lambda$ (nm)	0.4	0.02			0.02		
R	1,000	64,900			87,100		
f (mm)	100	100			100		
w_S (μm)	100	—			—		
b_{FPI} [mm]	—	20			20		
E (mm^2 sr)	$7.8 \cdot 10^{-3}$	$3 \cdot 10^{-2}$			$2.2 \cdot 10^{-2}$		
Rel. k	1	0.192			0.141		
Skylight							
		Blue sky	Aerosol layer	Cloud	Blue sky	Aerosol layer	Cloud
Rel. I (Figure 7)	1	$3 \cdot 10^{-3}$	$2 \cdot 10^{-2}$	$3 \cdot 10^{-1}$	$3 \cdot 10^{-4}$	$5 \cdot 10^{-3}$	10^{-1}
Budget							
δt [s]	30	30	30	30	30	30	30
N	10^8	$5.76 \cdot 10^4$	$3.84 \cdot 10^5$	$5.76 \cdot 10^6$	$4.23 \cdot 10^3$	$7.05 \cdot 10^4$	$1.41 \cdot 10^6$
$\Delta\tau = N^{-\frac{1}{2}}$	0.0001	0.0042	0.0016	0.0004	0.0152	0.0038	0.0008
$\delta\bar{\tau}_{volc}$			0.023			0.013	
SNR = $\frac{\delta\bar{\tau}_{volc}}{\Delta\tau}$		5.5	14.4	57.5	0.9	3.2	15.4

(Blumthaler et al., 1996). A sky overcast by thinner clouds above the volcanic plume would represent good measurement conditions. The presence of aerosol or broken-cloud sky conditions would also enable reasonable HF and HCl quantification, particularly as spectrograph measurements are hardly disturbed by background intensity variations.

Volcanic aerosol and condensed plumes can also serve as a light source. Although the light path in such measurement scenarios will not be well-defined, the evaluation of gas ratios (of gases absorbing in similar spectral ranges, such as HF and HCl) will still be possible (similar to the quantification of BrO/SO_2 by DOAS in the UV, see e.g., Lübcke et al., 2014).

The absorption cross section of other atmospheric gases (e.g., O_2, H_2O, CH_4, CO_2) in the respective spectral retrieval intervals are known. As in common DOAS routines, the absorption of these gases is accounted for in the evaluation and separated from the target trace gas absorption (see Platt and Stutz, 2008, for details).

We conclude that HF and HCl can be measured, similarly to volcanic SO_2, by RS with simple, robust and compact spectrographs using skylight as a light source. SO_2, HF, and HCl are basically chemically inert within the first minutes of plume evolution in the atmosphere (Beirle et al., 2014; Rüdiger et al., 2021). Thus, the ratio of these gases will provide an independent geochemical (or "purely volcanic") parameter without relying on atmospheric parameters, such as wind speed, plume height (SO_2 fluxes), or chemistry (BrO/SO_2 ratios). Autonomous ground-based (e.g., NOVAC-type, see Galle et al., 2010) and satellite-based platforms can be extended to measure HF and HCl in addition to SO_2 and provide real-time and continuous data during all stages of volcanic activity.

4 Conclusion and outlook

Nowadays techniques for RS of volcanic gases enable DOAS measurements of SO_2 emissions, which, when operated from autonomous platforms, provide global and continuous data (e.g., Carn et al., 2017; Theys et al., 2019; Arellano et al., 2021). Further species (e.g., H_2O, CO_2, SO_2, HF, HCl, CO) can be measured by more intricate techniques that almost exclusively provide data during dedicated field campaigns. We show here, that the use of high-resolution FPIs in spectrograph implementations could overcome the limitations of present-day volcanic gas RS techniques in many respects.

In the first part of this article, we describe volcanic field measurements with a FPI spectrograph prototype and demonstrate the feasibility of the quantification of volcanic OH radicals. While possibly playing a central role in the high-temperature chemistry of volcanic gases, no conventional sampling technique is able to measure volcanic OH. During the field measurements, the prototype set-up showed excellent stability and mobility. Furthermore, we introduce straight-forward evaluation approaches for the data generated by FPI spectrographs. The evaluation of a spectrum recorded above an active lava flow allows the quantification of SO_2 by its high resolution (picometre) absorption structures and the determination of a detection limit for OH to about 20 parts per billion. This means that, for an ideal sampling situation (i.e., light path traversing the hot plume), even our present (not fully optimised) prototype is able to quantify the OH mixing ratios predicted by high temperature chemistry models (parts per million range).

In the second part of this article, sample calculations prove the feasibility of DOAS-type measurements of HF and HCl using the light of the daytime sky. FPI spectrographs provide sufficient light throughput and high spectral resolution (for an accurate spectral detection of the trace gas) with a form factor comparable to that of a compact GS (focal length f = 100 mm). A GS with similar performance can only be implemented with a focal length of f > 10 m. Comparable FTS measurements will suffer from the skylight radiance variability, are intricate, expensive, and much less suited for continuous operation in a volcanic environment. Using skylight (i.e., scattered sunlight) for HF and HCl measurements will allow flexible measurement viewing geometries and thereby enable continuous measurements from autonomous platforms (similar to DOAS measurements of SO_2). This will provide real-time measurements and continuous records of ratios of inert volcanic gases, and thereby of a geochemical parameter that is independent of atmospheric influence (e.g., wind speed, chemistry). These data will substantially improve degassing models and volcanic monitoring capabilities through gas measurements.

OH measurements and HF and HCl DOAS measurements are only examples for the plenty of applications of FPI-based high-resolution spectroscopy to RS of volcanic gases. Besides improving the quality and lowering the detection limits of many state-of-the-art observations, further applications may include:

1. Similarly to FTSs, FPI spectrographs can be employed in solar occultation viewing geometry or with lamps or lava thermal emission as light source. The increased spectral resolution and higher light throughput leads to higher sensitivity of these measurements and might enable the quantification of further plume constituents, such as isotopes in CO_2 or H_2O.
2. Quantification of further reactive trace gas species within the high-temperature magma-atmosphere interface is essential for a better understanding of high-temperature volcanic emission processes. High-temperature sulfur chemistry is still bound to large uncertainties. Sulfanyl (SH) might be a central intermediate species in sulfur oxidation at high temperatures (Roberts et al., 2019; Kuhn, 2022) and shows sharp and strong absorption bands in the UV (ca. 324 nm, see Lewis and White, 1939).
3. High spectral resolution might enable RS of $^{34}SO_2$, based on slight shifts in spectral absorption in the UV (e.g., Danielache et al., 2008). This approach would circumvent fractionation issues as found for conventional sampling techniques (e.g., Mather et al., 2008).

FPI spectrographs rely on a basically very simple optical set-up (two lenses, a band-pass filter, a FPI etalon, and a detector). Low thermal expansion spacers of state-of-the-art FPIs ensure a high thermal stability of the instrument (Kuhn et al., 2021). Due to standardized manufacturing procedures of the intrinsically simple set-up of FPIs, FPI spectrographs are likely to cost a fraction of the price of a commercial FTS system. Moreover, the small size and high robustness makes them also ideal candidates for (miniature) satellite missions.

The combination of simple instrumentation and its striking potential to fill substantial gaps in present data suggests that FPI spectrographs will play a central role in the future of volcanic gas geochemistry.

Data availability statement

The original contributions presented in the study are included in the article/**Supplementary Material**, further inquiries can be directed to the corresponding author.

Author contributions

NB, GB, SC, GG, ML, KK and DT substantially supported the field measurements at Nyiragongo volcano. NB, TW, UP and JK contributed to the conceptualization and to interpretations of the study in frequent discussions. All co-authors reviewed and contributed to the refinement of earlier drafts of the manuscript. JK conceptualized, manufactured and characterized the FPI spectrograph prototype and the open-path set-up, developed the instrument model, conducted and evaluated the field measurements, conceptualized and performed the photon budget calculations, and wrote the draft of the manuscript.

Funding

This research has been partially funded by the German Research Foundation (DFG; project no. PL 193/23-1). For the publication fee we acknowledge financial support by Heidelberg University and the Deutsche For schungsgemeinschaft within the funding program “Open Access Publicationskosten”.

Acknowledgments

We are grateful to the Goma Volcano Observatory (OVG) for the invitation and logistic help. Further we thank the United Nations Organization Stabilization Mission in the Democratic Republic of the Congo (MONUSCO) and the Institut Congolais pour la Conservation de la Natur (ICCN) for providing the logistics inside the Virunga National Park. We thank SVG Geneve for providing the logistics to descent into Nyiragongo’s crater and particularly Pierre-Yves Burgi and Patrick Marcel for their support during the measurement. We thank SLS Optics Ltd., for their excellent services and kind support.

Conflict of interest

The authors declare that the research was conducted in the absence of any commercial or financial relationships that could be construed as a potential conflict of interest.

Publisher’s note

All claims expressed in this article are solely those of the authors and do not necessarily represent those of

their affiliated organizations, or those of the publisher, the editors and the reviewers. Any product that may be evaluated in this article, or claim that may be made by its manufacturer, is not guaranteed or endorsed by the publisher.

Supplementary material

The Supplementary Material for this article can be found online at: https://www.frontiersin.org/articles/10.3389/feart.2023.1039093/full#supplementary-material

References

Aiuppa, A., Baker, D., and Webster, J. (2009). Halogens in volcanic systems. *Chem. Geol.* 263, 1–18. doi:10.1016/j.chemgeo.2008.10.005

Ångström, A. (1929). On the atmospheric transmission of sun radiation and on dust in the air. *Geogr. Ann.* 11, 156–166. doi:10.1080/20014422.1929.11880498

Arellano, S., Galle, B., Apaza, F., Avard, G., Barrington, C., Bobrowski, N., et al. (2021). Synoptic analysis of a decade of daily measurements of SO_2 emission in the troposphere from volcanoes of the global ground-based network for observation of volcanic and atmospheric change. *Earth Syst. Sci. Data* 13, 1167–1188. doi:10.5194/essd-13-1167-2021

Beirle, S., Hörmann, C., Penning de Vries, M., Dörner, S., Kern, C., and Wagner, T. (2014). Estimating the volcanic emission rate and atmospheric lifetime of SO_2 from space: A case study for kīlauea volcano, Hawai`i. *Atmos. Chem. Phys.* 14, 8309–8322. doi:10.5194/acp-14-8309-2014

Beirle, S., Lampel, J., Lerot, C., Sihler, H., and Wagner, T. (2017). Parameterizing the instrumental spectral response function and its changes by a super-Gaussian and its derivatives. *Atmos. Meas. Tech.* 10, 581–598. doi:10.5194/amt-10-581-2017

Blumthaler, M., Gröbner, J., Huber, M., and Ambach, W. (1996). Measuring spectral and spatial variations of UVA and UVB sky radiance. *Geophys. Res. Lett.* 23, 547–550. doi:10.1029/96gl00248

Bobrowski, N., Giuffrida, G., Yalire, M., Lübcke, P., Arellano, S., Balagizi, C., et al. (2017). Multi-component gas emission measurements of the active lava lake of Niyragongo, DR Congo. *J. Afr. Earth Sci.* 134, 856–865. doi:10.1016/j.jafrearsci.2016.07.010

Butz, A., Dinger, A. S., Bobrowski, N., Kostinek, J., Fieber, L., Fischerkeller, C., et al. (2017). Remote sensing of volcanic CO_2, HF, HCl, SO_2, and BrO in the downwind plume of Mt. Etna. *Atmos. Meas. Tech.* 10, 1–14. doi:10.5194/amt-10-1-2017

Carn, S. A., Fioletov, V. E., McLinden, C. A., Li, C., and Krotkov, N. A. (2017). A decade of global volcanic SO_2 emissions measured from space. *Sci. Rep.* 7, 44095. doi:10.1038/srep44095

Cattolica, R. J., Yoon, S., and Knuth, E. L. (1982). OH concentration in an atmospheric-pressure methane-air flame from molecular-beam mass spectrometry and laser-absorption spectroscopy. *Combust. Sci. Technol.* 28, 225–239. doi:10.1080/00102208208952557

Crisp, D., Pollock, H. R., Rosenberg, R., Chapsky, L., Lee, R. A. M., Oyafuso, F. A., et al. (2017). The on-orbit performance of the orbiting carbon observatory-2 (OCO-2) instrument and its radiometrically calibrated products. *Atmos. Meas. Tech.* 10, 59–81. doi:10.5194/amt-10-59-2017

Crutzen, P. J. (1974). Photochemical reactions initiated by and influencing ozone in unpolluted tropospheric air. *Tellus* 26, 47–57. doi:10.3402/tellusa.v26i1-2.9736

Danielache, S. O., Eskebjerg, C., Johnson, M. S., Ueno, Y., and Yoshida, N. (2008). High-precision spectroscopy of ^{32}S, ^{33}S, and ^{34}S sulfur dioxide: Ultraviolet absorption cross sections and isotope effects. *J. Geophys. Res.* 113, D17314. doi:10.1029/2007jd009695

Fabry, C., and Buisson, H. (1908). Wavelength measurements for the establishment of a system of spectroscopic standards. *Astrophysical J.* 27, 169–196. doi:10.1086/141586

Fleischmann, O. C., Hartmann, M., Burrows, J. P., and Orphal, J. (2004). New ultraviolet absorption cross-sections of BrO at atmospheric temperatures measured by time-windowing Fourier transform spectroscopy. *J. Photochem. Photobiol. A Chem.* 168, 117–132. doi:10.1016/j.jphotochem.2004.03.026

Francis, P., Burton, M. R., and Oppenheimer, C. (1998). Remote measurements of volcanic gas compositions by solar occultation spectroscopy. *Nature* 396, 567–570. doi:10.1038/25115

Fuchs, C., Kuhn, J., Bobrowski, N., and Platt, U. (2021). Quantitative imaging of volcanic SO_2 plumes using Fabry–Pérot interferometer correlation spectroscopy. *Atmos. Meas. Tech.* 14, 295–307. doi:10.5194/amt-14-295-2021

Galle, B., Johansson, M., Rivera, C., Zhang, Y., Kihlman, M., Kern, C., et al. (2010). Network for observation of volcanic and atmospheric change (NOVAC) - a global network for volcanic gas monitoring: Network layout and instrument description. *J. Geophys. Res.* 115, D05304. doi:10.1029/2009JD011823

Gerlach, T. M. (2004). Volcanic sources of tropospheric ozone-depleting trace gases. *Geochem. Geophys. Geosystems* 5, 9. doi:10.1029/2004gc000747

Hörmann, C., Sihler, H., Bobrowski, N., Beirle, S., Penning de Vries, M., Platt, U., et al. (2013). Systematic investigation of bromine monoxide in volcanic plumes from space by using the GOME-2 instrument. *Atmos. Chem. Phys.* 13, 4749–4781. doi:10.5194/acp-13-4749-2013

Jacquinot, P. (1960). New developments in interference spectroscopy. *Rep. Prog. Phys.* 23, 267–312. doi:10.1088/0034-4885/23/1/305

Jacquinot, P. (1954). The luminosity of spectrometers with prisms, gratings, or Fabry–Pérot etalons. *J. Opt. Soc. Am.* 44, 761. doi:10.1364/josa.44.000761

Kern, C., Aiuppa, A., and de Moor, J. M. (2022). A golden era for volcanic gas geochemistry? *Bull. Volcanol.* 84, 43. doi:10.1007/s00445-022-01556-6

Kern, C., Masias, P., Apaza, F., Reath, K. A., and Platt, U. (2017). Remote measurement of high preeruptive water vapor emissions at sabancaya volcano by passive differential optical absorption spectroscopy. *J. Geophys. Res. Solid Earth* 122, 3540–3564. doi:10.1002/2017jb014020

Kuhn, J., Bobrowski, N., Lübcke, P., Vogel, L., and Platt, U. (2014). A Fabry–Perot interferometer-based camera for two-dimensional mapping of SO_2 distributions. *Atmos. Meas. Tech.* 7, 3705–3715. doi:10.5194/amt-7-3705-2014

Kuhn, J., Bobrowski, N., and Platt, U. (2022). The interface between magma and Earth's atmosphere. *Geochem. Geophys. Geosystems* 23. doi:10.1029/2022gc010671

Kuhn, J., Bobrowski, N., Wagner, T., and Platt, U. (2021). Mobile and high-spectral-resolution Fabry–Pérot interferometer spectrographs for atmospheric remote sensing. *Atmos. Meas. Tech.* 14, 7873–7892. doi:10.5194/amt-14-7873-2021

Kuhn, J. (2022). *Novel approaches to the analysis of volcanic degassing*. PhD Thesis. Heidelberg University. doi:10.11588/HEIDOK.00031922

Kuhn, J., Platt, U., Bobrowski, N., and Wagner, T. (2019). Towards imaging of atmospheric trace gases using Fabry–Pérot interferometer correlation spectroscopy in the UV and visible spectral range. *Atmos. Meas. Tech.* 12, 735–747. doi:10.5194/amt-12-735-2019

Le Guern, F. (1987). Mechanism of energy transfer in the lava lake of Nyiragongo (Zaire), 1959–1977. *J. Volcanol. Geotherm. Res.* 31, 17–31. doi:10.1016/0377-0273(87)90003-5

Levy, H. (1971). Normal atmosphere: Large radical and formaldehyde concentrations predicted. *Science* 173, 141–143. doi:10.1126/science.173.3992.141

Lewis, M. N., and White, J. U. (1939). The band spectrum of HS. *Phys. Rev.* 55, 894–898. doi:10.1103/physrev.55.894

Lübcke, P., Bobrowski, N., Arellano, S., Galle, B., Garzón, G., Vogel, L., et al. (2014). BrO/SO_2 molar ratios from scanning DOAS measurements in the NOVAC network. *Solid earth.* 5, 409–424. doi:10.5194/se-5-409-2014

Martınez-Lozano, J., Utrillas, M., Tena, F., and Cachorro, V. (1998). The parameterisation of the atmospheric aerosol optical depth using the ångström power law. *Sol. Energy* 63, 303–311. doi:10.1016/s0038-092x(98)00077-2

Mather, T., Pyle, D., and Heaton, T. (2008). Investigation of the use of filter packs to measure the sulphur isotopic composition of volcanic sulphur dioxide and the sulphur and oxygen isotopic composition of volcanic sulphate aerosol. *Atmos. Environ.* 42, 4611–4618. doi:10.1016/j.atmosenv.2008.01.052

Merten, A., Tschritter, J., and Platt, U. (2011). Design of differential optical absorption spectroscopy long-path telescopes based on fiber optics. *Appl. Opt.* 50, 738–754. doi:10.1364/AO.50.000738

Mori, T., and Burton, M. (2006). The SO_2 camera: A simple, fast and cheap method for ground-based imaging of SO_2 in volcanic plumes. *Geophys. Res. Lett.* 33, L24804. doi:10.1029/2006gl027916

Mori, T., Notsu, K., Tohjima, Y., and Wakita, H. (1993). Remote detection of HCl and SO_2 in volcanic gas from Unzen volcano, Japan. *Geophys. Res. Lett.* 20, 1355–1358. doi:10.1029/93gl01065

Moussallam, Y., Oppenheimer, C., and Scaillet, B. (2019). On the relationship between oxidation state and temperature of volcanic gas emissions. *Earth Planet. Sci. Lett.* 520, 260–267. doi:10.1016/j.epsl.2019.05.036

Notholt, J., Schütt, H., and Keens, A. (1997). Solar absorption measurements of stratospheric OH in the UV with a Fourier-transform spectrometer. *Appl. Opt.* 36, 6076. doi:10.1364/ao.36.006076

Notsu, K., and Mori, T. (2010). Chemical monitoring of volcanic gas using remote FT-IR spectroscopy at several active volcanoes in Japan. *Appl. Geochem.* 25, 505–512. doi:10.1016/j.apgeochem.2010.01.008

Perot, A., and Fabry, C. (1899). On the application of interference phenomena to the solution of various problems of spectroscopy and metrology. *Astrophysical J.* 9, 87. doi:10.1086/140557

Platt, U., Bobrowski, N., and Butz, A. (2018). Ground-based remote sensing and imaging of volcanic gases and quantitative determination of multi-species emission fluxes. *Geosciences* 8, 44. doi:10.3390/geosciences8020044

Platt, U., Lübcke, P., Kuhn, J., Bobrowski, N., Prata, F., Burton, M., et al. (2015). Quantitative imaging of volcanic plumes - results, needs, and future trends. *J. Volcanol. Geotherm. Res.* 300, 7–21. doi:10.1016/j.jvolgeores.2014.10.006

Platt, U., and Stutz, J. (2008). *Differential optical absorption spectroscopy*. Berlin Heidelberg: Springer. 978-3-540-21193-8.

Platt, U., Wagner, T., Kuhn, J., and Leisner, T. (2021). The "ideal" spectrograph for atmospheric observations. *Atmos. Meas. Tech.* 14, 6867–6883. doi:10.5194/amt-14-6867-2021

Pouclet, A., and Bram, K. (2021). Nyiragongo and nyamuragira: A review of volcanic activity in the kivu rift, Western branch of the East African Rift system. *Bull. Volkanology* 83, 10. doi:10.1007/s00445-021-01435-6

Prata, A. J., and Bernardo, C. (2014). Retrieval of sulfur dioxide from a ground-based thermal infrared imaging camera. *Atmos. Meas. Tech.* 7, 2807–2828. doi:10.5194/amt-7-2807-2014

Prata, A. J., and Bernardo, C. (2007). Retrieval of volcanic SO_2 column abundance from atmospheric infrared sounder data. *J. Geophys. Res.* 112, D20204. doi:10.1029/2006jd007955

Roberts, T., Dayma, G., and Oppenheimer, C. (2019). Reaction rates control high-temperature chemistry of volcanic gases in air. *Front. Earth Sci.* 7. doi:10.3389/feart.2019.00154

Rothman, L., Gordon, I., Babikov, Y., Barbe, A., Benner, D. C., Bernath, P., et al. (2013). The HITRAN2012 molecular spectroscopic database. *J. Quantitative Spectrosc. Radiat. Transf.* 130, 4–50. doi:10.1016/j.jqsrt.2013.07.002

Rüdiger, J., Gutmann, A., Bobrowski, N., Liotta, M., de Moor, J. M., Sander, R., et al. (2021). Halogen activation in the plume of masaya volcano: Field observations and box model investigations. *Atmos. Chem. Phys.* 21, 3371–3393. doi:10.5194/acp-21-3371-2021

Rufus, J., Stark, G., Smith, P. L., Pickering, J. C., and Thorne, A. P. (2003). High-resolution photoabsorption cross section measurements of SO_2, 2: 220 to 325 nm at 295 k. *J. Geophys. Res. Planets* 108, E2. doi:10.1029/2002je001931

Sawyer, G. M., Carn, S. A., Tsanev, V. I., Oppenheimer, C., and Burton, M. (2008). Investigation into magma degassing at nyiragongo volcano, democratic republic of the Congo. *Geochem. Geophys. Geosystems* 9, 2. doi:10.1029/2007gc001829

Serdyuchenko, A., Gorshelev, V., Weber, M., Chehade, W., and Burrows, J. P. (2014). High spectral resolution ozone absorption cross-sections - part 2: Temperature dependence. *Atmos. Meas. Tech.* 7, 625–636. doi:10.5194/amt-7-625-2014

Smittarello, D., Smets, B., Barrière, J., Michellier, C., Oth, A., Shreve, T., et al. (2022). Precursor-free eruption triggered by edifice rupture at nyiragongo volcano. *Nature* 609, 83–88. doi:10.1038/s41586-022-05047-8

Spilliaert, N., Metrich, N., and Allard, P. (2006). S-cl-f degassing pattern of water-rich alkali basalt: Modelling and relationship with eruption styles on mount etna volcano. *Earth Planet. Sci. Lett.* 248, 772–786. doi:10.1016/j.epsl.2006.06.031

Stephens, G. L., and Platt, C. (1987). Aircraft observations of the radiative and microphysical properties of stratocumulus and cumulus cloud fields. *J. Appl. Meteorology Climatol.* 26, 1243–1269. doi:10.1175/1520-0450(1987)026<1243:aootra>2.0.co;2

Stone, D., Whalley, L. K., and Heard, D. E. (2012). Tropospheric OH and HO2 radicals: Field measurements and model comparisons. *Chem. Soc. Rev.* 41, 6348. doi:10.1039/c2cs35140d

Strutt, J. (1871). XV. on the light from the sky, its polarization and colour. *Lond. Edinb. Dublin Philosophical Mag. J. Sci.* 41, 107–120. doi:10.1080/14786447108640452

Symonds, R. B., Rose, W. I., Bluth, G. J. S., and Gerlach, T. M. (1994). Volcanic-gas studies; methods, results, and applications. *Rev. Mineralogy Geochem.* 30, 1–66.

Taquet, N., Hernández, I. M., Stremme, W., Bezanilla, A., Grutter, M., Campion, R., et al. (2017). Continuous measurements of SiF 4 and SO 2 by thermal emission spectroscopy: Insight from a 6-month survey at the popocatépetl volcano. *J. Volcanol. Geotherm. Res.* 341, 255–268. doi:10.1016/j.jvolgeores.2017.05.009

Tedesco, D., Vaselli, O., Papale, P., Carn, S. A., Voltaggio, M., Sawyer, G. M., et al. (2007). January 2002 volcano-tectonic eruption of nyiragongo volcano, democratic republic of Congo. *J. Geophys. Res.* 112, B09202. doi:10.1029/2006jb004762

Theys, N., Hedelt, P., Smedt, I. D., Lerot, C., Yu, H., Vlietinck, J., et al. (2019). Global monitoring of volcanic SO_2 degassing with unprecedented resolution from TROPOMI onboard sentinel-5 precursor. *Sci. Rep.* 9, 2643. doi:10.1038/s41598-019-39279-y

Toon, G. C. (2015). *Solar line list for the tccon 2014 data release*. doi:10.14291/TCCON.GGG2014.SOLAR.R0/1221658

Valade, S., Ripepe, M., Giuffrida, G., Karume, K., and Tedesco, D. (2018). Dynamics of mount nyiragongo lava lake inferred from thermal imaging and infrasound array. *Earth Planet. Sci. Lett.* 500, 192–204. doi:10.1016/j.epsl.2018.08.004

Varon, D. J., Jervis, D., McKeever, J., Spence, I., Gains, D., and Jacob, D. J. (2021). High-frequency monitoring of anomalous methane point sources with multispectral sentinel-2 satellite observations. *Atmos. Meas. Tech.* 14, 2771–2785. doi:10.5194/amt-14-2771-2021

Vaughan, M. (1989). *The Fabry-Pérot interferometer history, theory, practice and applications*. Boca Raton: CRC Press. 978-08-527-4138-2.

Wagner, T., Apituley, A., Beirle, S., Dörner, S., Friess, U., Remmers, J., et al. (2014). Cloud detection and classification based on MAX-DOAS observations. *Atmos. Meas. Tech.* 7, 1289–1320. doi:10.5194/amt-7-1289-2014

Wagner, T., Dix, B., von Friedeburg, C., Frieß, U., Sanghavi, S., Sinreich, R., et al. (2004). MAX-DOAS O_4 measurements: A new technique to derive information on atmospheric aerosols - principles and information content. *J. Geophys. Res.* 109, D22205. doi:10.1029/2004JD004904

Wagner, T., Dörner, S., Beirle, S., Donner, S., and Kinne, S. (2021). Quantitative comparison of measured and simulated O_4 absorptions for one day with extremely low aerosol load over the tropical atlantic. *Atmos. Meas. Tech.* 14, 3871–3893. doi:10.5194/amt-14-3871-2021

Warnach, S., Bobrowski, N., Hidalgo, S., Arellano, S., Sihler, H., Dinger, F., et al. (2019). Variation of the BrO/SO_2 molar ratio in the plume of tungurahua volcano between 2007 and 2017 and its relationship to volcanic activity. *Front. Earth Sci.* 7. doi:10.3389/feart.2019.00132

Willbourn, A. H., and Hinshelwood, C. N. (1946). The mechanism of the hydrogen-oxygen reaction; the third explosion limit. *Proc. R. Soc. Lond. Ser. A. Math. Phys. Sci.* 185, 353–369. doi:10.1098/rspa.1946.0023

frontiers | Frontiers in Earth Science

TYPE Original Research
PUBLISHED 04 April 2023
DOI 10.3389/feart.2023.1088992

OPEN ACCESS

EDITED BY
Georg Rümpker,
Goethe University Frankfurt, Germany

REVIEWED BY
Philipson Bani,
UMR6524 Laboratoire Magmas et Volcans (LMV), France
Jean-François Smekens,
University of Oxford, United Kingdom

*CORRESPONDENCE
Thomas Charles Wilkes,
tcwilkes1@sheffield.ac.uk

SPECIALTY SECTION
This article was submitted to Volcanology, a section of the journal Frontiers in Earth Science

RECEIVED 03 November 2022
ACCEPTED 28 February 2023
PUBLISHED 04 April 2023

CITATION
Wilkes TC, Pering TD, Aguilera F, Layana S, Nadeau P, Kern C, McGonigle AJS, Aguilera M and Zhu C (2023), A new permanent, low-cost, low-power SO_2 camera for continuous measurement of volcanic emissions.
Front. Earth Sci. 11:1088992.
doi: 10.3389/feart.2023.1088992

A new permanent, low-cost, low-power SO_2 camera for continuous measurement of volcanic emissions

Thomas Charles Wilkes[1]*, Tom David Pering[1], Felipe Aguilera[2,3], Susana Layana[2], Patricia Nadeau[4], Christoph Kern[5], Andrew John Samuel McGonigle[6], Mauricio Aguilera[2,7] and Chengxi Zhu[8]

[1]Department of Geography, University of Sheffield, Sheffield, United Kingdom, [2]Millennium Institute on Volcanic Risk Research—Ckelar Volcanoes, Antofagasta, Chile, [3]Departamento de Ciencias Geológicas, Universidad Católica del Norte, Antofagasta, Chile, [4]U.S. Geological Survey, Hawaiian Volcano Observatory, Hilo, HI, United States, [5]U.S. Geological Survey, Cascades Volcano Observatory, Vancouver, WA, United States, [6]Department of Physics, University of Sydney, Sydney, NSW, Australia, [7]Programa de Magister en Ciencias Mención Geología, Universidad Católica del Norte, Antofagasta, Chile, [8]Cambridge Advanced Imaging Centre, University of Cambridge, Cambridge, United Kingdom

Since its introduction to volcanology in the mid-2000 s, the SO_2 camera has become an important instrument for the acquisition of accurate and high time-resolution SO_2 emission rates, aiding in hazard assessment and volcanological research. However, with the exception of a few locations (Stromboli, Etna, Kīlauea), hitherto the majority of measurements have been made on discrete field campaigns, which provide only brief snapshots into a volcano's activity. Here, we present the development of a new, low-cost, low-power SO_2 camera for permanent deployment on volcanoes, facilitating long-term, quasi-continuous (daylight hours only) measurements. We then discuss preliminary datasets from Lascar and Kīlauea volcanoes, where instruments are now in continuous operation. Further proliferation of such instrumentation has the potential to greatly improve our understanding of the transient nature of volcanic activity, as well as aiding volcano monitoring/eruption forecasting.

KEYWORDS

volcanology, sulphur dioxide, ultraviolet camera, remote sensing, raspberry pi

1 Introduction

Volcanic emissions are the manifestation of subsurface magmatic activity, therefore providing an insight into the state of a volcanic system and potentially providing a means of hazard forecasting through their measurement (e.g., Aiuppa et al., 2009; De Moor et al., 2016; Kunrat et al., 2022). Sulphur Dioxide (SO_2) is the most common gas species detected at open-vent volcanoes with remote sensing instrumentation, owing to its relative ease of detection that stems from two principal factors: Its relatively low background atmospheric concentration and its strong distinctive absorption bands at ultraviolet (UV) and infrared (IR) wavelengths (Platt and Stutz, 2008).

Since their development in the mid-2000s, ultraviolet (UV) SO_2 cameras (Mori and Burton, 2006; Bluth et al., 2007) have become extremely valuable tools for measuring volcanic emissions, due to their provision of high temporal (at times >1 Hz) and high spatial

resolution (providing two-dimensional, 2D, plume images) datasets. However, unlike the similarly popular differential optical absorption spectroscopy (DOAS) instruments, which have been installed as permanent/continuously operating instruments on a number of open-vent volcanoes worldwide (Burton et al., 2009; Galle et al., 2010; Arellano et al., 2021), SO_2 camera technology is yet to proliferate in this regard; to the best of our knowledge, previous permanent systems have been installed on only Stromboli (Burton et al., 2015), Etna (D'Aleo et al., 2016; Delle Donne et al., 2017), and Kīlauea (Kern et al., 2015), with the latter having to be removed from the field during the 2018 caldera collapse. Further installations may have been prevented, in part, by the cost of such equipment, which typically utilizes scientific grade UV cameras (≈1000s–10000 s USD per camera; 2 cameras per SO_2 camera system).

Discrete field campaigns with SO_2 cameras have regularly been conducted, as they are often easier and cheaper to undertake; however, recent research has emphasized the importance of gathering long-term time series, since a volcano can exhibit significant changes in activity over a wide range of time scales (e.g., Pering et al., 2019). Such datasets form the foundation of volcano monitoring, which often relies on identifying the departure of a volcano's activity away from some baseline (Phillipson et al., 2013), and also allow more detailed/reliable volcanological research. Indeed, the permanent SO_2 cameras currently in operation have already provided important new insights into volcanic activity, as well as instrument performance. On Etna, D'Aleo et al. (2016) captured shifts in activity from one vent to another over the course of an eruptive period, inferring shallow interconnections between the vents of the volcano. Delle Donne et al. (2019) observed a mild but detectable increase in SO_2 emission rate prior to the onset of paroxysmal activity on Etna in May 2016. At Stromboli, Burton et al. (2015) found reasonable agreement of camera data with a scanning DOAS network, whilst also highlighting that the high temporal resolution allows quantification of explosive events which are too brief to be captured by the scanning DOAS network. Delle Donne et al. (2017) then found that the frequency of explosion/puffing activity at Stromboli increased significantly prior to the onset of Stromboli's August-November 2014 effusive activity. More recently on Stromboli, Delle Donne et al. (2022) found that explosive degassing accounts for ≈10% of the total SO_2 emission budget, over a year-long observation period. They further showed that explosive SO_2 flux correlates well with both very-long-period (VLP) seismicity and passive SO_2 flux, inferring some commonality in the source processes involved in passive and explosive activity. In a somewhat different application, Elias et al. (2018) acquired highly-accurate SO_2 emission rates by combining UV camera-derived plume velocities with SO_2 measurements made by an array of upward-looking UV spectrometers. Their approach integrates the benefit of sophisticated DOAS retrievals of SO_2 column densities with the benefit of image-based plume speed estimation.

The work herein aims to contribute to the aforementioned growing need for long-term, quasi-continuous SO_2 emission rate data from active volcanoes. We present a new SO_2 camera which has significant potential to broaden the use of permanent SO_2 cameras in volcanology, owing largely to its relatively low-cost and low-power design, as well as its associated open-source code for data processing. The instrument is based on previously developed Raspberry Pi-based UV camera technology that exploits low-cost visible imaging cameras, modifying them to improve their UV sensitivity (Wilkes et al., 2016; Wilkes et al., 2017). We discuss installations of the system on 2 volcanoes, Lascar (Chile) and Kīlauea (Hawaii, United States), presenting preliminary datasets from both. We note that the instrument has also been installed on two other volcanoes (El Reventador, Ecuador; Lastarria, Chile); however, we do not yet have data from these instruments so they are not discussed further herein.

2 Materials and methods

2.1 SO_2 camera principles

The SO_2 camera works by exploiting the significant absorption of ultraviolet (UV) light by SO_2. Images are acquired at two distinct wavelengths (bands), using bandpass filters (≈10 nm full width at half maximum; FWHM) inserted into the camera optics. The on-band is located in a spectral region where SO_2 absorption is significant (≈310 nm), whilst the off-band is located in a nearby region where SO_2 absorption has diminished to be negligible in comparison (≈330 nm). Using the Beer-Lambert law of absorption, plume pixels in an image can be compared to the background sky radiance to calculate pixel optical depths in each band:

$$AA = \tau_{SO2} = \tau_{on} - \tau_{off} = \ln \frac{I_{0on}}{I_{on}} - \ln \frac{I_{0off}}{I_{off}}$$

where τ is the optical depth, I_0 is the background sky intensity, I is the in-plume intensity, and subscripts on and off refer to the on-band (310 nm) and off-band (330 nm) images, respectively. The off-band image is used to correct the on-band optical depths for radiative transfer effects that are relatively broadband in nature (thus change minimally between the on- and off-band images); this is principally scattering/absorption from aerosols in the plume.

SO_2 optical depth can be calibrated to SO_2 column densities using either gas cells of known SO_2 amounts or a co-aligned spectrometer retrieving contemporaneous SO_2 column densities from a small region within the field of view of the camera (Lübcke et al., 2013). For permanent SO_2 camera installations, the latter method is universally employed, since gas cell calibration would require the incorporation of moving parts into the system, such as a filter wheel, to cycle through cell calibrations a number of times each day. Moving parts are likely to result in failing components over the lifetime of a camera system, as well as adding more complexity to the initial design and construction. Furthermore, contemporaneous spectroscopic measurements can allow for more sophisticated retrievals, including correction for light dilution and in-plume scattering (Kern et al., 2013; Varnam et al., 2021).

An emission rate is retrieved by multiplying a plume cross-sectional mass (often referred to as integrated column amount; ICA) by the plume speed. Plume speed is primarily calculated by one of two methods: 1) cross-correlating time series from two parallel ICAs, one set downwind of the other, and therefore calculating the lag in plume motion over the series; 2) computer vision algorithms, principally optical flow, which estimate the motion of all features in an image from one frame to the next (e.g., Peters et al., 2015). The latter provides both a higher spatial (theoretically down

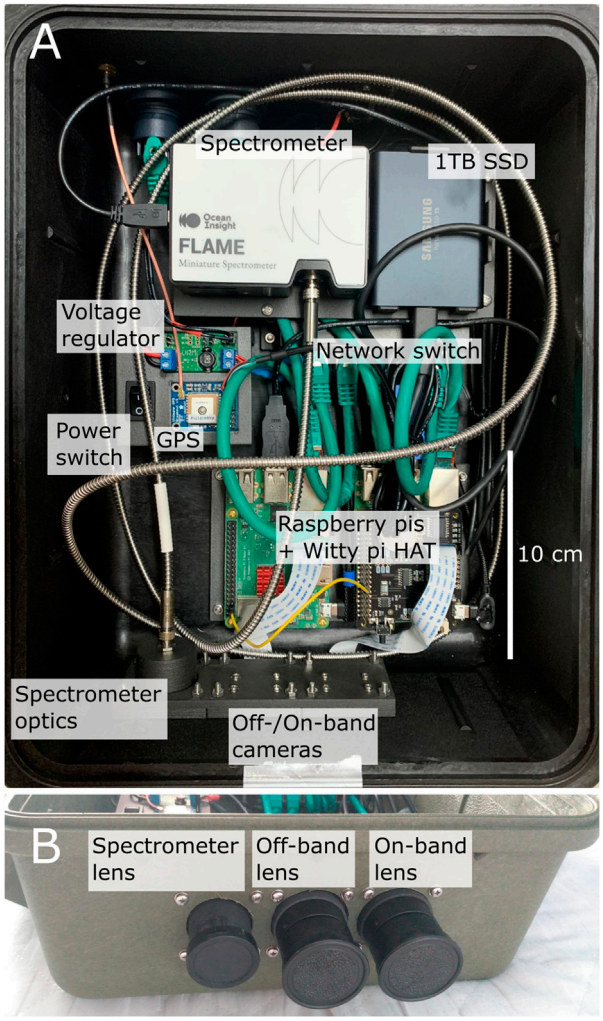

FIGURE 1
(A) Layout of permanent SO_2 camera. Most parts are mounted to the case using custom-designed three-dimensional prints. Whilst this system is housed inside a Peli Case 1,400 (306 × 234 × 130 mm), other systems have used the Peli Case 1,450 (380 × 266 × 153 mm) to provide extra space for mounting the system. **(B)** Front view of instrument optical systems.

to pixel-level) and temporal resolution (frame-by-frame) to plume speed estimation, relative to cross-correlation. An alternative cross-correlation technique, which can also provide frame-by-frame temporal resolution, uses a single plume transect line, this time parallel to plume motion, and cross-correlates this spatial profile in successive images to estimate velocity (Nadeau, 2011; Nadeau et al., 2011). However, this is less commonly found in the literature to date and, thus, is not currently available in our processing software.

2.2 Instrument design

The instrument makes use of sensors from Raspberry Pi cameras, which have been modified to enhance UV sensitivity by removal of their Bayer filter (Wilkes et al., 2016). This approach provides a significant cost reduction relative to the use of scientific-grade commercial UV cameras—100 s USD versus 1,000–10000 s USD for this component of the instrument (Wilkes et al., 2017). Following sensor modification, a UV transmissive optical system, designed in Zemax ray tracing software, was constructed and mounted to the sensor. A triplet design was used to improve upon the previous lower-cost plano-convex singlet (Wilkes et al., 2016; Wilkes et al., 2017), which suffered somewhat from spherical aberrations at the edges of images and had a reasonably low light throughput. Unlike our previous work, which constructed optics holders from three-dimensional (3D) prints, here the triplet mount was constructed in machined black anodised aluminium, for improved precision and longevity. The resulting instrument field of view (FOV) is 28° x 21°. The UV bandpass filters were mounted behind the triplet, to mitigate the effects of changing wavelength transmission that occurs with changing light incidence angle on the filter (Kern et al., 2010b).

The remainder of instrument design is similar to that of Kern et al. (2015), including a network switch for internal and external communications and a co-aligned spectrometer for calibration of the camera optical depths (Figure 1). The most notable difference, other than the different UV cameras used (which has a considerable influence on the overall cost of the instrument), is our omission of a thermoelectric cooler (TEC) for temperature control of the spectrometer. Whilst previous versions of the Ocean Optics (now Ocean Insight) spectrometers have shown notable temperature instabilities (pixel-wavelength calibration shift and change in instrument line shape with changing temperature), the relatively new Flame spectrometer series (c. 2015) has a much-improved thermal stability, both as quoted by the manufacturer and under external testing (see Supplementary Material S1). We therefore omitted the TEC, thereby significantly decreasing the power consumption of the instrument (the TEC consumed 3 W in Kern et al., 2015), as well as saving costs and reducing instrument complexity.

Power consumption of the system is relatively low, since the camera utilises a low-power CMOS sensor. All components of the instrument run from 5 V; however, the instrument contains a 12 to 5 V voltage regulator inside, such that the instrument accepts standard 12 V power supplies such as car batteries. Overall power consumption is summarised in Table 1. In full operation the instrument consumes a maximum of 12 W; however, in most cases, operation will occur during only a small fraction of a day, especially since the instrument cannot acquire at night due to the lack of UV radiation. Controlled by the scheduling on the WittyPi HAT, the Raspberry Pi components of the instrument can be powered down when not in operation, leaving only the network switch still running; this consumes 1 W, therefore a time-averaged power consumption (assuming 6 h of operation), may be as little as ≈3.75 W. This is approximately half the power of the system

TABLE 1 Instrument power consumption in different states.

Instrument state	Power consumption (Watts)
Sleep mode	0.96
On (not acquiring data)	6
On (acquiring data)	12

presented in Kern et al. (2015), which consumes ≈25 W in operation and ≈2 W in sleep mode. In locations where light conditions for solar power are poor, such as at high latitudes or regularly cloudy areas, this difference will be particularly beneficial. Lower power consumption should also mean that the instrument can be run on fewer and/or smaller solar panels and batteries, again further reducing the overall cost of the installation.

Overall, the cost of parts for a one-off instrument (bulk purchasing would reduce part costs) is ≈5000 USD, which is primarily controlled by the cost of the UV spectrometer (≈3500 USD for spectrometer and associated optics). Note, these costs do not include data transmission or powering options, which will vary from installation to installation, depending on what existing infrastructure a group may have or the availability of technology in specific countries/regions. Whilst this cost is a notable increase on our discrete field campaign instrument cost (≈500 USD), it remains considerably cheaper than the current alternatives, which employ scientific-grade UV cameras. For example, the instrument presented by Kern et al. (2015) had a part cost (not adjusted for inflation) of ≈18,000 USD (C. Kern, personal communication), not including software licenses which were also 1000 s USD; our use of open-source software also avoids this additional cost.

2.3 Data acquisition

Data acquisition is controlled by software written in Python 3, which is freely available at https://github.com/twVolc/PyCamPermanent. With the aim of making instrument control and processing of SO_2 camera data as accessible as possible, the code provides a graphical user interface (GUI) such that users should not need significant coding knowledge to work with the instrument. The principal aim is to ensure that robust and high-quality data capture and processing is as straightforward as possible for users.

The package contains a number of scripts that control the two cameras and spectrometer through a master script ("pycam_masterpi.py"), which also handles external communication (e.g., for adjusting settings or manual acquisition control). Once the instrument has been setup to acquire automatically, it can then run in a headless state, where connection to the GUI or an external computer is not required.

Automated image capture requires the automatic adjustment of camera and spectrometer shutter speed/integration time to avoid pixel saturation whilst ensuring sufficient light levels to obtain a good signal-to-noise ratio. To this end, image analysis performed on the instrument assesses the level of pixel saturation (relative to the maximum digital number measurable by the sensor—Defined by the sensor bit-depth) in every image/spectrum. User-defined parameters then allow the instrument to determine whether an increase or decrease in shutter speed/integration time is required for each image/spectrum. For images, the user predefines lower (α) and upper (β) limits for maximum pixel saturation (as a fraction), the number of pixels to average for this analysis (X), the number of image rows to use for the analysis, and whether to extract these rows from top-down or bottom-up. The option of only analysing a set number of rows allows us to only interrogate sky pixels in the analysis, omitting irrelevant pixels on the volcano flank. This is particularly important for snow-covered volcanoes, where snow-covered pixels appear very bright and would lead to an unwanted decrease in shutter speed if they were included in the analysis—It is important to optimise sky pixel intensity rather than the image as a whole. After this region of interest (ROI) has been extracted from the image, the brightest X pixels are found and the average digital number (DN) computed. Note, we choose to average a number of pixels rather than analysing only the brightest pixel, since erroneous "hot pixels" could interfere with the analysis. The saturation level of this average DN relative to the bit-depth DN is then computed. If this value is below α, the shutter speed of the next image will be increased; if the value is above β, the shutter speed of the next image will be decreased; for levels within the range α to β, the shutter speed will remain the same. For spectrometer integration time, the principle is the same; however, the user predefines a spectral window in which the saturation analysis takes place, rather than a spatial ROI. Typically this window may be 310–340 nm, ensuring that pixels do not become saturated in the spectrometer fitting window.

2.4 Data size and storage

The instrument holds a 1 TB SSD external storage device. This is the principal location for data storage. To ensure a backup, the data are also saved on the Raspberry Pi micro-SD card (128 GB), which can hold at least 100 GB of data (since it also holds the operating system of the Raspberry Pi). Images have a file size of 617 KB and spectra are 33 KB; of course, data accumulation depends on the acquisition rate and acquisition length per day. As a typical example, acquiring at a rate of 0.2 Hz for 6 h a day will generate ≈165 GB per month (2 TB per year); the storage will therefore be entirely full in 6 months, whilst back-up storage lasts less than 1 month. If frequent trips to download data are not possible, and data back-up is critical, an extra SSD external storage device could be added with relative ease; alternatively, larger SSDs are becoming more readily available. Data compression could also be explored in the future, to improve storage requirements. Where possible, telemetry of data would be desirable to allow near-real-time emission rate estimates and prevent the necessity for frequent trips to the instrument.

2.5 Data processing

Data processing can also be performed using the freely available PyCam software (https://github.com/twVolc/PyCamPermanent). Alongside in-house developed code, much of the processing makes use of the *pyplis* toolbox (Gliß et al., 2017), whilst spectrometer SO_2 retrievals are performed with *iFit* (Esse et al., 2020); light dilution correction of the spectrometer retrievals is also made possible using code associated with (Varnam et al., 2020). Information on the processing routines available can be found in those articles, and it is not within the scope of this paper to provide a detailed review of these routines. Using example datasets from Lascar and Kīlauea, Section 4 provides more details on some of the data processing algorithms available.

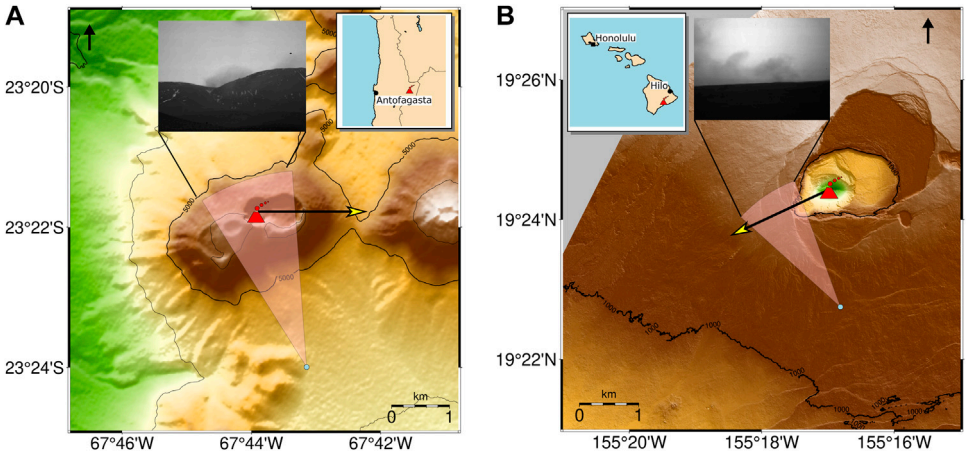

FIGURE 2
Digital elevation models (DEMs) of site locations with cameras shown as blue dots and their field of views extending from them, along with an example image from the on-band camera in each case. Red symbols indicate gas source locations. Typical plume motions are shown by yellow-headed arrows, but can vary significantly throughout the year. **(A)** Lascar (DEM from SRTM data); **(B)** Kīlauea (DEM from LiDAR data taken from Mosbrucker et al., 2020).

We note that absolute automation of SO_2 camera data processing remains troublesome, often requiring an expert user's retrospective interaction to ensure that processing routines have been optimally applied and to interrogate data quality. Others have achieved at least reasonable levels of automation (e.g., Kern et al., 2015; Delle Donne et al., 2017; Delle Donne et al., 2019), for instance, with the incorporation of a visibility index to omit data with poor visibility (Delle Donne et al., 2017) and a closed-path semi-circular integration line to capture gas emissions for all plume orientations (Kern et al., 2015). Of particular note, Delle Donne et al. (2019) investigated the difference between manual and automatic processing procedures, finding a reasonable agreement between their automatic processing routine and manual expert analysis ($r^2 \approx 0.75$); however, there clearly remains a notable disparity between the two, and this MATLAB-based (requiring a license) automation software is not open-source. In this respect, our work herein does not present any further steps in automation routines; however, it does provide open-source, user-friendly (with a graphical user interface) software which can promote the accessibility of SO_2 cameras to the wider volcanology community.

Data herein were processed with some manual interaction, for example, with the plume cross-sections optimized for the plume direction in each time series. Our software does, however, allow the use of multiple cross-sections, which would allow a quasi-semi-circular integration line, as in Kern et al. (2015), ensuring the capture of gas emissions for all plume orientations; future software development will include the option to use true semi-circular lines. Background sky intensities also require manual derivation at times, although automated procedures, which harness the *pyplis* functionality, are available within our GUI. In general, we have found that at times of non-perfect conditions (e.g., heterogeneous cloud cover), it was optimal to manually define the background sky region for an image sequence. Other automated background sky retrieval algorithms have been proposed (Osorio et al., 2017) and may offer improved performance when moving towards a fully automated processing procedure; again, this could be the focus of future software development.

3 Field sites

3.1 Lascar

Lascar (5,592 m; 23.37°S, 67.73°W) is a stratovolcano composed of 6 overlapping summit craters. It is predominantly andesitic-dacitic in composition. In 1993 a VEI 4 eruption created a column reaching 20–22 km altitude and resulted in ash fall as far away as Buenos Aires (1,500 km SE of the volcano) (Global Volcanism Program, 1993). Current activity is primarily confined to fumarolic activity within the active crater, although during the camera installation a few small explosions were possibly heard, albeit with no clear visible associated phenomena.

The camera system was installed on Lascar on 18th May 2022, approximately 4,300 m from the crater (Figure 2A). The camera location provides a near-orthogonal viewing direction relative to the prevailing westerly winds. However, the plume has a tendency to swirl and stagnate within Lascar's crater before drifting eastwards. We also note that the front of the crater can at times obscure full view of the gas, which may lead to underestimations in emission rates at times when the plume does not loft above the crater. The installation is displayed in Figures 3A, B.

3.2 Kīlauea

Kīlauea (1,247 m; 19.41° N, 155.28° W) is a shield volcano on the Island of Hawai'i. Starting in May 2018, a series of fissure eruptions in the lower East Rift Zone accompanied drainage from

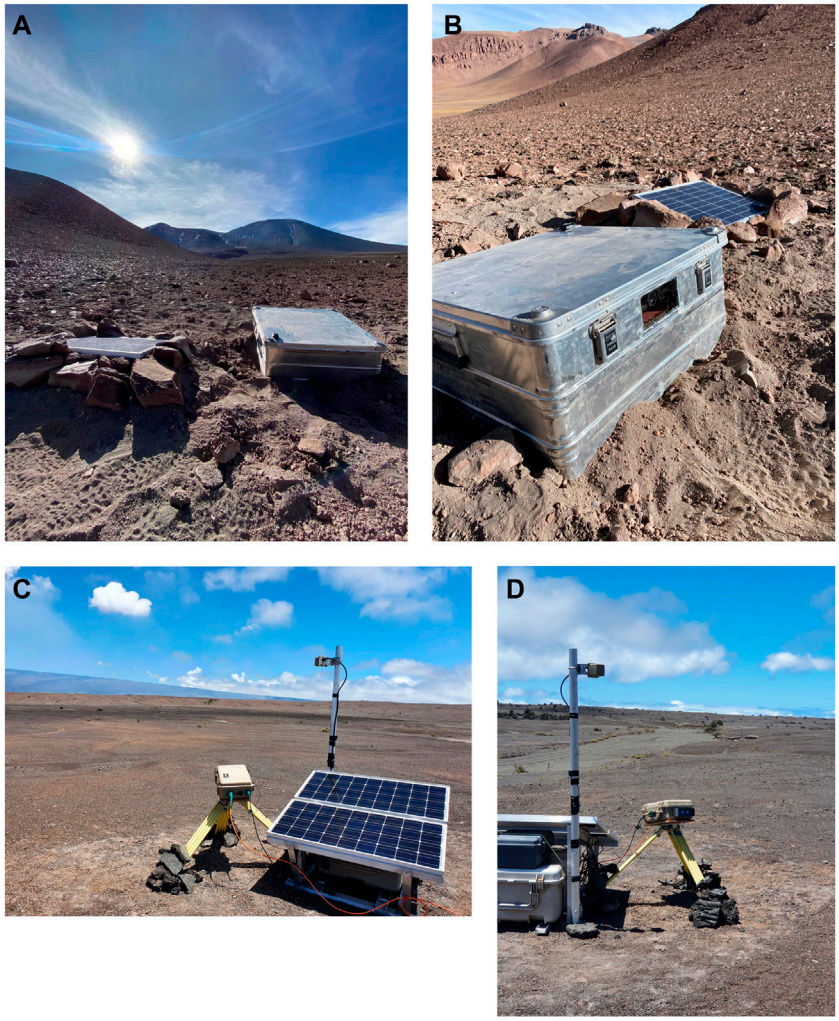

FIGURE 3
(A, B) Instrument installation on Lascar volcano, Chile (Photo credit: T. Wilkes). **(C, D)** Instrument installation on Kīlauea volcano, Hawaii, United States (Photo credit: T. Pering).

the Halemaʻumaʻu lava lake, which resulted in collapse of the summit caldera (Neal et al., 2019). During this period, SO_2 emission rates were estimated to have reached at least 200 kt/day (2,300 kg/s) (Kern et al., 2020). These extreme conditions were modelled to have significantly impacted air quality hundreds of kilometres downwind of the volcano (Kern et al., 2020), whilst in the local vicinity lava flows and seismicity caused substantial damage and destruction of infrastructure (Neal et al., 2019).

The system was installed on Kīlauea on 21st July 2022, approximately 2,700 m from the crater (Figure 2B). The north-easterly trade winds are relatively consistent, resulting in right to left gas motion through the image, which is almost exactly orthogonal to the viewing direction of the camera. This installation was augmented with data telemetry (up to 20 MB/s) from the instrument to a local observatory, allowing near-real-time processing of the data. This will enable rapid integration of SO_2 emission rates into hazard assessments at the volcano. The installation, along with radio antenna, is displayed in Figures 3C, D.

4 Results and discussion

4.1 Lascar

We here first present an in-depth analysis of a sample dataset retrieved shortly after camera installation on Lascar volcano, over the period 16:05:05–17:05:00 UTC on 20th May 2022. This is followed by a longer-term time series spanning 20th-21st May. Spectrometer FOV calibration is shown in Figure 4, along with the subsequent camera optical depth (τ_{SO2}) calibration. The FOV location is found through iterative calculation of the correlation coefficient between the spectrometer column density time series (Figure 4B) and τ_{SO2} time series of each pixel individually (Lübcke

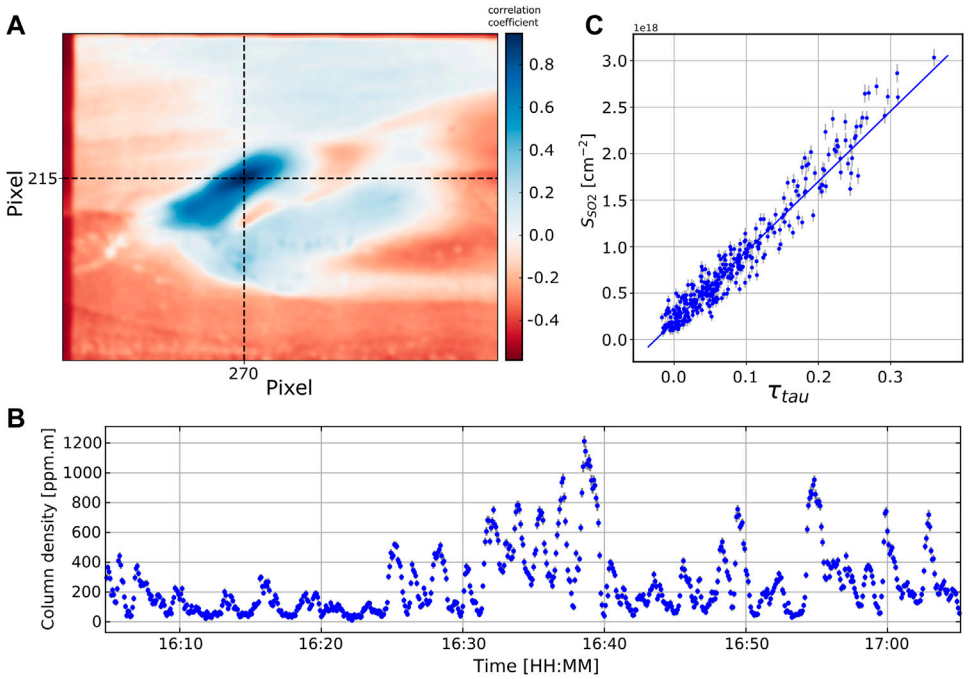

FIGURE 4
(A) Pearson correlation coefficients (colour scale) of spectrometer SO_2 retrievals with camera optical depths (τ_{SO2}), enabling determination of where the spectrometer field of view (FOV) is located within the camera image. In this case, the highest correlation coefficient is centered at pixel coordinate (270, 215). **(B)** Spectrometer-retrieved SO_2 slant column density retrieval time series (in UTC), highlighting that the FOV location is well-positioned to measure a wide range of column densities through time, therefore allowing a robust calibration of the camera optical depths. **(C)** Spectrometer SO_2 slant column density (S_{SO2}) retrievals versus camera optical depths measured in the spectrometer's FOV (as determined in A). The fitted calibration line is used to calibrate all pixel optical depths in the images.

et al., 2013; Gliß et al., 2017); Figure 4A displays the resulting correlation image and location of the spectrometer's FOV within the image. Once this is known, the spectrometer FOV can be fixed for subsequent datasets if desired. A regression between the spectrometer column densities and τ_{SO2} within the spectrometer's FOV can then be formed (Figure 4C), therefore allowing calibration of all pixel τ_{SO2} values. We note that the spectrometer's FOV is positioned just above the crater, such that it should be located within gas for most plume motions; however, there may still be periods of time where it is not located within the gas plume. In such periods it may be necessary to revert back to older calibrations, either earlier in the day or from previous days. Over time, we will build a catalog of instrument calibrations, which may then allow more robust selection of calibrations during periods where the plume is not in the spectrometer's FOV, for instance by identifying similar illumination conditions where a calibration was possible. A time series of the spectrometer SO_2 slant column density (SCD) retrievals (Figure 4C) also highlights that the spectrometer FOV is positioned such that it typically captures a wide range of SCDs in relatively short periods (<30 min). This ensures that camera optical depth calibration is unlikely to require significant extrapolation to larger values, which would result in greater measurement uncertainties. In this case the relationship between optical depth and SCDs was assumed linear, which is often reasonable for low SCDs. However, Kern et al. (2013) found that for high SO_2 burdens optical depths deviate significantly from the linear Beer-Lambert approximation, in part due to complex radiative transfer caused by in-plume aerosols and light dilution. The *pyplis* backend allows for non-linear regressions to be used in fitting camera optical depth to SCD, which can be changed within the pycam GUI.

Figure 5 shows a typical optical depth image from the instrument, also displaying the ICA line used to determine SO_2 emission rates for the time series discussed here. Emission rates can be retrieved using 4 distinct plume speed estimation algorithms; these are outlined in detail by Gliß et al. (2017), Gliß et al. (2018) and briefly summarised in Table 2. The cross-correlation technique introduced in Section 2.1 is represented by *flow_glob*, whilst the 3 other algorithms (*flow_raw*, *flow_histo*, *flow_hybrid*) utilise optical flow vectors with varying degrees of post-analysis. Figure 6 displays these effective velocities and the associated emission rate estimations; for clarity, we omit *flow_hybrid* from the plot, but these effective velocities, and thus emission rates, were extremely similar to the *flow_histo* algorithm. We note that, in this case and in our experience more generally, the optical flow algorithms typically estimate lower plume speeds than cross-correlation (*flow*_glob). This may be a result of cross-correlation preferentially fitting to larger pulsing events of gas (driven either by volcanic or meteorological factors), which have the most distinctive signature–notably standing out from general noise in a degassing

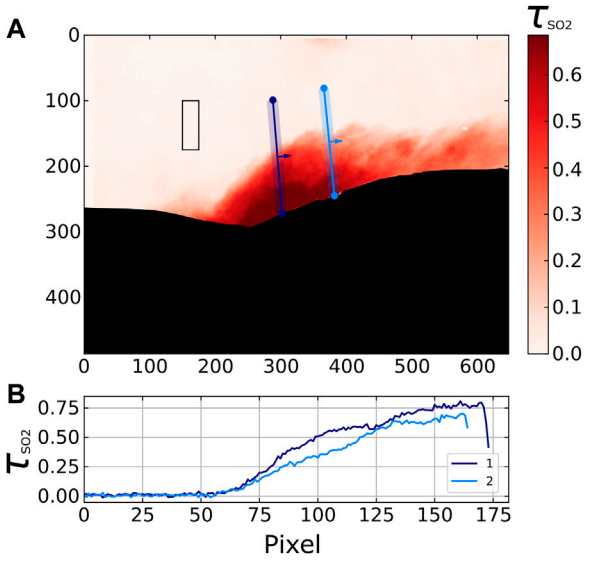

FIGURE 5
(A) Optical depth image of Lascar volcano from an acquisition at 14:00:35 UTC (10:00:35 CLT) on 25th May 2022. The black rectangle indicates the region of clear sky where the intensity I_0 was estimated. **(B)** Optical depth values across integration lines shown in **(A)**. The dark blue line was used for emission rate retrievals whilst the light blue was the secondary line used for cross-correlation plume speed estimation.

time series. This is supported by the higher optical flow speeds often coinciding with the larger mass loading along the ICA lines (peaks in the cross-correlation emission rate series); at these points the optical flow effective velocity is very similar to the cross-correlation plume speed (≈7.3 m/s in this case). In general, we therefore suggest the use of optical flow algorithms leads to more reliable emission rate estimates (Peters et al., 2015), especially the *flow_histo* (or *flow_hybrid*) algorithm (Gliß et al., 2018), which retrieves a local average flow velocity and can potentially mitigate unreliable retrievals from the raw Farnebäck algorithm. We note, however, that there are relatively frequent periods where the *flow_histo* algorithm fails, resulting in no emission rate for these points (e.g., see Figure 6 or the "*flow_histo* LD corrected" sheet in Lascar spreadsheet of supplementary materials). To account for such gaps, either interpolating between recent plume speeds, or reverting to the *flow_raw* or cross-correlation algorithm, are solutions. More detailed discussions of plume speed algorithms and associated uncertainties can be found elsewhere (Peters et al., 2015; Gliß et al., 2017; Klein et al., 2017; Elias et al., 2018; Gliß et al., 2018).

For the series shown in Figure 6, cross-correlation emission rates ranged between 1.3 and 6.0 kg/s, with a mean of 2.8 ± 0.7 (±1 SD) kg/s, whilst *flow_histo* generated a mean emission rate of 2.0 ± 0.7 kg/s, with the series ranging between 0.4 and 4.9 kg/s. The emission rate time series shows clear pulsing behaviour at Lascar, although it is difficult to definitively attribute this to volcanic activity, since the gas typically accumulates somewhat in the crater before exiting to where it can be observed by remote sensing equipment. It is therefore possible that wind turbulence at the summit is influencing the retrieved time series.

The above results were generated neglecting a light dilution (LD) correction, the phenomenon where light is scattered into the FOV of the instrument between the plume and the instrument; such light has not passed through the plume, so does not contain absorption features of SO_2, but contributes to the radiance at the detector. This can result in a significant underestimation of SO_2 emission rates (Mori et al., 2006; Kern et al., 2010a). Campion et al. (2015) proposed an image-based correction light dilution for camera optical depths, based on the changing measured intensity of the volcanic flank as it gets closer to the observer. We implement this correction using the *pyplis API*, finding that even in the dry Atacama air at >4,500 m altitude, there is still significant light dilution in the images (Figure 7). However, using this correction alone is only applicable to gas cell calibrated systems. Spectrometer-calibrated instruments require that the column densities measured by the spectrometer have also been corrected for associated light dilution effects; in fact, the spectrometer correction is much more critical than camera optical depth calibration, since the final calibration links column densities to somewhat arbitrary optical depths.

To correct the spectrometer-retrieved column densities we used the dual-band method proposed by Varnam et al. (2020). However, we found that the correction gave quite stochastic light-dilution factors that ranged from anywhere between 0 and 1. Correcting each spectrum individually therefore introduced large errors which resulted in a poor correlation between the spectrometer column densities and the associated optical depths in the camera images. The high correlation presented in Figure 4 suggests that the column density trend is accurate, even if absolute values are affected by light dilution. Below, we therefore present a method for stabilising the light dilution correction. Following Varnam et al. (2020), we first calculated the light dilution factor (LDF) and the associated corrected column density for each spectrum in the time series. We suggest the light dilution correction algorithm is likely to perform better on spectra with larger column densities, since the dual-band technique should see more disparity between the two bands than if fitting to low column densities. We therefore then discarded all spectra measuring column densities below 1E18 molecules cm^{-2}. We then took the median LDF of these

TABLE 2 Plume speed estimation algorithms, based on Gliß et al. (2017).

Name	Algorithm description
flow_glob	Cross-correlation
flow_raw	Raw output from Farnebäck optical flow algorithm
flow_histo	Histogram post-analysis to find a local average velocity vector for each integration line
flow_hybrid	Reliable motion vectors are used whilst unreliable ones are replaced based on histogram post-analysis

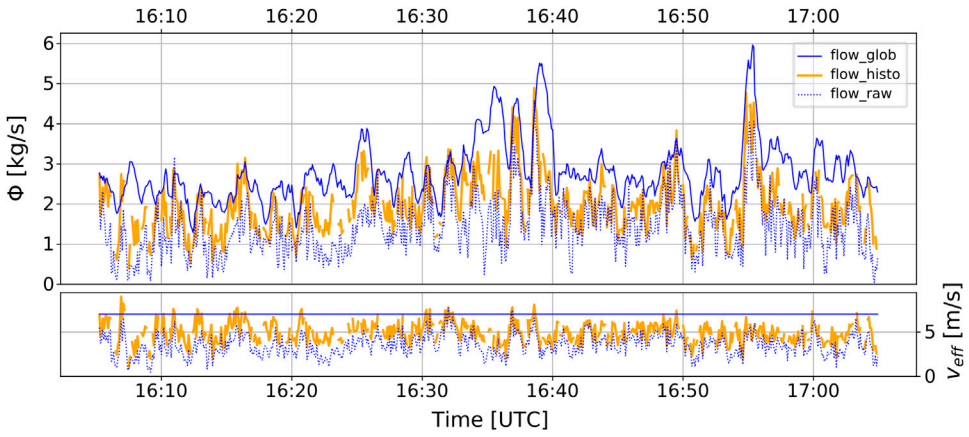

FIGURE 6
Emission rate (Φ) time series and associated effective velocity estimation (V_{eff}) using 3 different plume speed estimation algorithms. The single cross-correlation velocity is faster than optical flow velocities for the majority of the series, but peak optical flow velocities match quite well with this cross-correlation speed. We suggest *flow_histo* (bold orange) is likely to provide the most reliable data in general; however, at times this algorithm is unable to compute a reliable speed, therefore some parts of this time series are absent. Data from Lascar volcano on 20th May 2022; times are in UTC.

retrievals, in this case 0.25. Looking at the full time series again, we extracted all data points within ±20% of the median LDF (0.20 ≤ LDF ≤ 0.30). From this subset, a relationship between corrected and uncorrected column densities can be found, which is relatively linear within the range of values found here. This relationship was thus used to correct the initial column density time series. The correction increased the column densities by between ≈30% and ≈70%, depending on the initial uncorrected column density. This correction maintained the high >0.8 correlation between the spectrometer column densities and the associated optical depths within the spectrometer's FOV in the image series. We note, however, that this correction may be more complicated to implement in near-real-time when data are required rapidly for volcano monitoring purposes. Perhaps importantly, the general trends in the emission rates without a LD correction (Figure 6) are very similar to those with a LD correction (Figure 8), since the correction is relatively stable through time. This similartity suggests that emission rate time series without this correction could still have utility for rapid monitoring and response in real-time; the more accurate LD-corrected time series can then be generated *post hoc*.

The resulting light dilution-corrected emission rate time series increased somewhat (Figure 8A), with a mean cross-correlation emission rate of 3.8 ± 1.3 kg/s, whilst the *flow_histo* plume speed produced a mean emission rate of 2.8 ± 1.2 kg/s. From these mean values, the uncorrected retrievals therefore underestimate emission rates by 26% and 29% for *flow_glob* and *flow_histo*, respectively. These values are in the middle of the range of the examples presented by Campion et al. (2015); however, with the high altitude and dry conditions at Lascar, the level of light dilution is slightly higher than we had anticipated, highlighting that light dilution is likely to be a significant source of error for any measurements made at greater than 1–2 km from a volcano.

The longer-term series (Figure 8B), based on the same processing procedure outlined above (including light dilution correction), highlights the instrument's ability to perform shut-down/start-up sequences and adjust to changing light conditions throughout the day. Here, it is evident that the emission rates from the 2 days are significantly different. Whilst this could represent a true change in volcanic degassing, we cannot rule out the possibility that emission rates on 20th were incomplete measurements, with part of the plume being obscured by the crater as it drifted to the east. We note that plume speeds (v_{eff}) across the 2 days are relatively stable. The mean emission rate across the 2 days is 5.2 ± 3.1 kg/s, whilst the emission rate for only the 21st is 6.7 ± 3.1 kg/s. The emission rate is relatively variable, reaching a maximum of 17.5 kg/s; as mentioned above, this could be volcanogenic in nature but may also be associated with gas accumulation in the crater and subsequent large ejections driven by metrological conditions (e.g., wind turbulence).

Recent SO_2 camera measurements, in January 2019, are in good agreement with our measurements (4.7 ± 1.4 kg/s), suggesting relative stability of the volcanic system over the last few years (Layana, 2022). However, Layana (2022) also found that, during a period where satellite-derived thermal anomalies at the volcano were absent, SO_2 emissions (measured in March and June 2018) were significantly lower—close to or below the detection limit of their SO_2 camera. This highlights the importance of more continuous monitoring, which can identify changes in activity over a broad range of timescales (from the order of minutes to sub-annual/annual and beyond); Thus, again we emphasize that discrete field campaigns cannot provide a complete picture of a volcano's state. Our measurements are somewhat higher than NOVAC scanner data between 2013–2016, which retrieved a mean of 2.6 ± 1.4 kg/s (Bucarey et al., 2020; Arellano et al., 2021). This may be a result of changing subsurface conditions in recent years, or a product of the longer-term nature of the NOVAC time series incorporating days of lower activity too. Discrete campaigns have also measured a broad range of emission rates on Lascar: 6.4 ± 2.5 kg/s in December 2012 (Tamburello et al., 2014); 27.8 kg/s in January 2003 (Mather et al., 2004). The general trend

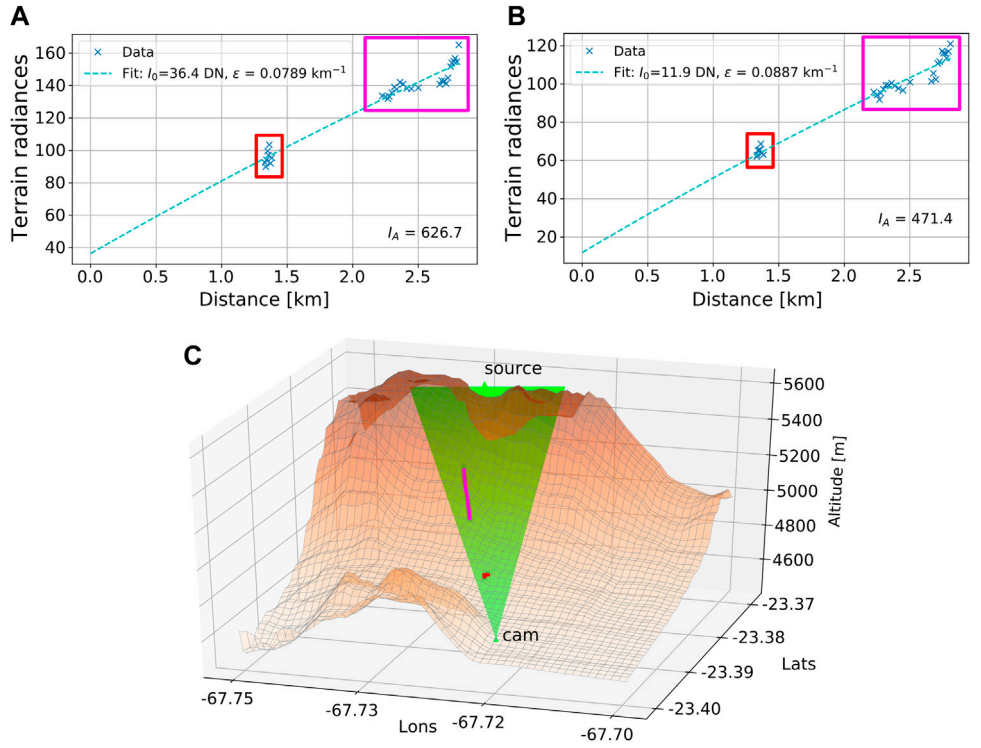

FIGURE 7
Image-based light dilution processing. **(A)** On-band image extinction coefficient calculation. **(B)** Off-band image atmospheric extinction coefficient calculation. **(C)** Digital elevation model of the camera viewing geometry on Lascar volcano; camera field of view is displayed in green. Magenta and red lines indicate the location of the extracted lines in the image in relation to the topography. Data points from these lines are outlined in A and B by their respective colours.

appears to be a steady decrease in SO_2 degassing (≈2003–2016), with perhaps a new increase in emissions in the last few years; this is something which the new installation will be able to elucidate further in the coming months/years.

4.2 Kīlauea

We present here data acquired from Kīlauea volcano on 25th July 2022. Figure 9 displays a representative optical depth image acquired by the camera. Within the time period of this camera dataset, 9 traverse-mode DOAS measurements were also made from a vehicle transecting the plume ≈1.5 km downwind of the Halemaʻumaʻu Crater. Wind speeds for emission rate calculations of these traverses were retrieved from a weather station located at Sand Hill, about 2 km west of the active vent. These were then scaled by a factor of 1.2 to account for systematic underestimation of the wind speeds aloft by our ground-based measurements (Elias et al., 2018). Spectral and spatial analysis of the traverse data was performed according to standard DOAS analysis procedures (Platt and Stutz, 2008) using the DOASIS software (Kraus, 2006) in combination with a custom MATLAB code ("mDOAS") specifically developed for spatial analysis of Mobile DOAS measurements.

Using the same method as in Section 4.1, we corrected the *iFit* spectrometer retrievals for light dilution. In this case, the image-based correction was not possible, due to the viewing geometry of the camera not providing enough volcanic flank. However, we propose that a first order light dilution correction should be possible simply by correcting the spectrometer retrievals, if we assume that image optical depths are uniformly affected by light dilution and that light dilution magnitude does not change significantly within a calibration window (typically 30–60 min). These assumptions are not strictly correct, however, since the correlation between image optical depth and column density (e.g., as in Figure 4B) remains strong following the spectrometer light dilution correction, correcting only the spectrometer retrievals may be adequate in many cases.

The traverse and camera datasets are displayed in Figure 10. Due to the significant differences in sampling frequency, and measurement location, exact comparison between the values is somewhat complicated and includes caveats; nevertheless, a basic comparison can still be useful. The 8 early DOAS traverses found an average emission rate of 18.7 ± 8.0 (±1 SD) kg/s, with a minimum measurement of 6.2 kg/s and maximum of 27.6 kg/s. Whilst there is a disparity, these measurements are in reasonably good agreement with the camera's contemporaneous first acquisition period (≈20:00–21:30 UTC), which has a mean emission rate of 12.7 ± 5 kg/s and a maximum of 28.0 kg/s. For the period 11:00–01:00 UTC (25/26th July), the difference in emission rates is more notable, with the single

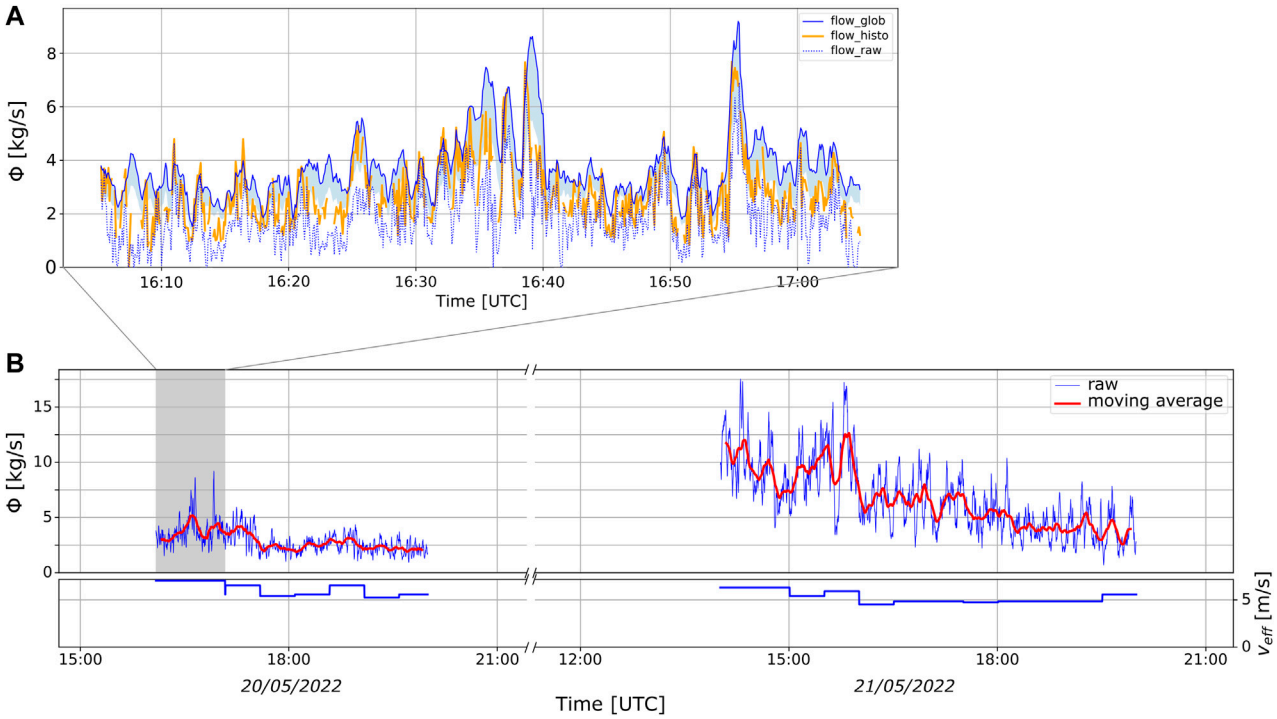

FIGURE 8
(A) Emission rate (Φ) time series as in Figure 6 but corrected for light dilution. Blue shaded region shows the difference between the uncorrected and corrected emission rates for the *flow_glob* series. **(B)** A longer-term series spanning 20th-21st May based on *flow_glob* plume speeds (blue) with a 10-min moving average (red). Plume speed (v_{eff}) is also displayed and is relatively consistent across the 2 days, unlike the emission rate which is significantly higher on the 21st.

traverse measurement of 23.5 kg/s, whilst the mean camera emission rate was just 7.5 ± 3.0 kg/s.

It is not clear what has caused this large disparity in the second period (albeit comparing with only one contemporaneous traverse measurement), although some possible influences may be: differences in wind speed estimates (and the sources of these estimates); In-plume aerosol scattering of light; incomplete capture of the full gas plume by the camera, due to its viewing geometry and the crater geometry; non-orthogonal plume motion relative to camera viewing direction (e.g., Klein et al., 2017). Regarding the latter, using the plume centers based on traverse measurements, we can calculate the difference between the plume's motion and the camera's focal plane azimuth. For the first acquisition period the difference ranged between 13° and 25°, whilst for the second period this difference was 17°. Although this can lead to an underestimation in emission rates, since the second period's angular deviation falls within the bounds of the first period, it is unlikely that this is the principal cause for the larger emission rate disparities in the second period. Alternatively, incomplete capture of the gas plume by the SO_2 camera could be a notable source of error for the camera measurements. The low lying crater geometry means that at times the plume can hug the ground, therefore making it difficult to fully capture emissions close to the source with the SO_2 camera. This would be particularly notable in stronger wind conditions, which would reduce the degree of plume lofting as it leaves the crater. It is difficult to quantify this error, but it certainly could contribute to a significant underestimation in emission rates. Using optical flow motion vectors, it should be possible to identify periods where plume motion is less buoyant (more horizontal motion) and flag such periods as potentially having unreliable emission rate estimates; longer-term datasets will allow deeper investigation into this.

Disparities in plume speeds, and associated emission rates, are somewhat more quantifiable; Although we note that direct comparisons may be troublesome, since the SO_2 camera images and weather stations are not collocated. Furthermore, neither technique is a direct measurement of the plume's velocity at its altitude above the traverse measurements. Details of the methodology employed for this comparison are outline in Supplementary Material S2. During the final traverse (23:56 UTC), in the second camera acquisition period, corrected image-based horizontal plume speeds had a mean of 6.0 m/s for optical flow analysis, whilst cross-correlation measured 9.0 m/s. As discussed in Section 4.1, the discrepancy is likely due to cross-correlation fitting to large pulses of gas exiting the crater, which are likely relate to larger gusts of wind and/or changes in volcanic degassing vigor. Indeed, much like in Figure 6, the optical flow speeds reach similar (and slightly larger) values at times; however, for the specific 10-min period of the traverse (adjusted for time for the plume to drift from crater to traverse location), the values are

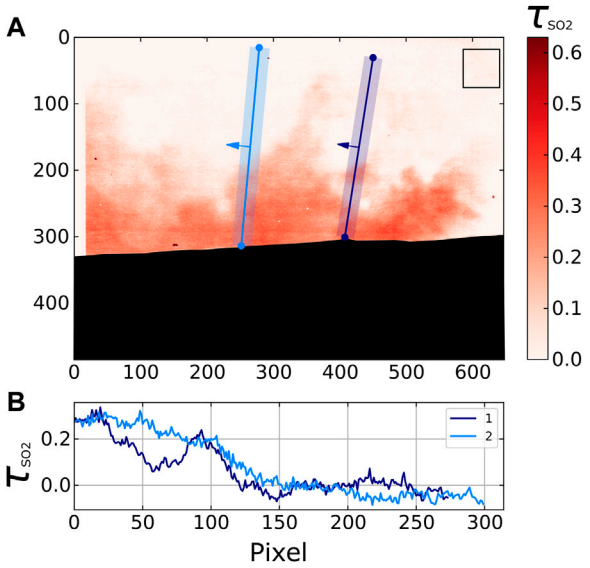

FIGURE 9
(A) Optical depth image of Kīlauea volcano from an acquisition at 20:21:35 UTC (10:21:35 HST) on 25th May 2022. The black rectangle indicates the region of clear sky where the intensity I_0 was estimated. **(B)** Optical depth values across integration lines shown in **(A)**. The dark blue line was used for emission rate retrievals whilst the light blue was the secondary line used for cross-correlation plume speed estimation.

notably lower. The Sand Hill weather station measurement at this time resulted in a scaled plume speed of 10 m/s. Using our plume measurements to rescale the traverse emission rates, we find emission rates of 14.1 and 21.2 kg/s for optical flow and cross-correlation, respectively. Whilst these values remain higher than the SO_2 camera average for this period, the camera data reach 12.9 kg/s at 23:53:15 UTC and 13.8 kg/s at 23:54:30 UTC; the center of the traverse was reached at 23:56:59 UTC and is located ≈2–3 min downwind (1.5 km from crater). For comparison, the difference between camera-derived and weather station-derived plume speeds for the first acquisition period (20:00–21:30 UTC) is markedly smaller; camera-derived speeds averaged 6.9 and 9.9 m/s, for optical flow and cross-correlation, respectively, whilst the weather station-derived speed was 9 m/s throughout.

Although it seems to be a contributing factor, it is very unlikely that the above plume speed difference is the only source of disparity between the traverse and SO_2 camera measurements. Whilst the academic literature currently lacks long-term comparisons between SO_2 camera measurements and traverse-/scanning-mode DOAS measurements, some previous work has found good agreement between DOAS traverses and UV camera data in discrete campaigns (Varnam et al., 2021). Conversely, however, de Moor et al. (2017) highlighted that their permanent scanning DOAS system systematically measured lower emission rates relative to contemporaneous traverse DOAS measurements. They suggest that one possible cause is having a sub-optimal scanning position that fails to capture the full plume in a large number of scans, due to variable wind direction blowing the plume away from fixed-location scanners. We note that similar issues, associated with camera location/viewing geometry, are particularly pertinent for permanent installations; during discrete field campaigns imaging location can be chosen on a daily (or sub-daily) basis depending on plume conditions. On many volcanoes it can be difficult to find a suitable viewing geometry to ensure that, given any wind direction and degassing strength, the camera will always be able to capture complete and robust emission rates. Indeed, in many cases it may be advisable to install multiple systems around a target, providing various vantage points that could facilitate more robust retrievals under a range of meteorological and volcanic conditions (e.g., Delle Donne et al., 2022). Scanning DOAS networks often do exactly this on the most comprehensively monitored volcanoes (Burton et al., 2009; Galle et al., 2010). The relatively low cost of our new permanent camera design would facilitate such ambitions. Additionally, we also suggest that longer-term comparisons

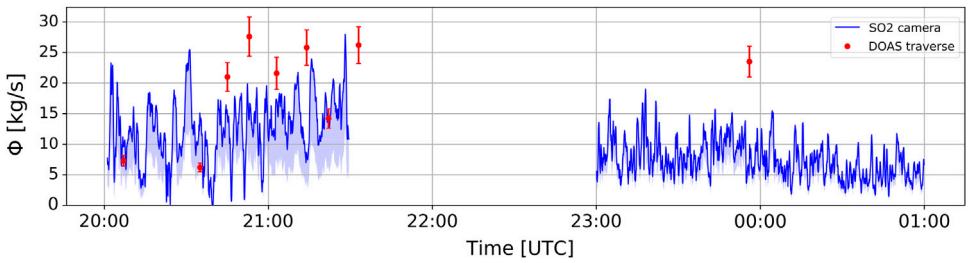

FIGURE 10
Permanent camera SO_2 emission rate (Φ) time series at Kīlauea on 25th and 26th July 2022 (UTC; all measurements were 25th July HST), with contemporaneous DOAS traverse measurements (red dots). Camera retrievals were made with the cross-correlation (*flow_glob*) plume speed estimation algorithm. The magnitude of the light dilution correction (applied through the instrument's spectrometer iFit retrievals) is displayed by the shaded blue region. Agreement between the camera and traverse measurements is reasonably good for the 25th measurements, whilst on the 26th the SO_2 camera retrieves significantly lower emissions rates, albeit with only one traverse measurement for comparison in this sequence. Note that the traverse measurements were performed ≈1.5 km downwind of the source, therefore with a plume speed of ≈8–10 m/s we may expect a lag in measurements of ≈150–190 s.

between SO_2 cameras and scanning-/traverse-mode DOAS measurements, as well as satellite retrievals (e.g., TROPOMI), are critical to understanding the validity of each measurement technique under a wide range of conditions.

5 Conclusion

We have presented the design of a new permanent UV camera system for volcanic SO_2 emission rate measurements, followed by installation of the instrument on 2 active volcanoes (Lascar, Chile; Kīlauea, Hawaii, United States). The instruments make use of a suite of previously developed open-source Python packages to supplement custom software, ensuring robust/standardised and comprehensive data analysis. We have highlighted how the relatively low cost and power consumption of these instruments makes them suitable for wide-scale deployment on volcanoes in a range of different environments around the globe. Although we note that longer-term testing of instrument performance is still required, such instruments have the potential to provide valuable datasets for comparison with alternative ground-based remote sensing instruments (i.e., DOAS scanning networks and traverse measurements) as well as ground-truthing satellite retrievals.

We provide example datasets from Lascar (Chile) and Kīlauea (Hawaii, United States). At Lascar, mean emission rates of 5.2 ± 3.1 kg/s agree well with recent (2019) measurements but are somewhat higher than earlier (2013-2016) longer term NOVAC time series (2.6 ± 1.4 kg/s). On Kīlauea we presented a comparison with contemporaneous traverse-mode DOAS measurements, which showed a reasonable agreement, albeit with the traverse emission rates (18.7 ± 8.0 kg/s) typically being higher than the camera-derived rates (12.7 ± 5 kg/s for the first series). A later measurement series gave lower camera-derived emission rates that were typically half the value of a traverse measurement in this window. We found that differences in wind speed estimates likely contributed significantly to the disparity; however, it is likely that other effects contributed too (e.g., in-plume scattering of light, incomplete capture of the entire plume by camera measurements).

We particularly emphasise the importance of permanent/continuous monitoring equipment in volcanic gas measurements, since volcanic activity is notably transient and variable in nature over a wide span of timescales. Whilst of course having significant value to the scientific community, the danger of discrete field campaigns is in interpreting such measurements as representative of that volcano outside of the measurement window. In some branches of volcanology (e.g., seismology), continuous monitoring is already somewhat commonplace; however, although there are a number of installations for permanent gas monitoring (e.g., most notably NOVAC), campaign-style measurements are still routine in a number of places across the globe. This is likely influenced by the cost and complexity of permanent systems. The instrument presented herein has the potential to aid the transition to more continuous geochemical monitoring of hazardous volcanoes across the globe, which in turn stands to improve our understanding of hazardous volcanic events and inform eruption forecasts (Kern et al., 2022).

Data availability statement

The original contributions presented in the study are included in the article/Supplementary Material, further inquiries can be directed to the corresponding author.

Author contributions

TW wrote the manuscript, developed the instrument and installed the instrument on Lascar. TP contributed to the manuscript, contributed to instrument development and installed the instrument on Kīlauea. FA contributed to instrument development. SL installed the instrument on Lascar and contributed to instrument development. PN and CK installed the instrument on Kīlauea; CK also contributed to instrument development. AM contributed to instrument development. MA contributed to field work in Chile. CZ contributed to instrument development.

Funding

TW acknowledges the support of a Leverhulme Early Career Fellowship (ECF-2020-107). We acknowledge the University of Sheffield Institutional Open Access Fund for covering the publication fees of this manuscript. For the purpose of open access, the author has applied a Creative Commons Attribution (CC BY) licence to any Author Accepted Manuscript version arising. This work has been partially funded by FONDECYT Regular project 1211220 and Antofagasta Regional Government, FIC-R project, code BIP N°30488832-0. SL is funded by Millennium Institute on Volcanic Risk Research - Ckelar Volcanoes, Millennium Scientific Initiative, code ICN2021_038. MA is funded by FONDECYT Regular project 1211220 and Master fellowship from Postgraduate Direction, Universidad Católica del Norte, Chile.

Acknowledgments

We would like to thank two reviewers whose comments have greatly improved the manuscript. TW would like to thank Jonas Gliß, Benjamin Esse and Mathew Varnam for their development of, and subsequent support with, their valuable Python packages. We also acknowledge the support of Silvana Hidalgo and colleagues at IGEPN for their work on the installation of an instrument on El Reventador, Ecuador. Any use of trade, firm, or product names is for descriptive purposes only and does not imply endorsement by the U.S. Government.

Conflict of interest

The authors declare that the research was conducted in the absence of any commercial or financial relationships that could be construed as a potential conflict of interest.

Publisher's note

All claims expressed in this article are solely those of the authors and do not necessarily represent those of their affiliated organizations, or those of the publisher, the editors and the reviewers. Any product that may be evaluated in this article, or claim that may be made by its manufacturer, is not guaranteed or endorsed by the publisher.

Supplementary material

The Supplementary Material for this article can be found online at: https://www.frontiersin.org/articles/10.3389/feart.2023.1088992/full#supplementary-material

References

Aiuppa, A., Federico, C., Giudice, G., Giuffrida, G., Guida, R., Gurrieri, S., et al. (2009). The 2007 eruption of Stromboli volcano: Insights from real-time measurement of the volcanic gas plume CO2/SO2 ratio. *J. Volcanol. Geotherm. Res.* 182, 221–230. doi:10.1016/j.jvolgeores.2008.09.013

Arellano, S., Galle, B., Apaza, F., Avard, G., Barrington, C., Bobrowski, N., et al. (2021). Synoptic analysis of a decade of daily measurements of SO₂ emission in the troposphere from volcanoes of the global ground-based Network for Observation of Volcanic and Atmospheric Change. *Earth Syst. Sci. Data* 13, 1167–1188. doi:10.5194/essd-13-1167-2021

Bluth, G. J. S., Shannon, J. M., Watson, I. M., Prata, A. J., and Realmuto, V. J. (2007). Development of an ultra-violet digital camera for volcanic SO2 imaging. *J. Volcanol. Geotherm. Res.* 161, 47–56. doi:10.1016/j.jvolgeores.2006.11.004

Bucarey, C., Arellano, S., Velasquez, G., and Galle, B. (2020). *SO2 flux of Lascar volcano from the NOVAC data-base*. doi:10.17196/novac.lascar.001

Burton, M. R., Caltabiano, T., Murè, F., Salerno, G. G., and Randazzo, D. (2009). SO2 flux from Stromboli during the 2007 eruption: Results from the FLAME network and traverse measurements. *J. Volcanol. Geotherm. Res.* 182, 214–220. doi:10.1016/j.jvolgeores.2008.11.025

Burton, M. R., Salerno, G. G., D'Auria, L., Caltabiano, T., Murè, F., and Maugeri, R. (2015). SO2 flux monitoring at Stromboli with the new permanent ingv SO2 camera system: A comparison with the flame network and seismological data. *J. Volcanol. Geotherm. Res.* 300, 95–102. doi:10.1016/j.jvolgeores.2015.02.006

Campion, R., Delgado Granados, H., Mori, T., Delgado-Granados, H., and Mori, T. (2015). Image-based correction of the light dilution effect for SO2 camera measurements. *J. Volcanol. Geotherm. Res.* 300, 48–57. doi:10.1016/j.jvolgeores.2015.01.004

D'Aleo, R., Bitetto, M., Delle Donne, D., Tamburello, G., Battaglia, A., Coltelli, M., et al. (2016). Spatially resolved SO 2 flux emissions from Mt Etna. *Geophys. Res. Lett.* 43, 7511–7519. doi:10.1002/2016GL069938

De Moor, J. M., Aiuppa, A., Avard, G., Wehrmann, H., Dunbar, N., Muller, C., et al. (2016). Turmoil at Turrialba Volcano (Costa Rica): Degassing and eruptive processes inferred from high-frequency gas monitoring. *J. Geophys. Res. Solid Earth* 121, 5761–5775. doi:10.1002/2016JB013150

de Moor, J. M., Kern, C., Avard, G., Muller, C., Aiuppa, A., Saballos, A., et al. (2017). A new sulfur and carbon degassing inventory for the southern central American volcanic arc: The importance of accurate time-series data sets and possible tectonic processes responsible for temporal variations in arc-scale volatile emissions. *Geochem. Geophys. Geosystems* 18, 4437–4468. doi:10.1002/2017GC007141

Delle Donne, D., Tamburello, G., Aiuppa, A., Bitetto, M., Lacanna, G., D'Aleo, R., et al. (2017). Exploring the explosive-effusive transition using permanent ultraviolet cameras. *J. Geophys. Res. Solid Earth* 122, 4377–4394. doi:10.1002/2017JB014027

Delle Donne, D., Aiuppa, A., Bitetto, M., D'Aleo, R., Coltelli, M., Coppola, D., et al. (2019). Changes in SO2 Flux regime at mt. etna captured by automatically processed ultraviolet camera data. *Remote Sens.* 11, 1201. doi:10.3390/rs11101201

Delle Donne, D., Coco, E. L., Bitetto, M., Paolo, F., La Monica, F. P., Lacanna, G., et al. (2022). Spatio-temporal changes in degassing behavior at Stromboli volcano derived from two co-exposed SO2 camera stations. *Front. Earth Sci.* 10, 1–17. doi:10.3389/feart.2022.972071

Elias, T., Kern, C., Horton, K. A., Sutton, A. J., and Garbeil, H. (2018). Measuring SO2 emission rates at Kīlauea volcano, Hawaii, using an array of upward-looking UV spectrometers, 2014–2017. *Front. Earth Sci.* 6, 1–20. doi:10.3389/feart.2018.00214

Esse, B., Burton, M. R., Varnam, M., Kazahaya, R., and Salerno, G. (2020). iFit: A simple method for measuring volcanic SO2 without a measured Fraunhofer reference spectrum. *J. Volcanol. Geotherm. Res.* 402, 107000. doi:10.1016/j.jvolgeores.2020.107000

Galle, B., Johansson, M., Rivera, C., Zhang, Y., Kihlman, M., Kern, C., et al. (2010). Network for observation of volcanic and atmospheric change (NOVAC)—a global network for volcanic gas monitoring: Network layout and instrument description. *J. Geophys. Res.* 115, D05304. doi:10.1029/2009JD011823

Gliß, J., Stebel, K., Kylling, A., Dinger, A., Sihler, H., and Sudbø, A. (2017). Pyplis–A Python software toolbox for the analysis of SO2 camera images for emission rate retrievals from point sources. *Geosciences* 7, 134. doi:10.3390/geosciences7040134

Gliß, J., Stebel, K., Kylling, A., and Sudbø, A. (2018). Improved optical flow velocity analysis in SO₂ camera images of volcanic plumes – implications for emission-rate retrievals investigated at Mt Etna, Italy and Guallatiri, Chile. *Atmos. Meas. Tech.* 11, 781–801. doi:10.5194/amt-11-781-2018

Kern, C., Deutschmann, T., Vogel, L., Wöhrbach, M., Wagner, T., and Platt, U. (2010a). Radiative transfer corrections for accurate spectroscopic measurements of volcanic gas emissions. *Bull. Volcanol.* 72, 233–247. doi:10.1007/s00445-009-0313-7

Kern, C., Kick, F., Vogel, L., Platt, U., and Wohrbach, M. (2010b). Theoretical description of functionality, applications, and limitations of SO₂ cameras for the remote sensing of volcanic plumes. *Atmos. Meas. Tech.* 3, 733–749. doi:10.5194/amt-3-733-2010

Kern, C., Werner, C., Elias, T., Sutton, a. J., and Lübcke, P. (2013). Applying UV cameras for SO2 detection to distant or optically thick volcanic plumes. *J. Volcanol. Geotherm. Res.* 262, 80–89. doi:10.1016/j.jvolgeores.2013.06.009

Kern, C., Sutton, J., Elias, T., Lee, L., Kamibayashi, K., Antolik, L., et al. (2015). An automated SO2 camera system for continuous, real-time monitoring of gas emissions from Kilauea Volcano's summit Overlook Crater. *J. Volcanol. Geotherm. Res.* 300, 81–94. doi:10.1016/j.jvolgeores.2014.12.004

Kern, C., Lerner, A. H., Elias, T., Nadeau, P. A., Holland, L., Kelly, P. J., et al. (2020). Quantifying gas emissions associated with the 2018 rift eruption of Kīlauea Volcano using ground-based DOAS measurements. *Bull. Volcanol.* 82, 55. in press. doi:10.1007/s00445-020-01390-8

Kern, C., Aiuppa, A., and Moor, J. M. D. (2022). A golden era for volcanic gas geochemistry? *Bull. Volcanol.* 84, 43. doi:10.1007/s00445-022-01556-6

Klein, A., Lübcke, P., Bobrowski, N., Kuhn, J., and Platt, U. (2017). Plume propagation direction determination with SO₂ cameras. *Atmos. Meas. Tech.* 10, 979–987. doi:10.5194/amt-10-979-2017

Kraus, S. G. (2006). *Doasis: A framework design for DOAS*. PhD thesis. Heidelberg: University of Heidelberg, 143. ISBN 978-3-8322-5452-0.

Kunrat, S., Kern, C., Alfianti, H., and Lerner, A. H. (2022). Forecasting explosions at Sinabung Volcano, Indonesia, based on SO2 emission rates. *Front. Earth Sci.* 10, 976928. doi:10.3389/feart.2022.976928

Layana, S. (2022). *Procesos que controlan el balance térmico-magmático en volcanes activos de la zona Volcánica Central (ZVC)*. PhD thesis. Antofagasta: Universidad Católica del Norte.

Lübcke, P., Bobrowski, N., Illing, S., Kern, C., Alvarez Nieves, J. M., Vogel, L., et al. (2013). On the absolute calibration of SO₂ cameras. *Atmos. Meas. Tech.* 6, 677–696. doi:10.5194/amt-6-677-2013

Mather, T. A., Tsanev, V. I., Pyle, D. M., Mcgonigle, A. J. S., Oppenheimer, C., and Allen, A. G. (2004). Characterization and evolution of tropospheric plumes from Lascar and Villarrica volcanoes, Chile. *J. Geophys. Res.* 109, D21303. doi:10.1029/2004JD004934

Mori, T., and Burton, M. R. (2006). The SO2 camera: A simple, fast and cheap method for ground-based imaging of SO2 in volcanic plumes. *Geophys Res. Lett.* 33, L24804. doi:10.1029/2006GL027916

Mori, T., Mori, T., Kazahaya, K., Ohwada, M., Hirabayashi, J., and Yoshikawa, S. (2006). Effect of UV scattering on SO2 emission rate measurements. *Geophys. Res. Lett.* 33, L17315–L17317. doi:10.1029/2006GL026285

Mosbrucker, A. R., Zoeller, M. H., and Ramsey, D. W. (2020). *Digital elevation model of Kīlauea Volcano, Hawai'i, based on July 2019 airborne lidar surveys*. U.S. Geological Survey data release. doi:10.5066/P9F1ZU8O

Nadeau, P. A., Palma, J. L., and Waite, G. P. (2011). Linking volcanic tremor, degassing, and eruption dynamics via SO2 imaging. *Geophys. Res. Lett.* 38, L01304. doi:10.1029/2010GL045820

Nadeau, P. A. (2011). *Ultraviolet digital imaging of volcanic plumes: Implementation and application to magmatic processes at basaltic volcanoes*. PhD thesis. Houghton, Michigan: Michigan Technological University.

Neal, C. A., Brantley, S. R., Antolik, L., Babb, J. L., Burgess, M., Calles, K., et al. (2019). The 2018 rift eruption and summit collapse of Kilauea Volcano. *Science* 363, 367–374. doi:10.1126/science.aav7046

Osorio, M., Casaballe, N., Belsterli, G., Barreto, M., Gómez, Á., Ferrari, J., et al. (2017). Plume segmentation from UV camera images for SO2 emission rate quantification on cloud days. *Remote Sens.* 9, 517. doi:10.3390/rs9060517

Pering, T. D., Ilanko, T., and Liu, E. J. (2019). Periodicity in volcanic gas plumes: A review and analysis. *Geosci* 9, 394. doi:10.3390/geosciences9090394

Peters, N., Hoffmann, A., Barnie, T., Herzog, M., and Oppenheimer, C. (2015). Use of motion estimation algorithms for improved flux measurements using SO2 cameras. *J. Volcanol. Geotherm. Res.* 300, 58–69. doi:10.1016/j.jvolgeores.2014.08.031

Phillipson, G., Sobradelo, R., and Gottsmann, J. (2013). Global volcanic unrest in the 21st century: An analysis of the first decade. *J. Volcanol. Geotherm. Res.* 264, 183–196. doi:10.1016/j.jvolgeores.2013.08.004

Platt, U., and Stutz, J. (2008). in *Differential optical absorption spectroscopy (DOAS)*. Editor M. W. Sigrist (Berlin, Heidelberg: Springer Berlin Heidelberg). doi:10.1007/978-3-540-75776-4

Tamburello, G., Hansteen, T. H., Bredemeyer, S., Aiuppa, A., and Tassi, F. (2014). Gas emissions from five volcanoes in northern Chile and implications for the volatiles budget of the Central Volcanic Zone. *Geophys. Res. Lett.* 41, 4961–4969. doi:10.1002/2014GL060653

Varnam, M., Burton, M. R., Esse, B., Kazahaya, R., Salerno, G., Caltabiano, T., et al. (2020). Quantifying light dilution in ultraviolet spectroscopic measurements of volcanic SO2 using dual-band modeling. *Front. Earth Sci.* 8, 1–11. doi:10.3389/feart.2020.528753

Varnam, M., Burton, M. R., Esse, B., Salerno, G., Kazahaya, R., and Ibarra, M. (2021). Two independent light dilution corrections for the SO2 camera retrieve comparable emission rates at masaya. *Remote Sens.* 13, 935. doi:10.3390/rs13050935

Global Volcanism Program (1993). "Report on lascar (Chile),". *Bulletin of the global volcanism network*. Editor E. Venzke (Smithsonian Institution), 18, 4. doi:10.5479/si.GVP.BGVN199304-355100

Wilkes, T. C., McGonigle, A. J. S., Pering, T. D., Taggart, A., White, B., Bryant, R., et al. (2016). Ultraviolet imaging with low cost smartphone sensors: Development and application of a raspberry pi-based UV camera. *Sensors* 16, 1649. doi:10.3390/s16101649

Wilkes, T. C., Pering, T. D., McGonigle, A. J. S., Tamburello, G., and Willmott, J. R. (2017). A low-cost smartphone sensor-based UV camera for volcanic SO2 emission measurements. *Remote Sens.* 9, 27. doi:10.3390/rs9010027

frontiers | Frontiers in Earth Science

TYPE Original Research
PUBLISHED 06 April 2023
DOI 10.3389/feart.2023.1062699

OPEN ACCESS

EDITED BY
Ryunosuke Kazahaya,
National Institute of Advanced Industrial Science and Technology (AIST), Japan

REVIEWED BY
Ben Esse,
The University of Manchester, United Kingdom
Jean-François Smekens,
University of Oxford, United Kingdom

*CORRESPONDENCE
N. Taquet,
noemi.taquet@gmail.com

SPECIALTY SECTION
This article was submitted to Volcanology, a section of the journal Frontiers in Earth Science

RECEIVED 06 October 2022
ACCEPTED 09 March 2023
PUBLISHED 06 April 2023

CITATION
Taquet N, Rivera Cárdenas C, Stremme W, Boulesteix T, Bezanilla A, Grutter M, García O, Hase F and Blumenstock T (2023), Combined direct-sun ultraviolet and infrared spectroscopies at Popocatépetl volcano (Mexico).
Front. Earth Sci. 11:1062699.
doi: 10.3389/feart.2023.1062699

Combined direct-sun ultraviolet and infrared spectroscopies at Popocatépetl volcano (Mexico)

N. Taquet[1]*, C. Rivera Cárdenas[1], W. Stremme[1], T. Boulesteix[2], A. Bezanilla[1], M. Grutter[1], O. García[3], F. Hase[4] and T. Blumenstock[4]

[1]Instituto de Ciencias de la Atmósfera y Cambio Climático, Universidad Nacional Autónoma de México, Mexico City, Mexico, [2]Volcanology Research Group, Department of Life and Earth Sciences, Instituto de Productos Naturales Y Agrobiología (IPNA-CSIC), San Cristóbal de La Laguna, Spain, [3]Centro de Investigación Atmosférica de Izaña (CIAI), Agencia Estatal de Meteorología (AEMet), Santa Cruz de Tenerife, Spain, [4]Karlsruhe Institute of Technology (KIT), Institute of Meteorology and Climate Research (IMK-ASF), Karlsruhe, Germany

Volcanic plume composition is strongly influenced by both changes in magmatic systems and plume-atmosphere interactions. Understanding the degassing mechanisms controlling the type of volcanic activity implies deciphering the contributions of magmatic gases reaching the surface and their posterior chemical transformations in contact with the atmosphere. Remote sensing techniques based on direct solar absorption spectroscopy provide valuable information about most of the emitted magmatic gases but also on gas species formed and converted within the plumes. In this study, we explore the procedures, performances and benefits of combining two direct solar absorption techniques, high resolution Fourier Transform Infrared Spectroscopy (FTIR) and Ultraviolet Differential Optical Absorption Spectroscopy (UV-DOAS), to observe the composition changes in the Popocatépetl's plume with high temporal resolution. The SO_2 vertical columns obtained from three instruments (DOAS, high resolution FTIR and Pandora) were found similar (median difference <12%) after their intercalibration. We combined them to determine with high temporal resolution the different hydrogen halide and halogen species to sulfur ratios (HF/SO_2, BrO/SO_2, HCl/SO_2, SiF_4/SO_2, detection limit of HBr/SO_2) and HCl/BrO in the Popocatépetl's plume over a 2.5-years period (2017 to mid-2019). BrO/SO_2, BrO/HCl, and HCl/SO_2 ratios were found in the range of $(0.63 \pm 0.06$ to $1.14 \pm 0.20) \times 10^{-4}$, $(2.6 \pm 0.5$ to $6.9 \pm 2.6) \times 10^{-4}$, and 0.08 ± 0.01 to 0.21 ± 0.01 respectively, while the SiF_4/SO_2 and HF/SO_2 ratios were found fairly constant at $(1.56 \pm 0.25) \times 10^{-3}$ and 0.049 ± 0.001. We especially focused on the full growth/destruction cycle of the most voluminous lava dome of the period that took place between February and April 2019. A decrease of the HCl/SO_2 ratio was observed with the decrease of the extrusive activity. Furthermore, the short-term variability of BrO/SO_2 is measured for the first time at Popocatépetl volcano together with HCl/SO_2, revealing different behaviors with respect to the volcanic activity. More generally, providing such temporally resolved and near-real-time time series of both primary and secondary volcanic gaseous species is critical for the management of volcanic emergencies, as well as for the understanding of the volcanic degassing processes and their impact on the atmospheric chemistry.

KEYWORDS

solar absorption spectroscopy, volcanic degassing, Popocatépetl, FTIR, DOAS, Pandora, dome cycle

1 Introduction

Volcanic plume composition measurements allow detection of significant changes in the magmatic processes from the magma chamber to the most superficial levels (Francis et al., 1995; Oppenheimer and McGonigle, 2004) and contribute to determining the degassing balance during eruptions (Gerlach and Graeber, 1985). Among the main magmatic volatile species involved in volcanic eruptions, halogens (F, Cl, Br, I) play a key role in the extrusive processes, affecting the physico-chemical properties of magmas (Dingwell and Mysen, 1985; Aiuppa, 2009), and having major implications for their transport towards the surface, their ascension speed, their potential to segregate a gas phase, their eruptability and the eruption dynamics/explosivity. In particular, based on their contrasted solubility in magma compared to sulfur, the temporal variability of halogen-to-sulfur ratios in plumes allowed deciphering the magmatic processes and eruptive dynamics (Mori et al., 1993; Burton et al., 2007; Schipper et al., 2019; Aiuppa et al., 2021).

For example, an increase of Cl/S ratios was observed during the eruptive periods with respect to quiescent periods, at, e.g., Mount Etna during the 2001 and 2002–2003 eruptions (Aiuppa et al., 2002; 2004; Notsu and Mori, 2010), which was interpreted in terms of solubility-controlled fractionation. The variability of the HCl/SO_2, CO_2/SO_2 in different eruptive contexts provides insights on the transition between quiet and explosive regimes, and on explosion mechanisms (Burton et al., 2007; Woitischek et al., 2020; Aiuppa et al., 2021). Edmonds et al. (2002) observed an increase of the HCl/SO_2 ratio at Soufrière Hills Volcano during lava extrusion, illustrating the shallow decompressional degassing of Cl.

Some of these halogen derivatives are reactive in volcanic plumes, obscuring the relationships between the plume composition and the magmatic/eruptive processes, which require both primary (magmatic) and secondary (in-plume) species to be accounted for in degassing balances. In-plumes reactions include SO_2 and HCl scavenging on volcanic ash (Martin et al., 2012; Delmelle et al., 2018), uptake by sulfate aerosols (Edmonds et al., 2003; Rodriguez et al., 2008; Rüdiger et al., 2021), and halogen chemistry (Bobrowski et al., 2007; Rudiger et al., 2021). The conversion of SO_2 to sulfate aerosols can be significant over long-term observation periods under humid conditions (Rodriguez et al., 2008), but seems to play a minor role in ash poor-plumes over a period of minutes to hours (McGonigle et al., 2004; Voigt et al., 2014). On the other hand, the characterization of the halogen activation mechanisms in volcanic plumes and their reaction kinetics is critical for both long and short-term studies, affecting the variability of primary species ratios and degassing balances.

Among the halogen secondary species, BrO was measured for the first time in a volcanic plume at Soufrière Hills (Montserrat) by Bobrowski et al. (2003), and then at a number of other volcanoes (Oppenheimer et al., 2006; Bobrowski and Platt, 2007; Kern et al., 2009; Heue et al., 2011; Rix et al., 2012; Donovan et al., 2014; Gliß et al., 2015; Dinger et al., 2018; Warnach et al., 2019; Dinger et al., 2021) including Popocatépetl (Boichu et al., 2011; Bobrowski and Giuffrida, 2012; Platt and Bobrowski, 2015; Fickel and Delgado Granados, 2017). Recent models succeeded in reproducing some observations of plume compositions at different plume ages (Rüdiger et al., 2021) and provide valuable information about the lifetimes and conversion rates of the primary (HCl, HF, HBr) and secondary (BrO, ClO, OClO, BrOH, Br_2, BrCl, $BrONO_2$) halogen species. However, the lack of simultaneous measurements of the different halogens species leaves some input parameters poorly constrained, and the influence of plume-mixing processes, relative humidity, presence of aerosols, photochemistry and/or redox conditions on the conversion rates remains still not fully understood. A review of the main recent findings on this topic is given in Gutmann et al. (2018). Some typical behaviors of the BrO/SO_2 ratios with respect to the volcanic activity were described at Mount Etna (Bobrowski and Giuffrida, 2012), Nevado del Ruiz (Lübcke et al., 2014), Tungurahua (Warnach et al., 2019) and Cotopaxi (Dinger et al., 2018), with low ratios prior to and during eruptions and/or explosive activity, while higher ratios occurred at the end of the eruptions or during passive degassing. On the other hand, Aiuppa et al. (2005) observed a coherent geochemical behaviour of halogen (F, Cl, Br, I) to sulfur ratios in the Mount Etna's plume before (increase of the ratio) and during (decrease of the ratio) the 2004 eruption. Unless Cl and F partition early in water/brines (Aiuppa, 2009; Shinohara, 2009), these species are generally exsolved from magma shallower than sulfur. The conditions of bromine exsolution from magma are not yet well understood, and both shallow and deep origins are still considered (Gutmann et al., 2018), complicating the interpretation of the BrO/SO_2 ratios in terms of magmatic processes.

SiF_4 is a byproduct of the reaction of HF with silicates either within the conduit or during the ash transport in the plume (Love et al., 1998; de Hoog et al., 2005). FTIR spectroscopy is the only method allowing its quantification together with HF (Mori et al., 2002). This compound has been detected at a few volcanoes such as Mount Etna and Satsuma-Iwojima, but especially at Popocatépetl (Love et al., 1998; Stremme et al., 2011; Stremme et al., 2012; Taquet et al., 2017; Taquet et al., 2019) where frequent ash-laden plumes and vigorous degassing through successive dome extrusions favors the formation of SiF_4 (de Hoog et al., 2005). The previous studies evidenced that both formation modes occur at Popocatépetl (Taquet et al., 2017; Taquet et al., 2019) and that the SiF_4/SO_2 ratio increases several minutes preceding (Love et al., 1998) and during dome-related explosions (Stremme et al., 2011; Taquet et al., 2017).

Many primary magmatic species (H_2O, CO_2, SO_2, HCl, HF, HBr, CO, OCS, H_2S) and their derivatives (BrO, OClO, SiF_4) can be remotely measured using satellite and ground-based spectroscopic techniques (from ultraviolet to thermal infrared) in both active and passive configurations. A complete review of the different ground-based techniques used to date for measuring and imaging the different species in volcanic plumes is given in Platt et al. (2018).

The use of DOAS instruments to measure SO_2 and reactive halogen species (BrO, OClO) has proven to be simple and effective, providing the possibility to automatize current instrumentation and create robust monitoring networks (Galle et al., 2010) such as the Network for Observation of Volcanic and Atmospheric Change (NOVAC). BrO/SO_2 ratios are measured by DOAS instruments using scattered sunlight (Gutmann et al., 2018) and Gliß et al. (2015) additionally measured the OClO species in the volcanic plume of Mount Etna using Multi-AXis DOAS (MAX-DOAS). FTIR spectroscopy has long been used to study the compositional variability (SO_2, HCl, HF, SiF_4, CO_2, OCS, CO, H_2S) of volcanic

plumes, mainly in open-path configuration, which requires an intense IR source (lava fountains and lakes or artificial), limiting its applicability. Solar occultation FTIR spectroscopy, using direct sunlight overcomes some of these limitations, allowing measurements during passive and active degassing phases (Francis et al., 1998; Oppenheimer et al., 1998; Burton et al., 2001; Stremme et al., 2011; Taquet et al., 2019). Few studies (Love et al., 1998; Love et al., 2000; Smekens et al., 2023) present simultaneous FTIR and UV measurements of volcanic plumes composition using thermal emission (in the LWIR range) and the solar radiation scattered by the atmosphere or clouds behind volcanic plumes. Thermal emission measurements have been performed recently at Popocatépetl (Taquet et al., 2017) and have proven to complement direct solar absorption measurements. Using thermal emission allows measuring with high frequency by just pointing towards the volcanic plume, but solving the radiative transfer and deriving the composition remain challenging (Love et al., 2000; Platt et al., 2018). Butz et al. (2017) combined for the first time direct-sun DOAS and FTIR measurements using portable instruments (EM27/SUN FTIR and UV spectrometers) to simultaneously measure SO_2, HCl, HF, CO_2, BrO species in Mount Etna's volcanic plume. In such configuration, the different instruments share the same line of sight and thus the same airmass. This allows straightforward comparisons of the retrieved vertical columns (VCs) and robust calculation of multiple volcanic species ratios, making this method one of the most reliable and adaptable for studying long-term variability of the volcanic plume composition.

In this contribution, we present 2.5 years (2017 to mid-2019) of high quality multispecies compositional data of Popocatépetl's plume combining ground-based DOAS and FTIR direct-sun measurements, with a focus over the most voluminous dome growth and destruction episode (February–April 2019) of the study period. The measurements were performed from the Altzomoni (ALTZ) observatory, one of the few stations pertaining to the Network for the Detection of Atmospheric Composition Change (NDACC) and to the Pandonia Gobal Network (PGN) located near a persistently degassing volcano. The site instruments (a high resolution (HR)-FTIR coupled with a DOAS and a Pandora spectrometers) and measurements benefit from standardized protocols, intercalibrations and comply with the measurement quality requirements. We studied the variability of both the primary and secondary species and of their ratios (i.e., BrO/SO_2, BrO/HCl, HCl/SO_2, HF/SO_2, SiF_4/SO_2) in the volcanic plume during different phases of the dome growth and relate it with the degassing processes and in-plume reactions.

2 Popocatépetl volcano and measurement site

Popocatépetl is an andesitic-dacitic stratovolcano of the trans-Mexican volcanic belt, located 70 km SE of Mexico City. Its past activity comprises destructive episodes of lateral flank collapses and plinian phases. Its historical activity is characterized by cycles of extrusion of lava domes and their destruction through a combination of compaction and explosions (Campion et al., 2018), interspersed with quiet periods with continuous passive degassing (Taquet et al., 2019). The long duration of the ongoing eruption (>28 years at the time of writing) and its relatively high degassing rate are ideal to explore the link between the volcanic activity and the variability of the plume composition, which is one of the few observable manifestations of the magmatic processes. The previously reported short- or long-term time series of the HCl, HF, SO_2, CO_2, SiF_4 species abundance and of their ratios in the Popocatépetl's plume (Goff et al., 1998; Love et al., 1998; Goff et al., 2001; Gerlach, 2004; Stremme et al., 2011; Stremme et al., 2012; Taquet et al., 2017; Taquet et al., 2019) gave valuable information on the behavior of these species with respect to the volcanic activity. However, the optimal combination of eruptive and meteorological conditions for measurements is seldom met multiple times during a single dome growth episode. We focused here on a 2.5-month time-series spanning the full cycle of construction and destruction of dome 82 (according to reports of the local institution in charge of the monitoring, i.e., Centro Nacional de Prevención de Desastres or CENAPRED). Following a relatively intense extrusive activity during September–December 2018, with the succession of the dome emplacement-destruction cycles #80 and #81 (CENAPRED daily reports; Caballero Jimenez et al., 2019), January 2019 is marked by a powerful explosion on day 22, apparently without a dome occupying the crater. Such explosions are rare, but they became more frequent following the earthquakes of 2017 (Boulesteix et al., 2022). A crater overflight was operated on day 27, which confirmed that the crater was still empty and that the conduit was permeable. Caballero and Valderrama (2020) indeed report the observation of a thermal anomaly coinciding with that of Sentinel-2 data (see, e.g., Mounts processing, Valade et al., 2019) and with the emission source of passive degassing plumes, as already proposed in previous thermal imaging studies at Popocatépetl (e.g., Wright et al., 2002). Based on CENAPRED reports, following this explosion and before the onset of the dome growth episode, daily averages of ~15 min of tremor, of 1.3 Volcano Tectonic (VT) earthquakes and of 150 exhalations (local term for low intensity explosions with little impulsive character) were recorded. On 15 February 2019, at approximately 2:55 UTC (14 February at 20:55, local time), the first 6 h-long LPs-tremor-explosions segment of this dome growth episode started. Its manifestation at the surface consisted in a "Strombolian-type" episode with sustained ash-venting, ejecting incandescent blocks on the external slopes of the cone. On 19 February 2019, an overflight confirmed the presence of a voluminous dome inside the crater with 200 m diameter (i.e., ~1.3 Mm^3 according to Valade et al., submitted). Similar 3–9 h-long tremor segments were recorded over the next days until day 27 summing to approximately 120 h. Another overflight on 28 February confirmed that the dome 82 was still occupying the crater. Between 26 February and 10 March 2019, 48 explosions were reported by CENAPRED (Figure 5), some of which (e.g., 1 and 9 March 2019) expelled incandescent blocks on the external slopes of the cone hundreds of meters downslope. This explosive activity resulted in 69 VAAC alerts, 29 of which occurred between 5–8 March. Strong degassing during the overflight on 7 March did not allow observations of the dome destruction. An image of 8 March in Google Earth offers a clear view on more than half of the crater floor, showing a stepped profile of the walls and clear marks of several explosions, confirming that the dome was destroyed during this explosion sequence. Eleven additional and sometimes large

explosions occurred until the end of March, with a large outreach of the blocks that set fire to the highest altitude vegetation on 27 March 2019. The explosions ceased during April and the activity declined significantly with, e.g., a threefold decrease of the number of exhalations. Dome forming activity only returned in mid-July (Caballero and Valderrama, 2020).

Currently, there are several strategies to remotely monitor the emission of gases from Popocatépetl volcano, both in mobile (Campion et al., 2018) and static configurations (Taquet et al., 2017; Schiavo et al., 2019; Taquet et al., 2019; Arellano et al., 2021). Since 2012, the installation of the ALTZ Atmospheric Observatory in the Izta-Popo-Zoquiapan National Park, 11 km from the Popocatépetl crater, allowed the ICAyCC-UNAM team to perform not only atmospheric measurements, but also volcanic plume measurements using solar, lunar absorption (Stremme et al., 2012; Krueger et al., 2013; Taquet et al., 2019) and thermal emission (Stremme et al., 2011; Stremme et al., 2012; Taquet et al., 2017) FTIR spectroscopic techniques. This site benefits from a number of advantages such as open and direct view to the volcano, a high altitude to minimize the interferences from water vapor and anthropogenic pollutants, a safe distance from the crater and from abundant ash-falls, and the availability of operational services (power and communication). Apart from the HR-FTIR spectrometer (a Bruker IFS-125HR), the station was also equipped with meteorological instruments, visible cameras, *in-situ* gas analyzers for atmospheric and environmental monitoring, among other instrumentation. Additionally, remote sensing equipments including a UV camera, a Pandora, another DOAS spectrometer coupled with the HR-FTIR instrument and a low-resolution FTIR spectrometer (a Bruker EM27-MIR), occasionally allow measuring Popocatépetl's plume composition with different configurations (solar absorption, thermal emission, UV scattered-light mode).

3 Instrumental set-up and analysis procedures

In this study, we present direct solar absorption measurements performed from the ALTZ station using the coupled HR-FTIR/DOAS set-up, and the Pandora spectrometer over a period of 2.5 years (2017-mid 2019). Plume measurements with this configuration are possible on days with clear sky conditions and only during favorable wind conditions, at times when the volcanic plume and the instrument are aligned with the Sun. Since both the DOAS instrument and Pandora are based on the DOAS technique, we hereafter referred to the DOAS integrated in the coupled HR-FTIR/DOAS set-up as "S2000 DOAS," and as "Pandora" for the Pandora instrument. In the same way, the DOAS measurements made by the Pandora will be referred to as "Pandora measurements" while the DOAS measurements of the HR-FTIR/DOAS set-up will be referred to as "S2000 DOAS measurements."

3.1 The combined FTIR-DOAS solar absorption measurements

A solar tracker (Camtracker; Gisi et al., 2011; Gisi et al., 2012; Gisi, 2012) located on the roof of the station collects the direct solar beam and reflects it into the container (see, e.g., Plaza-Medina et al., 2017; Taquet et al., 2019). A part of the solar beam is directed by mirrors toward the entrance of the S2000 DOAS optical fiber and the other part towards the FTIR spectrometer aperture (Figure 1).

The Bruker IFS-125HR FTIR spectrometer can provide a maximal optical path difference (OPDmax) of 257 cm corresponding to a spectral resolution of 0.0035 cm^{-1} (resolution = 0.9/OPDmax). The spectrometer operates with either KBr or CaF_2 beam splitters, three different detectors (MCT, InSb and InGaAs) and a set of seven optical filters installed in a rotating wheel. A remote control liquid-nitrogen filling system assures that the MCT and InSb detectors are properly cooled. The measurement routine was programmed to acquire high (0.005 cm^{-1}), moderate (0.02 cm^{-1}) and low (0.1 cm^{-1}) resolution spectra in the near-infrared (NIR) and mid-infrared (MIR) spectral ranges using the different filters. The complete normal-mode sequence lasts ~20 min. Every time the volcanic plume is observed in the optical path of the instrument, the acquisition is switched to a faster sequence, keeping only the NIR and the low resolution acquisitions with the NDACC filters three and 6 (~5 min for a complete sequence). The field of view varies between 2 and 4 mrad, depending on the used optical filter and measurement configuration.

For the DOAS measurements, spectra were collected using an Ocean Optics S2000 spectrometer (spectral resolution of ~0.6 nm) combined with an optical fiber and a band-pass filter (Hoya U330) which blocks visible light with wavelength between 360 and 640 nm. S2000 DOAS spectra were acquired using the DOASIS software (Kraus, 2006) adjusting automatically the exposure time to the Sun intensity. Collected spectra were averaged so that a final collection time of 1 min was achieved.

The container is thermally stabilized to provide optimal operating conditions for the different instruments. A remote-controlled dome cover and a microwave communication system (50 km line of sight to the university campus) allow us to fully control and perform the measurements remotely.

3.2 The Pandora measurements

A Pandora instrument (number 65) was implemented in the ALTZ station in 2018, and the data products have been available since January 2019. The Pandora head sensor is installed on the rooftop of the container, and points accurately to the Sun with a 2.5° field of view (FWHM SunFOV) using its own solar tracking system (SciGlob/NASA tracker). The head sensor is connected through an optical fiber to an Avantes spectrometer located in the thermally stabilized FTIR container. The spectrometer (model Avantes AvaSpec ULS 2048x64) has a 0.6 nm resolution (FWHM) covering the spectral range from 280 to 530 nm. Different bandpass and neutral density filters can be chosen and combined inside the optical head by two filter wheels, so that a large range of intensity is covered by the instrument and direct and indirect Sun or Moon light can be recorded. The measurement routine starts automatically in the morning, collecting direct solar spectra, but also hourly indirect sunlight spectra (zenith sky measurements, pointing above the crater and MAXDOAS-type measurements). During night time, lunar spectra are recorded, if possible. Spectra are sent to the central server of the PANDONIA Global Network (PGN, https://www.

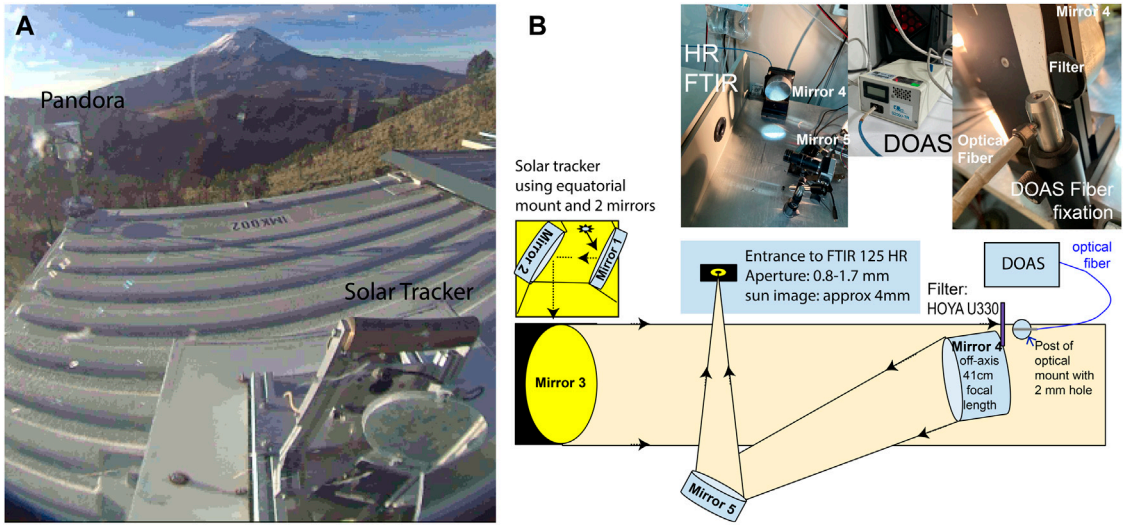

FIGURE 1
Set-up of the Pandora, HR-FTIR and S2000 DOAS instruments at the ALTZ station. **(A)** Global view of the instruments installed on the roof of the ALTZ station. **(B)** Instrumental set-up for the combined DOAS-FTIR measurements.

TABLE 1 Retrieval settings used for the S2000 DOAS and Pandora spectra analysis.

Instrument/Target species	Spectral windows (nm)	Interference species	Cross sections
S2000 DOAS			
SO_2	312.0–326.8	O_3	SO_2 at 298 K (Vandaele et al., 2009), O_3 at 221 K (Burrows et al., 1999)
BrO	330.6–356.3	SO_2, O_3, O_4, NO_2, OClO	BrO (Wilmouth et al., 1999), SO_2 at 298 K (Hermans et al., 2009), O_3 at 221 K (Burrows et al., 1999), O_4 (Hermans et al., 2003), NO_2 at 293 K (Voigt et al., 2002), OClO at 293 K (Bogumil et al., 2003)
Pandora			
SO_2	306.0–326.4	O_3, NO_2, HCHO, HONO, BrO	SO_2 (Vandaele et al., 2009), O_3 (Serdyuchenko et al., 2013), NO_2 (Vandaele et al., 1998), HCHO (Meller and Moortgat, 2000), HONO (Stutz et al., 2000) and BrO (Wilmouth et al., 1999)
BrO (from the PGN HCHO algorithm "fus5")	322.5–359.2	SO_2, O_3, NO_2, HCHO, HONO	O_3 (Serdyuchenko et al., 2013), NO_2 (Vandaele et al., 1998), SO_2 (Vandaele et al., 2009), HCHO (Meller and Moortgat, 2000), HONO (Stutz et al., 2000), and BrO (Wilmouth et al., 1999)

pandonia-global-network.org/) where the data are processed and analyzed.

3.3 Data analysis

3.3.1 UV analysis

3.3.1.1 Pandora data processing

In this study, we utilized the L2-rsus1p1-8 products available in the PGN server, in which the SO_2 total columns are retrieved using the code "sus1" of the BlickSFA algorithm (Cede et al., 2021). The PGN retrievals follow the Cede et al. (2021) Total Optical Absorption Spectroscopy approach. It is based on non-linear least square fitting of the absorption cross-sections of multiple atmospheric absorbers to the spectra, and uses a synthetic solar absorption reference spectrum, constructed from the measurements of the same spectrometer. SO_2 is fitted in the 306–326.4 nm spectral range (Table 1) with a fourth order smoothing polynomial function and includes the following cross sections: SO_2 (Vandaele et al., 2009), O_3 (Serdyuchenko et al., 2013), NO_2 (Vandaele et al., 1998), HCHO (Meller and Moortgat, 2000), HONO (Stutz et al., 2000) and BrO (Wilmouth et al., 1999). Additionally, we explored the BrO

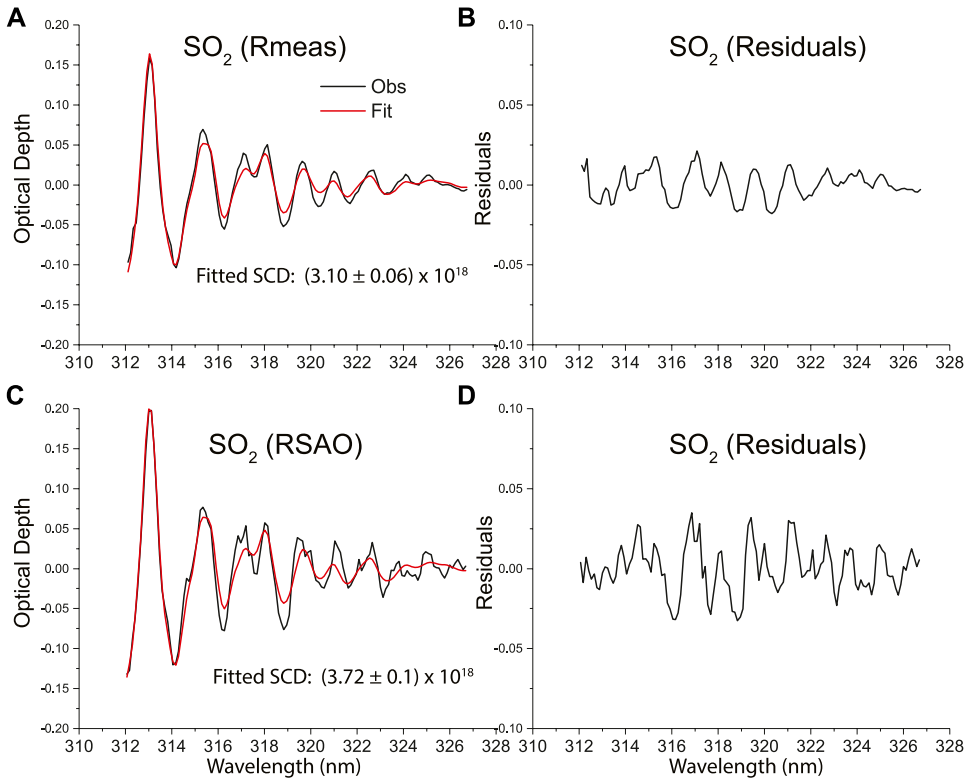

FIGURE 2
Example of fit of SO_2 analyzed in the 312.0–326.8 nm spectral window from the S2000 DOAS measurements at ALTZ station performed on 20 February 2019 using **(A)** the measured reference (Rmeas) and **(C)** the RSAO reference. The corresponding residues are presented in **(B,D)**, respectively. The retrieved slant column density (SCD, in molec/cm^2) is shown in the legend.

slant columns density (SCD) product, one of the outputs of the PGN "fus5" algorithm, officially used to retrieve the HCHO species in the 322.5–359.2 nm spectral range. In this algorithm, all of the O_3, NO_2, SO_2, HCHO, HONO, BrO species are fitted using the cross sections reported in Table 1. We converted the BrO SCDs to VCs to be compared with the S2000 DOAS products. Further details about the fitting procedures and calibrations can be found in Cede et al. (2021).

3.3.1.2 S2000 DOAS data processing

The UV spectra from the S2000 DOAS spectrometer were analyzed using the QDOAS software version 2.111 (Danckaert et al., 2013), developed by BIRA-IASB, which retrieves the SCDs of trace gases from the measured spectra, using a Marquardt Levenberg Non-Linear Least Squares (NLLS) Fitting algorithm. Wavelength calibration and slit function files were created with a low-density mercury lamp and were used as inputs in the QDOAS retrieval. An electronic offset correction was also measured and applied in the spectra analysis. SO_2 was retrieved in the 312.0–326.8 nm spectral window (Table 1) following the Butz et al. (2017) procedure. In the retrieval, two cross sections were used: SO_2 at 298 K (Vandaele et al., 2009) and O_3 at 221 K (Burrows et al., 1999) as an interfering gas and a fifth-order polynomial function was included in the fitting routine to remove broad band extinction. Intensity offset, non-linear wavelength shift and first order stretching corrections were included in the DOAS fit settings. In contrast to the scattered light radiance measurements, the direct-sun configuration is not affected by the Ring effect (Herman et al., 2009), so that we did not include it in the retrieval. The retrieval of SO_2 was performed applying two different strategies based on two different references. The "DOAS_v1" product is produced using the high resolution solar reference spectrum from Chance and Kurucz (2010) ("sao2010_solref_air.dat": hereafter "RSAO"), and the "DOAS_v2" product obtained with a measured clear sky reference spectrum (hereafter "Rmeas") acquired on 17 February 2019 with a solar zenith angle (SZA) close to zero. Fits and residuals obtained from the two strategies are presented in Figure 2. The use of a measured reference significantly improves the SO_2 fits, limiting the effect of interfering atmospheric gases and avoiding structures of the solar spectrum. To correct the I0 effect (Platt and Stutz, 2008), QDOAS performs an on-line approximation by correcting the cross sections with the high resolution solar Fraunhofer spectrum, considering a fixed predefined SCDI0. The I0 effect was corrected as following for the full time series: six SO_2 retrievals were performed using the QDOAS I0-correction algorithm for fixed SO_2 slant column values of 0.0, 1.0×10^{18}, 2.0×10^{18}, 3.0×10^{18}, 4.0×10^{18}, 5.0×10^{18} molec/cm^2 (the latter is close to the maximum uncorrected slant

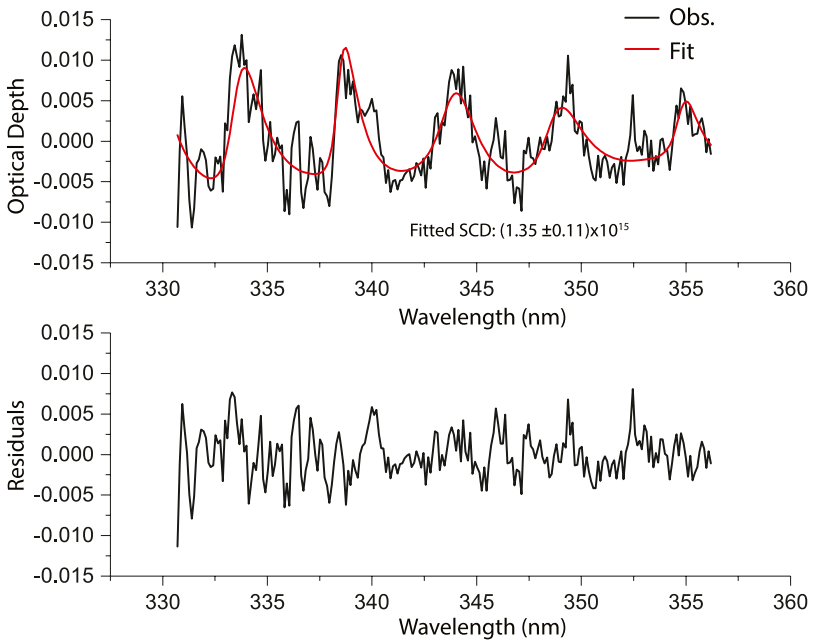

FIGURE 3
Example of fit of BrO analyzed in the (330.6–356.3 nm) spectral window from the DOAS measurements at ALTZ station performed on 20 February 2019. The retrieved slant column density (SCD, in molec/cm^2) is shown in the legend.

column). For each uncorrected datum, the most adequate I0-correction was interpolated from the five retrievals, depending on their slant column values. Only one iteration was required, since the difference between the slant columns obtained after the second and third iteration was lower than 1% of the retrieval error, so that the convergence was achieved after the second iteration. The O_3 cross section was also I0-corrected using the fixed slant column value of 1.0×10^{19} molec/cm^2, measured at Altzomoni by Plaza-Medina et al. (2017).

BrO was analyzed in the 330.6–356.3 nm spectral window (Table 1) according to Gliß et al. (2015), including the following cross sections: BrO at 298 K (Wilmouth et al., 1999), SO_2 at 298 K (Hermans et al., 2009), O_3 at 221 K (Burrows et al., 1999), O_4 (Hermans et al., 2003), NO_2 at 293 K (Voigt et al., 2002), OClO at 293 K (Bogumil et al., 2003) and a third-order polynomial function was included in the fitting routine. The I0 correction was applied to the O_3 cross-section. For the reference spectra, the same measured spectrum (Rmeas) as for the SO_2 retrieval was used. OClO was tentatively quantified from the same spectral window and settings, but it was not detected during the study period. Figure 3 shows an example of a BrO fit from DOAS measurements at ALTZ station. Data affected by the presence of clouds or without volcanic plume contribution were discarded using the SO_2 slant column uncertainties calculated by the QDOAS algorithm (based on the fit uncertainties) from the SO_2 analysis. We only consider data for which the relative SO_2 retrieval uncertainties were ≤20%. DOAS SO_2 and BrO SCDs were then converted into VCs to be compared with the FTIR and Pandora products, by dividing them by the SZA-dependent air mass factor (1/cos (SZA)).

3.3.2 FTIR analysis

SO_2, HCl, HF, and SiF_4 are retrieved from the high, medium and low resolution FTIR spectra using the PROFFIT9.6 retrieval code (Hase et al., 2004). Retrieval settings and strategies are detailed in Taquet et al. (2019) and summarized in Table 2. Examples of SO_2, HCl, HF, and SiF_4 fits are given in supplementary material (Supplementary Figures S3–S7). Importantly, this set-up allows the sequential analysis of the following pairs of gas species: SO_2 and HCl (InSb detector, NDACC filter 3), HF and HCl (InGaAs detector, Open) and SO_2 and SiF_4 (MCT detector, NDACC Filter 6), corresponding to different spectral regions (see Table 2). The different SO_2 (and HCl) products obtained using the different spectral ranges were calibrated and combined according to our previous study (Taquet et al., 2019). The only change with respect to Taquet et al. (2019) is the inclusion of the new spectral parameters for SiF_4 measured by Boudon et al. (2020), allowing retrievals of SiF_4 from both high (0.005 cm^{-1}) and low (0.1 cm^{-1}) resolution spectra. An estimation of the total error in the retrieved total columns is calculated by the PROFFIT code for all retrievals and includes systematic and statistical errors from different sources, such as the noise, baseline with channeling, Instrumental Line Shape (ILS), Line Of Sight (LOS) and spectroscopic parameters. The error analysis for this ALTZ instrument is described in more detail by Plaza-Medina et al. (2017). The channeling error (frequencies and amplitudes) for the instrument has been recently characterized and described by Blumenstock et al. (2020).

To evaluate the bias resulting from the use of the new spectroscopy in the SiF_4 analysis, we re-evaluated the SiF_4 VCs

TABLE 2 Spectral ranges and retrieval strategies (detailed in Taquet et al., 2019) applied for the SO_2, HCl, HF, and SiF_4 analysis from the FTIR data. TP refers to a profile retrieval with a Tikhonov-Phillips regularization, and Sc to a scaling retrieval.

	Spectral windows (cm^{-1}), (NDACC filter number, detector)	Spectral resolution (cm^{-1})	Retrieval strategy
SO_2	(2480.0–2520.0), (# 3, InSb) (1120.0–1180.0), (# 6, MCT)	0.1 and 0.005	Sc
HCl	(2727.0–2728.5); (2775.0–2776.50); (2818.75–2820.35); (2820.75–2822.35); (2843.0–2844.4); (2903.35–2904.85); (2923.0–2924.50); (2925.0–2926.75); (2942.0–2943.5); (2960.3–2961.825); (2962.3–2964.0); (2995.0–2996.5), (# 3, InSb) (5738.0–5740.0); (5767.0–5767.8); (5779.2–5779.9), (Open, InGaAs)	0.1 and 0.005 0.02	TP
HF	(3999.0–4003.5); (4036.5–4041.0), (Open, InGaAs)	0.1, 0.0075 and 0.02	TP
SiF_4	(1015.0–1035.0), (#6, MCT)	0.1 and 0.005	Sc

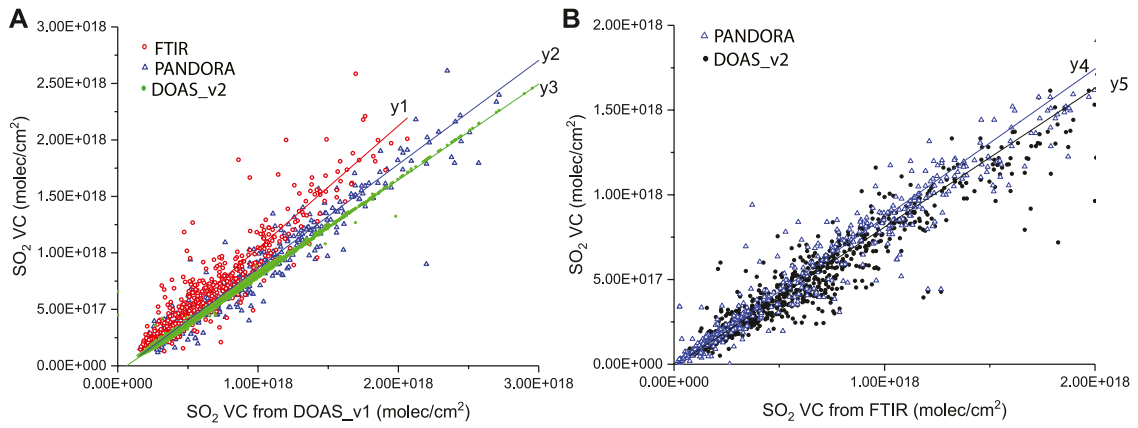

FIGURE 4
(A) Correlation plot of SO_2 VCs obtained from S2000 DOAS, Pandora, and FTIR instruments. **(B)** Determination of calibration factors with respect to the FTIR SO_2 product. Fit parameters are reported in Table 3.

TABLE 3 Linear fit parameters obtained from the intercomparison of the FTIR, S2000 DOAS and Pandora SO_2 products. R^2 stands for the determination coefficient.

Products	Regression label	Slope[a]	Intercept (molec/cm^2)	R^2
FTIR vs. DOAS_v1	y1	1.08 ± 0.02	$(-4.48 \pm 1.05) \times 10^{16}$	0.90
Pandora vs. DOAS_v1	y2	0.92 ± 0.01	$(-5.56 \pm 0.91) \times 10^{16}$	0.94
DOAS_v2 vs. DOAS_v1	y3	0.85 ± 0.01	$(-5.34 \pm 0.16) \times 10^{16}$	0.99
Pandora vs. FTIR	y4	0.88 ± 0.02	$(-8.17 \pm 4.04) \times 10^{15}$	0.90
DOAS_v2 vs. FTIR	y5	0.82 ± 0.01	$(-1.13 \pm 0.40) \times 10^{15}$	0.90

[a]Errors in the slope and intercept are given with a confidence interval of 0.95.

from the most significant SiF_4 events recorded at ALTZ on 06 March 2015 (Taquet et al., 2019). The re-analysis of the low resolution spectra provided SiF_4 columns slightly lower than previously published, by a factor of (0.94 ± 0.03) with a determination coefficient (R^2) of 0.96. The spectral fits are only slightly improved, but still a systematic artefact depending on the SZA, likely due to spectral interferences, was observed in the new SiF_4 time series. An empirical post-correction was applied to reduce this effect. A mean SiF_4 VC was calculated for all SZA (using bins of 5°). The so-generated airmass-dependent function was used for the whole time series and the intraday variability of SiF_4 was removed. Apart from increasing the number of SiF_4 data in the time series, the SiF_4 analysis from the high resolution spectra allows obtaining much lower total errors in the VCs than that for the low spectral resolution. For SiF_4 total columns higher than 2×10^{15} molec/cm^2, the SiF_4 VCs total errors are lower than 20%, while those obtained from the low resolution spectra occasionally reached 60%.

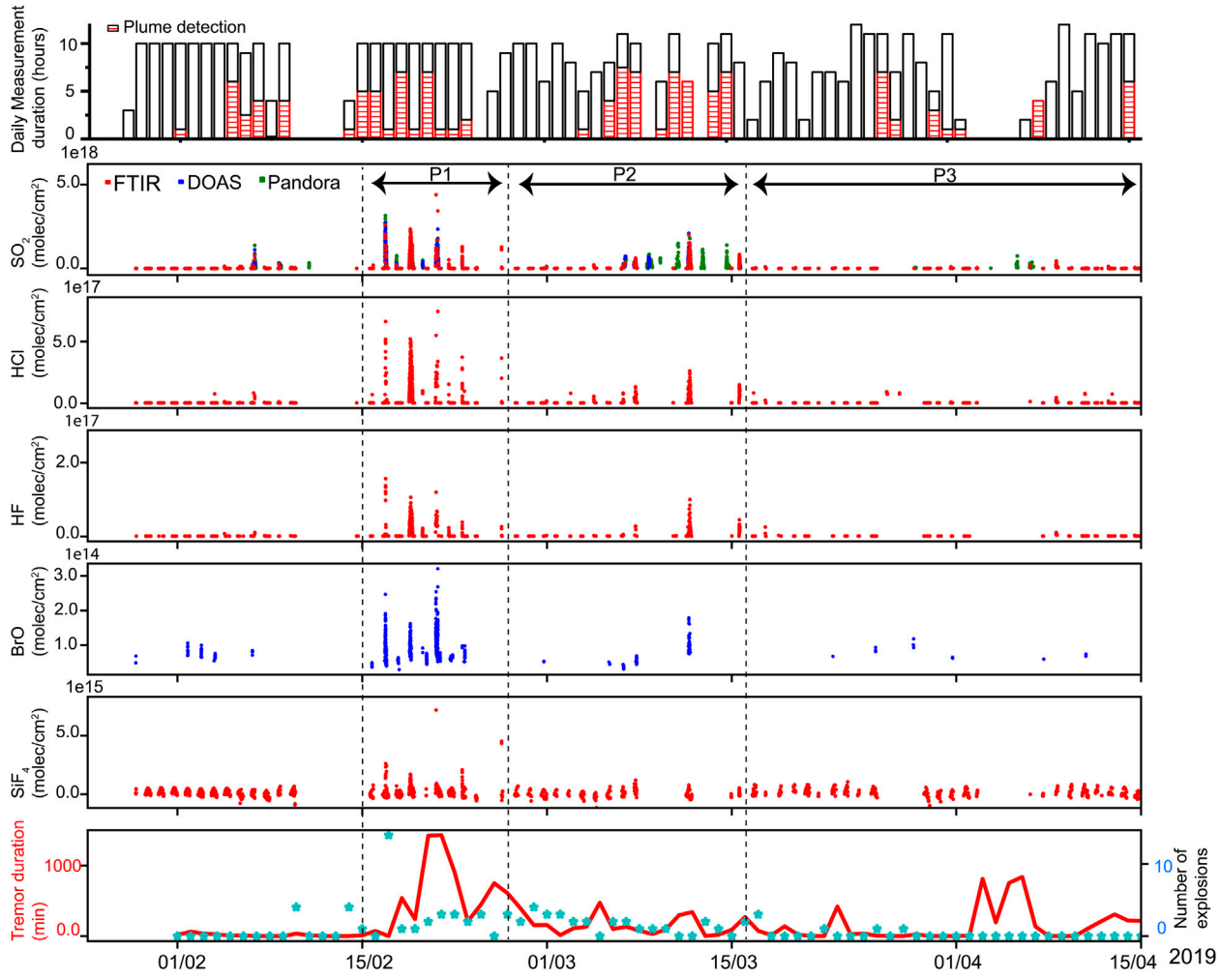

FIGURE 5
SO_2, HCl, HF, BrO, and SiF_4 VCs measured using S2000 DOAS, Pandora and FTIR instruments during the February–April 2019 period. The daily number of measurement hours and the number of hours affected by the presence of the volcanic plume are presented in the upper panel.

The quality control procedure described in Taquet et al. (2019) is applied for the different target species and an additional filter selecting SO_2 columns with relative total error <50% discards data with important uncertainties (presence of clouds, low signal, etc.).

4 Results

4.1 Intercomparison between the different instruments

4.1.1 SO_2 VCs from S2000 DOAS, FTIR, and Pandora

The intercomparison between the SO_2 VCs obtained from the FTIR, S2000 DOAS, and Pandora instruments is shown in Figure 4. Data pairs were chosen with a coincidence criterium equal to 1 min. Equations of regression lines (including uncertainties) are given in Table 3. SO_2 vertical columns obtained from the DOAS measurements using the two different strategies described in Section 3.3.1 (DOAS_v1 vs. DOAS_v2) are perfectly correlated (Figure 4A, in green) with a slope of 0.85 ± 0.01 (y3) and a determination coefficient of 0.99. In comparison with the DOAS products (measured with the highest temporal frequency), a good correlation ($R^2 \geq 0.90$) is observed in Figure 4A (Table 3) for the FTIR (y1) and Pandora (y2) SO_2 VCs products. The DOAS_v2 and the calibrated official Pandora SO_2 products are consistent, with respective bias of 0.85 ± 0.01 ($R^2 = 0.99$) and 0.92 ± 0.01 ($R^2 = 0.94$) to the DOAS_v1 product. Using the pre-calibrated RSAO reference (DOAS_v1) in the QDOAS retrieval instead of a "measured reference" allows obtaining "absolute" vertical columns directly comparable with those obtained from other instruments (Herman et al., 2009). However, the use of a measured reference (DOAS_v2 product) has the advantage to considerably reduce the noise in the absorbance spectrum (Figure 2) improving the fits and minimizing the total errors. The possible contamination of the

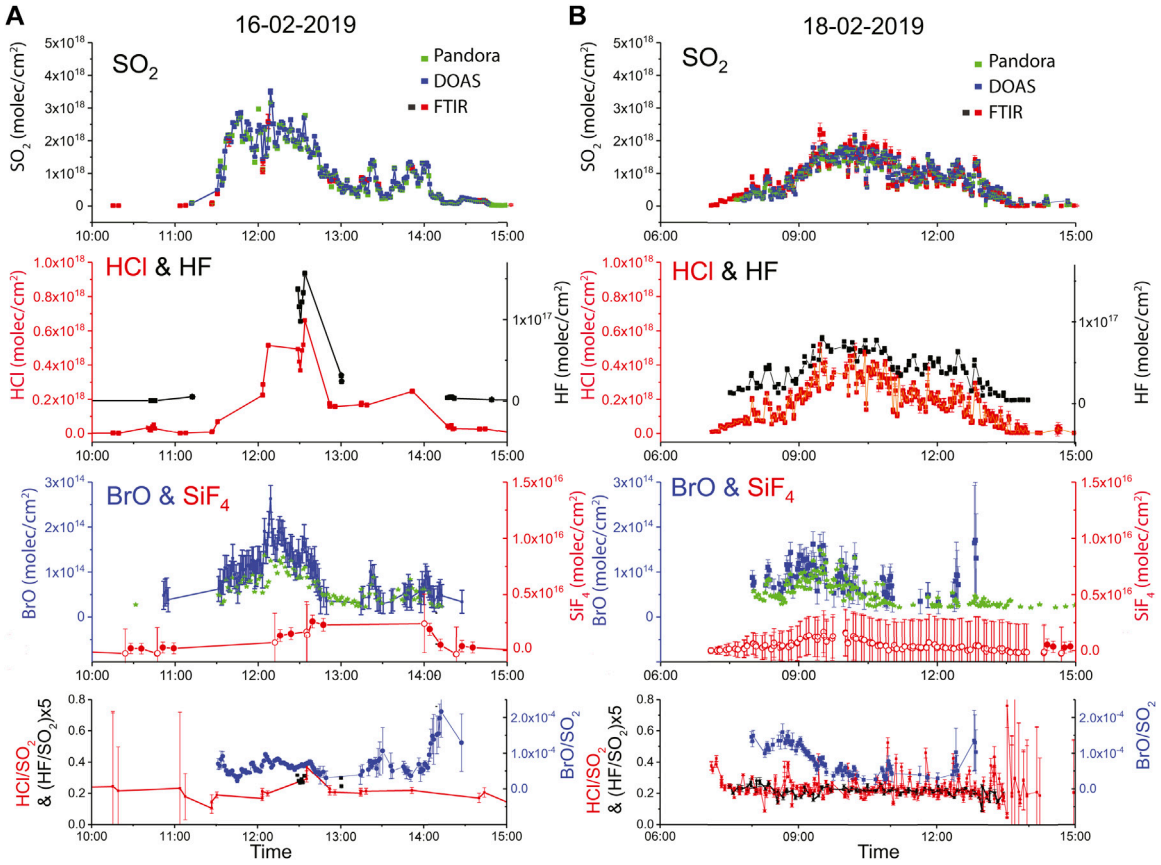

FIGURE 6
SO_2, HCl, HF, BrO, SiF_4 VCs intraday time series captured on the **(A)** 16 February 2019 and **(B)** 18 February 2019 using the S2000 DOAS, FTIR and Pandora instruments. For SiF_4, open and full circles correspond to the low and high resolution products, respectively. The BrO from the Pandora instrument [third **(A)** and **(B)** panels, in green] corresponds to a non-official PNG product and is only indicative of the S2000 DOAS and Pandora BrO VCs agreement. The lower panel shows the time series of the HCl/SO_2, HF/SO_2 (×5) and BrO/SO_2 ratios. See text for more details.

measured reference, however, has to be evaluated. For this, the measured reference used in the DOAS_v2 retrieval was pre-evaluated regarding its SO_2 content using a literature solar background spectrum as a Fraunhofer reference spectrum (Chance and Kurucz, 2010) which was convolved with the instrumental line spread function. The resulting SO_2 abundance of 9.1×10^{16} molec/cm^2 is of the same order of magnitude as the mean fit error ($5.0 \pm 4.0 \times 10^{16}$ molec/cm^2) of the SCDs and can be considered negligible in our measurement conditions.

Because of our longtime record of FTIR measurements at the ALTZ station (Stremme et al., 2009; Stremme et al., 2011; Stremme et al., 2012; Taquet et al., 2017; Taquet et al., 2019), the FTIR SO_2 product is hereafter used as our absolute reference, and the calibration factors defined in Figure 4B and reported in Table 3 were applied to the Pandora and DOAS_v2 products. The intercomparison was also examined at the intraday scale for different days, as shown in Figures 6A, B and Figures 7A, B, capturing explosive and passive degassing events during the dome growth episode of February 2019. The superimposition of the SO_2 VCs (median difference <12%) from the three instruments highlights the possibility to combine them, increasing the time resolution of the SO_2 time series and providing more pairs of coincident data for the calculation of the ratios.

4.1.2 BrO VCs from S2000 DOAS and Pandora

The Pandora and the DOAS BrO detections occurred on the same days (on the 16, 18 and 20/02/2019) during our 2.5-month time series. At the intraday scale (Figure 6), the BrO VCs from the two instruments agree within their uncertainties. However, the two time series are not well correlated (R^2 of 0.74) and show a slope DOAS/Pandora around 1.2. The PGN "fus5" retrieval is indeed not optimized for recovering BrO which is not a PGN official product, so that we will not consider it further for combination with the other products.

4.2 SO_2, HCl, HF, BrO and SiF_4 VCs measurements in the Popocatépetl's plume

The combination of the DOAS-FTIR instruments allowed the joint detection of more than 80 volcanic events during the whole measurement period (01/2017–05/2019), but the most significant

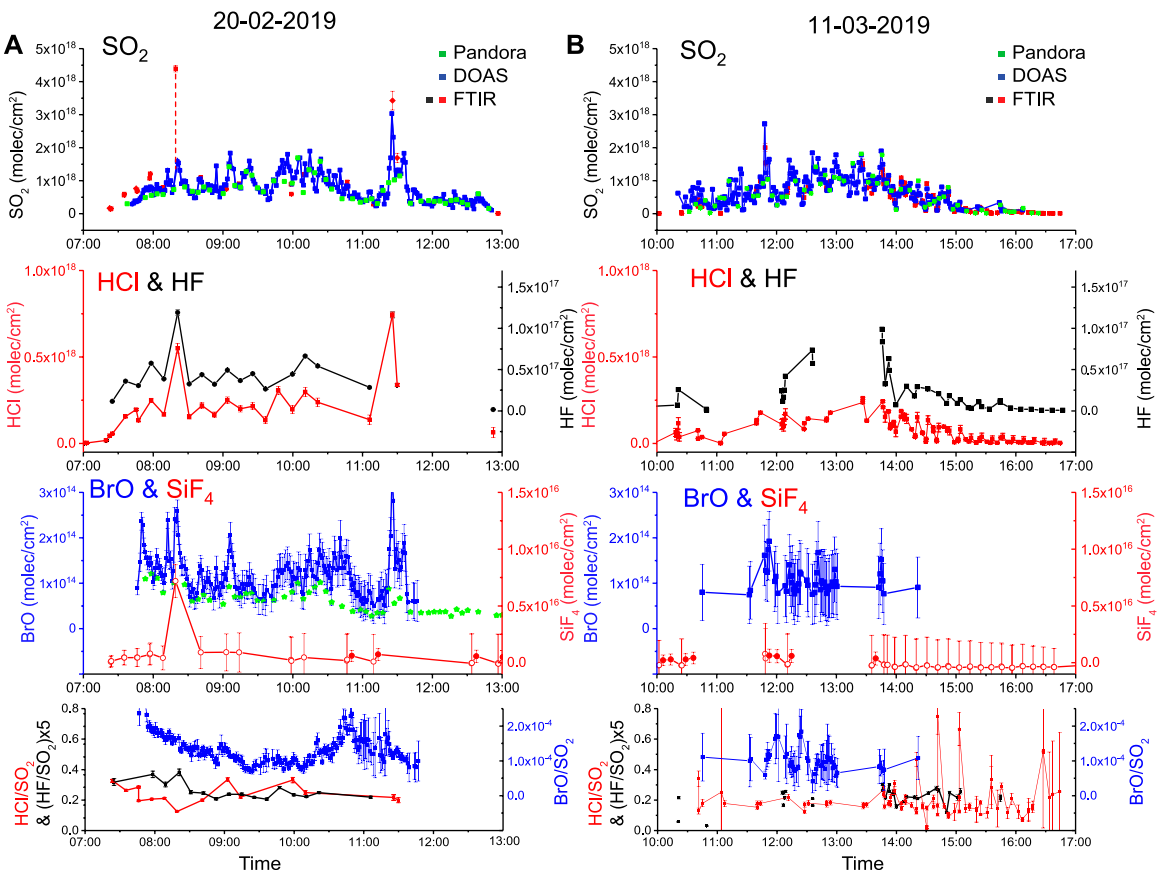

FIGURE 7
Same as Figure 6 for **(A)** 20 february 2019 and **(B)** 11 March 2019.

SO_2, HCl, HF, BrO, and SiF_4 columns were recorded during the main dome growth episodes. BrO was only detected during two (December 2017 and February 2019) of the 11 dome growth and destruction episodes that occurred during our 2.5-year time series (public CENAPRED annual and daily reports: https://www.cenapred.unam.mx/reportesVolcanGobMX/). The February-March 2019 dome growth episode is the only one during which we capture the volcanic plume over several consecutive days with the three (FTIR, S2000 DOAS and Pandora) instruments, with optimal meteorological conditions. Indeed over the 77 days of the period February–April 2019, 67 allowed measuring at least 1 h with the solar absorption configuration, cumulating a total of 558 h of measurements. The volcanic plume was captured by the different instruments over 118 h, distributed over 33 days. Figure 5 reports the SO_2, HCl, HF, BrO, SiF_4 time series during this crisis, concurrently with the tremor duration (from the daily CENAPRED reports), generally associated with short-term (several hours) extrusive periods. During this episode, we distinguished three main activity periods (see Introduction): P1 (15 February–26 February 2019), dominated by the dome growth manifestations such as "Strombolian-type activity" accompanied by spasmodic tremor; P2 (26 February–16 March 2019) characterized by the occurrence of strong explosions accompanying and following the dome destruction; and P3 (16 March–18 April 2019) with low volcanic activity and without dome occupying the crater.

Appreciable SO_2 columns were detected from 6 February 2019, at the same time as a small HCl and HF enhancement, unfortunately difficult to fully characterize on this day because of an unexpected interruption of the FTIR measurements. After that, even if small SO_2 short-term events were occasionally captured during the following days, the hydrogen halide and active halogen species VCs remained close to their detection limits until the first Strombolian-type episode started (on 15 February 2019). High SO_2, HCl, HF and BrO VCs were recorded during both the P1 and P2 periods, while significant columns of SiF_4 were only detected during P1. During P1, we captured volcanic plumes emitted between tremor episodes, sometimes accompanied with Strombolian-type phases (on 16, 18, 20, 21, and 22 February 2019). Two of these detections were facilitated by optimal northward wind conditions, driving the plume toward the ALTZ station for several hours. During P2, we captured an explosion plume (on 7 March 2019) and passive degassing (on 6, 11, and 15 March 2019). Examples of intraday time series corresponding to the different phases of the dome growth cycle are presented in Figures 6, 7. Intraday ratios are also calculated "point by point" from the measurement pairs to show the intraday variability of each species with respect to that of SO_2. Such ratios, occasionally combining VCs from different instruments (HF/SO_2)

TABLE 4 Linear fit parameters obtained from the correlation plots as presented in Figures 8 and 9. R^2 stands for the determination coefficient.

Species ratio	Regression label; Date	Slope	Intercept (molec/cm^2)	R^2
BrO/SO_2	y1a; 24/12/2017	$(1.14 \pm 0.2) \times 10^{-4}$	$(9.45 \pm 1.70) \times 10^{13}$	0.83
	y1b; 20/02/2019	$(8.70 \pm 0.82) \times 10^{-5}$	$(3.86 \pm 0.84) \times 10^{13}$	0.66
	y1c; 16/02/2019	$(6.28 \pm 0.65) \times 10^{-5}$	$(4.46 \pm 9.93) \times 10^{12}$	0.86
BrO/HCl	y2a; 24/12/2017	$(6.94 \pm 2.67) \times 10^{-4}$	$(6.10 \pm 4.13) \times 10^{13}$	0.89
	y2b; 20/02/2019	$(3.89 \pm 0.33) \times 10^{-4}$	$(3.59 \pm 0.76) \times 10^{13}$	0.84
	y2c; 16/02/2019	$(2.60 \pm 0.55) \times 10^{-4}$	$(0.6 \pm 1.7) \times 10^{13}$	0.92
HCl/SO_2	y3a; from 16/02 to 25/02/2019	(0.21 ± 0.01)	$(1.90 \pm 2.20) \times 10^{14}$	0.98
	y3b; from 07/03 to 15/03/2019	(0.16 ± 0.01)	$(1.34 \pm 1.27) \times 10^{15}$	0.96
	y3c; from 15/04 to 18/04/2019	(0.08 ± 0.01)	$(1.42 \pm 0.12) \times 10^{15}$	0.92
HF/SO_2	y4; from 16/02 to 18/04/2019	(0.049 ± 0.001)	$(1.45 \pm 1.44) \times 10^{14}$	0.96
SiF_4/SO_2	Figure 9	$(1.56 \pm 0.25) \times 10^{-3}$	$(2.08 \pm 1.87) \times 10^{14}$	0.96

[a]Errors in the slope and intercept are given with a confidence interval of 0.95.

and/or built upon species acquired within 1 min intervals, may be affected by noise errors and shall only be considered as indicative. For the longer-term comparison of the plume chemistry, we prefer the ratio obtained from daily correlation plots, averaging the noise and very short-term variations. Plume ages (±1 min) were estimated from the ALTZ webcams, capturing images every minute. All mentioned times are local winter times (UTC-6).

On 16 February 2019, our measurements take place during a passive degassing episode, a few hours after a ~3-h long Strombolian-type episode. An abrupt increase of SO_2 VCs was detected at 11:30, recording the arrival of the plume in the FTIR line of sight. This plume, aged of ~20 min and free of ash, corresponds to a continuous degassing period between two Strombolian-type episodes (from ~1:30 to ~4:30 and from ~16:00 to ~20:30), in the early phases of the dome construction. BrO was initially detected at the same time as SO_2, and abruptly increased around 12:05, as well as HF and HCl VCs. SO_2 and BrO are well correlated after this event (regression y1c in Table 4; Figure 8). The intraday BrO/SO_2 time series shows a small but statistically significant increase (>2 × Ratio error) between 11:45 and 13:00, coinciding with an apparent increase in the degassing (station's webcams). Although the time resolution of the FTIR time series is less than that of DOAS, HCl/SO_2 seems to show similar variations. The SiF_4 species is also detected on this day but with a very low abundance, close to its detection limit (VCs <1σ).

On 18 February 2019, we captured an ash-poor plume from continuous degassing during several hours, immediately following the end of a weak Strombolian-type episode (~21:30 to ~7:30 from CENAPRED reports) with few extra-crater projections. After a strong drop of ~30 min duration in the degassing activity (from ~6:30), an explosion occurred at 07:04, preceding the beginning of our measurements. Our measurements captured the return to a higher degassing regime. Wind speed was evaluated to more or less 20 m/s this day (from the GDAS/NOAA model), and the plume age can be estimated to be ~15 min using the station webcam. The HF, HCl, and SO_2 column variations remained perfectly correlated between them during the whole measured period as highlighted by the relatively constant HCl and HF to sulfur ratios of 0.20, 0.05 respectively. Although the intraday variability of the BrO VCs is the same order of magnitude as its total error, the BrO/SO_2 is less affected and allows observing a progressive decrease between 07:30 and 09:30. This decrease is mainly controlled by an increase in SO_2 columns during this period. Although the error of SiF_4 VCs is also important, its time series follows the general trend of the other species.

On 20 February 2019 (Figure 7A), the measurements started during an ~11-h long tremor episode and captured an ash-free plume, corresponding to continuous degassing. The wind conditions in the early morning drove the plume towards the ENE reaching the instruments field of view in about 21 min. At 07:52, a puff occurred (Supplementary Figure S2, supplementary material), and the plume reached the measurement line of sight at ~ 08:11. At ~8:45, the wind field changes towards the NE accompanying the rising Sun and the plume was progressively driven towards the station. A small puff occurred at 10:10, and an apparently more condensed plume was observed from 10:40 to 12:00 (Supplementary Figure S2, supplementary material). Despite the low time resolution of the FTIR measurements, SO_2, HCl and HF time series have a similar behaviour, with coincident peaks at 08:20 and 11:25. BrO VCs are on average about a factor of 1.5 higher than that observed on 18 February 2019, and although its variability is different from that of the other species, it shows the same significant peaks at 08:20 and 11:25. The peak observed at 08:20 coincides with the arrival of the first puff plume in the optical path of the instrument. The BrO/SO_2 linearly decreases with time until ~9:30 when it reaches a plateau, increases again from 10:15 to 10:50 and finally drops again until the end of the measurements. HCl/SO_2 and HF/SO_2 oscillate around their average ratio, except for the slight decrease of HF/SO_2 at the beginning of the time series until ~9:00. SiF_4 is detected over a short period (<30 min, two measurements: 7.2×10^{15} molec/cm^2) with VCs much higher than those of the other presented days, closer to the values recorded on 6 March 2015 (1.2×10^{16} molec/cm^2; Taquet et al., 2019). The BrO/SO_2 peak at 10:50 coincides with the

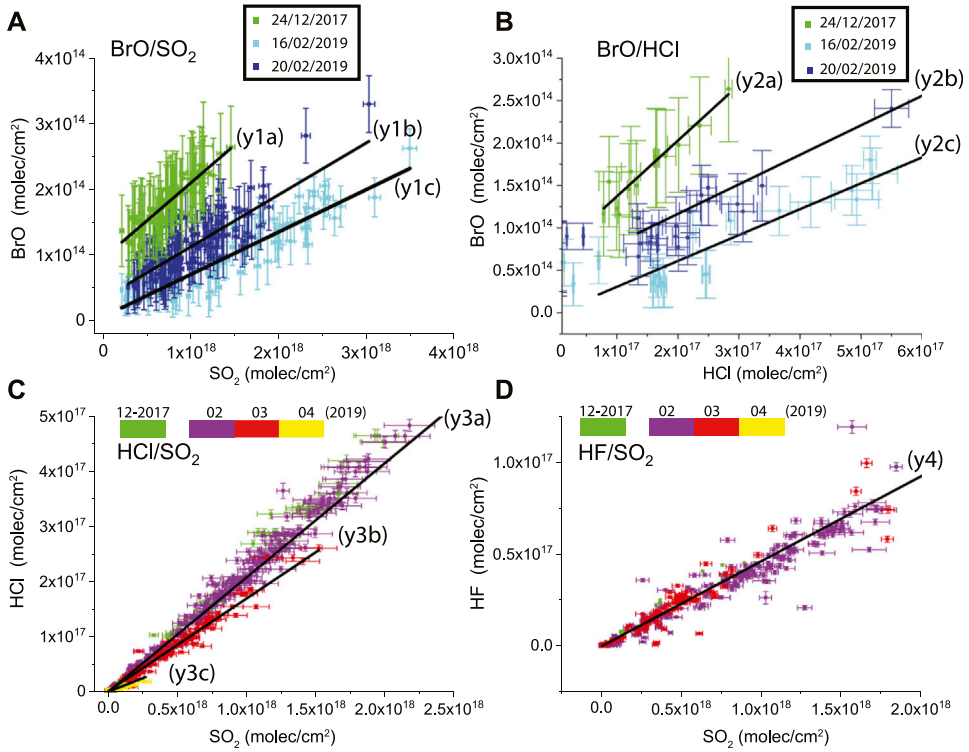

FIGURE 8
Correlation plots of **(A)** BrO vs. SO_2, **(B)** BrO vs. HCl, **(C)** HCl vs. SO_2 and **(D)** HF vs. SO_2 VCs combining DOAS and FTIR data on 24 December 2017 and during the February–April 2019 dome cycle. The BrO/SO_2, BrO/HCl, HCl/SO_2 and HF/SO_2 ratios were determined from the slopes of the correlation plots.

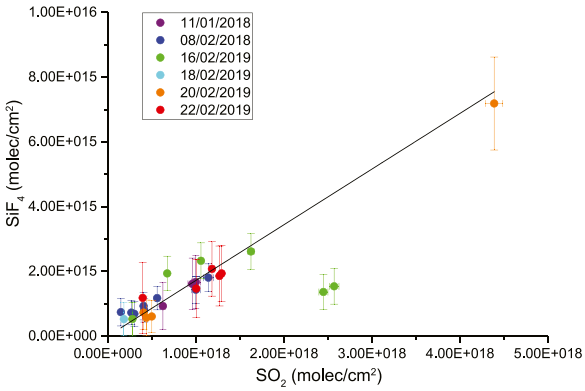

FIGURE 9
SiF_4/SO_2 correlation plot for the 2017–2019 measurement period. The slope is found to be (1.56 ± 0.25) × 10^{-3}. Error bars represent the total errors of the FTIR VCs measurements, detailed in the text.

arrival of the more condensed plume (after the puff at 10:10) in the optical path of the instrument.

On 11 March 2019 (Figure 7B), we captured a northward blown plume from passive degassing a few days after the end of the dome destruction. The plume entered the instruments line of sight around 10:30 until 15:00. The SO_2 peak at 11:46 corresponds to a plume coming from a small puff detected on the visible cameras above the crater at 11:30. HCl and SO_2 vary in time with the same magnitude, such that the HCl/SO_2 ratio is found to be almost constant. BrO is also detected, but contrary to the other days, BrO/SO_2 does not present a specific trend, oscillating around its mean value.

4.3 BrO/SO_2, HCl/SO_2, HF/SO_2, and BrO/HCl ratios at Popocatépetl

BrO/SO_2, HCl/SO_2, HF/SO_2, and BrO/HCl ratios have been calculated from the intraday correlation plots from February to April 2019 and reported in Figure 8. For the calculation of the HF/SO_2 (HF and SO_2 measured with two different NDACC filters) and BrO/HCl ratios, we interpolated the SO_2 and BrO S2000 DOAS time series (which have the highest time resolution) at the time of the FTIR measurements (HF, HCl). The interpolation is performed only if there are coincident data within an interval of 1 min for SO_2 or 2 min for BrO. An evaluation of the bias generated by the use of the SO_2 columns from the different instruments for the calculation of HF/SO_2 and BrO/SO_2 ratios is shown in supplementary material, Supplementary Figure S1. A maximum bias of 3% is found, making possible the combination of the different SO_2 products to increase

the number of coincident pairs, in particular for the HF/SO_2 ratio. S2000 DOAS and FTIR SO_2 products were therefore combined before the calculation of the different ratios, presented in Figure 8. Because of the rare occurrence of the BrO and SiF_4 species in our 2.5-month time series, we added the event of 24 December 2017 (Figure 8 in green) which was one of the most significant events of our 2.5-year time series to give an idea of their long-time variability.

BrO/SO_2 ratios (Figure 8A) are found in the range of [0.6–1.1] × 10^{-4}, with a significantly higher ratio on 24 December 2017 than those reported for 2019. This falls in the higher range of the few ratios previously reported for the Popocatépetl volcano between 0.04 × 10^{-4} and 1.4 × 10^{-4} (Boichu et al., 2011; Bobrowski and Giuffrida, 2012; Platt and Bobrowski, 2015; Fickel and Delgado Granados, 2017) and compiled in Gutmann et al. (2018).

BrO/HCl (Figure 8B) ranges between 2.6 and 6.9 × 10^{-4} and shows similar slopes (~3 × 10^{-4}) during the 2019 dome growth phase (on 16 and 20 February 2019) but different offsets.

HCl/SO_2 (Figure 8C) ranges between 0.08 ± 0.01 and 0.21 ± 0.01 and decreases with time during the 2019 dome growth cycle. Three different trend lines can be distinguished corresponding to three periods, from 15 to 25 February 2019, from 7 to 15 March 2019 and after this. The first two trend lines coincide with the dome growth (p1), and destruction (p2) periods described in Section 4.2, respectively. The third trend line (y3c), corresponding to the period p3, with very low HCl column abundances and low HCl/SO_2 ratios characterizes a new phase without extrusive activity.

HF/SO_2 (Figure 8D) correlation plot shows a more important dispersion, and only one trend line can be identified over the 2019 dome cycle, with a HF/SO_2 ratio around 0.049 ± 0.001. This value is in accordance with the previous values measured since 2012 (from 0.01 to 0.04) (Taquet et al., 2019).

Our previous studies on the long-term variability of the Popocatépetl's plume composition showed a link between the HCl/SO_2 and the main long-term changes in the deep and shallow magmatic processes (intrusions, long-term cessation of extrusive activity, etc). In this study we examined the variability of this ratio during a complete dome growth cycle (timescale of several months), and found a clear increase of HCl with respect to sulfur during the period of dome growth. It decreased during the period of destruction and reached very small values when no dome sits on the floor of the crater. HF/SO_2 does not show the same behavior and remains almost constant during the whole cycle. Its high intraday variability is likely due to in-plume reaction during the transport to the measurement locus.

Two types of SiF_4 detections occurred over the 2.5 years survey, either 1) as transient peaks generally occurring during explosions with ash-rich plumes, too short-termed for correlations with the SO_2 or HF to be clearly established, or 2) as several hour long enhancements with clear correlations with the other volcanic gas species, occurring only at the end of the dome growth episodes. Over the complete 2.5-years time series, only 6 days (Figure 9) allowed calculating an average SiF_4/SO_2 ratio, found equal to (1.56 ± 0.25) × 10^{-3}, similar to the lowest values found in 2012–2016 (1.0 − 9.9 × 10^{-3}; Taquet et al., 2019).

In our opinion, these two types of observation support the occurrence at Popocatépetl of both SiF_4 generation mechanisms, as previously reported (Love et al., 1998; Taquet et al., 2017), i.e., 1) the HF interaction with silica in the closing connected porosity of a mature dome and 2) the in-plume reaction of HF with ash. BrO/SO_2 and BrO/HCl have similar slopes on 16 and 20 February 2019, but further data are needed to explore its variability as a function of the dome growth phases. Finally, we compared our bromine to sulfur ratios with some of the meteorological parameters of interest available at the ALTZ station. The lowest ratio (6.3 ± 0.6 × 10^{-5}), obtained on 16 February 2019 is recorded on the day with the highest RH (>48%). On 18 February 2019, the RH even falls under 10% over the measurement period with a mid-range ratio (Figure 6). The highest ratios were obtained on 24 December 2017 and 20 February 2019, 2 days characterized with low humidity conditions <24% and <34%, respectively, which do not favor the formation of BrO (Oppenheimer et al., 2006). These observations suggest that atmospheric humidity might not be the main control on BrO conversion at Popocatépetl. Furthermore, on 20 February 2019, the highest ratios are measured at ~7:46, during sunrise, with a solar irradiance as low as 133 W/m^2, which appears sufficient to allow the conversion of HBr into detectable amounts of BrO.

5 Discussion and conclusion

In this contribution, we explored the feasibility and performance of combining direct-sun measurements from S2000 DOAS, Pandora and HR-FTIR instruments to study the short-term variability of Popocatépetl's plume composition. The SO_2 vertical columns obtained from the three instruments were found similar after their intercalibration (median difference <12%), making it possible to combine the different products to increase the number of coincident data pairs in the ratios calculation. Although the DOAS instrument is generally used in "scattering" mode to continuously measure BrO/SO_2 in volcanic plumes, there are important advantages of direct-sun such as the straightforward conversion from slant to vertical columns using a simple geometric determination of the airmass factor, and the absence of ring effect, thus considerably reducing the total errors. Moreover, this configuration is one of the most reliable allowing direct comparison with VCs from other techniques (FTIR) and determining ratios of species that are not detectable with the same technique. FTIR SiF_4 retrieval was improved compared to that published in Taquet et al. (2019) using the new spectroscopy from Boudon et al. (2020) and allowing the treatment of high resolution spectra. The VCs total errors obtained from the low resolution products are only slightly improved, but the results obtained from the high resolution spectra are significantly more precise with total error <20% for total columns >2.0 × 10^{15} molec/cm^2 when those from the low resolution spectra occasionally reached 60%.

The BrO/SO_2 ratio was successfully quantified at a distance of 11 km from the crater, found between 0.6 and 1.1×10^{-4}, in the range of the few values previously reported (Bobrowski and Giuffrida, 2012; Platt and Bobrowski, 2015; Fickel and Delgado Granados, 2017). However, HBr analysis from the high resolution FTIR spectra is not straightforward at this distance from the crater, and so as in Taquet et al. (2019), only a detection limit of 5.0×10^{14} molec/cm^2 was calculated. Following this study and assuming the average Br/Cl ratio for arc volcanoes ($2.2 \pm 2.0 \times 10^{-3}$; Gerlach, 2004), we calculate a speculative primitive HBr/SO_2 for the surveyed period from the average HCl/SO_2 ratio (0.21 ± 0.01) of $(4.6 \pm 4.2) \times 10^{-4}$. Assuming the maximum value (8.8×10^{-4}) within the uncertainty interval for this (HBr/SO_2) ratio, our measured BrO/SO_2 ratios would thus correspond to minimum HBr conversion rates of the order of 10%, which is in the range for plumes with an age equal to or higher than 15 min (Rüdiger et al., 2021). Using this detection limit, the maximum HBr/BrO ratio would then be between 0.11 and 0.19.

For the first time, the BrO/SO_2, HCl/SO_2, HF/SO_2, BrO/HCl, and SiF_4/SO_2 ratios have been simultaneously measured in the Popocatépetl's plume and their behavior with respect to the volcanic activity was explored at the scale of a dome growth cycle (several weeks). The decrease of the HCl/SO_2 ratio after the dome destruction at the end of February 2019 suggests that halogen emissions are higher during the dome growth periods, i.e., during sustained ascension of the magma column, confirming the long-term observations reported in Taquet et al. (2019). HF/SO_2 ratios apparently remain constant during the February to April 2019 period and show a high intraday variability. SiF_4/SO_2 was quantified on various occasions during the dome cycle period and apparently remains constant, equal to $(1.56 \pm 0.25) \times 10^{-3}$ compatible with previous results (Goff et al., 1998; Love et al., 1998; Stremme et al., 2012; Taquet et al., 2017; Taquet et al., 2019). Considering a HF/SO_2 average ratio of 0.049 ± 0.001 over the dome cycle period, we determine an average SiF_4/HF ratio of 0.031 ± 0.001.

BrO/SO_2 and HCl/SO_2 apparently show different long-term variability, at least for the three examples presented here (on 24 December 2017 and on 16 and 20 February 2019), for which two significantly different BrO/SO_2 ratios were found while the HCl/SO_2 was found to be constant (Figure 8).

On a few occasions, clear patterns appear in the BrO/SO_2 intraday time series (Figures 6, 7A) while the HCl/SO_2 remains almost constant (flat baseline). These patterns, generally a few hours long, consisted either in decreasing trends (e.g., the first hours of 18 and 20 February) or increase/decrease sequences (e.g., 10:00–12:00 on 20 February). In particular, 2 days (16 and 20 February 2019) show significant BrO/SO_2 variations, which are not dominated by the SO_2 columns variability. The most significant variations (20 February 2019 between 10:50 and 12:00) occur coincidentally with a change in the aspect of the plume and might be related to changes in the plume moisture content, although further studies are needed to explore this aspect in more details. Surprisingly, the highest average BrO/SO_2 ratio (recorded on 20 February 2019) is not observed during meteorological and sunlight intensity conditions (RH <34%, and solar irradiance ~133 W/m^2) that favour HBr conversion to BrO (c.f. Oppenheimer et al., 2006; Kern et al., 2009). Since the BrO content in the Popocatépetl's plume may not be mainly controlled by the meteorological conditions or sunlight intensity, the impact of plume aerosol content has to be explored in future studies. BrO/HCl was quantified for the first time at Popocatépetl (from 2.6 to 6.9×10^{-4}). It is found almost constant at the intraday scale but with significant day to day variability. Considering the BrO as full conversion from HBr, this is already a factor of 1.5–3.5 higher than the lower bound of Gerlach. (2004) Br/Cl range, and thus constitutes a first minimum constraint on this ratio at Popocatépetl. The maximum conversion rates ever described (65% at Ambrym, Vanuatu; Bani et al., 2009; Gutman et al., 2018) would provide a higher bound for this ratio at Popocatépetl of 1.08×10^{-3}.

This study is a new step towards the establishment of a comprehensive highly time-resolved database of volcanic gas ratios for Popocatépetl by integrating multiple spectroscopic techniques. Such database should provide insight for, e.g., 1) delineating the degassing processes at Popocatépetl occurring during both passive degassing and extrusive phases, 2) refining the degassing balance by taking into account the in-plume interactions, and 3) comparing the degassing processes observed at Popocatépetl with those of analogue volcanoes.

Our study shows the benefits and performance of implementing a UV-Vis spectrometer on an existing HR-FTIR NDACC instrument to simultaneously measure the main primary and secondary volcanic gaseous species. Such implementation does not either disturb or interrupt the continuous solar absorption atmospheric measurements performed for the networks. This experiment could be reproduced at any other NDACC stations located near volcanoes, such as, e.g., the Izaña Observatory which recently recorded atmospheric data during the 2021-La Palma (Canary Islands, Spain) eruption (Garcia et al., 2022), at Maïdo observatory (La Réunion Island, France), or Mauna Loa Observatory (Hawaii), providing quasi-near-real-time critical data for the management of volcanic emergencies. High spectral resolution spectroscopic data also have the advantage to provide simultaneous atmospheric vertical profiles of both atmospheric and some volcanic species, giving new insight into the effect of volcanic emissions on the atmospheric chemistry and climate change.

Data availability statement

The raw data supporting the conclusion of this article will be made available by the authors, without undue reservation.

Author contributions

All the co-authors contributed in the development and the discussion of concepts, and to the preparation of the manuscript. NT, CR, and WS were responsible of the DOAS and FTIR measurements and the data analysis. MG and WS lead the ALTZ station development and its long-term operation. TBo participated to the measurements and to the interpretation. AB was responsible of the maintenance of the

instruments at the Altzomoni station. OG contributes for the FTIR/DOAS intercomparison and discussions. TBl leads at KIT the German-Mexican collaboration for the deployment of the high resolution FTIR spectrometer and supports its long-term operation as part of NDACC. FH has helped in the design and setup of the spectrometer and solar tracker before it was shipped to Mexico. He has developed the retrieval code PROFFIT and gives continuously support to the UNAM group for its use and in operating the spectrometer.

Funding

We acknowledge financial support from grants UNAM-PAPIIT IA101620 and IN111521. NT and TBo also thank the stipend given by the Mexican Foreign Affairs Department (Secretaría de Relaciones Exteriores) and its AMEXCID program. Financial support from Conacyt-AEM through grant No. 275239 is acknowledged.

Acknowledgments

We thank the two reviewers for their very constructive comments, which help to significantly improve the manuscript. We thank R. Campion for fruitfull discussions on the degassing and activity of the Popocatépetl. We thank all the personnel of the CENAPRED for realizing the Popocatépetl activity reports. We thank the PGN team for the Pandora data processing. The PGN is a bilateral project supported with funding from NASA and ESA. We thank to C. Fayt, M. Van Roozendael, and A. Merlaud for their help to use the QDOAS software.

Conflict of interest

The authors declare that the research was conducted in the absence of any commercial or financial relationships that could be construed as a potential conflict of interest.

Publisher's note

Supplementary material

The Supplementary Material for this article can be found online at: https://www.frontiersin.org/articles/10.3389/feart.2023.1062699/full#supplementary-material

References

Aiuppa, A., Bellomo, S., D'Alessandro, W., Federico, C., Ferm, M., and Valenza, M. (2004). Volcanic plume monitoring at Mount Etna by diffusive (passive) sampling. *J. Geophys. Res.* 109, D21308. doi:10.1029/2003JD004481

Aiuppa, A., Bitetto, M., Delle Donne, D., La Monica, F. P., Tamburello, G., Coppola, D., et al. (2021). Volcanic CO_2 tracks the incubation period of basaltic paroxysms. *Sci. Adv.* 7, eabh0191. doi:10.1126/sciadv.abh0191

Aiuppa, A. (2009). Degassing of halogens from basaltic volcanism: Insights from volcanic gas observations. *Chem. Geol.* 263 (1-4), 99–109. doi:10.1016/j.chemgeo.2008.08.022

Aiuppa, A., Federico, C., Antonio, P., Giovannella, P., and Mariano, V. (2002). S, Cl and F degassing as an indicator of volcanic dynamics: The 2001 eruption of Mount Etna. *Geophys. Res. Lett.* 29, 1559. doi:10.1029/2002GL015032

Aiuppa, A., Federico, C., Franco, A., Giudice, G., Gurrieri, S., Inguaggiato, S., et al. (2005). Emission of bromine and iodine from Mount Etna volcano. *Geochem. Geophys.* 6 (8). doi:10.1029/2005GC000965

Arellano, S., Galle, B., Apaza, F., Avard, G., Barrington, C., Bobrowski, N., et al. (2021). Synoptic analysis of a decade of daily measurements of SO_2 emission in the troposphere from volcanoes of the global ground-based Network for Observation of Volcanic and Atmospheric Change. *Earth Syst. Sci. Data* 13 (3), 1167–1188. doi:10.5194/essd-13-1167-2021

Bani, P., Oppenheimer, C., Tsanev, V. I., Carn, S. A., Cronin, S. J., Crimp, R., et al. (2009). Surge in sulphur and halogen degassing from Ambrym volcano, Vanuatu. *Vanuatu. Bull. Volcanol.* 71, 1159–1168. doi:10.1007/s00445-009-0293-7

Bobrowski, N., and Giuffrida, G. (2012). Bromine monoxide/sulphur dioxide ratios in relation to volcanological observations at Mt. Etna 2006–2009. *Solid earth.* 3, 433–445. doi:10.5194/se-3-433-2012

Bobrowski, N., Hönninger, G., Galle, B., and Platt, U. (2003). Detection of bromine monoxide in a volcanic plume. *Nature* 423, 273–276. doi:10.1038/nature01625

Bobrowski, N., and Platt, U. (2007). Bromine monoxide studies in volcanic plumes. *J. Volcanol. Geotherm. Res.* 166, 147–160.doi:10.5194/acp-13-4749-2013

Bobrowski, N., Von Glasow, R., Aiuppa, A., Inguaggiato, S., Louban, I., Ibrahim, O. W., et al. (2007). Reactive halogen chemistry in volcanic plumes. *J. Geophys. Res. Atmos.* 112 (D6), D06311. doi:10.1029/2006jd007206

Bogumil, K., Orphal, J., Homann, T., Voigt, S., Spietz, P., Fleischmann, O. C., et al. (2003). Measurements of molecular absorption spectra with the SCIAMACHY pre-flight model: Instrument characterization and reference data for atmospheric remote sensing in the 230-2380 nm region. *J. Photochem. Photobiol. A Chem.* 157, 167–184. doi:10.1016/S1010-6030(03)00062-5

Boichu, M., Oppenheimer, C., Roberts, T. J., Tsanev, V., and Kyle, P. R. (2011). On bromine, nitrogen oxides and ozone depletion in the tropospheric plume of Erebus volcano, *Atmos. Environ.* 45, 3856–3866. doi:10.1016/j.atmosenv.2011.03.027

Boudon, V., Manceron, L., and Richard, C. (2020). High-resolution spectroscopy and analysis of the ν3, ν4 and 2ν4 bands of SiF_4 in natural isotopic abundance. *J. Quantitative Spectrosc. Radiat. Transf.* 253, 107114. doi:10.1016/j.jqsrt.2020.107114

Boulesteix, T., Legrand, D., Taquet, N., Coppola, D., Laiolo, M., Valade, S., et al. (2022). Modulation of Popocatépetl's activity by regional and worldwide earthquakes. *Bull. Volcanol.* 84, 80. doi:10.1007/s00445-022-01584-2

Burrows, J. P., Richter, A., Dehn, A., Deters, B., Himmelmann, S., Voigt, S., et al. (1999). Atmospheric remote-sensing reference data from GOME: Part 2. Temperature-Dependent absorption cross-sections of O_3 in the 231-794 nm range. *J. Quant. Spectrosc. Radiat. Transf.* 61, 509–517. doi:10.1016/S0022-4073(98)00037-5

Burton, M., Allard, P., Muré, F., and La Spina, A. (2007). Magmatic gas composition reveals the source depth of slug-driven strombolian explosive activity. *Science* 317, 227–230. doi:10.1126/science.1141900

Burton, M. R., Oppenheimer, C., Horrocks, L. A., and Francis, P. W. (2001). Diurnal changes in volcanic plume chemistry observed by lunar and solar occultation spectroscopy. *Geophys. Res. Lett.* 28 (5), 843–846. doi:10.1029/2000gl008499

Butz, A., Dinger, A. S., Bobrowski, N., Kostinek, J., Fieber, L., Fischerkeller, C., et al. (2017). Remote sensing of volcanic CO_2, HF, HCl, SO_2, and BrO in the downwind plume of Mt. Etna. *Atmos. Meas. Tech.* 10, 1–14. doi:10.5194/amt-10-1-2017

Caballero, G., and Valderrama, S. (2020). *Actividad del volcán Popocatépetl 2019. México*. Mexico City: Centro Nacional de Prevención de Desastres.

Caballero Jimenez, G., Valderrama, S., and Espinasa Perena, R. (2019). *Actividad del volcan Popocatépetl 2018*. Mexico City: Centro Nacional de Prevención de Desastres.

Capion, R., Delgado-Granados, H., Legrand, D., Taquet, N., Boulesteix, T., Pedraza-Espitía, S., et al. (2018). Breathing and coughing: The extraordinarily high degassing of Popocatépetl volcano investigated with an SO2 camera. *Front. Earth Sci.* 6, 163. doi:10.3389/feart.2018.00163

Cede, A., Tiefengraber, M., Gebetsberger, M., and Spinei Lind, E. (2021). Pandonia global network data products readme document. Version 1.8-5. Available at: https://

www.pandonia-global-network.org/wp-content/uploads/2022/01/PGN_DataProducts_Readme_v1-8-5.pdf.

Chance, K., and Kurucz, R. (2010). An improved high-resolution solar reference spectrum for Earth's atmosphere measurements in the ultraviolet, visible, and near infrared. *J. Quant. Spectrosc. Ra.* 111, 1289–1295. doi:10.1016/j.jqsrt.2010.01.036

Danckaert, T., Fayt, C., Van Roozendael, M., De Smedt, I., Letocart, V., Merlaud, A., et al. (2013). *QDOAS Software user manual.* Belgium: Belgian Institute for Space Aeronomy.

De Hoog, J. C., Van Bergen, M. J., and Jacobs, M. H. (2005). Vapour-phase crystallisation of silica from SiF_4-bearing volcanic gases. *Ann. Geophys.* 48 (4–5). doi:10.4401/ag-3233

Delmelle, P., Wadsworth, F. B., Maters, E. C., and Ayris, P. M. (2018). High temperature reactions between gases and ash particles in volcanic eruption plumes. *Rev. Mineral. Geochem.* 84, 285–308. doi:10.2138/rmg.2018.84.8

Dinger, F., Bobrowski, N., Warnach, S., Bredemeyer, S., Hidalgo, S., Arellano, S., et al. (2018). Periodicity in the BrO/SO_2 molar ratios in the volcanic gas plume of Cotopaxi and its correlation with the Earth tides during the eruption in 2015. *Solid earth.* 9, 247–266. doi:10.5194/se-9-247-2018

Dinger, F., Kleinbek, T., Dörner, S., Bobrowski, N., Platt, U., Wagner, T., et al. (2021). SO_2 and BrO emissions of Masaya volcano from 2014 to 2020. *Atmos. Chem. Phys.* 21, 9367–9404. doi:10.5194/acp-21-9367-2021

Dingwell, D. B., and Mysen, B. O. (1985). Effects of water and fluorine on the viscosity of albite melt at high pressure: A preliminary investigation. *Earth Planet. Sci. Lett.* 74, 266–274. doi:10.1016/0012-821X(85)90026-3

Donovan, A., Tsanev, V., Oppenheimer, C., and Edmonds, M. (2014). Reactive halogens (BrO and OClO) detected in the plume of Soufriere Hills Volcano during an eruption hiatus. *Geochem. Geophys. Geosyst.* 15, 3346–3363. doi:10.1002/2014GC005419

Edmonds, M., Herd, R. A., Galle, B., and Oppenheimer, C. M. (2003). Automated, high time-resolution measurements of SO_2 flux at Soufrière Hills Volcano, Montserrat. *Bull. Volcanol.* 65, 578–586. doi:10.1007/s00445-003-0286-x

Edmonds, M., Pyle, D., and Oppenheimer, C. (2002). HCl emissions at Soufrière Hills Volcano, Montserrat, west indies, during a second phase of dome building: November 1999 to october 2000. *Bull. Volcanol.* 64, 21–30. doi:10.1007/s00445-001-0175-0

Fickel, M., and Delgado Granados, H. (2017). On the use of different spectral windows in DOAS evaluations: Effects on the estimation of SO_2 emission rate and mixing ratios during strong emission of Popocatépetl volcano. *Chem. Geol.* 462, 67–73. doi:10.1016/j.chemgeo.2017.05.001

Francis, P., Burton, M. R., and Oppenheimer, C. (1998). Remote measurements of volcanic gas compositions by solar occultation spectroscopy. *Nature* 396 (6711), 567–570. doi:10.1038/25115

Francis, P., Maciejewski, A., Oppenheimer, C., Chaffin, C., and Caltabiano, T. (1995). SO_2:HCl ratios in the plumes from Mt. Etna and vulcano determined by fourier transform spectroscopy. *Geophys. Res. Lett.* 22, 1717–1720. doi:10.1029/95GL01657

Galle, B., Johansson, M., Rivera, C., Zhang, Y., Kihlman, M., Kern, C., et al. (2010). Network for observation of volcanic and atmospheric change (NOVAC)—a global network for volcanic gas monitoring: Network layout and instrument description. *J. Geophys. Res.* 115, D05304. doi:10.1029/2009JD011823

García, O., Stremme, W., Taquet, N., Hase, F., Ortega, I., Hannigan, J., et al. (2022). Sulphur dioxide from ground-based Fourier transform infrared spectroscopy: Application to volcanic emissions. *TCCON/COCCON/NDACC 2022 Jt. Meet.*

Gerlach, T., and Graeber, E. (1985). Volatile budget of Kilauea volcano. *Nature* 313, 273–277. doi:10.1038/313273a0

Gerlach, T. M. (2004). Volcanic sources of tropospheric ozone-depleting trace gases. *Geochem. Geophys. Geosystems* 5 (9), Q09007. doi:10.1029/2004GC000747

Gisi, M., Hase, F., Dohe, S., and Blumenstock, T. (2011). Camtracker: A new camera controlled high precision solar tracker system for ftir-spectrometers. *Atmos. Meas. Tech.* 4, 47–54. doi:10.5194/amt-4-47-2011

Gisi, M., Hase, F., Dohe, S., Blumenstock, T., Simon, A., and Keens, A. (2012). XCO2-measurements with a tabletop FTS using solar absorption spectroscopy. *Atmos. Meas. Tech.* 5, 2969–2980. doi:10.5194/amt-5-2969-2012

Gisi, M. (2012). Setup of precise camera based solar tracker systems and greenhouse gas measurements using a modified portable spectrometer. Doctoral dissertation. Karlsruhe: Karlsruher Institut für Technologie (KIT). doi:10.5445/IR/1000031248

Gliß, J., Bobrowski, N., Vogel, L., Pöhler, D., and Platt, U. (2015). OClO and BrO observations in the volcanic plume of Mt. Etna – implications on the chemistry of chlorine and bromine species in volcanic plumes. *Atmos. Chem. Phys.* 15, 5659–5681. doi:10.5194/acp-15-5659-2015

Goff, F., Janik, C. J., Delgado, H., Werner, C., Counce, D., Stimac, J. A., et al. (1998). Geochemical surveillance of magmatic volatiles at Popocatépetl volcano, Mexico. *Geol. Soc. Am. Bull.* 110, 695–710. doi:10.1130/0016-7606(1998)110<0695:GSOMVA>;2.3.CO;2

Goff, F., Love, S. P., Warren, R., Counce, D., Obenholzner, J., Siebe, C., et al. (2001). Passive infrared remote sensing evidence for large, intermittent CO_2 emissions at Popocatépetl volcano, Mexico. *Chem. Geol.* 177, 133–156. doi:10.1016/S0009-2541(00)00387-9

Gutmann, A., Bobrowski, N., Roberts, T. J., Rüdiger, J., and Hoffmann, T. (2018). Advances in bromine speciation in volcanic plumes. *Front. Earth Sci.* 6, 213. doi:10.3389/feart.2018.00213

Hase, F., Hannigan, J., Coffey, M., Goldman, A., Hopfner, M., Jones, N., et al. (2004). Intercomparison of retrieval codes used for the analysis of highresolution, ground-based FTIR measurements. *J. Quant. Spectrosc. Radiat. Transf.* 87, 25–52. doi:10.1016/j.jqsrt.2003.12.008

Herman, J., Cede, A., Spinei, E., Mount, G., Tzortziou, M., and Abuhassan, N. (2009). NO2 column amounts from ground-based Pandora and MFDOAS spectrometers using the direct-sun DOAS technique: Intercomparisons and application to OMI validation. *J. Geophys. Res.* 114,D13307. doi:10.1029/2009JD011848

Hermans, C., Vandaele, A. C., Fally, S., Carleer, M., Colin, R., Coquart, B., et al. (2003). Absorption cross-section of the collision-induced bands of oxygen from the UV to the NIR. *Proc. NATO Adv. Res. Workshop, Weakly Interact. Mol. Pairs Unconv. Absorbers Radiat. Atmos. France. NATO Sci. Ser. IV Earth Environ. Sci.* 27, 193–202. doi:10.1007/978-94-010-0025-3_16

Hermans, C., Vandaele, A., and Fally, S. (2009). Fourier transform measurements of SO_2 absorption cross sections: I. Temperature dependence in the 24 000–29 000 cm^{-1} (345–420 nm) region. *J. Quant. Spectrosc. Ra.* 110, 756–765. doi:10.1016/j.jqsrt.2009.01.031

Heue, K.-P., Brenninkmeijer, C. A. M., Baker, A. K., Rauthe-Schöch, A., Walter, D., Wagner, T., et al. (2011). SO_2 and BrO observation in the plume of the eyjafjallajökull volcano 2010: CARIBIC and GOME-2 retrievals. *Atmos. Chem. Phys.* 11, 2973–2989. doi:10.5194/acp-11-2973-2011

Kern, C., Sihler, H., Vogel, L., Rivera, C., Herrera, M., and Platt, U. (2009). Halogen oxide measurements at Masaya Volcano, Nicaragua using active long path differential optical absorption spectroscopy. *Bull. Volcanol.* 71, 659–670. doi:10.1007/s00445-008-0252-8

Kraus, S. (2006). *Doasis: A framework design for DOAS.* Germany: Shaker Verlag GmbH.

Krueger, A., Stremme, W., Harig, R., and Grutter, M. (2013). Volcanic SO_2 and SiF_4 visualization using 2-D thermal emission spectroscopy - Part 2: Wind propagation and emission rates. *Atmos. Meas. Tech.* 6, 47–61. doi:10.5194/amt-6-47-2013

Love, S. P., Goff, F., Counce, D., Siebe, C., and Delgado, H. (1998). Passive infrared spectroscopy of the eruption plume at Popocatépetl volcano, Mexico. *Nature* 396, 563–567. doi:10.1038/25109

Love, S. P., Goff, F., Schmidt, S. C., Counce, D., Pettit, D., Christenson, B. W., et al. (2000). Passive infrared spectroscopic remote sensing of volcanic gases: Ground-based studies at white Island and ruapehu, New Zealand, and Popocatepetl, Mexico. *Geophys. Monograph-American Geophys. Union* 116, 117–138. doi:10.1029/GM116p0117

Lübcke, P., Bobrowski, N., Arellano, S., Galle, B., Garzón, G., Vogel, L., et al. (2014). BrO/SO_2 molar ratios from scanning DOAS measurements in the NOVAC network. *Solid earth.* 5, 409–424. doi:10.5194/se-5-409-2014

Martin, R. S., Wheeler, J. C., Ilyinskaya, E., Braban, C. F., and Oppenheimer, C. (2012). The uptake of halogen (HF, HCl, HBr and HI) and nitric (HNO_3) acids into acidic sulphate particles in quiescent volcanic plumes. *Chem. Geol.* 296-297, 19–25. doi:10.1016/j.chemgeo.2011.12.013

McGonigle, A. J. S., Delmelle, P., Oppenheimer, C., Tsanev, V. I., Delfosse, T., Williams-Jones, G., et al. (2004). SO_2 depletion in tropospheric volcanic plumes. *Geophys Res. Lett.* 31, L13201. doi:10.1029/2004GL019990

Meller, R., and Moortgat, G. K. (2000). Temperature dependence of the absorption cross sections of formaldehyde between 223 and 323 K in the wavelength range 225-375 nm. *J. Geophys. Res.* 105 (6), 7089–7101. doi:10.1029/1999JD901074

Mori, T., Notsu, K., Tohjima, Y., and Wakita, H. (1993). Remote detection of HCl and SO_2 in volcanic gas from Unzen volcano, Japan. *J. Geophys. Res.* 13, 1355–1358. doi:10.1029/93gl01065

Mori, T., Sato, M., Shimoike, Y., and Notsu, K. (2002). High SiF_4/HF ratio detected in Satsuma-Iwojima volcano's plume by remote FT-IR observation. *Earth Planets Space* 54, 249–256. doi:10.1186/BF03353024

Notsu, K., and Mori, T. (2010). Chemical monitoring of volcanic gas using remote FT-IR spectroscopy at several active volcanoes in Japan. *Appl. Geochem.* 25 (4), 505–512. doi:10.1016/j.apgeochem.2010.01.008

Oppenheimer, C., Francis, P., and Maciejewski, A. J. H. (1998). Spectroscopic observation of HCl degassing from Soufriere Hills volcano, Montserrat. *Geophys. Res. Lett.* 25 (19), 3689–3692. doi:10.1029/98gl01584

Oppenheimer, C., and McGonigle, A. J. (2004). Exploiting ground-based optical sensing technologies for volcanic gas surveillance. *Ann. Geophys.* 47 (4).

Oppenheimer, C., Tsanev, V. I., Braban, C. F., Cox, R. A., Adams, J. W., Aiuppa, A., et al. (2006). BrO formation in volcanic plumes. *Geochim. Cosmochim. Acta* 70 (12), 2935–2941. doi:10.1016/j.gca.2006.04.001

Platt, U., Bobrowski, N., and Butz, A. (2018). Ground-based remote sensing and imaging of volcanic gases and quantitative determination of multi-species emission fluxes. *Geosciences* 8 (2), 44. doi:10.3390/geosciences8020044

Platt, U., and Bobrowski, N. (2015). "Quantification of volcanic reactive halogen emissions," in *Volcanism and global environmental change* (Cambridge: University Press), 115–132.

Platt, U., and Stutz, J. (2008). *Differential optical absorption spectroscopy (DOAS), principle and applications*. Heidelberg: Springer-Verlag.

Plaza-Medina, E. F., Stremme, W., Bezanilla, A., Grutter, M., Schneider, M., Hase, F., et al. (2017). Ground-based remote sensing of O_3 by high- and medium-resolution FTIR spectrometers over the Mexico City basin. *Atmos. Meas. Tech.* 10, 2703–2725. doi:10.5194/amt-10-2703-2017

Rix, M., Valks, P., Hao, N., Loyola, D., Schlager, H., Huntrieser, H., et al. (2012). Volcanic SO_2, BrO and plume height estimations using GOME-2 satellite measurements during the eruption of Eyjafjallajökull in May 2010. *J. Geophys. Res.* 117, D00U19. doi:10.1029/2011JD016718

Rodríguez, L. A., Watson, I. M., Edmonds, M., Ryan, G., Hards, V., Oppenheimer, C. M. M., et al. (2008). SO_2 loss rates in the plume emitted by Soufrière Hills volcano, Montserrat. *J. Volcanol. Geotherm. Res.* 173, 135–147. doi:10.1016/j.jvolgeores.2008.01.003

Rüdiger, J., Gutmann, A., Bobrowski, N., Liotta, M., de Moor, J. M., Sander, R., et al. (2021). Halogen activation in the plume of masaya volcano: Field observations and box model investigations. *Atmos. Chem. Phys.* 21, 3371–3393. doi:10.5194/acp-21-3371-2021

Schiavo, B., Stremme, W., Grutter, M., Campion, R., Guarin, C. A., Rivera, C., et al. (2019). Characterization of a UV camera system for SO_2 measurements from Popocatépetl Volcano. *J. Volcanol. Geotherm. Res.* 370, 82–94. doi:10.1016/j.jvolgeores.2018.09.001

Schipper, C. I., Castro, J. M., Kennedy, B. M., Christenson, B. W., Aiuppa, A., Alloway, B., et al. (2019). Halogen (Cl, F) release during explosive, effusive, and intrusive phases of the 2011 rhyolitic eruption at Cordón Caulle volcano (Chile). *Volcanica* 2 (1), 73–90. doi:10.30909/vol.02.01.7390

Serdyuchenko, A., Gorshelev, V., Weber, M., Chehade, W., and Burrows, J. P. (2013). High spectral resolution ozone absorption cross-sections - Part 2: Temperature dependence. *Atmos. Meas. Tech. Discuss.* 6, 6613–6643. doi:10.5194/amtd-6-6613-2013

Shinohara, H. (2009). A missing link between volcanic degassing and experimental studies on chloride partitioning. *Chem. Geol.* 263 (1-4), 51–59. doi:10.1016/j.chemgeo.2008.12.001

Smekens, J. F., Mather, T. A., Burton, M. R., La Spina, A., Kabbabe, K., Esse, B., et al. (2023). Quantification of gas, ash, and sulphate aerosols in volcanic plumes from open path Fourier transform infrared (OP-FTIR) emission measurements at Stromboli volcano, Italy. *Front. Earth Sci.* 10, 1005738. doi:10.3389/feart.2022.1005738

Stremme, W., Krueger, A., Harig, R., and Grutter, M. (2012). Volcanic SO_2 and SiF_4 visualization using 2-D thermal emission spectroscopy - Part 1: Slant-columns and their ratios. *Atmos. Meas. Tech.* 5, 275–288. doi:10.5194/amt-5-275-2012

Stremme, W., Ortega, I., and Grutter, M. (2009). Using ground-based solar and lunar infrared spectroscopy to study the diurnal trend of carbon monoxide in the Mexico City boundary layer. *Atmos. Chem. Phys.* 9, 8061–8078. doi:10.5194/acp-9-8061-2009

Stremme, W., Ortega, I., Siebe, C., and Grutter, M. (2011). Gas composition of Popocatépetl volcano between 2007 and 2008: FTIR spectroscopic measurements of an explosive event and during quiescent degassing. *Earth Planet. Sci. Lett.* 301, 502–510. doi:10.1016/j.epsl.2010.11.032

Stutz, J., Kim, E. S., Platt, U., Bruno, P., Perrino, C., and Febo, A. (2000). UV-visible absorption cross sections of nitrous acid. *J. Geophys. Res. Atmos.* 105 (11), 14585–14592. doi:10.1029/2000jd900003

Taquet, N., Hernández, I. M., Stremme, W., Bezanilla, A., Grutter, M., Campion, R., et al. (2017). Continuous measurements of SiF_4 and SO_2 by thermal emission spectroscopy: Insight from a 6-month survey at the Popocatépetl volcano. *J. Volcanol. Geotherm. Res.* 341, 255–268. doi:10.1016/j.jvolgeores.2017.05.009

Taquet, N., Stremme, W., Grutter, M., Baylón, J., Bezanilla, A., Schiavo, B., et al. (2019). Variability in the gas composition of the Popocatépetl volcanic plume. *Front. Earth Sci.* 7, 114. doi:10.3389/feart.2019.00114

Valade, S., Ley, A., Massimetti, F., D'Hondt, O., Laiolo, M., Coppola, D., et al. (2019). Towards global volcano monitoring using multisensor Sentinel missions and artificial intelligence: The MOUNTS monitoring system. *Remote Sens.* 11, 1528. doi:10.3390/rs11131528

Vandaele, A. C., Hermans, C., and Fally, S. (2009). Fourier transform measurements of SO_2 absorption cross sections: II. Temperature dependence in the 29000-44000 cm^{-1} (227-345 nm) region. *J. Quant. Spectrosc. Radiat. Transf.* 110, 2115–2126. doi:10.1016/j.jqsrt.2009.05.006

Vandaele, A. C., Hermans, C., Simon, P. C., Carleer, M., Colin, R., Fally, S., et al. (1998). Measurements of the NO_2 absorption cross-section from 42,000 cm^{-1} to 10,000 cm^{-1} (238-1000 nm) at 220 K and 294 K. *J. Quant. Spectrosc. Radiat. Transf.* 59, 171–184. doi:10.1016/S0022-4073(97)00168-4

Voigt, C., Jessberger, P., Jurkat, T., Kaufmann, S., Baumann, R., Schlager, H., et al. (2014). Evolution of CO_2, SO_2, HCl, and HNO_3 in the volcanic plumes from Etna. *Geophys. Res. Lett.* 41, 2196–2203. doi:10.1002/2013GL058974

Voigt, S., Orphal, J., and Burrows, J. (2002). The temperature and pressure dependence of the absorption cross-sections of NO_2 in the 250–800 nm region measured by Fourier-transform spectroscopy. *J. Photoch. Photobio. A* 149, 1–7. doi:10.1016/S1010-6030(01)00650-5

Warnach, S., Bobrowski, N., Hidalgo, S., Arellano, S., Sihler, H., Dinger, F., et al. (2019). Variation of the BrO/SO2 molar ratio in the plume of Tungurahua volcano between 2007 and 2017 and its relationship to volcanic activity. *Front. Earth Sci.* 7, 132. doi:10.3389/feart.2019.00132

Wilmouth, D. M., Hanisco, T. F., Donahue, N. M., and Anderson, J. G. (1999). Fourier transform ultraviolet spectroscopy of the $A\ ^2\Pi_{3/2} \leftarrow X\ ^2\Pi_{3/2}$ transition of BrO. *J. Phys. Chem. A* 103, 8935–8945. doi:10.1021/jp991651o

Woitischek, J., Woods, A. W., Edmonds, M., Oppenheimer, C., Aiuppa, A., Pering, T. D., et al. (2020). Strombolian eruptions and dynamics of magma degassing at Yasur Volcano (Vanuatu). *J. Volcanol. Geotherm. Res.* 398, 106869. doi:10.1016/j.jvolgeores.2020.106869

Wright, R., La Cruz-Reyna DeServando, H., Andrew, F., Luke, G-P., and Jose, J. (2002). Infrared satellite monitoring at Popocatépetl: Explosions, exhalations, and cycles of dome growth. *J. Geophys Res.* 107 (8), 2153. doi:10.1029/2000JB000125

frontiers | Frontiers in Earth Science

TYPE Original Research
PUBLISHED 20 April 2023
DOI 10.3389/feart.2023.1063922

OPEN ACCESS

EDITED BY
Ryunosuke Kazahaya,
National Institute of Advanced Industrial Science and Technology (AIST), Japan

REVIEWED BY
Jian Xu,
Chinese Academy of Sciences (CAS), China
Toshiya Mori,
The University of Tokyo, Japan

*CORRESPONDENCE
Alexander Nies,
alexander.nies@cnrs-orleans.fr

RECEIVED 07 October 2022
ACCEPTED 04 April 2023
PUBLISHED 20 April 2023

CITATION
Nies A, Heimann J, Fuchs C, Kuhn J, Bobrowski N and Platt U (2023), Quantifying BrO and SO_2 distributions in volcanic plumes—Recent advances in imaging Fabry-Pérot interferometer correlation spectroscopy.
Front. Earth Sci. 11:1063922.
doi: 10.3389/feart.2023.1063922

Quantifying BrO and SO_2 distributions in volcanic plumes—Recent advances in imaging Fabry-Pérot interferometer correlation spectroscopy

Alexander Nies[1,2]*, Jaro Heimann[1], Christopher Fuchs[1,3], Jonas Kuhn[1], Nicole Bobrowski[1,4] and Ulrich Platt[1]

[1]Institute of Environmental Physics, Heidelberg University, Heidelberg, Germany, [2]Laboratoire de Physique et de Chimie de l`Environnement et de l`Espace, CNRS/University Orleans, Orleans, France, [3]Institute for Atmospheric and Climate Science, ETH Zurich, Zurich, Switzerland, [4]Istituto Nazionale di Geofisica e Vulcanologia—Osservatorio Etneo, Catania, Italy

Bromine monoxide (BrO) and sulphur dioxide (SO_2) are two gases frequently observed in volcanic plumes by spectroscopic techniques capable of continuous gas monitoring like, e.g., Differential Optical Absorption Spectroscopy (DOAS). The spatio-temporal resolution of DOAS measurements, however, only allows to determine average gas fluxes (minutes to hours resolution). In particular, it is insufficient to record two-dimensional images of SO_2 and BrO in real-time (seconds time resolution). Thus, it is impossible to resolve details of chemical conversions of reactive plume constituents. However, these details are vital for further understanding reactive halogen chemistry in volcanic plumes. Therefore, instruments that combine high spatio-temporal resolution and high gas sensitivity and selectivity are required. In addition, these instruments must be robust and compact to be suitable for measurements in harsh and remote volcanic environments. Imaging Fabry-Pérot interferometer (FPI) correlation spectroscopy (IFPICS) is a novel technique for atmospheric trace gas imaging. It allows measuring atmospheric gas column density (CD) distributions with a high spatial and temporal resolution, while at the same time providing selectivity and sensitivity comparable to DOAS measurements. IFPICS uses the periodic transmission spectrum of an FPI, that is matched to the periodic narrowband (vibrational) absorption features of the target trace gas. Recently, IFPICS has been successfully applied to volcanic SO_2. Here we demonstrate the applicability of IFPICS to much weaker (about two orders of magnitude) trace gas optical densities, such as that of BrO in volcanic plumes. Due to its high reactivity, BrO is extremely difficult to handle in the laboratory. Thus, based on the similarity of the UV absorption cross sections, we used formaldehyde (HCHO) as a spectral proxy for BrO in instrument characterization measurements. Furthermore, we present recent advances in SO_2 IFPICS measurements and simultaneous measurements of SO_2 and BrO from a field campaign at Mt Etna in July 2021. We find photon shot-noise limited detection limits of 4.7×10^{17} molec $s^{0.5}$ cm^{-2} for SO_2 and of 8.9×10^{14} molec $s^{0.5}$ cm^{-2} for BrO at a spatial resolution of 512 × 512 pixels and 200 × 200 pixels, respectively. Furthermore, an estimate for the BrO to SO_2 ratio (around 10^{-4}) in the volcanic plume is given. The prototype instrument presented here provides spatially resolved measurements of the reactive volcanic plume component BrO. The

temporal resolution of our approach allows studies of chemical conversions inside volcanic plumes on their intrinsic timescale.

KEYWORDS

remote sensing, Fabry-Perot interferometer, imaging, bromine monoxide, sulphur dioxide, volcanic plumes, IFPICS

1 Introduction

Despite of their low atmospheric mixing ratios, halogen radicals substantially influence atmospheric processes and impact the overall oxidative capacity of the atmosphere. Several volcanoes are strong sources yielding comparatively high atmospheric mixing ratios of halogen radicals (particularly bromine species) inside volcanic plumes (e.g., Bobrowski, et al., 2003). Bromine radicals influence the oxidation capacity of the atmosphere. For instance, they catalyze ozone (O_3) destruction, interfere with the NO_x-reaction cycle, and may enhance the hydroxyl radical to hydroperoxyl (OH/HO_2) ratio. Hypophalus acids like hypobromous acid (HOBr, formed from BrO) can accelerate the formation of sulphate in aqueous particles and bromine atoms can oxidize mercury and therefore reduce its atmospheric lifetime (e.g., Platt & Bobrowski 2015). Moreover, in the atmosphere near active volcanoes, bromine almost exclusively originates from the volcanoes itself, which additionally might make it a good tracer for volcanic activity (e.g., Platt & Bobrowski 2015). Therefore, it is of great interest to study the abundance and behavior of these species.

Ground based remote sensing techniques are a common tool to measure gases in volcanic plumes. SO_2 and BrO can be measured and continuously monitored readily by DOAS (see, e.g., Platt & Stutz 2008). However, the spatio-temporal resolution of typical DOAS instruments is too low to resolve fast chemical evolution processes. Beside the atmospheric impact, those processes need to be better understood in order to link, for example, the BrO amount in volcanic plumes to volcanological parameters (e.g., the bromine emission). The formation of BrO in the atmosphere is explained by the autocatalytic oxidation of bromide, also known as 'bromine explosion' (Platt & Lehrer 1997), which was found to occur in marine and polar boundary layers (Barrie et al., 1988), over salt lakes (Stutz et al., 2002) and also has been observed in volcanic plumes (Bobrowski et al., 2003). The presence of BrO in volcanic plumes has a number of consequences for atmospheric chemistry, for instance O_3 destruction is catalyzed (e.g., Bobrowski et al., 2007; Vance et al., 2010).

Fast and spatially resolved measurements of BrO can yield important insights into the chemical processes occurring in volcanic plumes. An ideal instrument for such observations combines a high spatial resolution (on the order of meters) to resolve the spatial distribution of trace gas gradients and a high temporal resolution (on the order of seconds) for the observation of fast chemical conversions of trace gases. These properties should not come at the expense of high selectivity and sensitivity of the instrument towards the gas to be measured. Also, the instrument should be compact and robust to be operable in remote locations.

Here we present a prototype imaging instrument based on the IFPICS technology proposed by Kuhn et al. (2014) and applied to measure volcanic SO_2 distributions by Fuchs et al. (2021). It utilizes the periodic transmission spectrum of an FPI in a camera setup, which results in a high selectivity and sensitivity, while retaining high spatio-temporal resolution (see Section 2.1).

This work demonstrates the applicability of the IFPICS technology to atmospheric absorbers with—compared to SO_2—low differential optical densities (of the order of 10^{-3}) like BrO. We present imaging measurements of HCHO gas cells. Due to the similarity of the UV absorption cross sections, HCHO can serve as a spectral proxy for BrO absorption in characterization measurements. Furthermore, advances in SO_2 imaging and parallel imaging measurements of volcanic SO_2 and BrO performed at Mt Etna in July 2021 are presented and compared to DOAS measurements.

2 Materials and methods

2.1 Imaging Fabry-Pérot interferometer correlation spectroscopy (IFPICS)

IFPICS combines the benefits of line-scanning "hyperspectral" cameras (or imaging DOAS, see, e.g., Lohberger et al., 2004; Louban et al., 2009) and of filter-based cameras (like the "SO_2 camera," see, e.g., Mori & Burton 2006; Bluth et al., 2007) by using an FPI as a wavelength selective element. In other words, IFPICS combines high sensitivity and selectivity with high spatio-temporal resolution. The FPI and its transmission spectrum is designed to match periodic components of the absorption cross section of a target trace gas. This approach yields a much higher selectivity and sensitivity compared to filter-based cameras (see Kuhn et al., 2014; Kuhn et al., 2019; Fuchs et al., 2021 for details). Lambert-Beers law states that, the optical density of the target trace gas τ is given by the logarithmic ratio of the incoming radiance without the targeted trace gas absorption I_0 to the incoming radiance including trace gas absorption I, i.e., $\tau = \ln(I_0/I)$. Similar to trace gas detection with filter-based SO_2 cameras, IFPICS relies on recording spatial distributions of trace gas optical densities in two (or more) wavelength channels (obtained by tuning the FPI transmission spectrum). This concept is illustrated in Figure 1 for the trace gases BrO, HCHO, and SO_2. First, in an on-band channel "A" the transmission maxima of the FPI are tuned (by tilting the FPI element) to the absorption maxima of the target gas. The optical density τ_A is recorded when the FPI transmission exhibits maximum correlation with the narrowband absorption structure of the target trace gas (e.g., the vibrionic bands in the UV for SO_2 and BrO). Then, τ_A is compared to the optical density τ_B, recorded in an off-band channel "B," when the FPI transmission maxima are slightly tuned (shifted around 1–2 nm by tilting the FPI element) to coincide with the absorption minima of the target gas. In this setting, the FPI transmission anti-correlates with the absorption structure of the

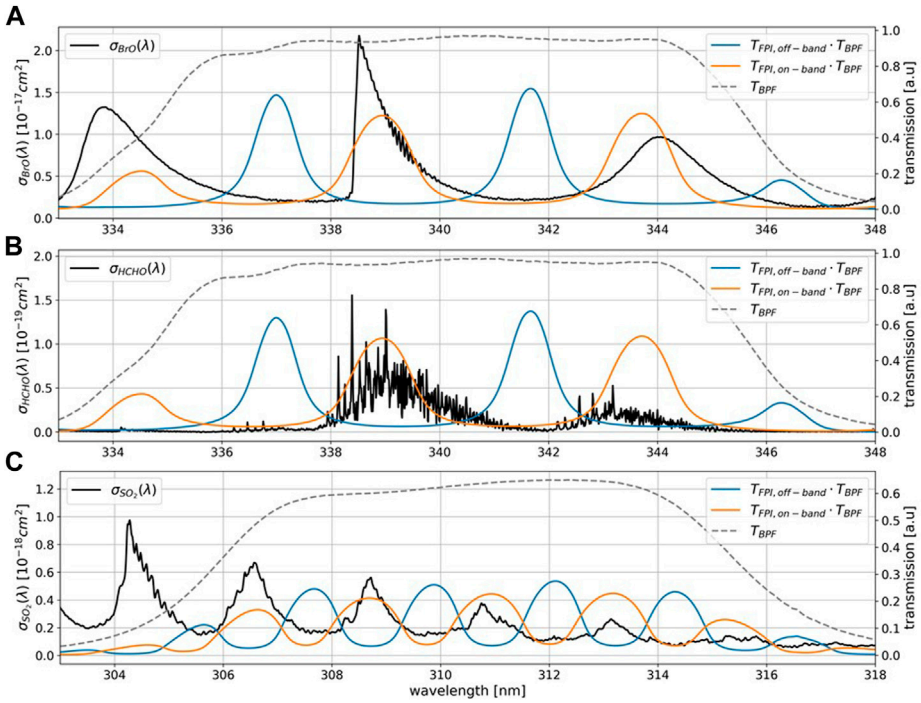

FIGURE 1
Trace gas detection principle of the IFPICS technique for BrO **(A)**, HCHO **(B)** and SO_2 **(C)**. The absorption cross sections σ_{BrO}, σ_{HCHO}, and σ_{SO2} of the trace gases are marked in black. The dashed line corresponds to the transmission curve of the broadband bandpass filter T_{BPF} with a central wavelength of 340 nm for BrO and HCHO and 310 nm for SO_2. The colored lines correspond to the FPI transmission spectrum T_{FPI} multiplied with the bandpass filter transmission in on-band position A (orange) and off-band position B (blue).

TABLE 1 Instrumental and optical parameters of both camera systems with uncertainties.

Parameter	SO_2 camera	BrO camera	Description
d [μm]	21.684 ± 0.002	12.366 ± 0.002	FPI mirror separation
R	0.65	0.70	FPI reflectivity
F	7.15	8.54	FPI finesse
n	1.00029	1.00029	Refractive index (air)
α_A [°]	8.35 ± 0.02	9.45 ± 0.02	FPI tilt, on-band
α_B [°]	6.80 ± 0.02	6.07 ± 0.02	FPI tilt, off-band
$T_{BPF,max}$	0.63	0.85	BPF peak transmission
λ_{BPF} [nm]	310.5	340.4	BPF central wavelength
δ_{BPF} [nm]	9.0	10.0	BPF FWHM
f [mm]	47 ± 2	47 ± 2	Lens system 1 focal length
a [mm]	1.60 ± 0.05	1.10 ± 0.05	Aperture diameter
Θ_{FOV} [°]	17	17	Imaging FOV

target trace gas. Differential evaluation (equivalent to rationing) of both channels yields the so-called apparent absorbance (AA). The AA is a quantity proportional to the target trace gas CD S. The instrument sensitivity k is determined by the difference of the mean weighted absorption cross sections $\bar{\sigma}_A$ and $\bar{\sigma}_B$ of the two wavelength channels, respectively:

$$AA = \tau_A - \tau_B = \ln\left(\frac{I_{A,0} I_B}{I_A I_{B,0}}\right) = (\bar{\sigma}_A - \bar{\sigma}_B) \cdot S = k \cdot S \quad (1)$$

Here I_A and I_B describe the incoming radiances with the target trace gas in the light path and $I_{A,0}$, $I_{B,0}$ the background radiances without the target trace gas absorption (i.e., pixels within the FOV that do not cover the volcanic plume). Matching of the transmission curve of the FPI to the periodicity of the target molecule is accomplished by choosing appropriate physical FPI parameters, i.e., choosing the mirror separation and the finesse (given essentially by the mirror reflectivity) of the FPI. An assessment of the signal to noise ratio gives an optimal finesse for the FPI (Kuhn et al., 2014). The two FPI positions (A, B, see above) are achieved by altering the angle of incidence on the FPI (α_A, α_B), in our case by about 3° for BrO and 1° for SO_2 (see Table 1). Additionally, a bandpass filter (BPF) is used to select the wavelength range (typically around 10 nm width) with high correlation between FPI transmission and absorption spectrum and low cross interferences. The choice of the FPI instrument parameters and wavelength windows is based on simulations by Kuhn et al., 2019.

The optical density of the individual spectral channels is not only sensitive to the absorption of the target trace gas, but also to extinctions resulting from scattering by aerosols and clouds, or by absorption of other trace gases. However, due to the small spectral shift (1–2 nm) of the FPI transmission between channels

A and B, broadband influences essentially cancel out in the evaluation. Furthermore, the selectivity achieved by the matched transmission spectrum of the FPI minimizes interferences with other trace gases absorbing in the same wavelength region.

2.2 The IFPICS instruments

The two IFPICS instruments (for BrO and SO_2, respectively, based on the design by Fuchs et al., 2021) used in this study are prototypes optimized for harsh environmental conditions and easy handling with compact dimensions of 200 mm × 350 mm × 130 mm, low weight of approximately 5 kg and a low power consumption (<10 W). The BrO and the SO_2 cameras are of the same design except for different FPIs and band-pass filters (see Section 2.1). The wavelength range for the SO_2 camera is (310 ± 5) nm and for the BrO camera (340 ± 5) nm. All instrumental parameters are summarized in Table 1.

Several improvements compared to the design of Fuchs et al., 2021 are introduced. 1) A major difference is the addition of a second optics next to the IFPICS optics to include a coaligned DOAS instrument with a narrow field of view (FOV) of 0.5° which is inside the FOV of the IFPICS instrument. It allows for a real-time SO_2 DOAS evaluation (see Luebcke et al., 2013) to trace the volcanic plume and to validate the model calibration (see Section 2.3). 2) We use a temperature-stabilized CMOS sensor (pco.edge bi 4.2 UV provided by Excelitas PCO GmbH) with a spatial resolution of 2048 × 2048 pixels. It allows for a time optimized acquisition of images, which results in a time resolution of ca. 2 Hz (BrO camera) and ca. 0.5 Hz (SO_2 camera). 3) The SO_2 camera BPF in Fuchs et al., 2021 was inclined by about 10° towards the optical axis. In the new SO_2 camera setup the filter was used without inclination. The operating wavelength range is thereby shifted by 2 nm towards higher wavelength, resulting in a more linear instrument response and higher photon yield. 4) The instrument software has been revised and optimized for field measurements.

The imaging optics are implemented as image side telecentric optics, with approximately uniform incidence angles of the incoming radiation on the FPI. This ensures that each pixel of the detector sees the same transmission spectrum on the FPI for the entire FOV. A detailed description of the instrument optics can be found in Fuchs et al., 2021. In principle, other optical setups are possible as discussed in Kuhn et al., 2014. Both cameras have a FOV of 17°. The spatial resolution for a given trace gas detection limit is limited by the FPI aperture size (Kuhn et al., 2019). The circular shape of the image aperture causes a circular image on the square detector area. In addition, the magnification of this image on the detector can be adjusted by the imaging optics and allows to shrink the imaging FOV to a reduced sensor area for low light conditions.

2.3 The instrument model

In order to convert the AA (see Eq. 1) into the trace gas CD S, we use the IFPICS instrument model as described in Fuchs et al., 2021. The model calculates the spectral instrument transmission, based on the FPI parameters and BPFs used in the camera setups. The radiances $I_0(\lambda)$ are taken from a solar atlas spectrum (Chance & Kurucz 2010) and are scaled with λ^{-4} to approximate a Rayleigh scattering atmosphere. Moreover, stratospheric O_3 absorption is included, as it governs the UV radiance that reaches Earth's surface at lower UV wavelengths, which particularly effects the SO_2 measurement. The absorption cross sections of O_3, SO_2, HCHO, and BrO are obtained from Serdyuchenko et al., 2014, Bogumil et al., 2003, Chance & Orphal 2011 and Fleischmann et al., 2004, respectively.

In order to determine the FPI tilt angles α_A and α_B (see Table 1), we calculate the integrated radiances $I_{FPI}(\alpha)$ containing the target trace gas absorption and the radiances $I_{0,FPI}(\alpha)$ without target trace gas absorption as a function of the incidence angle α (i.e., an interferogram). The progression of τ_{FPI} under variation of the incidence angle α of incoming radiation represents the shift of the FPI transmission across the trace gas absorption spectrum and allows to find the optimum FPI tilt angles (α_A and α_B) for on-band and off-band measurements, respectively. The modelled interferograms for BrO and HCHO are displayed in Figure 2. The optimal tilt angles for a measurement of BrO and HCHO are equal within the scale of the resolution of the stepper motor (0.02°). For optimal tilt angles, a calibration curve is calculated. The incidence angles are kept constant at α_A and α_B and the CD S of the target trace gas is varied, which gives the calibration curve from $AA_{FPI} = k \cdot S$. The instrument sensitivity k is determined by a linear fit for BrO and a polynomial fit for SO_2 of the calibration curve.

3 Results

3.1 Laboratory measurements of HCHO

As described above, we use the similarities of the BrO and HCHO spectral absorption in the instruments' operating wavelength range (335 nm–345 nm, see Figures 1A, B, 2) for the characterization of the BrO camera. HCHO is chemically more stable than BrO and thus easier to handle in the laboratory, e.g., in calibration cells. Thus, HCHO is used as a spectral proxy for BrO in order to characterize the instrument. The HCHO cell was prepared by initially filling a quartz cell with para-formaldehyde (PFA, produced by Sigma-Aldrich with an assay of 95.0%–100.5%), in the form of a white powder. It is then evaporated by heating the cell with a heat gun to form gaseous HCHO. During cooling the gaseous HCHO repolymerizes to PFA and settles on the walls of the gas cell. This leads to a gradually decreasing HCHO signal during the course of the experiment (e.g., shown with the various colors in Figure 3).

The instrument model (see Section 2.3; Figure 2) confirms that both gases can be detected with equal FPI instrument parameters. The modeled optimal angles α_A and α_B for the on- and off-band FPI setting (A, B) can be validated by recording an interferogram (the transmitted intensity for a continuous sequence of FPI tilt angles) of a HCHO gas cell. Such an interferogram of a HCHO gas cell where scattered skylight is used as a light source is presented in Figure 3. Here the mean value of the optical density τ within the gas cell is plotted as a function of the angle of incidence α of the collimated light beam on the FPI. The interferogram is recorded with a resolution of 0.2° in a range between 4° and 11.2°. This range is chosen as a trade-off between the effective finesse decrease for higher

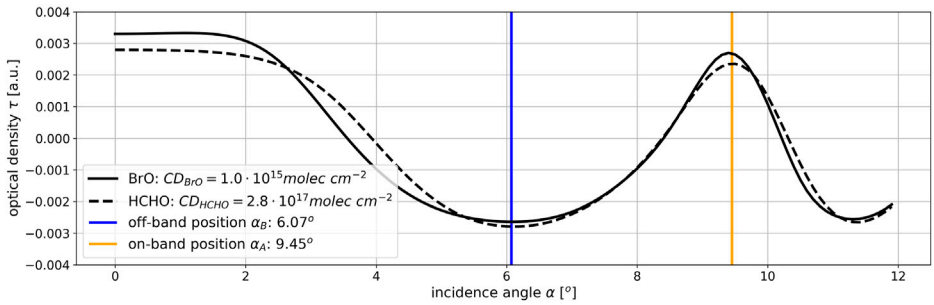

FIGURE 2
Modelled interferograms for BrO (CD_{BrO} = 1.0 × 10^{15} molec cm^{-2}) and HCHO (CD_{HCHO} = 2.8 × 10^{17} molec cm^{-2}). The BrO CD is chosen as atypical value for volcanic plumes and the HCHO CD is scaled according to have a similar absorption signal. The vertical lines show the on-band (orange line) and off-band (blue line) measurement angles for the BrO measurement. On-band and off-band measurement angles for BrO and HCHO are almost identical in the spectral region of the used bandpass filter.

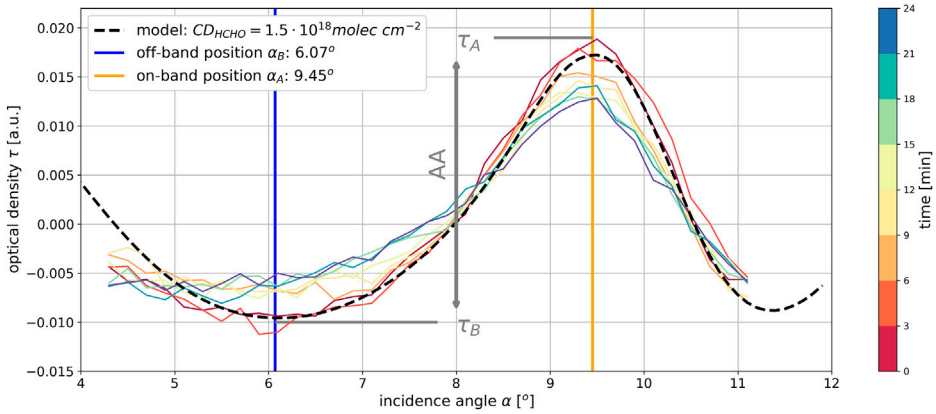

FIGURE 3
IFPICS interferogram of a HCHO gas cell, i.e., the optical density τ as a function of the FPI incidence (tilt) angle α, where the color scale indicates the time after initial heating of the HCHO gas cell. Since the gaseous HCHO repolymerizes to PFA during gas cell cooling, a decrease in AA signal (difference between τ_A and τ_B, see Section 2.3) is observed, which is indicated by the different colored lines. Black dashed line: model simulation for a HCHO CD of 1.5 × 10^{18} molec cm^{-2}. The measurement and the model simulation are normalized to their respective mean value. The vertical lines show the chosen on-band position α_A of 9.45° (orange) and off-band position α_B of 6.07° (blue) obtained from the comparison of measurement and model simulation.

FPI incidence angles and to avoid disturbing reflections for incidence angles lower than 4° inside the instrument optics on the detector (Fuchs et al., 2021). The results shown in Figure 3 yield the optimal angles α_A and α_B to achieve ideal on-band and off-band positions and show excellent agreement between the measurement and our model (dashed black line in Figure 3). The following FPI tilt angles optimizing the measurement of HCHO and BrO were used: an on-band position (A) of α_A = 9.45° and an off-band position (B) of α_B = 6.07°. The difference between minimum (τ_B) and maximum (τ_A) in this graph (vertical grey line) represents the AA, which is around 0.025. This is converted *via* a modelled calibration curve into a HCHO CD of 1.5 x 10^{18} molec cm^{-2}. The corresponding model interferogram is shown as the black dashed line in Figure 3. To illustrate the applicability of the IFPICS technique to imaging measurements of BrO, we show a measurement of two HCHO gas cells using scattered skylight as a light source in Figure 4A). The measurement is calibrated with a co-aligned narrow-FOV DOAS measurement, measuring the HCHO CD inside the smaller gas cell (see Figure 4B). The CD gained by the DOAS measurements is plotted as a function of IFPICS AA and fitted with a linear function, yielding a calibration curve for HCHO CDs. The measurement shows a nearly linear trend with increasing CD of the HCHO gas cells, but a deviation of approximately 17% to the model prediction for high HCHO optical densities is observed. Possible reasons are systematical errors in the DOAS evaluation due to the high HCHO optical densities, reflections at the cell (e.g., influencing the light path inside the cell), slight misalignments of the DOAS telescope optics and small errors introduced by the temperature dependence of the HCHO cross-section.

Instrument characterization measurements (such as the absolute calibration of the motor angle) are extremely simplified by

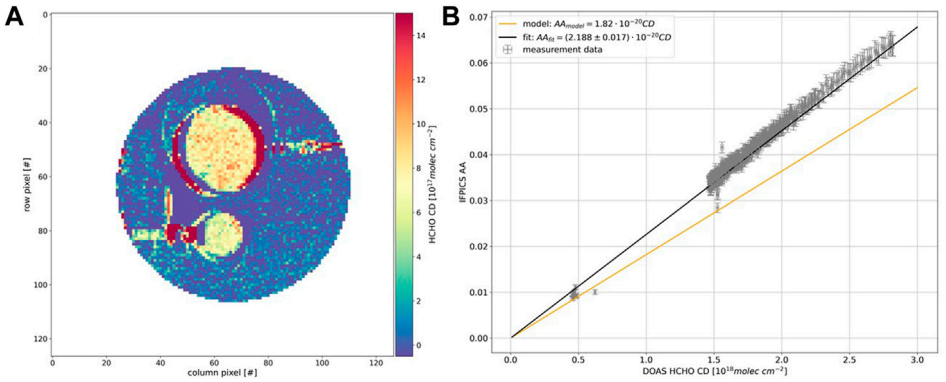

FIGURE 4
(A) Imaging measurement of two HCHO gas cells (Ø 50 mm and Ø 22 mm) with the IFPICS instrument from 19th of September 2020 at 08:03 UTC using scattered skylight as a light source. The measurement has a time resolution of 3 s and 8 × 8 pixel binning has been applied, resulting in an approximate spatial resolution of 80 × 80 pixels. The color scale shows the HCHO CD calibrated with a co-aligned DOAS measurement. **(B)** Calibration curve for the HCHO measurement shown in panel **(A)**. The DOAS instrument measures the CD inside the small gas cell and the DOAS calibration curve (black line) is compared to the model prediction (orange line). The gap between values around 5 × 10^{17} molec cm^{-2} and 1.5 × 10^{18} molec cm^{-2} originates from heating the gas cell, where the low CD measurements are prior to heating of the cell. The deviation between model prediction and measurement calibration is around 17%, possibly caused by errors in the DOAS evaluation, reflections at the cell, or slight misalignment of the DOAS telescope optics.

interferograms recorded with a gas cell with a high amount of the target trace gas (or a spectral tracer gas, like in our case HCHO). We note that the cross-sensitivity of our instrument to HCHO will generally have negligible impact on volcanic BrO measurements, since HCHO levels in volcanic plumes as well as background gradients within a typical instrument FOV are commonly low (typically below 10^{16} molec cm^{-2} corresponding to an optical density of 0.0002, see Figure 4B). Nevertheless, caution is necessary in regions with extensive biomass burning activities or wildfires. The applicability of the IFPICS technique to low differential optical densities (such as the BrO optical density of volcanic plumes, i.e., ca. 10^{-3}) has been shown by theoretical calculations of Kuhn et al., 2019. Furthermore, a more detailed investigation of the BrO camera prototype detection limit is shown in Supplementary Figures S1, S2. These laboratory studies show that gas cells with a high amount of HCHO can be used to characterize the BrO camera for volcanic applications.

3.2 Field campaign at Mt Etna July 2021

In order to test the performance of our instruments in the field we conducted simultaneous IFPICS measurements of BrO and SO_2 at Mt Etna volcano, Italy. The measurements were performed mainly during quiescent degassing periods.

3.2.1 15 July 2021: SO_2 flux measurements

The SO_2 flux measurement presented here was recorded on the 15th of July 2021 at the mountain ridge "Schiena dell'Asino" at a location of 37°42′35″ N 15°01′39″ E [1,900 m above sea level (a.s.l)] between 08:05 and 10:20 UTC. The camera points into a viewing direction of 327° N with an elevation angle of 20° in an approximate distance of 5.3 km to the crater area (see Figure 6B). The wind direction was 102° E with an approximate windspeed of 5 m s^{-1} (see Supplementary Figure S3). Images are taken with 1 s of exposure time, leading to a total image acquisition time for two consecutive images (with FPI setting A and B) of 2.3 s, because additional 0.3 s are lost due to movement of the stepper motor (tilting the FPI between on- and off-band position) and data acquisition.

The here presented SO_2 flux measurements illustrate the development of the SO_2 camera and flux calculations since Fuchs et al., 2021. With similar spatial resolution, higher frame rates (by about a factor of 2) are achieved through developments in the software and a more compatible detector (see Section 2.3). Figure 5A shows an exemplary image of the SO_2 CD inside the volcanic plume during the measurement period. A video of the complete measurement timeseries is included in the Supplementary Material. The SO_2 AA is calibrated using the instrument model (Section 2.3) and assuming an O_3 VCD of (312 ± 10) DU, obtained from TROPOMI satellite measurements (closest available data from the 24th of July 2021, see Geoservice 2022). The model accounts for the variation of the total O_3 column amount in the background spectrum introduced by the changing solar zenith angle (SZA, see also Fuchs et al., 2021). Figure 5B shows the model calibration curve for the beginning and the end of the measurement time series examined here. The calibration is performed dynamically according to actual SZA. The influence of O_3 on the sensitivity is similarly observed for traditional filter-based SO_2 cameras (Kern et al., 2010). But there it can only be corrected by frequent in-field calibration. The AA corresponding to the detection limit has a value 1.4 × 10^{-2} for an SZA of 55°, an integration time of 2.4 s and a spatial resolution of 400 × 400 pixel. We assume that the detection limit is determined by photon shot-noise, i.e., inversely proportional to the square exposure time. This corresponds to photon shot-noise limited detection limit of 4.7 × 10^{17} molec $s^{0.5}$ cm^{-2} normalized to 1 s of exposure time.

In order to calculate the SO_2 flux, the SO_2 CD is integrated along a transect of the plume (Supplementary Figure S4 and black

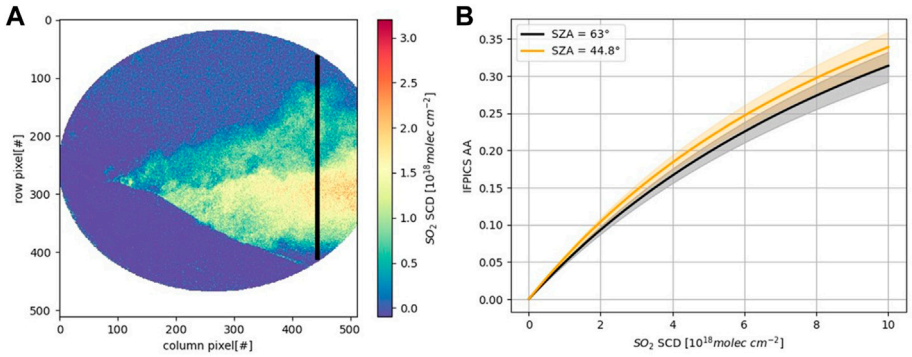

FIGURE 5
(A) SO_2 IFPICS image acquired at the 15th of July at the mountain ridge "Schiena dell'Asino" in an approximate distance of 5.3 km to the crater area. The image has a spatial resolution of 400 × 400 pixels and a time resolution of 2.4 s. The vertical black line shows the line of integration for the SO_2 flux calculation. **(B)** Exemplary model calibration curves of the SO_2 IFPICS instrument. The shaded area marks the model error. The black curve marks the first calibration (SZA = 63°) for the measurement time series and the orange curve the last one (SZA = 44.8°). In between the calibration curve is dynamically adapted according to the SZA.

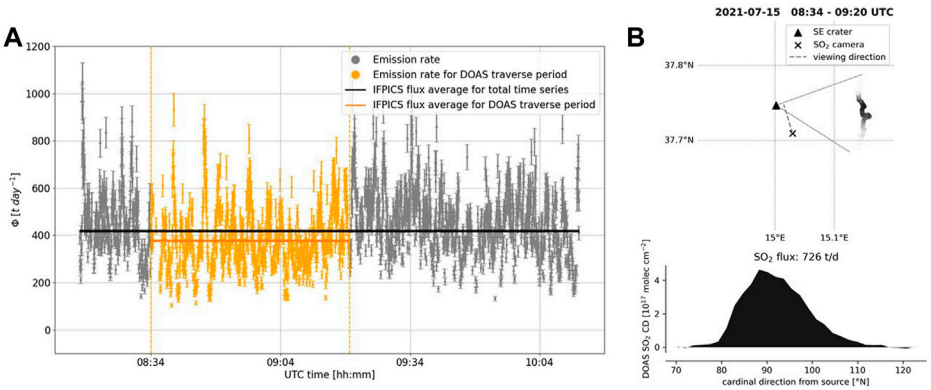

FIGURE 6
SO_2 flux measurements from 15th July 2021 (see Figure 5) **(A)** IFPICS SO_2 flux measured in an approximate distance of 5.3 km to the crater area of Mt Etna between 08:05 and 10:20 UTC. The orange part of the IFPICS data marks the time period of a DOAS car traverse measurement shown in panel **(B)**. The horizontal lines mark the average flux for the complete time series (black, (418 ± 138) t day^{-1}) and for the traverse time [orange, (378 ± 129) t day^{-1})]. **(B)** DOAS car traverse measurement of SO_2 flux between 08:34 and 09:20 UTC. The upper panel shows the location and direction of the plume and the viewing direction of the SO_2 camera. The lower panel shows the SO_2 CD during the plume traverse.

vertical line in Figure 5A and multiplied with the plume propagation velocity along the image plane (see Supplementary Figure S3). The plume's instantaneous propagation velocity (or the effective wind speed) is obtained by evaluating the optical flow field (using the algorithm by Farneback 2000) between two consecutive images at the transect of interest (see, e.g., Gliß et al., 2018). Figure 6A shows the resulting flux time series of the total emission of Mt Etna obtained on the 15th of July 2021 between 08:17 and 10:13 UTC. The mean flux for this timeframe is 418 t day^{-1} with a standard deviation of 138 t day^{-1}. The high frequency natural variability of the SO_2 emission is clearly visible and by far dominates the noise of the individual measurements (which amounts to a relative error of about 10%). The mean flux is compared to a DOAS car traverse measurement which was recorded during the IFPICS measurement timeseries between 08:34 and 09:20 UTC (see Figure 6B). This time period is marked by orange color in Figure 6A. The volcanic SO_2 emission flux determined by the DOAS car traverse is 726 t day^{-1}. It was calculated using the average plume propagation velocity obtained by the IFPICS measurement during the traverse period. The deviation by almost a factor of two is likely to be introduced by the following effects: 1) The SO_2 camera measurement during that time only captured a part of the plume (a rather small but unknown part was masked by topography). 2) Radiative transfer effects, in particular light dilution (e.g., Kern et al., 2009; Campion et al., 2015) are not accounted for in our evaluations. As the SO_2 camera is further away from the plume (5.3 km) and operates at lower wavelength than the DOAS, this could partially account for the observed deviation. 3) The DOAS car traverse was recorded during a

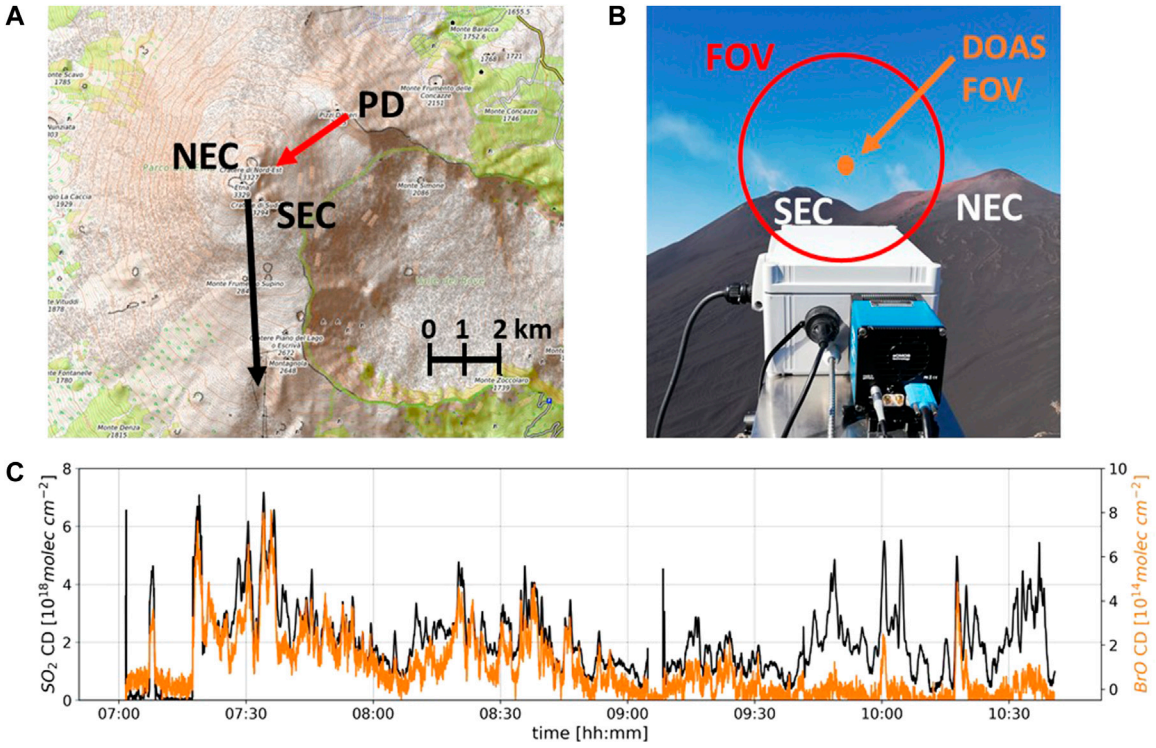

FIGURE 7
(A) Topographic map (OpenTopoMap, 2022) of the measurement location from 24th of July 2021, close to the Pizzi Deneri (PD) observatory, showing the viewing direction of the camera (205° SW, red arrow) and the plume direction (178° S, black arrow). Additionally, the South Eastern crater (SEC) and the North Eastern crater (NEC) of Mt Etna are marked. The measurement location has an approximate distance of 2.5 km to the crater area. **(B)** Image of the BrO camera with SEC and NEC in the background. The red circle marks the FOV of the camera. The plume is faintly visible between the two craters. The DOAS FOV is marked with an orange circle and it points directly into the plume. **(C)** Time series of the DOAS measurement (location marked with orange circle in panel B). The black line (left *y*-axis) shows the SO_2 CD and the orange line (right *y*-axis) the BrO CD between 07:00—10:30 UTC. BrO and SO_2 CDs are correlated up to approximately 10:45 UTC, when the plume shows a stronger condensation and also clouds start to form inside the plume.

rather long time (almost 30 min within the plume). During that time the plume might have slightly moved (e.g., meandering) in driving direction, which might have increased the apparent plume size.

3.2.2 24 July 2021: BrO and SO_2 measurements

For the BrO measurement we present a measurement from the 24th of July 2021 between 07:38 and 08:24 UTC which was recorded close to the Osservatorio Vulcanologico Pizzi Deneri at a location of 37°45′48″ N and 15°01′12″ E (ca. 2,800 m a.s.l., see Figure 7). The SO_2 and the BrO cameras were pointed towards the crater area at an approximate distance of 2.5 km. The centers of the FOVs were aligned in a direction of 205° SW with an elevation angle of 18° for the BrO camera and 15° for the SO_2 camera. The wind direction was 178° S with a wind speed of approximately 6 m s^{-1} (IFPICS optical flow retrieval, see Section 3.2.1). Measurements were performed nearly simultaneously with an exposure time of 0.3 s per image for the BrO camera and 1 s per image for the SO_2-camera. The integration time difference originates from the different skylight radiance in the respective operating wavelength ranges. A narrow-FOV DOAS measurement was performed simultaneously in the FOV of the BrO camera (see Figure 7B).

3.2.2.1 BrO detection

In order to reduce photon shot noise up to an AA of 10^{-3}, which corresponds to a detection limit of ca. 1×10^{14} molec cm^{-2}, 10 consecutively recorded measurement images are co-added and a spatial binning of 8×8 pixels is applied resulting in a temporal resolution of 10 s and a spatial resolution of approximately 200×200 pixels with a size of 3.7×3.7 m^2 per pixel at the distance of the plume (2.5 km). A detailed investigation of the detection limit of the BrO camera is shown in Supplementary Figures S1, S2. The narrow-FOV DOAS time series (Figure 7C) shows BrO column densities that range up to 1×10^{15} molec cm^{-2}, this corresponds to an approximate signal to noise ratio (SNR) of 10. Figure 8A shows an exemplary image of the BrO CD inside the volcanic plume. In fact, the plume is clearly distinguishable from the atmospheric background and the crater flank from the southeast crater of Mt Etna (see Figure 8B). The image is calibrated using the narrow-FOV DOAS measurement within the FOV of the camera (see Luebcke et al., 2013; Sihler et al., 2017), which is shown in Figure 9. Fitting of the calibration curve is performed with an orthogonal distance regression method (Boggs & Rogers 1990) from the SciPy python library (Virtanen et al., 2020), which considers errors in x-and *y*-direction. The DOAS calibration curve (black line in Figure 9)

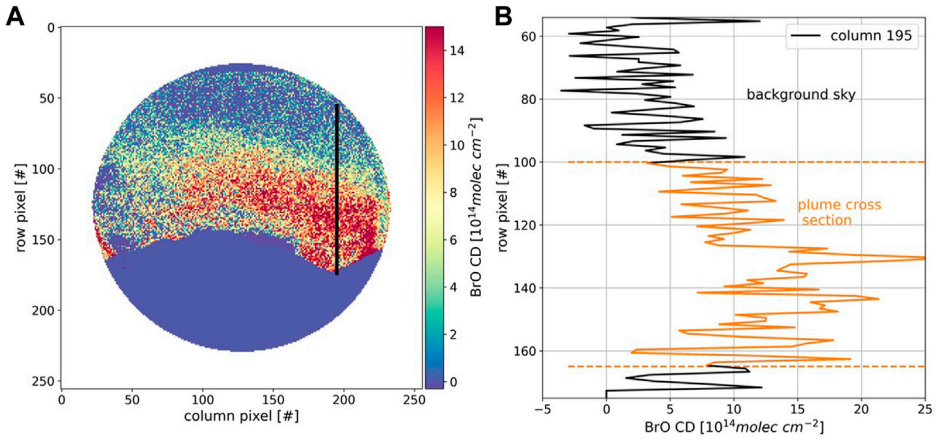

FIGURE 8
(A) BrO CD measured with the IFPICS prototype instrument and calibrated with the linear part of the narrow-FOV DOAS measurement (see Figure 7B and Figure 9). The image has a spatial resolution of 200 × 200 pixels and a time resolution of 10 s. The area of the crater flank is masked and set to zero to enhance the contrast between sky, plume and the crater flank. **(B)** Exemplary plot of column 195 [indicated as black line in **(A)**] from image. The volcanic plume signal (between row 100 and 165) in the range of 1.2 × 10^{15} molec cm^{-2} is clearly distinguishable from the background.

gives a slope of k_{IFPICS} = (5.50 ± 0.85) × 10^{-18} cm^2 $molec^{-1}$ which is in good agreement with the model prediction of k_{model} = 5.288 × 10^{-18} cm^2 $molec^{-1}$ (orange line in Figure 9). While the slope represents the expected BrO sensitivity of the instrument, we observe an apparently constant offset between the BrO CD determined by DOAS and that determined by the IFPICS technique (i.e., the BrO camera). Since the background sky is set to zero BrO by subtracting a mean value of the plume-free sky background in the IFPICS evaluation it is very likely that the effect causing the offset is due to some kind of interference within the volcanic plume (Supplementary Figure S2 shows that the background sky has a flat distribution on the order of 10^{-3}). This interference could be due to 1) unrecognized trace gases or 2) radiation transport effects. The influence of possible cross interferences of other gaseous absorbers was thoroughly studied by Kuhn et al., 2019 and are not plausible on the observed scale (extremely high HCHO levels can be ruled out on the basis of data from the narrow-FOV DOAS). However, since the plume was slightly condensed (visible but not opaque, Figure 7B) the offset could be due to radiative transfer changes introduced by the plume, i.e., scattering at plume aerosol leads to significant different atmospheric light paths for the plume and the background sky. The influence of light path enhancement (or shortening) on the measured CD is the same for IFPICS and DOAS. Differences in inelastic scattering effects (Grainger & Ring 1962) between plume and background sky are accounted for by the DOAS measurement (by the well-known procedure of adding a pseudo "Ring" absorber to the fit). However, they are presently ignored by the evaluation procedure of the IFPICS technique. This limitation restricts measurements with the present BrO camera prototype to aerosol-free plumes and demands further studies that quantify influences such as the differential Ring effect (Grainger & Ring 1962) between plume and background sky for the IFPICS technique. Nevertheless, the detection limit of the BrO camera (for aerosol-free conditions) can be estimated by the investigation of the 1-σ-pixel-pixel standard deviation in a plume free region of the background sky. This analysis was performed for a range of temporal (1 s–100 s) and spatial (no binning—32 × 32 pixel binning) binning parameters to optimize the trade-off between temporal and spatial resolution and the necessary reduction in photon shot-noise (see Supplementary Figure S1). For a spatial resolution of ca. 200 × 200 pixels (8 × 8 binning) and 10 s integration time the 1-σ-pixel-pixel standard deviation of the AA within the background sky is 1.5 × 10^{-3}. According to the calibration, this corresponds to a BrO CD of 2.8 × 10^{14} molec cm^{-2}. Consequently, the detection limit normalized to 1 s exposure is 8.9 × 10^{14} molec $s^{0.5}$ cm^{-2}, which closely matches the theoretical prediction of Kuhn et al., 2019.

3.2.2.2 BrO/SO_2 ratio

The BrO/SO_2 ratio is commonly observed in many volcanic plumes, for instance by the NOVAC network (e.g., Luebcke et al., 2014; Dinger et al., 2021). Since SO_2 can serve as a quasi-conservative tracer for dilution this ratio can give important insights in plume chemistry (von Glasow et al., 2009) but can be also related to volcanic activity (e.g., Warnach et al., 2019). Imaging measurements of this ratio can help to understand the complex chemical conversion mechanism within early plume stages, which is so far not well understood (see, e.g., Kuhn et al., 2022).

The BrO/SO_2 ratio inside the plume determined with the IFPICS measurements is compared to the narrow-FOV DOAS measurement inside the cameras FOV. Figure 10 shows a comparison of the BrO and SO_2 camera images. Both images are scaled to the same resolution and tailored to share approximately the same FOV. Despite the lower SNR of the BrO image (Figure 10A), the outline of the plume is well matched to the SO_2 image (Figure 10B). Furthermore, the instruments operate at different time resolutions. To account for this effect, the BrO and SO_2 time series from the DOAS measurement are individually compared to the respective IFPICS signals to obtain the FOV of the DOAS instrument within the IFPICS FOV(Sihler et al., 2017).

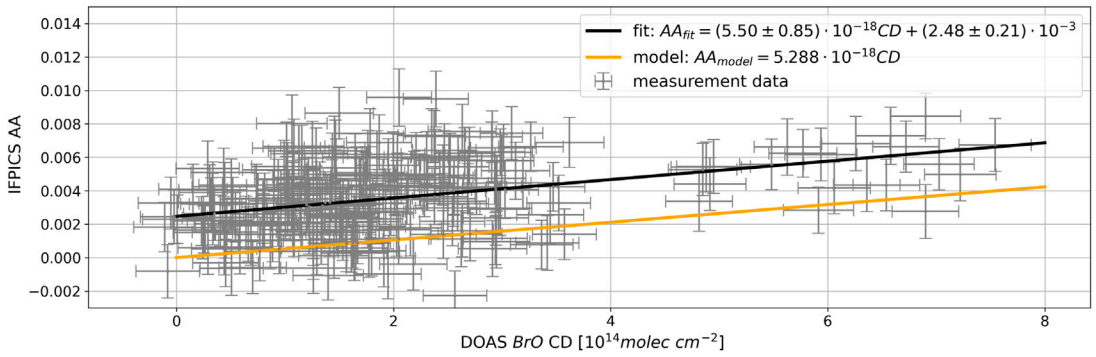

FIGURE 9
Calibration curve of the BrO measurement on the 24th of July 2021 between 07:38 and 08:24 UTC. The IFPICS AA inside the FOV of the narrow FOV DOAS is plotted against the BrO CD density obtained from the DOAS measurement. A linear fit (solid black line) gives the calibration curve of the BrO camera. The solid orange line shows the IFPICS model prediction.

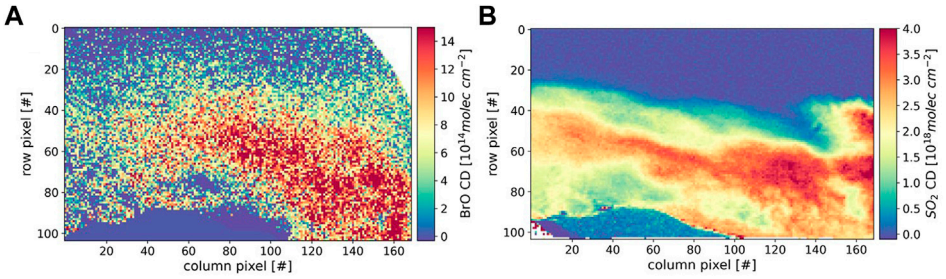

FIGURE 10
Cutout of BrO and SO_2 images acquired at the 24th of July with the IFPICS instruments. The plume originating from the Bocca Nuova crater moves from right to left through the image above the south eastern crater of Mt Etna. Panel **(A)** shows the BrO camera image and panel **(B)** the SO_2 camera image. The images are cutout to show the same FOV and scaled to have a similar temporal (10 s) and spatial resolution (104 × 169 pixels).

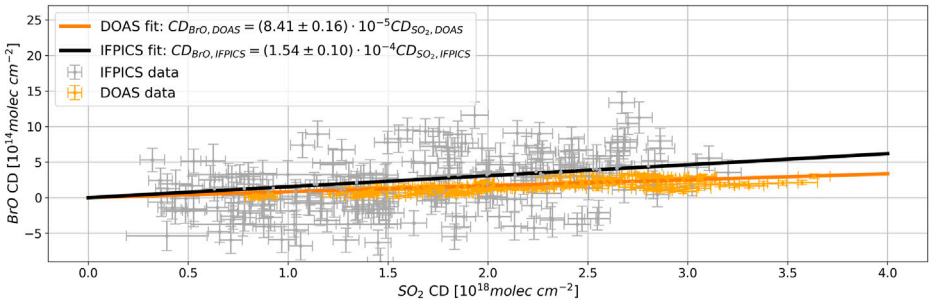

FIGURE 11
BrO/SO_2 ratio calculated from both instruments for the time period between 07:38 and 08:24 UTC. The pixels compared correspond to the FOV of the infield DOAS. The orange points show the infield DOAS measurement fitted with a linear function (solid orange line). The grey points mark the IFPICS measurement evaluated in the infield DOAS FOV also fitted with a linear function (black solid line).

The resulting BrO and SO_2 column densities at the IFPICS pixels corresponding to the DOAS FOV are calibrated with the IFPICS instrument model, interpolated to the time resolution of the BrO measurement and plotted in a scatter plot to retrieve the BrO/SO_2 ratio seen by the IFPICS instruments. In the calibration the offset in the BrO IFPICS data is subtracted (see Figure 9). The result is shown in Figure 11 (grey dots) and fitted with a linear function (solid black line) resulting in a BrO/SO_2 ratio of (8.41 ± 0.16) x 10^{-5} with a correlation coefficient of R = 0.37. This ratio is compared to the DOAS measurement of the BrO/SO_2 ratio (orange color in

Figure 11) which gives a value of $(1.54 \pm 0.10) \times 10^{-4}$ with a correlation coefficient of R = 0.90. The error of the slope is given as the standard deviation of the estimate. The values have a factor of 1.5 difference probably due to uncertainties in the alignment of the FOVs, the DOAS FOV retrieval and interpolation to account for different time resolutions. Nevertheless, the retrieved BrO/SO_2 ratio is comparable to previous measurements at Mt Etna (e.g., Bobrowski & Platt 2007). Future studies should also allow for two-dimensional BrO/SO_2 ratios, by improving the alignment of the FOVs of the IFPICS instruments under field conditions and optimization of the image evaluation.

4 Discussion and conclusion

Imaging of weakly absorbing trace gases in the atmosphere remains a challenging task. In this work, we showed that the IFPICS technique enables imaging remote sensing measurements of volcanic plume constituents other than SO_2. Imaging measurements of HCHO gas cells excellently matched the model predictions and first attempts to measure weak absorbers like BrO in the field showed promising results.

The determined detection limit of 2.8×10^{14} molec cm^{-2} for an exposure time of 10 s (corresponding to a differential optical density of approximately 1.5×10^{-3} for 10 s exposure time, two orders of magnitude smaller compared to common SO_2 measurements) is in good accordance with the performance expected from theoretical calculations (Kuhn et al., 2019). Moreover, field data of the IFPICS BrO AA confirm the modeled sensitivity when compared with DOAS measurements. However, for the presented measurement, we still observe a seemingly constant offset between the BrO data retrieved with DOAS and IFPICS, respectively. This offset is likely to indicate disturbing influences rooted in light path differences between (condensed) plume and blue sky background. In particular, the influence of, for instance, the differential Ring effect between plume and background sky needs to be investigated in future studies and might be reduced by adding additional wavelength channels. In the present state, the IFPICS BrO camera should only be applied to aerosol-free volcanic emissions.

We present advances in SO_2 flux measurements with the IFPICS technique. The flux difference found between DOAS car traverse measurement and the SO_2 camera in the presented example can be explained by not covering the whole plume in the camera FOV, radiative transfer effects and plume movements during the traverse measurement. The drastically enhanced SO_2 selectivity of the IFPICS technique in comparison to filter-based SO_2 cameras and the high temporal resolution compared to DOAS measurements demonstrate the possibility to study the variability of the SO_2 emission flux on short timescales with high accuracy and enables the use of the technique for weak emitters.

In addition, parallel SO_2 and BrO images recorded at Mt Etna are evaluated to give a value of $(8.41 \pm 0.16) \times 10^{-5}$ on the BrO/SO_2 ratio. The factor of 1.5 difference compared to the DOAS measurement might be due to inelastic scattering effects (Grainger & Ring 1962) between plume and background sky which are accounted for by the DOAS measurement but not yet in the IFPICS measurement (causing a BrO offset), uncertainties in calibration of both instruments and also imperfect alignment of the two IFPICS instruments. Improvements in the individual measurements of BrO and SO_2, better alignment and extended studies of inelastic scattering will also be reflected in the ratio of both gases.

In following up measurements of this type there is a great potential to study the distribution of both species within volcanic plumes and thus allowing detailed studies of the combined effects of mixing (of ambient air and thus O_3 and hydrogen radicals into the plume) and chemistry (e.g., the formation of BrO by the bromine explosion mechanism and the destruction of O_3). Future studies will also include two-dimensional BrO/SO_2 ratios.

Similarities between the absorption features of HCHO and BrO in the UV around 340 nm limit the measurement to low backgrounds of the respective interfering species, but also allows to use HCHO measurements as a proxy for BrO in volcanic plumes, because it is easier to handle under laboratory conditions. Imaging of BrO distributions can be useful to study processes in other environments, e.g., the polar boundary layer or above salt lakes. In turn, the IFPICS BrO could be used to quantify higher HCHO amounts (e.g., wildfires) in low BrO environments.

Furthermore, several other trace gases which show nearly periodic patterns in their absorption cross section will be detectable with the IFPICS technology, for example, nitrogen dioxide (NO_2), chlorine dioxide (OClO) or iodine oxide (IO).

Data availability statement

The raw data supporting the conclusion of this article will be made available by the authors, without undue reservation.

Author contributions

JK, NB, and UP developed the research question. AN, JH, CF, JK, and NB conducted the field campaign. CF designed and constructed the instrument. AN and JH characterized the instruments. AN evaluated the data, and wrote the manuscript, with all authors contributing by revising it within several iterations.

Funding

Support from the Deutsche Forschungsgemeinschaft (project DFG PL 193/23-1) and Terrestrial and Magmatic Systems (TeMaS - collaborative effort of the Universities of Mainz, Heidelberg and Frankfurt) is gratefully acknowledged.

Acknowledgments

We would like to thank SLS Optics Ltd. for sharing their expertise in designing and manufacturing the etalons.

Conflict of interest

The authors declare that the research was conducted in the absence of any commercial or financial relationships that could be construed as a potential conflict of interest.

Publisher's note

All claims expressed in this article are solely those of the authors and do not necessarily represent those of their affiliated organizations, or those of the publisher, the editors and the reviewers. Any product that may be evaluated in this article, or claim that may be made by its manufacturer, is not guaranteed or endorsed by the publisher.

Supplementary material

The Supplementary Material for this article can be found online at: https://www.frontiersin.org/articles/10.3389/feart.2023.1063922/full#supplementary-material

SUPPLEMENTARY FIGURE S1
Plot of the detection limit investigation of the BrO camera showing the 1-σ-pixel-pixel standard deviation of the IFPICS AA σ_{AA} in a plume-free background sky region as a function of the integration time. The right x-axis shows the BrO CD calibrated with the IFPICS model giving the detection limit of the BrO camera.

SUPPLEMENTARY FIGURE S2
Background measurement of the IFPICS BrO camera showing homogeneity of the background sky. **(A)** Image of the measurement conditions from 11 July 2021 at the southern side of Mt Etna at the "Piano Vetore" plateau (position of 37°41′37″ N and 14°58′45″ E). The distance to the crater area is approximately 6.3 km. The red circle marks the FOV of the IFPICS instrument and the black box marks the cutout shown in panel **(B)**. **(B)** IFPICS AA signal of the sky background for an image with a spatial resolution of 200 × 200 pixels and a time resolution of 10 s. **(C)** Exemplary plot of row 20, showing that the variation in the IFPICS AA is on the order of 10^{-3}.

SUPPLEMENTARY FIGURE S3
Plume propagation velocity vplume retrieved from the optical flow calculation between two consecutive SO_2 camera images for the time series shown in Figure 6A. The windspeed is determined pixelwise at the position of the plume transect (see vertical black line in Figure 5A).

SUPPLEMENTARY FIGURE S4
Integrated transect of the SO_2 CD (SO_2 CD multiplied with the plume cross section σ_{plume}) for the time period of the SO_2 flux measurement in Figure 6A. The orange points denote the measurements during the DOAS car traverse.

References

Barrie, L., Bottenheim, J. W., Schnell, R. C., Crutzen, P. J., and Rasmussen, R. A. (1988). Ozone destruction and photochemical reactions at polar sunrise in the lower Arctic atmosphere. *Nature* 334, 138–141. doi:10.1038/334138a0

Bluth, G., Shannon, J., Watson, I. P. I., and Realmuto, V. (2007). Development of an ultra-violet digital camera for volcanic SO_2 imaging. *J. Volcanol. Geotherm. Res.* 161, 47–56. doi:10.1016/j.jvolgeores.2006.11.004

Bobrowski, N., Hoenninger, G., Galle, B., and Platt, U. (2003). Detection of bromine monoxide in a volcanic plume. *Nature* 423, 273–276. doi:10.1038/nature01625

Bobrowski, N., and Platt, U. (2007). SO_2/BrO ratios studied in five volcanic plumes. *J. Volcanol. Geotherm. Res.* 166, 147–160. doi:10.1016/j.jvolgeores.2007.07.003

Bobrowski, N., von Glasow, R., Aiuppa, A., Inguaggiato, S., Louban, I., Ibrahim, O. W., et al. (2007). Reactive halogen chemistry in volcanic plumes. *JGR Atmos.* 112, D06311. doi:10.1029/2006jd007206

Boggs, J., and Rogers, J. (1990). "Orthogonal distance regression," in *Contemporary mathematics*, 186. s.l.:s.n., p.

Bogumil, K., Orphal, J., Homann, T., Voigt, S., Spietz, P., Fleischmann, O., et al. (2003). Measurements of molecular absorption spectra with the SCIAMACHY pre-flight model: Instrument characterization and reference data for atmospheric remote-sensing in the 230–2380 nm region. *J. Photochem. Photobiol. A Chem.* 157, 167–184. doi:10.1016/s1010-6030(03)00062-5

Campion, R., Delgado-Granados, H., and Mori, T. (2015). Image-based correction of the light dilution effect for SO_2 camera measurements. *J. Volcanol. Geotherm. Res.* 300, 48–57. doi:10.1016/j.jvolgeores.2015.01.004

Chance, K., and Kurucz, R. (2010). An improved high-resolution solar reference spectrum for earth's atmosphere measurements in the ultraviolet, visible, and near infrared. *J. Quantitative Spectrosc. Radiat. Transf.* 111, 1289–1295. doi:10.1016/j.jqsrt.2010.01.036

Chance, K., and Orphal, J. (2011). Revised ultraviolet absorption cross sections of H_2CO for the HITRAN database. *J. Quantitative Spectrosc. Radiat. Transf.* 112, 1509–1510. doi:10.1016/j.jqsrt.2011.02.002

Dinger, F., Kleinbek, T., Dörner, S., Bobrowski, N., Platt, U., Wagner, T., et al. (2021). SO_2 and BrO emissions of Masaya volcano from 2014 to 2020. *Atmos. Chem. Phys.* 21, 9367–9404. doi:10.5194/acp-21-9367-2021

Farneback, G. (2000). *Fast and accurate motion estimation using orientation tensors and parametric motion models*. s.l., s.n. 135–139.

Fleischmann, O., Hartmann, M., Burrows, J., and Orphal, J. (2004). New ultraviolet absorption cross-sections of BrO at atmospheric temperatures measured by time-windowing Fourier transform spectroscopy. *J. Photochem. Photobiol.* 168, 117–132. doi:10.1016/j.jphotochem.2004.03.026

Fuchs, C., Kuhn, J., Bobrowski, N., and Platt, U. (2021). Quantitative imaging of volcanic SO_2 plumes using Fabry–Pérot interferometer correlation spectroscopy. *Atmos. Meas. Tech.* 14, 295–307. doi:10.5194/amt-14-295-2021

Geoservice, E. (2022). Sentinel-5P TROPOMI L3 daily composites - EOC geoservices. [Online] Available at: https://geoservice.dlr.de/web/maps/s5p:tropomi:l3 (Accessed 10 08 2022).

Gliß, J., Strebel, K., Kylling, A., and Sudbo, A. (2018). Improved optical flow velocity analysis in SO_2 camera images of volcanic plumes – implications for emission-rate retrievals investigated at Mt Etna, Italy and Guallatiri, Chile. *Atmos. Meas. Tech.* 11 (2), 781–801. doi:10.5194/amt-11-781-2018

Grainger, J. F., and Ring, J. (1962). Anomalous fraunhofer line profiles. *Nature* 193, 762. doi:10.1038/193762a0

Kern, C., Deutschmann, T., Vogel, L., Wöhrbach, M., Wagner, T., and Platt, U. (2009). Radiative transfer corrections for accurate spectroscopic measurements of volcanic gas emissions. *Bull. Volcanol.* 72, 233–247. doi:10.1007/s00445-009-0313-7

Kern, C., Kick, F., Lübcke, P., Vogel, L., Wöhrbach, M., and Platt, U. (2010). Theoretical description of functionality, applications, and limitations of SO_2 cameras for remote sensing of volcanic plumes. *Atmos. Meas. Tech.* 3 (3), 733–749. doi:10.5194/amt-3-733-2010

Kuhn, J., Bobrowski, N., Lübcke, P., Vogel, L., and Platt, U. (2014). A Fabry–Perot interferometer-based camera for two-dimensional mapping of SO_2 distributions. *Atmos. Meas. Tech.* 7, 3705–3715. doi:10.5194/amt-7-3705-2014

Kuhn, J., Bobrowski, N., and Platt, U. (2022). The interface between magma and Earth's atmosphere. *Geochem. Geophys. Geosystems* 23 12. doi:10.1029/2022gc010671

Kuhn, J., Platt, U., Bobrowski, N., and Wagner, T. (2019). Towards imaging of atmospheric trace gases using Fabry–Pérot interferometer correlation spectroscopy in the UV and visible spectral range. *Atmos. Meas. Tech.* 12, 735–747. doi:10.5194/amt-12-735-2019

Lohberger, F., Hoenninger, G., and Platt, U. (2004). Ground-based imaging differential optical absorption spectroscopy of atmospheric gases. *Appl. Opt.* 43, 4711–4717. doi:10.1364/ao.43.004711

Louban, I., Bobrowski, N., Rouwet, D., Inguaggiato, S., and Platt, U. (2009). Imaging DOAS for volcanological applications. *Bull. Vulcanology* 71, 753–765. doi:10.1007/s00445-008-0262-6

Luebcke, P., Bobrowski, N., Arellano, S., Galle, B., Garzón, G., Vogel, L., et al. (2014). BrO/SO_2 molar ratios from scanning DOAS measurements in the NOVAC network. *Solid earth.* 5 (1), 409–425.

Luebcke, P., Bobrowski, N., Illing, S., Kern, C., Alvarez Nieves, J. M., Vogel, L., et al. (2013). On the absolute calibration of SO_2 cameras. *Atmos. Meas. Tech.* 6, 677–696. doi:10.5194/amt-6-677-2013

Mori, T., and Burton, M. (2006). The SO_2 camera: A simple, fast and cheap method for ground-based imaging of SO_2 in volcanic plumes. *Geophys. Res. Lett.* 33, L24804. doi:10.1029/2006gl027916

OpenTopoMap (2022). OpenTopoMap. [Online]. Available at: https://opentopomap.org/#map=14/37.74992/15.01702 (Accessed 19 April 2022).

Platt, U., and Bobrowski, N. (2015). "Quantification of volcanic reactive halogen emissions," in *Volcanism and global environmental change*. Editors A. Schmidt, K. Fristad, and L. Elkins-Tanton (Cambridge University Press), 115–132. s.l.

Platt, U., and Lehrer, E. (1997). *Arctic tropospheric ozone chemistry, ARCTOC*. Heidelberg: s.n: Final Report of the EU-Project EV5V-CT93-0318.

Platt, U., and Stutz, J. (2008). *Differential optical absorption spectroscopy* 1 ed. Heidelberg: Springer Berlin. s.l.

Serdyuchenko, A., Gorshelev, V., Weber, M., Chehade, W., and Burrows, J. P. (2014). High spectral resolution ozone absorption cross-sections – Part 2: Temperature dependence. *Atmos. Meas. Tech.* 7, 625–636. doi:10.5194/amt-7-625-2014

Sihler, H., Lübcke, P., Lang, R., Beirle, S., de Graaf, M., Hörmann, C., et al. (2017). In-operation field-of-view retrieval (IFR) for satellite and ground-based DOAS-type instruments applying coincident high-resolution imager data. *Atmos. Meas. Tech.* 10, 881–903. doi:10.5194/amt-10-881-2017

Stutz, J., Ackermann, D., Fast, J. D., and Barrie, L. (2002). Atmospheric reactive chlorine and bromine at the great salt lake, Utah. *Geophys. Res. Lett.* 29 (10), 18-1–18-4. doi:10.1029/2002gl014812

Vance, A., McGonigle, A. J. S., Aiuppa, A., Stith, J. L., Turnbull, K., and von Glasow, R. (2010). Ozone depletion in tropospheric volcanic plumes. *Geophys. Res. Lett.* 37 22. doi:10.1029/2010gl044997

Virtanen, P., Gommers, R., Oliphant, T. E., Haberland, M., Reddy, T., Cournapeau, D., et al. (2020). SciPy 1.0: Fundamental algorithms for scientific computing in Python. *Nat. Methods* 17 (3), 261–272. doi:10.1038/s41592-019-0686-2

von Glasow, R., Bobrowski, N., and Kern, C. (2009). The effects of volcanic eruptions on atmospheric chemistry. *Chem. Geol.* 263 (1 - 4), 131–142. doi:10.1016/j.chemgeo.2008.08.020

Warnach, S., Bobrowski, N., Hidalgo, S., Arellano, S., Sihler, H., Dinger, F., et al. (2019). Variation of the BrO/SO_2 molar ratio in the plume of tungurahua volcano between 2007 and 2017 and its relationship to volcanic activity. *Front. Earth Sci. Vulcanology* 7. doi:10.3389/feart.2019.00132

frontiers | Frontiers in Earth Science

TYPE Original Research
PUBLISHED 20 April 2023
DOI 10.3389/feart.2023.1114001

OPEN ACCESS

EDITED BY
Ryunosuke Kazahaya,
National Institute of Advanced Industrial Science and Technology (AIST), Japan

REVIEWED BY
Taryn Lopez,
University of Alaska Fairbanks, United States
Marco Liuzzo,
National Institute of Geophysics and Volcanology, Italy

*CORRESPONDENCE
Susana Layana,
susana.layana@ckelar.org

RECEIVED 02 December 2022
ACCEPTED 03 April 2023
PUBLISHED 20 April 2023

CITATION
Layana S, Aguilera F, Inostroza M, Tassi F, Wilkes TC, Bredemeyer S, González C, Pering TD and McGonigle AJS (2023), Evolution of the magmatic-hydrothermal system at Lastarria volcano (Northern Chile) between 2006 and 2019: Insights from fluid geochemistry.
Front. Earth Sci. 11:1114001.
doi: 10.3389/feart.2023.1114001

Evolution of the magmatic-hydrothermal system at Lastarria volcano (Northern Chile) between 2006 and 2019: Insights from fluid geochemistry

Susana Layana[1,2,3]*, Felipe Aguilera[1,3,4], Manuel Inostroza[1], Franco Tassi[5], Thomas Charles Wilkes[6], Stefan Bredemeyer[7,8], Cristóbal González[1,2], Tom David Pering[6] and Andrew John Samuel McGonigle[9]

[1]Millennium Institute on Volcanic Risk Research—Ckelar Volcanoes, Antofagasta, Chile, [2]Programa de doctorado en Ciencias mención Geología, Universidad Católica del Norte, Antofagasta, Chile, [3]Centro de Investigación para la Gestión Integrada del Riesgo de Desastres (CIGIDEN), Santiago, Chile, [4]Departamento de Ciencias Geológicas, Universidad Católica del Norte, Antofagasta, Chile, [5]Dipartamento di Scienze della Terra, Università degli Studi di Firenze, Firenze, Italy, [6]Department of Geography, The University of Sheffield, Sheffield, United Kingdom, [7]GEOMAR Helmholtz Centre for Ocean Research Kiel, Kiel, Germany, [8]Helmholtz Centre Potsdam, GFZ German Research Centre for Geosciences, Potsdam, Germany, [9]School of Physics, University of Sydney, Camperdown, NSW, Australia

One of the major problems in the volcanic surveillance is how data from several techniques can be correlated and used to discriminate between possible precursors of volcanic eruptions and changes related to non-eruptive processes. Gas chemical surveys and measurements of SO_2 emission rates performed in the past (2006–2019) at Lastarria volcano in Northern Chile have revealed a persistent increment of magmatic sourced gas emissions since late November 2012, following a 13 years period of intense ground uplift. In this work, we provide new insights into the gas-chemical evolution of Lastarria's fumarolic discharges obtained from direct sampling (2006–2019) and SO_2 emission rates using UV camera and DOAS instruments (2018–2019) and link these to pre-existing information on ground deformation (1998–2016) in order to determine the origin of observed degassing and ground deformation processes. We revise the four mechanisms originally proposed as alternatives by Lopez et al. (Geosphere, 2018, 14 (3), 983–1007) to explain the changes observed in the fluid geochemistry and ground deformation between 2009 and 2012, in order to explain major changes in gas-geochemistry over an extended period between 1998 and 2019. We hypothesize that a continuous sequence of processes explains the evolution in the fluid geochemistry of fumarolic discharges. Two mechanisms are responsible of the changes in the gas composition during the studied period, corresponding to a 1) deep magma chamber (7–15 km depth) pressurized by volatile exsolution (1998–2020), which is responsible of the large-scale deformation; followed by 2) a crystallization-induced degassing (2001–2020) and pressurization of the hydrothermal system (2003-early November 2012), where the former process induced the changes in the gas composition from hydrothermal-dominated to magmatic-dominated, whereas the last produced the small-scale deformation at Lastarria volcano. The changes in the gas composition since late November 2012, which were strongly dominated by magmatic volatiles, produced two consecutive processes: 1) acidification (late November 2012–2020)

and 2) depletion (2019–2020) of the hydrothermal system. In this work we have shown that a long-term surveillance of the chemistry of fluid discharges provides valuable insights into underlying magmatic/volcanic processes, and consequently, for forecasting future eruptions.

KEYWORDS

volcanic degassing, volatile flux, central volcanic zone of the andes, PiCam, ground-based remote gas measurements, direct sampling

1 Introduction

Changes in volcanic activity can be tracked by the variations in the data obtained from several monitoring techniques as seismicity, degassing, thermal energy released, ground deformation, among others. Those variations can be in some cases indicative of eruptions (Spampinato et al., 2019; Caudron et al., 2021), although in other cases only represent changes in the internal activity of volcanoes, not necessarily finishing with an eruption (Galetto et al., 2019; Guo et al., 2019). For decades, several investigations have focused on determining the internal behavior of volcanic systems and to track pre-eruptive activity, in order to find possible precursor signals, to anticipate the eruptive activity, and consequently, to reduce the risks related to volcanic processes (Williams-Jones and Rymer, 2002; Dempsey et al., 2020). Geophysical parameters, such as seismicity, ground deformation and gravimetry have been measured and monitored individually or combined to detect several internal processes, such as influx of new magma, ascent of magma, magma crystallization, perturbations of hydrothermal systems, among others (Tizzani et al., 2009; Tizzani et al., 2015; Calahorrano-Di Patre et al., 2019). For example, increasing frequency and intensity of earthquakes, and occurrence of swarms (e.g., low frequency events; Bell et al., 2018; Roman and Cashman, 2018) are considered a typical precursor of volcanic activity (e.g., Cameron et al., 2018). Although volcanic eruptions are common after episodes of strong inflation (Segall, 2013), a global study carried out by Biggs et al. (2014) demonstrated that only ~46% of volcanoes which presented deformation erupted, while 94% of non-deforming volcanoes did not erupt. Similar results were obtained by Galetto et al. (2022), who suggest that magma inflow rates are more reliable in forecasting eruption, at least at basaltic calderas. Complementary, increasing CO_2/SO_2 ratios can allow detection of the pre-eruptive degassing of rising magma (Aiuppa et al., 2007). Therefore, changes in seismic and ground-deformation data, as well as in the degassing rate, fumarolic fluid composition, and emitted thermal energy, have been used to try to forecast eruptions (Reath et al., 2019; Coppola et al., 2022), although in some cases strong changes in activity and precursory signals have not been followed by eruptive events (Ebmeier et al., 2018; Lopez et al., 2018; Layana et al., 2020).

Lastarria volcano (Northern Chile) is one of the most intense persistently degassing volcanoes in the Central Volcanic Zone of the Andes (CVZA) (Tamburello et al., 2014; Lopez et al., 2018), which has been continuously degassing since at least late XIX century (González-Ferrán, 1995). Since 1998, the volcanic chain constituted by Lastarria, Cordón del Azufre, and Cerro Bayo volcanoes, and also known as Lazufre, has undergone a continuous large scale ground deformation process related to a deep-magmatic source, and Lastarria volcano exhibited localized small-scale deformation processes (2003–2005) related to a pressurization of its hydrothermal system (e.g., Froger et al., 2007; Ruch et al., 2008). Chemical compositions of gases discharged by Lastarria volcano between 2006 and 2009 were dominated by hydrothermally sourced gas (Aguilera et al., 2012). Data obtained by Tamburello et al. (2014) using MultiGAS, filter pack, and ground-based remote techniques during a field campaign in late November 2012 in contrast indicate a clear magmatic composition. Similarly, Lopez et al. (2018) combined the results of direct gas sampling, MultiGAS, filter pack, ground-based remote techniques, and diffuse CO_2 sampling acquired by the participants of the 2014 International Association of Volcanology and Chemistry of the Earth's Interior (IAVCEI) Commission on the Chemistry of Volcanic Gases (CCVG) 12th Gas Workshop in November 2014, detecting major changes in the gas composition. They proposed 4 alternative models in order to explain the changes in the gas composition between 2009 and 2012 considering the contemporary ground deformation process. These geophysical and geochemical changes may be interpreted as precursory signs of a potential eruptive phase (Lopez et al., 2018).

Despite of the first attempt of Lopez et al. (2018), any correlation between large-and-small scale ground deformation and the changes observed in the gas composition remains elusive. Here we present a unique and large database (due to the frequency of sampling, the number of techniques involved, and the time span considered) of fumarolic gas compositions and emission rates of Lastarria volcano, comprising previously published (May 2006- June 2009) and new unpublished (June 2010-November 2019) data obtained from direct sampling, UV Camera (May 2018-November 2019) and Differential Optical Absorption Spectrometry-DOAS (January and November 2019). The aim of this work is to establish the source(s) of gases, to determine the processes explaining the changes observed in gas composition between 2006 and 2019, and to link with the previously published ground deformation studies (Pritchard and Simons, 2002; Pritchard and Simons, 2004; Froger et al., 2007; Ruch et al., 2008; Anderssohn et al., 2009; Pearse and Lundgren, 2013; Henderson et al., 2017; Pritchard et al., 2018). Consequently, our contribution will point to provide more evidence that the combination of several techniques can be used to detect possible precursors for future eruptions in arc-related volcanoes.

2 Geological setting

2.1 Volcanological evolution

Lastarria *sensu stricto* (*ss*) is an active stratovolcano located in the southern portion of the Central Volcanic Zone of the Andes (CVZA) which extends along the Chile-Argentina border (Figure 1). Lastarria *ss* is part of the Lastarria Volcanic Complex (LVC), which

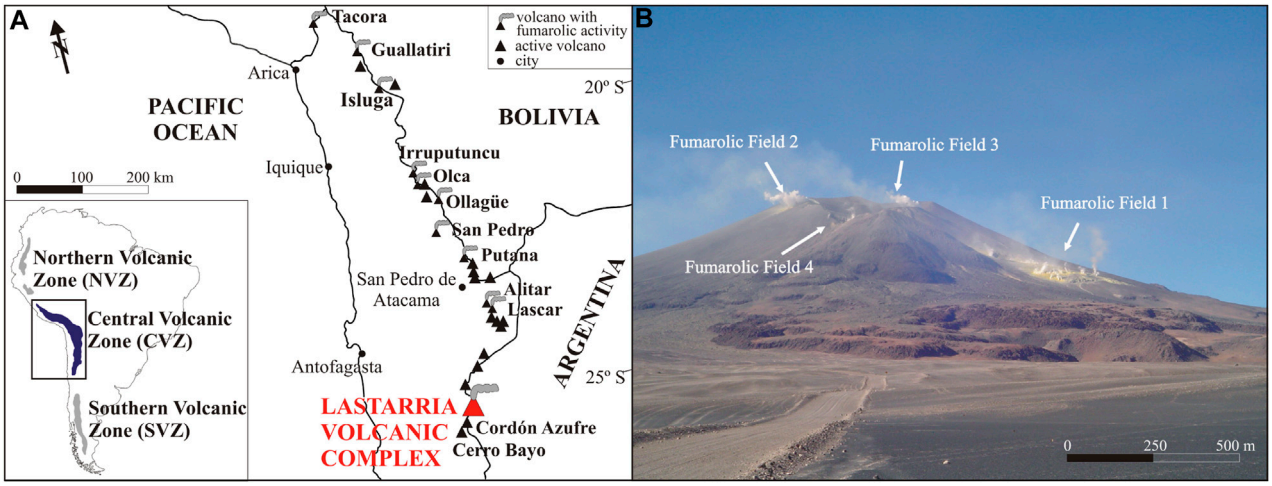

FIGURE 1
(A) Location map of the Lastarria Volcanic Complex and **(B)** picture of the 4 fumarolic fields (seen from the North).

also includes the Negriales lava field and Espolón Sur volcano (Naranjo, 2010). Negriales volcano (from 400 ± 60 to 116 ± 26 ka) is composed of andesitic-to-dacitic lava flows, coulees, and domes, whereas Espolón Sur volcano (150 ± 50 ka) is constituted of andesitic lava and pyroclastic flow deposits. Lastarria *ss* is the only active structure of the complex and has evolved through 10 eruptive stages (from 260 ± 20 to 2.46 ± 0.050 ka; Naranjo, 2010). Their volcanic products correspond to andesitic-to-dacitic lava flows and domes, pyroclastic flows and fallout deposits, and debris avalanche deposits (Naranjo, 1992; Naranjo, 2010). Although there are no records of historical eruptive activity, a persistent degassing has been observed since the early 19th century (Casertano, 1963; González-Ferrán, 1995), which is concentrated in four fumarolic fields (Figure 1) located in the northwestern flank (fumarolic field 1), in the eastern and western rim of crater IV (fumarolic fields 2 and 3) ,and inside of crater V (fumarolic field 4) (Aguilera et al., 2012).

2.2 Ground deformation

Large-scale deformation, as detected by InSAR (Interferometric synthetic-aperture radar) and geodetic measurements, has been observed since 1998 in the Lazufre area, which consists of, from north to south, LVC, Cordón del Azufre and Bayo volcanoes. The zone of uplift has been extending over a ~45 × 37 km NNE-oriented elliptical area (Pritchard and Simons, 2002; Pritchard and Simons, 2004; Froger et al., 2007; Ruch et al., 2008; Anderssohn et al., 2009; Pearse and Lundgren, 2013; Henderson et al., 2017; Pritchard et al., 2018). The maximum average uplift was observed until 2010 with a rate of 3 cm/yr (Pearse and Lundgren, 2013), whilst between 2011 and 2016 the uplift rate was reduced to <1.5 cm/yr, and should continue to decrease over the next decades, until uplift is anticipated to stop (Henderson et al., 2017). Six alternative models have been proposed to explain this large-scale deformation: 1) magma injection; 2) thermal expansion due to assimilation of wall rock; 3) thermally induced volatile exsolution produced by magma crystallization; 4) lateral expansion due to the intrusion of a sill-like magmatic body (Pritchard and Simons, 2004; Froger et al., 2007; Ruch et al., 2008; Anderssohn et al., 2009; Pearse and Lundgren, 2013); 5) a pulse of heat from the magmatic system into an overlying hydrothermal aquifer without changes in magma reservoir volume (Froger et al., 2007); 6) exsolved volatiles from a melt and temporally trapped at relative deep levels (>10 km) that cause pressurization of a deep reservoir, and consequently ground uplift (Pritchard et al., 2018). The source of the large-scale deformation has been located in a range between 7 and 15 km deep (Pritchard and Simons, 2004; Froger et al., 2007; Ruch et al., 2008; Anderssohn et al., 2009; Pearse and Lundgren, 2013; Henderson et al., 2017; Pritchard et al., 2018). A secondary small-scale deformation affecting an area of 6 km^2 was observed below Lastarria *ss* edifice between 2003 and 2005, with a deformation rate of ~9 mm/yr, which has been related to a pressurized shallow source (hydrothermal aquifer) lying <1,000 m below Lastarria *ss* edifice (Froger et al., 2007).

Spica et al. (2015), using seismic tomography, further identified a shallow magmatic source located between 3 and 6 km depth (not previously identified), and a shallow hydrothermal source located at 0.4 km depth. Stechern et al. (2017) using petrological approaches (mostly related to Holocene explosive events), identified two magmatic sources, the shallower located at 5–8 km depth, as well as a deeper reservoir between 11 and 15 km depth. Díaz et al. (2015) using resistivity measurements identified three resistivity zones, which are coincident with the shallow hydrothermal system, and the two magmatic reservoirs previously described.

3 Methodologies

3.1 Direct sampling and analytical procedures

Gas samples from fumarolic emissions were collected using a 50 cm in length and 25 mm in inner diameter titanium tube and pyrex glass dewared pipes connected with metallic clips and Teflon

FIGURE 2
Location of measurements with UV Picam and DOAS at Lastarria volcano. The blue and black circle correspond to locations of UV Picam measurements, and the yellow tripods correspond to DOAS measurements. The numbers correspond to the correlative location points in the Table 1.

plugs. A 60 mL pre-evacuated glass flask equipped with a Thorion® valve and partially filled (20 mL) with an alkaline suspension (4 M NaOH and 0.15 M $Cd(OH)_2$) was assembled in the titanium-glass line (Montegrossi et al., 2001). Incondensable species (He, Ar, N_2, O_2, CH_4, H_2, CO, and light hydrocarbons) remained in the headspace, soluble (water vapor), acidic species (SO_2, HCl, HF) and CO_2 dissolved into solution, whereas H_2S precipitated as CdS.

The chemical compositions of incondensable, dissolved, and precipitated species were determined at the Laboratory of Fluid Geochemistry of the Department of Earth Sciences, University of Florence, Italy. Incondensable species from the headspace were analyzed by gas chromatography (GC) using the Shimadzu 15, 14 A and Thermo Focus equipment. The liquid phase was analyzed by ionic chromatography (IC; Metrohm 761), where the concentration of Cl^- (from HCl dissolution), F^- (from HF dissolution), and SO_4^{2-} (from SO_2 dissolution) were determined. Acidic titration (AT; Metrohm Basic Titrino) was used to determine the concentration of CO_2^{3-} (from CO_2 dissolution). Solid CdS was dissolved using H_2O_2 to analyze H_2S as SO_4^{2-} by IC (Montegrossi et al., 2001). Analytical error for GC, AT, and IC analysis was <5%.

3.2 UV camera

SO_2 emission rates of Lastarria volcano were measured using a PiCam, a low-cost UV camera, developed at University of Sheffield, United Kingdom (Wilkes et al., 2016; 2017). This instrument consists of two cameras with a field of view (FOV) of 23.1° × 17.3°. Each camera has a bandpass filter with a transmission wavelength on-band and off-band for SO_2 absorption, corresponding to 310 and 330 nm, respectively. The instrument is connected to a laptop via WiFi, with the Picam then controlled through Python 3 code (Aguilera et al., 2020). Prior to each measurement sequence the Picam was calibrated with gas cells with column densities of 100, 467, and 1,989 parts per million by meter (ppm m). Additionally, dark and clear sky corrections were performed, in order to correct the residual noise with a black image, and correction of vignetting through a mask in the clear sky, respectively.

The measurements were carried out on 12, 13 May and 1, 2 November 2018, on 17, 18 January and 21, 22 November 2019 at a distance of 2–5 km from the plume, with a range of geographic altitude from 4,600 to 5,000 m above sea level (m a.s.l. Figure 2; Table 1). On each day of measurement, calibration was performed every hour, with measurements possible for up to 6 h each time.

The sequences were processed using a python-based code in order to determine SO_2 emission rates (Wilkes et al., 2017; Aguilera et al., 2020). Plume velocity was calculated using cross-correlation technique, because the error with this technique is minor, considering the high temporal and spatial resolution of UV camera (McGonigle et al., 2005; Kantzas et al., 2010).

All the measurements presented in this article have uncertainties inherent to field conditions and characteristics of the instrument, which could affect the quality of data. Following Ilanko et al. (2020); Aguilera et al. (2020), uncertainties were determined (Table 2) associated with plume velocity, gas cell concentration and calibration drift, column density across line integration, light dilution. Uncertainties due to plume direction were negligible given near perpendicularity to the plume (Klein et al., 2017), while the plume was near transparent meaning errors from in-plume scattering were also negligible. Despite some uncertainty

TABLE 1 Technical information about measurements with PiCam, coordinates in decimal degrees, m a.s.l.: meters about sea level, OCV: openCV method for post processing. CP: control points method for post processing (N° of control points used).

Date		12-May-18	13-May-18	13-May-18	01-November-18	02-November-18	17-January-19	18-Januaru-19	21-November-19	22-November-19
Location in geographic coordinates		−25.146550	−25.130754	−25.117851	−25.123110	−25.117222	−25.122590	−25.117966	−25.121163	−25.1409
		−68.533683	−68.512288	−68.25718	−68.518197	−68.517222	−68.515253	−68.524152	−68.520477	−68.5383
N° Point		1	2	3	4	5	6	7	8	9
Geographic altitude (m a.s.l)		4,682	4,615	4,426	4,507	5,000	4,526	4,426	4,472	4,559
Position measurement in relation with the plume (°)		147°	85°	102°	94°	91°	89°	100°	97°	140°
Distance to the plume (km)		1.8	2	3	4.2	5	4.5	4.2	4	3
Hour measurement (UTC-3)		15:39	11: 50–13:37	12:10–13: 08–16:01	11:25–12:10–13: 17–15:15	13:24	11:04–12:40: 14:19	13:30	13:15	11:04–12:03 -13:16
Shutter Speed	Lens A	600	600, 700	600	420, 500, 530,550, 600	700, 800, 850	520, 650	450	400	350, 370
	Lens B	100	75, 100	100	70, 80, 90, 100	100, 150	100, 110	90	80	70, 80
Frequency (Hz)		0.2	0.2	0.2	0.2	0.2	0.2	0.2	0.2	0.2
Sequences		2	2	3	4	1	3	1	1	3
N° images per secuence		22, 533	533, 537	554, 537, 233	97, 539, 230, 362	101	540, 531, 722	710	890	92, 398, 518
Type of processing		OCV, CP (7)	OCV, CP (8)	OCV, CP(7)	OCV, CP(12)	CP(6)	OCV, CP (8)	CP(7)	CP (7)	CP(7)

related to grounding plumes affecting 19% of the data, in this work we have processed UV camera data using integration lines which include the border between ground and plume, and in several positions along the plume, in order to reduce to the minimum that uncertainty. An estimation of this uncertainty has not been carried out.

The plume speed uncertainty depends on the distance between the PiCam and the plume (and consequently the distance between the two integrated columns amounts (ICA)), and the difference in time of the plume movement between one ICA and another during cross-correlation. Considering the distance errors of 200 m, the uncertainty related to the plume speed of our measurements is of ±27%. In the case of calibration drift, we considered variations in the illumination because of the changes in the sun position along 1 day of measurements, selecting and comparing all calibrations carried out and used for the processing of images, in the same site and same day, as per Ilanko et al. (2019). Low uncertainties were calculated for calibration drift, with values ranging from < ±0.46% to ±10%. Uncertainties in column density across line integration were low, with a minimum of ±0.25% and a maximum of ±20%, which were calculated according to Wilkes et al. (2017). In the case of uncertainties related to the light dilution, which is generated by scattering of photons into the FOV of the camera between the plume and the PiCam, we have considered the specific atmospheric conditions in the northern Chile Altiplano, as relatively low atmospheric pressure, very low humidity and scarce aerosol concentrations. According to these conditions; Aguilera et al. (2020) based on Campion et al. (2015) suggest that measurements carried out at distance <3 km, light dilution is negligible, whereas for distances between 3 and 6 km, this will be at least up to +20%. In relation to the above, at Lastarria volcano, we have estimated a negligible light dilution error in the case of 13 May 2018 measurements (distance from the plume <3 km), 1 November 2018, 17, 18 January 2019, and 21 November 2019 an uncertainty variable between +13 and +15% (distance of 4–4.5 km from the plume) and +25% for 2 November 2018 measurements (5 km distance from the plume), the above as a proportion in relation to the indicated by Aguilera et al. (2020). Uncertainty related to gas cell calibration is provided by the manufacturer (Resonance Ltd.), and is ±10% for 100, 467 and 1,989 ppm m cells.

Finally, the total error percentage calculated by the root mean square error (RMS) varies in a range of −19% and +17% (Table 2).

3.3 Portable scanning Mini-DOAS

In this work we have used two different Differential Optical Absorption Spectroscopy (DOAS) instruments, the first one

TABLE 2 Uncertainties in each measurement. Total RMS error (root mean square) is included (%). (-) represent a despicable error.

Uncertainty		13-May- 18	01-November-18	17-January-19	18-January-19	21-November-19
Plume distance	Min	± 1.7	± 1	± 1.1	± 1.1	± 1.3
	Max	± 10	±4.8	± 4.4	± 4.5	± 5
Time	Min	± 25	± 25	± 17	± 17	± 25
	Max	± 25	± 25	± 25	± 25	± 25
Plume Speed	Min	± 25	± 25	± 17	± 17	± 25
	Max	± 27	± 25	± 18	± 18	± 26
Calibration Drift	Min	± 0.46	± 10	± 6.7	—	—
	Max	± 2.4	± 10	± 9	—	—
Gas Cell Callibration		±10	±10	±10	±10	±10
Light Dilution		0	+13/+15	+14	+14	+13
SO2 Detection	Min	±0.57	±0.5	±0.31	±0.74	—
	Max	±1.6	±20	±1.7	±0.74	—
Plume Direction		—	—	—	—	—
Multiple Sccatering		—	—	—	—	—
Total RMS error	Min	−14/+12	±14	−10/+11	−10/+12	−19/+17
	Max	−15/+13	−18/+17	−11/+12	± 12	−19/+ 17

developed by The University of Sheffield, UK (Linear Scanning Spectrometer- LSS), whilst the second one was a portable scanning Mini-DOAS station of the NOVAC-type, which was equipped with conical scanning optics (see Galle et al., 2010; Conde et al., 2014 for details on the instrument). Both instruments were used for scanning DOAS measurements.

LSS instrument allowed us to determine the SO_2 column densities, from the light spectra scanned by the spectrometer, whose slit entrance is 50 μm wide, with the optical bench set up to provide a spectral range of ~240–400 nm and a spectra resolution of ~0.65 nm. It uses a Sony ILX511 detector with a 2,048 element linear array CCD and 16- bits ADC. The scanning is performed by a mirror mounted to a stepper motor, which is covered by a 3D-printed scanner head and UV-transmissive curved Perspex window. Python software "SpecScan", also developed by The University of Sheffield, is used to control the spectrometer and the scanning instrument, and subsequently retrieve column densities of SO_2 from the spectra. The PiSpec measurements were performed on 20, 21, and 22 November 2019, at 4 km N and 3.1 km NW from the summit of Lastarria volcano, 4,558 and 4,566 m a.s.l., respectively (Figure 2; Table 3). Scanning sequences lasted between 31 min, and 4 h and 54 min, being carried out between 9:44 and 14:39 h local time (UTC -3). Integration time used varied in a range of 550–700 ms, whilst the scanning range varied from 90° to 140°. The wind speed data was measured 1) *in situ* by a handheld anemometer measurements at ground level, and 2) obtained from the plume speed estimated by the UV Camera measurements. The spectra were processed post-acquisition using "SpecScan" for determination of SO_2 emission rates.

The SO_2 emission rate measurements from the NOVAC-type instrument were carried out on 17, 18 January 2019. On each acquisition day, the instrument was deployed for several hours at accessible locations roughly beneath the gas plume and about 4–8 km downwind of the emission sources on Lastarria (Figure 2; Table 3). For data acquisition, the DOAS instrument scans across the sky collecting spectra of incoming scattered UV light at 51 angular steps of 3.6° along a semi-conical surface in order to obtain SO_2 column density profiles perpendicular to the transport direction of the volcanic gas plume. Prior to each scan, exposure times (50–1,000 ms) used for the recording of individual spectra were automatically adjusted by the instrument depending on previously measured UV light intensity. Resulting acquisition times ranged between 5 and 15 min for a complete scan from horizon to horizon.

Scans were evaluated using the DOAS method (Platt and Stutz, 2008) in order to retrieve SO_2 column densities from the sunlight spectra measured across the gas plume. DOAS fits were performed in the 310–325 nm wavelength range of the measurement spectra, additionally including reference absorption spectra of SO_2 (Vandaele et al., 1994) and O_3 (Voigt et al., 2001), the latter being the main interfering gaseous UV absorber relevant for SO_2 retrieval in this spectral range. Furthermore, a Ring reference spectrum (Chance and Spurr, 1997) was included in the DOAS fit to reduce the undesired effects of rotational Raman scattering, and spectral shifts of measured spectra were determined and corrected for by means of comparison with a solar reference spectrum (Chance and Kurucz, 2010). Reference spectra were calibrated to match the spectral resolution of the two spectrometers by means of convolution with the slit function of respective spectrometers.

SO_2 emission rates were calculated using auxiliary information on plume transport height and direction constraining location of the

10.3389/feart.2023.1114001

TABLE 3 Technical information of measurements with DOAS. m a.s.l.: meters above sea level. *Average flux calculated using wind speed from GDAS and ground level measurements. ** Average flux calculated using wind speed from PiCam.

Date	17-January-2019	18-January-2019	18-January-2019	20-November-19	21-November-19	22-November-19
Location in geographic coordinates	−25.122590	−25.138700	−25.117966	−25.122800	−25.122800	−25.140900
	−68.515253	−68.544700	−68.524152	−68.507400	−68.507400	−68.538300
N° Point	6	10	7	11	8	9
Geographic altitude (m a.s.l.)	4,526	4,507	4,426	4,558	4,558	4,559
Distance to the plume (km)	4.5	3.8	4.2	4	4	3
Hour measurements (UTC-3)	14:14–15:35	13:39–14:27	16:56–17:27	09:44–14:39	11:30–12:01	10:33–14:25
Wind speed GDAS and ground level measurements (m/s)	3.9–4.7	6.1	7.4	7.3	10.8	3.5
Wind Speed PiCam (m/s)	9.8	—	—	—	11.7	—
Average flux (t/d)*	172 ± 78	626 ± 85	286 ± 64	506 ± 241	1,416 ± 568	467 ± 235
Average flux (t/d)**	418 ± 217	—	—	—	1,534 ± 485	—

gas plume within the measurement geometry of the scanning DOAS, and information on the speed of gas transport. Plume heights were estimated by visual inspection of plume photographs. Knowing the locations of both emission source and DOAS instrument, the plume transport directions were also determined by means of triangulation using the center of SO_2 mass in measured plume cross-sections and estimated plume heights as reference. For evaluation of the data, plume speeds required to eventually calculate emission rate were approximated using modeled wind speeds obtained from archived data of the Global Forecast System (GFS) provided by National Oceanic and Atmospheric Administration (NOAA), and by cross-correlation of plume features in image sequences obtained from contemporary UV-camera measurements.

3.4 Calculation of H_2O, CO_2, H_2S, and HCl emission rates

H_2O, CO_2, H_2S, and HCl emission rates were calculated using Eq. 1 (López et al., 2013) combining determined daily average SO_2 emission rate (F_{SO_2}), measured by ground-based remote techniques, and the concentrations of fumarolic compounds obtained from direct sampling technique.

$$F_{volatiles} = F_{SO_2}\left(\frac{M_{volatiles} \times X_{volatiles}}{M_{SO_2} \times X_{SO_2}}\right) \quad (1)$$

where $M_{volatiles}$ is the molecular weight of each major species, in the case of SO_2 (M_{SO_2}) is 64 gr/mol, $X_{volatiles}$ is the average mole percent of each volatile species present in the fumarolic gases. Summing up the emission rates of all major gaseous compounds finally yielded the total volatile inventory of Lastarria.

4 Results

4.1 Gas chemistry obtained by direct sampling

Here we present a large database of 63 samples, 29 corresponding to the period May 2006–April 2009 (Aguilera et al., 2012), 1 sample from June 2010 (this work), 4 samples of November 2014 (2 from Lopez et al. (2018) and 2 this work), and 29 samples between May 2011 and November 2019 (this work). Altitude (m a.s.l.), temperature (°C) and chemical composition (mol %) of fumarolic gas discharge at Lastarria volcano, are presented in the Table 4. Fumaroles for the period May 2006-November 2019 presented outlet gas temperatures between 80.1°C and 408°C. Gas composition can be described in two different periods:

1. May 2006-November 2012: Water vapor and CO_2 were the predominant compounds whose concentrations were 81–91 and 7.2–17 mol%, respectively. SO_2 concentrations were within the range of 0.01 and 0.68 mol%, while H_2S concentrations varied from 0.01 to 0.3 mol%. Significant amounts of HCl (0.001–0.12 mol%), HF (0.0001–0.05 mol %), N_2 (0.03–0.51 mol%) and H_2 (0.0005–0.24 mol%) were also found in fumarolic gases. Minor amounts of carbon-bearing compounds such as CH_4 (≤0.001 mol%) and CO

TABLE 4 Temperature (in °C) and chemical composition (in mol%) of fumarolic gases from Lastarria volcano.

Date	T°	H_2O	CO_2	SO_2	H_2S	HCl	HF	N_2	O_2	H_2	CH_4	Co	He	Ar
2006	278	84.6	14.3	0.40	0.01	0.06	0.00896	0.47	0.00769	0.14	0.00096	0.00045	0.00003	0.00039
	217	83.0	16.0	0.35	0.01	0.06	0.00829	0.46	0.00999	0.12	0.00093	0.00045	0.00004	0.00042
	278	82.6	16.3	0.37	0.01	0.06	0.00852	0.48	0.00626	0.12	0.00092	0.00044	0.00003	0.00040
	82.8	90.1	9.42	0.15	0.25	0.00	0.00063	0.06	0.00022	0.00	0.00042	0.00001	0.00002	0.00008
	85.1	90.7	8.87	0.15	0.21	0.01	0.00076	0.08	0.00042	0.00	0.00050	0.00001	0.00002	0.00009
	90	90.4	9.10	0.16	0.26	0.01	0.00082	0.05	0.00019	0.00	0.00046	0.00001	0.00001	0.00011
	94.1	92.7	7.20	0.01	0.03	0.00	0.00009	0.04	0.00001	0.00	0.00057	0.00003	0.00007	0.00006
	95	91.5	8.41	0.01	0.04	0.00	0.00008	0.04	0.00001	0.00	0.00062	0.00002	0.00005	0.00006
	86.1	90.9	9.01	0.01	0.04	0.00	0.00007	0.04	0.00001	0.00	0.00063	0.00002	0.00004	0.00007
	80.1	90.4	9.09	0.21	0.30	0.00	0.00070	0.04	0.00009	0.00	0.00045	0.00000	0.00005	0.00008
	81.4	91.9	7.74	0.21	0.15	0.00	0.00069	0.03	0.00007	0.00	0.00039	0.00000	0.00006	0.00007
	80.9	91.5	8.14	0.21	0.10	0.01	0.00064	0.03	0.00001	0.00	0.00036	0.00000	0.00003	0.00004
	80.8	89.9	9.76	0.19	0.11	0.00	0.00054	0.03	0.00002	0.00	0.00040	0.00001	0.00003	0.00007
	96.1	91.7	7.93	0.20	0.12	0.01	0.00065	0.03	0.00003	0.00	0.00040	0.00000	0.00005	0.00006
	83.7	91.4	8.21	0.20	0.15	0.01	0.00073	0.03	0.00008	0.00	0.00036	0.00000	0.00004	0.00006
2008	287	85.3	13.6	0.41	0.02	0.06	0.00774	0.51	0.00136	0.17	0.00095	0.00051	0.00003	0.00036
	319	83.4	15.5	0.43	0.01	0.07	0.00915	0.46	0.00154	0.18	0.00102	0.00050	0.00003	0.00029
	120	85.8	13.5	0.22	0.06	0.03	0.00564	0.27	0.00223	0.16	0.00087	0.00049	0.00003	0.00037
	191.9	84.4	14.9	0.19	0.06	0.05	0.00552	0.31	0.00035	0.15	0.00066	0.00047	0.00002	0.00041
	94.8	92.5	7.42	0.01	0.03	0.00	0.00049	0.05	0.00007	0.00	0.00065	0.00001	0.00006	0.00016
	254	82.6	16.5	0.30	0.02	0.05	0.00663	0.36	0.00069	0.14	0.00075	0.00046	0.00002	0.00029
	84.3	92.4	7.48	0.01	0.04	0.00	0.00048	0.06	0.00006	0.00	0.00055	0.00001	0.00005	0.00019
	84.2	92.3	7.57	0.02	0.03	0.00	0.00040	0.05	0.00007	0.00	0.00069	0.00001	0.00007	0.00021
2009	345	82.3	16.4	0.60	0.01	0.06	0.02385	0.38	0.00062	0.24	0.00027	0.00099	0.00005	0.00028
	367	84.4	14.5	0.48	0.01	0.06	0.02070	0.42	0.00087	0.14	0.00025	0.00094	0.00002	0.00052
	295	84.7	14.5	0.28	0.01	0.04	0.01453	0.33	0.00167	0.14	0.00031	0.00051	0.00006	0.00060
	400	82.3	16.2	0.62	0.01	0.07	0.03447	0.51	0.00028	0.24	0.00035	0.00111	0.00004	0.00027

(Continued on following page)

10.3389/feart.2023.1114001

TABLE 4 (*Continued*) Temperature (in °C) and chemical composition (in mol%) of fumarolic gases from Lastarria volcano.

Date	T°	H_2O	CO_2	SO_2	H_2S	HCl	HF	N_2	O_2	H_2	CH_4	Co	He	Ar
	336	82.7	16.2	0.52	0.01	0.07	0.01991	0.29	0.00045	0.17	0.00045	0.00078	0.00004	0.00033
	408	81.1	17.4	0.68	0.01	0.09	0.05582	0.39	0.00159	0.22	0.00040	0.00126	0.00003	0.00049
2010	370	84.2	14.6	0.42	0.01	0.05	0.02761	0.48	0.00033	0.20	0.00025	0.00078	0.00003	0.00028
2011	313	84.1	14.9	0.50	0.01	0.10	0.01542	0.27	0.00033	0.14	0.00052	0.00084	0.00004	0.00035
	307	83.1	16.0	0.43	0.01	0.09	0.01420	0.21	0.00019	0.12	0.00044	0.00074	0.00006	0.00025
	168	85.2	14.2	0.15	0.04	0.05	0.00459	0.27	0.00022	0.12	0.00061	0.00043	0.00002	0.00031
	169	86.1	13.4	0.12	0.03	0.04	0.00361	0.23	0.00017	0.12	0.00050	0.00046	0.00004	0.00025
	400	83.6	15.2	0.51	0.01	0.11	0.05100	0.32	0.00026	0.18	0.00048	0.00084	0.00005	0.00025
	86	92.1	7.79	0.02	0.03	0.002	0.00055	0.05	0.00012	0.004	0.00062	0.00001	0.00008	0.00020
	305	82.6	16.5	0.46	0.01	0.09	0.01514	0.19	0.00021	0.15	0.00061	0.00049	0.00004	0.00028
	400	83.5	15.5	0.49	0.01	0.12	0.01848	0.21	0.00031	0.16	0.00048	0.00051	0.00004	0.00021
	86	91.4	8.50	0.01	0.03	0.003	0.00069	0.05	0.00012	0.004	0.00077	0.00001	0.00006	0.00021
2012	290	87.7	11.9	0.14	0.18	0.02	0.00185	0.08	0.00018	0.01	0.00053	0.00032	0.00003	0.00047
	291	89.2	10.3	0.12	0.20	0.02	0.00097	0.08	0.00017	0.04	0.00055	0.00042	0.00003	0.00027
	334	90.5	9.18	0.13	0.10	0.03	0.00105	0.03	0.00010	0.02	0.00025	0.00046	0.00003	0.00018
	355	86.7	12.7	0.29	0.16	0.03	0.00333	0.06	0.00039	0.06	0.00048	0.00037	0.00003	0.00016
	229	87.9	11.6	0.16	0.16	0.02	0.00194	0.06	0.00044	0.07	0.00054	0.00023	0.00003	0.00019
	223	89.5	10.1	0.16	0.13	0.01	0.00053	0.06	0.00035	0.04	0.00029	0.00035	0.00002	0.00025
2014	328	93.7	3.30	1.50	0.78	0.39	0.0081	0.15	0.00011	0.16	0.00006	0.000002	0.00008	0.00054
	320	91.9	5.60	1.20	0.85	0.36	0.0074	0.07	0.00024	0.05	0.00003	0.000001	0.00007	0.00038
	260	93.1	5.00	1.03	0.61	0.15	0.0051	0.07	0.000003	0.02	0.00003	0.00001	0.00015	0.00016
	180	96.4	2.00	0.69	0.51	0.27	0.012	0.04	0.00001	0.09	0.00022	0.00001	0.00013	0.00012
2017	265	89.3	7.10	2.10	0.91	0.29	0.0045	0.22	0.00043	0.08	0.00008	0.000001	0.00009	0.00099
	265	92.4	4.50	1.70	0.76	0.36	0.0077	0.16	0.00017	0.13	0.00003	0.00003	0.00006	0.00056
	85	93.1	3.90	1.30	0.51	0.32	0.0069	0.13	0.00011	0.16	0.00005	0.00004	0.00006	0.00041

(Continued on following page)

10.3389/feart.2023.1114001

10.3389/feart.2023.1114001

TABLE 4 (*Continued*) Temperature (in °C) and chemical composition (in mol%) of fumarolic gases from Lastarria volcano.

Date	T°	H_2O	CO_2	SO_2	H_2S	HCl	HF	N_2	O_2	H_2	CH_4	Co	He	Ar
2018	314	88.1	7.90	2.20	1.20	0.39	0.011	0.12	0.00069	0.11	0.00003	0.00002	0.00008	0.00063
	273	87.2	8.20	2.60	1.50	0.21	0.0089	0.16	0.00078	0.16	0.00004	0.00004	0.00007	0.00051
	83	86.3	9.10	3.10	0.87	0.35	0.013	0.18	0.00056	0.13	0.00003	0.00006	0.00005	0.00035
	212	89.1	6.80	2.70	0.95	0.26	0.0085	0.11	0.00084	0.12	0.00003	0.00003	0.00007	0.00047
	285	87.6	7.50	2.90	1.20	0.44	0.015	0.16	0.00063	0.18	0.00002	0.00008	0.00006	0.00036
January 2019	268	70.3	17.5	3.30	0.56	0.46	0.069	0.96	0.0016	6.80	0.00001	0.00087	0.00011	0.00560
	360	69.9	18.6	4.10	0.32	0.52	0.088	0.91	0.00085	5.50	0.00001	0.00079	0.00015	0.00610
	290	68.2	18.8	3.90	0.49	0.49	0.079	0.88	0.00091	7.10	0.00001	0.00096	0.00009	0.00790
April 2019	304	86.0	9.50	2.40	1.20	0.31	0.031	0.23	0.00032	0.29	0.00004	0.00006	0.00008	0.00055
November 2019	311	91.6	5.60	1.60	0.55	0.15	0.008	0.19	0.00060	0.29	0.00005	0.00005	0.00007	0.00069
	126	94.4	4.10	1.00	0.96	0.09	0.005	0.24	0.0011	0.11	0.00013	0.00001	0.00009	0.00087

(≤0.001 mol%) were found, whereas noble gases (He and Ar) have values ≤0.0002 mol%, and concentrations of O_2 were below 0.01 mol%.

2. November 2014-November 2019: Water vapor and CO_2 were still the predominant compounds with concentrations of 68–96 mol % and 2–19 mol%, respectively, although large differences were observed in January 2019, when water vapor concentrations dropped to their lowest concentrations, whereas CO_2 reached the highest concentrations. SO_2 and H_2S increase in comparison with the previous period with concentrations of 0.69–4.1 mol%, and 0.32–1.5 mol%, respectively. HCl (0.09–0.52 mol%), HF (0.005–0.09 mol%), and N_2 (0.04–0.96 mol%) also increased in concentration, although H_2 showed more significant increases (0.02–7.1 mol%), especially during January 2019. Minor species, such as CH_4 (≤0.0002 mol%), CO (≤0.001 mol%), He (≤0.0002 mol%), Ar (≤0.008 mol%), and O_2 (≤0.002 mol%), maintained low concentrations.

4.2 SO_2 emission rates obtained by UV camera

The results of the UV camera measurements were determined for individual and/or combined fumarolic fields, and corresponding to SO_2 emission rates ±1 standard deviation, the last representing the variability of the data during the measurement process, are presented in the Table 5, and summarized as follows:

On 13 May 2018 we measured SO_2 sequences with a total of 1,070 images obtained, where fumarolic fields 1 and 2 were measured individually, obtaining rates of 113 ± 25 and 76 ± 15 t/d, respectively, whereas the rates by combination of the emissions from the fumarolic fields 3 and 4 was 93 ± 21 t/d. The overall average emission rate considering the four fumarolic fields for 13 May 2018 was 282 ± 20 t/d.

SO_2 measurements on 1 November 2018 averaged 786 ± 40 t/d, which is an increase in comparison with SO_2 measurements carried out in May 2018, for all fumarole fields combined. Considerable increases were observed in field 1 (234 ± 54 t/d), and the plume produced by combination of fumaroles from fumarolic fields 1, 3, and 4 (500 ± 94 t/d).

On 17 January 2019 the overall emission rate measured was 726 ± 74 t/d, similar to those measured on 1 November 2018, and with an emission rate for fumarolic fields 1, 2, 3, and 4 of 298 ± 105, 282 ± 69, 73 ± 22, and 72 t/d, respectively. On 18 January 2019, the plume moved in an atypical direction (west), and only the fumarolic field 1 could be measured, obtaining a minimum emission rate of 137 ± 38 t/d.

The overall SO_2 emission rate estimated for 21 November 2019 (1 sequence and 890 images) was 359 ± 29 t/d, with a low SO_2 emission rate in the fumarolic field 1 (24 ± 23 t/d) in comparison to the measurements of November 2018 and January 2019.

If we consider the root mean square error (RMS) expressed in percentage (Table 2), the final emission rates for the same dates, and expressed as a range, where minimum and maximum values correspond to the overall average emission rate plus negative and positive maximum RMS error, the SO_2 emission rates correspond to 240–319 t/d (13 May 2018), 645–935 t/d (1 November 2018), 646–813 t/d (17 January 2019), and 291–420 t/d (21 November 2019).

TABLE 5 SO_2 fluxes obtained in the different measurements in t/d. The measured fields are indicated. nm: not measured; 1 Results presented only as a reference; 2 Fluxes estimated from the difference between the bulk plume and individual fumarolic fields measurements and/or difference between combined and individual fumarolic fields.

Date	Field 1	Field 2	Field 3	Field 4	Fields 1 year 3	Fields 1, 3 years 4	Fields 3 years 4	NW	Total SO_2 flux
13-May-18	113 ± 25	76 ± 15	45[2]	48[2]	nm	nm	93 ± 21	nm	282 ± 20
01-Nov-18	234 ± 54	449*	102 ± 17	nm	299 ± 95	51 ± 38	nm	500 ± 94	786 ± 40
17-Jan-19	298 ± 105	282 ± 69	73 ± 22	72*	n.m	293 ± 74[1]	146 ± 48	418 ± 124	726 ± 74
18-Jan-19	137 ± 38	nm	nm	nm	nm	nm	nm	nm	
21-Nov-19	24 ± 23	101 ± 31	90 ± 32	145[2]	nm	259[2]	nm	359 ± 100	359 ± 29

4.3 SO_2 emission rates obtained by DOAS

The results of the measurements carried out with mini-DOAS in bulk plume are presented in the Table 3. On 17 January 2019, using wind speed values of 3.9 and 4.7 m/s, both obtained from GDAS1 at 500 hPa (corresponding at ~5,600 m a.s.l.), the total SO_2 emission rate obtained was 172 ± 78 t/d. Recalculating the total SO_2 emission rate using the plume speed average values obtained from simultaneous measurements with the PiCam (9.8 m/s), the total SO_2 emission rate increased to 418 ± 217 t/d. On 18 January 2019, measurements were carried out at two different locations. At point 7, using a wind speed of 6.1 m/s (GDAS1 at 400 hPa), the total SO_2 emission rate obtained was 282 ± 64 t/d. At the point 10, using a wind speed 7.4 m/s (GDAS1 at 400 hPa), the total SO_2 emission rate obtained was 626 ± 85 t/d. The overall SO_2 emission rate for both days was 376 ± 111 t/d.

On 20–22 November 2019, we used average ground level wind speed (by use of an anemometer) of 7.3, 10.8, and 3.5 m/s, respectively, because the mean wind speeds obtained by the GFS model (GDAS1 at 500 hPa) were on average 40% lower than those observed in the field. The SO_2 emission rate (average ± 1SD) was 506 ± 241, 1,416 ± 568, and 467 ± 235 t/d, respectively. Whereas using the PiCam plume speed (11.7 m/s), the recalculated measurement increased to 1,534 ± 485 t/d on 21 November 2019 (the only day with a reliable plume speed obtained by PiCam). The overall SO_2 emission rate for 3 days was 981 ± 382 t/d.

4.4 H_2O, CO_2, H_2S, and HCl emission rates

The results of emission rates of gases for the years 2014, 2018, and 2019 are presented in Table 6, where only high temperature fumaroles were considered. Here we present the results for each period considering the average of direct sampling data obtained from the different fumaroles, and using the variations of the SO_2 emission rates based on the RMS error presented in the Section 4.2. For November 2014 we estimated the emission rates of main species using the average SO_2 emission rate measured by Lopez et al. (2018) corresponding to 604 t/d, and we used the ±50% error reported for remote measurements, corresponding to a range between 302 and 906 t/d. Consequently, for November 2014, the emission rates of H_2O, CO_2, H_2S, and HCl ranged 7,208–21,626, 747–2,241, 100–299, and 46–137 t/d. In the following years, the H_2O, H_2S, and HCl decrease, reaching the lowest ranges during January 2019, corresponding to 3,351–4,217, 42–52, and 48–60 t/d, whereas CO_2 increases to its highest range in the same period (2,158–2,716 t/d). During November 2019, the emission rates of H_2O and H_2S increase to values similar to the November 2018 (5,823–8,405 and 90–130 t/d, respectively), whereas CO_2 and HCl reached the lowest flux along the whole revised period (746–1,077 and 15–22 t/d, respectively).

5 Discussions

5.1 Evolution of the fumarolic gas composition

The chemical composition of the fumarolic discharges from Lastarria volcano, which were investigated by Aguilera et al. (2012), covering a period between May 2006 and June 2009 (Table 4), showed that fluids have two origins: 1) a deep magmatic and 2) a shallow hydrothermal source. Along the whole range of fumarolic discharge temperatures (80°C–408°C) acid species such as SO_2, HCl, and HF were present, indicating a significant fluid contribution from magma degassing. Additionally, water isotopic composition (δD and $\delta^{18}O$) showed a pristine magmatic origin, poorly affected by meteoric contributions (Aguilera et al., 2012). However, concentrations of species like SO_2 and HF are lower than expected for magmatically dominated arc volcanoes (Fischer et al., 1998; Lewicki et al., 2000), especially if only fumaroles with temperatures above the saturated steam vapor at the local atmospheric pressure (120°C–408°C; Table 4) are considered. The latter suggests that secondary processes modified the original composition of magmatic volatiles, which include gas-rock interaction and salt deposition. The hydrothermal reservoir corresponds to a shallow boiling aquifer producing gases such as H_2S and CH_4. Magmatic volatiles are cooled and scrubbed at shallower depth, decreasing the concentration of highly soluble gases and the temperatures down to levels where condensation can occur. According to the model presented by Aguilera et al. (2012), the mixed distribution of low (<96°C) and high (>120°C) temperatures is explained by the occurrence of a discontinuous shallow aquifer, where water vaporization is catalyzed by the

TABLE 6 Total volatile fluxes and fluxes for each gas specie in t/d. Minimum (min), maximum (max) and average (ave) fluxes are shown.

Date		H_2O	CO_2	SO_2	H_2S	HCl	Total
2014	Min	7,208	747	302	100	46	8,402
	Max	21,623	2,241	906	299	137	25,206
	Ave	14,415	1,494	604	200	91	16,804
2018	Min	5,887	1,297	645	145	45	8,020
	Max	8,535	1,881	935	210	65	11,626
	Ave	7,174	1,581	786	177	55	9,773
January 2019	Min	3,351	2,158	646	42	48	6,244
	Max	4,217	2,716	813	52	60	7,858
	Ave	3,766	2,425	726	47	54	7,017
November 2019	Min	5,823	746	291	90	15	6,966
	Max	8,405	1,077	420	130	22	10,054
	Ave	7,184	921	359	111	19	8,594

rising of hot magmatic volatiles. Consequently, for the period May 2006-June 2009, Lastarria can be considered as a volcano dominated by hydrothermal discharges (Figure 3), with some contributions of magmatic volatiles. According to our new data presented here (Table 4), the gas composition between May 2011 and 11 November 2012 remained stable without major changes and was dominated by hydrothermal fluids, similar to observations of the previous years (Figure 3). A major change in gas composition was detected only 2 weeks later by Tamburello et al. (2014) who used a combination of MultiGAS, filter packs, and ground-based remote measurements of SO_2 emission rates on 27–29 November 2012. Their data in comparison to previous measurements showed a clear increase of SO_2 and HCl contents, and a decrease of CO_2, which is considered compatible with an increasing magmatic signature. Tamburello et al. (2014) explained these changes by (1) dissimilar sampling conditions, where MultiGAS were carried out in the "bulk" plume, whereas previous direct sampling was concentrated in few fumaroles which could be more affected by secondary processes, therefore not representative of the bulk emissions; or (2) a consequence of a real evolution of the volcanic system from hydrothermal-to-more magmatic degassing. Lopez et al. (2018) confirmed the changes in the gas composition by combination of direct gas sampling, MultiGAS, filter pack, ground-based remote, and CO_2 diffuse measurements, describing an evolution of fluids to a stronger magmatic signature, as the increasing SO_2 and HCl concentrations suggest (Figure 3; Table 4). Unpublished data from February 2017 to November 2018 (Table 4) showed similar concentrations to the November 2014 data, confirming the increasing of SO_2 and HCl, although an increase of N_2 by one order of magnitude was also observed. In January 2019, new changes were observed in the gas compositions (Table 4), H_2O decreased to 68.2–70.3 mol%, whereas CO_2, HF and H_2 increased one order of magnitude in comparison with 2014–2018 data, corresponding to the highest concentrations throughout the studied period. Between April and November 2019 gas concentrations returned to the values observed during February 2017 and November 2018 (Table 4).

According to the evolution of gas composition previously described a noticeable evolution from hydrothermal-dominated to magmatic-dominated volatiles is observed in Lastarria volcano since May 2006 up to November 2019 (Figure 3). Despite the presence of magmatic gases like SO_2 and HF, hydrothermal compounds predominated between May 2006 and early November 2012, which have been attributed to secondary water-rock interaction processes such as interaction of magmatic gases with rocks and/or salt deposition/precipitation with decreasing temperatures, promoting the scrubbing of highly soluble species such as SO_2, HCl, and HF (Aguilera et al., 2012; Lopez et al., 2018). The magmatic-dominated compositions observed since late November 2012, are compatible with a shallow degassing process, due to the decreasing of CO_2, and the increasing of SO_2 and HCl concentrations (Figure 3). The increase of the more soluble species was likely caused by a more restricted scrubbing in the shallow hydrothermal system. The decreasing of the scrubbing process could be attributed to the increased input of magmatic volatiles, followed by the acidification and partial consumption of the hydrothermal system. Increase of SO_2 emission rate has been observed in the period between November 2018 and January 2019, which will be discussed in the following sections. Acidification of the hydrothermal system explains the decrease of H_2O/SO_2 and H_2O/HCl, which started in late November 2012 (Figure 4). In January 2019 the lowest concentrations of water vapor were observed (68.2–70.3 mol%; Table 4), which could be related to consumption of the hydrothermal system caused by the enhanced hot magmatic fluid inputs that led to an increase of the reservoir ebullition. The input of magmatic volatiles caused an increase in the temperature of the hydrothermal reservoir increasing the concentration of the temperature dependent gases, such as H_2 and CO (Table 4). This process was concordant with the first ever witnessed active sulfur flows at this volcano. In April and November 2019, the returning of gas composition to values close February 2017-November 2018 seems to represent a subtle recovery of the previously depleted hydrothermal system.

5.2 Changes in the SO_2 emission rates

Similar to fumarolic gas composition, changes have been observed in the SO_2 emission rates in the period between November 2012 and November 2019 (Figure 5). The first SO_2 emission rates reported for Lastarria volcano were acquired using mini-DOAS from the summit of Lastarria (Tamburello et al., 2014). The daily rates (expressed as average ±1 standard deviation) were 1,917 ± 607, 473 ± 188, and 433 ± 314 t/d for 27, 28, and 29 November 2012, with an overall value for the 3 days of 884 ± 779 t/d and a much lower median of merely 538 t/d, the latter reflecting the outlier nature of the much higher emission rates obtained for 27 November 2012. SO_2 emission rates of 27 November 2012 generally were a factor ~5 larger than those of 28 and 29 November 2017, and temporarily peaked at 36.14 kg/

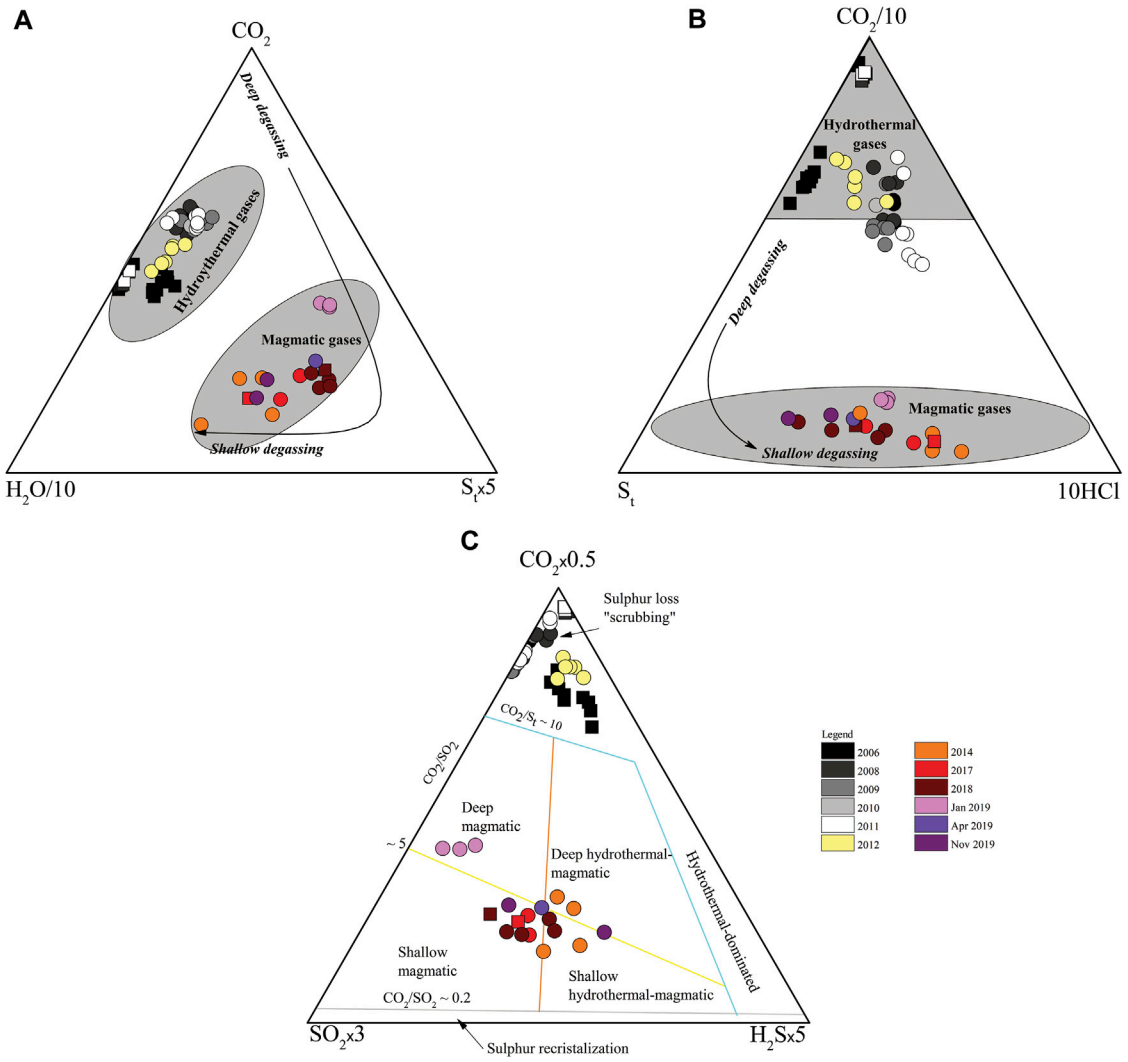

FIGURE 3
Ternary diagrams for Lastarria volcano gas compositions. **(A)** $H_2O/10$-CO_2-S_tx5; **(B)** S_t-$CO_2/10$-HClx10; **(C)** SO_2x3-CO_2x0.5-H_2Sx5. <96°C fumaroles are shown as filled squares; >120°C fumaroles are shown as filled circles. Hydrothermal and magmatic gases fields are highlighted in grey. Transition of deep-to-shallow degassing is shown as long black arrows. Classification of gases and limits of compositional fields for **(C)** diagram were adopted from Lages et al. (2019). S_t correspond to to SO_2+H_2S.

sec (which would correspond to 3,123 t/d). These observations were carried out in stormy and gusty conditions (wind speeds of up to 17 m/sec) during the passage of a low-pressure frontal system causing air pressure to drop by 10 hPa in 12 h (9:00–21:00) which may have enforced gas release on that day, and thus these emission rates may be considered as exceptionally high and likely not representative in the long-term. As to not overrate the measurements of November 27, we consider the median SO_2 emission rate of 538 t/d of the November 2012 campaign as representative of this period. Lopez et al. (2018) present data on 22 November 2014 based on UV camera and DOAS measurements, with an overall SO_2 emission rate of 604 ± 296 t/d. Although the SO_2 emission rate in November 2014 probably was slightly higher than November 2012, the high standard deviation and high error reported (±50%; Lopez et al., 2018) make it unclear whether this is related to increasing of degassing caused by rising of deep magmatic volatiles. Our UV camera data (Table 5) show clearly an increasing of SO_2 emission rate on 1 November 2018 and 17 January 2019 (786 ± 40 and 726 ± 74 t/d) (Figure 6) in comparison with May 2018 (282 ± 20 t/d), decreasing subsequently on 21 November 2019 (359 ± 29 t/d) (Figures 5, 6). These data show high stability (low standard deviation) and lower errors (−19 and +17%; Table 2) compared with Tamburello et al. (2014); Lopez et al. (2018) data, which can be considered as highly reliable. This behavior is compatible with the changes observed in the fumarolic gas composition, where the most magmatic signature of gas is coincident with the highest SO_2 emission rates in November 2018 and January 2019. Consequently, the increase of SO_2 emission rates could be explained by rising of magmatic volatiles, which caused a decrease of scrubbing, as argued in the previous section. The decrease of SO_2 emission rate in November 2019 is also coincident with the returning of the fumarolic gas composition

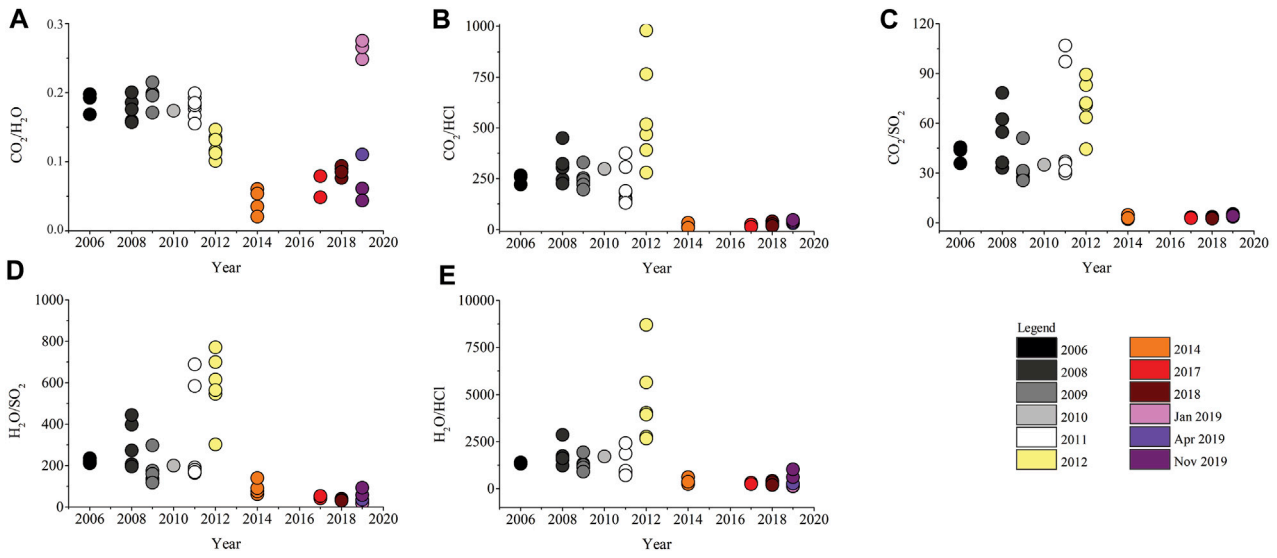

FIGURE 4
Gas ratios of Lastarria volcano fumarolic discharges **(A)** CO_2/H_2O; **(B)** CO_2/HCl; **(C)** CO_2/SO_2; **(D)** H_2O/SO_2; **(E)** H_2O/HCl. Only fumaroles with temperatures >120°C were considered.

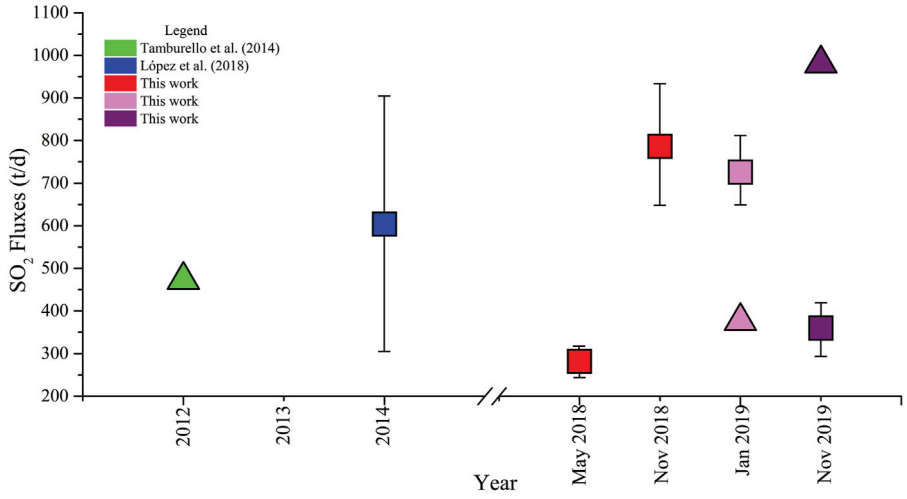

FIGURE 5
SO_2 emission rates (t/d) of Lastarria volcano during the period 2012–2019. Filled squares correspond to UV camera measurements (except Lopez et al., 2018, which was calculated on the base of UV camera and DOAS data), filled triangles correspond to DOAS measurements. Moreover, SO_2 emission rates obtained by Tamburello et al. (2014), in this work we merely consider the DOAS data of 28 November 2012. SO_2 emission rates from UV camera correspond to the Total SO_2 flux column from the Table 5, whereas SO_2 emission rates from our DOAS instruments correspond to the overall emission rate among measured days. Root mean square (RMS) obtained from UV camera measurements are shown as error bars.

to values of 2017. This decrease led to an increase of magmatic gas scrubbing and, consequently, a partial recovery of the hydrothermal system, as was previously discussed. We have not considered in this analysis the DOAS data from January and November 2019, because the scanning was done in a geometry not able to cover the total of the plume during January 2019, which produced an underestimation of the SO_2 emission rate. In the case of measurements carried out in November 2019, the overestimation of the emission rates is also related to the scanning geometry, where semi-horizontal scanning covered an "excess" of plume.

5.3 Volatile budgets from emission rates of main gas species

We have calculated the volatile budgets combining the emission rates of main species (H_2O, CO_2, SO_2, H_2S, and HCl; Table 6) for four different periods (November 2014, November 2018, January and November 2019), considering the species measured by direct sampling (Table 4). We have not combined our direct sampling data with SO_2 emission rates from Tamburello et al. (2014) due to large differences between our gas composition (hydrothermal-

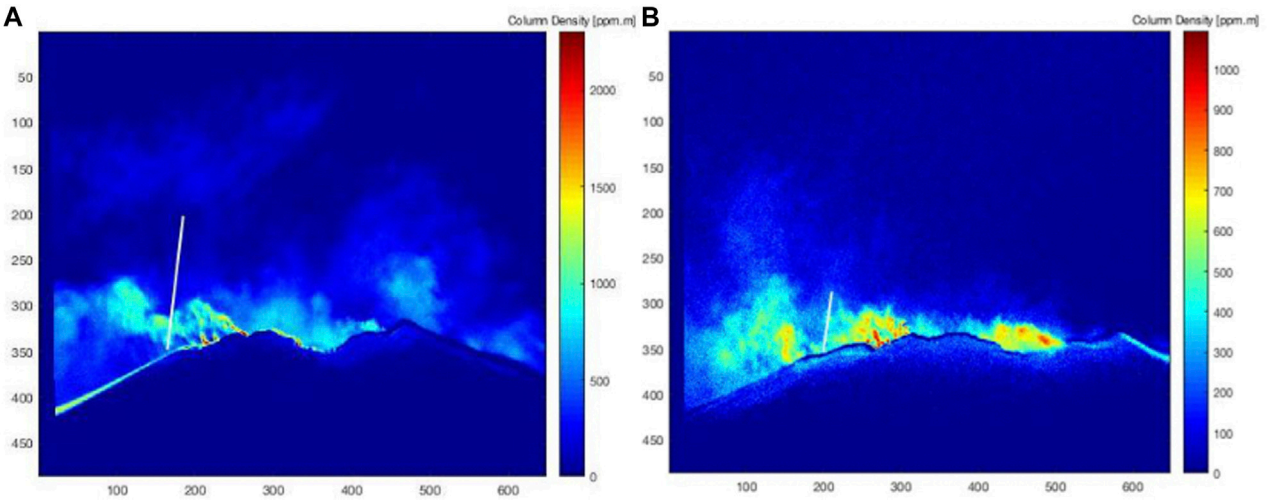

FIGURE 6
Images obtained with the PiCam UV Camera of Lastarria volcano gas plume, indicating the total SO_2 emission rates obtained from the four fumarolic fields. **(A)** 17 January 2019; **(B)** 21 November 2019. The white lines correspond to cross-plume profiles along which Integrated Column Amount (ICA) have been determined. The color bar displays column density in ppm•m.

dominated) and that reported during late November 2012, which show magmatic-dominated composition. Consequently, here we assume that the enhanced SO_2 emission rates which were measured during late November 2012 were related to the magmatic signature. The volatile budget of November 2014 averaged at 16,804 t/d (with a minimum of 8,402 t/d and maximum 25,206 t/d), which is close to that calculated by Lopez et al. (2018) for the same date (average 12,401 t/d), and the budget calculated for November 2012 (13,480 t/d; Tamburello et al., 2014). Lopez et al. (2018) present large differences between minimum and maximum emission rates in their work—3,579 and 38,311 t/d, respectively—whereas in our case the differences are more restricted, with a minimum flux of 8,402 t/d and a maximum of 25,206 t/d. Lopez et al. (2018) calculated the volatile fluxes including the variations in the SO_2 emission rates and the changes in the gas compositions, whereas in our case, we used the average of the gas composition and the SO_2 emission rate average and their related RMS error. We consider our data more reliable due the very low variability of the SO_2 emission rates, and because our gas composition was standardized by the same sampling and analyzing methods, in the last case even using the same laboratory. On the contrary, Lopez et al. (2018) combined data from different direct sampling methods applying analyzing methods from different laboratories. The volatile budget decreased in November 2018 and January 2019 to 9,773 and 7,017 t/d, respectively, and in November 2019 it further increased subtly to 8,594 t/d. Here we have considered only our UV camera data, due to the under and overestimation observed for our DOAS data in January and November 2019, and discussed in the Section 5.2. The same pattern was followed by H_2O and H_2S, which is compatible with a progressive depletion of the hydrothermal system. On the contrary, CO_2 emission rates increase up to January 2019 when their highest values were reached, descending again in November 2019. The progressive increase of CO_2 emission rates could be related to the incorporation of deep magmatic volatiles, similar to the trend in direct sampling data.

In the regional context of the CVZA, Ubinas and Sabancaya volcanoes presented average total volatile fluxes of 23,898 and 5,469 t/d respectively, whereas average CO_2 and SO_2 emission rates ranged 1,222–1,366 and 988–1,325 t/d, respectively (both in November 2015; Moussallam et al., 2017). In the case of Ubinas volcano, the measurements were carried out during an eruptive period, and in the case of Sabancaya measurements were a few months before the beginning of a new eruptive cycle. According to Tamburello et al. (2014), Lascar volcano had a total flux of 6,517 t/d, while CO_2 and SO_2 emission rates were 534 and 554 t/d, measurements carried out during a passive degassing period without eruptive activity involved. Lastarria volcano average total fluxes varied in a range of 7,017–16,804 t/d, CO_2 emission rates from 921 to 2,425 t/d, and SO_2 emission rates between 359 and 786 t/d, making Lastarria volcano one of the most strongly degassing volcanoes of the CVZA, especially in the case of CO_2.

5.4 Relationship between the degassing and ground deformation

5.4.1 A revision of the previous mechanisms

Several studies have shown changes in the deformation rates of the large-scale deformation area (Lazufre), with an initial rate of 1 cm/yr in the period 1998–2003 (Pritchard and Simons, 2002), changing to 2.5–3 cm/yr for 2003–2010 (Froger et al., 2007; Ruch et al., 2008; Anderssohn et al., 2009; Ruch et al., 2009; Pearse and Lundgren, 2013), decreasing and stabilizing at ~1.5 cm/yr between 2011 and 2016 (Henderson et al., 2017) (Figure 7). In the case of the small-scale deformation area (Lastarria volcano), a deformation rate of ~9 mm/yr was detected between 2003 and 2008 (Froger et al., 2007; Ruch et al., 2009) (Figure 7). No studies have been carried out

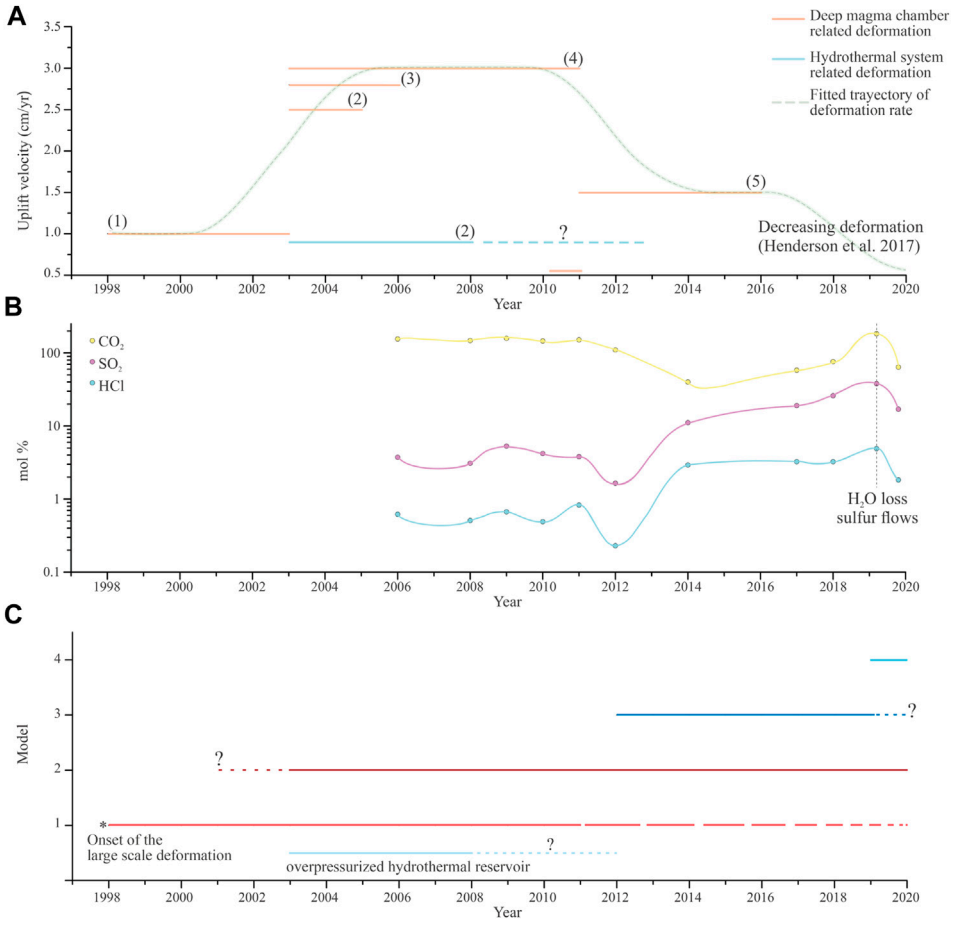

FIGURE 7
Time series of **(A)** ground deformation data, **(B)** direct sampling degassing data, and **(C)** the sequence of mechanisms that explain degassing/deformation processes. In the diagrams **(A)** the orange lines correspond to the deformation related to the deep magma chamber, the blue one related to the shallow hydrothermal system deformation, and the green short-dashed line corresponds to a fitted possible trajectory of the deformation rate 1) Pritchard and Simons (2002), 2) Froger et al. (2007), 3) Ruch et al. (2008), 4) Pritchard et al. (2018), and 5) Henderson et al. (2017). In **(B)**, the black short-dashed line marks the occurrence of sulfur flows.

to detect deformation in this area in the period 2008–2014, whilst no deformation has been observed in this area after 2014 (Thomas Walter, pers. comm.). If a temporal comparison between ground-deformation and degassing data is performed (Figure 7), it is clear that a correlation exists between both processes. In order to better understand the possible linkage between both processes, we invoke the mechanisms proposed by Lopez et al. (2018) to explain the changes in the gas composition of Lastarria volcano:

Mechanism 1: Decompression-induced magma ascent and degassing in the shallow crust.
Mechanism 2: Crystallization-induced degassing of a stalled magma body.
Mechanism 3: Acidification of the hydrothermal system.
Mechanism 4: Depletion of the hydrothermal system due to heating, changes in the local stress, and/or minimal precipitation.

The mechanism 1 could explain the initial deep large-scale deformation in the period 1998–2003, and then the increasing deformation between 2003 and 2010. Additionally, this process could explain the high concentrations of CO_2, and relative high CO_2/SO_2 ratio (Figure 4) in the fumarolic gas composition between 2006 and early November 2012. Lopez et al. (2018) modelled the degassing depths by use of melt compositions and volatile solubilities, suggesting that Lastarria degassing process is a combination of an open-system and close-system end members (with a 1 wt% exsolved volatiles), with an initial deep degassing at depth between 10.5 and 6.6 km in the period 2006–2009, followed by degassing in a broad range of depths between 9 and 1.2 km depth (2014). According to this, mechanism 1 is possible only if shallow small-scale deformation (2003–2008) is magma-related, and inflation also continued after 2008. However, the evidence of shallow deformation suggests that it is sourced <1 km depth and due to the overpressure of the hydrothermal system, and not to magma rising (e.g., Froger et al., 2007). In fact, Díaz et al. (2015); Spica et al. (2015) showed the presence of a hydrothermal system at similar depths (~1 km), while a shallow magma body is located at 3–6 km depth. Similarly, the mechanisms that explain the deep large-scale deformation show no evidence of magma rising (Pritchard and Simons, 2004; Froger et al., 2007; Ruch et al.,

2008; Anderssohn et al., 2009; Pearse and Lundgren, 2013; Pritchard et al., 2018). Mechanism 2 could explain the gas composition prior to late November 2012, and the deformation between 1998 and 2010, if the stalled magma corresponds to the deep reservoir (7–18 km depth; Stechern et al., 2017; Pritchard et al., 2018). In fact, thermally induced volatile exsolution produced by magma crystallization has been suggested as a possible explanation of the deep large-scale deformation (e.g., Froger et al., 2007). On the other hand, this mechanism explains the gas composition after late November 2012 only if the stalled magma is located in the shallow magma reservoir (3–6 km depth), which is compatible with a shallow degassing and high concentrations of SO_2 and HCl. Similar to mechanism 1, this mechanism cannot explain the depth and source of the shallow deformation in the period 2003–2008. Mechanism 3 provides explanation of the gas composition since late 2014, due to the increasing of acid species as SO_2, HCl, and HF. Lopez et al. (2018) suggest that no shallow deformation should be involved, consequently, the absence of shallow deformation, at least since 2008, is concordant with this mechanism. Mechanism 4 explains exclusively a single event, corresponding to the "excessive" loss of water vapor observed during January 2019, which was accompanied by the emission of sulfur flows. The heating of the hydrothermal system and the changes in local stress are plausible processes, in the first case by ascent of volatiles related to a deep magma chamber and/or increase of gas flux, while in the last, Ruch et al. (2009) have proposed changes in the local stress as a process that can explain the shallow small-scale deformation at Lastarria in the period 2003–2008. The minimal precipitation can be ruled out since Lastarria is located in a hyper arid environment, and lack of precipitation is permanent, not an exception. Lopez et al. (2018) suggest that mechanisms 1 and 2 fit better to explain the observed changes in the gas composition and deformation data. However, considering that Lopez et al. (2018) included only the early years of changes (2 years) in the degassing process, several uncertainties were still present. Here we show that the four mechanisms worked as a continuous and linked process, where the mechanisms 1 and 2 explain the linkage between deformation and degassing processes, encompassing changes through the years, and how both triggered the mechanisms 3 and 4 (Figures 7, 8).

5.4.2 Deep magma chamber pressurized by volatile exsolution (1998–2020)

According to Pritchard et al. (2018), the deep large-scale deformation observed since 1998 and currently ongoing in the Lazufre area, occurs due to exsolved volatiles from a partial melting and temporally trapped at relative deep levels (>10 km) that cause pressurization of a deep magma chamber. Following Pritchard et al. (2018), and assuming that volatiles are originated exclusively from the deep magma chamber, we can expect that the gas composition of fumarolic discharges is dominated by water vapor and CO_2. We observed gas compositions corresponding to hydrothermally-dominated fluids between 2006 and early November 2012. Although there is no information about fluid composition before 2006, if we assume that the hydrothermally-dominated composition was constant since 1998, when the deformation started, the hypothesis of a deep magma chamber pressurized by exsolution of volatiles from a melt and temporally trapped at relative deep levels allows us to explain the initial deep large-deformation and the gas composition between 2006 and early November 2012. The increase of deformation rate up to 3 cm/yr in the period between 2003 and 2010 could be related to the maximum volatile exsolution, and consequently, the maximum pressure and deformation rate. As mentioned previously, Lopez et al. (2018) indicate that in the period 2006–2009 the degassing was sourced from a depth of 6.6–10.5 km, which is coincident with the location of the deep and large magma chamber (Figure 8A).

5.4.3 Crystallization-induced degassing (2001–2020) and pressurization of the hydrothermal system (2003-early November 2012)

In the period 2003–2008, the small and shallow (<1 km) deformation zone below Lastarria volcano was active, and was originally attributed to the pressurization of the hydrothermal system (Figure 8B; Froger et al., 2007). The gas composition in the same period was characterized by a hydrothermal signature, where water vapor and CO_2 were the most abundant species, which correlate with the interpretation of Froger et al. (2007). Although no information exists about further deformation at Lastarria volcano between 2008 and 2012, if we assume the shallow inflation process was continuous, and then finished during 2012, the changes in the gas composition observed since late November 2012 and discussed in the previous section, would be intimately linked with this shallow inflation, and consequently, related with major changes in the hydrothermal system. Ruch et al. (2009) propose that a stress changes in the wall of the reservoir (in this case a hydrothermal reservoir) may have caused linkage of pre-existing fractures, increasing rock permeability, and thus promoting the release of fluids to the atmosphere. Changes in the stress regime can be induced by the internal pressure exerted by the accumulation of volatiles (Heap et al., 2010). The original pressurized hydrothermal reservoir due to accumulation of volatiles then started to release higher volatile fluxes, decompressing the hydrothermal system, and consequently, stopping the shallow deformation. However, the changes in the gas composition since late November 2012 cannot be explained simply by the last reviewed processes. As was discussed in the previous sections, the gas composition between late November 2012 and November 2018 was characterized by a magmatic signature, with high concentrations of SO_2 and HCl, depleted in CO_2, and low H_2O/SO_2, CO_2/SO_2, and CO_2/HCl ratios (Figures 4, 7), suggesting an increase of magmatic degassing. These changes can be related to the degassing of a shallow magma chamber, which in the case of Lastarria volcano is located between 3 and 6 km (Díaz et al., 2015; Spica et al., 2015). Lopez et al. (2018) suggest that the crystallization-induced degassing of a stalled magma body can produce the fluid signature observed after November 2012. In this case, the rising of an "excess" of volatiles from a deep source could "reactivate" the shallow magma chamber (probably a cooler and more evolved magma), for example, inducing crystallization, forcing convection and, consequently, degassing. Evidence of an evolved and degassed shallow magma chamber below Lastarria volcano has been provided by Robidoux et al. (2020), according to the low R/Ra ratios measured in melt inclusions found in pyroclastic samples that are dated to late Holocene. Lopez et al. (2018) propose that magma rising is also responsible for the changes in gas composition after November 2012; although the rising of

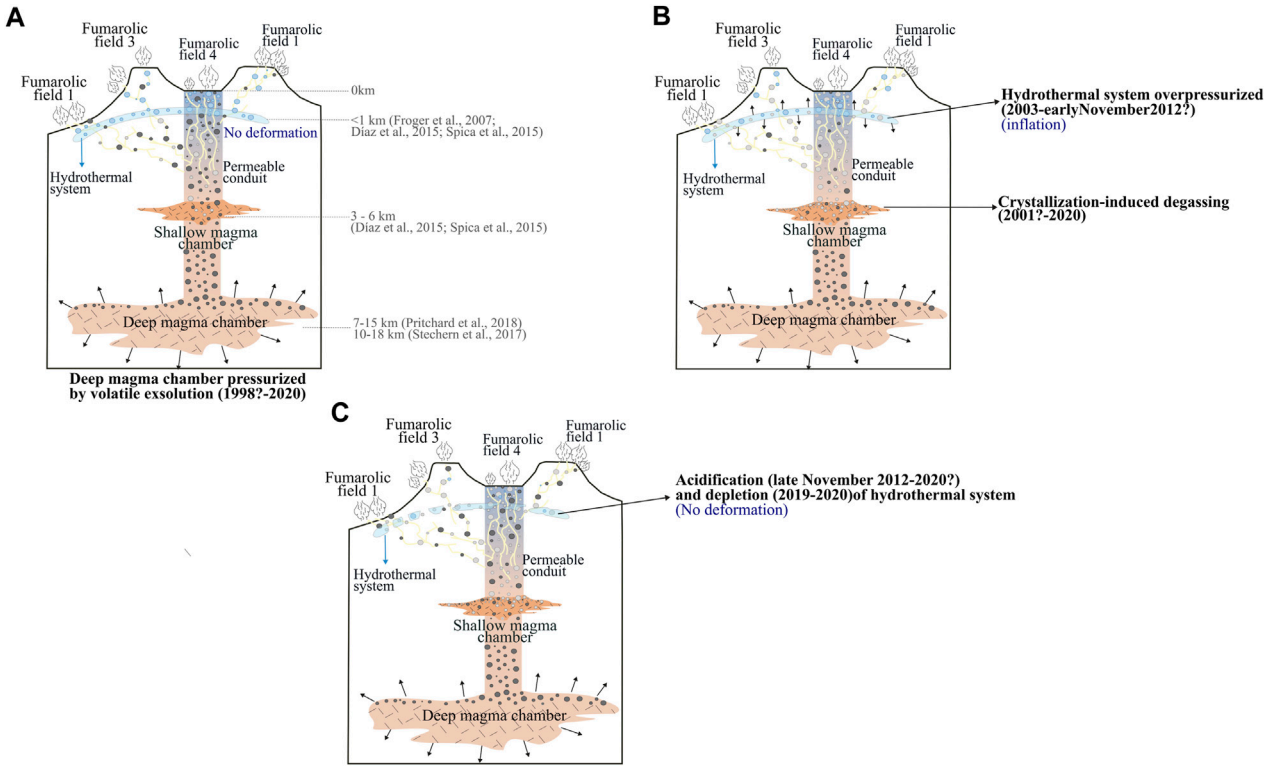

FIGURE 8
Conceptual sketches the sequence of mechanisms that explain the deformation and gas composition in the studied period. **(A)** Accumulation of deep-derived fluids (1998–2011), **(B)** Crystallization induced degassing in the shallow magma chamber (2003–2019) and over-pressurization of the shallow hydrothermal system (2003–2009). **(C)** Acidification and drying of hydrothermal system (2003–2019). Dark grey bubbles represent volatiles exsolved from a deep magmatic source, light grey bubbles correspond to volatiles exsolved from a shallow magmatic source, and blue bubbles are volatiles from a boiling aquifer. Black arrows represent inflation of both magmatic and hydrothermal systems.

magma is a plausible explanation of these changes, we suggest that more evidence is necessary to confirm such. It is expected that crystallization induced degassing rather would produce deflation of the shallow magma chamber, whereas magma rising, which could finish in the replenishment of the shallow magma chamber, would produce inflation. However, no deformation related to the shallow magma chamber has been observed throughout the study period. According to Girona et al. (2014), passive degassing may reduce the pressure of shallow magma chambers in only a few months to years. Considering that no eruptions have been involved during this period, and the degassing has been only passive, no deformation can be expected for both processes. Considering that the deformation started at least during 1998, the ascent of "excess" volatiles from a deep source should be a continuous process which started previously. Further, we hypothesize that the crystallization-induced degassing of a stalled magma (Figure 8B) should have started upon gradual cooling of the previously heated magma body a few months or years after large-scale deformation began. Consequently, the over-pressure of the hydrothermal system, which produced the shallow deformation, could be induced by the increasing of volatile flux from the shallow magma chamber. Following Ruch et al. (2009), changes in the stress field of the hydrothermal reservoir caused the release of fluids to the atmosphere, which as we can show were dominated by fluids enriched in magmatic compounds degassed from a shallow magma chamber.

5.4.4 Acidification (late November 2012–2020) and depletion (2019–2020) of the hydrothermal system

As consequence, the "excessive" release of acid gases since late November 2012, produced changes in the hydrothermal reservoir, including its acidification. The acidification of the hydrothermal system (Figure 8C) has been a continuous process until November 2019. Another consequence of the increase of magmatic volatile fluxes (as observed in November 2018 and January 2019; Sections 5.2, 5.3), is the depletion of the hydrothermal system (Figure 8C), caused by an intense vaporization of the boiling aquifer, which could lead to the total consumption of parts of the aquifer. Although a depletion of the hydrothermal system could produce a shallow deflation, in this case the extension seems to be limited to only small areas of the fumarolic fields.

6 Conclusion

Lastarria volcano has undergone changes in its fumarolic gas composition in the last 8 years, following a period of both, large scale deformation in the Lazufre area at least since 1998 and

localized small-scale deformation in the hydrothermal fields of Lastarria volcano since 2003, respectively. The present study has shown that a sequence of linked processes explains the changes in both degassing and deformation data, starting in 1998 with the accumulation of volatiles causing pressurization of a deep magma chamber, which in turn produced a large zone of uplift. The rising of volatiles from a deep magma chamber later probably induced the "reactivation" of a shallow magmatic chamber. Subsequent cooling of previously formed partial melts eventually led to the crystallization-induced degassing of this shallow stalled magma. The volatiles released from the shallow and deep magma body in 2003 started to accumulate below the partially sealed hydrothermal system, which explains its pressurization and, consequently, the shallow-sourced ground inflation until 2008. During this period and until mid-November 2012 the superficial degassing was dominated by hydrothermal fluids, with H_2O and CO_2 as the most abundant species. Volatiles related to the degassing of the shallow magma chamber started to be emitted to the atmosphere since late November 2012, most likely as a response to changes in the local stress field of the hydrothermal reservoir, which re-established pre-existing degassing paths. This enhancement in degassing activity allowed for decompression of the hydrothermal system, which explains why shallow inflation at Lastarria volcano was not detected in the following years. The fluids emitted since late November 2012 presented a typical magmatic signature related to a shallow degassing process (high concentrations of SO_2 and HCl, partially depleted in CO_2, and low H_2O/SO_2, CO_2/SO_2, and CO_2/HCl ratios). These changes may indicate the acidification and depletion of the hydrothermal system, which is why acid gas species were less scrubbed in the hydrothermal environment due to an increase of magmatic fluid fluxes, and enhanced vaporization of water from the boiling aquifer. In this work we have shown that a long-term surveillance of the chemistry of fluid discharges provides valuable insights into underlying magmatic/volcanic processes, and consequently, for forecasting the occurrence of future eruptions.

Data availability statement

The original contributions presented in the study are included in the article/supplementary material, further inquiries can be directed to the corresponding author.

Author contributions

SL measured and process UV camera data, carried out direct sampling campaigns, conceptualized, and wrote the manuscript; FA carried out direct sampling campaigns, conceptualized, and wrote the manuscript; MI and FT carried out direct sampling campaigns and wrote the manuscript; TW built the UV camera and one of the DOAS, wrote the manuscript, and reviewed the English; SB carried out DOAS measurements and processed the data, and wrote the manuscript; CG carried out DOAS measurements and processed the data; TP and AM built the UV camera and one of the DOAS and reviewed the English.

Funding

SL was funded by Beca Doctorado Nacional ANID-PCHA/Doctorado Nacional/21160276 (Agencia Nacional de Investigación y Desarrollo-ANID). This work was partially funded by the ANID Iniciativa Milenio-ICN2021_038 "Instituto Milenio de Investigación en Riesgo Volcánico—Ckelar Volcanes", ANID-FONDAP 15110017 project "Centro de Investigación para la Gestión Integrada del Riesgo de Desastres, CIGIDEN", FIC-R BIP 30488832-0 project "Mitigación de los Riesgos Asociados a Procesos Volcánicos en la Región de Antofagasta", funded by the Antofagasta Regional Government, National Research Funding Competition FONDECYT Regular 2021 Code 1211220, and Special Project 2017 (277/2017) Vicerrectoría de Investigación y Desarrollo Tecnológico, Universidad Católica del Norte, "Procesos que controlan el balance de masa en volcanes activos del Norte de Chile".

Conflict of interest

The authors declare that the research was conducted in the absence of any commercial or financial relationships that could be construed as a potential conflict of interest.

Publisher's note

All claims expressed in this article are solely those of the authors and do not necessarily represent those of their affiliated organizations, or those of the publisher, the editors and the reviewers. Any product that may be evaluated in this article, or claim that may be made by its manufacturer, is not guaranteed or endorsed by the publisher.

References

Aguilera, F., Layana, S., Rojas, F., Arratia, P., Wilkes, T. C., González, C., et al. (2020). First measurements of gas flux with a low-cost smartphone sensor-based UV camera on the volcanoes of northern Chile. *Remote Sens.* 12 (13), 2122.

Aguilera, F., Tassi, F., Darrah, T., Moune, S., and Vaselli, O. (2012). Geochemical model of a magmatic–hydrothermal system at the Lastarria volcano, northern Chile. *Bull. Volcanol.* 74 (1), 119–134. doi:10.1007/s00445-011-0489-5

Aiuppa, A., Moretti, R., Federico, C., Giudice, G., Gurrieri, S., Liuzzo, M., et al. (2007). Forecasting Etna eruptions by real-time observation of volcanic gas composition. *Geology* 35 (12), 1115–1118. doi:10.1130/g24149a.1

Anderssohn, J., Motagh, M., Walter, T. R., Rosenau, M., Kaufmann, H., and Oncken, O. (2009). Surface deformation time series and source modeling for a volcanic complex system based on satellite wide swath and image mode interferometry: The Lazufre system, central Andes. *Remote Sens. Environ.* 113 (10), 2062–2075. doi:10.1016/j.rse.2009.05.004

Bell, A. F., Naylor, M., Hernandez, S., Main, I. G., Gaunt, H. E., Mothes, P., et al. (2018). Volcanic eruption forecasts from accelerating rates of drumbeat long-period earthquakes. *Geophys. Res. Lett.* 45, 1339–1348. doi:10.1002/2017gl076429

Biggs, J., Ebmeier, S. K., Aspinall, W. P., Lu, Z., Pritchard, M. E., Sparks, R. S. J., et al. (2014). Global link between deformation and volcanic eruption quantified by satellite imagery. *Nat. Commun.* 5 (1), 3471–3477. doi:10.1038/ncomms4471

Calahorrano-Di Patre, A., Williams-Jones, G., Battaglia, M., Mothes, P., Gaunt, E., Zurek, J., et al. (2019). Hydrothermal fluid migration due to interaction with shallow magma: Insights from gravity changes before and after the 2015 eruption of Cotopaxi volcano, Ecuador. *J. Volcanol. Geotherm. Res.* 387, 106667. doi:10.1016/j.jvolgeores.2019.106667

Cameron, C. E., Prejean, S. G., Coombs, M. L., Wallace, K. L., Power, J. A., and Roman, D. C. (2018). Alaska volcano observatory alert and forecasting timeliness: 1989-2017. *Front. Earth Sci.* 6, 86. doi:10.3389/feart.2018.00086

Campion, R., Delgado-Granados, H., and Mori, T. (2015). Image-based correction of the light dilution effect for SO_2 camera measurements. *J. Volcanol. Geotherm. Res.* 300, 48–57. doi:10.1016/j.jvolgeores.2015.01.004

Casertano, L. (1963). General characteristics of active Andean volcanoes and a summary of their activities during recent centuries. *Bull. Seismol. Soc. Am.* 53 (6), 1415–1433. doi:10.1785/bssa0530061415

Caudron, C., Girona, T., Jolly, A., Christenson, B., Kane Savage, M., Carniel, R., et al. (2021). A quest for unrest in multiparameter observations at Whakaari/White Island volcano, New Zealand 2007–2018. *Earth Planets Space* 73, 195. doi:10.1186/s40623-021-01506-0

Chance, K., and Kurucz, R. L. (2010). An improved high-resolution solar reference spectrum for earth's atmosphere measurements in the ultraviolet, visible, and near infrared. *J. quantitative Spectrosc. Radiat. Transf.* 111 (9), 1289–1295. doi:10.1016/j.jqsrt.2010.01.036

Chance, K. V., and Spurr, R. J. (1997). Ring effect studies: Rayleigh scattering, including molecular parameters for rotational Raman scattering, and the fraunhofer spectrum. *Appl. Opt.* 36 (21), 5224–5230. doi:10.1364/ao.36.005224

Conde, V., Nilsson, D., Galle, B., Cartagena, R., and Muñoz, A. (2014). A rapid deployment instrument network for temporarily monitoring volcanic SO₂ emissions – A case study from telica volcano. *Geoscientific Instrum. Methods Data Syst.* 3 (2), 127–134. doi:10.5194/gi-3-127-2014

Coppola, D., Valade, S., Masias, P., Laiolo, M., Massimetti, F., Campus, A., et al. (2022). Shallow magma convection evidenced by excess degassing and thermal radiation during the dome-forming Sabancaya eruption (2012–2020). *Bull. Volcanol.* 84 (2), 16–19. doi:10.1007/s00445-022-01523-1

Dempsey, D., Cronin, S., Mei, S., and Kempa-Liehr, A. (2020). Automatic precursor recognition and real-time forecasting of sudden explosive volcanic eruptions at Whakaari, New Zealand. *Nat. Commun.* 11 (1), 3562–3568. doi:10.1038/s41467-020-17375-2

Díaz, D., Heise, W., and Zamudio, F. (2015). Three-dimensional resistivity image of the magmatic system beneath Lastarria volcano and evidence for magmatic intrusion in the back arc (northern Chile). *Geophys. Res. Lett.* 42 (13), 5212–5218. doi:10.1002/2015gl064426

Ebmeier, S. K., Andrews, B. J., Araya, M. C., Arnold, D. W. D., Biggs, J., Cooper, C., et al. (2018). Synthesis of global satellite observations of magmatic and volcanic deformation: Implications for volcano monitoring and the lateral extent of magmatic domains. *J. Appl. Volcanol.* 7, 2. doi:10.1186/s13617-018-0071-3

Fischer, T., Giggenbach, W., Sano, Y., and Williams, S. (1998). Fluxes and sources of volatiles discharged from Kudryavy, a subduction zone volcano, Kurile Islands. *Earth Planet. Sci. Lett.* 160, 81–96. doi:10.1016/s0012-821x(98)00086-7

Froger, J. L., Rémy, D., Bonvalot, S., and Legrand, D. (2007). Two scales of inflation at Lastarria-Cordon del Azufre volcanic complex, central Andes, revealed from ASAR-ENVISAT interferometric data. *Earth Planet. Sci. Lett.* 255 (1-2), 148–163. doi:10.1016/j.epsl.2006.12.012

Galetto, F., Acocella, V., Hooper, A., and Bagnardi, M. (2022). Eruption at basaltic calderas forecast by magma flow rate. *Nat. Geosci.* 15, 580–584. doi:10.1038/s41561-022-00960-z

Galetto, F., Bagnardi, M., Acocella, V., and Hooper, A. (2019). Noneruptive unrest at the Caldera of Alcedo Volcano (Galápagos Islands) revealed by InSAR data and geodetic modeling. *J. Geophys. Res. Solid Earth* 124 (4), 3365–3381. doi:10.1029/2018jb017103

Galle, B., Johansson, M., Rivera, C., Zhang, Y., Kihlman, M., Kern, C., et al. (2010). Network for observation of volcanic and atmospheric change (NOVAC)—a global network for volcanic gas monitoring: Network layout and instrument description. *J. Geophys. Res. Atmos.* 115 (D5), D05304. doi:10.1029/2009jd011823

Girona, T., Costa, F., Newhall, C., and Taisne, B. (2014). On depressurization of volcanic magma reservoirs by passive degassing. *J. Geophys. Res. Solid Earth* 119 (12), 8667–8687. doi:10.1002/2014jb011368

González-Ferrán, O. (1995). *Volcanes de Chile*. Santiago: Instituto Geográfico Militar.

Guo, Q., Xu, C., Wen, Y., Liu, Y., and Xu, G. (2019). The 2017 noneruptive unrest at the Caldera of Cerro Azul Volcano (Galápagos Islands) revealed by InSAR observations and geodetic modelling. *Remote Sens.* 11 (17), 1992. doi:10.3390/rs11171992

Heap, M., Faulkner, D., Meredith, P., and Vinciguerra, S. (2010). Elastic moduli evolution and accompanying stress changes with increasing crack damage: Implications for stress changes around fault zones and volcanoes during deformation. *Geophys. J. Int.* 183, 225–236. doi:10.1111/j.1365-246x.2010.04726.x

Henderson, S. T., Delgado, F., Elliott, J., Pritchard, M. E., and Lundgren, P. R. (2017). Decelerating uplift at Lazufre volcanic center, Central Andes, from AD 2010 to 2016, and implications for geodetic models. *Geosphere* 13 (5), 1489–1505. doi:10.1130/ges01441.1

Ilanko, T., Pering, T. D., Wilkes, T. C., Choquehuayta, F. E. A., Kern, C., Moreno, A. D., et al. (2019). Degassing at Sabancaya volcano measured by UV cameras and the NOVAC network. *Volcanica* 2 (2), 239–252. doi:10.30909/vol.02.02.239252

Kantzas, E. P., McGonigle, A. J., Tamburello, G., Aiuppa, A., and Bryant, R. G. (2010). Protocols for UV camera volcanic SO_2 measurements. *J. Volcanol. Geotherm. Res.* 194 (1-3), 55–60. doi:10.1016/j.jvolgeores.2010.05.003

Klein, A., Lübcke, P., Bobrowski, N., Kuhn, J., and Platt, U. (2017). Plume propagation direction determination with SO₂ cameras. *Atmos. Meas. Tech.* 10 (3), 979–987. doi:10.5194/amt-10-979-2017

Lages, J., Chacón, Z., Burbano, V., Meza, L., Arellano, S., Liuzzo, M., et al. (2019). Volcanic gas emissions along the Colombian arc segment of the northern volcanic zone (CAS-NVZ): Implications for volcano monitoring and volatile budget of the andean volcanic belt. *Geochem. Geophys. Geosystems* 20 (11), 5057–5081. doi:10.1029/2019gc008573

Layana, S., Aguilera, F., Rojo, G., Vergara, Á., Salazar, P., Quispe, J., et al. (2020). Volcanic Anomalies monitoring System (VOLCANOMS), a low-cost volcanic monitoring system based on Landsat images. *Remote Sens.* 12 (10), 1589. doi:10.3390/rs12101589

Lewicki, J., Fischer, T., and Williams, S. (2000). Chemical and isotopic compositions of fluids at cumbal volcano, Colombia: Evidence for magmatic contribution. *Bull. Volcanol.* 62, 347–361. doi:10.1007/s004450000100

Lopez, T., Aguilera, F., Tassi, F., De Moor, J. M., Bobrowski, N., Aiuppa, A., et al. (2018). New insights into the magmatic-hydrothermal system and volatile budget of Lastarria volcano, Chile: Integrated results from the 2014 IAVCEI CCVG 12th Volcanic Gas Workshop. *Geosphere* 14 (3), 983–1007. doi:10.1130/ges01495.1

López, T., Ushakov, S., Izbekov, P., Tassi, F., Cahill, C., Neill, O., et al. (2013). Constraints on magma processes, subsurface conditions, and total volatile flux at Bezymianny Volcano in 2007–2010 from direct and remote volcanic gas measurements. *J. Volcanol. Geotherm. Res.* 263, 92–107. doi:10.1016/j.jvolgeores.2012.10.015

McGonigle, A. J. S., Hilton, D. R., Fischer, T. P., and Oppenheimer, C. (2005). Plume velocity determination for volcanic SO_2 flux measurements. *Geophys. Res. Lett.* 32 (11). doi:10.1029/2005GL022470

Montegrossi, G., Tassi, F., Vaselli, O., Buccianti, A., and Garofalo, K. (2001). Sulfur species in volcanic gases. *Anal. Chem.* 73 (15), 3709–3715. doi:10.1021/ac001429b

Moussallam, Y., Tamburello, G., Peters, N., Apaza, F., Schipper, C. I., Curtis, A., et al. (2017). Volcanic gas emissions and degassing dynamics at Ubinas and Sabancaya volcanoes; implications for the volatile budget of the central volcanic zone. *J. Volcanol. Geotherm. Res.* 343, 181–191. doi:10.1016/j.jvolgeores.2017.06.027

Naranjo, J. A. (1992). Chemistry and petrological evolution of the Lastarria volcanic complex in the north Chilean Andes. *Geol. Mag.* 129 (6), 723–740. doi:10.1017/s0016756800008451

Naranjo, J. (2010). *Geología del Complejo Volcánico Lastarria, Región de Antofagasta: Servicio Nacional de Geología y Minería Carta Geológica de Chile*, 123.

Pearse, J., and Lundgren, P. (2013). Source model of deformation at Lazufre volcanic center, central Andes, constrained by InSAR time series. *Geophys. Res. Lett.* 40 (6), 1059–1064. doi:10.1002/grl.50276

Platt, U., and Stutz, J. (2008). "Differential absorption spectroscopy," in *Differential optical absorption spectroscopy* (Berlin, Heidelberg: Springer), 135–174.

Pritchard, M., de Silva, S., Michelfelder, G., Zandt, G., McNutt, S., Gottsmann, J., et al. (2018). Synthesis: Plutons: Investigating the relationship between pluton growth and volcanism in the central Andes. *Geosphere* 14 (3), 954–982. doi:10.1130/ges01578.1

Pritchard, M., and Simons, M. (2002). A satellite geodetic survey of large-scale deformation of volcanic centres in the central Andes. *Nature* 418 (6894), 167–171. doi:10.1038/nature00872

Pritchard, M., and Simons, M. (2004). An InSAR-based survey of volcanic deformation in the central Andes. *Geochem. Geophys. Geosystems* 5 (2). doi:10.1029/2003gc000610

Reath, K., Pritchard, M., Poland, M., Delgado, F., Carn, S., Coppola, D., et al. (2019). Thermal, deformation, and degassing remote sensing time series (CE 2000–2017) at the 47 most active volcanoes in Latin America: Implications for volcanic systems. *J. Geophys. Res. Solid Earth* 124 (1), 195–218. doi:10.1029/2018jb016199

Robidoux, P., Rizzo, A. L., Aguilera, F., Aiuppa, A., Artale, M., Liuzzo, M., et al. (2020). Petrological and noble gas features of Lascar and Lastarria volcanoes (Chile): Inferences on plumbing systems and mantle characteristics. *Lithos* 370, 105615. doi:10.1016/j.lithos.2020.105615

Roman, D. C., and Cashman, K. V. (2018). Top-down precursory volcanic seismicity: Implications for 'stealth' magma ascent and long-term eruption forecasting. *Front. Earth Sci.* 6, 124. doi:10.3389/feart.2018.00124

Ruch, J., Anderssohn, J., Walter, T., and Motagh, M. (2008). Caldera-scale inflation of the Lazufre volcanic area, south America: Evidence from InSAR. *J. Volcanol. Geotherm. Res.* 174 (4), 337–344. doi:10.1016/j.jvolgeores.2008.03.009

Ruch, J., Manconi, A., Zeni, G., Solaro, G., Pepe, A., Shirzaei, M., et al. (2009). Stress transfer in the Lazufre volcanic area, central Andes. *Geophys. Res. Lett.* 36 (22), L22303. doi:10.1029/2009gl041276

Segall, P. (2013). Volcano deformation and eruption forecasting. *Geol. Soc. Lond. Spec. Publ.* 380 (1), 85–106. doi:10.1144/sp380.4

Spampinato, S., Langer, H., Messina, A., and Falsaperla, S. (2019). Short-term detection of volcanic unrest at Mt. Etna by means of a multi-station warning system. *Sci. Rep.* 9, 6506. doi:10.1038/s41598-019-42930-3

Spica, Z., Legrand, D., Iglesias, A., Walter, T., Heimann, S., Dahm, T., et al. (2015). Hydrothermal and magmatic reservoirs at Lazufre volcanic area, revealed by a high-resolution seismic noise tomography. *Earth Planet. Sci. Lett.* 421, 27–38. doi:10.1016/j.epsl.2015.03.042

Stechern, A., Just, T., Holtz, F., Blume-Oeste, M., and Namur, O. (2017). Decoding magma plumbing and geochemical evolution beneath the Lastarria volcanic complex (northern Chile)—evidence for multiple magma storage regions. *J. Volcanol. Geotherm. Res.* 338, 25–45. doi:10.1016/j.jvolgeores.2017.03.018

Tamburello, G., Hansteen, T. H., Bredemeyer, S., Aiuppa, A., and Tassi, F. (2014). Gas emissions from five volcanoes in northern Chile and implications for the volatiles budget of the Central Volcanic Zone. *Geophys. Res. Lett.* 41 (14), 4961–4969. doi:10.1002/2014gl060653

Tizzani, P., Battaglia, M., Castaldo, R., Pepe, A., Zeni, G., and Lanari, R. (2015). Magma and fluid migration at Yellowstone Caldera in the last three decades inferred from InSAR, leveling, and gravity measurements. *J. Geophys. Res. Solid Earth* 120 (4), 2627–2647. doi:10.1002/2014jb011502

Tizzani, P., Battaglia, M., Zeni, G., Atzori, S., Berardino, P., and Lanari, R. (2009). Uplift and magma intrusion at Long Valley caldera from InSAR and gravity measurements. *Geology* 37 (1), 63–66. doi:10.1130/g25318a.1

Vandaele, A., Simon, P., Guilmot, J., Carleer, M., and Colin, R. (1994). SO_2 absorption cross section measurement in the UV using a Fourier transform spectrometer. *J. Geophys. Res. Atmos.* 99 (D12), 25599–25605. doi:10.1029/94jd02187

Voigt, S., Orphal, J., Bogumil, K., and Burrows, J. (2001). The temperature dependence (203–293 K) of the absorption cross sections of O3 in the 230–850 nm region measured by Fourier-transform spectroscopy. *J. Photochem. Photobiol. A Chem.* 143 (1), 1–9. doi:10.1016/s1010-6030(01)00480-4

Wilkes, T. C., McGonigle, A. J., Pering, T. D., Taggart, A. J., White, B. S., Bryant, R. G., et al. (2016). Ultraviolet imaging with low cost smartphone sensors: development and application of a Raspberry Pi-based UV camera. *Sensors* 16 (10), 1649. doi:10.3390/s16101649

Wilkes, T., Pering, T., McGonigle, A., Tamburello, G., and Willmott, J. (2017). A low-cost smartphone sensor-based UV camera for volcanic SO_2 emission measurements. *Remote Sens.* 9 (1), 27. doi:10.3390/rs9010027

Williams-Jones, G., and Rymer, H. (2002). Detecting volcanic eruption precursors: A new method using gravity and deformation measurements. *J. Volcanol. Geotherm. Res.* 113 (3-4), 379–389. doi:10.1016/s0377-0273(01)00272-4

frontiers | Frontiers in Earth Science

TYPE Original Research
PUBLISHED 05 May 2023
DOI 10.3389/feart.2023.1088056

OPEN ACCESS

EDITED BY
Nick Varley,
University of Colima, Mexico

REVIEWED BY
Simon Carn,
Michigan Technological University,
United States
Felipe Aguilera,
Catholic University of the North, Chile

*CORRESPONDENCE
Christoph Kern,
ckern@usgs.gov

RECEIVED 03 November 2022
ACCEPTED 19 April 2023
PUBLISHED 05 May 2023

CITATION
Kern C and Kelly PJ (2023), Weak degassing from remote Alaska volcanoes characterized with a new airborne imaging DOAS instrument and a suite of *in situ* sensors.
Front. Earth Sci. 11:1088056.
doi: 10.3389/feart.2023.1088056

Weak degassing from remote Alaska volcanoes characterized with a new airborne imaging DOAS instrument and a suite of *in situ* sensors

Christoph Kern* and Peter J. Kelly

United States Geological Survey, Volcano Science Center, Vancouver, WA, United States

Gas emissions from volcanoes occur when volatile species exsolve from magmatic and hydrothermal systems and make their way to the surface. Measurements of emitted gases therefore provide insights into volcanic processes. On 16 July 2021, we made airborne measurements of weak gas plumes emitted from four remote Alaska volcanoes: Iliamna Volcano, Mount Douglas, Mount Martin, and Mount Mageik. Integrated into a small fixed-wing aircraft, a new Imaging Differential Optical Absorption Spectroscopy (DOAS) instrument was used to map the spatial extent of SO_2 plumes as they drifted downwind. Contrary to conventional Mobile DOAS instruments, which provide only a single viewing direction, the Imaging DOAS simultaneously measures SO_2 column density along 48 individual viewing directions oriented in a swath above or below the aircraft. Each of the individual measurements have a comparable precision and sensitivity to those obtained by conventional instruments. Together, they provide high resolution 2D imagery of the volcanic plumes and allow calculation of limited emission rate time series information. Although zenith-facing DOAS measurements achieve greater accuracy and are performed here, the application of the Imaging DOAS in a nadir-facing setup is also discussed and compared to satellite observations made in similar geometries. Also onboard the aircraft, a suite of electrochemical and optical sensors measured the relative abundances of the six major volcanic volatile species H_2O, CO_2, SO_2, H_2S, HCl, and HF as the aircraft passed through the plumes. Mean SO_2 emission rates of 90 $\pm$ 10, 20 $\pm$ 3, and 13 $\pm$ 3 t/d were measured at Iliamna Volcano, Mount Douglas, and Mount Martin, respectively. SO_2 emissions were below the DOAS detection limit at Mount Mageik but CO_2 and H_2S could be measured with the *in situ* sensors. The information gleaned from these measurements was used to assess and compare activity at these volcanoes, all of which were found to be in a state of background degassing but whose emissions pointed to different source conditions ranging from mixed magmatic-hydrothermal to purely hydrothermal in character. Additional measurements at Mount Spurr, Redoubt Volcano, and Augustine Volcano failed to detect the very weak gas concentrations downwind of these persistently degassing vents.

KEYWORDS

volcanic gases, DOAS, spectroscopy, remote sensing, volatiles, imaging, volcanic plumes, hydrothermal systems

Introduction

The state of Alaska is home to more than 130 volcanoes and volcanic fields, 54 of which have been active since 1700 CE (Cameron et al., 2022a), and hardly a year passes without an eruption (Cameron et al., 2022b). Most of these volcanoes are located along the Alaska-Aleutian arc where the northward-moving Pacific Plate is pushed beneath the North American Plate at a rate of ~6 cm per year (Syracuse and Abers, 2006). Although most of these volcanoes are in relatively remote locations, they can still pose significant hazards to aviation. More than 60,000 passengers can be expected to be traveling on commercial aircraft in the airspace downwind of Alaska's active volcanoes on a daily basis (Ewert et al., 2018). Explosive volcanic eruptions can produce ash clouds that, if flown through by jet aircraft, can cause engine damage or failure. Eruptions from volcanoes in the Cook Inlet (Mount Spurr, Redoubt Volcano, Iliamna Volcano, and Augustine Volcano) can have the most severe impacts as these are nearest to Anchorage, Alaska's largest population center and a major cargo airport hub (Figure 1). For example, a series of eruptions from Redoubt Volcano in 1989–1990 caused airport closures and airline cancellations in Anchorage and on the Kenai Peninsula (Casadevall, 1994), and disrupted air traffic as far away as Texas. Just 2 years later, in 1992, three eruptions of Mount Spurr's Crater Peak closed the Anchorage airport again and disrupted air traffic as far east as the eastern United States and Canada (Keith, 1995).

Due to these potential hazards, the United States Geological Survey's (USGS) Alaska Volcano Observatory (AVO) is tasked with monitoring Alaska's active volcanoes and providing timely information about volcanic activity to stakeholders and the public at large. For this purpose, AVO maintains a network of visual, geophysical, and geodetic monitoring instrumentation on many of the most active volcanoes in the region. However, the harsh environmental conditions and remote nature of many of the volcanoes make maintaining permanent monitoring infrastructure extremely challenging. AVO therefore relies heavily on campaign-type measurements and satellite remote sensing data to compliment observations from sensors on the ground and produce reliable information on volcanic events (Poland et al., 2020). Information on volcanic degassing, in particular, is currently obtained almost entirely through remote sensing observations or manual ground-based or airborne surveys, though efforts are underway to install limited continuous geochemical monitoring on volcanoes where such data are deemed particularly important for eruption forecasting and detection.

Anomalous gas emissions are often the first indicators of volcanic unrest, particularly at "open system" volcanoes at which volatiles exsolved from magma at depth can travel independently to the surface and degas to the atmosphere. Notable examples include the order-of-magnitude increase in sulfur dioxide (SO_2) emissions weeks before the 2005 eruption of Santa Ana volcano, El Salvador (Olmos et al., 2007), the anomalous carbon dioxide (CO_2) degassing identified ~6 months prior to the 2009 eruption of Redoubt Volcano, Alaska (Werner et al., 2013), and the increase in CO_2 degassing observed weeks to months before the deadly 2019 paroxysms at the ordinarily benign Stromboli volcano, Italy (Aiuppa et al., 2021). Pre-eruptive degassing occurs when magma ascends in a volcanic system, leading to a decrease in pressure and

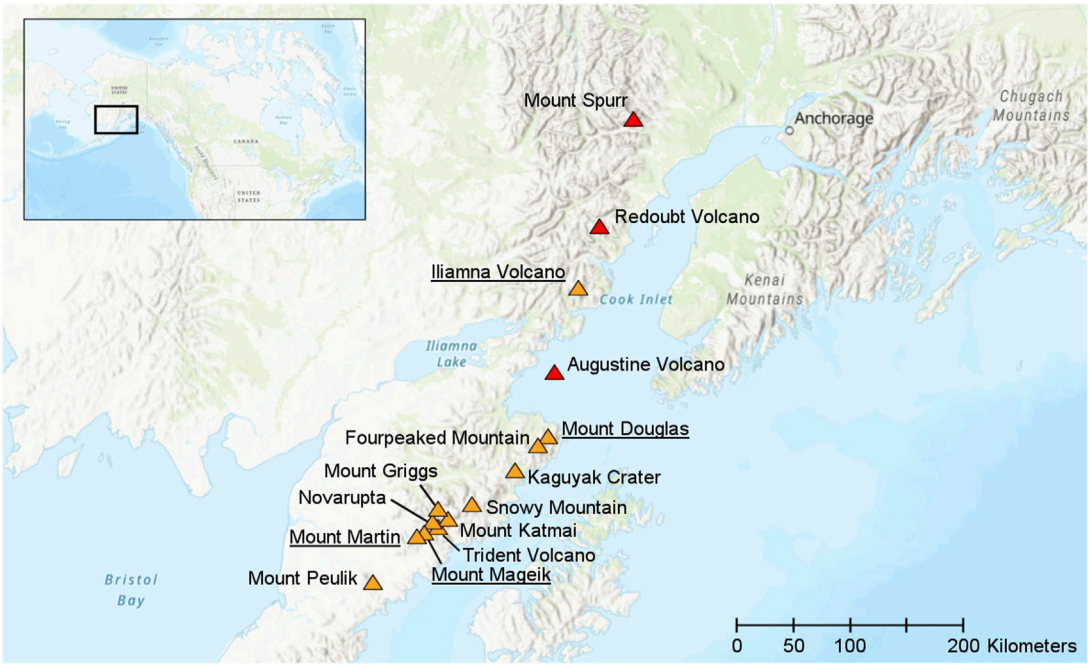

FIGURE 1
"High" (orange) and "Very High" (red) threat volcanoes of the Cook Inlet and northern Alaska Peninsula. Underlined names indicate volcanoes at which gas plumes could be detected on 16 July 2021 using our airborne gas monitoring instrumentation. Threat ranking according to Ewert et al. (2018). Base map from Esri (2022) and its licensors.

partitioning of dissolved volatile species to a separate fluid phase that can move upward toward the surface (Edmonds and Wallace, 2017). In such cases, the rate at which gases are emitted to the atmosphere, typically given in kg/s or metric tons per day (t/d), tracks the volume of rising magma to first order. Because volatile species have vastly different solubilities in melt, their exsolution occurs at different pressures/depths, with CO_2 typically being the first to exsolve at depths >10 km (Wallace et al., 2015), followed by sulfur and water vapor as the magma moves closer to the surface (Edmonds and Wallace, 2017; Werner C. et al., 2020). The relative abundance of these species in volcanic gas emissions therefore provides information on the depth from which they originate (Aiuppa et al., 2007; Burton et al., 2007; de Moor et al., 2016; Werner C. et al., 2020).

Due to their diagnostic utility, volcano observatories are increasingly interested in tracking volcanic gas emission rates and chemical compositions over time (Kern et al., 2022). In some cases, this is accomplished with geochemical monitoring stations permanently installed on active volcanoes. The most common continuous gas monitoring instruments are Scanning Differential Optical Absorption Spectrometers (Scanning DOAS, Galle et al., 2010; Arellano et al., 2021), which measure the SO_2 emission rate, and multi-GAS instruments (Aiuppa et al., 2005; Shinohara, 2005), which measure the relative abundance of the major volcanic gas species (H_2O, CO_2, SO_2, and H_2S). However, these instruments provide only limited spatial information, making it difficult to study processes like plume heterogeneity, dynamics, or chemical evolution. Additional spatial information can be obtained by mounting DOAS or multi-GAS instruments on mobile platforms such as vehicles or aircraft, but even then, the instruments only provide information at a single location at a given time. Relatively novel SO_2 camera technology (Mori and Burton, 2006; Bluth et al., 2007) now allows acquisition of 2D imagery of gas plumes from stationary instruments, thus providing insights into SO_2 distributions in the atmosphere. However, these instruments can only measure SO_2 and have not been proven to work well on moving platforms.

In this study, we aim to improve the ability to obtain spatially resolved measurements of volcanic gases by introducing a novel Imaging DOAS instrument designed for airborne surveys. As we show in the following sections, this instrument can provide 2D imagery of gas plumes from moving platforms while also capturing the full, moderate-resolution (<1 nm) spectral information required for measuring multiple gas species at high sensitivity.

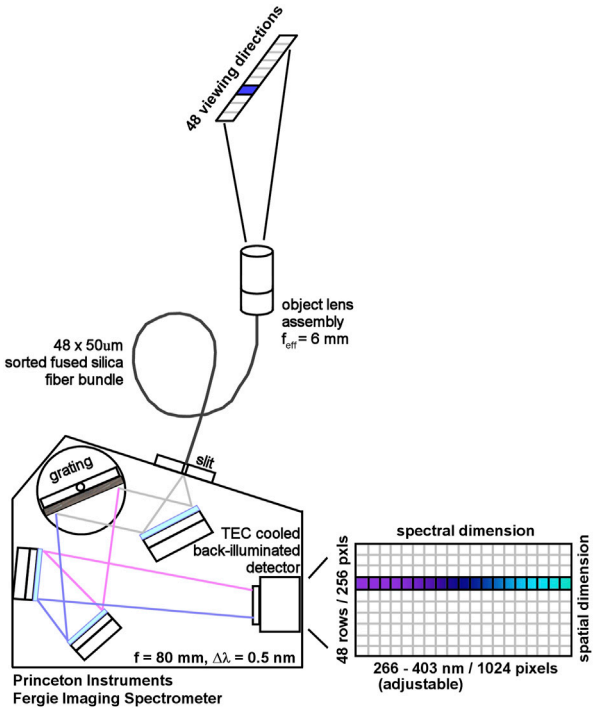

FIGURE 2
Optical design of the airborne Imaging DOAS instrument integrated into the Alaska Volcano Observatory airborne gas laboratory. Scattered sunlight is collected by an object lens assembly and coupled into a linear fiber bundle. The sorted fiber bundle transfers the light into the aircraft and ends in the focal plane of the imaging spectrometer. An adjustable dispersion grating maps the ultraviolet spectrum onto the horizontal dimension of a two-dimensional back-illuminated detector. The spatial swath collected with the fiber bundle is mapped onto the vertical dimension of the detector. The aircraft's motion scans the swath across the sky, thus providing the second spatial dimension of the imagery (see Figure 5).

Materials and methods

A new airborne Imaging DOAS instrument

Measurement principle

Since its first application to volcanic gases approximately 20 years ago (Galle et al., 2002; Edmonds et al., 2003), DOAS has become a standard technique for quantifying SO_2 emission rates from volcanoes. DOAS instruments measure the absorption of ultraviolet (UV) radiation by SO_2 and, in certain cases, some other plume constituents [e.g., bromine monoxide (BrO), chlorine dioxide (OClO), iodine monoxide (IO), and water vapor (H_2O)] (Galle et al., 2002; Bobrowski et al., 2003; Bobrowski et al., 2007; Kern et al., 2017; Schönhardt et al., 2017). By selectively measuring the narrow-band absorbance related to known ro-vibronic transitions of trace gas molecules in the light path, the measurements yield trace gas column densities (Platt and Stutz, 2008). These are typically given in molecules/cm^2, ppmm, or for satellite remote sensing observations, Dobson Units (DU, 1 DU = $2.69{\cdot}10^{16}$ molecules/cm^2).

Most DOAS observations of volcanic plumes use sunlight scattered in the atmosphere as their light source. This affords great flexibility with regards to measurement geometry, as instruments can be aimed in practically any viewing direction and measure the slant column density (SCD, typically given in molecules/cm^2) along the line-of-sight. In contrast to *in situ* measurements that measure trace gas concentrations at a single point in space, the integrative nature of the DOAS measurements allows derivation of emission rates. The SO_2 burden in a cross-section of a volcanic plume can be determined by passing the instrument along a traverse above or below the plume, or by scanning through the plume from a fixed location. Multiplication of this burden with the wind speed at plume height then yields the emission rate (Galle et al., 2002; Kern, 2009; Galle et al., 2010).

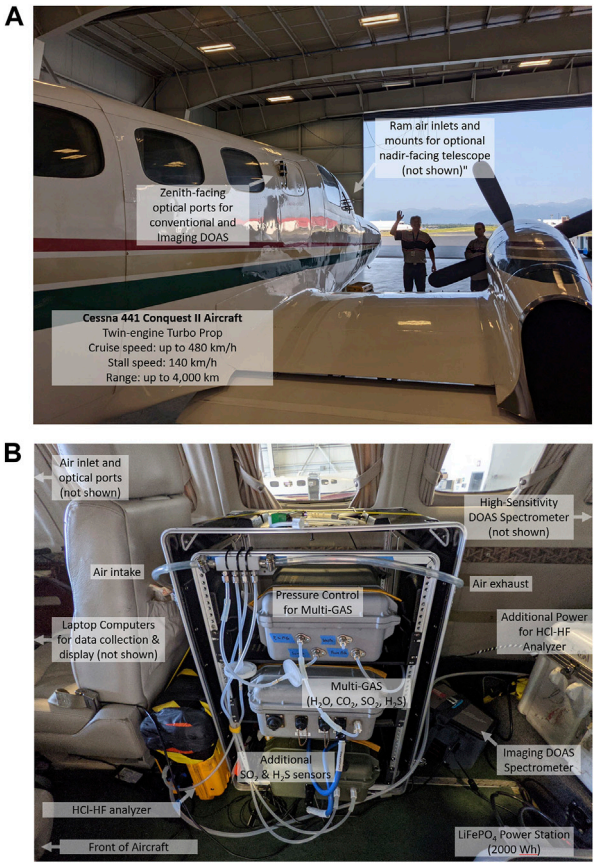

FIGURE 3
The AVO airborne gas lab pictured on board a Cessna Conquest aircraft in July 2021. **(A)** While circling a volcano at speeds of ~180 km/h, forward-facing metal inlets at the front of the aircraft divert ram-air into tubing leading to the *in situ* sensors inside. Farther back, two zenith-facing ports allow integration of C-Mount optical ports, in this case a conventional DOAS telescope and the Imaging DOAS object lens assembly. **(B)** Inside the aircraft, the *in situ* gas sensors actively pull air off the ram air manifold. The Imaging DOAS Spectrometer is strapped to the floor just aft of the *in situ* rack assembly. A fused-silica fiber bundle transmits light in from the external optical port. A second, high-sensitivity DOAS spectrometer is located just off the photo to the right (aft). Photos by Christoph Kern, USGS.

While conventional DOAS instruments measure the trace gas column density along a single, narrow field of view, Imaging DOAS instruments can provide multi-dimensional images of gas distributions in the atmosphere (Lohberger et al., 2004; Bobrowski et al., 2006; Louban et al., 2009). In the "push-broom" imaging technique, light is coupled into a spectrometer with a 2D detector. While one detector dimension measures the spectrum of incident radiation, the other detector dimension allows multiple spatial pixels to be measured at the same time. In this manner, trace gas column densities along an entire swath of the atmosphere can be measured simultaneously. This swath can then be scanned across an area of interest (e.g., a volcanic plume), thus providing a 2D image of the trace gas column density distribution (Platt et al., 2014). Often used for imaging volcanic gas plumes from space, the Ozone Monitoring Instrument (OMI) and the Tropospheric Monitoring Instrument (TROPOMI) both use the same push-broom technique to capture 2D imagery from low-Earth orbit.

Integration into the AVO airborne gas laboratory

For this study, we implemented an Imaging DOAS system based on a Teledyne Princeton Instruments FERGIE spectrometer (Figure 2). The FERGIE instrument features a variant of a Czerny-Turner spectrograph with an 80.8 mm focal length modified to correct for spherical and field astigmatism (McClure, 2013; McClure, 2014). The spectrograph's entrance plane is mapped onto a 2D cooled, back-illuminated CCD detector with 256 × 1024 (row × column) pixels. Blazed for maximum efficiency at 300 nm, an echelette grating with 1200 grooves/mm provides diffraction along the detector's horizontal dimension. Mounted on a rotary stage, the grating can be turned to adjust the captured wavelength range. In the measurements presented here, we recorded the 266–403 nm region. Light is coupled into the system through a fiber bundle with 48 individual fused silica fibers, each with a 50 µm diameter (+10 µm cladding) aligned in a sorted, linear array on either end. One end of the fiber bundle is positioned in the entrance plane of the spectrograph and thus the fiber array itself emulates a 50 µm entrance slit. In this configuration, the spectrometer achieves a spectral resolution of 0.45 nm throughout the detector plane. The other end of the fiber bundle is positioned in the focal plane of a wide-angle object lens with an effective focal length of f_{eff} = 6 mm which thereby collects radiation from a swath of 27.2-degree width.

The Imaging DOAS was developed in a modular design such that it could easily be installed into various aircraft. For the measurements presented here, we integrated the system into the AVO airborne gas laboratory on board a Cessna Conquest twin-engine aircraft (Figure 3A). For this purpose, an emergency exit door over the starboard wing was modified such that two C-mount telescopes could be mounted in zenith-facing direction adjacent to one another. One of these mounts held the Imaging DOAS wide-angle telescope while the other held a standard, f = 30 mm narrow-beam telescope running to a conventional DOAS instrument used for comparison (see the Supplementary Material for a complete description of the conventional DOAS). Two additional small holes beneath the optical mounts allowed optical fibers attached to the telescopes to enter the aircraft.

Inside the airplane, the Imaging DOAS was positioned just aft of the sensor package used for measuring plume composition *in situ* (Figure 3B). For this initial survey, the FERGIE spectrometer was simply strapped to the floor of the aircraft, with the carpeted interior providing some vibration dampening. The required 80 W (maximum) of electrical power were provided by a 2,000 Wh LiFePO4 power station with integrated circuit protection. Data acquisition was performed with a laptop computer running a custom MATLAB application. The spectrometer was set to continuous acquisition mode in which successive CCD images (Figure 4) are acquired with a fixed exposure time (typically 1–2 s) and cached onboard. Using the MATLAB program, the operator can request cached imagery be downloaded to the laptop at the push of a button while the aircraft is not transecting the gas plume. The download occurs through a USB3.0 interface and can take several 10 s of seconds, depending on how much imagery was cached since the last download. Once the

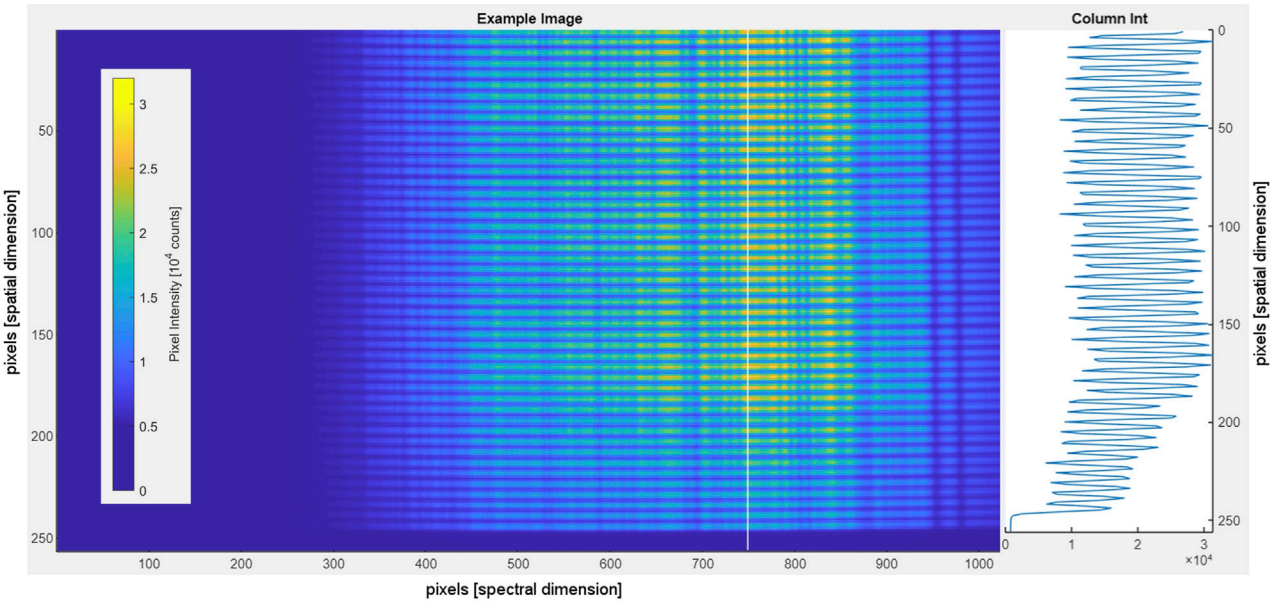

FIGURE 4
Example multispectral image recorded with the airborne Imaging DOAS. Each of the 48 fibers in the bundle produces a spectrum, which is mapped horizontally on the detector. Areas between fibers (cladding) appear as dark rows. The intensity along the white vertical line is plotted at right (in detector counts).

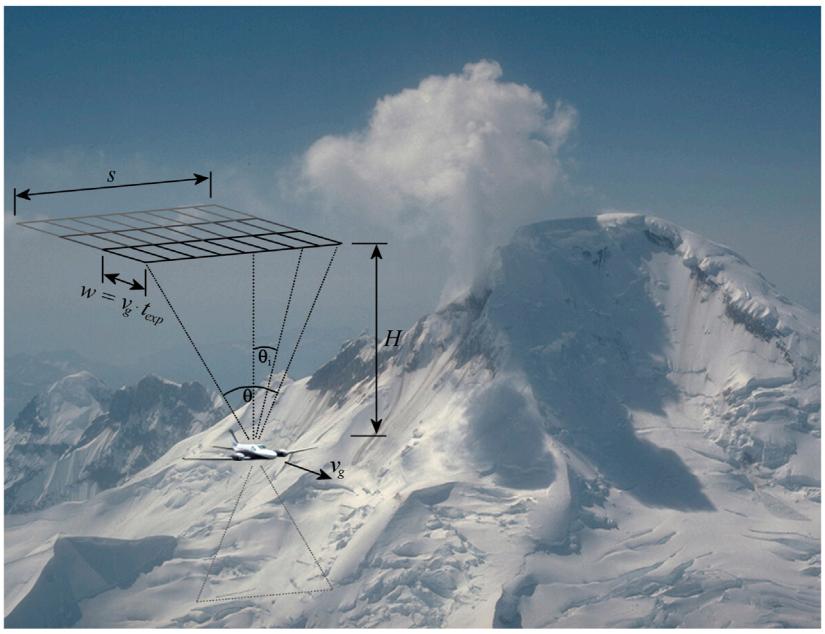

FIGURE 5
Schematic of push-broom imaging DOAS observations performed with a fixed-wing aircraft flying beneath a volcanic gas plume. The swath angle θ is fixed at 27.2 deg. The swath width s thus depends on the distance H between the aircraft and the gas plume. The swath is divided into 48 pixels, corresponding to the 48 fibers in the fiber bundle. The spatial resolution in the flight direction is given by the product of the aircraft's ground speed v_g and the Imaging DOAS exposure time t_{exp} (Schönhardt et al., 2015). Indicated in gray, additional optical ports allow nadir-facing observations, but this geometry was not used in the measurements presented here. Photograph of 1986 activity at Iliamna Volcano by R.G. McGimsey, USGS.

download is complete, the illumination conditions are assessed, and the next measurement sequence is automatically initialized with an appropriate exposure time.

Installed in this manner, the Imaging DOAS instrument measured scattered solar radiation originating from a 27.2-deg swath of sky above the aircraft (Figure 5). The motion of the aircraft then scans this swath across the sky, thus generating 2D images of the overhead trace-gas column densities. The along-track spatial resolution of the images depends on the utilized exposure times, which in turn depend on the lighting conditions. In this study, spectra were recorded at approximately 0.5–1 Hz, which, when combined with the aircraft's flight speed of approximately 50 m/s (180 km/h) during observation segments, leads to an along-track resolution of 50–100 m. The cross-track resolution depends on the distance between the aircraft and the gas plume, with the pixel width increasing by about 10 m per km plume distance. In this study, our cross-track pixel length was generally around 10–20 m, with the exact size varying with plume and flight altitude.

Spectral retrieval

Analysis of the recorded Imaging DOAS data first requires a spectral retrieval in which trace gas column densities are derived from the measured radiance spectra. First, we split each recorded 2D CCD image into 48 individual spectra by binning adjacent detector rows such that pixels collecting light from an individual fiber in the linear bundle are combined. This process generates 48 spectra for each acquisition, with each spectrum corresponding to a different viewing angle. While we found the optical resolution and instrument line shape to be remarkably constant and independent of the position on the CCD detector, imperfect alignment of the fiber bundle at the entrance of the spectrometer did lead to a slight variation in the pixel-wavelength calibration between different viewing angles. We therefore treated each of the 48 viewing directions separately in the spectral retrieval, only comparing spectra recorded in a specific viewing direction with others from the same direction.

The spectral retrieval itself follows the standard DOAS methodology (Platt and Stutz, 2008): Each measurement spectrum is corrected for stray light by subtracting the average intensity recorded at wavelengths shorter than 300 nm where the stratospheric ozone (O_3) blocks radiation. Then the logarithm is taken. Next, a non-linear least-squares fit is used to fit a model spectrum to the measurement. The model spectrum consists of a linear combination of the logarithm of a clear-sky reference spectrum recorded away from the volcanic gas plume, the trace gas absorption cross-sections of SO_2 and ozone (O_3) (Bogumil et al., 2003; Vandaele et al., 2009), a Ring correction spectrum to account for the effect of inelastic Raman scattering in the atmosphere (Grainger and Ring, 1962), and a 3rd order polynomial to account for broadband scattering and absorption effects (Platt and Stutz, 2008). A new set of clear-sky spectra was recorded at each volcano, with each viewing direction in the swath using its own reference. The clear-sky measurements were selected by choosing an acquisition close in time and space to the volcanic plume measurements, but which lacked the absorption signature of SO_2 in all viewing directions.

Once the best fit between measurement and model spectrum is achieved, the fit coefficients yield the slant column densities (SCDs) of SO_2 and O_3 relative to those contained in the clear-sky spectrum. For our zenith-facing observations, the vertical column density was then determined by simply accounting for the geometric air mass factor, i.e., each slant column was multiplied by the cosine of the measurement zenith angle θ_i (see Figure 5). BrO and OClO column densities can be retrieved in an analogous manner from the Imaging DOAS spectra (Gliß et al., 2015), but both were below the instrument's detection limit during the measurements presented here.

Detection limit

The precision of spectroscopic measurements is limited by shot noise (Platt and Stutz, 2008). Pure shot noise increases with $n^{1/2}$, where n denotes the number of photons collected. Since the measured radiance signal increases with n, the signal-to-noise ratio increases with $n^{1/2}$. The precision of a measurement can therefore be improved by increasing the exposure time, co-adding subsequent exposures or, in the case of scattered light measurements, increasing the solid angle from which light is collected in each acquisition. In an Imaging DOAS spectrometer, the latter can be achieved by binning adjacent rows of the CCD detector, sacrificing spatial resolution for increased measurement precision. In practice, care must be taken to only combine measurements of the same trace gas column densities. Co-adding spectra representative of different column densities can have unintended consequences, as the spectra are weighted by their individual light intensities so their sum may not be representative of the average column density in the region of interest.

We assessed the detection limits of our Imaging DOAS system by dividing two clear-sky spectra by one another and taking the logarithm to obtain the optical depth as a function of wavelength. Deviations from 0 in this optical depth spectrum are attributed to noise, as the two spectra recorded the same clear-sky scene. To be detectable, the differential optical depth of a trace gas absorption band τ'_{TG} would need to exceed the noise level in the clear-sky differential optical depth τ'_{noise}

$$\tau'_{TG} = \sigma'_{TG} \cdot SCD_{TG} > \tau'_{noise} \quad (1)$$

Here, σ'_{TG} represents the differential (narrow band) absorption cross-section of the respective trace gas. Solving for the trace gas slant column density SCD_{TG} (see Eq. 3 for a definition) then yields an equation for the instrument detection limit.

$$SCD_{TG} > \tau'_{noise} / \sigma'_{TG} \quad (2)$$

The detection limit therefore depends on the noise level τ'_{noise} and the magnitude of the differential (narrow band) features of the trace gas absorption cross-section σ'_{TG} in the analyzed wavelength region.

We applied this methodology to clear-sky spectra recorded during our airborne survey in the Cook Inlet, Alaska, on 16 July 2021. Taking two spectra with 1-s exposure times recorded at 12:20 local time (corresponding to a solar zenith angle of 40°), we determined the 1-s SO_2 detection limit of an individual spatial pixel recorded by our Imaging DOAS system (with 5 detector rows binned to combine light from a single fiber) to be approximately 1.2×10^{17} molecules/cm^2. This corresponds to about 4.5 Dobson Units (DU) or 50 ppmm assuming normal temperature and pressure. Note that this value strongly depends on the UV clear-sky radiance, which is itself dependent on the solar zenith angle, as stratospheric O_3 removes UV radiation more

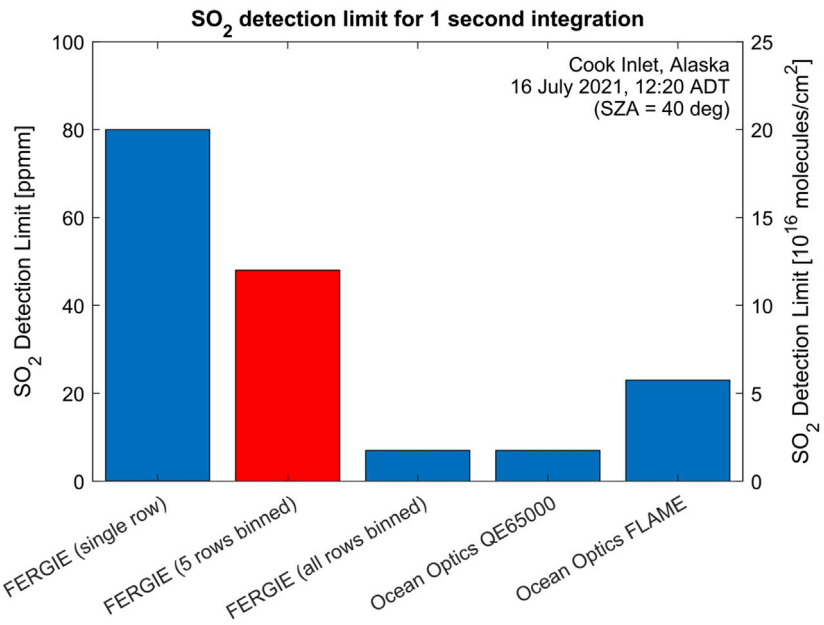

FIGURE 6
SO_2 detection limits of the airborne Imaging DOAS (Princeton Instruments FERGIE Spectrometer) compared with two Ocean Optics spectrometers also commonly used by AVO for airborne measurements. The fiber bundle utilized in our setup allows binning of 5 detector rows without loss of spatial information, and this setting was used for the measurements described below. All detection limits were measured at the indicated time except for that of the FLAME spectrometer, which was estimated based on a direct comparison with the QE65000 performed on 6 September 2022 in Vancouver, Washington.

efficiently when light passes through the O_3 layer obliquely. Hence, this detection limit will improve for measurements made at lower latitudes. Still, the Imaging DOAS detection limit is comparable to that of other consumer-grade spectrometers often used for DOAS applications (Figure 6). Research grade spectrometers with detectors especially sensitive to UV radiation can achieve lower detection limits but lack imaging capabilities, a setup that could be replicated with similar results by binning all detector rows of the FERGIE spectrometer.

Sensitivity to trace gas plumes

As is the case for all DOAS measurements, the sensitivity of the Imaging DOAS instrument to a gas plume depends not only on instrumental characteristics (see previous section) but also on the effective light path of scattered UV radiation between the Sun and the instrument. DOAS instruments measure the slant column density (SCD) of the trace gases to which they are sensitive. The slant column density is given by the integral of the trace gas concentration c_{TG} along the effective light path L.

$$SCD_{TG} = \int_L c_{TG} \cdot dl \tag{3}$$

Longer effective light paths in the volcanic plume result in higher column densities, regardless of the trace gas concentration inside the plume. This can be problematic if the effective light path is not well known or changes with time. The vertical column density (VCD) provides a more quantitative measure. The VCD is defined as the integral of the trace gas concentration c_{TG} along a straight vertical path Z through the atmosphere, from the ground to space.

$$VCD_{TG} = \int_Z c_{TG} \cdot dz \tag{4}$$

The sensitivity of a measurement to a region of interest, in our case the volcanic plume, is then given by the air mass factor (AMF). The AMF is defined as the ratio of the trace gas SCD to its VCD.

$$AMF = \frac{SCD}{VCD} \tag{5}$$

AMFs > 1 indicate an enhancement of the light path through the trace gas layer, e.g., due to multiple scattering by aerosols within the plume. AMF values < 1 indicate a shorter light path in the plume, which leads to a diminished sensitivity to the trace gas in question.

For measurements performed with zenith-facing DOAS instruments on moving platforms (typically referred to as "Mobile DOAS"), it is often assumed that the instrument is measuring the VCD directly (AMF = 1). In other words, the instrument is passing beneath the plume, sunlight is scattered in the atmosphere above the plume, and the light passes through it along a straight, vertical line. Strictly speaking, our Imaging DOAS measurements do not fulfill these assumptions because light is collected from a range of angles forming a swath above the aircraft. Therefore, each SCD must be multiplied by the cosine of the measurement zenith angle to obtain a geometrical approximation of the vertical column density (General et al., 2014b). However, as our swath angle θ is 27.2 deg (Figure 5), the maximum measurement zenith angle during level flight is only 13.6 deg, which yields a geometrical correction of less than 3%. This is negligible when compared to the effects of uncertain radiative

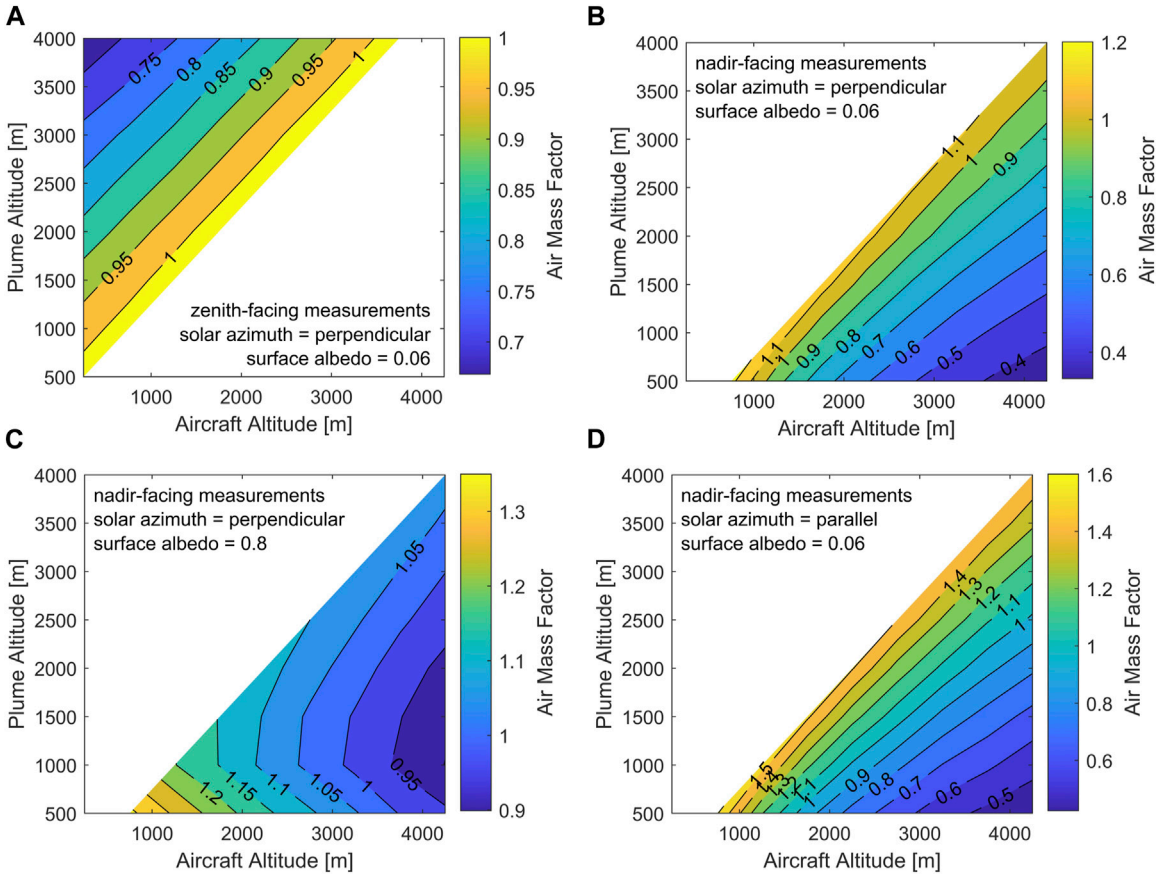

FIGURE 7
Simulated air mass factors (AMFs) for DOAS traverses beneath **(A)** and above **(B–D)** an SO_2 plume. **(A)** The sensitivity of zenith-facing measurements decreases slightly with the distance between the aircraft and the plume. **(B)** When flying over water or snow-free terrain (surface albedo = 0.06), nadir-facing air mass factors decrease about twice as quickly with plume distance as in the zenith-facing case. **(C)** Looking down at snow or sea ice (surface albedo = 0.8) significantly increases the measurement sensitivity, particularly for low plumes. **(D)** SO_2 column densities may be overestimated if the solar azimuth aligns with the plume propagation direction. See the Supplementary Material for a full description of the radiative transfer model parameters used for the simulations presented here.

transfer in and around volcanic plumes (see below). Generally, the simplification that zenith-facing DOAS instruments measure the VCD of trace gases contained in overhead plumes is reasonable for optically thin plumes measured at close range but fails if the plume is measured at long range, if the plume is opaque/optically thick, or if clouds/fog obstruct the instrument's view of the plume (Millan, 1980; Mori et al., 2006; Kern et al., 2010a, Kern et al., 2013, Kern et al., 2020).

Although the measurements we report in this study were all made using a zenith-facing geometry, our Imaging DOAS can also be run in a nadir-facing configuration. In this case, the aircraft must fly above the volcanic plume and the instrument measures light that has been scattered in the atmosphere beneath it or reflected on the ground, analogous to measurements performed from satellite platforms. The nadir-viewing geometry offers more flexibility in choosing the distance between the aircraft and the plume and thus the across-track spatial resolution of the recorded imagery. Also, in the case of ash-rich plumes, nadir observations avoid the need to fly under or within regions that may contain ash concentrations hazardous to the aircraft's operation. However, as we will show, the radiative transfer associated with this measurement configuration is more complex than in the zenith-facing geometry, and though the instrument is facing straight down, it is generally not appropriate to assume it is measuring the vertical column density directly (Tack et al., 2019; Schwaerzel et al., 2020).

To investigate the sensitivity of our Imaging DOAS instrument to volcanic plumes, we ran simulations of the radiative transfer at 313 nm in and around an idealized volcanic plume using the 3D Monte Carlo radiative transfer model McArtim (Deutschmann et al., 2011). We configured the model parameters to resemble the conditions we encountered in our measurements from 16 July 2021 (see Section 3). We placed a homogeneous, cylindrical plume of infinite length and 500 m diameter in a clean background atmosphere at various altitudes. At its center, the plume was modeled to have an SO_2 vertical column density of 2.5×10^{17} molecules/cm^2, an aerosol optical depth of 0.1, and an aerosol single scatter albedo of 0.9 representative of a sulfate aerosol. An instrument was placed at various altitudes above and beneath the plume, always aimed at the plume center. The full details of the

radiative transfer model parameterization for the simulations we ran are given in Supplementary Table S1.

For zenith-facing observations (Figure 7A), the simulations confirmed that our measured SCDs through the optically thin plume approximately matched the VCDs (i.e., AMF ≈ 1). Regardless of plume altitude, AMFs were within 10% of unity if the aircraft was flown no more than 1.2 km below the plume center. Only when the distance between aircraft and plume increased beyond this value did the AMF decrease farther, reaching about 0.7 for measurements made >3 km beneath the plume center. These results did not change significantly when we varied the surface albedo or solar azimuth angle as discussed below, and essentially confirm that our measured SCDs from weak degassing volcanoes in Alaska can be treated as VCDs within an uncertainty of about 10%.

If installed in a nadir-facing geometry, the sensitivity of our instrument is expected to be more variable. Figure 7B shows the simulated AMFs for nadir-facing measurements over snow/ice-free terrain with a surface albedo of approximately 0.06 at 313 nm (Kleipool et al., 2008). In this scenario, the AMF decreases more rapidly with distance between aircraft and the plume. As was true for the zenith-facing geometry, SCD and VCD are still within 10% of one another if the aircraft is flown within ~1 km of the plume's altitude. However, the AMF decreases to <0.5 if measurements are made 3 km above the plume center. This decrease in sensitivity stems from measured UV radiation being scattered at various altitudes beneath the aircraft, only some of which has passed through the plume on its way to the sensor.

However, the reduced sensitivity of nadir-facing measurements is only true for low surface albedos. Our simulations show a marked increase in AMF if a surface albedo of 0.8 is used (Figure 7C), consistent with the albedo of snow or sea ice (Kleipool et al., 2008). In this situation, the high surface reflectivity means that measured UV radiation is more likely to have been reflected on the ground back toward the instrument, rather than being scattered at various altitudes in the atmosphere. Therefore, most radiation has passed through the plume (at least once) before reaching the spectrometer, regardless of the plume and aircraft altitude. We also note that the detection limit of measurements performed while flying over reflective surfaces is particularly good, as the absolute radiance entering the instrument at 313 nm is expected to be more than twice the value expected during zenith-facing observations.

Finally, we found that 3D effects also play a role when making nadir-facing DOAS measurements of localized SO_2 plumes, as has been shown previously for nitrogen dioxide (NO_2) measurements in the visible spectral region (Schwaerzel et al., 2020). Figure 7D shows the results of a simulation identical to that shown in Figure 7B, except for the chosen solar azimuth angle. In Figure 7B, the solar azimuth was selected such that sunlight entered the scene perpendicular to the plume axis at a 40-degree solar zenith angle. In Figure 7D, the solar zenith angle remained 40°, but this time light entered the model space at an azimuth parallel to that of the plume axis. This circumstance greatly increases the probability of radiation passing through the plume twice: once on its way down, and again after being scattered up toward the instrument. This leads to AMFs as high as 1.5 for overpasses made in close proximity to volcanic plumes over snow-free terrain (Figure 7D). In fact, we found that AMFs can approach 2 when solar azimuth and plume direction align over snow-covered terrain. In such situations, assuming that SCD ≈ VCD, as we do with our zenith-facing observations, would lead to an overestimation of gas masses or emission rates by almost a factor of 2.

In situ instrumentation

Integration into the AVO airborne gas laboratory

The *in situ* gas sensing payload of the AVO airborne gas laboratory included two instruments that together measured the six most abundant volcanic gases, H_2O, CO_2, SO_2, hydrogen sulfide (H_2S), hydrogen chloride (HCl), and hydrogen fluoride (HF), in real time at 1 Hz resolution. The instruments were secured aft of the passenger seats in the aircraft cabin and supplied sample air from a forward-facing ram air inlet installed in a window blank on the forwardmost-starboard side of the aircraft. Ram air was conveyed by ~3 m of 0.953 cm inner diameter (ID) Teflon tubing to a manifold mounted in the instrument rack. The manifold outlet was connected to a port near the rear of the aircraft with another length of 0.953 cm ID Teflon tubing to exhaust excess ram air. We did not quantitatively measure the ram air flow rate during this survey, but a similar setup in a slower Piper Navajo aircraft routinely yielded flow rates ~25 lpm (Kelly et al., 2013), which is much greater than the instruments' demand. To minimize instrument response times and sorption effects of sticky gases like HCl and HF on tubing, the instruments sampled air from the ram air manifold with short (<50 cm) individual lengths of 0.318 cm ID polyethylene (Bev-a-line IV) tubing.

In situ measurements of H_2O, CO_2, SO_2, and H_2S

Since 2009, *in situ* measurements of H_2O, CO_2, SO_2, and H_2S gases during annual fixed-wing gas surveys in Alaska have been accomplished using the VERP system (Volcano Emissions Research Package; Kelly et al., 2013). VERP achieved excellent analytical precision with a typical 1-sigma precision of 0.15 parts-per-million by volume (ppmv) for CO_2, 2 parts-per-billion by volume (ppbv) for SO_2, and 1 ppbv for H_2S, all achieved at 1 Hz sampling rate (Kelly et al., 2013). However, the system was large (60 cm × 51 cm × 84 cm), heavy (>40 kg), and difficult for non-experts to operate. Thus, for this study we attempted to adapt a much smaller (47 cm × 36 cm × 18 cm), lighter (~10 kg), and easier to use USGS "campaign" multi-GAS instrument to measure H_2O, CO_2, SO_2, and H_2S. This model of multi-GAS has been extensively utilized for ground-based and helicopter-borne surveys (Gunawan et al., 2017; Werner et al., 2017, Werner et al., 2020a., Werner et al., 2020a) and has been described previously. Briefly, the multi-GAS was powered by a small, internal 6 Ah $LiFePO_4$ battery and included an integrated GPS receiver (Garmin GPS 18x LVC), a non-dispersive infrared CO_2 and H_2O analyzer (LI-COR, Inc., LI-840A, 0–5,000 ppmv for CO_2, 0–80,000 ppmv for H_2O), and electrochemical SO_2 (City Technology, Ltd., T3ST/F, 0–100 ppmv) and H_2S sensors (City Technology, Ltd., T3H, 0–100 ppmv). Miniature pressure sensors (Phidgets 1141) measured the pressure in the instrument's sample line and the ambient pressure inside the aircraft's cabin. All data were logged at 1 Hz to the multi-GAS datalogger (Campbell Scientific, CR1000) and displayed in real time with a tablet. To mitigate potential analytical problems associated with transient pressure changes in

the ram air inlet during aircraft maneuvers and with sampling gases at a broad range of altitudes (ca. 1,300–3,800 m), the multi-GAS was integrated with an experimental pressure control unit set to maintain constant pressure and flow (~1 lpm) at 650 hPa.

The CO_2, SO_2, and H_2S sensors were calibrated five times in-flight at ambient pressures from 804–686 hPa (~1,800–3,000 m altitude) using standard gases stored in 25-L capacity tedlar bags (CO_2 = 448 ppmv, SO_2 = 2.1 ppmv, H_2S, = 2.0 ppmv; all gases certified at ±2% accuracy). As part of each calibration, the H_2O/CO_2 analyzer's baseline response was checked using small soda lime and anhydrite cartridges to remove H_2O and CO_2 from ambient air, and the sulfur sensors' baselines were derived from their responses while sampling clean ambient air. The in-flight random noise (1-sigma at 1 Hz sampling rate) on the H_2O, CO_2, SO_2, and H_2S measurements were ±24, ±6.7, ±0.081, and ±0.037 ppmv, respectively. The average baseline-corrected response of each sensor to the five in-flight calibrations was used to scale the raw CO_2, SO_2, and H_2S sensor data, and the measurements' precision was calculated based on the reproducibility of the calibration tests. Using this method, the overall 1-sigma precision of the CO_2, SO_2, and H_2S measurements during the entire flight were ±1.1%, ±32%, and ±12%, respectively. We note that the CO_2, SO_2, and H_2S measurements collected using the smaller multi-GAS system were approximately 40 times noisier than measurements obtained with the larger VERP system. Expressed in terms of 3-sigma detection limits, the multi-GAS's CO_2, SO_2, and H_2S detection limits were ±20, ±0.24, and ±0.11 ppmv, respectively, as compared to VERP's CO_2, SO_2, and H_2S 3 s detection limits of 0.45, 0.006, and 0.003 ppmv. The relatively poor precision of the multi-GAS clearly illustrates the unfavorable analytical tradeoffs for using the much smaller and more convenient multi-GAS analyzer for this type of application.

In situ measurement of HCl and HF

In addition to the multi-GAS, the *in situ* sensing payload included an "Ultraportable" H_2O-HCl-HF analyzer manufactured by Los Gatos Research (LGR), Inc., (Kelly et al., 2017). The LGR instrument is a laser-absorption spectrometry system that measures H_2O, HCl, and HF simultaneously using an Off-Axis Integrated Cavity Output Spectroscopy (OA-ICOS) approach (Baer et al., 2002). The instrument contains two tunable diode lasers and a high finesse optical cavity that achieves an effective optical pathlength >3 km through the sample cell, which enables measurement of very low levels of HCl and HF at a high sampling rate (typical 1-sigma precision at 1 Hz sampling rate: HCl < 0.4 ppbv, HF < 0.1 ppbv). The instrument and its external pump require ~90 W of power, which wwas supplied by two 12 V, 35 Ah lead-acid batteries and a pure sine wave AC inverter. Raw absorption spectra were stored on the instrument's onboard computer. Digital results in sensible units (i.e., ppmv) were recorded along with time, location, and altitude information from a GPS (Garmin GPS 18x LVC) with a Campbell Scientific CR300-WIFI datalogger and displayed in-flight with a tablet. The GPS timestamp was used to synchronize the LGR output with the multi-GAS data during post-processing.

Results

Due to the hazards associated with potential volcanic eruptions near Anchorage, the AVO attempts to perform airborne gas measurements at high threat volcanoes in the Cook Inlet on at least an annual basis. One such survey was flown on 16 July 2021, with the new Imaging DOAS system integrated into the airborne gas laboratory for the first time, along with the *in situ* sensor suite described above. Measurements were attempted at 7 volcanoes in the Cook Inlet and northern Alaska Peninsula: Mount Spurr, Redoubt Volcano, Iliamna Volcano, Augustine Volcano, Mount Douglas, Mount Mageik and Mount Martin. Gas emissions were detected at Iliamna Volcano, Mount Douglas, Mount Martin, and Mount Mageik (Figure 1). These measurements are described in more detail below. Note that all reported measurement uncertainties refer to the 1-sigma standard deviation and relative compositions are given as molar ratios.

Iliamna Volcano

General observations

Iliamna Volcano (60.0325°N, 153.0880°W, 3,007 m) is a composite stratovolcano composed of interbedded andesite lava flows and pyroclastic rocks (Miller et al., 1998) located about 225 km southwest of Anchorage, Alaska. Though no historical eruptions have been recorded at Iliamna Volcano, two non-cohesive lahar deposits have been found and dated to <305 years before present (Waythomas et al., 2000). Iliamna Volcano exhibits typical signs of ongoing magmatic activity, with persistent seismic activity and the presence of fumaroles near the summit of the edifice. Airborne measurements performed on a recurring basis since 1990 have documented relatively stable gas emissions with Iliamna Volcano continuously degassing ~50–100 t/d of SO_2 during quiescence (Doukas, 1995; Doukas and McGee, 2007; Werner et al., 2011; Werner et al., 2022). Notable increases to around 500 t/d SO_2 occurred in 1996 and 2012 (Roman et al., 2004; Werner et al., 2022), both of which were likely associated with magma movement in the volcano's plumbing system but did not lead to eruptions (Roman and Power, 2011; Werner et al., 2011).

On 16 July 2021, our airborne gas survey approached Iliamna Volcano at 19:45 UTC. Following our standard procedure, the volcano was first visually surveyed from altitudes greater than its summit elevation to assess overall activity and meteorological conditions. As has been the case in past years, two active fumarole fields on the volcano's southeast flank at an elevation of about 2,800 m exhibited visible degassing (Figure 8). Light winds out of the north allowed the condensed plumes to rise along the steep walls of the edifice before re-evaporating as they became diluted with background air and, though invisible now, presumably drift south. We next began surveying the atmosphere above the southern sector of the volcano beginning at 3,600 m directly over the fumaroles and successively dropping to as low as 1,300 m altitude at 6 km from the summit as Iliamna Volcano's topography forced transects to be flown successively farther out as we descended. We then climbed back to >3,000 m and made several more passes through the gas plume to characterize its composition with the *in situ* sensors.

FIGURE 8
Iliamna Volcano viewed from the south on 16 July 2021. The location of the main active fumaroles is indicated **(A)**, as well as that of a secondary, less vigorous fumarole field **(B)**. Photo by Peter Kelly, USGS.

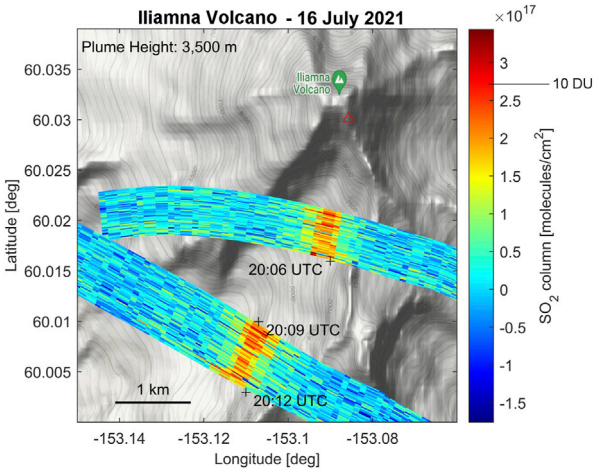

FIGURE 9
Imaging DOAS measurements of SO_2 emitted from Iliamna Volcano on 16 July 2021. The volcanic gas plume was clearly identified drifting south of the edifice in three traverses beneath the plume, two of which (12:09, 12:12 UTC) were performed at a similar distance from the vent and thus overlap in the plot. At the time of measurements, SO_2 was being emitted from fumaroles on the southeast side of the volcano at a rate of 90 ± 10 t/d. For the purposes of our analysis, we assumed a single source location corresponding to that of the main active fumaroles (see Figure 8), as indicated by a red triangle on the map. The cross-track resolution depends on the distance between the aircraft and the plume. The plume altitude is assumed to be constant at 3,500 m, consistent with the *in situ* observations. The variable along-track spatial resolution of the imagery stems from the use of a variable acquisition rate in the Imaging DOAS system. Base map: Google.

Analysis of the collected remote sensing and *in situ* sensor data shows that the aircraft passed beneath or through the gas plume a total of 15 times. As indicated by our measurements, the plume drifted south at altitudes between 3,000 and 3,500 m and appeared to rise slightly (toward the upper end of this range) as it moved downwind. The most diagnostic remote sensing data we were able to collect stem from 3 traverses flown beneath the plume (at ~2,100 m altitude) at distances ranging from 1.3 to 3.0 km from the active fumarole fields. During these traverses, which passed beneath the plume at 20:06, 20:09, and 20:12 UTC, respectively, the Imaging DOAS detected the overhead gas plume. A map of the retrieved SO_2 column densities reveals a ~400 m-wide plume drifting south, then southwest following the ridge along the southern edge of Iliamna Volcano's Umbrella Glacier (Figure 9). Maximum SO_2 column densities of ~3 × 10^{17} molecules/cm^2 (~11 DU) were detected in the plume center. At 3,500 m altitude, this corresponds to approximately 180 ppmm, so maximum SO_2 mixing ratios likely exceeded 1 ppm in the plume center, broadly consistent with the *in situ* measurements (see below).

Wind speed and direction

As described earlier, one of the main advantages of the DOAS technique is that it allows retrieval of gas emission rates. However, this calculation relies on knowledge of the speed at which the plume is traveling downwind. To obtain a robust estimate of plume speed at Iliamna Volcano during our survey, we performed a so-called "wind circle" maneuver in which the aircraft flies a standard turn at constant thrust and altitude while being pushed downwind (Doukas, 2002). Figure 10A shows the GPS location of the aircraft during the 4 complete wind circles flown just southeast

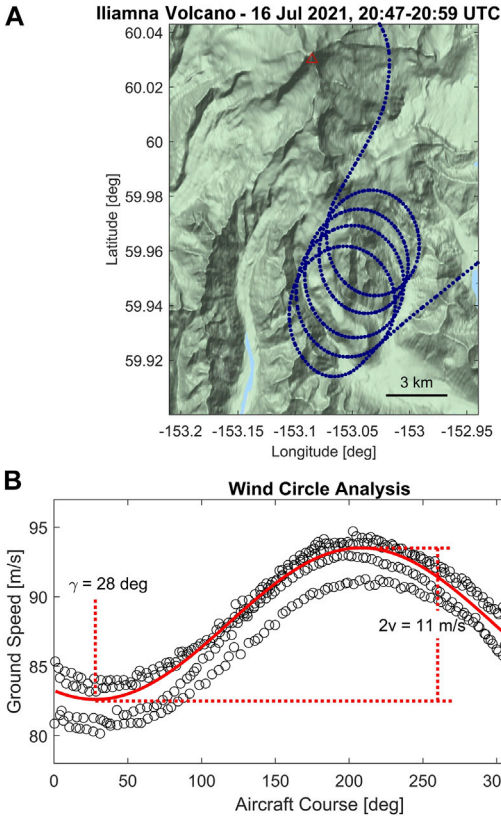

FIGURE 10
The plume speed at each volcano was obtained by flying "wind circles" in which the pilot performs a standard rate turn with constant thrust and altitude. **(A)** The GPS track of the aircraft shows how it was pushed downwind during the wind circles flown at Iliamna Volcano. Base map: Google. **(B)** The wind speed v and direction γ can be calculated by fitting a sinusoid to the aircraft ground speed as a function of its course. The course at which the minimum ground speed is realized corresponds to the wind direction. The amplitude of the sinusoid corresponds to the wind speed. Our wind circles at Iliamna Volcano yielded $\gamma = 28 \pm 10$ deg; v = 5.5 ± 0.5 m/s. The aircraft course and wind direction are both measured in degrees east of true north.

of the volcano. Improving upon previous work in which the plume speed was estimated simply from the difference between the highest and lowest measured ground speed (Doukas, 2002), we used the entire dataset to obtain a more reliable result. In ideal conditions, plotting the GPS-determined aircraft ground speed v_g as a function of the aircraft course β should yield a cosine function.

$$v_g = -v_w \cdot \cos(\beta - \gamma) + v_a \quad (6)$$

Here, the amplitude of the observed sine wave is given by the wind speed v_w, while its phase is determined by the meteorological wind direction γ. The curve is offset from 0 by the aircraft speed relative to the air surrounding it (airspeed, v_a). Plotting our flight data accordingly and fitting the above cosine function using a least-squares regression varying v_w and γ (Figure 10B), we obtain a wind speed of 5.5 ± 0.5 m/s and a wind direction of 28 ± 10 deg for our measurements at Iliamna Volcano. This same procedure was repeated for all other volcanoes at which emission rates were determined during our survey (see Table 1).

Time series of SO_2 emission rates

With the wind information in hand, SO_2 emission rates can be retrieved. A conventional DOAS system flown for comparison measured cross-sectional SO_2 burdens of 0.196, 0.204, and 0.217 kg/m on the 3 traverses pictured in Figure 9 (see Supplementary Figure S1 for example results from the conventional DOAS traverses). Multiplication with the plume speed yields SO_2 emission rates of 1.08, 1.12, and 1.19 kg/s, respectively. These measurements, combined with two additional traverses flown farther downwind yielding slightly lower values (0.91 and 0.98 kg/s), constrained the SO_2 emission rate to 1.04 ± 0.1 kg/s or 90 ± 10 t/d, consistent with previous measurements of background degassing at Iliamna Volcano (Doukas, 1995; Doukas and McGee, 2007; Werner et al., 2022).

However, the Imaging DOAS measurements can provide additional information and, as we show below, can even be used to derive limited time series data. Although the signal-to-noise level in each Imaging DOAS viewing direction is somewhat inferior to that of the research-grade conventional DOAS (Figure 6), the imaging spectrometer records spectra along 48 independent tracks corresponding to the 48 fibers in the fiber bundle. When flown beneath the gas plume roughly perpendicular to the wind direction, each of these rows records the cross-sectional SO_2 burden at a slightly different distance to the gas vent. In an approach analogous to that used to derive time series information from satellite remote sensing data (Merucci et al., 2011; Theys et al., 2013, Theys et al., 2019; Queißer et al., 2019), cross-sectional SO_2 burdens X measured at distance d from a vent correspond to gas emission rates $\phi(t)$ that occurred $\Delta t = d/v_w$ prior to the measurement time t_m.

$$\phi\left(t_m - \frac{d}{v_w}\right) = X(d) \cdot v_w \cdot \cos(\delta) \quad (7)$$

Here, δ represents the angle between the wind direction and the normal vector of the plane in which the plume cross-section X was measured, and multiplication with the cosine ensures that only the perpendicular component of the wind speed is considered when calculating the emission rate. Using Eq. 7, we can convert the 48 plume cross-sections measured during each Imaging DOAS traverse to a time series of 48 emission rates. Repeating this process for all three transects shown in Figure 9, we obtain a time series of SO_2 emission rates spanning ~6 min from 19:59 to 20:05 UTC on 16 July 2021 (Figure 11A). Note that the second traverse, although recorded 3 min after the first, provides information on the earliest emission rates because this traverse was performed 3 km rather than just 1.3 km downwind of the fumaroles.

According to the Imaging DOAS results, the mean SO_2 emission rate during this brief observation period was 1.11 kg/s (95.6 t/d), and the standard deviation around this mean was 0.32 kg/s (27.4 t/d). The SO_2 time series can readily be compared to other volcano monitoring data. As an example, the seismic waveform measured at the AVO seismic station ILS, located about 7.5 km southeast of the volcano, is plotted in Figure 11B. A magnitude 4.0 regional earthquake occurring at 20:01:34 on the Alaska-Aleutian subduction zone 475 km southeast of Iliamna Volcano (see www.earthquake.usgs.gov) caused shaking at the site beginning at 20:02:45, but our data indicate that this event did

TABLE 1 Gas compositions and emission rates measured during the airborne gas survey on 16 July 2021. "S_t" refers to total sulfur, which is assumed to be equal to the sum of SO_2 and H_2S emissions. 1 sigma errors for gas ratios were calculated using the combined analytical and regression error estimates (typical regression error was ~7.25%). HF concentrations were below the detection limit of the HCl-HF analyzer throughout the survey. Mount Spurr, Redoubt Volcano, and Augustine Volcano are not listed because all species were below the detection limits of our instruments at those locations.

	Iliamna Volcano[a]	Mount Douglas	Mount Martin	Mount Mageik
Relative gas composition (molar ratio)				
H_2O/CO_2	132 ±10		146 ± 11	
CO_2/SO_2	5.1 ± 1.0		11.1 ± 3.7	
CO_2/H_2S	31 ± 8		5.0 ± 0.7	10.1 ± 1.2
CO_2/S_t	4.4 ± 1.7		3.5 ± 1.2	
H_2S/SO_2	0.16 ± 0.06		2.2 ± 0.8	
HCl/SO_2	0.040 ± 0.01		0.018 ± 0.01	
Bulk composition (molar)				
H_2O	99.074%		99.126%	
CO_2	0.749%		0.677%	
SO_2	0.147%		0.061%	
H_2S	0.024%		0.135%	
HCl	0.006%		0.001%	
Emission rates (metric tons per day)[b]				
H_2O	17000 ± 6,000		6,000 ± 2,400	
CO_2	320 ± 130		99 ± 40	
SO_2	90 ± 10	20 ± 3	13 ± 3	
H_2S	7.8 ± 2.9		15 ± 6.6	
HCl	2.0 ± 0.7		0.13 ± 0.05	

[a]CO_2 mixing ratios were below the detection limit of our instruments at Iliamna Volcano. The presented CO_2 composition and emission rate were calculated by combining the measured X/SO_2 ratios (where X = H_2O, H_2S, and HCl) with the average molar CO_2/SO_2 ratio (5.1 ± 1.0) measured between 2009 and 2013 (Werner et al., 2022), excluding data from unrest in 2012.
[b]Emission rates were calculated by scaling the DOAS-derived SO_2 emission rate with *in situ* X/SO_2 ratios (where X = H_2O, CO_2, H_2S, and HCl).

not have a measurable effect on the SO_2 emission rate within the first 2 min after the onset of ground motion.

Gas composition

Additional information on the gases emitted from Iliamna Volcano comes from the suite of *in situ* sensors contained in the AVO airborne gas laboratory (Table 1). Clear in-plume H_2O, SO_2, H_2S, and HCl peaks were measured at ~2,875 m altitude and ~200 m downwind from Iliamna Volcano (ΔH_2O_{max} = 1,900 ppmv, ΔSO_{2max} = 1.0 ppmv, ΔH_2S_{max} = 0.15 ppmv, ΔHCl_{max} = 0.052 ppmv, where Δ = mixing ratio above ambient background), but CO_2 could not be resolved above ambient background and HF was not detected. To our knowledge, these are the first reported measurements of H_2O and HCl emissions from Iliamna Volcano. Sulfur was present mainly as SO_2 (SO_2/H_2S = 6.1 ± 2.1), similar to typical long-term average values (SO_2/H_2S = 7.6 ± 2.2, excluding data from unrest in 2012; Werner et al., 2022). The plume composition was water-rich (H_2O/S_t = 580 ± 204, where S_t represents total sulfur, which is assumed to be emitted exclusively as SO_2 or H_2S) and HCl-poor (HCl/S_t = 0.034 ± 0.012) compared to typical high-temperature magmatic gases (global arc-volcanic gas average H_2O/S_t = 69, HCl/S_t = 0.5; Taran and Zelenski, 2015). The lack of detectable HF was not surprising given that it is usually an order of magnitude less abundant than HCl in emissions from arc volcanoes (Taran and Zelenski, 2015), and the failure to resolve CO_2 is also not surprising due to the poor precision of the CO_2 analyzer, the relatively low in-plume sulfur mixing ratios, and because Iliamna Volcano's typical C/S is relatively low (average CO_2/SO_2 = 5.1 ± 1.0 from 2009 to 2013, excluding data from unrest in 2012; Werner et al., 2022).

Mount Douglas

Mount Douglas (58.8596°N, 153.5351°W, 2,140 m) is an ice-clad stratovolcano at the northern end of the Alaska Peninsula, just south of Kamishak Bay. No historical eruptive activity has been reported at Mount Douglas (Wood and Kienle, 1990), but active degassing occurs from the summit crater which hosts a ~250 m diameter crater lake (Figure 12A). Observations of activity on 16 July and in August of 2021 (M. Loewen, USGS, written personal communication from 21 February 2023) showed visual degassing occurring on the western margin of the crater lake, and additional gas may also have been emitted through the lake itself.

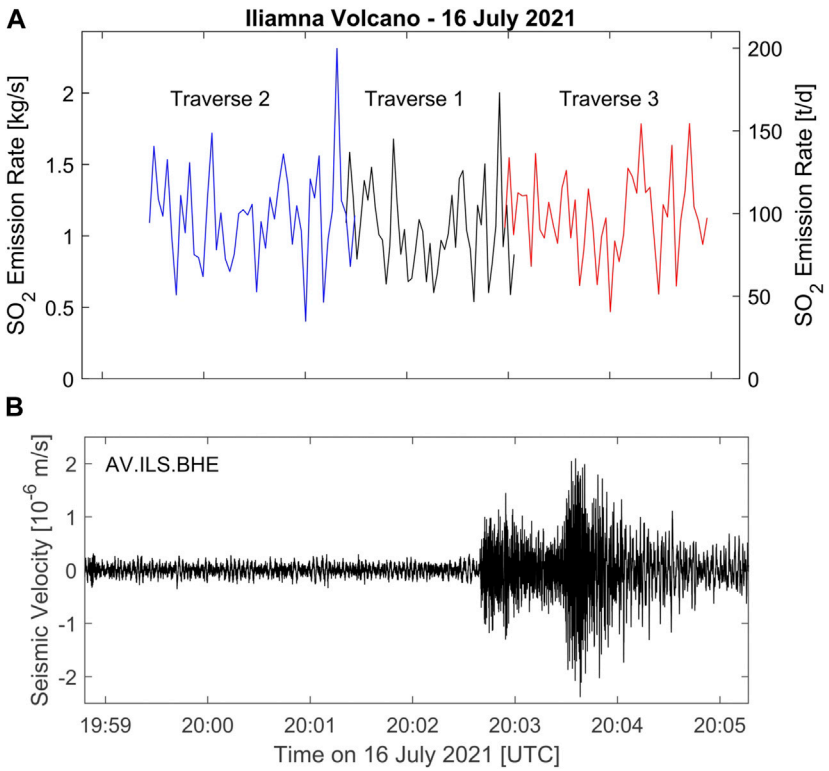

FIGURE 11
(A) Time series of SO_2 emission rate from Iliamna Volcano on 16 July 2021. This time series was compiled from the three Imaging DOAS traverses shown in Figure 8. Each viewing direction provides an independent measurement of SO_2 burden in the plume cross-section, which, when multiplied by the wind speed (see Figure 9), yields an emission rate (see text for details). **(B)** Seismic velocity measured at seismic station ILS, approximately 7.5 km southeast of Iliamna Volcano summit. Beginning at 20:02:45, the seismometer measured shaking from a regional earthquake, but this event did not appear to affect degassing. The velocity is filtered above 0.4 Hz to remove long-period noise.

Our observation flight on 16 July 2021 approached Mount Douglas from the northeast. After some high-level reconnaissance, we descended to approximately 2,100 m altitude and flew several transects through the plume directly above the west edge of the crater lake. As we flew through the plume, the *in situ* sensor suite registered some small apparent SO_2 peaks (~0.1 ppmv) but we are not confident in the detections because the peak values were below the sensor's 3s detection limit (±0.24 ppmv). All other species (H_2O, CO_2, H_2S, HCl, HF) were also below the detection limits of the instruments or were indistinguishable from ambient concentrations.

We proceeded to descend to about 1,600 m and flew two transects beneath the plume which we later realized could clearly be identified in our Imaging DOAS measurements drifting south of the edifice (Figure 12B). Based on wind circles flown immediately after the mapping survey, winds were out of 23 ± 13 deg at 3.6 ± 0.2 m/s. Maximum SO_2 column densities in the plume center were ~2.5×10^{17} molecules/cm^2, and the SO_2 emission rate was quantified to 20 ± 3 t/d. Just barely above the detection limit of the Imaging DOAS, this weak plume did not allow for a reliable time series calculation as performed for Iliamna Volcano.

Mount Martin

Mount Martin (58.1692°N, 155.3566°W, 1860 m) is located near the southern end of the Mount Katmai volcanic cluster, just 15 km southwest of the Novarupta vent that famously erupted in June of 1912 (Hildreth and Fierstein, 2002). Mount Martin's summit cone features a crater that is approximately 300 m in diameter and breached on its southeast side. Vigorous degassing has occurred at Mount Martin since at least 1913 (Griggs, 1922), and although there is no conclusive evidence of an eruption in historical times, visible plumes containing steam, gas, and possibly ash have been observed to rise as high as 600 m above the volcano's summit vent and extend downwind for up to 20 km (Miller et al., 1998).

Our 16 July 2021 airborne survey approached Mount Martin from the northeast at about 2,000 m altitude. Circling to the southeast side of the volcano offered a clear view of the crater lake and active fumarole field on its northwest shore (Figure 12C). On the day of our survey, emissions from the fumaroles were evident as condensed water plumes drifting upward to the rim of the summit crater. From there on, the plumes became transparent as ambient conditions led to re-evaporation of plume water. We proceeded to fly several plume intercepts directly over the top of the crater, briefly intersecting the volcanic gas plume each time. Our *in situ* sensor package registered a water-rich ($H_2O/S_t \approx 500$) plume (ΔH_2O_{max} = 2,150 ppmv) containing approximately twice as much H_2S as SO_2 (H_2S/SO_2 = 2.2 ± 0.8; ΔSO_{2max} = 0.6 ppmv, ΔH_2S_{max} = 1.0 ppmv). Intercepting the gas above the summit of the volcano, CO_2 was also detected above the atmospheric background (ΔCO_{2max} = 25 ppm). Behind H_2O, CO_2 was the second most abundant species, with CO_2/S_t = 3.4 ± 1.1. Finally, HCl was also identified (ΔHCl_{max} = 0.27 ppmv) in the volcanic gas plume though its relative

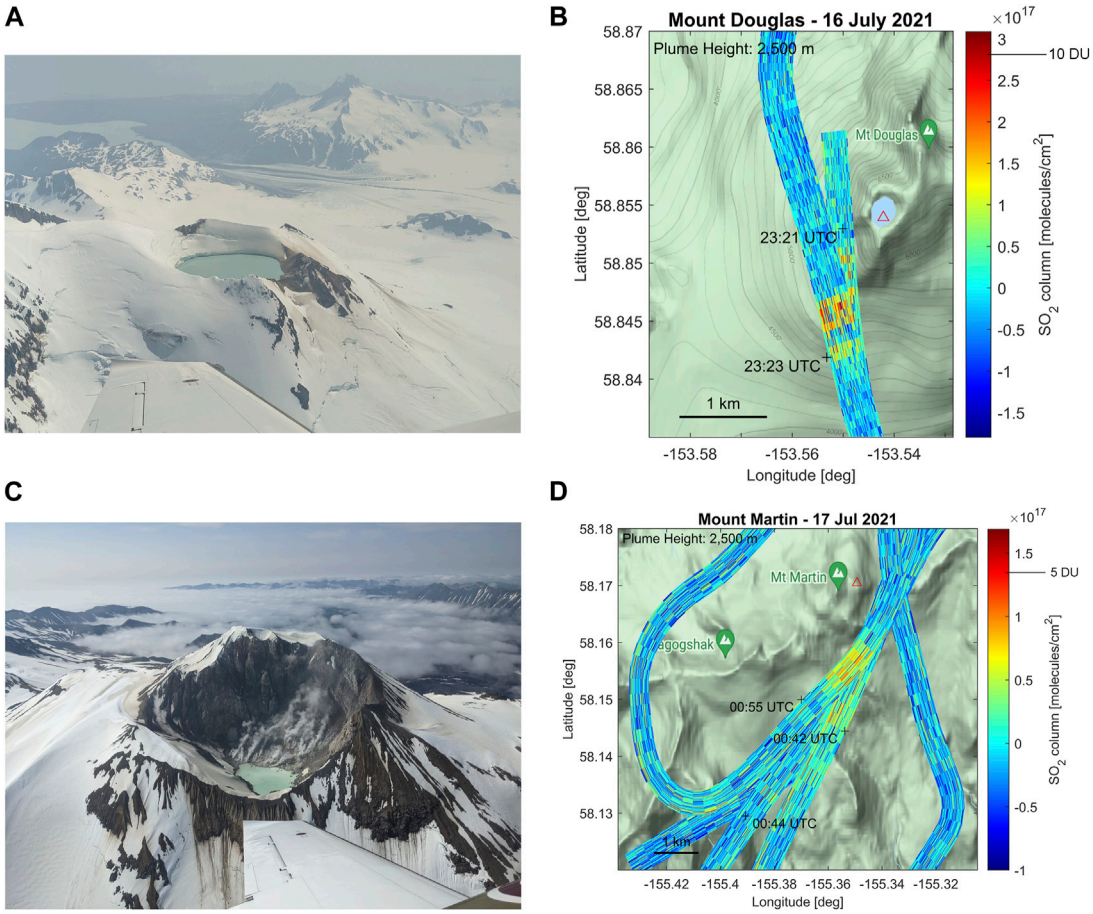

FIGURE 12
(A) Mount Douglas viewed from the northwest during our airborne survey on 16 July 2021. The volcano's summit crater hosts a lake. Degassing occurs through and along the edges of this lake. **(B)** Imaging DOAS SO_2 column densities retrieved downwind of Mount Douglas. A weak plume was detected southwest of the volcano. **(C)** Viewed from the southeast in this photo taken during our survey, Mount Martin also hosts a crater lake, but visible degassing occurs from a large fumarole field on its northwest shore. **(D)** Imaging DOAS SO_2 column densities reveal a very weak plume drifting south of the volcano. Both plumes were assumed to have a constant altitude of 2,500 m, consistent with the *in situ* observations. Note that measurements at Mount Martin were made on the same day as the others, with the 17 July date stamp referring to traverse time in UTC. Photos by Christoph Kern, USGS. Base maps: Google.

abundance in the plume was low (HCl/SO_2 = 0.018 ± 0.01, see Table 1 for details). HF was not detected above the detection limit of the instrumentation.

Following the plume intercepts, we moved farther from the volcano's summit allowing us to descend to approximately 1,500 m. At this flight level, we performed three traverses beneath the gas plume, which we intersected approximately 1.5 km south of the crater (Figure 12D). At this distance, our DOAS instruments detected overhead SO_2 column densities up to 1.1 × 10^{17} molecules/cm^2 while under the plume center. Again, applying the wind circle technique, winds were determined to be out of 9 ± 7 deg at 1.9 ± 0.2 m/s. Multiplying the DOAS-derived plume cross-sectional SO_2 burdens with these values, the volcanic SO_2 emission rate was constrained to 0.15 ± 0.03 kg/s (13 ± 3 t/d).

We had previously determined the SO_2 detection limit of our Imaging DOAS instrument to be approximately 1.2 × 10^{17} molecules/cm^2 (see Materials and Methods section). Yet despite the overhead SO_2 column densities not exceeding this value at our traverse location, the volcanic plume can be identified in the imagery retrieved from the Imaging DOAS data collected 1.5 km downwind of Mount Martin's summit (Figure 12D). This is a consequence of the large number of independent measurements collected by the imaging spectrometer and illustrates an advantage of this technique. Even though the SO_2 column density derived at each individual pixel does not exceed the noise level, the plume is probed at approximately 250 independent locations during each traverse and the distribution of column densities retrieved in this area is skewed toward higher values than is true for the regions surrounding the gas plume.

Mount Mageik

Mount Mageik (58.1946°N, 155.2544°W, 2,165 m) is a broad, cone-shaped stratovolcano located just 7 km northeast of Mount Martin and resting on the same basement ridge (Miller et al., 1998).

Mount Mageik's summit area consists of four separate volcanic cones. A 350-m-wide phreatic crater on the northeast side of the central cone hosts an acidic crater lake and an active fumarole field. The easternmost cone is a Holocene edifice, but Mount Mageik has no known historical eruptions, and the configuration of the crater has not changed in the last century (Fenner, 1930; Hildreth and Fierstein, 2000).

During our observation flight on 16 July 2021, this crater was the only identifiable source of degassing at Mount Mageik. Bubbles several meters in diameter were observed breaching the lake surface, and a raft of what appeared to be sulfur spherules was seen floating on the water (Supplementary Figure S2). Flying from north to south and *vice versa*, we performed 6 plume intercepts directly above the crater at an altitude of approximately 2,000 m. The onboard gas sensors registered up to 4 ppm of H_2S and 40 ppm CO_2 above the atmospheric background. SO_2, HCl, and HF remained below the detection limit of the *in situ* instruments on all transects of the plume, consistent with previous measurements of the bulk plume with multi-GAS and sampling of the fumaroles on the north crater wall performed in 2013 (Lopez et al., 2017).

Other volcanoes included in the airborne survey

Applying the techniques described above, airborne gas measurements were attempted at 3 additional Alaska volcanoes on 16 July 2021. Measurements at Mount Spurr, Redoubt Volcano, and Augustine Volcano failed to detect any volcanic gas species with either the remote sensing or *in situ* instruments. While quantitative measurements have sometimes been possible at these volcanoes in past years, the ability to measure gases depends not only on the volcanic emission rates but also decisively on the meteorological conditions present during the respective surveys. Although we could not quantify gas emissions at these volcanoes on this flight, visual observations appeared to confirm very low levels of degassing consistent with background activity.

Discussion

Volcanic activity in the Cook Inlet and northern Alaska Peninsula

All volcanoes in the Cook Inlet and northern Alaska Peninsula were exhibiting typical background activity during our 16 July 2021 airborne gas survey. Each of the four volcanoes at which gases were measured (Iliamna Volcano, Mount Douglas, Mount Martin, and Mount Mageik) produced only very weak plumes, with SO_2 emission rates of 90 ± 10, 20 ± 3, and 13 ± 3 t/d measured at Iliamna Volcano, Mount Douglas, and Mount Martin, respectively (Table 1). SO_2 emissions at Mount Mageik were below the detection limit of our instruments. These comparatively low SO_2 emission rates are consistent with a lack of rising, volatile rich magma and, taken together with the gas composition measurements, gas-water-rock interactions which are removing SO_2 from the gas stream before it reaches the atmosphere (see below). However, they do indicate a magmatic origin for at least part of the emitted gas at the volcanoes where SO_2 was detected.

At Iliaman Volcano, the presence of SO_2 and HCl in the plume reveals a clear magmatic origin of the gases (Symonds et al., 2001), but the overall water-rich and HCl-poor character of the plume (Gerlach, 2004) suggests that gases are interacting with groundwaters of either meteoric or magmatic origin on their path to the surface. Chemical reactions involving volcanic gases, water, and rocks remove water-soluble species like SO_2 and HCl from the gas phase in a process called "scrubbing" (Symonds et al., 2001), and the removal of S and HCl and addition of non-magmatic H_2O could well be contributing to the observed high H_2O/S_t ratio and low HCl/S_t ratio.

Mount Douglas also emits measurable SO_2, evidence of a magmatic component in the volcanic system. The lack of significant H_2S in the gas plume is interesting, as the presence of at least some reduced sulfur gases would be expected in emissions from water-rich systems, as Mount Douglas's crater lake would appear to imply it is. However, several recent studies have identified some volcanic crater lakes that appear to emit SO_2-rich, H_2S-poor gases (Shinohara et al., 2015; Tamburello et al., 2015; Gunawan et al., 2017) and attributed this phenomenon to a preferential removal of H_2S from the gas stream occurring at low temperatures via the reaction,

$$SO_2 + 2H_2S \rightarrow 2H_2O + 3S_e \quad (8)$$

This reaction (Mizutani and Sugiura, 1966; Giggenbach, 1987) deposits elemental sulfur S_e, a circumstance that is consistent with prior observations of solid material floating on the surface of Mount Douglas's crater lake (Wood and Kienle, 1990), and might therefore be responsible for the apparent lack of H_2S in the Mount Douglas plume.

The gas emissions observed at Mount Martin during our survey are generally consistent with previous observations from a significantly more rigorous gas sampling campaign conducted 10–22 July 2013 (Lopez et al., 2017), with the notable exception of our lower gas emission rate [only 13 ± 3 t (SO_2)/d as opposed to the ~75 t/d reported for 2013]. Also, these are the first reported HCl compositions and emission rates from Mount Martin because its crater was too difficult to access for ground-based sampling in 2013 (Lopez et al., 2017). As the authors of this previous work suggest, the presence of SO_2 is consistent with degassing from an active magmatic-hydrothermal system, while the relatively low CO_2/S_t ratio generally indicates degassing from a relatively shallow magma body or one that has been previously depleted in CO_2. Overall, Mount Martin appears to host a mixed magmatic-hydrothermal system and tracking gas compositions and emission rates will likely be useful in assessing the relative contributions of the two components over time.

At Mount Mageik, the lack of significant concentrations of acid gases (SO_2, HCl, HF) and the relatively high CO_2/S_t ratio (10 ± 1.2) we measured are both typical for degassing of active hydrothermal systems, and we did not find evidence for a distinct magmatic component in the volcano's emissions during our survey.

Airborne Imaging DOAS offers new possibilities for plume characterization

The Imaging DOAS measurements of weak SO_2 plumes emitted from Alaska volcanoes described above allude to the new

possibilities for plume characterization that the technique provides. Contrary to conventional airborne Mobile DOAS measurements which only offer 1D transects of overhead gas plumes, the imaging spectrometer allows for 2D mapping of the plumes as they drift downwind. Though all plumes measured as part of this survey were weak, with a maximum SO_2 emission rate of only 90 t/d measured at Iliamna Volcano, the gas clouds could still be clearly distinguished from the background at distances exceeding 5 km from the degassing vents. With this sensitivity, the instrument will be able to track more vigorous plumes, e.g., immediately prior to or during eruptive activity, for many tens to hundreds of kilometers downwind, thus providing actionable information to the AVO and other institutions tasked with monitoring the emission rate and atmospheric dispersion of volcano emissions. The ability to derive limited, continuous time series information of gas emission rates for comparison with other monitoring data (e.g., seismic, geodetic, thermal, see Figure 11) is also a novel capability for an airborne remote sensing package and such measurements may help advance the scientific understanding of shallow degassing processes as more such measurements are made. But beyond these concepts, which we were able to demonstrate during our 16 July 2021 survey, the Imaging DOAS provides a few novel capabilities that tie into ongoing related research and are discussed below.

Comparison to satellite measurements

One particularly interesting aspect of the Imaging DOAS data products is that they are directly comparable to satellite observations of trace gas plumes, as both measure the spatial distribution of trace-gas VCDs. The observation geometry of the Imaging DOAS is more flexible, allowing for both zenith and nadir-facing observations. We showed that zenith-facing observations will generally be more accurate due to better constraints on radiative transfer leading to AMFs close to unity. To some degree, they will also avoid the complex 3D radiative transfer effects of nadir-facing geometries (Schwaerzel et al., 2020; Wagner et al., 2022). However, even the AMFs of nadir-facing measurements will typically be better constrained for the airborne imaging when compared to those of satellite measurements, as light dilution/light mixing effects are minimized when the aircraft passes over the plume at shorter distances. Our modeling suggests nadir-imaging clear-sky AMFs in the 0.5–1.5 range (at 313 nm) for SO_2 plumes in the lowermost few kilometers of the atmosphere, compared to values ranging from about 0.3 to 3 for the Tropospheric Monitoring Instrument (TROPOMI) on board the Copernicus Sentinel-5 Precursor satellite (Theys et al., 2017). Thus, airborne Imaging DOAS measurements will generally be more accurate and lend themselves to validation studies.

Besides the better constrained instrument sensitivity, another powerful feature of the Imaging DOAS measurements is the greatly enhanced spatial resolution when compared to satellite-based trace gas measurements. The highest quality space-based volcanic SO_2 products currently come from the aforementioned TROPOMI instrument, which provides SO_2 VCDs at 3.5 km × 5.5 km resolution. This pixel size is only slightly smaller than the 5.5 km × 5.5 km map segment shown in Figure 9. Our map shows a plume with a mean SO_2 VCD of approximately 2×10^{17} molecules/cm^2 filling a region that extends about 0.25 km × 5 km. Assuming a similar orientation of the plume in the TROPOMI pixel as in Figure 9, the plume would fill only approximately 6% of the pixel area. Further assuming the pixel illumination is homogeneous (which is reasonable for cloud-free conditions and uncondensed plumes as encountered here), the TROPOMI AMF would thus be reduced to 6% of the AMF for the entire pixel. On the other hand, the pixel size of the Imaging DOAS instrument was smaller than the extent of the plume and therefore our sensitivity did not suffer from this effect.

The TROPOMI instrument passed over Iliamna Volcano at 23:49 UTC on 16 July 2021 (Orbit 19473), approximately 3.5 h after our measurements. Downloaded from the Sentinel-5 Precursor Open Access Data Hub (https://s5phub.copernicus.eu/dhus/#/home), the Level 2 Offline SO_2 SCDs derived over the Cook Inlet region in the 312–326 nm range are shown in Supplementary Figure S3. The SO_2 SCD immediately south of Iliamna Volcano is not enhanced above the noise of the measurement in this regional sector, which was determined to be 4.1×10^{16} molecules/cm^2 at 3 sigma[1]. At the time of the satellite overpass, the TROPOMI AMF calculated for the location of Iliamna Volcano was approximately 2. Had the plume filled the entire pixel, the SO_2 absorption signal would have been about an order of magnitude above the instrument's detection limit. However, since the SO_2 plume filled only 6% of the pixel, the AMF corresponding to the plume itself was only 0.12, making the TROPOMI SO_2 VCD detection limit 3.4×10^{17} molecules/cm^2 (at 3 sigma). Therefore, TROPOMI was not able to detect the weak SO_2 degassing from Iliamna Volcano even in these relatively ideal measurement conditions (cloud-free, high surface albedo, close to summer solstice). However, this example demonstrates how high-sensitivity, high-resolution Imaging DOAS data can be used to validate satellite measurements of trace gas plumes from point sources in the future.

Imaging volcanic gases other than SO_2

As described in the Material and Methods section, the Imaging DOAS technique enables 2D measurements of trace gas distributions. Two other techniques have recently come into focus that also allow imaging of gas plumes, particularly in the context of measuring volcanic emissions: SO_2 cameras use narrow-band optical filters placed in front of UV or IR-sensitive cameras to measure the incident radiance at multiple wavelength bands (McElhoe and Conner, 1986; Mori and Burton, 2006; Bluth et al., 2007). Sensitivity to SO_2 comes from comparing radiances at wavelengths corresponding to SO_2 absorption bands with those at nearby wavelengths without SO_2 absorption (Kern et al., 2010b, Kern et al., 2013; Lübcke et al., 2013). A second method for imaging trace gas distributions uses Fabry-Perot interferometry to slide a transmission comb across the incident spectral radiance (Platt et al., 2014). Careful selection of the interferometer's optical path length difference and finesse allows the transmission peaks to be alternatingly tuned such that they coincide with periodic trace gas absorption bands and troughs between

1 We use a 3-sigma threshold above the noise level to define the instrument detection limit, as suggested by (Theys et al., 2019). We note, however, that our TROPOMI image of the Cook Inlet (Supplementary Figure S3) contains 5785 pixels, 16 of which are expected to fall outside the 3-sigma threshold based on noise statistics alone (false detections). We therefore suggest using a 4-sigma confidence level or higher for a more robust single-pixel detection limit.

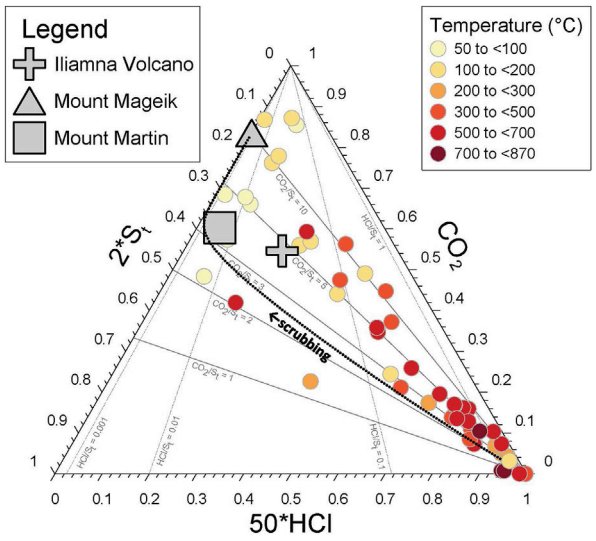

FIGURE 13
Ternary diagram showing CO_2-S_t-HCl compositions of gases from Iliamna Volcano, Mount Mageik, and Mount Martin. Note that the indicated CO_2 composition from Iliamna Volcano is based on S_t and HCl compositions measured in 2021 and the average CO_2/SO_2 ratio (5.1 ± 1.0) measured between 2009 and 2013 (Werner et al., 2022), excluding data from unrest in 2012. For comparison, filled circles indicate literature gas compositions from four volcanoes (Augustine Volcano, Meakandake, Ruapehu, White Island) where direct samples and vent temperatures were recorded from high-temperature fumaroles proximal to the strongest degassing areas and lower-temperature, distal gas vents (Giggenbach and Sheppard, 1989; Symonds et al., 1992; Christenson, 2000; Shinohara et al., 2011). The curve labelled "scrubbing" illustrates the general compositional trend expected for the evolution of a magmatic gas interacting with near-surface meteoric water. The initial composition of the model gas was 50% CO_2, 25% SO_2, and 25% HCl, and the solubilities (by mass) in 20°C water at 1 atm were set to 0.172% for CO_2, 10.548% for SO_2 (Wilhelm et al., 1977), and 73% for HCl (O'Neil, 2013).

bands, thereby again allowing a comparison of on and off-band radiance (Kuhn et al., 2014; Fuchs et al., 2021).

Both methods have the advantage that a full 2D image can generally be obtained quite quickly because on and off-band images can either be taken in rapid succession or, in the case of the SO_2 camera, simultaneously (if using two detectors). The Imaging DOAS requires scanning the area of interest line by line, which generally takes longer. However, the SO_2 camera and Fabry Perot imagers are specifically designed to target an individual trace gas (e.g., SO_2 or BrO), with the dispersive elements (optical filters, optical path difference and finesse) customized to maximize sensitivity to this species. The Imaging DOAS, on the other hand, measures the full near-UV spectrum at moderate resolution (0.45 nm in our setup). This enables measurements of numerous volcanic and atmospheric trace gases, including SO_2, BrO, OClO, IO, O_3, H_2O, NO_2, nitrous acid (HNO_2), formaldehyde (CH_2O), glyoxal ($C_2H_2O_2$), and oxygen dimers (O_4).

Though their column densities were below the detection limits of our instrument in the weak plumes encountered during our survey on 16 July 2021, the halogen oxides BrO, OClO, and IO have all been measured in more vigorous volcanic plumes with DOAS instruments (Bobrowski et al., 2003; Theys et al., 2009,Theys et al., 2014; Bobrowski and Giuffrida, 2012; General et al., 2014a; Donovan et al., 2014; Gliß et al., 2015; Schönhardt et al., 2017; Kern and Lyons, 2018). These species are not primarily emitted from volcanoes, but instead are formed from primary volcanogenic emissions in a complex series of chemical reactions that occur as the plume ages and constituents are mixed with background air (Gerlach, 2004; Oppenheimer et al., 2006; Bobrowski et al., 2007; von Glasow, 2010; Kelly et al., 2013; Gutmann et al., 2018). These reactions affect the oxidation capacity of the atmosphere on local to regional scales (von Glasow et al., 2009). Future measurements with our Imaging DOAS instrument will allow us to characterize the spatial distribution of these species in chemically evolving plumes, measurements that could lead to a better understanding of halogen chemistry and thus allow us to better constrain primary volcanic halogen emissions from measurements of these secondary species. Initial studies have already uncovered some interesting findings including a decrease in BrO/SO_2 ratios in the months leading up to the 30 June 2012 eruption of Nevado del Ruiz volcano, Colombia (Lübcke et al., 2014), and a 2 to 5-fold increase in BrO/SO_2 ratios accompanying Vulcanian to Strombolian transitions in eruptive behaviour at Tungurahua volcano, Ecuador (Warnach et al., 2019). Furthermore, since halogen oxides are accessible to the common scanning DOAS instruments that make up the global Network for Observation of Volcanic and Atmospheric Change [NOVAC (Galle et al., 2010; Arellano et al., 2021); www.novac-community.org], better constraints on plume chemistry and the volcanological implications of changes in halogen emissions would be immediately applicable to the >35 volcanoes monitored in this manner.

The development of such standardized continuous gas monitoring instruments and the expansion of global networks that cover an increasing number of volcanoes will allow us to better measure the gas-geochemical signals associated with the full progression of quiescence to unrest to eruption. The goals are to gain insights into volcanic processes occurring at depth and develop an understanding of the geochemical signatures that can be used to forecast future volcanic events. However, the remote location and harsh environment of many active volcanoes, e.g., those in Alaska, means that this endeavor will necessarily also rely on intermittent campaign observations and satellite remote sensing data. The Imaging DOAS and *in situ* sensor package described here allow airborne characterization of volcanic degassing at remote vents. These observations can provide geochemical assessments of volcanic systems even during times of weak background degassing and, through comparison and validation, will help refine space-based measurements such that they can better track global volcanic gas emissions.

Conclusion

In this study, we have implemented an Imaging DOAS system specifically for observation of volcanic degassing from airborne platforms. The instrument can be operated either in zenith or nadir-facing geometry, with the zenith-facing measurements providing the highest accuracy due to the well-constrained radiative transfer in the overhead volcanic plumes. However, the nadir-facing geometry offers an improved measurement signal-to-noise ratio and detection limit when observations are made over snow cover, as is often the case for volcanoes in Alaska. Our instrument achieved a single-pixel SO_2 detection limit of 1.2×10^{17}

molecules/cm^2 (~50 ppmm) during our zenith-facing measurements in mid-July, but since volcanic plumes are probed in numerous viewing directions simultaneously, these can be detected even at lower column densities (e.g., see the presented results from Mount Martin). The spatial information provided by the Imaging DOAS can be used to assess the heterogeneity of gas abundances in volcanic plumes and track their extent as they propagate downwind. Using our measurements at Iliamna Volcano as an example, we also demonstrate how limited time series information can be derived from airborne Imaging DOAS data. The time series of SO_2 emission rates can then readily be compared to other time-resolved geophysical monitoring streams.

In addition to the Imaging DOAS, a suite of *in situ* sensors was used to characterize the major chemical composition of the volcanic gas plumes. These sensors measured H_2O, CO_2, SO_2, H_2S, HCl, and HF, as well as temperature, pressure, and relative humidity in the ambient air as the aircraft intercepted the gas plumes. Gas compositions measured at Iliamna Volcano, Mount Douglas, Mount Martin, and Mount Mageik indicate that gas-water-rock interactions ("scrubbing") are important to varying degrees at these volcanoes, yet comparisons to CO_2-S_t-HCl compositions from other well-sampled volcanoes show that emissions from Iliamna Volcano and Mount Mageik are most similar to samples collected from lower-temperature fumaroles (ca. < 200°C) as opposed to higher-temperature fumaroles with abundant HCl (Figure 13). Both Iliamna Volcano and Mount Martin have relatively low CO_2/St ratios, which suggests that degassing is sustained by relatively shallow magma. At Mount Douglas, gases passing through or around the crater lake appear to be depositing native sulfur via low-temperature Reaction 8, which requires a mixed magmatic-hydrothermal input to the shallow aquifer and/or crater lake. At Mount Mageik, on the other hand, all sulfur emissions occurred in the form of H_2S. This, combined with the high CO_2/St ratio of about 10, indicates a purely hydrothermal source, with some portion of the sulfur gases possibly being scrubbed from the gas stream by the crater lake.

By implementing an Imaging DOAS and a suite of *in situ* sensors on a small, fixed-wing aircraft, we were able to acquire detailed geochemical information on several Alaska volcanoes in a single airborne survey. The information we collected allowed us to characterize the volcanic systems and provided useful information on current activity levels. By comparing future measurements to this baseline, signals associated with a transition of a system towards eruptive activity may be captured ahead of time and assist in hazard assessments and eruption forecasts.

Data availability statement

The datasets presented in this study can be found in online repositories. The names of the repository/repositories and accession number(s) can be found below: Data uploaded to the USGS ScienceBase repository: https://doi.org/10.5066/P9YTK9PE.

Author contributions

CK led the development and integration of the airborne Imaging DOAS instrument. PK led the development and integration of the *in situ* sensor suite. CK and PK performed the measurements on 16 July 2021 and analyzed the collected data. CK wrote the first draft of the manuscript. PK wrote sections of the manuscript. Both authors contributed to manuscript revision and approved the submitted version.

Funding

The funding for this study was provided by the United States Geological Survey's Volcano Hazards Program and through Grant/Cooperative Agreement No. G19AC00060 with the State of Alaska Department of Natural Resources.

Acknowledgments

The authors would like to thank Jason Ward, Chuck Werly and the Security Aviation team for their assistance integrating our instruments into the Cessna Conquest aircraft. These measurements would not have been possible without the piloting skills of Jeff McMillan. Thanks to John Lyons for help with retrieving and plotting seismic data for comparison, and to Matt Loewen for providing an internal review of the manuscript. Any use of trade, product, or firm names is for descriptive purposes only and does not imply endorsement by the United States Government.

Conflict of interest

The authors declare that the research was conducted in the absence of any commercial or financial relationships that could be construed as a potential conflict of interest.

Publisher's note

Supplementary material

The Supplementary Material for this article can be found online at: https://www.frontiersin.org/articles/10.3389/feart.2023.1088056/full#supplementary-material

References

Aiuppa, A., Bitetto, M., Donne, D. D., Paolo, F., Monica, L., Tamburello, G., et al. (2021). Volcanic CO_2 tracks the incubation period of basaltic paroxysms. *Sci. Adv.* 7, eabh0191. doi:10.1126/sciadv.abh0191

Aiuppa, A., Federicao, C., Giudice, G., and Gurrieri, S. (2005). Chemical mapping of a fumarolic field: La fossa crater, vulcano Island (aeolian islands, Italy). *Geophys. Res. Lett.* 32, L13309. doi:10.1029/2005GL023207

Aiuppa, A., Moretti, R., Federico, C., Giudice, G., Gurrieri, S., Liuzzo, M., et al. (2007). Forecasting Etna eruptions by real-time observation of volcanic gas composition. *Geology* 35, 1115. doi:10.1130/G24149A.1

Arellano, S., Galle, B., Apaza, F., Avard, G., Barrington, C., Bobrowski, N., et al. (2021). Synoptic analysis of a decade of daily measurements of SO_2 emission in the troposphere from volcanoes of the global ground-based network for observation of volcanic and atmospheric change. *Earth Syst. Sci. Data* 13, 1167–1188. doi:10.5194/essd-13-1167-2021

Baer, D., Paul, J., Gupta, M., and O'Keefe, A. (2002). Sensitive absorption measurements in the near-infrared region using off-axis integrated-cavity-output spectroscopy. *Appl. Phys. B* 75, 261–265. doi:10.1007/s00340-002-0971-z

Bluth, G. J. S., Shannon, J. M., Watson, I. M., Prata, A. J., and Realmuto, V. J. (2007). Development of an ultra-violet digital camera for volcanic SO_2 imaging. *J. Volcanol. Geotherm. Res.* 161, 47–56. doi:10.1016/j.jvolgeores.2006.11.004

Bobrowski, N., and Giuffrida, G. (2012). Bromine monoxide/sulphur dioxide ratios in relation to volcanological observations at Mt. Etna 2006–2009. *Solid earth.* 3, 433–445. doi:10.5194/se-3-433-2012

Bobrowski, N., Hönninger, G., Galle, B., and Platt, U. (2003). Detection of bromine monoxide in a volcanic plume. *Nature* 423, 273–276. doi:10.1038/nature01625

Bobrowski, N., Honninger, G., Lohberger, F., and Platt, U. (2006). Idoas: A new monitoring technique to study the 2D distribution of volcanic gas emissions. *J. Volcanol. Geotherm. Res.* 150, 329–338. doi:10.1016/j.jvolgeores.2005.05.004

Bobrowski, N., von Glasow, R., Aiuppa, A., Inguaggiato, S., Louban, I., Ibrahim, O. W., et al. (2007). Reactive halogen chemistry in volcanic plumes. *J. Geophys. Res.* 112, D06311. doi:10.1029/2006JD007206

Bogumil, K., Orphal, J., Homann, T., Voigt, S., Spietz, P., Fleischmann, O. C., et al. (2003). Measurements of molecular absorption spectra with the SCIAMACHY pre-flight model: Instrument characterization and reference data for atmospheric remote-sensing in the 230–2380 nm region. *J. Photochem. Photobiol. A Chem.* 157, 167–184. doi:10.1016/S1010-6030(03)00062-5

Burton, M., Allard, P., Mure, F., and La Spina, A. (2007). Magmatic gas composition reveals the source depth of slug-driven strombolian explosive activity. *Science* 317, 227–230. doi:10.1126/science.1141900

Cameron, C. E., Crass, S. W., and Staff, A. V. O. (2022b). Geologic database of information on volcanoes in Alaska (GeoDIVA). *Alaska Div. Geol. Geophys. Surv. Digital Data Ser.* 20. doi:10.14509/30901

Cameron, C. E., Schaefer, J. R., and Perreault, J. M. (2022a). Historically active volcanoes of Alaska. *Alsk. Div. Geol. Geophys. Surv* Misc. Publ. 133 ver. 5 2 sheets doi:10.14509/30851

Casadevall, T. J. (1994). Volcanic ash and aviation safety: Proceedings of the first international symposium on volcanic ash and aviation safety. *U. S. Geol. Surv. Bull.* 2047, 464. doi:10.3133/b2047

Christenson, B. W. (2000). Geochemistry of fluids associated with the 1995-1996 eruption of Mt. Ruapehu, New Zealand: Signatures and processes in the magmatic-hydrothermal system. *J. Volcanol. Geotherm. Res.* 97, 1–30. doi:10.1016/S0377-0273(99)00167-5

de Moor, J. M., Aiuppa, A., Avard, G., Wehrmann, H., Dunbar, N., Muller, C., et al. (2016). Turmoil at Turrialba Volcano (Costa Rica): Degassing and eruptive processes inferred from high-frequency gas monitoring. *J. Geophys. Res. Solid Earth* 121, 5761–5775. doi:10.1002/2016JB013150

Deutschmann, T., Beirle, S., Frieß, U., Grzegorski, M., Kern, C., Kritten, L., et al. (2011). The Monte Carlo atmospheric radiative transfer model McArtim: Introduction and validation of Jacobians and 3D features. *J. Quant. Spectrosc. Radiat. Transf.* 112, 1119–1137. doi:10.1016/j.jqsrt.2010.12.009

Donovan, A., Tsanev, V., Oppenheimer, C., and Edmonds, M. (2014). Reactive halogens (BrO and OClO) detected in the plume of soufriere hills Volcano during an eruption hiatus. *Geochem. Geophys. Geosystems* 15, 3346–3363. doi:10.1002/2014GC005419

Doukas, M. P. (1995). A compilation of sulfur dioxide and carbon dioxide emission-rate data from Cook inlet volcanoes (Redoubt, Spurr, Iliamna, and augustine), Alaska during the period from 1990 to 1994. *U.S. Geol. Surv*, 16. Open-File Rep. 95-55 doi:10.3133/ofr9555

Doukas, M. P. (2002). A new method for GPS- based wind speed determinations during airborne volcanic plume measurements. *U.S. Geol. Surv.*, 1–13. Open-File Rep. 02-395 doi:10.3133/ofr02395

Doukas, M. P., and McGee, K. A. (2007). A compilation of gas emission-rate data from volcanoes of Cook inlet (Spurr, Crater Peak, Redoubt, Iliamna, and augustine) and Alaska Peninsula (Douglas, fourpeaked, griggs, Mageik, Martin, peulik, ukinrek maars, and veniaminof), Alaska, from 1995-2006. *U.S. Geol. Surv.*, 16. Open-File Rep. 2007-1400 doi:10.3133/ofr20071400

Edmonds, M., Herd, R. A., Galle, B., and Oppenheimer, C. M. (2003). Automated, high time-resolution measurements of SO_2 flux at Soufriere Hills Volcano, Montserrat. *Bull. Volcanol.* 65, 578–586. doi:10.1007/s00445-003-0286-x

Edmonds, M., and Wallace, P. J. (2017). Volatiles and exsolved vapor in volcanic systems. *Elements* 13, 29–34. doi:10.2113/gselements.13.1.29

Ewert, J. W., Diefenbach, A. K., and Ramsey, D. W. (2018). 2018 update to the U.S. Geological survey national volcanic threat assessment. *USGS Sci. Investig*, 50. Rep. 2018– 5140 doi:10.3133/sir20185140

Fenner, C. N. (1930). Mount Katmai and Mount Mageik. *Z. für Vulkanol.* 13, 1–24.

Fuchs, C., Kuhn, J., Bobrowski, N., and Platt, U. (2021). Quantitative imaging of volcanic SO_2 plumes using Fabry-Pérot interferometer correlation spectroscopy. *Atmos. Meas. Tech.* 14, 295–307. doi:10.5194/amt-14-295-2021

Galle, B., Johansson, M., Rivera, C., Zhang, Y., Kihlman, M., Kern, C., et al. (2010). Network for observation of volcanic and atmospheric change (NOVAC)—a global network for volcanic gas monitoring: Network layout and instrument description. *J. Geophys. Res.* 115, D05304. doi:10.1029/2009JD011823

Galle, B., Oppenheimer, C., Geyer, A., Mcgonigle, A. J. S., Edmonds, M., and Horrocks, L. (2002). A miniaturised ultraviolet spectrometer for remote sensing of SO_2 fluxes: A new tool for volcano surveillance. *J. Volcanol. Geotherm. Res.* 119, 241–254. doi:10.1016/S0377-0273(02)00356-6

General, S., Bobrowski, N., Pöhler, D., Weber, K., Fischer, C., and Platt, U. (2014a). Airborne I-DOAS measurements at Mt. Etna: BrO and OClO evolution in the plume. *J. Volcanol. Geotherm. Res.* 300, 175–186. doi:10.1016/j.jvolgeores.2014.05.012

General, S., Pöhler, D., Sihler, H., Bobrowski, N., Frieß, U., Zielcke, J., et al. (2014b). The Heidelberg airborne imaging DOAS instrument (HAIDI) – A novel imaging DOAS device for 2-D and 3-D imaging of trace gases and aerosols. *Atmos. Meas. Tech. Discuss.* 7, 2187–2257. doi:10.5194/amtd-7-2187-2014

Gerlach, T. M. (2004). Volcanic sources of tropospheric ozone-depleting trace gases. *Geochem. Geophys. Geosystems* 5, 1–16. doi:10.1029/2004GC000747

Giggenbach, W. F. (1987). Redox processes governing the chemistry of fumarolic gas discharges from White Island, New Zealand. *Appl. Geochem.* 2, 143–161. doi:10.1016/0883-2927(87)90030-8

Giggenbach, W. F., and Sheppard, D. S. (1989). "Variations in the temperature and chemistry of White Island fumarole discharges 1972–1985," in *The 1976-82 eruption sequence at white Island volcano (whakaari), bay of plenty, New Zealand*. Editors B. F. Houghton and I. A. Nairn (New Zealand Geological Survey bulletin 103), 119–126. Available at: https://shop.gns.cri.nz/b103-pdf/.

Gliß, J., Bobrowski, N., Vogel, L., Pöhler, D., and Platt, U. (2015). OClO and BrO observations in the volcanic plume of Mt. Etna-implications on the chemistry of chlorine and bromine species in volcanic plumes. *Atmos. Chem. Phys.* 15, 5659–5681. doi:10.5194/acp-15-5659-2015

Grainger, J. F., and Ring, J. (1962). Anomalous fraunhofer line profiles. *Nature* 193, 762. doi:10.1038/193762a0

Griggs, R. F. (1922). *The Valley of ten thousand smokes*. Washington, D.C.: National Geographic Society.

Gunawan, H., Caudron, C., Pallister, J., Primulyana, S., Christenson, B., Mccausland, W., et al. (2017). "New insights into Kawah Ijen ' s volcanic system from the wet volcano workshop experiment," in *Geochemistry and geophysics of active volcanic lakes.* Editors T. Ohba, B. Capaccioni, and C. Caudron (Geological Society of London). doi:10.1144/SP437.7

Gutmann, A., Bobrowski, N., Roberts, T. J., Rüdiger, J., and Hoffmann, T. (2018). Advances in bromine speciation in volcanic plumes. *Front. Earth Sci.* 6. doi:10.3389/feart.2018.00213

Hildreth, W., and Fierstein, J. (2002). Geologic map of the Katmai volcanic cluster, Katmai national park, Alaska. *U.S. Geol. Surv. IMAP* 2778. doi:10.3133/i2778

Hildreth, W., and Fierstein, J. (2000). Katmai volcanic cluster and the great eruption of 1912. *Bull. Geol. Soc. Am.* 112, 1594–1620. doi:10.1130/0016-7606(2000)112<1594:KVCATG>2.0.CO;2

Keith, T. E. C. (1995). The 1992 eruptions of Crater Peak vent, Mount Spurr volcano, Alaska. *USGS Bull.* 2139. doi:10.3133/b2139

Kelly, P. J., Kern, C., Roberts, T. J., Lopez, T., Werner, C., and Aiuppa, A. (2013). Rapid chemical evolution of tropospheric volcanic emissions from Redoubt Volcano, Alaska, based on observations of ozone and halogen-containing gases. *J. Volcanol. Geotherm. Res.* 259, 317–333. doi:10.1016/j.jvolgeores.2012.04.023

Kelly, P., Sutton, A., Elias, T., Kern, C., Clor, L., and Baer, D. (2017). "Real-time, high frequency (1 Hz), *in situ* measurement of HCl and HF gases in volcanic plumes with a novel cavity-enhanced, laser-based instrument," in *AGU fall meeting abstracts (new orleans)*. Available at: https://agu.confex.com/agu/fm17/meetingapp.cgi/Paper/239617.

Kern, C., Aiuppa, A., and de Moor, J. M. (2022). A golden era for volcanic gas geochemistry? *Bull. Volcanol.* 84, 43–11. doi:10.1007/s00445-022-01556-6

Kern, C., Deutschmann, T., Vogel, L., Wöhrbach, M., Wagner, T., and Platt, U. (2010a). Radiative transfer corrections for accurate spectroscopic measurements of volcanic gas emissions. *Bull. Volcanol.* 72, 233–247. doi:10.1007/s00445-009-0313-7

Kern, C., and Kelly, P. (2023). *Airborne survey of gas emissions from volcanoes in the Cook inlet and northern Alaska Peninsula, 2021*. U.S. Geological Survey data release. doi:10.5066/P9YTK9PE

Kern, C., Kick, F., Lübcke, P., Vogel, L., Wöhrbach, M., and Platt, U. (2010b). Theoretical description of functionality, applications, and limitations of SO_2 cameras for the remote sensing of volcanic plumes. *Atmos. Meas. Tech.* 3, 733–749. doi:10.5194/amt-3-733-2010

Kern, C., Lerner, A. H., Elias, T., Nadeau, P. A., Holland, L., Kelly, P. J., et al. (2020). Quantifying gas emissions associated with the 2018 rift eruption of Kīlauea Volcano using ground-based DOAS measurements. *Bull. Volcanol.* 82, 55. doi:10.1007/s00445-020-01390-8

Kern, C., and Lyons, J. J. (2018). Spatial distribution of halogen oxides in the plume of Mount Pagan volcano, Mariana Islands. *Geophys. Res. Lett.* 45, 9588–9596. doi:10.1029/2018GL079245

Kern, C., Masias, P., Apaza, F., Reath, K. A., and Platt, U. (2017). Remote measurement of high preeruptive water vapor emissions at Sabancaya volcano by passive differential optical absorption spectroscopy. *J. Geophys. Res. Solid Earth* 122, 3540–3564. doi:10.1002/2017JB014020

Kern, C. (2009). Spectroscopic measurements of volcanic gas emissions in the ultra-violet wavelength region. Available at: http://www.ub.uni-heidelberg.de/archiv/9574.

Kern, C., Werner, C., Elias, T., Sutton, A. J., and Lübcke, P. (2013). Applying UV cameras for SO_2 detection to distant or optically thick volcanic plumes. *J. Volcanol. Geotherm. Res.* 262, 80–89. doi:10.1016/j.jvolgeores.2013.06.009

Kleipool, Q. L., Dobber, M. R., de Haan, J. F., and Levelt, P. F. (2008). Earth surface reflectance climatology from 3 years of OMI data. *J. Geophys. Res. Atmos.* 113, D18308–D18322. doi:10.1029/2008JD010290

Kuhn, J., Bobrowski, N., Lübcke, P., Vogel, L., and Platt, U. (2014). A Fabry-Perot interferometer-based camera for two-dimensional mapping of SO_2 distributions. *Atmos. Meas. Tech.* 7, 3705–3715. doi:10.5194/amt-7-3705-2014

Lohberger, F., Hönninger, G., and Platt, U. (2004). Ground-based imaging differential optical absorption spectroscopy of atmospheric gases. *Appl. Opt.* 43, 4711–4717. doi:10.1364/AO.43.004711

Lopez, T., Tassi, F., Aiuppa, A., Galle, B., Rizzo, A. L., Fiebig, J., et al. (2017). Geochemical constraints on volatile sources and subsurface conditions at MountMount Martin, Mount Mageik, and trident volcanoes, Katmai volcanic cluster, Alaska. *J. Volcanol. Geotherm. Res.* 347, 64–81. doi:10.1016/j.jvolgeores.2017.09.001

Louban, I., Bobrowski, N., Rouwet, D., Inguaggiato, S., and Platt, U. (2009). Imaging DOAS for volcanological applications. *Bull. Volcanol.* 71, 753–765. doi:10.1007/s00445-008-0262-6

Lübcke, P., Bobrowski, N., Arellano, S., Galle, B., Garzón, G., Vogel, L., et al. (2014). BrO/SO_2 molar ratios from scanning DOAS measurements in the NOVAC network. *Solid earth.* 5, 409–424. doi:10.5194/se-5-409-2014

Lübcke, P., Bobrowski, N., Illing, S., Kern, C., Alvarez Nieves, J. M., Vogel, L., et al. (2013). On the absolute calibration of SO_2 cameras. *Atmos. Meas. Tech.* 6, 677–696. doi:10.5194/amt-6-677-2013

McClure, J. P. (2013). Anastigmatic imaging spectrograph. Available at: https://patents.google.com/patent/WO2013106307A1.

McClure, J. P. (2014). "The Schmidt-Czerny-Turner spectrograph," in *SPIE opt. Eng. + appl. Proc. Vol. 9189, photonic innov. Solut. Complex environ. Syst. II* doi:10.1117/12.2061559

McElhoe, H. B., and Conner, W. D. (1986). Remote measurement of sulfur dioxide emissions using an ultraviolet light sensitive video system. *J. Air Pollut. Control Assoc.* 36, 42–47. doi:10.1080/00022470.1986.10466043

Merucci, L., Burton, M., Corradini, S., and Salerno, G. G. (2011). Reconstruction of SO_2 flux emission chronology from space-based measurements. *J. Volcanol. Geotherm. Res.* 206, 80–87. doi:10.1016/j.jvolgeores.2011.07.002

Millan, M. (1980). Remote sensing of air pollutants. A study of some atmospheric scattering effects. *Atmos. Environ.* 14, 1241–1253. doi:10.1016/0004-6981(80)90226-7

Miller, T. P., McGimsey, R. G., Richter, D. H., Riehle, J. R., Nye, C. J., Yount, M. E., et al. (1998). Catalog of the historically active volcanoes of Alaska. *U.S. Geol. Surv.*, 104. Open-File Rep. 98-582 doi:10.3133/ofr98582

Mizutani, Y., and Sugiura, T. (1966). The chemical equilibrium of the $2H_2S+SO_2=3S+2H_2O$ reaction in solfataras of the nasudake volcano. *Bull. Chem. Soc. Jpn.* 39, 2411–2414. doi:10.1246/bcsj.39.2411

Mori, T., and Burton, M. (2006). The SO_2 camera: A simple, fast and cheap method for ground-based imaging of SO_2 in volcanic plumes. *Geophys Res. Lett.* 33, L24804. doi:10.1029/2006GL027916

Mori, T., Mori, T., Kazahaya, K., Ohwada, M., Hirabayashi, J., and Yoshikawa, S. (2006). Effect of UV scattering on SO_2 emission rate measurements. *Geophys. Res. Lett.* 33, L17315–5. doi:10.1029/2006GL026285

Olmos, R., Barrancos, J., Rivera, C., Barahona, F., López, D. L., Henriquez, B., et al. (2007). Anomalous emissions of SO_2 during the recent eruption of Santa Ana volcano, El Salvador, central America. *Pure Appl. Geophys.* 164, 2489–2506. doi:10.1007/s00024-007-0276-6

O'Neil, M. J. (2013). *The merck index: An encyclopedia of chemicals, drugs, and biologicals* 15th ed. Cambridge, UK: Royal Society of Chemistry.

Oppenheimer, C., Tsanev, V., Braban, C., Cox, R., Adams, J., Aiuppa, A., et al. (2006). BrO formation in volcanic plumes. *Geochim. Cosmochim. Acta* 70, 2935–2941. doi:10.1016/j.gca.2006.04.001

Platt, U., Lübcke, P., Kuhn, J., Bobrowski, N., Prata, F., Burton, M., et al. (2014). Quantitative imaging of volcanic plumes — results, needs, and future trends. *J. Volcanol. Geotherm. Res.* 300, 7–21. doi:10.1016/j.jvolgeores.2014.10.006

Platt, U., and Stutz, J. (2008). *Differential optical absorption spectroscopy - Principles and applications*. Berlin, Heidelberg: Springer. doi:10.1007/978-3-540-75776-4

Poland, M. P., Lopez, T., Wright, R., and Pavolonis, M. J. (2020). Forecasting, detecting, and tracking volcanic eruptions from space. *Remote Sens. Earth Syst. Sci.* 3, 55–94. doi:10.1007/s41976-020-00034-x

Queißer, M., Burton, M., Theys, N., Pardini, F., Salerno, G., Caltabiano, T., et al. (2019). TROPOMI enables high resolution SO_2 flux observations from Mt. Etna, Italy, and beyond. *Sci. Rep.* 9, 957–1012. doi:10.1038/s41598-018-37807-w

Roman, D. C., and Power, J. A. (2011). Mechanism of the 1996-97 non-eruptive volcano-tectonic earthquake swarm at Iliamna Volcano, Alaska. *Bull. Volcanol.* 73, 143–153. doi:10.1007/s00445-010-0439-7

Roman, D. C., Power, J. A., Moran, S. C., Cashman, K. V., Doukas, M. P., Neal, C. A., et al. (2004). Evidence for dike emplacement beneath Iliamna Volcano, Alaska in 1996. *J. Volcanol. Geotherm. Res.* 130, 265–284. doi:10.1016/S0377-0273(03)00302-0

Schönhardt, A., Altube, P., Gerilowski, K., Krautwurst, S., Hartmann, J., Meier, A. C., et al. (2015). A wide field-of-view imaging DOAS instrument for two-dimensional trace gas mapping from aircraft. *Atmos. Meas. Tech.* 8, 5113–5131. doi:10.5194/amt-8-5113-2015

Schönhardt, A., Richter, A., Theys, N., and Burrows, J. V. P. (2017). Space-based observation of volcanic iodine monoxide. *Atmos. Chem. Phys.* 17, 4857–4870. doi:10.5194/acp-17-4857-2017

Schwaerzel, M., Emde, C., Brunner, D., Morales, R., Wagner, T., Berne, A., et al. (2020). Three-dimensional radiative transfer effects on airborne and ground-based trace gas remote sensing. *Atmos. Meas. Tech.* 13, 4277–4293. doi:10.5194/amt-13-4277-2020

Shinohara, H. (2005). A new technique to estimate volcanic gas composition: Plume measurements with a portable multi-sensor system. *J. Volcanol. Geotherm. Res.* 143, 319–333. doi:10.1016/j.jvolgeores.2004.12.004

Shinohara, H., Matsushima, N., Kazahaya, K., and Ohwada, M. (2011). Magma-hydrothermal system interaction inferred from volcanic gas measurements obtained during 2003-2008 at Meakandake volcano, Hokkaido, Japan. *Bull. Volcanol.* 73, 409–421. doi:10.1007/s00445-011-0463-2

Shinohara, H., Yoshikawa, S., and Miyabuchi, Y. (2015). "Degassing activity of a volcanic crater lake: Volcanic plume measurements at the yudamari crater lake, aso volcano, Japan," in *Volcanic lakes. Advances in Volcanology*. Editors D. Rouwet, B. Christenson, F. Tassi, and J. Vandemeulebrouck (Berlin Heidelberg), 201–217. doi:10.1007/978-3-642-36833-2_8

Symonds, R. B., Gerlach, T. M., and Reed, M. H. (2001). Magmatic gas scrubbing: Implications for volcano monitoring. *J. Volcanol. Geotherm. Res.* 108, 303–341. doi:10.1016/S0377-0273(00)00292-4

Symonds, R. B., Reed, M. H., and Rose, W. I. (1992). Origin, speciation, and fluxes of trace-element gases at Augustine volcano, Alaska: Insights into magma degassing and fumarolic processes. *Geochim. Cosmochim. Acta* 56, 633–657. doi:10.1016/0016-7037(92)90087-Y

Syracuse, E. M., and Abers, G. A. (2006). Global compilation of variations in slab depth beneath arc volcanoes and implications. *Geochem. Geophys. Geosystems* 7. doi:10.1029/2005GC001045

Tack, F., Merlaud, A., Meier, A. C., Vlemmix, T., Ruhtz, T., Iordache, M. D., et al. (2019). Intercomparison of four airborne imaging DOAS systems for tropospheric NO_2 mapping - the AROMAPEX campaign. *Atmos. Meas. Tech.* 12, 211–236. doi:10.5194/amt-12-211-2019

Tamburello, G., Agusto, M., Caselli, A., Tassi, F., Vaselli, O., Calabrese, S., et al. (2015). Intense magmatic degassing through the lake of Copahue volcano, 2013–2014. *J. Geophys. Res. Solid Earth* 120, 6071–6084. doi:10.1002/2015JB012160

Taran, Y., and Zelenski, M. (2015). "Systematics of water isotopic composition and chlorine content in arc-volcanic gases," in *The role of volatiles in the genesis, evolution and eruption of arc magmas*. Editors G. F. Zellmer and S. M. Straub (London: Geological Society), 237–262. doi:10.1144/SP410.5

Theys, N., Campion, R., Clarisse, L., Brenot, H., van Gent, J., Dils, B., et al. (2013). Volcanic SO_2 fluxes derived from satellite data: A survey using OMI, GOME-2, IASI and MODIS. *Atmos. Chem. Phys.* 13, 5945–5968. doi:10.5194/acp-13-5945-2013

Theys, N., De Smedt, I., Roozendael, M. V., Froidevaux, L., Clarisse, L., and Hendrick, F. (2014). First satellite detection of volcanic OClO after the eruption of Puyehue-Cordon Caulle. *Geophys. Res. Lett.* 41, 667–672. doi:10.1002/2013GL058416

Theys, N., De Smedt, I., Yu, H., Danckaert, T., Van Gent, J., Hörmann, C., et al. (2017). Sulfur dioxide retrievals from TROPOMI onboard Sentinel-5 Precursor: Algorithm theoretical basis. *Atmos. Meas. Tech.* 10, 119–153. doi:10.5194/amt-10-119-2017

Theys, N., Hedelt, P., De Smedt, I., Lerot, C., Yu, H., Vlietinck, J., et al. (2019). Global monitoring of volcanic SO_2 degassing from space with unprecedented resolution. *Sci. Rep.* 9, 2643–2710. doi:10.1038/s41598-019-39279-y

Theys, N., Van Roozendael, M., Dils, B., Hendrick, F., Hao, N., and De Mazière, M. (2009). First satellite detection of volcanic bromine monoxide emission after the Kasatochi eruption. *Geophys. Res. Lett.* 36, 1–5. doi:10.1029/2008GL036552

Vandaele, A. C., Hermans, C., and Fally, S. (2009). Fourier transform measurements of SO_2 absorption cross sections: II. Temperature dependence in the 29 000-44 000 cm-1 (227-345 nm) region. *J. Quant. Spectrosc. Radiat. Transf.* 110, 2115–2126. doi:10.1016/j.jqsrt.2009.05.006

von Glasow, R. (2010). Atmospheric chemistry in volcanic plumes. *Proc. Natl. Acad. Sci. U. S. A.* 107, 6594–6599. doi:10.1073/pnas.0913164107

von Glasow, R., Bobrowski, N., and Kern, C. (2009). The effects of volcanic eruptions on atmospheric chemistry. *Chem. Geol.* 263, 131–142. doi:10.1016/j.chemgeo.2008.08.020

Wagner, T., Warnach, S., Beirle, S., Bobrowski, N., Jost, A., Pukite, J., et al. (2022). Investigation of 3D-effects for UV/vis satellite and ground based observations of volcanic plumes. *Atmos. Meas. Tech. Discuss.*, 1–44. doi:10.5194/amt-2022-253

Wallace, P. J., Kamenetsky, V. S., and Cervantes, P. (2015). Melt inclusion CO_2 contents, pressures of olivine crystallization, and the problem of shrinkage bubbles. *Am. Mineral.* 100, 787–794. doi:10.2138/am-2015-5029

Warnach, S., Bobrowski, N., Hidalgo, S., Arellano, S., Sihler, H., Dinger, F., et al. (2019). Variation of the BrO/SO_2 molar ratio in the plume of Tungurahua volcano between 2007 and 2017 and its relationship to volcanic activity. *Front. Earth Sci.* 7, 1–14. doi:10.3389/feart.2019.00132

Waythomas, C. F., Miller, T. P., and Begét, J. E. (2000). Record of late holocene debris avalanches and lahars at Iliamna Volcano, Alaska. *J. Volcanol. Geotherm. Res.* 104, 97–130. doi:10.1016/S0377-0273(00)00202-X

Werner, C. a., Doukas, M. P., and Kelly, P. J. (2011). Gas emissions from failed and actual eruptions from Cook Inlet Volcanoes, Alaska, 1989–2006. *Bull. Volcanol.* 73, 155–173. doi:10.1007/s00445-011-0453-4

Werner, C. A., Kern, C., and Kelly, P. J. (2020a). Chemical evaluation of water and gases collected from hydrothermal systems located in the central Aleutian arc, August 2015. *USGS Sci. Investig*, 35. Rep. 2020–5043 doi:10.3133/sir20205043

Werner, C., Kelly, P. J., Doukas, M., Lopez, T., Pfeffer, M., McGimsey, R., et al. (2013). Degassing of CO_2, SO_2, and H_2S associated with the 2009 eruption of Redoubt Volcano, Alaska. *J. Volcanol. Geotherm. Res.* 259, 270–284. doi:10.1016/j.jvolgeores.2012.04.012

Werner, C., Kern, C., Coppola, D., Lyons, J. J., Kelly, P. J., Wallace, K. L., et al. (2017). Magmatic degassing, lava dome extrusion, and explosions from Mount Cleveland volcano, Alaska, 2011-2015: Insight into the continuous nature of volcanic activity over multi-year timescales. *J. Volcanol. Geotherm. Res.* 337, 98–110. doi:10.1016/j.jvolgeores.2017.03.001

Werner, C., Power, J., Kelly, P., Prejean, S., and Kern, C. (2022). Characterizing unrest: A retrospective look at 20 years of gas emissions and seismicity at Iliamna Volcano, Alaska. *J. Volcanol. Geotherm. Res.* 422, 107448. doi:10.1016/j.jvolgeores.2021.107448

Werner, C., Rasmussen, D. J., Plank, T., Kelly, P. J., Kern, C., Lopez, T., et al. (2020b). Linking subsurface to surface using gas emission and melt inclusion data at Mount cleveland volcano, Alaska. *Geochem. Geophys. Geosystems* 21, 1–33. doi:10.1029/2019GC008882

Wilhelm, E., Battino, R., and Wilcock, R. J. (1977). Low-pressure solubility of gases in liquid water. *Chem. Rev.* 77, 219–262. doi:10.1021/cr60306a003

C. A. Wood and J. Kienle (Editors) (1990). *Volcanoes of north America: United States and Canada* (New York: Cambridge University Press).

frontiers | Frontiers in Earth Science

TYPE Original Research
PUBLISHED 18 May 2023
DOI 10.3389/feart.2023.1145343

OPEN ACCESS

EDITED BY
Thorvaldur Thordarson,
University of Iceland, Iceland

REVIEWED BY
Muhammad Aufaristama,
University of Twente, Netherlands
Francesco Marchese,
National Research Council (CNR), Italy

*CORRESPONDENCE
Ryo Tanaka,
r_tanaka@sci.hokudai.ac.jp

RECEIVED 16 January 2023
ACCEPTED 05 May 2023
PUBLISHED 18 May 2023

CITATION
Yamaguchi K, Tanaka R, Morita M, Mori T and Kazahaya R (2023), Sulfur dioxide flux measurement at Mount Tokachi, Japan, with TROPOspheric Monitoring Instrument.
Front. Earth Sci. 11:1145343.
doi: 10.3389/feart.2023.1145343

Sulfur dioxide flux measurement at Mount Tokachi, Japan, with TROPOspheric Monitoring Instrument

Kensuke Yamaguchi[1], Ryo Tanaka[2]*, Masaaki Morita[3], Toshiya Mori[4] and Ryunosuke Kazahaya[5]

[1]Department of Natural History Sciences, Graduate School of Science, Hokkaido University, Sapporo, Japan, [2]Faculty of Science, Institute of Seismology and Volcanology, Hokkaido University, Sapporo, Japan, [3]Earthquake Research Institute, The University of Tokyo, Tokyo, Japan, [4]Graduate School of Science, The University of Tokyo, Tokyo, Japan, [5]Geological Survey of Japan, National Institute of Advanced Industrial Science and Technology (AIST), Tsukuba, Japan

Introduction: Monitoring the volcanic activity of a potentially hazardous volcano is essential for eruption warning and hazard mitigation. The SO_2 flux from the volcano is one of the most important measures to understand its activity. Mount Tokachi, in Japan, is an active volcano that experienced three magmatic explosive eruptions in the 20th century (in 1926, 1962, and 1988–1989). Since 2006, geodetic observations have captured ground deformation, suggesting an inflation beneath the main crater. Moreover, since 2020 daily visual observations have detected the increase in plume heights and the occurrence of volcanic glow at the main crater. The high-time-resolution estimation of SO_2 flux will help monitor the activity of Mount Tokachi and clarify the associating mechanisms. Furthermore, satellite remote sensing can estimate the vertical column density (VCD) of sulfur dioxide (SO_2), enabling the daily determination of SO_2 flux without the need to visit the site. Due to the improved spatial resolution, the TROPOspheric Monitoring Instrument (TROPOMI) has advanced satellite-based volcanic gas flux measurements.

Methods: We have analyzed the available TROPOMI data and conducted ground-based observations to estimate the SO_2 flux from Mount Tokachi at 100–2,000 tons/day.

Result and Discussion: The average annual SO_2 flux has been increasing since 2021, on par with the increase in plume height and volcanic glow. TROPOMI data enabled quantification of the annual SO_2 flux, with a sufficient temporal resolution to monitor the volcanic activity at Mount Tokachi. However, a high flux, such as in excess of 2,000 tons/day, was observed in the winter season. The flux from the satellite data was similar to that from ground-based observations during the summer. However, a seasonal change in flux from the satellite data was observed in winter, with the flux being larger than that in summer, possibly because the flux increases during winter. Another possible reason is the influence of snow cover on satellite observations due to its high surface reflectance. We reanalyzed some TROPOMI data during the winter, in which the ground snow cover was misidentified as clouds at low altitudes. This procedure suppresses the error caused by the high surface reflectance due to winter snow coverage and improves the quality of the annual SO_2 flux from satellite observations. This methodology is

applicable to other high-latitude or high-altitude volcanoes during specific seasons characterized by frequent fluctuations in snow cover conditions.

KEYWORDS

SO_2 flux, remote sensing, Mount Tokachi, TROPOspheric Monitoring Instrument, volcano monitoring

1 Introduction

Volcanic gas degassed from magma provides crucial clues about magmatic processes within the shallow part of volcanoes. Sulfur dioxide (SO_2) in a volcanic plume is used as a proxy for volcanic gas flux because it is easily measured using ultraviolet (UV) remote sensing techniques, and the atmosphere is mostly SO_2-free. Moreover, the volcanic SO_2 flux is thought to reflect the supply rate of degassing magma (Wallace, 2001; Shinohara, 2008) and movements of magma and magmatic fluids inducing seismicity or ground deformation (Nadeau et al., 2011; Kazahaya et al., 2011; Kazahaya et al., 2015a; Kazahaya et al., 2015b; McGonigle et al., 2017). Notably, volcanic SO_2 flux has been measured since the 1970s (Stoiber et al., 1983; Edmonds et al., 2003; Salerno et al., 2009; Galle et al., 2010). Fluctuations in SO_2 flux in association with volcanic unrest have been reported for many active volcanoes (e.g., Daag et al., 1996; Poland et al., 2009; Kazahaya et al., 2015a; Mori et al., 2017), demonstrating the importance of monitoring SO_2 flux to implement eruption warnings and mitigate hazards.

The TROPOspheric Monitoring Instrument (TROPOMI) has advanced satellite-based volcanic gas flux measurements (Theys et al., 2017). This instrument provides a snapshot of the volcanic SO_2 plume with high temporal (mostly daily) and spatial ($3.5 \times 5.5\ km^2$) resolutions. The SO_2 is retrieved from band 3 (310–405 nm), with a typical spectral resolution of 0.54 nm and a signal-to-noise ratio of about 1,000. Theys et al. (2019) estimated SO_2 flux during eruptions at Mayon in the Philippines and Popocatepetl in Mexico using TROPOMI. Moreover, Queißer et al. (2019) applied back-trajectory modeling for the non-eruptive SO_2 plume from Mt. Etna, Italy, detected using TROPOMI to derive hourly SO_2 flux time series. These results were compared with ground-based observations to validate the quantitative performance of TROPOMI. Notably, besides eruptive dense SO_2 plumes, non-eruptive diluted plumes (lower SO_2 flux) can be detected and quantified using this novel technique.

Mount (Mt.) Tokachi is an active volcano located in central Hokkaido, Japan (**Figure 1A**), and has experienced three magmatic explosive eruptions in 1926, 1962, and 1988–1989 (Katsui et al., 1990). The 1926 eruption triggered lahars (Uesawa, 2014), which reached the town at the foot of the volcano, killing 144 people (Tada and Tsuya, 1927; Committee for Prevention of the Natural Disaster of Hokkaido, 1971). Uesawa (2014) proposed that hydrothermal fluids released due to a sector collapse caused by the eruption played a role in the long runout of the lahar. Based on the resistivity structure, Tanaka et al. (2021) pointed out that the volume of hydrothermal fluids existing just below the crater area of Mt. Tokachi is comparable to the volume affecting the 1926 lahar. Notably, lahars are common at Mt. Tokachi, taking place once every 250 years over the last 2,000 years (Nanri et al., 2008). Due to the increasing population of towns at the foot of the mountain, and more frequent tourist visitations, a lahar of the same magnitude as that of 1926 are a threat to population centers, tourists and infrastructure. Therefore, volcanic eruptions at Mt. Tokachi have the potential to cause large-scale volcanic disasters. Consequently, the volcano should be monitored at least monthly or better still weekly.

Notably, unrest has been observed at Mt. Tokachi; volcanic gas plumes are currently emitting from three craters (**Figure 1B**): Crater 62–2, of the 1962 eruption; Taisho Crater, formed in the 1926 eruption; and the Furikosawa Fumaroles, which appeared in 1972 and expanded its fumarolic zone during the 1988–1989 eruption. Recently, the main fumarolic activity has been at Crater 62–2 (Japan Meteorological Agency, 2021). Furthermore, Japan Meteorological Agency (JMA) has reported on pre-2005 fumarolic activity at Crater 62–2 was active before 2005, with a monthly maximum plume height in excess of 500 m (JMA, 2021). However, since 2005, this fumarolic activity has been sluggish. In addition, intermittent localized ground deformation observed since 2006 indicates inflation at the shallow part beneath the 62–2 crater (Regional Volcanic Observation and Warning Center, Sapporo Regional Headquarters, JMA, 2018). Also, annual magnetic total-field measurements have revealed demagnetization, indicating heating at a shallow depth beneath the crater (Hashimoto et al., 2010). Tanaka et al. (2017) suggested that these unrest episodes are triggered by the obstruction of the plume conduit. Additionally, they have pointed out that outgassing from the crater should be monitored to track and better understand this unrest at Mt. Tokachi. According to the JMA monthly volcanic activity report of Mt. Tokachi (https://www.data.jma.go.jp/svd/vois/data/tokyo/STOCK/monthly_v-act_doc/sapporo/22m10/108_22m10.pdf), an increase in plume height has been observed since 2018. Volcanic glow has occasionally been observed at crater 62–2 since June 2020. Therefore, geochemical and geophysical monitoring of this activity at Mt. Tokachi is paramount.

SO_2 flux is part of the monitoring of Mt. Tokachi activity. SO_2 flux measurements at Mt. Tokachi are conducted using ground- and satellite-based observations. Mori et al. (2013), using car and walking traverses, estimated the SO_2 flux at Mt. Tokachi in 2003 and 2006 to be approximately 200 tons/day. However, it is difficult to maintain such flux measurements using the ground-based traverses at sufficient frequency due to the limited number of routes suitable for ground traverse measurements around Mt. Tokachi (**Figure 1A**). Firstly, there are no suitable routes to the north, and secondly, the southern route (① of **Figure 1A**) is too far away (30 km) for the typical plume magnitudes at Mt. Tokachi. Thirdly, the route on the west side (② of **Figure 1A**) is at an adequate distance for this type of measurement, but the weather is often poor at times of easterly winds, and it is closed in winter because of snow. Fourthly, the eastern route (③ of **Figure 1A**) features many tunnels and trees that severely limit the sections where SO_2 can be

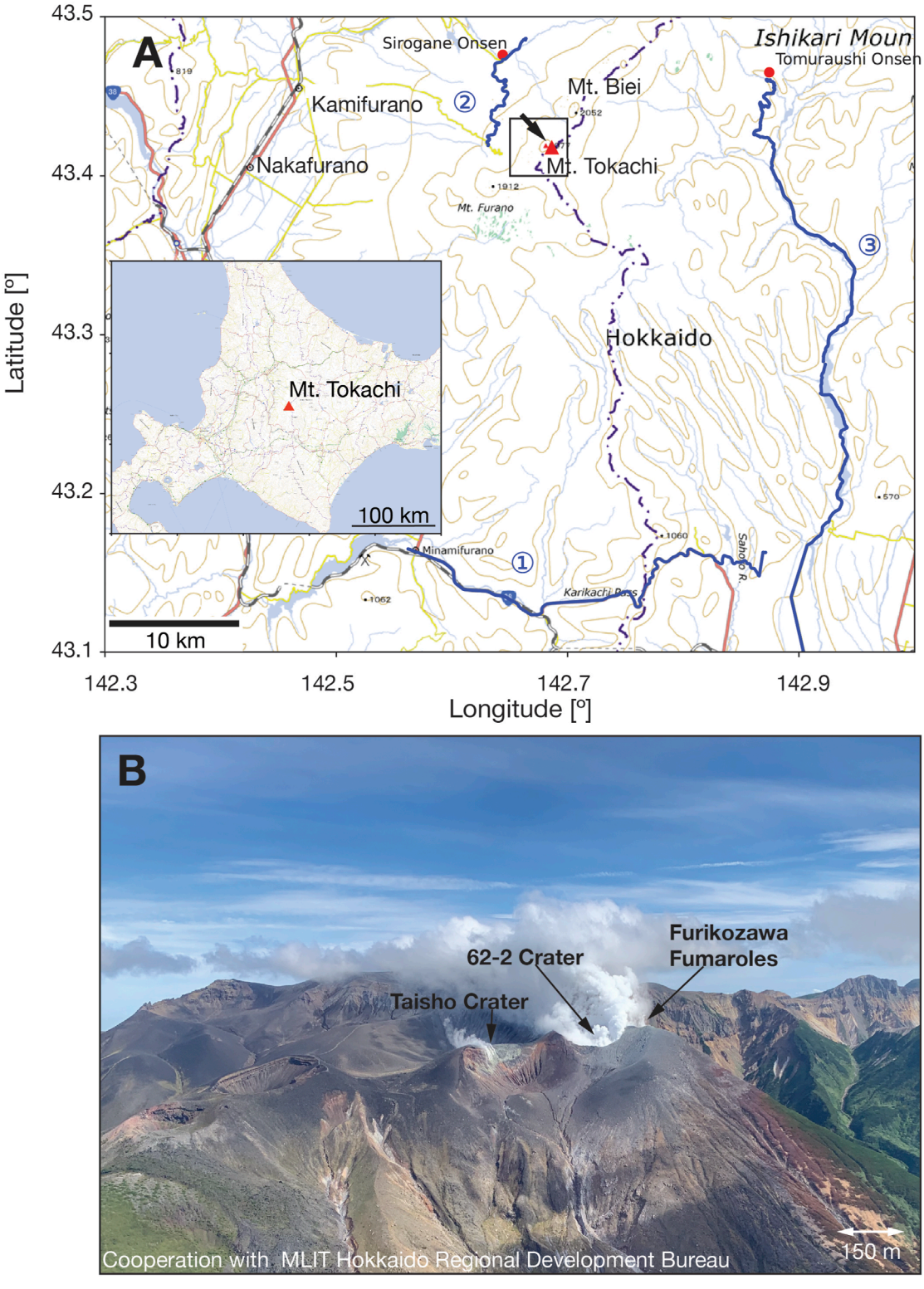

FIGURE 1
Location map of Mt. Tokachi and photograph of Mt. Tokachi. **(A)** Map of central Hokkaido (inset = Hokkaido) showing the location of Mt. Tokachi. The SO_2 flux measurement traverses route by car is indicated by the blue line. The lahars in 1926 reached Kamifurano and Nakafurano towns located west of Mt. Tokachi. The black arrow near the volcano indicates the direction of the Photograph **(B)**. **(B)** Photograph of the crater of Mt. Tokachi taken by Ryo Tanaka on 2 September 2022.

measured. Furthermore, measurements of the SO_2 flux by walking traverses around the craters have been undertaken every year since 2014. In 2015 and 2016, the traverse quantified the SO_2 flux as 200–500 tons/day (**Supplementary Material**). However, such traverses did not provide an estimate of the SO_2 flux in other years because the mountain can only be climbed in summer when the weather is good. Additionally, the extent of the walking paths is limited; hence, wind direction determines whether SO_2 flux can be measured.

Using satellite observations, Carn et al. (2017) estimated an average SO_2 flux at Mt. Tokachi of 135 tons/day between 2005 and 2015. However, they only reported on the annual average flux and used averaging or oversampling procedures to resolve the potential locations of SO_2 emissions. Furthermore, the Ozon Monitoring Instrument (OMI) used by Carn et al. (2017) had a low spatial resolution ($13 \times 24\ km^2$ at the nadir). High temporal resolution observations of small plumes are difficult with OMI because their estimation requires processing like done by Carn et al. (2017).

This study aims to demonstrate the applicability of TROPOMI in assessing SO_2 flux during 2019–2022 (non-eruptive period) at Mt. Tokachi and as such can be used to monitor ongoing but periodic volcanic unrest. We analyze data obtained via satellite- and ground-based observations at Mt. Tokachi, Japan. The ground-based data are used to validate the satellite observations.

2 Materials and methods

We analyzed satellite-based data obtained with TROPOMI between August 2019 and October 2022 and conducted ground-based measurements of car traverses as often as possible between June 2021 and March 2022.

For the satellite-based data, we used the TROPOMI SO_2 Level 2 data products processed by the European Space Agency (ESA) (Copernicus Sentinel data processed by ESA, German Aerospace Center DLR, 2019; Copernicus Sentinel data processed by ESA, German Aerospace Center DLR, 2020). We estimated the SO_2 flux based on the method proposed by Theys et al. (2019) with some modifications to apply to a relatively small-scale plume. The Level 2 products contain Vertical Column Density (VCD), assuming the presence of SO_2 plumes centered at 1, 7, and 15 km. Based on these data, the VCD for each pixel was estimated by linear interpolation, assuming that the SO_2 plume was located at an altitude of 2000 m (**Figure 2A**). This height was based on visual observations of the plume height routinely operated by JMA (Japan Meteorological Agency, 2021) that showed the data of 200–400 m above the crater rim (the rim of Crater 62–2 is approximately 1800 m). First, pixels with solar zenith angles > 70° were excluded, because they typically have large noise amplitudes. Second, we excluded pixels with VCD values smaller than the VCD error values (**Figure 2B**). Although Theys et al. (2019) used Slant Column Density (SCD) and SCD error × 3 as criteria, they are too strict for detecting the plume from Mt. Tokachi. We also tried to use the SCD error × 1–3 and the VCD error × 1–3 as the criteria. Among them, the criteria as the VCD error × 1 was the best at extracting plumes. Additionally, to further exclude isolated pixels that did not correspond to the plumes, we applied a median filter that employed the median of nine adjacent cells and excluded pixels whose median value was less than the VCD error value (**Figure 2C**).

Next, the days for flux estimation were selected based on plume continuity which was determined using concentric circles (distance windows), indicating the distance of the plume advection from the volcano. We set a distance window as 10 km width based on TROPOMI's pixel size. At TROPOMI's pixel size, a 10 km width contains at least two pixels. Although a time window with a fixed time (30 min) regardless of wind speed was used by Theys et al. (2019), the width (distance) of the time window became wider, and fewer plumes filled a single time window as the wind speed increased. Therefore, we adopted distance windows with a constant width independent of the wind speed. Next, we drew distance windows corresponding to the advection distance within 6 h, assuming a constant wind speed around the volcano (**Figure 2C**). Regarding the constant wind speed, we used the average wind speed of the grid point value (GPV) data obtained from the mesoscale numerical weather prediction model (MSM) designed by JMA at 800 MPa isobars (corresponding to 2,000 m altitude) above Mt. Tokachi. Additionally, regarding the days for flux estimation, we visually picked days when the plume extended over two or more distance windows. Notably, days with wind speeds of $\geq 2\ m\ s^{-1}$ were included in the analysis because the plume may be retained around the crater if the wind speed is low.

The distance windows for flux estimation were determined using the following procedures. First, pixels with cloud fractions (including the L2 products) > 0.5 were masked to exclude cloud effects (**Figure 2D**). Next, the distance windows where the plume crosses more than two such windows, even with cloud masking, were used to integrate the VCD. Whether a plume crosses two or more windows was determined by visual inspection. The window closest to the volcano was excluded from the VCD integration to avoid overestimation due to stagnation of the plume near the crater or underestimation due to a narrow width of the plume against the area of the pixel. Additionally, the area outside 90° to the direction of the plume flow was masked to remove noise unrelated to the plume (**Figure 2E**). The direction of the plume flow was visually determined from the VCD map and corrected in 15° increments relative to the GPV wind direction. When the plume direction was masked at 90° or 180° to the GPV wind direction without any correction. The former caused slightly off-center plumes to be missed, and the latter caused the enhanced noise level, which was problematic.

Lastly, SO_2 flux was determined as follows. First, the cloud mask was removed because if it partially masks pixels within the range for integration, it may cause underestimation (**Figure 2E**). Next, the VCDs within the selected distance windows were integrated. Subsequently, the daily flux was estimated using the integrated VCDs and advection times corresponding to the distance windows used. Some pixels with a cloud fraction > 0.5 may be included in the integration range, which may result in underestimation of the SO_2 flux. Nevertheless, the crater of Mt. Tokachi is at 1800 m, often above the clouds; therefore, not all days with cloud cover resulted in an underestimation of the flux. Additionally, we labeled days that met the conditions listed above "good" and days that did not slightly meet some of the conditions or with some problems but attempted to estimate flux were designated "poor".

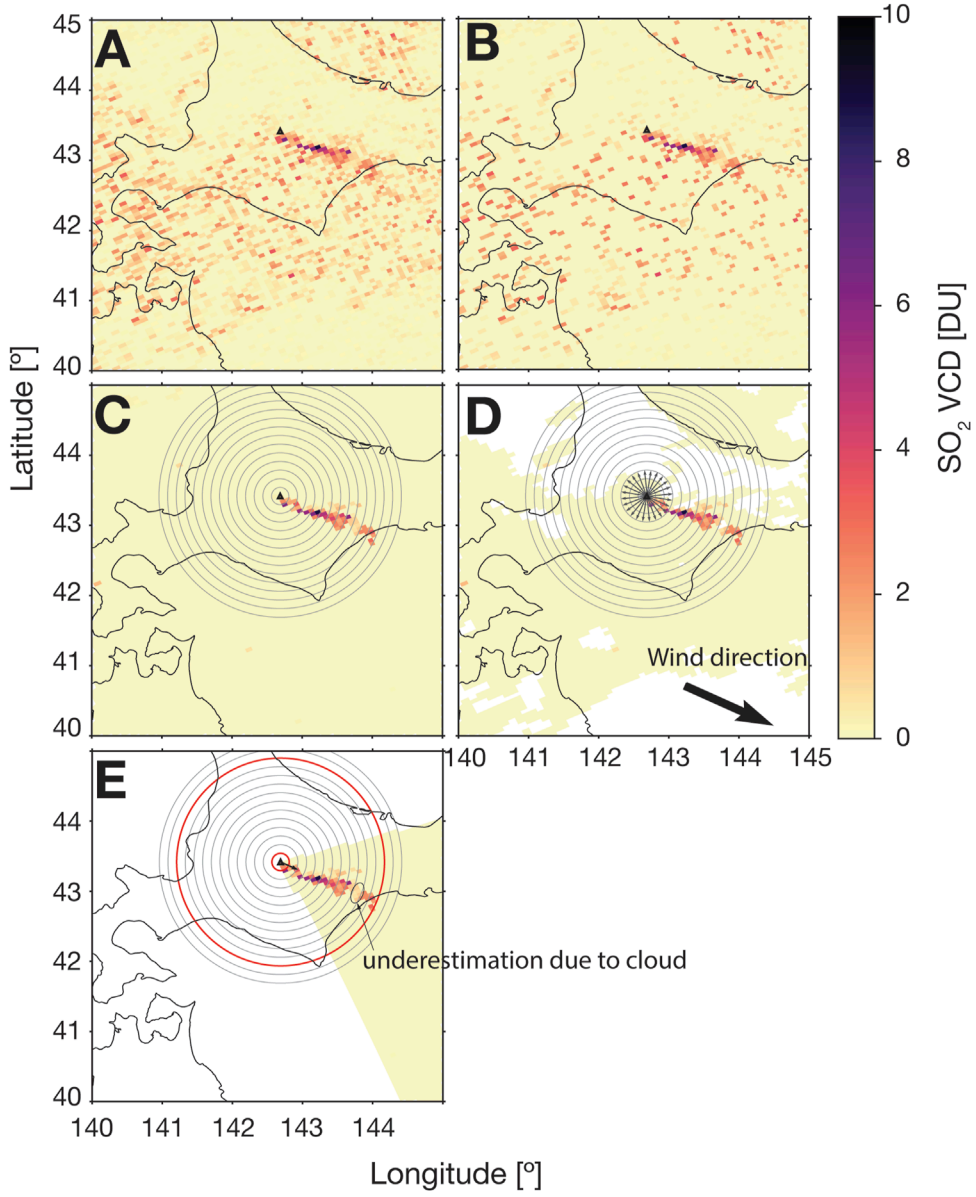

FIGURE 2
SO_2 vertical column density (VCD) distribution during the procedure to calculate the flux by satellite data. **(A)** VCD distribution linearly interpolated by plume altitude. The plume altitude is assumed to be 2000 m and linearly interpolated from 1 km to 7 km data in the TROPOMI L2 data set. **(B)** VCD distribution after filtering pixels with 1) solar zenith angle > 70°, 2) VCD value less than the VCD error. **(C)** VCD distribution with isolated signals removed using a median filter. **(D)** VCD distribution masked cloud fraction (> 50%) with the distance windows (~ 10 km, black circles), the wind direction (black arrow), and gray arrows for the correction of the plume direction. We determined the distance windows for the flux estimation with this figure. **(E)** VCD distribution for the integration of VCD and the estimation of the flux. The mask by cloud fraction is removed. The outside of the direction of the plume (±45°) is now masked. We integrated the area between two red circles and estimated the SO_2 flux.

Ground-based observations were conducted using the car traverse method. A miniature UV spectrometer (USB 2000+, Ocean Optics, Inc.) was mounted on the vehicle and passed under the plume to measure the VCD of SO_2. The VCD was obtained using Mobile DOAS software (Arellano et al., 2019) through the three routes shown in **Figure 1**. The software collects UV spectra of the zenith sky during the traverse, automatically analyze the spectra for SO_2 VCD by DOAS (Differential Optical Absorption Spectroscopy) method (Platt and Stutz, 2008) in real-time, and records the calculated VCD together with GPS positions. Next, the SO_2 flux was estimated by multiplying the plume advection velocity by the integral of the VCDs in the cross-section perpendicular to the direction of the plume advection using the Mobile DOAS. Regarding plume advection velocity, we used an average wind speed of GPV data obtained from the mesoscale numerical weather prediction model (MSM) designed by JMA at 800 MPa isobars (corresponding to 2000 m altitude) above Mt. Tokachi.

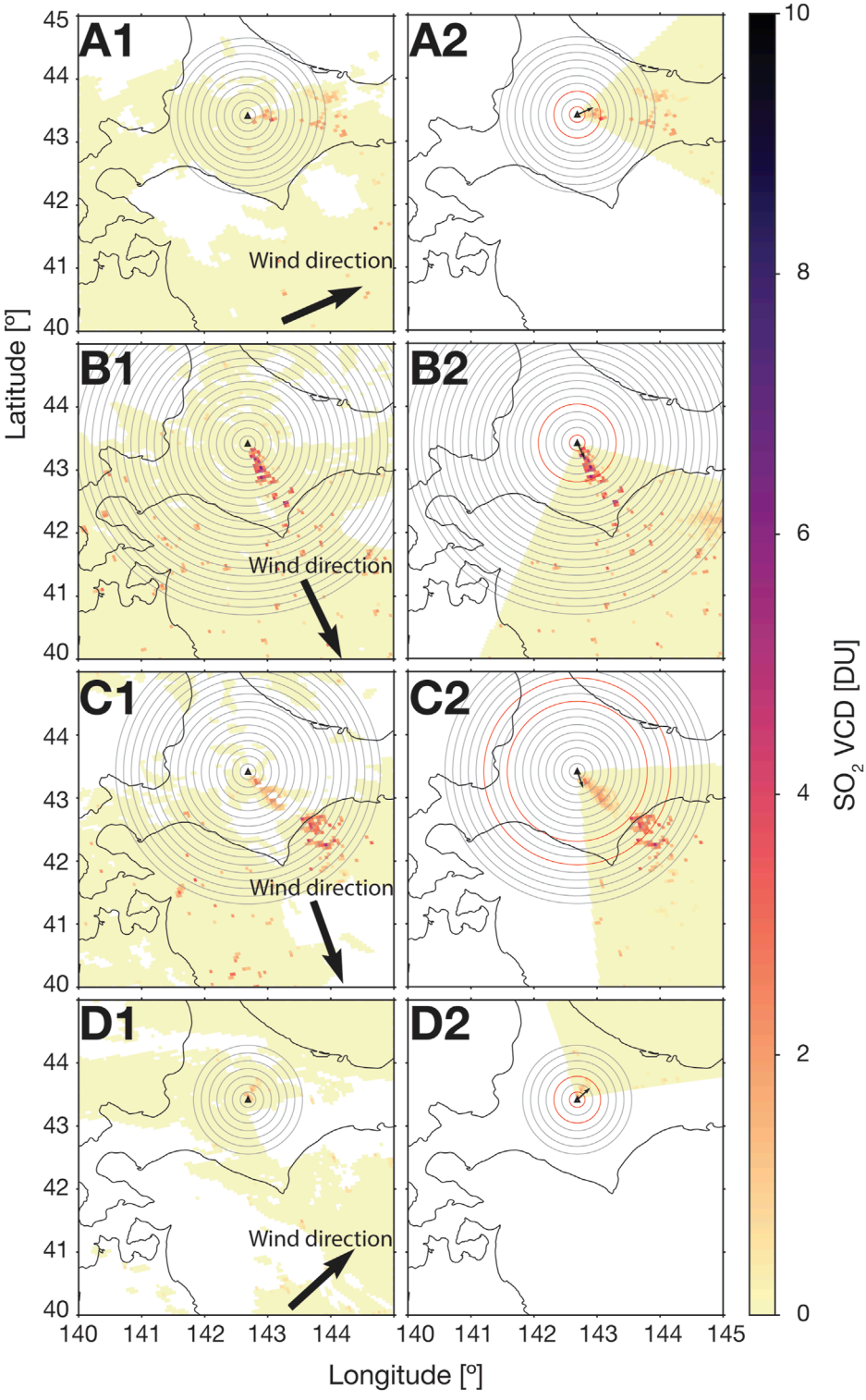

FIGURE 3
Examples of "good" VCD distribution for SO_2 flux estimation (1: masked by cloud fraction, 2: for VCD integration). Black circles are distance windows. The black arrow represents the wind direction. We integrated VCDs between two red circles. **(A)** 7 August 2019, example of the day with low wind velocity; wind velocity v = 4.6 m s^{-1}, SO_2 flux M = 185.9 ± 34.1 tons/day. **(B)** 20 July 2021, example of the day with high wind velocity; wind velocity v = 10.2 m s^{-1}, SO_2 flux M = 931.9 ± 202.7 tons/day. **(C)** 28 July 2022, example of the plume fragmented by cloud mask. We estimated SO_2 flux using the detached area. Wind velocity v = 7.7 m s^{-1}, SO_2 flux M = 389.0 ± 119.0 tons/day. **(D)** 3 October 2019, example of the day with low flux; wind velocity v = 3.2 m s^{-1}, SO_2 flux M = 66.1 ± 15.8 tons/day.

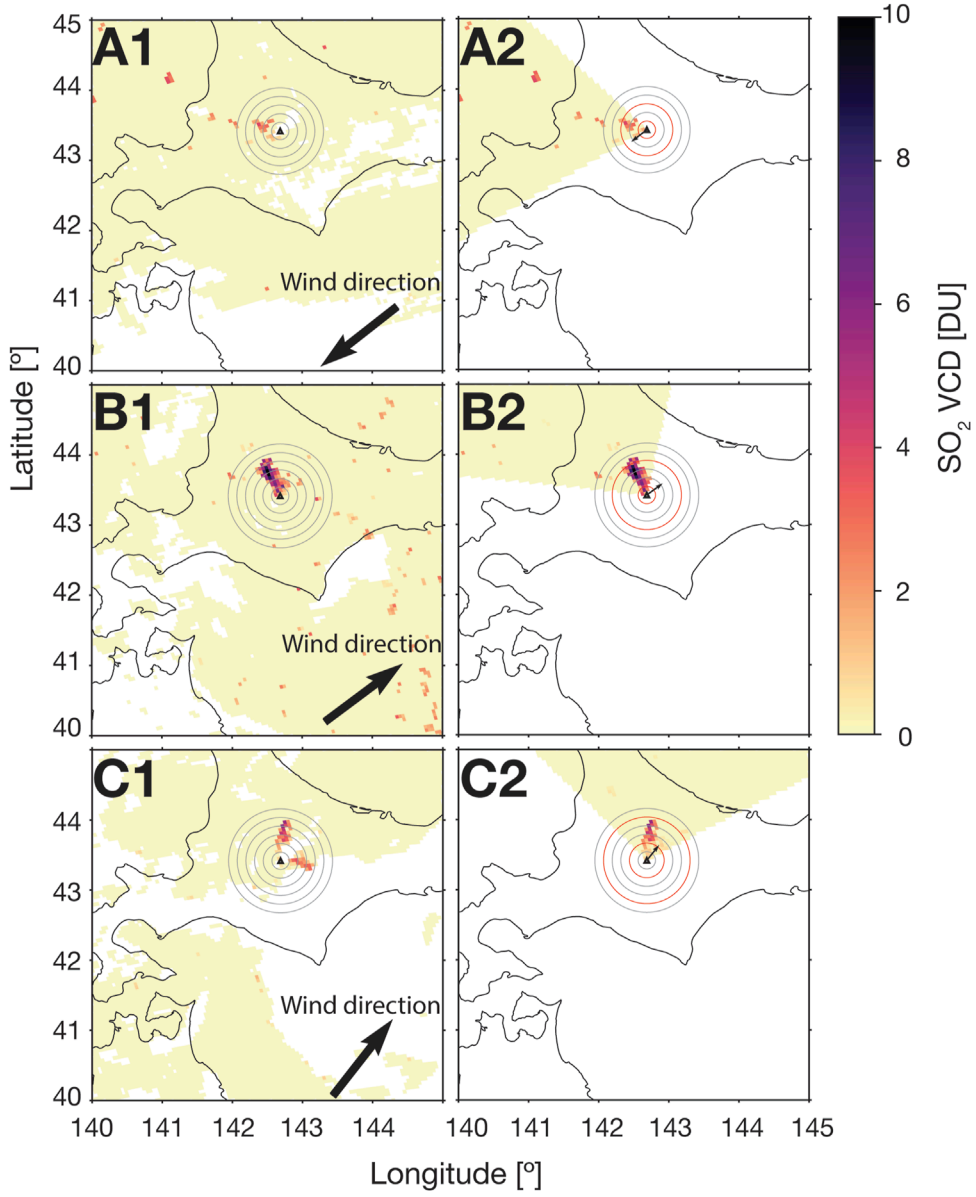

FIGURE 4
Example of SO_2 flux measurements with a few unsatisfactory or problematic conditions (1: masked by cloud fraction, 2: for the integration of VCD). Black circles are distance windows. The black arrow represents the wind direction. We integrated VCDs between two red circles. These days are labeled as "poor" and plotted with black symbols in **Figure 5**. **(A)** 13 April 2020, example of the day that slightly fails to satisfy the requirement of being across two distance windows; wind velocity v = 2.2 m s^{-1}, SO_2 flux M = 150.1 ± 44.7 tons/day. **(B)** 21 August 2021, example of significant difference (≤ 60°) between wind and plume directions; wind velocity v = 2.5 m s^{-1}, SO_2 flux M = 469.0 ± 89.6 tons/day. **(C)** 11 September 2021, example of plume advecting in two directions; wind velocity v = 2.5 m s^{-1}, SO_2 flux M = 229.3 ± 39.2 tons/day. We integrated only the plume with higher VCDs than others.

3 Results

We estimated the SO_2 flux from Mt. Tokachi, regardless of the wind direction and speed. **Figure 3** shows "good" examples of the VCD distribution on a day suitable for flux estimation. **Figure 3A** shows an example from 7 August 2019, of a day with a low wind velocity. Near the volcano a continuous plume is observed, and the flux is estimated using pixels crossing two distance windows. **Figure 3B** shows an example from 20 July 2021, a day with high wind velocity. The distance windows enabled us to integrate the plume at an appropriate length, even if plume continuity was lost at ~ 50 km distance from the source vent. We included in our analysis cases when continuity was confirmed in the absence of the cloud mask, even if the plume is fragmented by the application of a cloud mask, as shown for 28 July 2022 (**Figure 3C**). In such a case, we only used the pixels with lower cloud fractions for the flux estimation. Lastly, 3 October 2019, is an example of one of the lowest observed fluxes (**Figure 3D**). The high spatial resolution of TROPOMI enabled us to quantify SO_2 plumes of < 100 tons/day under suitable conditions. All analyzed data are shown in the **Supplemental Material**.

We analyzed the data with a few unsatisfactory or problematic conditions labeled as "poor" and examples are shown on Figure 4. An example that marginally fails to satisfy the condition of crossing two distance windows is shown in Figure 4A. In such cases, we integrated the VCDs within a single distance window. An example of a significant difference between wind and plume directions is illustrated in Figure 4B. Here, we defined a significant difference as ≥ 60° and treated the data as problematic because it is not given that the wind velocity matches may not match the advection velocity of the plume. As shown in Figure 4C, the plume was advected in two directions and most likely caused by variations in the wind direction with altitude. If integration is not carried out in both directions the SO_2 flux may be underestimated. Also, as wind speeds may differ in relation to direction, only the plume matching roughly to the wind direction was integrated into this case. This situation was observed for only 1 day during the analyzed period. All "poor" data are shown in the Supplemental Material.

Ground-based observations obtained a flux of 80–600 tons/day in 2021 (Table 1). Only the measurements on 2 March 2022, indicated high SO_2 flux of 1,287 ± 643 tons/day. As we reside in Sapporo, Hokkaido, 150–225 km from Mt. Tokachi, only days with a promising weather forecast and favorable wind direction were selected for traverse measurements. For this study only 5 days produced reliable measurements.

On the other hand, we obtained measurements of the daily SO_2 flux at Mt Tokachi from 108 days using satellite-based observations. Figure 5 shows the temporal variation in SO_2 flux. The minimum time interval at which the flux could be estimated by analyzing the satellite data was 1 day, the maximum was approximately 2 months, and the average was approximately 10 days. Analyzing satellite data made it possible to quantify SO_2 flux throughout the year and the temporal resolution is high enough to monitor volcanic activity. The SO_2 flux from Mt. Tokachi in 2019–2022 ranged from ~ 100–2,000 tons/day. However, fluxes exceeding 2,000 tons/day, were only obtained in winter, while the flux estimated from the ground and satellite observations was consistent and stable during the summer.

TABLE 1 Results of ground observation.

Day	Route	Number of trials	Wind speed [m/s]	Flux [tons/day]
2021/6/9	1 and 3	7	13	349 ± 255
2021/6/23	2	6	3	551 ± 78
2021/8/13	3	2	1	80 ± 16
2021/12/9	3	4	2	207 ± 162
2022/3/2	3	6	13	1,287 ± 643

4 Discussion

Two factors influence the seasonal variation: 1) the winter effect (i.e., the snow cover) on satellite data and 2) enhancement of the volcanic activity in winter. First, we address the influence of snow cover on satellite data. The blue bars in Figure 5 show the snow depth at an AMeDAS station (Kamishihoro) located 53 km east-southeast of Mt. Tokachi. The strong positive correlation between snow depth and enhanced SO_2 flux suggests that the seasonal flux-increase might be induced by greater surface reflectance because of the snow cover. TROPOMI measures SCD, which is converted to VCD using a conversion factor—Air Mass Factor (AMF). AMF considers observations' geometrical information, total ozone absorption, clouds, and surface albedo (Theys et al., 2019). According to Romahn et al. (2020), the AMF of TROPOMI was calculated using the climatological monthly minimum Lambertian equivalent reflector (minLER) measured by OMI as the surface

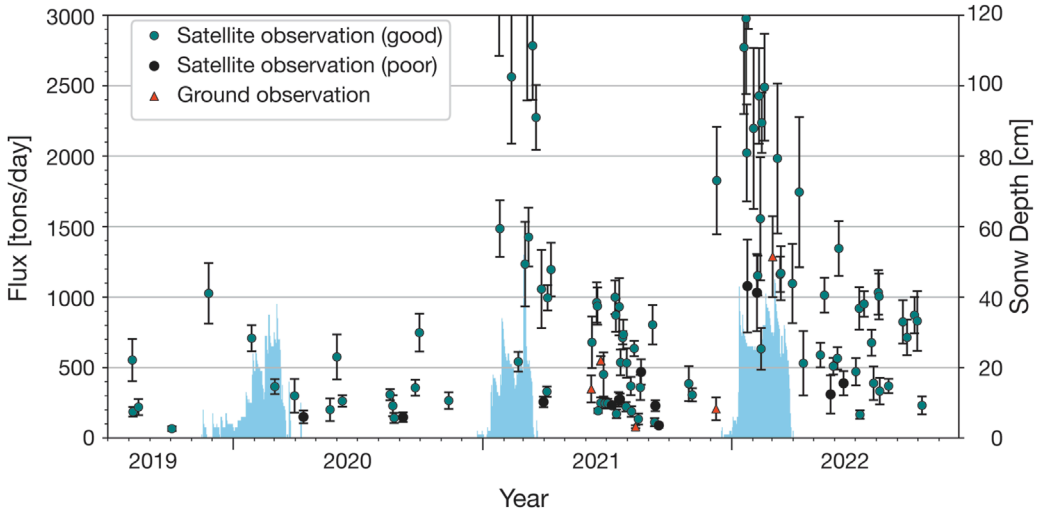

FIGURE 5
Temporal variation in the SO_2 flux at Mt. Tokachi according to satellite data and ground-based observations. The green and black circles represent the flux measured by satellite observations. The red triangles represent ground-based observations. The blue bar indicates the snow thickness at AMeDAS, located approximately 53 km east-southeast of Mt. Tokachi. SO_2 flux of approximately 100–2,000< tons/day can be quantified throughout the year. However, seasonal variations are observed, with a larger flux in winter than in summer.

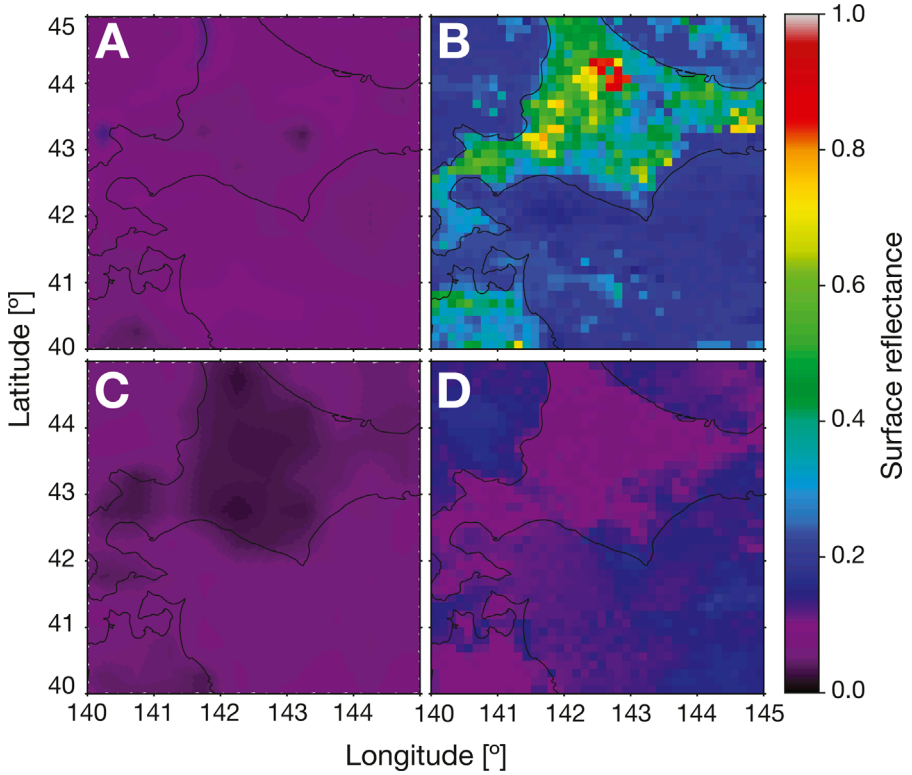

FIGURE 6
Examples of surface reflectance. **(A)** Surface reflectance (minLER for 328 nm) in January observed by OMI used in TROPOMI's AMF calculations included in TROPOMI L2 products. Despite the fact that the observations are from the winter season, the reflectivity is on par with the summer values. **(B)** Surface reflectance (minLER in snow and ice condition for 328 nm) in January observed by TROPOMI (Tilstra, 2022). The reflectance is relatively high. **(C)** July surface reflectance (minLER for 328 nm) observed by OMI used in TROPOMI's AMF calculations included in TROPOMI L2 products. **(D)** July surface reflectance (minLER in snow and ice-free condition for 328 nm) observed by TROPOMI (Tilstra, 2022).

reflectance (**Figures 6A, C**, data are included in TROPOMI L2 products). No significant difference was observed between January (**Figure 6A**) and July (**Figure 6C**), even though surface reflectance may be more significant in winter due to snow cover. **Figures 6B, D** show the minLER of 328 nm UV light in the TROPOMI data products, which is close to the actual reflectance (Tilstra, 2022). The reflectance in January (**Figure 6B**) was higher than that in July (**Figure 6D**). Furthermore, by comparing the OMI data with the TROPOMI data for winter (January), TROPOMI data have a considerably higher reflectance. According to Theys et al. (2017), AMF values near the ground surface vary significantly with surface albedo by a factor of 2–3 compared with albedo values of 0.06 and 0.8. Therefore, an overestimation of SO_2 VCD due to AMF calculated using an albedo smaller than the actual situation may influence the tendency of SO_2 flux to increase during winter.

To monitor volcanic activity from satellites throughout the year, SO_2 VCD must be estimated correctly during the snow season (winter). Notably, calculating the AMF using the appropriate albedo input is the most appropriate correction method. However, this is labor-intensive and must be calculated using a radiative transfer program, such as VLIDORT (Spurr, 2006). Herein, we propose a correction method based on the fact that there were days when snow cover was recognized as clouds in the TROPOMI products. For example, in the visible satellite image on 9 March 2021, no clouds appeared over Hokkaido (**Figure 7A**). On the other hand, the cloud height data in the TROPOMI dataset shows clouds (cloud fraction of approximately 1.0) near the ground surface (**Figures 7B,C**), indicating that snow cover may be misidentified as a cloud. This area was masked by cloud fraction in the previous SO_2 flux estimation procedure (**Figure 7D**). Next, the VCD map was recreated without a cloud mask because the actual cloud cover was not present (**Figure 7E**). The VCD in the black circle of **Figure 7E** was calculated with high cloud reflectivity, comparable to snow reflectivity, and represented a more realistic VCD. Additionally, the VCD was lower than the surrounding area, and the SO_2 flux was calculated using this area where snow cover is erroneously identified as a cloud (**Figure 7F**). The flux decreased from $1,425.3 \pm 208.0$ to 502.7 ± 83.2 tons/day. Supposing the lower value was correct, incorrect ground reflectances would have resulted in an approximately 2.8 times overestimation. **Figure 7G** shows the temporal variation of the flux with the reanalyzed data, in which the snow cover was misidentified as winter clouds. Although the number of days analyzed was small, the fluxes reanalyzed were not significantly higher than the initial values. Also, they are in the same range as those in the summer. Using this method, we can obtain the flux with a probability of accuracy in other high latitude or high altitude volcanoes, although under set of specific conditions. This evaluation contributes to the understanding and monitoring of volcanic activity.

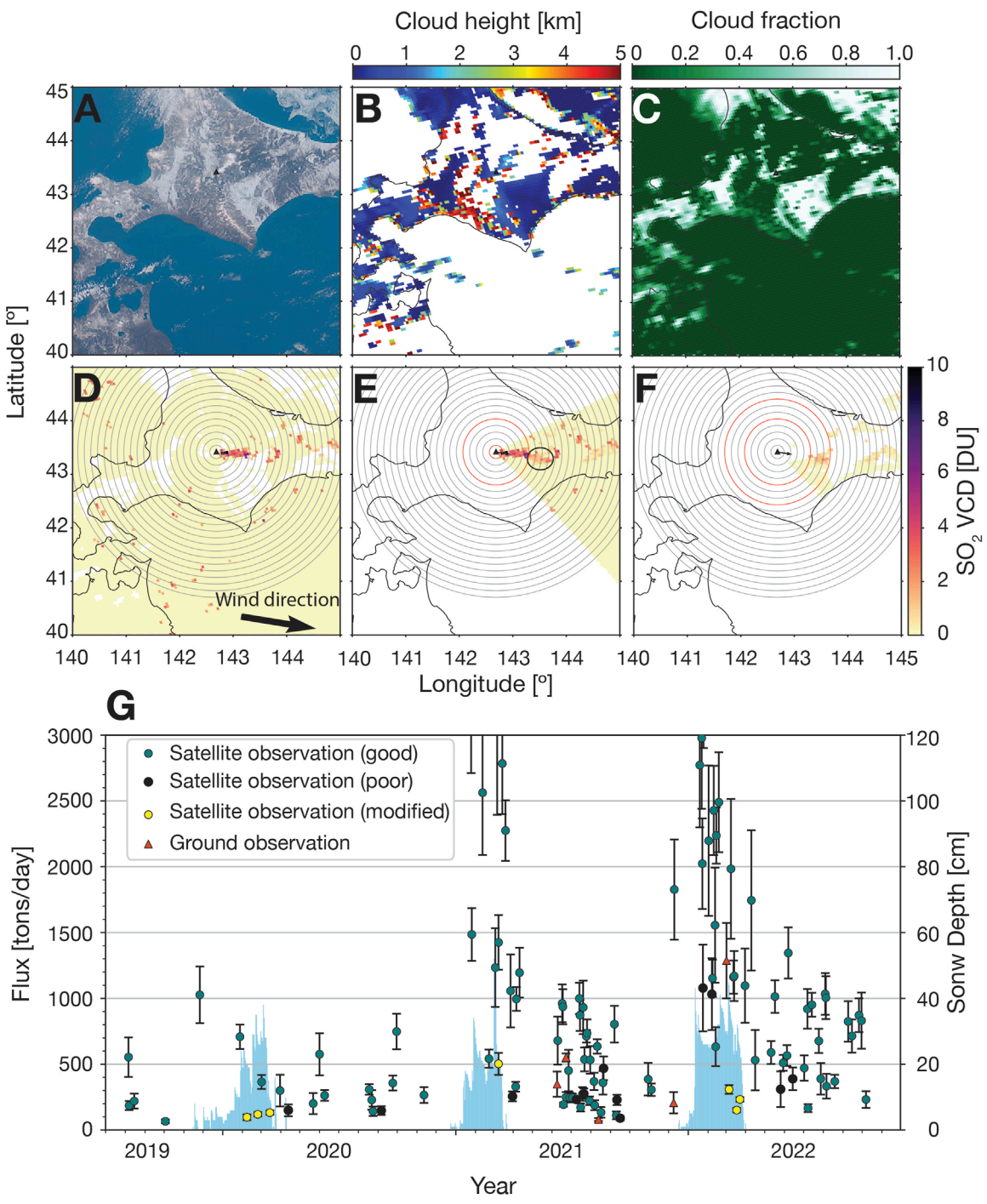

FIGURE 7
Processes and results of the newly proposed method. **(A)** Satellite visible image on 9 March 2021. There are no clouds over Hokkaido. **(B)** Cloud height as indicated in TROPOMI data products. Clouds are seen near the ground surface. **(C)** Cloud fraction as indicated in TROPOMI data products. Although there are no clouds over Hokkaido, some areas are covered high cloud fraction. **(D)** VCD distribution with cloud mask used for determination of the distance windows for the flux estimation. Black circles are distance windows. The black arrow represents the wind direction. The gray arrows are displayed for the correction of the plume direction. **(E)** VCD distribution is used for flux estimation by the conventional method. The area (in the black circle) masked by clouds in **(D)** has a lower VCD value than other areas. The black arrow indicates the wind direction. We integrated VCDs between two red circles. **(F)** VCD distribution for flux estimation by the new method. The pixels with low cloud fractions (< 0.5) are masked. The black arrow indicates the wind direction. We integrated VCDs between two red circles. **(G)** Time series with some of the data reanalyzed with the new method (yellow symbols). Seasonal variations appear to have been suppressed, although the number of days that could be analyzed is small.

Next, we address the possibility of increased winter SO_2 emissions at Mt. Tokachi as indicated by satellite-based measurements and hinted at by ground-based measurements on 2 March 2022. Here, we consider scrubbing (Kusakabe et al., 2000; Symonds et al., 2001) and S formation reactions (Shinohara et al., 2011) as the possible cause for seasonal changes in the SO_2 emissions. Scrubbing is a process that reduces emissions during reactions between magmatic gas, water, and, occasionally, rock (Symonds et al., 2001). Symonds et al. (2001) reported that scrubbing with water can remove significant amounts of SO_2. Furthermore, Tanaka et al. (2021) has suggested a significant amount of water contained within the hydrothermal system beneath 62–2 craters according to Audio-Magnetotelluric measurements during summer. Moreover, precipitation occurs throughout the year around Mt. Tokachi, and there is always a recharge of meteoritic water to the hydrothermal system; however, the recharge may decrease in winter due to snow accumulation. Therefore, a decline in groundwater volume could decrease the effectiveness of scrubbing, thereby increasing the actual SO_2 emissions during winter.

Breakdown of sulfur species produces water and sulfur from SO_2 and H_2S. This reaction occurs below 200°C–250°C. The temperature at crater 62–2, measured in summer using an infrared thermometer, was approximately 200°C–400°C in 2020 and approximately 300°C after 2021 (Japan Meteorological Agency, 2021). However, the crater temperature in winter is unknown because it has not been observed. Nevertheless, assuming lower temperatures in winter, this reaction will be accelerated, producing S and consuming SO_2; however, if it increases, the opposite reaction consumes S and produces SO_2. If the recharge rate decreases in winter, the amount of rainwater mixed with hydrothermal fluids may decrease, and the fumarolic temperature will increase and so will the SO_2 emissions. To differentiate between these possible causes for the apparent seasonal changes in detected SO_2 flux, more frequent ground-based observations and observations of the compositional ratios of volcanic gases during winter are needed.

Satellite-based SO_2 flux measurements at Mt. Tokachi have enabled us to monitor the SO_2 flux throughout the year, although flux assessment during winter is challenging. SO_2 flux averaged between May and September of each year was 203 ± 44 tons/day in 2019 (August only), 330 ± 85 tons/day in 2020, 462 ± 93 tons/day in 2021, and 680 ± 124 tons/day in 2022. Previous studies estimated the SO_2 flux at Mt. Tokachi to be 200 tons/day in 2003 and 2006 (Mori et al., 2013) and 135 tons/day between 2005 and 2015 (Carn et al., 2017). Notably, the SO_2 flux between 2019 and 2020 is comparable to that between 2003 and 2015 but lower than that between 2021 and 2022. In 2003, the monthly maximum plume height at crater 62–2 (~ 800 m) was higher than in 2022, and the monthly average of the daily maximum (~ 300 m) was similar to that in 2022 (JMA: Monthly volcanic activity report of Mt. Tokachi, https://www.data.jma.go.jp/svd/vois/data/tokyo/STOCK/monthly_v-act_doc/sapporo/22m10/108_22m10.pdf). This suggests changes in the volcanic gases currently released at Mt. Tokachi are more SO_2-rich. The recent trend of increasing plume height and volcanic glow at crater 62–2 is consistent with these results. If there is an escalation of the activity at Mt. Tokachi and a rapid increase in SO_2 flux, as demonstrated here, the TROPOMI data are sufficient for such detection and long term monitoring, although it may be difficult to detect it in winter. For clarification, the high frequency of SO_2 flux measurements using satellites is essential to consider the mass balance and to determine the mechanisms of ground deformation and total magnetic field changes which reflect the magma and magmatic fluids movements below crater 62–2 and monitor the activity of Mt. Tokachi.

5 Conclusion

We attempted to quantify the SO_2 flux from Mt. Tokachi, Japan, using TROPOMI. We analyzed the satellite data and ground-based observations at Mt. Tokachi during the non-eruptive period and compared them to validate satellite-based estimates. Although the ground-based observations succeeded only on 5 days from June 2021 to March 2022, the satellite-based observations enabled us to collect a daily SO_2 flux for 108 days between August 2019 and October 2022. The satellite-based observations using TROPOMI have the potential to monitor the SO_2 flux from volcanoes where ground-based measurements are generally difficult to be performed. Satellite-based SO_2 flux estimation at Mt. Tokachi enabled us to estimate SO_2 flux at high frequencies throughout the year, although seasonal changes were recognized. Moreover, the SO_2 flux from Mt. Tokachi in 2019–2022 was approximately 100–2,000 tons/day. Comparing our results with previous studies, the flux from Mt. Tokachi has increased recently. This trend is consistent with that of plume height and the occurrence of volcanic glow. Additionally, the results of the ground and satellite observations were consistent in the summer. The seasonal change may be attributed to snow cover's effect on satellite observations and the actual flux increase in winter. Nevertheless, continuous ground-based observations are needed to determine whether the actual SO_2 emissions during winter are increasing. Furthermore, it is necessary to correctly estimate SO_2 VCD during the snow season to monitor volcanic activity from satellites throughout the year. We proposed a method for estimating flux using only those regions of satellite data that misidentified snow cover as clouds. This method may be applied to other high latitude and altitude volcanoes in certain seasons when snow cover condition is frequently changing (e.g., ending or beginning of the summer season at Antarctic and Icelandic volcanoes). The high frequency of SO_2 flux measurements using satellites is essential to determine the mechanisms of unrest that reflect the magma and magmatic fluids movements.

Data availability statement

The original contributions presented in the study are included in the article/**Supplementary Material**, further inquiries can be directed to the corresponding author.

Author contributions

KY collected, analyzed, and discussed the data. RT drafted the manuscript, collected data, and discussed the data. MM, TM, and RK contributed to the data collection, analysis, and discussion. All authors contributed to the manuscript revision and read and approved the submitted version. All authors contributed to the article and approved the submitted version.

Acknowledgments

We acknowledge the free use of the TROPOMI surface DLER database provided by the Sentinel- 5p+ Innovation project of the European Space Agency (ESA). The TROPOMI Surface DLER database was created by the Royal Netherlands Meteorological Institute (KNMI). We would like to thank Editage (www.editage.com) for English language editing.

Conflict of interest

The authors declare that the research was conducted in the absence of any commercial or financial relationships that could be construed as a potential conflict of interest.

Publisher's note

All claims expressed in this article are solely those of the authors and do not necessarily represent those of their affiliated organizations, or those of the publisher, the editors and the reviewers. Any product that may be evaluated in this article, or claim that may be made by its manufacturer, is not guaranteed or endorsed by the publisher.

Supplementary material

The Supplementary Material for this article can be found online at: https://www.frontiersin.org/articles/10.3389/feart.2023.1145343/full#supplementary-material

References

Arellano, S., Kern, C., and Norgaard, D. (2019). *Mobile DOAS v6.1 software manual*.

Carn, S., Fioletov, V., McLinden, C., Li, C., and Krotkov, N. (2017). A decade of global volcanic SO_2 emissions measured from space. *Sci. Rep.* 7, 44095–44112. doi:10.1038/srep44095

Committee for Prevention of the Natural Disaster of Hokkaido (1971). *Tokachidake: The report on the volcanoes of hokkaido, part 1*. (in japanese).

Copernicus Sentinel data processed by ESA, German Aerospace Center (DLR) (2020). *Greenbelt, MD, USA, goddard Earth sciences data and information services center (GES DISC)*.

Copernicus Sentinel data processed by ESA, German Aerospace Center (DLR) (2019). *Sentinel-5P TROPOMI sulphur dioxide SO_2 1-orbit L2 5.5km x 3.5km*. Greenbelt, MD, USA: Goddard Earth Sciences Data and Information Services Center (GES DISC.

Daag, A. S., Tubianosa, B. S., Newhall, C., Tungol, N., Javier, D., Dolan, M., et al. (1996). *Monitoring sulfur dioxide emission at mount pinatubo*. Philippines: Fire and mud: Eruptions and lahars of Mount Pinatubo, 409–414.

Edmonds, M., Herd, R., Galle, B., and Oppenheimer, C. (2003). Automated, high time-resolution measurements of SO2 flux at Soufrire Hills Volcano, Montserrat. *Bull. Volcanol.* 65, 578–586. doi:10.1007/s00445-003-0286-x

Galle, B., Johansson, M., Rivera, C., Zhang, Y., Kihlman, M., Kern, C., et al. (2010). Network for observation of volcanic and atmospheric change (novac)—A global network for volcanic gas monitoring: Network layout and instrument description. *J. Geophys. Res. Atmos.* 115, D05304. doi:10.1029/2009jd011823

Hashimoto, T., Nishimura, M., Arita, S., Yamamoto, T., Ogiso, M., Shigeno, N., et al. (2010). Heat accumulation beneath Tokachidake volcanoes inferred from magnetic changes. *Goephys Bull. Hokkaido Univ.* 73, 269–280.

Japan Meteorological Agency (2021). *Annual report for 2021 volcanic activity of Tokachidake volcano*.

Katsui, Y., Kawachi, S., Kondo, Y., Ikeda, Y., Nakagawa, M., Gotoh, Y., et al. (1990). The 1988-1989 explosive eruption of Tokachi-dake, Central Hokkaido, its sequence and mode: Special section: The 1988-1989 eruption of Mt. Tokachi, Central Hokkaido. *SECOND Ser. Bull. Volcanol. Soc. Jpn.* 35, 111–129.

Kazahaya, R., Aoki, Y., and Shinohara, H. (2015a). Budget of shallow magma plumbing system at asama volcano, Japan, revealed by ground deformation and volcanic gas studies. *J. Geophys. Res. Solid Earth* 120, 2961–2973. doi:10.1002/2014jb011715

Kazahaya, R., Maeda, Y., Mori, T., Shinohara, H., and Takeo, M. (2015b). Changes to the volcanic outgassing mechanism and very-long-period seismicity from 2007 to 2011 at mt. asama, Japan. *Earth Planet. Sci. Lett.* 418, 1–10. doi:10.1016/j.epsl.2015.02.034

Kazahaya, R., Mori, T., Takeo, M., Ohminato, T., Urabe, T., and Maeda, Y. (2011). Relation between single very-long-period pulses and volcanic gas emissions at mt. asama, Japan. *Geophys. Res. Lett.* 38. doi:10.1029/2011gl047555

Kusakabe, M., Komoda, Y., Takano, B., and Abiko, T. (2000). Sulfur isotopic effects in the disproportionation reaction of sulfur dioxide in hydrothermal fluids: Implications for the δ34s variations of dissolved bisulfate and elemental sulfur from active crater lakes. *J. Volcanol. Geotherm. Res.* 97, 287–307. doi:10.1016/s0377-0273(99)00161-4

McGonigle, A. J., Pering, T. D., Wilkes, T. C., Tamburello, G., D'Aleo, R., Bitetto, M., et al. (2017). Ultraviolet imaging of volcanic plumes: A new paradigm in volcanology. *Geosciences* 7, 68. doi:10.3390/geosciences7030068

Mori, T., Morita, M., Iguchi, M., and Headquarters, F. R. (2017). Sulfur dioxide flux monitoring using a regular service ferry after the 2014 eruption of kuchinoerabujima volcano, Japan. *J. Nat. Disaster Sci.* 38, 105–118. doi:10.2328/jnds.38.105

Mori, T., Shinohara, H., Kazahaya, K., Hirabayashi, J., Matsushima, T., Mori, T., et al. (2013). Time-averaged SO_2 fluxes of subduction-zone volcanoes: Example of a 32-year exhaustive survey for Japanese volcanoes. *J. Geophys. Res. Atmos.* 118, 8662–8674. doi:10.1002/jgrd.50591

Nadeau, P. A., Palma, J. L., and Waite, G. P. (2011). Linking volcanic tremor, degassing, and eruption dynamics via so2 imaging. *Geophys. Res. Lett.* 38. doi:10.1029/2010gl045820

Nanri, T., Makinou, T., Yonekawa, K., Harada, N., Ando, H., and Yamada, T. (2008). Volcanic mudflow chronology in Furano river of Mt. Tokachi, Hokkaido. *Sabo Gakkaishi* 60, 23–30. doi:10.11475/sabo1973.60.5_23

Platt, U., and Stutz, J. (2008). *Differential absorption spectroscopy*. Berlin, Heidelberg: Springer Berlin Heidelberg, 135–174. doi:10.1007/978-3-540-75776-4_6

Poland, M. P., Sutton, A. J., and Gerlach, T. M. (2009). Magma degassing triggered by static decompression at kilauea volcano, hawai 'i. *Geophys. Res. Lett.* 36, L16306. doi:10.1029/2009gl039214

Queißer, M., Burton, M., Theys, N., Pardini, F., Salerno, G., Caltabiano, T., et al. (2019). Tropomi enables high resolution so2 flux observations from mt. etna, Italy, and beyond. *Sci. Rep.* 9, 957–1012. doi:10.1038/s41598-018-37807-w

Regional Volcanic Observation and Warning Center, Sapporo Regional Headquarters, JMA (2018). *Volcanic activity of Tokachidake volcano during the last 10 years (2006–2016). Report of the coordinating committee for prediction of volcanic eruptions 127*.

Romahn, F., Pedergnana, M., Loyola, D., Apituley, A., Sneep, M., and Veefkind, J. P. (2020). *Sentinel-5 precursor/TROPOMI Level 2 product user manual sulphur dioxide SO_2*.

Salerno, G., Burton, M., Oppenheimer, C., Caltabiano, T., Randazzo, D., Bruno, N., et al. (2009). Three-years of so2 flux measurements of mt. etna using an automated uv scanner array: Comparison with conventional traverses and uncertainties in flux retrieval. *J. Volcanol. Geotherm. Res.* 183, 76–83. doi:10.1016/j.jvolgeores.2009.02.013

Shinohara, H. (2008). Excess degassing from volcanoes and its role on eruptive and intrusive activity. *Rev. Geophys.* 46. doi:10.1029/2007rg000244

Shinohara, H., Hirabayashi, J., Nogami, K., and Iguchi, M. (2011). Evolution of volcanic gas composition during repeated culmination of volcanic activity at kuchinoerabujima volcano, Japan. *J. Volcanol. Geotherm. Res.* 202, 107–116. doi:10.1016/j.jvolgeores.2011.01.011

Spurr, R. J. (2006). Vlidort: A linearized pseudo-spherical vector discrete ordinate radiative transfer code for forward model and retrieval studies in multilayer multiple scattering media. *J. Quantitative Spectrosc. Radiat. Transf.* 102, 316–342. doi:10.1016/j.jqsrt.2006.05.005

Stoiber, R., Maliconico, L., and Williams, S. (1983). "Use of the correlation spectrometer at volcanoes," in *Forecasting volcanic events*. Editor S. J. Tazieff H (Amsterdam: Elsevier), 425–444.

Symonds, R., Gerlach, T., and Reed, M. (2001). Magmatic gas scrubbing: Implications for volcano monitoring. *J. Volcanol. Geotherm. Res.* 108, 303–341. doi:10.1016/s0377-0273(00)00292-4

Tada, F., and Tsuya, H. (1927). The eruption of the tokachidake volcano, Hokkaido, on may 24th, 1926. *Bull. Earthq. Res. Inst. Univ. Tokyo* 2, 49–84.

Tanaka, R., Hashimoto, T., Matsushima, N., and Ishido, T. (2017). Permeability-control on volcanic hydrothermal system: Case study for Mt. Tokachidake, Japan, based on numerical simulation and field observation. *Earth, Planets Space* 69, 39–24. doi:10.1186/s40623-017-0623-5

Tanaka, R., Yamaya, Y., Tamura, M., Hashimoto, T., Okazaki, N., Takahashi, R., et al. (2021). Three-dimensional inversion of audio-magnetotelluric data acquired from the crater area of Mt. Tokachidake, Japan. *Earth, Planets Space* 73, 172–211. doi:10.1186/s40623-021-01502-4

Theys, N., De Smedt, I., Yu, H., Danckaert, T., van Gent, J., Hörmann, C., et al. (2017). Sulfur dioxide retrievals from TROPOMI onboard sentinel-5 precursor: Algorithm theoretical basis. *Atmos. Meas. Tech.* 10, 119–153. doi:10.5194/amt-10-119-2017

Theys, N., Hedelt, P., De Smedt, I., Lerot, C., Yu, H., Vlietinck, J., et al. (2019). Global monitoring of volcanic SO_2 degassing with unprecedented resolution from TROPOMI onboard Sentinel-5 Precursor. *Sci. Rep.* 9, 2643–2710. doi:10.1038/s41598-019-39279-y

Tilstra, L. (2022). *TROPOMI ATBD of the directionally dependent surface lambertian-equivalent reflectivity*. KNMI Report S5P-KNMI-L3-0301-RP.

Uesawa, S. (2014). A study of the Taisho lahar generated by the 1926 eruption of Tokachidake volcano, central Hokkaido, Japan, and implications for the generation of cohesive lahars. *J. Volcanol. Geotherm. Res.* 270, 23–34. doi:10.1016/j.jvolgeores.2013.11.002

Wallace, P. (2001). Volcanic so2 emissions and the abundance and distribution of exsolved gas in magma bodies. *J. Volcanol. Geotherm. Res.* 108, 85–106. doi:10.1016/s0377-0273(00)00279-1

frontiers | Frontiers in Earth Science

TYPE Original Research
PUBLISHED 01 June 2023
DOI 10.3389/feart.2023.1049670

OPEN ACCESS

EDITED BY
Silvana Hidalgo,
Escuela Politécnice Nacional, Ecuador

REVIEWED BY
Daniel Sierra,
Escuela Politécnice Nacional, Ecuador
Mariana Patricia Jacome Paz,
National Autonomous University of Mexico, Mexico

*CORRESPONDENCE
Nicole Bobrowski,
nicole.bobrowski@ingv.it

RECEIVED 20 September 2022
ACCEPTED 20 April 2023
PUBLISHED 01 June 2023

CITATION
Gutiérrez X, Bobrowski N, Rüdiger J, Liotta M, Geil B, Hoffmann T, Gutiérrez E, Dinger F, Montalvo F, Villalobos M and Escobar D (2023), Geochemical characterization of volcanic gas emissions at Santa Ana and San Miguel volcanoes, El Salvador, using remote-sensing and *in situ* measurements. *Front. Earth Sci.* 11:1049670. doi: 10.3389/feart.2023.1049670

Geochemical characterization of volcanic gas emissions at Santa Ana and San Miguel volcanoes, El Salvador, using remote-sensing and *in situ* measurements

Xochilt Gutiérrez[1], Nicole Bobrowski[2,3]*, Julian Rüdiger[4], Marcello Liotta[5], Bastien Geil[1], Thorsten Hoffmann[1], Eduardo Gutiérrez[1], Florian Dinger[2,6], Francisco Montalvo[7], Mirian Villalobos[7] and Demetrio Escobar[7]

[1]Institute of Inorganic and Analytical Chemistry, Johannes Gutenberg—University Mainz, Mainz, Germany, [2]Institute of Environmental Physics, University of Heidelberg, Heidelberg, Germany, [3]Istituto Nazionale di Geofisica e Vulcanologia—Osservatorio Etneo, Catania, Italy, [4]Umweltbundesamt, Langen, Germany, [5]Instituto Nazionale di Geofisica e Vulcanologia—Sezione di Palermo, Palermo, Italy, [6]Max-Planck Institute for Chemistry, Mainz, Germany, [7]Observatorio Ambiental, Área de Vulcanología, Ministerio de Medio Ambiente y Recursos Naturales, San Salvador, El Salvador

Volcanic degassing provides important information for the assessment of volcanic hazards. Santa Ana and San Miguel are open vent volcanoes along the Central American Volcanic Arc–CAVA, where the magmatism, basaltic to dacitic, is related to the near-orthogonal convergence of the Caribbean Plate and the subducting Cocos Plate. Both volcanoes are the most active ones in El Salvador with recent eruptive events in October 2005 (Santa Ana) and December 2013 (San Miguel), but still not much data on gas composition and emission are available today. At each volcano, SO_2 emissions are regularly monitored using ground-based scanning Differential Optical Absorption Spectrometer (Scan-DOAS) instruments that are part of the global "Network for Observation of Volcanic and Atmospheric Change" (NOVAC). We used the data series from these NOVAC stations in order to retrieve SO_2 and minimum bromine emissions, which can be retrieved from the same spectral data for the period 2006–2020 at Santa Ana and 2008–2019 at San Miguel. However, BrO was not detected above the detection limit. SO_2 emission ranged from 10 to 7,760 t/d, and from 10 to 5,870 t/d for Santa Ana and San Miguel, respectively. In addition, the SO_2 emissions are complemented with *in situ* plume data collected during regular monitoring surveys (2018–2020) and two field campaigns in El Salvador (2019 and 2020). MultiGAS instruments recorded CO_2, SO_2, H_2S and H_2 concentrations. We determined an average CO_2/SO_2 ratio of 2.9 $\pm$ 0.6 when peak SO_2 concentration exceeded 15 ppmv at Santa Ana, while at San Miguel the CO_2/SO_2 ratio was 7.4 $\pm$ 1.8, but SO_2 levels reached only up to 6.1 ppmv. Taking into account these ratios and the SO_2 emissions determined in this study, the resulting CO_2 emissions are about one order of magnitude higher than those determined so far for the two volcanoes. During the two field campaigns Raschig tubes (active alkaline trap) were used to collect plume samples which were analyzed with IC and ICP-MS to identify and quantify CO_2, SO_2, HCl, HF, and HBr. Additionally, also 1,3,5-trimethoxybenzene (TMB)-coated denuders were applied and subsequently analyzed by GC-MS to determine the sum of the reactive halogen species (RHS: including Cl_2, Br_2, interhalogens,

hypohalous acids). The RHS to sulfur ratios at Santa Ana and San Miguel lie in the range of 10^{-5}. Although no new insights could be gained regarding changes with volcanic activity, we present the most comprehensive gas geochemical data set of Santa Ana and San Miguel volcanoes, leading to a solid data baseline for future monitoring purposes at both volcanoes and their improved estimate of CO_2, SO_2 and halogens emissions. Determining the reactive fraction of halogens is a first step towards a better understanding of their effects on the atmosphere.

KEYWORDS

Santa Ana, San Miguel, volcanic gas emissions, SO_2 emissions, halogen emissions, (min.5-max. 8)

1 Introduction

Magma degassing and post-magmatic processes (e.g., processes occurring in hydrothermal systems and/or volcanic aquifers) contribute to the chemical composition of volcanic gas emissions. Studying changes in volcanic gas release and separating these processes allows volcanologists to understand the processes that control volcanic activity and, when this occurs over time, to detect signs of unrest. SO_2 emissions are considered a fundamental monitoring tool, which can be measured using remote sensing techniques. Differential optical absorption spectroscopy (DOAS) is a well-established method to measure volcanic SO_2 emission rates on a regular basis. In the global Network for Observation of Volcanic and Atmospheric Change (NOVAC), approximately 80 DOAS scanners are in operation at 37 volcanoes (Galle et al., 2010; Arellano et al., 2021). Typically, SO_2 flux measurements are combined with *in situ* gas measurements of SO_2 and other volatiles (e.g., CO_2, H_2S) to assess changes in the volcanic activity. Multisensor instruments (MultiGAS) are often used for this purpose, allowing real-time measurements of multiple gases simultaneously (Aiuppa et al., 2005; Shinohara, 2005; Roberts et al., 2014). When suitable real-time sensors are not available for the species of interest, *in situ* measurements can be made by using for instance sampling flasks filled with alkaline solutions (e.g., Noguchi and Kamiya, 1993; Symonds et al., 1994; Wittmer et al., 2014). Recently, Rüdiger et al. (2017) presented an *in situ* method to quantify the amount of reactive halogen species (Cl_2, Br_2, interhalogens, hypohalous acids) using *in situ* derivatizing agents applied in diffusion denuders. This method has demonstrated the importance of *in situ* measurements not only for monitoring volcanic emissions, but also for increasing our knowledge of the role of volcanic halogen emissions in the atmosphere. Each of the aforementioned techniques has individual advantages and disadvantages, but their simultaneous application allows for an integrated approach to the geochemical characterization of a volcano (Symonds et al., 1994; Aiuppa, 2015).

In the beginning of the study we will summarize the limited existing measurements from two volcanic systems Santa Ana and San Miguel, in El Salvador. This summary underscores the importance and need for further studies to determine the gas composition of these volcanoes. The purpose of our comprehensive geochemical gas study is to improve the understanding of the state of volcanic activity of San Miguel and Santa Ana by analyzing long-term SO_2 measurements from NOVAC stations, complemented by MultiGAS data collected during regular monitoring (2018–2020) and dedicated field campaigns (2019–2020) including other species (e.g., halogens).

1.1 Santa Ana

Santa Ana volcano (13.853°N, 89.630°W), also known as Ilamatepec, is the highest volcano in El Salvador (2,381 m above sea level (a.s.l)), and is located 40 km west of the capital city, San Salvador (>1.7°million inhabitants) and 15 km from Santa Ana city (>550,000 inhabitants). This active stratovolcano is part of the Santa Ana-Izalco-Coatepeque volcanic complex Figure 1 A and B, which lies in a late Pliocene or early Pleistocene depression (Central American Graben; e.g., Mann et al., 2004) On its northeast flank is the Coatepeque caldera, an elliptical depression of 6.5 × 10.5 km, and on its south-southeast flank, are Izalco volcano and other numerous older cinder cones and explosion craters in the area. The edifice consists of a large cone with four concentric craters on its summit, the largest one with a radius of 1.5 km, and the innermost one with a radius of 0.5 km. The latter crater was formed after the 1904 eruption and hosts a small (~200 m diameter) acidic lake and an adjacent fumarole field on the western crater wall (Bernard et al., 2004; Laiolo et al., 2017).

Continuous activity and at least 12 explosive eruptions have been documented since the first Spanish expedition to El Salvador in the 16th century. Meyer-Abich. (1956) reported that the activity of Ilamatepec was limited to hydrothermal or phreatic activity since the 1920 eruption, which almost completely evaporated the crater lake at that time. In January 2000, the presence of a high-temperature fumarole (532°C) was observed on the west side of the lake, followed by an increase in the degassing rate without increase of seismicity (Bernard et al., 2004). In February 2001 very high fumarole temperatures of up to 875°C were measured and Rodriguez et al. (2004) reported sulfur dioxide emission rates that ranged from 30 to 280 t/d at Santa Ana volcano, undertaking ground-based correlation spectrometer (COSPEC) measurements in the same month. In March 2001 SO_2 fluxes measured again by stationary and vehicular COSPEC ranged from 244 to 393 t/d (Global Volcanism Program, 2001—GVP Bulletin). In addition, Salazar et al. (2004) determined the diffuse emission of carbon dioxide from the Santa Ana-Izalco-Coatepeque volcanic complex using the accumulation chamber technique during a survey in March 2001. The total diffuse CO_2 emission for this volcanic complex was estimated to be ~600 t/d. These studies constitute the first published data from measurements of emitted gases at this

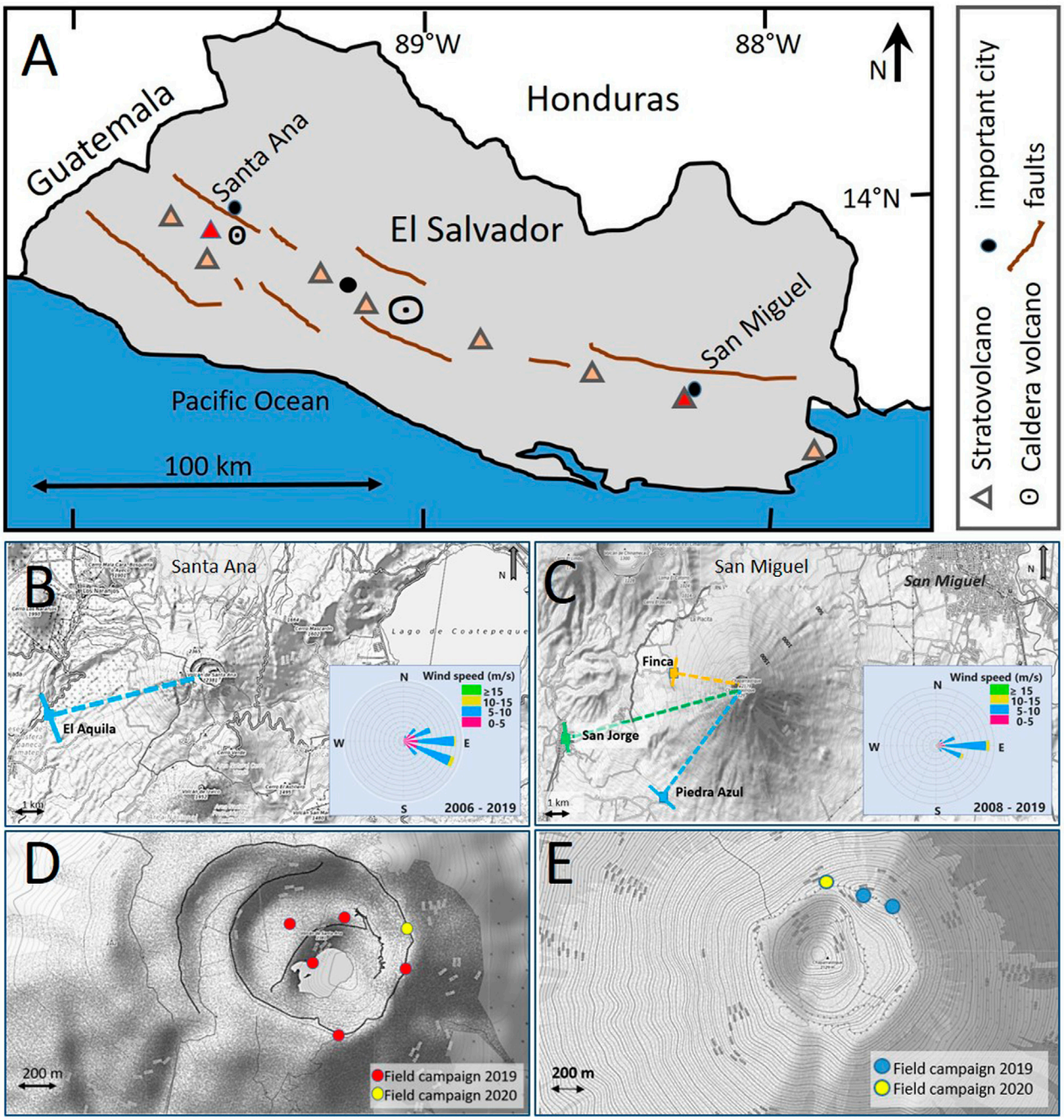

FIGURE 1
Geographical and geological information on the study area **(A)** overview of the major volcano-structural features in El Salvador adapted from Mann et al., 2004. In **(B)** and **(C)** Scan geometry and wind rose displaying from where the wind is blowing at **(B)** El Águila station, 5.8 Km from Santa Ana volcano and **(C)** Piedra Azul, Finca and San Jorge stations downwind San Miguel volcano. *In-situ* sampling sites are displayed in **(D)** for Santa Ana volcano, and **(E)** San Miguel volcano during the 2019 and 2020 surveys.

volcano. In a further field survey in January 2002, Rodriguez et al. (2004) determined SO_2 emission rates in a similar range with values ranging between 10 and 220 t/d.

Signs of unrest were observed at the crater in mid-2004 (e.g., intense degassing, hydrothermal activity and high-temperature fumaroles), that culminated in the 01 October 2005 eruption. The activity and evolution of the crater lake before and after this event are well documented (Bernard et al., 2004; Hernández et al., 2007; Colvin et al., 2013; Laiolo et al., 2017). Table 1 shows the variations in temperature (16–66°C), pH (≤1–2.5) and chemistry of the crater lake. SO_2 fluxes determined with mobile and stationary differential optical spectrometers (scanning-DOAS) in 2004–2005 were also reported (Olmos et al., 2007). These studies allowed the calculations of SO_2 fluxes listed in Table 2. For many

TABLE 1 Santa Ana volcano crater lake chemistry.

Period	pH	T (°C)	Cl (mg/L)	SO_4 (mg/L)	TDS (mg/L)	SO_4/Cl
1992–1993a	≤1–2.5	n.d	~3,500–75,000	1900–9,000	9,300–82,000	<1
2000–2002b	~1	19–30	5,500–8,700	8,400–13,000	18,000–26,800	~1.5
2002–2005a	~1–2.0	16–31	1,100–9,200	4,500–14,000	6,700–25,000	1.2–2.6
2005c	n.d	29	n.d	n.d	n.d	n.d
2006c	n.d	67	n.d	n.d	n.d	n.d
2007a	≤1–1.3	19–66	3,200–22,300	2,500–9,800	10,000–36,000	0.4–0.8
2008days		30–40				

[a]Colvin et al., 2013.
[b]Bernard et al., 2004.
[c]Hernández et al., 2007.
[d]Informe SNET.
[e]d: no data.

TABLE 2 Published sulfur dioxide fluxes emitted by Santa Ana volcanoes between 2000–2018.

Period	T (°C)	SO_2 (t/d)	Instrument	Activity	Source
2000–2001	523	244–393	COSPEC	Fuming/Incandescence	GVP Bulletin, 2001
2001–2002	532–875[a]	30–280	COSPEC	Fumarolic degassing	Rodríguez et al. (2004)
2004–2005	360[a]	110–4,300	COSPEC/DOAS	Hydrothermal/phreatic	Olmos et al. (2007)
2007	n.d	16–1,600	DOAS	Phreatic explosion	Colvin et al. (2013)
2017–2018	n.d	41–329	DOAS	Degassing through lake	Hasselle et al. (2019)

[a]Temperatures from fumaroles from Hernández et al., 2007.
[b]d - no data.

years thereafter, very few studies have published SO_2 fluxes and water composition data (Colvin et al., 2013; Hasselle et al., 2019; Arellano et al., 2021).

In a study presented by Hasselle et al. (2019), SO_2 fluxes (Table 2) and measurements of gas composition (H_2O, CO_2, SO_2, H_2S and H_2) from gas plumes released from the crater lake were determined using the observatory's NOVAC station and a multicomponent gas analyzer system (MultiGAS), respectively. Total volatile fluxes of 20,200–30,200 ton/d and 900–10,167 t/d were reported for 2017 and 2018, respectively, which includes water vapor. These results highlight the dynamic nature of the lake, the rapid changes in its composition and the need for further monitoring.

1.2 San Miguel

San Miguel volcano, also called Chaparrastique, is an active volcano in the eastern part of El Salvador (13.434°N, 88.269°W). It rises 2,310 m a.s.l near and is located at about 11 km distance from the municipalities of San Miguel, El Tránsito, San Rafael Oriente, and San Jorge. It lies on the eastern section of the Central Graben of the country, which is crossed by the regional NW-SE fault system (Bonforte et al., 2016). Its northern flank extends to the San Esteban river, while its western flank is truncated against the Ojo de Agua (Cerro El Limbo) and Chinameca (Cerro El Pacayal) volcanoes (Chesner et al., 2004).

This stratovolcano has a symmetrical cone shape. The edifice consists of two main cones, the ancestral cone to the east of the summit, and a younger cone formed by the collapse of the ancestral one with a central crater ~900 m in diameter and several adventive cones (Escobar, 2003).

Over the past 500 years, more than 28 volcanic eruptions and unrest periods have been recorded (Escobar, 2003; Chesner et al., 2004). According to the local observatory, the 1699 eruption was identified as the first historical eruption, consisting of a large lava flow that descended about 8 km from its source vent to the southeast flank of the volcano at 480 m a.s.l (Jiménez et al., 2020). During the period from January 1999 to December 2000, measurements of diffuse soil gases (radon, thoron, mercury and carbon dioxide) were made at San Miguel volcano to understand gas flow within the volcanic edifice and the status of volcanic activity. The low CO_2 fluxes obtained in that study (less than 0.1–5.0 g/m^{2}d), were interpreted as low permeability of the volcanic edifice caused by lava flows which covered the sampling locations rather than with low gas fluxes (Cartagena et al., 2004).

Later, Pérez et al. (2006) reported an average CO_2 fluxes of 29.4 g/m^{2}d for the period of November 2001 to March 2002, using

TABLE 3 NOVAC stations settings for Santa Ana and San Miguel volcanoes.

Volcano	Station	Instrument number	Coordinates	Altitude (m a.s.l)	Distance (Km)	Scan plane	Operation time
Santa Ana	El Águila	D2J2167	13.8509	1,014	5.8	66°	2008—present
			-89.6295				
San Miguel	Piedra Azul	D2J2170	13.3962	373	5.0	43°	2008–2010
			-88.3045				
San Miguel	San Jorge	I2J9304	13.4148	339	7.9	70°	2012–2014
			-88.3444				
San Miguel	Finca	D2J2205	13.4349	884	2.8	99°	2014–2016
			-88.2997				
San Miguel	San Jorge	I2J9304	13.4148	339	7.9	70°	2017 - present
			-88.3444				

an automated station on the eastern flank of San Miguel volcano (594 m a.s.l). In this survey the authors detected an increased flux (270 g/m^{2}d) for the January 2002 short-term unrest at San Miguel volcano and statistically estimated a rate of 16 g/m^{2}d as a background value for the volcano, considering larger rates as anomalous.

Sulfur dioxide fluxes were first estimated by Rodriguez et al. (2004) based on ground-based COSPEC measurements during the January 2002 unrest. The average emission was between 220 and 280 t/d. No previous measurements have been documented and there are no published data for more than 10 years after the ones from Rodriguez et al. (2004). In December 2013, San Miguel volcano erupted after 46 years of weak activity. Granieri et al. (2015) reported SO_2 emissions gained by the NOVAC stations, ~8 km from the summit crater and normally used for continuous monitoring by the observatory; and a FLAME station, located 2.7 km from the crater, used by INGV between January 30 and 21 February 2014. The observed rates were: ~310 t/d, 1 year before the eruption; between 330–2,200 t/d during eruption; and 680 t/d after eruption.

Moreover, average 640 t/d CO_2 emission rates calculated from MultiGAS system data and the scan-DOAS station data for the period January-February 2014 are presented in that study. In addition, the first halogen emission rates using FTIR spectrometer measurements were presented for the same period (~90 t/d for HCl and ~10 t/d for HF).

2 Methods

2.1 DOAS measurements

In this study, SO_2 emissions are determined by using two scanning DOAS systems, one of which is installed at Santa Ana volcano and one at San Miguel volcano, nowadays at 6 and 8 km downwind, respectively. These stations are part of NOVAC, which is operated in El Salvador by the Ministerio de Medio Ambiente y Recursos Naturales (MARN) - Observatorio Ambiental, the national institution responsible for the study and research of natural phenomena in the country. The El Águila (Santa Ana volcano) and Piedra Azul (San Miguel volcano) stations (spectrometer number D2J2167 and D2J2170, respectively) have been in operation since 2006 and 2008, respectively. However, the instrument at Piedra Azul was removed due to technical problems, and a new station with a different spectrometer was established at San Jorge. From 2014 to 2016 the NOVAC station at Piedra Azul was replaced by another instrument which had been installed at a distance of only 2.8 km from the summit, at Finca (see Figure 1). Afterwards, in 2017, the former San Jorge station could be reactivated and since then it is the only working NOVAC-station at San Miguel volcano. Summary information about the stations and their locations is presented in Table 3.

Each station records spectra during daylight hours (6 a.m.–6 p.m.). Each instrument consists of an UV-spectrometer (Ocean Optics®, S2000: 274.3–424.8 nm for El Águila; 277.1–425.8 nm for Piedra Azul; 278.7–424.4 nm for Finca and 474.4–409.0 nm for San Jorge), connected to a telescope (field of view 8 mrad) via a quartz fiber and collecting backscattered sunlight through a motor-driven mirror; each measurement sequence scans the sky in a vertical plane of 180°, from horizon to horizon, with angular steps of 3.6°. More details about the NOVAC instruments can be found in Galle et al. (2010). The instrument is controlled by a microcomputer, which is also used to store and transmit the measurements via radio link to the observatory, where the measurements are downloaded and analyzed using the Novac Program (Galle et al., 2010). Data collected from the stations were used here to retrieve SO_2 and BrO gas emissions from Santa Ana and San Miguel volcanoes for the period 2006–2020 and 2008–2019, respectively. Datasets were provided by the observatory, with some gaps due to instrument failures. The analysis is based on Lübcke et al., 2014 and Dinger et al. (2021), who performed the following: 1) a quality check of individual spectra from a scan, 2) a retrieval of the spatial SO_2 distribution, 3) a spectral addition of scan spectra to perform the SO_2 and BrO DOAS fitting, 4) a spectral addition of successive scans to further improve the signal-to-noise of the BrO fitting. The results of this evaluation are time series of SO_2 and BrO slant column densities (SCDs) (Figure 2); and in principle daily BrO/SO_2 ratios. Unfortunately, BrO was not significantly exceeding the detection limit. In addition, this approach

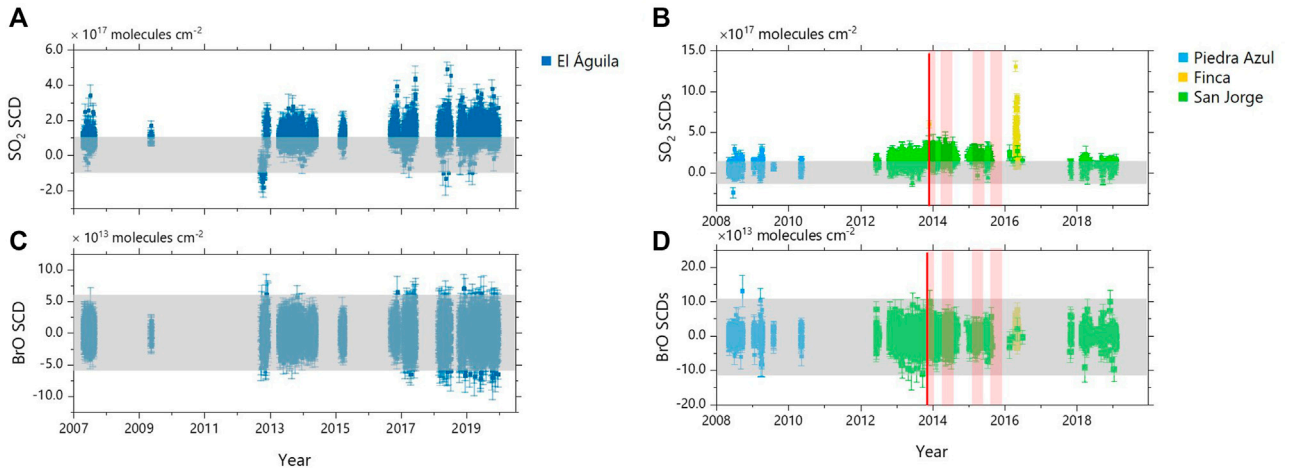

FIGURE 2
Time series of SCD's of SO_2 and BrO for Santa Ana **(A–C)** and San Miguel **(B–D)**. Red line indicates eruption, red shadow points out periods of increase of activity, including ash emissions. NOVAC stations are indicated by different colors. Gray shadow indicates the limit of detection (LOD).

allows the calculation of the SO_2 emission fluxes when meteorological data are available via

$$F_{SO_2} = M_{SO_2} \times v \times \cos(\omega - \beta) \times H \times \int_{-\infty}^{\infty} V_{SO_2}(\varepsilon)\, d(\tan(\varepsilon))$$

where M_{SO_2} is the SO_2 molar mass, v is the absolute wind speed, ω is the absolute wind direction, β is the orientation of the scanning plane, H is the plume height and $\int_{-\infty}^{\infty} V_{SO_2}(\varepsilon)\, d(\tan(\varepsilon))$ is the SO_2 VCDs (vertical column densities) angular integral. In this work, the meteorological data were taken from the ERA5 re-analysis database of the European Center for Medium-Range Weather Forecasts (ECMWF, DOI: 10.24381/cds.bd0915c6) since no local meteorological data are available. The ERA5 covers the period from 01.01.1979 to the present. This model and reanalysis system has a spatial resolution of 37 vertical levels up to one hPa. For each volcano, the wind information (wind speed and direction) was calculated based on the horizontal and vertical wind components, with a temporal resolution of 6 h, on a horizontal grid of 0.25° × 0.25°, close to the location of the volcanic vent and vertically interpolated to an altitude of 2,381 m a.s.l. for Santa Ana and 2,130 m a.s.l for San Miguel, using four wind vectors (including data on wind direction and velocity) two with pressure levels above each volcano's summit altitude, two with pressure levels below each volcano's summit altitude and performing then a linear interpolation, determining a wind vector for the exact altitude of the summit of both volcanoes.

2.2 *In-situ* measurements

Sampling locations were selected based on accessibility and prevailing wind direction to obtain measurements of the fumarole degassing on the inner flanks of the summit crater of each volcano (Figures 1D, E), given that it is difficult to sample the fumaroles directly. Measurements were made as part of regular monitoring surveys by the local observatory and during our field campaigns for detailed studies.

2.2.1 MultiGAS

Two different portable instruments were used during the field campaigns: Pitsa (PT) (Tirpitz et al., 2019) and Sunkist (SK) (Rüdiger et al., 2018), both developed by the University of Heidelberg, Germany. PT was used only for measurements on Santa Ana's plateau (~200 m from the crater lake), during the 2019 survey. The SK instrument (Hasselle et al., 2019) is a smaller MultiGAS version designed for use onboard an unmanned aerial vehicle (UAV). In February 2019, measurements with SK were made over the crater lake at Santa Ana, with the UAV flying between several tens of meter above the lake and staying below the height of the crater rim and on the ground at the rim of San Miguel. The observatory conducted measurements with a third portable MultiGAS instrument, here called SN, for gas measurements of CO_2, SO_2 and H_2S and H_2 on the plateau and rim of Santa Ana and San Miguel as regular monitoring of the volcanoes between 2018 and 2020. This system also includes sensors for temperature (T), pressure (P) and relative humidity (Rh), which allow the calculation of H_2O mixing ratios.

In the field, each device draws the volcanic gases through a PTFE (Polytetrafluorethylene) inlet filter with a pore size of 45 µm to the corresponding gas sensors. The sensors are read by a microcontroller equipped with a microSD card logger (Rüdiger et al., 2018). Sensor from PT and SK were calibrated in the laboratory using test gas standards (200 ppm SO_2 in N_2, 5,000 ppm CO_2 in N_2, All-in-Gas e.K., München, Germany) prepared in different gas mixtures in Tedlar® bags. The sensors were exposed to these gas mixtures by pumping the gas through the MultiGAS system before every field campaign for six different gas mixtures for SO_2 (2–200 ppm) and two gas mixtures for CO_2 (2,500–5,000 ppm). The recorded field data were post-processed using the RatioCalc program (Tamburello, 2015) to obtain time series of X/SO_2 mixing ratios (X: CO_2, H_2S, H_2, H_2O). Specific acquisition time windows or subintervals were selected, and molar ratios were determined by the best-fitting regression line in scatter plots

TABLE 4 SO_2 and BrO SCD's in the gas plume of Santa Ana and San Miguel volcanoes between 2008–2020.

Volcano	SO_2 SCD (× 10^{17} molecules cm^{-2})					BrO SCD (× 10^{13} molecules cm^{-2})					Total days
	Mean	SD	Max	Error	LOD	Mean	SD	Max	Error	LOD	
Santa Ana	1.04	0.43	4.92	0.37	0.49	-2.49	1.52	7.06	2.17	3.0	1,213
San Miguel	1.33	1.04	13.1	0.64	0.70	0.049	1.93	13.08	4.58	3.76	772

of volatile pairs. If volcanic gases were excessively dilute (e.g., SO_2 < 3.0 ppmv) or if the correlation coefficient was low (R^2 < 0.5), no ratio calculated during the subintervals was considered.

2.2.2 Active alkaline trap

Active alkaline traps, as used in this work, refers to the use of a Raschig-tube device (RT) (Wittmer et al., 2014), consisting of a glass cylinder containing little glass rings (Raschig rings), wetted with 50 ml of aqueous 1 M NaOH solution (EMSURE® ≥ 99.0%, Sigma Aldrich) as trapping medium. Homogeneous wetting is achieved by rotating the RT during the sampling period using a geared motor. Before each measurement, the tube is cleaned with ultra-pure water. During sampling, the RT collects the acid gases through an inlet with a flow rate of 4 L min^{-1} using a GilAir Plus™ pump (Sensidyne, St. Petersburg, FL, United States). The collected samples were stored, prepared and analyzed according to Wittmer et al. (2014) at the Instituto Nazionale di Geofisica e Vulcanologia–Sezione di Palermo in Italy. For this purpose, an ion chromatograph (Dionex ICS-1100, Thermo Fischer Scientific, Massachusett, United States) was equipped with an AS14A column (1 ml min^{-1} flow rate), an AERS 500e suppressor, and a 100 µL sample loop. This instrument was used to analyze Cl^-, SO_4^{2-} and F^- species. In addition, samples from the 2019 survey were also analyzed for HBr and HI by ICP-MS (Agilent 7500 CE). Carbon dioxide in this type of samples was determined by volumetric titration adding 0.1 M HCl solution to 0.5 ml of the sample dissolved in 35 ml of CO_2-free water (Geil, 2021).

2.2.3 Gas diffusion denuder

Reactive halogen species were collected using TMB-coated denuders prepared with brown borosilicate glass tubes (6 mm i.d., length 50 cm) and a 15 mM TMB (≥99.0%, Merck Germany) solution in methanol (HPLC-Grade, Merck Germany) according to Rüdiger et al. (2017). *In-situ* sampling was performed at Santa Ana and San Miguel volcanoes, using two denuders in a serial setup with a GilAir Plus pump at a flow of 250 ml min^{-1}. The measurements were performed simultaneously with the RT-instrument. The collected samples were analyzed following Rüdiger et al. (2017), at the Institute of Inorganic and Analytical Chemistry, JGU Mainz in Germany, using an Agilent 6850 Network GC and Agilent 5973 Network Mass Selective Detector (Agilent Technologies, Inc. Santa Clara, CA, United States).

3 Results

3.1 SO_2 and BrO SCDs

Here we present a description of the SO_2 and BrO SCD's retrieved from the NOVAC stations at Santa Ana and San Miguel volcanoes, with its respective limit of detection (LOD), calculated as four times the fitting error (Stutz and Platt, 1996; Lübcke et al., 2014). At Santa Ana, ~50% of the total SO_2 SCD's exceed the LOD, while at San Miguel ~40% of the data exceed this limit (Table 4). Our results demonstrate relatively low SO_2 emissions compared to high emitting volcanoes (e.g., Etna, Nyiragongo, Cotopaxi, Masaya) that have SO_2 SCDs >2 × 10^{18} molecules cm^{-2} (Bobrowski et al., 2007; Bobrowski and Giuffrida, 2012; Dinger et al., 2021; Dinger et al., 2021). BrO was not detected above the LOD (6.0 × 10^{13} molecules cm^{-2} and 11.0 × 10^{13} molecules cm^{-2} for Santa Ana and San Miguel, respectively). Expected SCDs for this gas would be in the range between (1.0–10) × 10^{13} molecules cm^{-2} during quiescent periods (e.g., Pacaya), and eventually (1.5–6.0) × 10^{14} molecules cm^{-2} during eruptive periods (e.g., Masaya). Although the maximum values (in total a number of fourteen values for Santa Ana and one for San Miguel) are above our respective LOD, these correspond to single measurements within the 10 + years of recorded measurements. Each of those spectra were manually checked and none of them showed a visible clear definite absorption structure. However, BrO production within the plume cannot be excluded, but it has not been detectable.

3.2 SO_2 emission fluxes

SO_2 fluxes were calculated as described in section 2.1, using the SO_2 SCDs of each volcano and assuming a fixed plume height according to the summits' height (Figure 3). The daily average SO_2 flux (±1 standard deviation) for Santa Ana results in 470.0 ± 414.69 t/d with a maximum of 7,757.98 t/d in January 2009 and a minimum of 10.28 t/d in June 2008 (Table 5). San Miguel shows a daily average of 903.88 ± 599.49 SO_2 t/d with a maximum of 5,868.93 t/d in July 2014, and a minimum of 10.47 t/d in June 2015.

During the analyzed period at San Miguel an eruption was recorded on 29 December 2013. Our results show that: 1) before the unrest of the volcano, between July 2008 and September 2012, the SO_2 emission had an average value of 474.0 ± 376.57 t/d, 2) in the year of the eruption, between January and December 2013, the SO_2 emissions increased with a daily mean of 1,032.13 ± 581.47 t/d, 3) during the eruption, on 29 and 30 December 2013 the daily mean SO_2 rate increased to a maximum value of 2,378.85 ± 978.21 t/d, 4) during the post-eruption period when smaller explosions were reported by the local observatory, between February 2014 and September 2016, the SO_2 rates observed had a small decrease with a daily mean of 1,077.41 ± 590.86 t/d, and 5) between October 2017 and April 2019, a passive degassing period has followed with an average SO_2 emissions of 765.710 ± 610.14 t/d. The average SO_2 rates of the eruptive event were ~23–40% higher

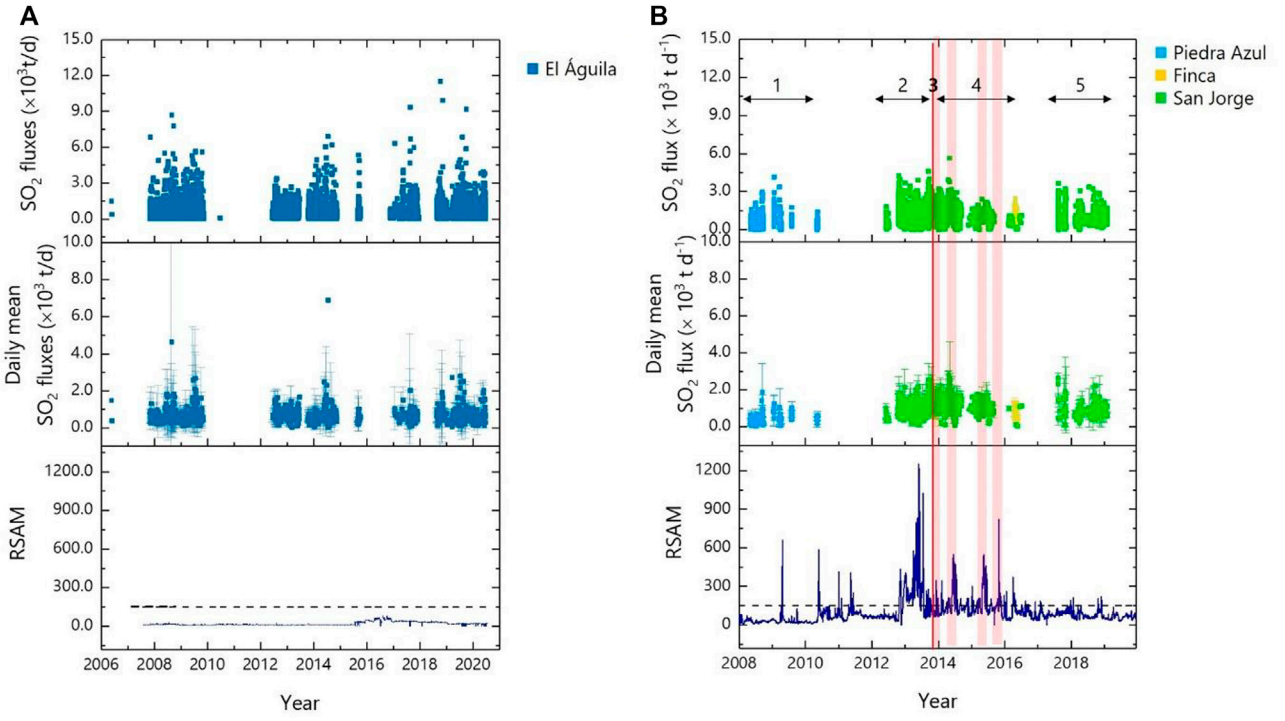

FIGURE 3
Temporal variation of SO_2 fluxes and RSAM of **(A)** Santa Ana and **(B)** San Miguel volcanoes. Red line indicates eruption, red shadow points out periods of increase of activity, black dash line shows the RSAM threshold.

TABLE 5 SO_2 in the gas plume of Santa Ana and San Miguel volcanoes between 2008–2020.

Volcano	SO_2 fluxes (t d^{-1})				Total days	Wind speed (m s^{-1})		Wind direction (°)	
	Mean	SD	Min	Max		Mean	SD	Mean	SD
Santa Ana	470.53	414.69	10.28	7,757.98	1,259	5.8	2.8	56.7	31.5
San Miguel	903.88	599.49	10.47	5,868.93	777	6.8	2.4	89.25	39.15

than those of the passive degassing periods and ~50% higher than those of the preceding and post-eruptive periods. Granieri et al. (2015) reported an average value of SO_2 emissions of 310 ± 170 t/d for the year 2013, values between 640 and 1,240 t/d during the eruption on 29 and 30 December, and an average of 680 ± 220 t/d for the period following the eruption in January - February 2014. These emissions are ~25% higher than those of the year 2013 and >50% higher than the post-eruptive months, which is in agreement with our estimations.

3.3 Molar carbon dioxide, hydrogen and water to sulfur dioxide ratios (X/SO_2)

During our observations between 2018 and 2020, both volcanoes were in a state of passive degassing activity with plumes associated with their respective fumaroles and Santa Ana crater lake. The maximum gas concentrations we measured using the MultiGAS instruments were: 33.6 ppmv SO_2, 73.2 ppmv CO_2, 63.4 ppmv H_2 and 11.0 ppmv H_2S for Santa Ana and 12.65 ppmv SO_2, 76.9 ppmv CO_2, 8.9 ppmv H_2 and 1.7 ppmv H_2S for San Miguel. The recorded datasets from the MultiGAS instruments were post-processed using the RatioCalc program (Tamburello, 2015) to obtain concentration ratios from the correlation of the measured gases. Ratios calculated from subintervals were not considered if excessive volcanic gas dilution was present (e.g., SO_2 < 3.0 ppmv) or a low correlation coefficient was determined (R^2 < 0.5) between gases (Table 6), following Aiuppa et al. (2018).

Figure 4A shows the molar X/SO_2 ratios as time series for both volcanoes. Moderate variations were observed for Santa Ana's CO_2/SO_2 ratios, ranging from 2.1 to 10.1, while San Miguel ratios range from 5.2 to 9.2. Previous studies have described that CO_2/SO_2 ratio population is often inversely correlated to peak SO_2 concentrations in diluted-plume conditions (low peak SO_2) (Shinohara et al., 2008;

TABLE 6 Daily mean gas mixing ratios observed at Santa Ana and San Miguel volcanoes, using the portable MultiGAS devices.

Date	Instrument	Place	SO_2 max (ppmv)	CO_2/SO_2	H_2S/SO_2	H_2/SO_2	H_2O/SO_2
Santa Ana							
29.01.2019	SN	Plateau	33.6	2.5 ± 0.4	0.1 ± 0.02	0.4 ± 0.08	
30.01.2019	SN	Plateau	23.7	3.2 ± 0.6	0.1 ± 0.02	0.5 ± 0.1	56.4 ± 12.4
30.01.2019	PT	Plateau	12.5	5.1 ± 0.3	b.l.d		
30.01.2019	SK	Lake (dron flight 1)	16.3	3.0 ± 1.5	b.l.d		
31.01.2019	SN	Plateau	12.0	6.2 ± 2.0	0.1 ± 0.02	0.5 ± 0.2	83.2 ± 29.3
31.01.2019	PT	Plateau	10.8	5.7 ± 0.7	b.l.d		
31.01.2019	SK	Lake (dron flight 1)	17.3	2.1 ± 1.6	b.l.d		
31.01.2019	SK	Lake (dron flight 3)	19.6	3.7 ± 1.4	b.l.d		
08.08.2019	SN	Crater rim	4.6	10.1 ± 5.9	0.2 ± 0.04		42.9 ± 22.3
24.10.2019	SN	Crater rim	3.0		0.1 ± 0.05		
17.12.2019	SN	Crater rim	12.7	3.8 ± 1.7	0.1 ± 0.04	0.4 ± 0.2	67.7 ± 33.9
23.01.2020	SN	Crater rim	15.8	2.9 ± 1.7	0.2 ± 0.05		41.8 ± 19.1
30.09.2020	SN	Crater rim	11.0	6.7 ± 2.9	0.1 ± 0.04	0.5 ± 0.1	163.4 ± 64.2
03.12.2020	SN	Crater rim	7.9	4.4 ± 1.9	0.1 ± 0.03		176.9 ± 86.8
		Average		4.6 ± 2.2	0.14 ± 0.03	0.47 ± 0.05	90.3 ± 56.5
San Miguel							
13.07.2018	SN	Plateau	3.5	9.2 ± 4.7	0.1 ± 0.04		
06.02.2019	SN	Crater rim	5.3	7.0 ± 2.1	0.1 ± 0.02		140.5 ± 42.2
07.02.2019	SN	Crater rim	5.7	5.2 ± 1.5	0.1 ± 0.02		70.5 ± 29.5
27.03.2019	SN	Crater rim	6.1	8.3 ± 3.2	0.2 ± 0.04		97.6 ± 32.9
		Average		7.4 ± 1.8	0.1 ± 0.04		102.9 ± 35.3

Aiuppa et al., 2018; Battaglia et al., 2018; Woitischek et al., 2020). In this study, the calculated CO_2/SO_2 population is scattered at low concentrations (<15 ppmv SO_2), along with observations at other volcanoes (e.g., Etna, Masaya, Pacaya) and they converge at more concentrated plume conditions (>15 ppmv SO_2) with values in the range of 2.1–3.3 (2.9 ± 0.6), behaving within the CAVA (2.0 ± 1.1) and the global arc gas signature (~2.5) (Aiuppa et al., 2017). Hasselle et al. (2019) already reported this behavior from measurements taken at Santa Ana, suggesting the scattering of the ratios due to the diluted nature of the plume and/or because of contributions from multiple gas sources (e.g., weakly degassing hydrothermal fumaroles and soil diffuse degassing on the inner crater slope). However, changes in the wind speed and direction should also be considered since some of the measurements were performed in a time span between 2 and 4 h, bringing different gas concentrations to the sampling point. A similar behavior is observed for the H_2O/SO_2 ratio (4c), where low ratios are obtained in denser plumes (peak SO_2 concentrations >15 ppmv). The extent of variation in the ratios clearly depends on the sampling location. For example, at the outer rim of Santa Ana estimated CO_2/SO_2 ratios ranged from 2.9 to 10.1 (mean: 4.8 ± 2.37) indicating the influence of several sources, while a smaller range was observed over Santa Ana's crater lake (2.1–3.7, mean: 2.9 ± 0.8) pointing to a single distinct source. In the case of San Miguel the mean value of CO_2/SO_2 is 6.8 ± 1.6 for the rim, while 9.2 ± 4.7 is observed on the plateau, at a distance of ~0.4 km and ~0.25 km from the summit, respectively. These variations are related to the SO_2 concentration in the plume at the time of sampling. As shown in Figure 4B, the CO_2/SO_2 populations calculated from San Miguel were obtained from measurement at dilute plume concentrations (<15 ppmv SO_2). The ratios are higher than those reported by Granieri et al. (2015) for San Miguel volcano (see Figure 5) because they measured a few days after the eruption of the volcano, when even higher amounts of SO_2 were emitted in comparison to the lower emission measured during our study (quiescent phase).

H_2/SO_2 ratios determined for Santa Ana ranged from 0.4 to 0.5 (0.47 ± 0.05), with no difference between sites. This differs from the results of Hasselle et al. (2019), who found large differences between sites (Lake: 0.42 ± 11, and Plateau: 2.39 ± 0.27), which was attributed to an additional contribution of H_2 by diffuse degassing. However, at the end of their study (May–June 2018), also lower H_2/SO_2 ratios were measured with daily mean values ranging between 0.37 and 0.39 on the Santa Ana plateau. Our results are consistent with these later observations, suggesting that additional gas supply has decreased since 2018. No data are available from San Miguel for the H_2/SO_2 ratio, as no correlation between the two gases was observed. H_2S/SO_2 ratios were also estimated and showed the same mean value for both volcanoes (0.1 ± 0.03). However, the cross-sensitivity of the H_2S measurement with respect to SO_2 is also in this range, so these values should be interpreted with caution.

3.4 Total halogen to sulfur ratios (Y/S)

The determined halogens are abbreviated here as Y (Y = F, Cl, Br, I). Supplementary Table S7 summarizes the determined concentration of halogens in the Santa Ana and San Miguel plumes, while Table 7 shows the obtained molar ratios of halogens to sulfur for each volcano. Figure 6 shows the overall ratio of halogens to sulfur, which varies by sampling location. The

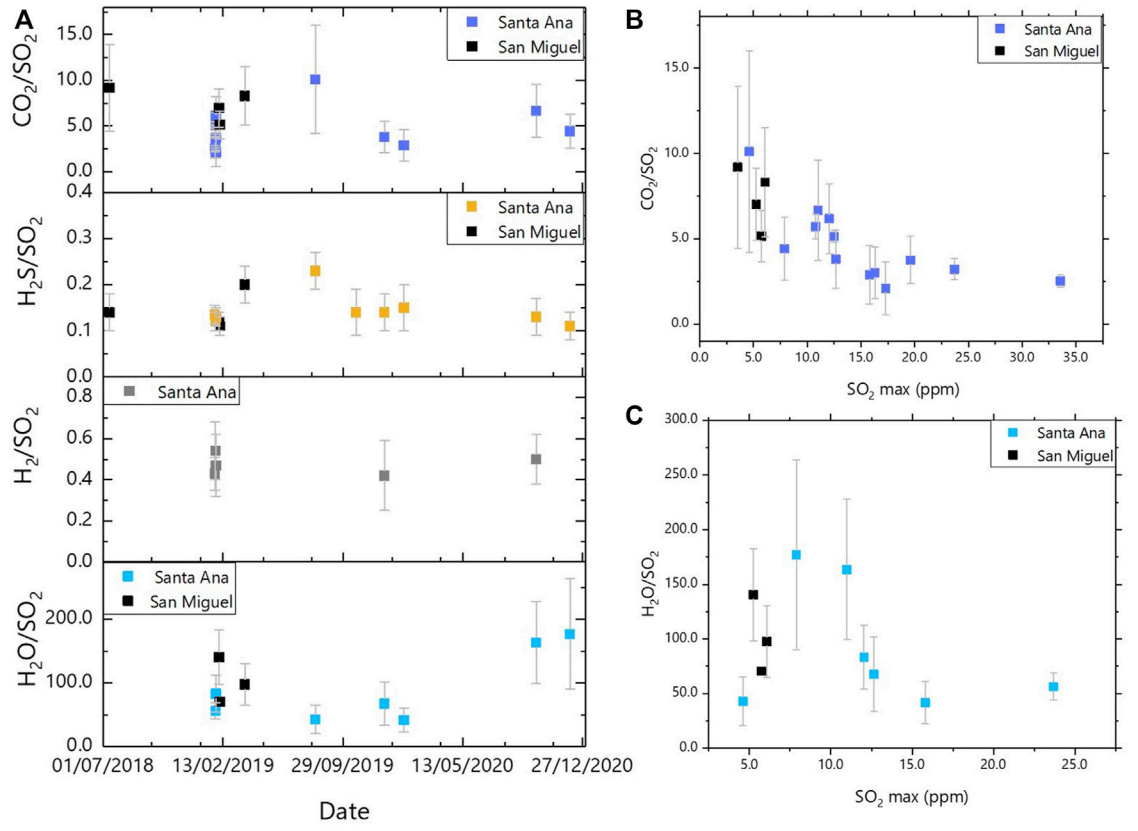

FIGURE 4
(A) Time series of carbon, hydrogen sulfide, hydrogen and water to sulfur molar ratios for Santa Ana and San Miguel corresponding to the 2018–2020 time period. **(B, C)** are the CO_2/SO_2 and H_2O/SO_2 *versus* the peak SO_2 concentration (maximum concentration within each evaluation window).

mean Y/S ratios for the Santa Ana rim are 0.2 ± 0.03 for fluorine, 0.7 ± 0.2 for chlorine, and (8.0 ± 5.3) × 10^{-5} for bromine, while on the plateau only Cl/S was detected with a value of 0.1 ± 0.02. No large variations were found between campaigns. At the San Miguel rim, Cl, Br, and I were detected in the plume with mean Y/S ratios of 1.0 ± 0.08 for chlorine, (5.2 ± 1.0) × 10^{-4} for bromine, and (1.8 ± 0.63) × 10^{-5} for iodine. No ratio was obtained for F/S because the fluorine values detected were below the detection limit (Table 7). Figure 6B shows the Y/S ratios obtained during the two field campaigns at San Miguel. No large variations are observed between the surveys, indicating the quiet state of the volcano. First measurements of Cl/S plume ratios for San Miguel volcano were done using a solar occultation FTIR (Fourier transform infrared) spectrometer between January and February 2014, obtaining an average of 0.13 (Granieri et al., 2015), a smaller value than those obtained in this study which might be interpreted as a consequence of the different state of activity at the time of the surveys (post-eruptive period and quiescent period).

Reactive bromine (BrX) was determined in 14 of 22 samples for Santa Ana, all samples from San Miguel were below the detection and quantitation limits (LOD_{Br2} = 0.13 ng and LOQ_{Br2} =0.4 ng). Reactive chlorine (ClX) was determined in four of the 22 samples from Santa Ana and at two of 10 samples for San Miguel (LOD_{Cl2} = 0.18 ng and LOQ_{Cl2} = 0.5 ng). The results for these samples are given in Table 8, along with the ratios of reactive to total halogen and reactive halogen to total sulfur ratios in (mol/mol). Uncertainties were calculated using the Gaussian error propagation by using an error of 5% for the sampled volume and 10% for the measured analyte amounts (Rüdiger et al., 2021). These are the first RHS measurements performed at both volcanos. The Santa Ana RHS ranged from 1.1 to 9.1 pptv BrX and from 3.6 to 35.3 pptv ClX, whereas only ClX was detected in the San Miguel samples (1.2–1.7 pptv). These data represent less than 1% of the total chlorine content of the RT samples. Several studies suggest halogen activation within the volcanic plume as a function of the distance from the crater (e.g., von Glasow, 2010; Bobrowski and Giuffrida, 2012; Roberts et al., 2014; Surl et al., 2021). Our results are within this expected behavior, showing low ratios when the measurement locations are closer to the emission vent and increasing ratios for bromine when they are farther from it (Figure 7). For example, BrX/S increases from (3.7 ± 0.9) × 10^{-7}, on the Santa Ana plateau, to (1.9 ± 0.09) × 10^{-5} at the crater rim, while BrX/Br increases from 0.02 ± 0.01 to 0.16 ± 0.04. ClX/S and ClX/Cl have been calculated for Santa Ana's plateau ((0.12 ± 0.02) × 10^{-5} and (0.95 ± 0.16) × 10^{-5}, respectively). Observations and model studies at other volcanoes (e.g., Etna, Masaya) have also shown that ClX/Cl is significantly smaller in the plume compared to BrX/Br (Roberts et al., 2009; Gliß et al., 2015; Rüdiger et al., 2021). In the case of San Miguel volcano, samples were collected only at its crater rim because the plateau and fumaroles are not easily accessible.

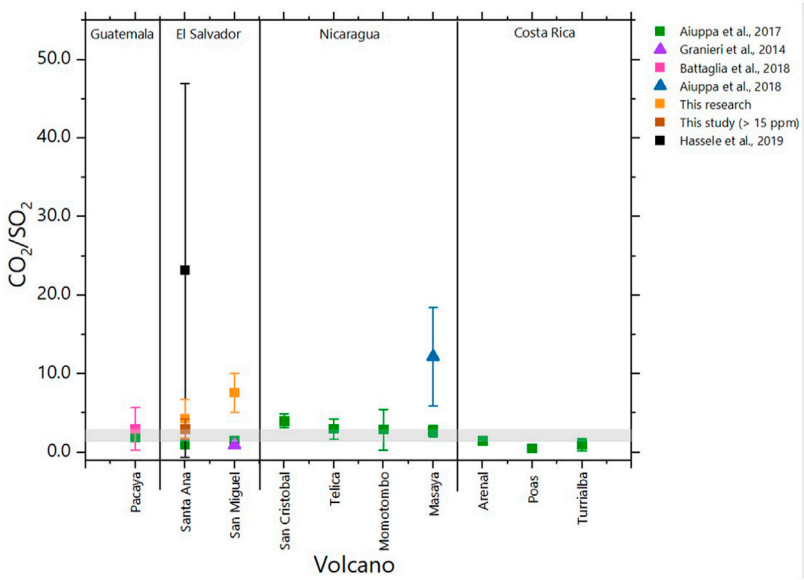

FIGURE 5
Comparison of published CO_2/SO_2 molar ratios of volcanoes belonging to the CAVA arc segment and the ones obtained in this work. Gray shadow indicates the CO_2/S_t signature assigned to the arc (Aiuppa et al., 2017). Triangles present data taken during eruptive periods. Squares refer to data taken during quiescent degassing periods. Average ratios obtained in this study with all measurements are in light orange while average ratio obtained at concentrated plumes conditions (>15 ppm SO_2) is in dark orange.

TABLE 7 Molar ratios (±error) calculated from data in Supplementary Table S6.

Date	Place	F/S	Cl/S	Br/S × 10^{-5}	I/S × 10^{-6}	CO_2/S
Santa Ana						
29.01.2019	Rim	n.a	0.5 ± 0.1	4.3 ± 1.0	n.a	116.1 ± 27.9
30.01.2019	Plateau	n.a	0.1 ± 0.03	n.a	n.a	46.0 ± 11.0
31.01.2019	Plateau	n.a	0.1 ± 0.02	n.a	n.a	33.3 ± 8.0
02.12.2020	Rim	0.5 ± 0.1	1.5 ± 0.4	n.a	n.a	889.7 ± 216.3
03.12.2020	Rim	0.0005 ± 0.0001	0.2 ± 0.05	1.17 ± 0.28	n.a	235.7 ± 56.7
San Miguel						
06.02.2019	Rim	n.a	0.9 ± 0.2	45.1 ± 10.9	2.2 ± 0.5	100.2 ± 24.1
07.02.2019	Rim	n.a	1.1 ± 0.3	59.2 ± 14.2	13.1 ± 3.1	100.0 ± 24.0

n.a.: not available.

4 Discussion

4.1 Comparison of SO_2 with NOVAC repository

In sections 1.1 and 1.2, we have described all SO_2 flux studies we are aware of at the two volcanoes where measurements were taken over at least a 1–2-year period. More recently, Arellano et al. (2021) presented a global compilation of SO_2 fluxes obtained from all NOVAC stations, including Santa Ana and San Miguel stations, for a 12-year period between 2005 and 2017. Fluxes were calculated using the NOVAC post-processing-program (Galle et al., 2010) and wind speed downloaded from the ERA-Interim re-analysis database, considering valid spectra the ones that have position, time, total duration (≤ 15 min) and adequate intensity (≤ 10% of saturation); and a chi-square (χ^2) value of 9 × 10^{-3} as DOAS fit threshold for the retrieval of SO_2. Less data were evaluated in the repository due to less data available on the NOVAC database. An average of 169.5 ± 48.7 SO_2 t/d was obtained for Santa Ana volcano, corresponding to 22 days between June 2008 and September 2009. The average obtained for the same days with our evaluation is 472.90 ± 375.45 t/d, being more than 2.5 times higher. The difference is caused by the meteorological data used (Supplementary Tables S1, S2). In the case of San Miguel, an average of 1,828.7 ± 262.5 SO_2 t/d was reported as the mean value for the period of 2005–2017, calculated with 4 days that correspond to the last 2 days of December 2013 and 2 days of February 2014 (Arellano et al., 2021). Our results for the same days show a mean SO_2 emission rate of 1,686.43 ± 470.01 t/d, which is within the confidence interval of the NOVAC inventory. The

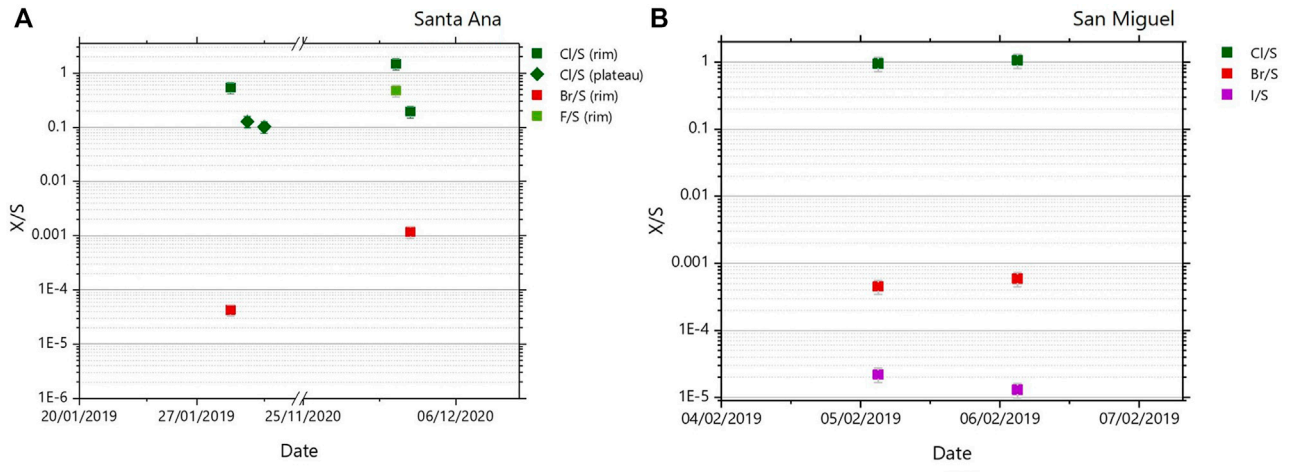

FIGURE 6
Halogen-to-sulfur molar ratios (X/S, where X = F, Cl, Br, I) measured at different sampling sites at Santa Ana volcano (left) and at San Miguel's rim (right).

TABLE 8 Molar mixing ratios of reactive halogens, obtained from denuders, to total halogens and total sulfur, obtained at different sampling sites.

Date	Location	Distance to the vent m)	Reactive halogens		BrX/Br	BrX/S × 10^{-5}	ClX/Cl × 10^{-5}	ClX/S× 10^{-5}
			BrX (pptv)	ClX (pptv)				
Santa Ana								
29.01.2019	Rim	480	9.1 ± 1.5	b.l.d	0.46 ± 0.11	1.95 ± 0.46	n.a	n.a
30.01.2019	Plateau	230	6.3 ± 0.8	3.6. ± 0.1	n.a	0.21 ± 0.04	0.95 ± 0.16	0.12 ± 0.02
31.01.2019	Rim	370	1.1 ± 0.2	35.3. ± 2.5	n.a	n.a	n.a	n.a
31.01.2019	Plateau	260	2.0 ± 0.3	b.l.d	n.a	0.04 ± 0.004	n.a	n.a
02.12.2020	Rim	570	3.1 ± 0.5	b.l.d	n.a	1.8 ± 0.4	n.a	n.a
San Miguel								
05.02.2019	Rim	366	b.l.d	1.2 ± 0.2	n.a	n.a	0.14 ± 0.03	n.a
07.12.2019	Rim	430	b.l.d	1.7 ± 0.3	n.a	n.a	0.12 ± 0.03	0.13 ± 0.03

[a]l.d: below limit of detection.
n.a:not available.

comparison shows the overall consistency of the calculated SO_2 fluxes at San Miguel and a discrepancy with Santa Ana estimations.

4.2 Comparison of SO_2 fluxes with seismic data

Real-time Seismic-Amplitude Measurement–RSAM (Endo and Murray, 1991), is the average signal size over a given period of time (10 min) acquired by the seismic network of the local Observatory. At Santa Ana volcano, the seismic station called San Blas (13.8393-89.6230) is located 1.0 km from the vent, while at San Miguel the VSM station (13.4413-88.2725) used to obtain the seismic data are at 0.9 km from the crater. For both volcanoes, the Observatory has assigned 150 RSAM units as the threshold. Data above this value represent an anomaly. This threshold was set arbitrarily, but is based on long-term monitoring experience. Figure 3 shows the temporal variation of SO_2 fluxes and RSAM value, demonstrating the quiet degassing of Santa Ana volcano, although an increase in the seismic data are observed between 2016 and 2018. However, these values are still at background level. Seismic data from San Miguel volcano show several periods when RSAM values were above threshold, which fits with events or phases before the volcano increased its activity. Figure 3 shows anomalous RSAM values during 2013 (151.0–1,252. RSAM units) prior to the eruption when SO_2 fluxes ranged from 25.9 to 1,863.2 t/d. On December 29, 1,275 RSAM

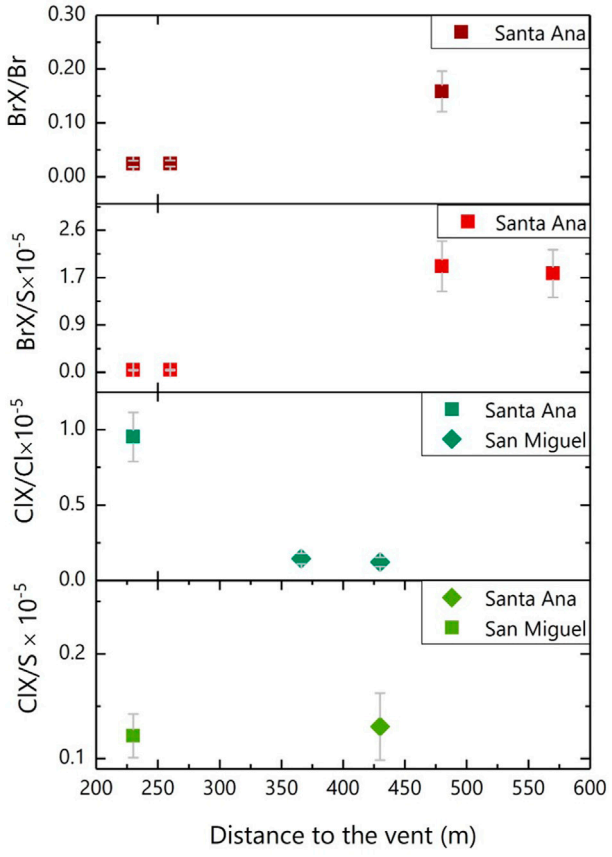

FIGURE 7
RHS molar ratios calculated from the concentrations detected at Santa Ana and San Miguel's crater.

units were recorded with SO_2 emissions varying between 727 and 3,390 t/d. After this event, the observatory reported smaller explosions (reddish shading in Figure 3) with values between 199.5 and 1,218.5 RSAM units and SO_2 emission rates that varied between 111.0 and 2,789.8 t/d. Although this study does not examine the specific seismic events that occurred during the study period (i.e., long-period volcano-tectonic events, tremors), the RSAM signatures follow overall general trend such as the SO_2 emission rates for San Miguel volcano, which also correlates with the visual observations of changes in the volcanic activity reported by the observatory.

4.3 Plume Gas composition

CO_2/SO_2 and H_2O/SO_2 ratios determined with the MultiGAS instrument both varied widely (Table 6). Using each pair of ratios recorded together, the molar fractions (in mol%) were calculated for the three main volatiles (Fischer and Chiodini, 2015; Symonds et al., 1994). The derived compositions range from 79.1 to 97.0 mol% H_2O, 2.4–18.6 mol% CO_2 and 0.5–2.2 mol% SO_2 for Santa Ana, while San Miguel has compositions of 91.1–94.5 mol% H_2O, 4.7–7.7 mol% CO_2 and 0.7–1.3 mol% SO_2. Larger variations are observed for Santa Ana than for San Miguel, of the global volcanic arc gases (Aiuppa, 2015; Edmonds, 2021). Furthermore, our results position Santa Ana in the list of low-carbon volcanoes in the CAVA segment when considering only data with >15 ppmv SO_2, in agreement with Mather et al. (2006) and Aiuppa et al. (2017). Furthermore, we see a medium to rich amount of water in the plume, when measurements were made under concentrated plume conditions (>15 ppm SO_2). Previous studies have reported variations in gas composition due to a combination of both scrubbing and meteorological conditions such as precipitation (e.g., Symonds et al., 2001; Colvin et al., 2013; Aiuppa, 2015; Hasselle et al., 2019). Field campaigns in this study were conducted during the dry season with sunny or cloudy days and no rain, so the above-mentioned effect did not influence our data.

Aiuppa et al. (2019) reported on the volcanic CO_2 inventory of several volcanoes, including Santa Ana and San Miguel, by scaling satellite-based SO_2 observations during 2005–2015, and CO_2/SO_2 ratios in high-temperature gases and calculating 66 ± 125 t/d and 91 ± 139 t/d, respectively. The SO_2 fluxes calculated here show a high variability and include observations of mainly quiescent degassing periods with few exceptions for San Miguel. Nevertheless, our mean SO_2 emission fluxes result in higher mean SO_2 fluxes than those of Carn et al., 2017, which covered a 10-year period (2005–2015) that partially overlaps with the period reported here (2006–2020 and 2008–2019 for Santa Ana and San Miguel, respectively) but is based on less frequent plume detection. In Carn et al., 2017, Santa Ana and San Miguel are 77th and 78th on the global list of volcanic SO_2 emission observed from space. In this study, CO_2 emission rates were estimated using the daily mean SO_2 fluxes obtained from the NOVAC stations between 2006 and 2019 for Santa Ana and 2008 and 2019 for San Miguel, and CO_2/SO_2 ratios obtained from MultiGAS with high SO_2 concentrations considered representative of magmatic composition, yielding CO_2 output rates of 1,585.4 ± 866.6 t/d for Santa Ana volcano.

The difference of these findings with the previously described results is noteworthy, since, based on our measurements, significantly higher CO_2 emission results. However, the previous datasets (Granieri et al., 2015; Aiuppa et al., 2019) were based on a comparatively small database. This alone can be a problem, as emphasized by Werner et al. (2019), for example, if few measurements obtained during periods of increased activity are the basis of the estimates. Therefore, longer time series are an important scientific basis, for improved emission estimation. In this study, we report time series of more than 10 years for SO_2 emissions and also MultiGAS data repeatedly collected over a 3-year period (2018–2020), which we believe leads to a more representative data set. In the case of San Miguel and Santa Ana volcanoes, previous sparse measurements apparently tended to underestimate CO_2 emissions. More long-term ground- and space-based measurement series are undoubtedly needed for a more accurate determination of global volcanic degassing.

5 Conclusion

We summarized earlier SO_2 emission rates for Santa Ana and San Miguel which cover periods often of only 1–2 years or even less (Bernard et al., 2004; Cartagena et al., 2004; Rodriguez et al., 2004; Pérez et al., 2006; Olmos et al., 2007; Arellano et al., 2021) and

extended those time series significantly. We obtained a daily average of 903.88 ± 599.49 t/d for San Miguel and 470.53 ± 414.69 t/d for Santa Ana. These new data were recorded from NOVAC stations installed downwind of the craters on the SW flanks of both volcanoes. Most of the data were recorded during quiescent volcanic activity, with the exception of the events at San Miguel shown in Figure 3, where peak SO_2 fluxes were observed along with some changes in the seismic data recorded for the same period.

The remote sensing data were complemented with *in situ* sampling conducted during field campaigns in 2019–2020, to further characterize the chemical signature of the gas plumes at Santa Ana and San Miguel. Plume composition at Santa Ana is H_2O-intermediate (79.1–97.0 mol%), with a typical CAVA CO_2/SO_2 signature of 2.9 ± 0.6 while San Miguel is H_2O-rich (91.1–94.5 mol %) with relatively high CO_2/SO_2 ratios obtained from diluted and discontinuous plume signatures (< 10 ppm SO_2), likely containing contributions from low-temperature hydrothermal gases characterized by sulfur scrubbing (Aiuppa et al., 2017).

We also report the total halogen fraction of the emitted gases with their corresponding halogen to sulfur ratios. At San Miguel, halogen to sulfur ratios were obtained with mean values for HCl/SO_2, HBr/SO_2 and HI/SO_2 of (1.0 ± 0.2, (5.2 ± 1.3) × 10^{-4} and (1.8 ± 0.4) × 10^{-5}, while at Santa Ana we found average values of HCl/SO_2, HF/SO_2 and HBr/SO_2 of 0.5 ± 0.1, 0.2 ± 0.3, (6.8 ± 1.6) × 10^{-5}, respectively. In addition, we present the first measurements of RHS (sum of reactive bromine and chlorine species) made at these two El Salvadorean volcanoes using TMB coated denuders. The data show activation of halogens as a function of distance from the emission vent, i.e., higher RHS concentrations are measured at greater distances, consistent with measurements on other locations and model studies (von Glasow, 2010; Roberts et al., 2014). These field observations provide new data on RHS, especially for low-emission volcanoes. As a result, the global data set on halogen speciation in volcanic plumes is complemented. This contributes to a better understanding of the relationship between emitted halogen species and measurable halogen compounds—i.e., better understanding the chemistry in volcanic plumes. Overall, we present the most comprehensive geochemical gas dataset of the Santa Ana and San Miguel volcanoes, with the aim of creating a significantly expanded database of their gas emissions. The CO_2 flux determined in this study is about an order of magnitude higher than previous estimates. The database presented is an essential prerequisite not only for a better understanding of basic volcanological processes, but also as a basis for the scientific assessment of the significance of changes in the emission rate of released gases or their compounds later formed in the volcanic plume. In addition, on the long-term this allows to reliably use the gas emissions as indicators of volcanic unrest.

Data availability statement

The datasets presented in this study can be found in online repositories. The names of the repository/repositories and accession number(s) can be found below: https://github.com/xguti83/ESA_gas_emissions; https://novac.chalmers.se/.

Author contributions

XG, NB, JR, FM, MV, and DE collected samples. XG produced research results and processed data. FD provided scripts to evaluate DOAS data. ML and BG contributed research results. JR and NB provided input on the analysis of the results. EG and FM contributed with the logistic of the field campaigns. XG, NB, and TH wrote the paper with input from ML and BG.

Funding

XG thanks the Deutscher Akademischer Austauschdienst for the financial support. Field campaigns were supported from TeMaS (Terrestrial Magmatic Systems, a collaborative effort of the Universities of Mainz, Frankfurt and Heidelberg) and the Max Planck Graduate Center (MPGC).

Acknowledgments

We would like to thank the park rangers, Comandos de Salvamento de El Salvador and Policía Nacional Civil (PNC) as well as the colleagues from observatory for their collaboration during the surveys, especially Manuel Díaz, Gerente de Geología, for facilitating the cooperation with us. XG thanks Carlos Alberti, Institute of Meteorology and Climate Research (IMK-ASF), Karlsruhe Institute of Technology (KIT), Karlsruhe, Germany; for his input with the evaluation scripts. We also thank the two reviewers and the editor for revising our manuscript and all constructive comments to improve the article.

Conflict of interest

The authors declare that the research was conducted in the absence of any commercial or financial relationships that could be construed as a potential conflict of interest.

Publisher's note

Supplementary material

The Supplementary Material for this article can be found online at: https://www.frontiersin.org/articles/10.3389/feart.2023.1049670/full#supplementary-material

References

Aiuppa, A., Federico, C., Franco, A., Giudice, G., Gurrieri, S., Inguaggiato, S., et al. (2005). Emission of bromine and iodine from Mount Etna volcano. *Geochem. Geophys. Geosyst.* 6 (8), n/a. doi:10.1029/2005gc000965

Aiuppa, A., Fischer, T. P., Plank, T., and Bani, P. (2019). CO_2 flux emissions from the Earth's most actively degassing volcanoes, 2005 - 2015. *Sci. Rep.* 9, 5442. doi:10.1038/s41598-019-41901-y

Aiuppa, A., Fischer, T. P., Plank, T., Robidoux, P., and Di Napoli, R. (2017). Along-arc, inter-arc and arc-to-arc variations in volcanic gas CO 2/S T ratios reveal dual source of carbon in arc volcanism. *Earth-Science Rev.* 168, 24–47. doi:10.1016/j.earscirev.2017.03.005

Aiuppa, A., Moor, J. M. D., Arellano, S., Coppola, D., Francofonte, V., Galle, B., et al. (2018). Tracking Formation of a lava lake from ground and space: Masaya volcano (Nicaragua), 2014-2017. *Geochem. Geophys. Geosyst.* 19 (2), 496–515. doi:10.1002/2017GC007227

Aiuppa, A. (2015). "Volcanic-gas monitoring," in *Volcanism and global environmental change*. Editors A. Schmidt and E. Kirsten (Cambridge: Cambridge University Press), 81–96.

Arellano, S., Galle, B., Apaza, F., Avard, G., Barrington, C., Bobrowski, N., et al. (2021). Synoptic analysis of a decade of daily measurements of SO_2 emission in the troposphere from volcanoes of the global ground-based Network for Observation of Volcanic and Atmospheric Change. *Earth Syst. Sci. Data* 13 (3), 1167–1188. doi:10.5194/essd-13-1167-2021

Battaglia, A., Bitetto, M., Aiuppa, A., Rizzo, A. L., Chigna, G., Watson, I. M., et al. (2018). The magmatic gas signature of Pacaya Volcano, with implications for the volcanic CO2 flux from Guatemala. *Geochemistry,Geophysics, Geosystems* 19, 667–692. doi:10.1002/2017GC007238

Bernard, A., Escobar, C. D., Mazot, A., and Gutierrez, R. E. (2004). "The acid volcanic lake of Santa Ana volcano, El Salvador," in *Natural Hazards in El salvado* (Boulder, CO: Geological Society of America).

Bobrowski, N., and Giuffrida, G. (2012). Bromine monoxide/sulphur dioxide ratios in relation to volcanological observations at Mt. Etna 2006–2009. *Solid earth.* 3 (2), 433–445. doi:10.5194/se-3-433-2012

Bobrowski, N., Glasow, R. V., Aiuppa, A., Inguaggiato, S., Louban, I., Ibrahim, O. W., et al. (2007). Reactive halogen chemistry in volcanic plumes. *J. Geophys. Res.* 112 (D6), D06311. doi:10.1029/2006JD007206

Bonforte, A., Hernandez, D. A., Gutiérrez, E., Handal, L., Polío, C., Rapisarda, S., et al. (2016). The unrest of the san Miguel volcano (El Salvador, central America): Installation of the monitoring network and observed volcano-tectonic ground deformation. *Nat. Hazards Earth Syst. Sci.* 16, 1755–1769. doi:10.5194/nhess-16-1755-2016

Carn, S. A., Fioletov, V. E., McLinden, C. A., Li, C., and Krotkov, N. A. (2017). A decade of global volcanic SO2 emissions measured from space. *Sci. Rep.* 7 (1), 44095. doi:10.1038/srep44095

Cartagena, R., olmos, R., López, D. L., Soriano, T., Barahona, F., Hernández, P. A., et al. (2004). "Diffuse soil degassing of carbon dioxide, radon and mercury at San Miguel volcano, El Salvador," in *natural hazards in El Salvador* (Boulder, CO: Special Paper of the Geological Society of America).

Chesner, C. A., Pullinger, C. R., and Escobar, C. D. (2004). "Physical and chemical evolution of San Miguel volcano, El Salvador," in *Natural hazards in El Salvador* (Boulder, CO: Geological Society of America).

Colvin, A., Rose, W. I., Varekamp, J. C., Palma, J. L., Escobar, D., Gutierrez, E., et al. (2013). "Crater lake evolution at Santa Ana Volcano (El Salvador) following the 2005 eruption," in *Understanding open-vent volcanism and related hazards*. Editors W. I. Rose, J. L. Palma, H. Delgado Granados, and N. Varley (Geological Society of America Special Paper), 23–43. doi:10.1130/2013.2498(02

Dinger, F., Kleinbek, T., Dörner, S., Bobrowski, N., Platt, U., Wagner, T., et al. (2021). SO_2 and BrO emissions of Masaya volcano from 2014 to 2020. *Atmos. Chem. Phys.* 21 (12), 9367–9404. doi:10.5194/acp-21-9367-2021

Edmonds, M. (2021). "Geochemical monitoring of volcanoes and the mitigation of volcanic gas hazards," in *Forecasting and Planning for Volcanic Hazards, Risks and Disasters*. Editors J. Schroder and P. Papale. doi:10.1016/C2018-0-02632-8

Endo, E. T., and Murray, T. (1991). Real-time seismic amplitude measurement (RSAM): a volcano monitoring and prediction tool. *Bull. Volcanol.* 53 (7), 533–545. doi:10.1007/BF00298154

Escobar, C. D. (2003). *San Miguel volcano and its volcanic hazards, El Salvador, Central America*. Houghton, WA: Michigan Technological University. PhD thesis.

Fischer, T. P., and Chiodini, G. (2015). "Volcanic, Magmatic and Hydrothermal Gases," in *The Encyclopedia of Volcanoes*. Editors H. Sigurdsson, B. Houghton, S. R. McNutt, H. Rymer, and J. Stix doi:10.1016/C2015-0-00175-7

Galle, B., Johansson, M., Rivera, C., Zhang, Y., Kihlman, M., Kern, C., et al. (2010). Network for observation of volcanic and atmospheric change (NOVAC)—a global network for volcanic gas monitoring: Network layout and instrument description. *J. Geophys. Res.* 115 (D5), D05304. doi:10.1029/2009JD011823

Geil, B. (2021). *Methodenentwicklung zur Halogenbestimmung von Vulkanischen Systemen mittels Basischer Fallen und Diffusionsabscheidern/Entwicklung einer Permeablen Chlorgasquelle (Master thesis)*. Mainz, Germany: Johannes Gutenberg Universität Mainz.

Gliß, J., Bobrowski, N., Vogel, L., Pöhler, D., and Platt, U. (2015). OClO and BrO observations in the volcanic plume of Mt. Etna – implications on the chemistry of chlorine and bromine species in volcanic plumes. *Atmos. Chem. Phys.* 15, 5659–5681. doi:10.5194/acp-15-5659-2015

Granieri, D., Salerno, G., Liuzzo, M., La Spina, A., Giuffrida, G., Caltabiano, T., et al. (2015). Emission of gas and atmospheric dispersion of SO 2 during the December 2013 eruption at San Miguel volcano (El Salvador, Central America). *Geophys. Res. Lett.* 42 (14), 5847–5854. doi:10.1002/2015GL064660

Hasselle, N., Montalvo, F., Rouwet, D., Battaglia, A., Bitetto, M., Escobar, D., et al. (2019). The crater lake of Ilamatepec (Santa Ana) volcano, El Salvador: Insights into lake gas composition and implications for monitoring. *Bull. Volcanol.* 81 (11), 66. doi:10.1007/s00445-019-1331-8

Hernandez, P., Pérez, N., Varekamp, J., Henríquez, B., Hernández De la Cruz, A., Barrancos, J., et al. (2007). *crater lake temperature changes of the 2005 eruption of Santa Ana volcano, El Salvador Pure and applied geophysics, Springer*. Central America. doi:10.1007/978-3-7643-8720-4_9

Jiménez, D., Becerril, L., Bartolini, S., Escobar, D., and Martí, J. (2020). Making a qualitative volcanic-hazards map by combining simulated scenarios: An example for San Miguel Volcano (El Salvador). *J. Volcanol. Geotherm. Res.* 395, 106837–110273. doi:10.1016/j.jvolgeores.2020.106837

Laiolo, M., Coppola, D., Barahona, F., Benitez, J. E., Cigolini, C., Escobar, D., et al. (2017). Evidences of volcanic unrest on high-temperature fumaroles by satellite thermal monitoring: The case of Santa Ana volcano, El Salvador. *Journa Volcanolgy Geotherm. Res.* 340, 170–179. doi:10.1016/j.jvolgeores.2017.04.013

Lübcke, P., Bobrowski, N., Arellano, S., Galle, B., Garzón, G., Vogel, L., et al. (2014). BrO/SO_2 molar ratios from scanning DOAS measurements in the NOVAC network. *Solid earth.* 5 (1), 409–424. doi:10.5194/se-5-409-2014

Mann, C. P., Stix, J., Vallance, J. W., Richer, M., Rose, W. I., Bommer, J. J., et al. (2004). "Subaqueous intracaldera volcanism, ilopango caldera, El Salvador, central America," in *Natural hazards in El Salvador* (Boulder, Colorado: Geological Society of America Special Paper).

Mather, T. A., Pyle, D. M., Tsanev, V. I., McGonigle, A. J. S., Oppenheimer, O., and Allen, A. G. (2006). "A reassessment of current volcanic emissions from the Central American arc with specific examples from Nicaragua," in *Journal of Volcanology and Geothermal Research* 149, 297–311. doi:10.1016/j.jvolgeores.2005.07.021

Meyer-Abbich, H. (1956). *Anales servicio geologico nacional*. El Salvador: Anales del Servicio Geologico Nacional.

Noguchi, K., and Kamiya, H. (1963). Prediction of volcanic eruption by measuring the chemical composition and amounts of gases. *B. Volcanol.* 26, 367–378. doi:10.1007/bf02597298

Olmos, R., Barrancos, J., Rivera, C., Barahona, F., López, D. L., Henriquez, B., et al. (2007). Anomalous emissions of SO2 during the recent eruption of Santa Ana volcano, El Salvador, central America. *Pure Appl. Geophys.* 164 (12), 2489–2506. doi:10.1007/s00024-007-0276-6

Pérez, N. M., Hernández, P. A., Padrón, E., Cartagena, R., Olmos, R., Barahona, F., et al. (2006). Anomalous diffuse CO2 emission prior to the january 2002 short-term unrest at san Miguel volcano, El Salvador, central America. *Pure Appl. Geophys.* 163, 883–896. doi:10.1007/s00024-006-0050-1

Roberts, T. J., Braban, C. F., Martin, R. S., Oppenheimer, C., Adams, J. W., Cox, R. A., et al. (2009). Modelling reactive halogen formation and ozone depletion in volcanic plumes. *Chem. Geol.* 263 (1-4), 151–163. doi:10.1016/j.chemgeo.2008.11.012

Roberts, T. J., Martin, R. S., and Jourdain, L. (2014). Reactive bromine chemistry in mount etna's volcanic plume: The influence of total Br, high-temperature processing, aerosol loading and plume–air mixing. *Atmos. Chem. Phys.* 14 (20), 11201–11219. doi:10.5194/acp-14-11201-2014

Rodríguez, L. A., Watson, I. M., Rose, W. I., Branan, Y. K., Bluth, G. J. S., Chigna, G., et al. (2004). SO2 emissions to the atmosphere from active volcanoes in Guatemala and El Salvador, 1999–2002. *J. Volcanol. Geotherm. Res.* 138 (3-4), 325–344. doi:10.1016/j.jvolgeores.2004.07.008

Rüdiger, J., Bobrowski, N., Liotta, M., and Hoffmann, T. (2017). Development and application of a sampling method for the determination of reactive halogen species in volcanic gas emissions. *Anal. Bioanal. Chem.* 409 (25), 5975–5985. doi:10.1007/s00216-017-0525-1

Rüdiger, J., Gutmann, A., Bobrowski, N., Liotta, M., Moor, J. M. D., Sander, R., et al. (2021). Halogen activation in the plume of Masaya volcano: Field observations and box model investigations. *Atmos. Chem. Phys.* 21 (5), 3371–3393. doi:10.5194/acp-21-3371-2021

Rüdiger, J., Tirpitz, J., Moor, J. M. D., Bobrowski, N., Gutmann, A., Liuzzo, M., et al. (2018). Implementation of electrochemical, optical and denuder-based sensors and sampling techniques on UAV for volcanic gas measurements: Examples from Masaya,

turrialba and stromboli volcanoes. *Atmos. Meas. Tech.* 11 (4), 2441–2457. doi:10.5194/amt-11-2441-2018

Salazar, J. M., Hernández, P. A., Pérez, N. M., Olmos, R., Barahona, F., Cartagena, R., et al. (2004). "Spatial and temporal variations of diffuse CO2 degassing at Santa Ana-Izalco-Coatepeque volcanic complex, El Salvador, Central America," in *Natural Hazards*. Editors W. Rose, J. J. Bommer, D. Lopez, M. J. Carr, and J. J. Major

Shinohara, H. (2005). A new technique to estimate volcanic gas composition: Plume measurements with a portable multi-sensor system. *J. Volcanol. Geotherm. Res.* 143 (4), 319–333. doi:10.1016/j.jvolgeores.2004.12.004

Shinohara, H., Aiuppa, A., Giudice, G., Gurrieri, S., and Liuzzo, M. (2008). Variation of H2O/CO2 and CO2/SO2 ratios of volcanic gases discharged by continuous degassing of Mount Etna volcano, Italy. *J. Geophys. Res.* 113 (B9), 5185. doi:10.1029/2007JB005185

Stutz, J., and Platt, U. (1996): Numerical analysis and estimation of the statistical error of differential optical absorption spectroscopy measurements with least-squares methods. *Applied optics* 35(30), 6041–6053.

Surl, L., Roberts, T., and Bekki, S. (2021): Observation and modelling of ozone-destructive halogen chemistry in a passively degassing volcanic plume. *Atmos. Chem. Phys.* 21(16), 12413–12441. doi:10.5194/acp-21-12413-2021

Symonds, R. B., Rose, W. I., Bluth, G. J. S., and Gerlach, T. M. (1994): VOLCANIC-GAS studies: METHODS, results, and applications," in *Volatiles in magmas*. Editors M. R. Carroll and J. R. Holloway (Berlin, Boston: De Gruyter), 1–66. doi:10.1515/9781501509674-007

Symonds, R. B., Gerlach, T. M., and Reed, M. H. (2001). Magmatic gas scrubbing: Implications for volcano monitoring. *J. Volcanol. Geotherm. Res.* 108, 303–341. doi:10.1016/s0377-0273(00)00292-4

Tamburello, G. (2015). Ratiocalc: Software for processing data from multicomponent volcanic gas analyzers. *Comput. Geosciences* 82, 63–67. doi:10.1016/j.cageo.2015.05.004

Tirpitz, J. L., Pöhler, D., Bobrowski, N., Christenson, B., Rüdiger, J., Schmitt, S., et al. (2019). Non-dispersive UV absorption spectroscopy: A promising new approach for *in-situ* detection of sulfur dioxide. *Front. Earth Sci.* 7, 2. doi:10.3389/feart.2019.0002

von Glasow, R. (2010). Atmospheric chemistry in volcanic plumes In PNAS 107(15), 6594–6599. doi:10.1073/pnas.0913164107

Werner, C., Fischer, T. P., Aiuppa, A., Edmonds, M., Cardellini, C., Carn, S., et al. (2019). "Carbon dioxide emissions from subaerial volcanic regions," in *Deep carbon past to present* (Cambridge, Great Britain: Cambridge University Press).

Wittmer, J., Bobrowski, N., Liotta, M., Giuffrida, G., Calabrese, S., and Platt, U. (2014). Active alkaline traps to determine acidic-gas ratios in volcanic plumes: Sampling techniques and analytical methods. *Geochem. Geophys. Geosyst.* 15 (7), 2797–2820. doi:10.1002/2013GC005133

Woitischek, J., Woods, A. W., Edmonds, M., Oppenheimer, C., Aiuppa, A., Pering, T. D., et al. (2020). Strombolian eruptions and dynamics of magma degassing at Yasur volcano (Vanuatu). *J. Volcanol. Geotherm. Res.* 398, 106869. doi:10.1016/j.jvolgeores.2020.106869

Global Volcanism Program (2001). "Report on Santa Ana (El Salvador)," in *Bulletin of the global volcanism network*. Editor R. Wunderman (Washington, DC: Smithsonian Institution), 4. doi:10.5479/si.GVP.BGVN200104-343020

frontiers | Frontiers in Earth Science

TYPE Original Research
PUBLISHED 12 July 2023
DOI 10.3389/feart.2023.1088768

OPEN ACCESS

EDITED BY
Nick Varley,
University of Colima, Mexico

REVIEWED BY
Jan-Lukas Tirpitz,
Heidelberg University, Germany
Ben Esse,
The University of Manchester,
United Kingdom

*CORRESPONDENCE
S. Arellano,
santiago.arellano@chalmers.se

RECEIVED 03 November 2022
ACCEPTED 29 June 2023
PUBLISHED 12 July 2023

CITATION
Galle B, Arellano S, Johansson M, Kern C and Pfeffer MA (2023), An algorithm for correction of atmospheric scattering dilution effects in volcanic gas emission measurements using skylight differential optical absorption spectroscopy. *Front. Earth Sci.* 11:1088768. doi: 10.3389/feart.2023.1088768

An algorithm for correction of atmospheric scattering dilution effects in volcanic gas emission measurements using skylight differential optical absorption spectroscopy

B. Galle[1], S. Arellano[1]*, M. Johansson[1], C. Kern[2] and M. A. Pfeffer[3]

[1]Department of Space, Earth and Environment, Chalmers University of Technology, Gothenburg, Sweden, [2]U.S. Geological Survey, Volcano Science Center, Vancouver, WA, United States, [3]Icelandic Meteorological Office, Reykjavik, Iceland

Differential Optical Absorption Spectroscopy (DOAS) is commonly used to measure gas emissions from volcanoes. DOAS instruments measure the absorption of solar ultraviolet (UV) radiation scattered in the atmosphere by sulfur dioxide (SO_2) and other trace gases contained in volcanic plumes. The standard spectral retrieval methods assume that all measured light comes from behind the plume and has passed through the plume along a straight line. However, a fraction of the light that reaches the instrument may have been scattered beneath the plume and thus has passed around it. Since this component does not contain the absorption signatures of gases in the plume, it effectively "dilutes" the measurements and causes underestimation of the gas abundance in the plume. This dilution effect is small for clean-air conditions and short distances between instrument and plume. However, plume measurements made at long distance and/or in conditions with significant atmospheric aerosol, haze, or clouds may be severely affected. Thus, light dilution is regarded as a major error source in DOAS measurements of volcanic degassing. Several attempts have been made to model the phenomena and the physical mechanisms are today relatively well understood. However, these models require knowledge of the local atmospheric aerosol composition and distribution, parameters that are almost always unknown. Thus, a practical algorithm to quantitatively correct for the dilution effect is still lacking. Here, we propose such an algorithm focused specifically on SO_2 measurements. The method relies on the fact that light absorption becomes non-linear for high SO_2 loads, and that strong and weak SO_2 absorption bands are unequally affected by the diluting signal. These differences can be used to identify when dilution is occurring. Moreover, if we assume that the spectral radiance of the diluting light is identical to the spectrum of light measured away from the plume, a measured clean air spectrum can be used to represent the dilution component. A correction can then be implemented by iteratively subtracting fractions of this clean air spectrum from the measured spectrum until the respective absorption signals on strong and weak SO_2 absorption bands are consistent with a single overhead SO_2 abundance. In this manner, we can quantify the magnitude of light dilution in each individual measurement spectrum as well as obtaining a dilution-corrected value for the SO_2 column density along the line of sight of the instrument. This paper first presents the theory

behind the method, then discusses validation experiments using a radiative transfer model, as well as applications to field data obtained under different measurement conditions at three different locations; Fagradalsfjall located on the Reykjanaes peninsula in south Island, Manam located off the northeast coast of mainland Papua New Guinea and Holuhraun located in the inland of north east Island.

KEYWORDS

DOAS, scattering, volcanic gas, sulfur dioxide, emission monitoring

1 Introduction

Volcanic plumes are common occurrences at active volcanoes around the world. These plumes contain volatile species exsolved from magma rising from depth. The chemical signature of volcanic plumes depends on magma chemistry, the interaction of rising volatiles with rocks and water, and potentially condensation and re-evaporation from hydrothermal systems. Plumes may contain gases and aerosols, with the latter consisting of cloud droplets, ash, and secondary aerosols from the oxidation of volcanogenic gas species. The gas phase of high-temperature volcanic plumes predominantly consists of water vapor (H_2O), carbon dioxide (CO_2), and sulfur dioxide (SO_2), with lesser amounts of hydrogen sulfide (H_2S), hydrogen halides (HCl, HF, HBr), and a variety of minor trace components including hydrogen, helium, reduced carbon species, and metals/metalloids (Giggenbach 1996; Gerlach 2004; Oppenheimer et al., 2014). Tracking changes in the emission rate and composition of gas emissions can provide crucial information on volcanic processes occurring at depth and provide input into eruption forecasts (e.g., Aiuppa et al., 2007, 2021; Burton et al., 2007; de Moor et al., 2016a, 2016b; Kunrat et al., 2022). Furthermore, volcanic plumes can be transported long distances from their sources, causing impact on air quality, air traffic, fumigation of soils and water bodies, health, and infrastructure. Therefore, routine monitoring of volcanic plumes has become one of the key components of modern volcanic and atmospheric surveillance (Sparks et al., 2012; Kern et al., 2022).

The most commonly measured gas species in volcanic plumes is SO_2. This is because this species is a marker of magmatic activity, the background concentration in air is usually of a few parts per billion (ppb), and measurement is facilitated by passive remote sensing techniques sensitive to the strong light absorption of SO_2 in the near ultraviolet wavelengths. Since the 1970s, correlation spectroscopy (COSPEC) has been used to measure SO_2 remotely from ground by analysis of the absorption of diffused solar light at discrete narrow wavelength bands in the 305–330 nm spectral range (Moffat and Millán, 1971). This technique has been gradually replaced by differential optical absorption spectroscopy (DOAS), which instead analyses the absorption features of a continuous spectrum in the same range (Galle et al., 2003). The technique is now used at dozens of volcanoes for routine monitoring with stationary scanning DOAS systems, or by traversing under the plume with zenith-looking DOAS instruments (Edmonds et al., 2003; Johansson et al., 2008; Galle et al., 2010; Platt et al., 2015; Arellano et al., 2021).

The DOAS method is based on absorption spectroscopy and uses the UV-light from the Sun, scattered within the atmosphere as it travels to the instrument. The conventional application of the method assumes that all the measured light comes from above the plume and has passed through the plume in route to the instrument. The last scattering event of the measured light occurs above the plume and, from there, crosses the plume along the instrument's line of sight. However, a fraction of the light that reaches the instrument may come from atmospheric scattering without first passing through the plume. This light causes a "dilution" of the amount of gas measured. In clean-air conditions and with short distance between the instrument and the plume, this dilution effect is small, but if conditions get hazier, and/or the distance to the plume increases, this effect may become severe. Thus, as elevated plumes or opaque atmospheres are common on many volcanoes, this effect is regarded as a major error source in volcanic SO_2 emission monitoring using UV spectroscopy (Millán, 1980; Mori et al., 2006; Kern et al., 2010).

Already in the COSPEC era it was recognized that this atmospheric scattering could severely affect the measurements of gas emissions from volcanoes and industrial sources (Millán, 1980). Now that the mini-DOAS systems are commonly applied to quantify volcanic gas emissions, this problem has received increased attention (Mori et al., 2006; Kern et al., 2010), and the error in typical emission rate measurements due to atmospheric scattering is today estimated to be 10%–100% depending on geometric and meteorological conditions. Several attempts have been made to model the phenomena (Kern et al., 2012), and the physical mechanisms are now relatively well understood. However, applying such models to retrieve volcanic emission rates requires knowledge of the local aerosol composition and distribution, both inside the plume and in the background atmosphere, parameters that are rarely known with the required accuracy. Thus, practical algorithms to quantitatively correct for the effect are needed. We here propose one such algorithm.

Mori and collaborators recognized that when DOAS measurements of SO_2 in volcanic plumes were made over longer distances, atmospheric scattering between the instrument and the plume caused underestimation in the derived SO_2 columns and that this dilution was stronger at shorter wavelengths and at higher SO_2 columns (Mori et al., 2006). They suggested that evaluating SO_2 columns in different wavelength bands in the region 303–320 nm could be used to qualitatively detect if there is significant underestimation in the DOAS measurements due to atmospheric scattering. Fickel and Delgado Granados also conclude that different wavelength bands yield different column densities, and suggested using evaluation in longer wavelength bands, when possible, to minimize but not eliminate the dilution effect (Fickel and Delgado Granados, 2017). Varnam et al. (2020) suggested a method for quantitative correction of the atmospheric scattering dilution based on evaluation in two different wavelength bands in the range 306–322 nm. They use synthetically modelled spectra (Esse et al.,

2020), with varying SO_2 column and atmospheric scattering dilution. These spectra were then evaluated in the two wavelength bands and the results were used to build a look-up table. The results from evaluating measured plume spectra in the same two wavelength bands were then compared with the corresponding data in the look-up table, providing a dilution factor that facilitates a quantitative correction of the measured plume spectra.

The approach to quantify the scattering effect described here is based on taking advantage of the non-linearity of the Beer-Lambert law for absorption, as well as the difference in light intensity in the plume spectrum caused by SO_2 broadband absorption, combined with the assumption that the spectral distribution of the light scattered below the plume is similar to the spectral distribution of the light scattered without the plume. The method is applicable when multiple scattering inside the plume can be neglected (low amounts of ash and other aerosols). The method is more robust when the measured gas columns are high enough to cause significant non-linearity and broadband intensity reduction in the absorption spectra studied.

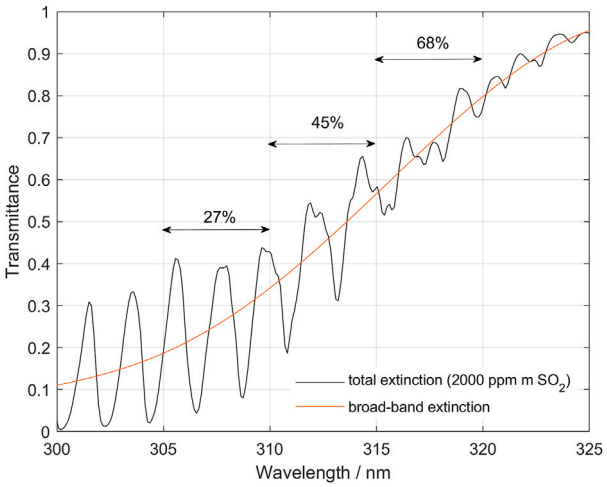

FIGURE 1
Theoretical transmittance spectrum for light passing through 2,000 ppm m SO_2. Notice that SO_2 broadband absorption is unequal for the three wavelength bands: 305–310, 310–315 and 315–320, which causes different dilution effects. Here it can be seen that due to the broad-band absorption in SO_2 the actual average intensity in the plume at the three wavelength bands used is only 27%, 45% and 68% respectively of the plume intensity without SO_2.

2 Experimental details

The basic mini-DOAS system consists of a pointing telescope fiber-coupled to a spectrograph. The narrow field of view telescope gathers ultraviolet light from the Sun, scattered from aerosols and molecules in the atmosphere. Light is transferred from the telescope to the spectrometer by an optical fiber. The spectra are digitalized and logged on a computer for analysis using DOAS (Platt and Stutz, 2008). In this way, the slant column density of various gases in the viewing direction of the telescope is derived (Galle et al., 2003). Two different setups are commonly used, the MobileDOAS and the ScanningDOAS.

In the MobileDOAS setup measurements are made from a mobile platform. The telescope is pointing towards zenith while traversing under the plume at the same time as the position of the platform is logged by a GPS. In this way the total number of SO_2 molecules in a cross-section of the plume may be derived, and after multiplication with the wind speed at plume height the emission in kg s^{-1} is obtained.

In the ScanningDOAS setup the telescope is motorized to automatically scan the field of view of the instrument over 180°. In a typical measurement the instrument is located under the plume, and scans are made, from horizon to horizon, in a plane perpendicular to the wind-direction. Thus, automatic unattended measurements of the SO_2 emission with 5–10 min time resolution can be made. This is the concept used in the NOVAC network (Galle et al., 2010).

In this paper we focus on the MobileDOAS application. In the MobileDOAS application measurements of sky and plume are made in the same zenith direction, while in the ScanDOAS application the plume spectra are taken in varying directions different from the clean air sky spectrum which may complicate the use of the here suggested algorithm.

A correct unit to use for column measurement of a gas is molec/cm^2. In our case, volcanic gas emissions, this means numbers of the order 10^{16}–10^{19}. In connection with COSPEC measurements a more practical unit, ppm m, was introduced and has become widely used in the volcano gas community, yielding results in the order 10–10,000 ppm m. It should be noted, however, that the instruments measure mass units not mixing ratio. Nevertheless, we define 1 ppm m as $2.5{\cdot}10^{15}$ molec/cm^2 (its true value for STP) and for clarity use this unit throughout this paper. Thus, to convert any data in this paper expressed in ppm m to mass units one should simply multiply with $2.5{\cdot}10^{15}$, without any correction for pressure or temperature.

3 Methods

3.1 Qualitative description

The conventional DOAS method applied in routine remote sensing of volcanic SO_2 assumes that all the measured light has been last scattered into the field of view above the plume and has passed in a straight line through the plume. In practice, however, a fraction of the light that reaches the instrument originates from atmospheric scattering on molecules and aerosols below the plume and thus has not passed through the plume. This causes a “dilution” of the slant column retrieved by the DOAS method.

We define the following:

- Sky spectrum: a spectrum of the skylight that has not passed through the plume. This can be measured in a location with plume free zenith view.
- Plume spectrum: a spectrum of the skylight that has passed through the volcanic plume but not undergone dilution afterwards. Not directly measurable.

- Dilution spectrum: a spectrum of skylight that is scattered into the field-of-view of the measurement device from the atmosphere below the plume and has thus never passed through the plume. Not directly measurable.
- Measured spectrum: the spectrum as observed by the instrument while aimed at the volcanic plume, hence the combined plume and dilution spectrum.
- Dilution factor k: the fraction of the sky spectrum, that is obtained after iterative subtraction of fractions of the sky spectrum (normalized as described in Section 3.2) from the measured spectrum.

Figure 1 shows a theoretical SO_2 transmittance spectrum covering the region commonly used in DOAS evaluations, with the three narrow evaluation intervals used in this paper highlighted (305–310, 310–315, and 315–320 nm). When a certain fraction of the measured light has not passed through the plume, it will dilute the measured spectrum and act to reduce the measured absorption. If we assume that the spectral shape of this diluting light is identical to that of the sky spectrum, then the different absorption bands will be diluted with the same fraction. However, if the absorption is strong enough that the absorption features in the shorter wavelength bands, which have the strongest absorption, do not respond linearly to the dilution, then this dilution of the measured spectrum will change the differential absorptions more in the shorter wavelength bands compared to the longer wavelength bands where the absorption is weaker. Hence, performing a DOAS evaluation of the different bands highlighted above will give different SO_2 column in each band (Fickel and Delgado Granados, 2017).

Also, the SO_2 broadband absorption contributes to this imbalance because although the different bands have equal absolute dilution, expressed as the ratio of the dilution to the sky spectrum, the effective intensity of light coming from the plume is different in the different bands and thus the relative dilution, with respect to the measured spectrum, will differ. Figure 1 shows the absorbance spectrum of 2,000 ppm m SO_2. Here it can be seen that due to the broadband absorption in SO_2 the actual intensity in the plume at the three wavelength bands used is only 27, 45, and 68%, respectively, of the plume intensity without SO_2. Thus, a dilution factor of 0.1 (10% of the normalized sky spectrum contribution to the measured spectrum), will effectively result in a dilution of the differential SO_2 absorption corresponding to about 37, 22, and 15% in the respective wavelength bands. Note that if there is no dilution then this difference in intensity between the evaluation bands caused by the broadband SO_2 absorption is not a problem as it is taken care of by the DOAS evaluation procedure. However, when dilution is present, this difference in intensity contribution from the plume results in a different effective dilution between the bands. In the following we refer to this effect as an "imbalance" in the absorption and make use of this effect to indicate presence of "below-the-plume" scattering and quantitatively correct for its diluting effect. As will be discussed further later in this paper, some other wavelength dependent processes, like plume aerosol extinction and atmospheric ozone concentration, may also contribute to the "imbalance" when dilution is present.

The method presented here relies on the assumption that the fraction of diluting light, i.e., the ratio of the light scattered below the plume, the dilution spectrum, to the spectrum of light scattered above the plume, the sky spectrum, is constant within a narrow spectral interval. By narrow we mean a band not wider than 10 nm.

The method is applied as follows: first, we perform conventional DOAS evaluations on two adjacent or slightly overlapping bands encompassing an interval at least 5 nm and not larger than 10 nm wide (e.g., 305–310 and 310–315 nm) to derive the apparent columns of SO_2 in the two bands, using a measured spectrum outside of the plume as the background. If there is dilution below the plume and the actual SO_2 column is sufficiently high, then the two retrieved columns will differ with the column retrieved at the stronger absorption band being lower than that from the weaker absorption band and both being lower than the true column. Notice that the spectral fit obtained at both bands may still look good (no significant systematics in the fit residual) because the effect of dilution on the spectral shape in such narrow spectral intervals is often not evident. If a difference in columns is found between the two bands, we proceed to iteratively subtract a constant fraction of the sky spectrum from the measured spectrum until a fraction is found where the evaluated columns in the two bands coincide. To obtain a quantifiable parameter for the dilution, the sky spectrum used in the iterative subtraction is normalized to become of equal intensity to the measured spectrum at 350 nm, which is chosen to be close to the SO_2 absorption region but not significantly affected even by strong absorptions of SO_2. Hereby we quantitatively obtain the amount of spectral dilution (the dilution factor k, see above) as well as a corrected value for the column. The process is described in more detail and with illustrations in Figures 2, 3.

3.2 Formalization

In the following we formalize the method. For the sake of clarity, we assume that any instrumental effect that may be present in the plume and sky spectra, such as dark current, offset spectra, or possible changes in the instrumental line function or wavelength calibration, have been corrected.

We can represent the algorithm mathematically in the following way: the measured spectrum, $I_m(\lambda)$ is expressed as the sum of the plume spectrum, $I_p(\lambda)$, and the dilution spectrum, $I_d(\lambda)$:

$$I_m(\lambda) = I_p(\lambda) + I_d(\lambda) \quad (1)$$

It is convenient to relate the measured spectrum to the sky spectrum. Both may be measured under different conditions, for instance at different elevation angles or under unequal background scattering conditions. This results in intensities that may vary even in spectral intervals where absorption by the plume is expected to be negligible. We can start by defining a 'scaled sky spectrum' as the product of the sky spectrum by a factor equal to the ratio of the intensities of the measured and sky spectrum at a wavelength with negligible SO_2 absorption. We choose the intensities averaged over 5 nm at 350 nm for this scaling:

$$I_S'(\lambda) = I_s(\lambda)\left[\frac{I_m(350\,nm)}{I_s(350\,nm)}\right] \quad (2)$$

The scaling is not problematic because it is equivalent to allowing a free scaling between the measured spectrum and the sky spectrum in the standard DOAS formalism.

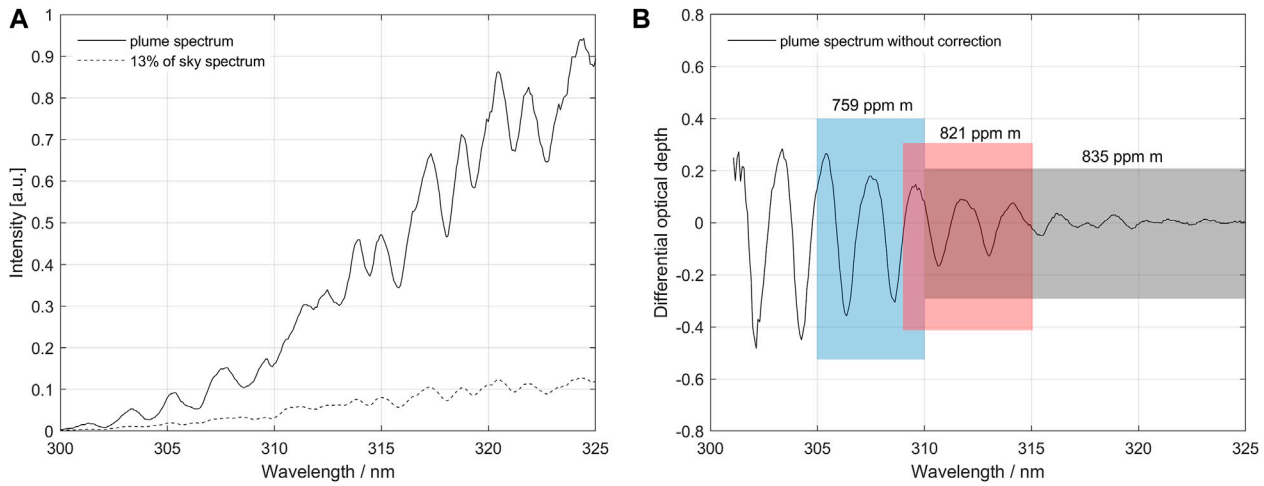

FIGURE 2
(A) Example of a measurement affected by dilution taken on a traverse on 18 March 2013 at Turrialba volcano, Costa Rica. The measured plume spectrum contains an unknown fraction of scattered sunlight from below the plume, the dilution spectrum. The picture also shows a dilution spectrum scaled in intensity to be 13% of the sky spectrum at 350 nm. **(B)** Differential absorption optical depth spectrum derived from the original spectra. The standard evaluation using DOAS in the fit-region of 310–325 nm gives a slant column density (SCD) of 835 ppm m. Evaluations in fit-regions 1 (305–310 nm) and 2 (309–315 nm) give 759 and 821 ppm m, respectively. This imbalance is caused by below-the-plume-scattering, in combination with the logarithmic dependence of the Beer-Lambert law, and intensity variation in the plume spectrum caused by SO_2 broadband absorption.

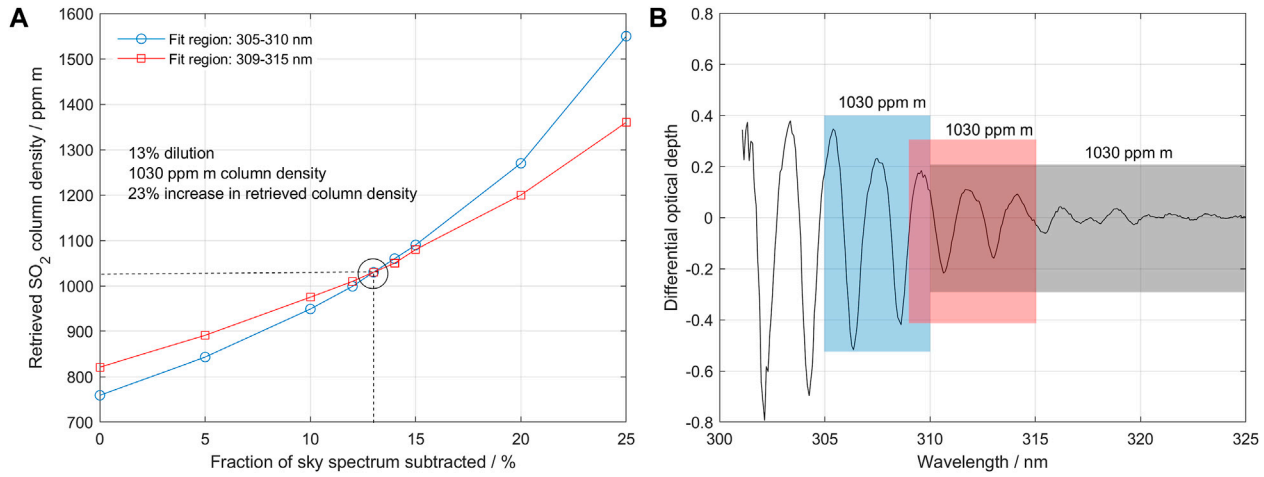

FIGURE 3
(A) Retrieved SCDs using fit regions 1 and 2 as a function of the amount of scattered light that has been subtracted from the original measured spectrum. A subtraction of 13% scattered light yields equal values in both fit regions of 1,030 ppm m. This is defined as a dilution factor of 0.13. **(B)** Differential absorption optical depth spectrum after subtraction of 13% scattered light. Now all fit regions yield the same SCD value of 1,030 ppm m. After applying the scattering correction algorithm, the slant column is increased by 23% from 835 (standard evaluation) to 1,030 ppm m.

The dilution spectrum is assumed to be proportional to the scaled sky spectrum $I_s(\lambda)$ within a narrow wavelength interval:

$$I_d(\lambda) = kI_S'(\lambda) \quad (3)$$

With the constant $k > 0$ defined as the dilution factor.

The plume spectrum must then correspond to the complementary fraction $(1-k)$ of the scaled sky spectrum multiplied by a Beer-Lambert law term with a relative optical depth $\tau(\lambda)$ between the plume and scaled sky spectra. This relative optical depth not only contains the effect of absorption by SO_2 in the plume but also the effect of all other processes that make both spectra different, namely: difference in O_3 absorption, difference in elastic and inelastic (Ring effect) molecular scattering, or difference in extinction due to aerosols.

$$I_p(\lambda) = (1-k)I_S'(\lambda)e^{-\tau(\lambda)} \quad (4)$$

The meaning of the complementary factor $(1-k)$ is to normalize the transmittance of the measured spectrum with

respect to the scaled sky spectrum. We do this by noting that in the limit of zero relative optical depth the measured and scaled sky spectrum must be equal.

Then follows that the measured spectrum is equal to:

$$I_m(\lambda) = I_S'(\lambda)\left[(1-k)e^{-\tau(\lambda)} + k\right] \quad (5)$$

The method we propose iteratively subtracts a fraction of the normalized sky spectrum $I_s'(\lambda)$ from the measured spectrum $I_m(\lambda)$, normalizes the new transmittance spectrum to compensate for the subtracted term, and applies the DOAS retrieval on two adjacent wavelength intervals. In each iteration, we find a set of fit parameters that minimize the difference between the logarithms of the modelled and measured spectra. These parameters are the coefficients of a polynomial that represents broadband structures of the relative optical depth (between scaled sky and measured spectra), and the relative column densities of atmospheric gases or pseudo-absorbers (O_3, Ring-effect) with absorption features in the interval of evaluation, as well as an apparent column density of SO_2, S_i.

Let us use the notation $R_{i,\Delta\lambda}(I_m(\lambda)) \rightarrow S_{i,\Delta\lambda}$ to represent the retrieval of an apparent column density S_i at a spectral interval $\Delta\lambda$ applied to the spectrum $I_m(\lambda)$. We apply the retrieval in two adjacent narrow spectral intervals on modified spectra formed by subtracting a fraction of the scaled sky spectrum from the measured spectrum, followed by re-normalization:

$$R_{i,\Delta\lambda}\left(\frac{I_m(\lambda) - x_i I_s'(\lambda)}{1 - x_i}\right) \rightarrow S_{i,\Delta\lambda} \quad (6)$$

This iteration is applied until we find the constant fraction x_i that would make the retrieved columns S_i at the two adjacent spectral intervals equal. In other words, we vary x_i until $S_{i,\Delta\lambda1} = S_{i,\Delta\lambda2}$. We can see from equations [1–5] that this occurs when $x_i = k$, i.e., when we subtract from the measured radiance the component that was added by scattering of radiation not passing through the plume. In this way, we find not only the true column S, but also the dilution factor k, assumed to be constant along the two wavelength intervals used in the analysis.

3.3 Further considerations

Depending on the available amount of UV-light and actual SO_2 column strength, different wavelength intervals can be chosen for the evaluation. The idea is to select two wavelength intervals $\Delta\lambda1$ and $\Delta\lambda2$, wide enough to facilitate a good DOAS evaluation (~5 nm), located close enough to encounter a similar dilution effect from atmospheric scattering, while still having a distinct difference in absorption cross-section. In addition, the absorption cross-section should be large enough so that at least one of the included absorption bands encounters non-linearity due to the Beer-Lambert law, given the actual SO_2 columns. Ideally, the intervals would also be differently affected by broadband SO_2 absorption. These conditions imply that different pairs may be optimal under different conditions; optically weak plumes need to be measured at short wavelengths to obtain enough non-linearity effects in the absorption, while optically thicker plumes, may need to be measured at longer wavelengths and thus weaker absorption as the stronger absorption bands may be saturated.

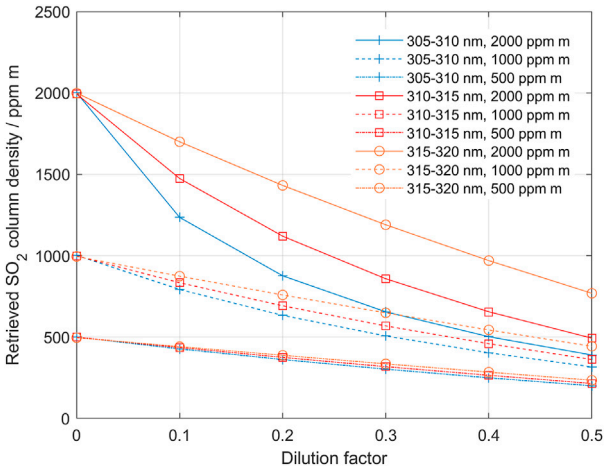

FIGURE 4
The underestimation of derived SO_2 column as a function of dilution, when using the different evaluation bands; 305–310 nm (blue), 310–315 nm (red) and 315–320 (orange) for SO_2 columns of 500, 1,000 and 2,000 ppm m, respectively. By following a pair of evaluated columns from high to low dilution the behavior of the iterative process in the dilution correction algorithm can be studied (see, for example Figure 3 above and Figure 11 below).

For the method to be able to determine a corrected column and dilution factor it is necessary that the difference between the columns derived using the two different bands can be clearly distinguished so that a well-defined cross-over point can be established. Thus, the true column and dilution must be high enough that the Beer-Lambert law non-linearity or SO_2 broad-band absorption cause a difference between the columns in the bands used that overcomes the noise level. This is illustrated in Figure 4, which shows how the columns derived in the three evaluation bands: 305–310, 310–315, and 315–320 nm are affected by dilution, for SO_2 columns of 500, 1,000 and 2000 ppm m, respectively. These plots are based on theoretical data. In a real case a difference between the columns of 5–10 ppm m is needed to overcome the noise level.

For SO_2 columns below 500 ppm m, the columns derived from the two lower bands, 305–310/310–315, respond almost linearly to increased dilution and the method will not converge and thus will fail to quantify the dilution. However, the dilution is still there and affects the column data linearly (15% dilution gives approximately 15% lower SO_2 column). For SO_2 columns higher than about 600 ppm m the difference between the two lower bands, at 10% dilution, is more than 10 ppm m and thus this pair can be used for evaluation of the dilution. In the same way, for SO_2 columns higher than about 800 ppm m also the higher pair 310–315/315–320 gives an imbalance response enough for evaluation at 10% dilution. At the other end, for SO_2 columns higher than 5,000 ppm m, saturation effects due to the limited spectral resolution start to cause problems for the lower pair. The longer-wavelengths pair is for the same reason limited to about 8,000 ppm m. Thus, for low to moderate SO_2 columns (600–2,000 ppm m) the lower pair is preferred due to its higher sensitivity, provided that the UV light level is high enough at 305 nm to overcome the noise level. For medium to high SO_2

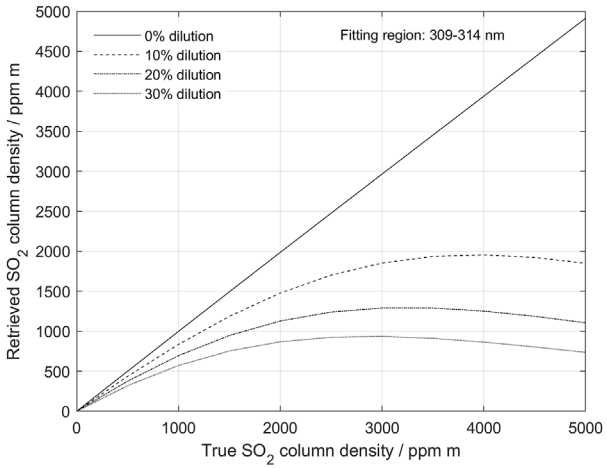

FIGURE 5
The apparent SO_2 column, evaluated in the evaluation band 309–314 nm, as a function of true SO_2 column, for different dilution factors.

columns (1,000–5,000 ppm m) the higher pair may instead be used, especially when the UV level at 305–310 nm is too low for accurate measurements. Of course, it is not possible to know the actual column before the correction, therefore evaluation at three bands may be necessary to explore the range of variation before choosing the pair of wavelength intervals that would maximize the quality of the retrieval based on the considerations given above.

In the examples and discussion above we assumed a dilution of 10%. With less dilution even higher true SO_2 columns are needed to give a reliable detection. This is also illustrated in Figure 4. The band with weakest absorption (315–320 nm) drops almost linearly with increasing dilution, while the band with the strongest absorption drops off faster than linearly initially and then drops more linearly, almost in parallel to the weak band. This is because with increasing dilution, the apparent column gets smaller and smaller and eventually the stronger absorption bands also become linear. By following the two curves belonging to a specific true SO_2 column from high to low dilution, one can simulate how the dilution correction method works. Notably, in the case of strong dilution (for example 50%) and strong true SO_2 column (for example, 2,000 ppm m), the apparent columns in the two stronger absorption bands initially diverge when dilution is decreased and then, as dilution continues to decrease, the lines of retrieved columns at the two bands start to converge. Thus, the iterative correction algorithm must allow for both convergence and divergence until the retrieved values are close enough and the column obtained at the weaker band is not lower than that obtained at the stronger band.

It is also interesting to note that, although the two processes of non-linearity and broad-band absorption both act to enhance the imbalance described above, the two processes in a way counterbalance each other. Figure 5 shows how the apparent SO_2 column, evaluated in the evaluation window 309–314 nm, varies with true SO_2 column for different dilution factors.

For a given dilution constant, the effect of dilution due to broad-band SO_2 absorption becomes stronger and stronger with increasing SO_2 column density at the same time as the monotonous increase in apparent column due to non-linearity gets smaller and smaller. This results in a turnover making the apparent column decrease with increasing true SO_2 column. As a consequence, for a given evaluation band and dilution factor there is a maximum column that can be obtained in a DOAS evaluation. This effect has been pointed out by others (Mori et al., 2006; Varnam et al., 2020) and constitutes a limitation in standard DOAS evaluations as well as in some existing schemes for dilution correction. However, this is not a limitation for our method, as we just keep iterating until we reach the convergence point.

Besides the effect of dilution, conditions where light with dramatically different SO_2 column are superimposed in a single spectrum may also cause such an imbalance. This can occur when spectra containing different columns are co-added into a single spectrum, or if the field-of-view of the receiving optics cover a wider angle than represented by typical variations in total column in the plume, e.g., when a single spectrum contains light from both strong and weak columns. A typical example of this situation is when measurements are made at the beginning and end of a traverse where dramatic changes in column occur over short traverse distances. These effects can, to some extent, be avoided by using a narrow field-of-view and high sampling rate, and by excluding data from the traverse edges in the scattering correction dilution estimate.

Other processes resulting in similar effects are straylight in the spectrometer and scattering within the plume itself. The amount of straylight in the spectrometer depends on type of spectrometer as well as its condition and can to some extent be reduced by filtering out light with wavelengths outside the studied wavelength region. Moreover, the impact that straylight has on the imbalance can be checked by performing a measurement with a gas cell using a clean air background, with high enough gas column in the cell to reveal imbalance in the extinction law, with a nominal column value of 1,000 ppm m or more. If an imbalance in the absorption is detected in this cell measurement, straylight is likely to be present.

Eliminating effects of scattering within the plume is more difficult. One approach to study the impact of scattering within the plume on the spectral imbalance used in our method is modelling. The results from a study using the radiative transfer model McArtim (Deutschmann et al., 2011) is shown in the chapter 5.1 below. This modelling study indicates that the method presented here may give somewhat reduced column densities, especially for the case of a non-condensing plume above an opaque atmosphere. Plumes with high aerosol optical depths tend to offset this effect producing higher columns, probably due to multiple scattering.

A crucial condition in the method is that the clean air spectrum used in the iterative subtraction, and the true dilution spectrum caused by scattering below the plume, have similar shape over the two wavelength intervals used in the analysis. If this condition is not fulfilled, then the “crossover point” between the bands in the iterative process will be wrong. This problem is minimized by using two narrow wavelength bands located close to each other and to perform the sky and plume measurements close in time. Special care should be taken when cloud conditions differ significantly between sky and plume measurements. One way to check this is to compare the slope of the spectra in the actual wavelength interval, after dividing sky spectra taken before and after the plume traverse. Ozone has strong broadband absorption in the

spectral regions suggested here and a difference in ozone between the sky spectrum and the plume spectrum may have an impact on the imbalance between the two evaluation bands. However, the impact of ozone is dominated by its stratospheric slant column density (O_3SCD), which is determined by the solar zenith angle (SZA, Eq. 6). Thus, if the sky spectrum is taken close in time to the plume spectrum, or if measurements are made close to noon, then the impact of ozone is negligible. If these conditions are not fulfilled, then the effect of ozone may still be eliminated by evaluating the relative ozone slant column density before and after passing the plume in the traverse. Using GPS data, time, and location, one can then derive the SZA related to each of these measurements and calculate the ozone vertical column density (O_3VCD) for the time of the traverse. Knowing the O_3VCD one can then use the GPS data of each spectrum to derive the O_3SCD of each spectrum and use the known absolute ozone absorption cross-sections to eliminate the effect of the difference in O_3SCD between the sky spectrum and the plume spectrum (including the dilution spectrum).

If we denote:

O_3SCD_{sky} ozone slant column density in sky spectrum

O_3SCD_{plume} ozone slant column density in plume spectrum

O_3VCD ozone vertical column density (common to sky and plume)

SZA solar zenith angle (different for sky and plume)

$$O_3VCD = \frac{O_3SCD_{plume} - O_3SCD_{sky}}{\frac{1}{\cos SZA_{plume}} - \frac{1}{\cos SZA_{sky}}} \quad (6a)$$

3.4 Software

The method described above has been implemented in software, ScatteringCorrection, written in C++ and the initialization parameters are further described in the Supplementary Annex to this article. The software reads measured spectra saved in the extended standard (*.std) format, e.g., used by the MobileDOAS software (Johansson, 2009) and, for each measured spectrum, performs DOAS evaluations in two aforementioned narrow wavelength intervals and in one wider wavelength interval. If the SO_2 column in the wide wavelength interval exceeds a user-defined limit (approx. 500 ppm m), determined from when the non-linearity of the Beer-Lambert law begins, and there is a difference in SO_2 column between the two short wavelength intervals, then the software will attempt to perform a dilution correction of the measurement as described above.

The software performs a search for the optimal dilution factor k by attempting to minimize the difference between the evaluated SO_2 columns in the bands of longer and shorter wavelengths λ_1 and λ_2. $S_{i,\Delta\lambda1} < S_{i,\Delta\lambda2}$ implies the applied dilution factor k is too small, while $S_{i,\Delta\lambda1} > S_{i,\Delta\lambda2}$ implies k is too large. This fact is used to determine the direction of the search in each step of the iteration in which k is varied. Notice, however, that if the search has stepped too far beyond the optimum dilution factor k, the above relationship may fail. This fact must be accounted for in the search, most easily by also verifying that the DOAS fit is valid, e.g., by requiring a maximum permissible standard deviation in the fit residual. In our implementation, the search begins by attempting to determine the upper bound for k by stepping up k in relatively large steps until $S_{I,\Delta\lambda1} > S_{i,\Delta\lambda2}$. During this stepping up of k, the software also determines the largest lower bound on the dilution factor, as the largest k_i, which yielded $S_{i,\Delta\lambda1} < S_{i,\Delta\lambda2}$. The second phase of the search is to determine the optimum dilution factor k between the upper and lower bounds. In the case of valid DOAS fits for both the lower and upper bounds, this is done using a linear interpolation between the two as this method has been found to be the fastest. In the case of an invalid fit on either bound, which typically occurs when the upper bound has stepped too far, a binary search is applied instead.

4 Results

4.1 Modelling

To improve our understanding on how different parameters like plume height, SO_2 concentration, and aerosol burden in and below volcanic plumes influence our light dilution correction, we applied the method to spectra simulated with the radiative transfer model McArtim (Deutschmann et al., 2011). The model can be used to simulate UV/vis spectra expected in a wide range of user-defined atmospheric and plume conditions, and thus allows us to test the ability to derive accurate SO_2 SCDs using our scattering correction technique. For the purposes of this study, the spectra produced by the model were adapted to standard DOAS std format and then analyzed using the developed ScatteringCorrection program (see details in Supplementary Annex).

We study three scenarios: 1) a clean Rayleigh atmosphere and a plume with zero aerosol optical depth (clean atmosphere/clean plume); 2) the same plume but in an opaque atmosphere where a 1 km thick layer with aerosol optical depth of 0.2 is placed at ground level (opaque atmosphere/clean plume); and 3) an opaque plume with aerosol optical depth of 1, immersed in a clean atmosphere (clean atmosphere/opaque plume). For the three scenarios the plume has a vertical column density of 2,000 ppm m and has a cylindrical shape with 500 m diameter and horizontal orientation. The plume altitude is varied between 0 and 3,000 m above ground level (plume-bottom), which is assumed to be at 50 m above sea level. The Sun shines with a relative azimuth of 90° with respect to the plume axis and a solar zenith angle of 30°. The field of view of the instrument is set to 8 mrad. The instrument is located below the plume axis at 50 m altitude and pointed to the zenith. Other parameters of the simulation are given in the Supplementary Appendix.

Dividing each spectrum of the three scenarios by the respective clean air "sky" spectrum produces transmittance spectra, as shown in Figure 6.

Some correction algorithms have been proposed on the assumption that the diluting light follows the Koschmieder formula using either a Rayleigh scattering coefficient, or another coefficient suggested by the measurement conditions (Koschmieder, 1938; Mori et al., 2006; Vogel et al., 2011; Campion et al., 2015; Varnam et al., 2020). One way to test the assumptions of our model, that assumes a wavelength-independent dilution term, and the predictions of a wavelength-dependent term, is to test predictions of both on synthetic spectra. Our proposed model assumes that the dilution spectrum is a constant fraction of the sky spectrum, whereas in other methods the dilution spectrum is equal to

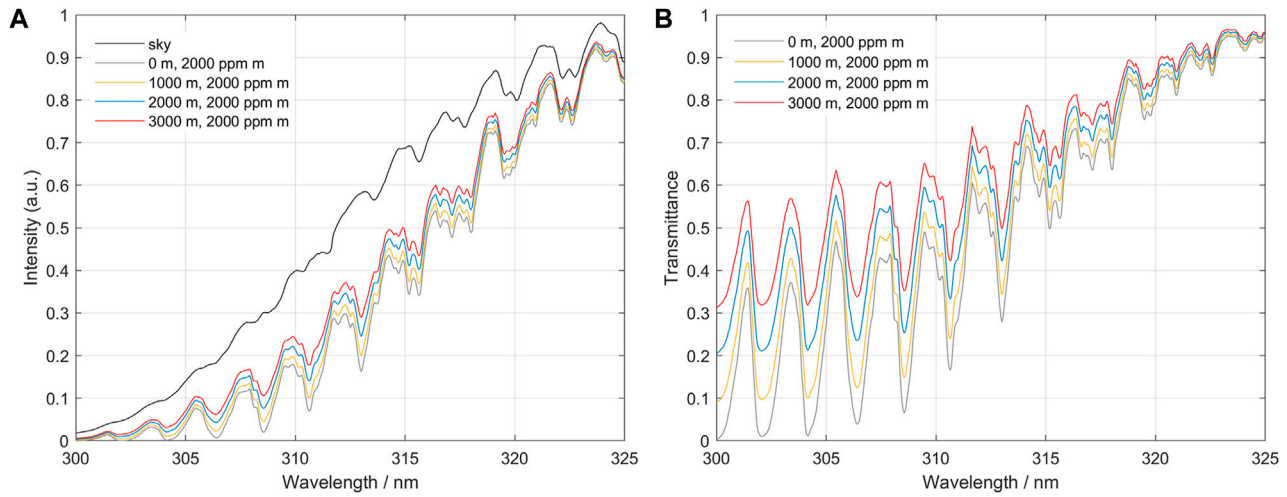

FIGURE 6
(A) Simulated spectra: a clean air "sky" spectrum and simulated measurement spectra of an SO_2 plume located at 0, 1,000, 2,000 and 3,000 m above ground level. We can see clearly that spectra from higher plumes have higher intensity due to added light from dilution. **(B)** The spectra from various plume heights, divided by the clean air "sky" reference. Note the spectral distortion for the spectra from elevated plumes, as well as the SO_2 broadband absorption.

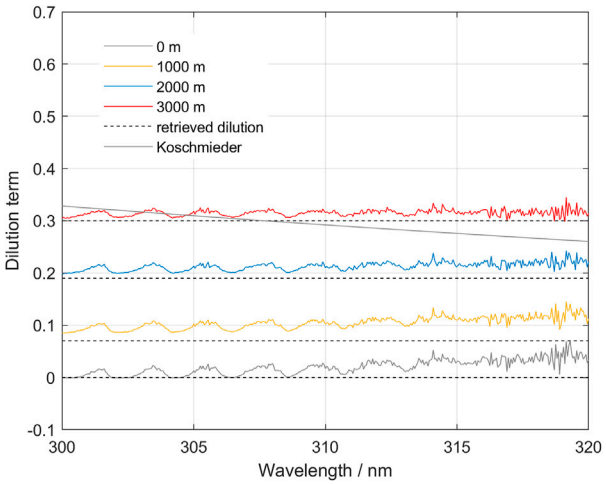

FIGURE 7
The spectral shape of the dilution function for various plume heights in the clean atmosphere, clean plume scenario. Notice that the overall shape is relatively flat over the wavelength intervals 305–315 and 310–320 used in the scattering correction method. Also notice a residual SO_2 that indicates that the effective column does not correspond exactly to the nominal column of 2,000 ppm m in this inversion. The "Koschmieder" prediction is also shown for a plume located at 3,000 m altitude.

the sky spectrum scaled by a wavelength dependent scattering efficiency. Using the spectra simulated with McArtim in which the true SO_2 column density is known we derived the wavelength-dependency of the dilution factor k (Figure 7).

Our results indicate that the trend in the dilution term is nearly independent of wavelength, a circumstance that is in good agreement with our proposed model. There are some structures that are correlated with the absorption of SO_2 which may be due to incomplete compensation of the term involving SO_2 in our model. This may be due to radiative transfer effects that produced an effective column that is not equal to the prescribed vertical column density used to model the different spectra. In the interpretation given by Kern et al. (2010), this could be caused by different effective pathlengths due to different absorption strength of SO_2 for different wavelengths.

Applying the ScatteringCorrection software using the lower bands 305–310/310–315 nm, we obtain the following results for retrieved column and dilution factor (Figure 8).

The modelling results indicate that our proposed method can deal relatively well with spectra taken under conditions of clear and opaque atmospheres and clear and opaque plumes. In all scenarios, we notice the increase of dilution factor with distance to the plume and with increase in scattering conditions below the plume. The retrieved SO_2 column densities without correction show a systematic decrease with increasing dilution, but aerosols in the plume seem to reduce the amount of dilution, possibly due to enhanced forward scattering towards the instrument. The retrieved column values after correction lie within 10% accuracy of the nominal values, being worst for the case of an opaque atmosphere and slightly better for the case of an opaque plume. We think this reflects the effect of two processes: one is that the percentage of radiation that reaches the instrument passing through the plume may be larger for an opaque plume due to higher forward scattering, and the other is that the aerosols may increase the mean path of radiation in the plume due to multiple scattering. The modelling results also show that the assumption of constant dilution within a narrow wavelength interval is reasonable.

4.2 Measurements

Next, we tested our scattering correction on real-world DOAS traverse measurements. Three different cases are shown, representing

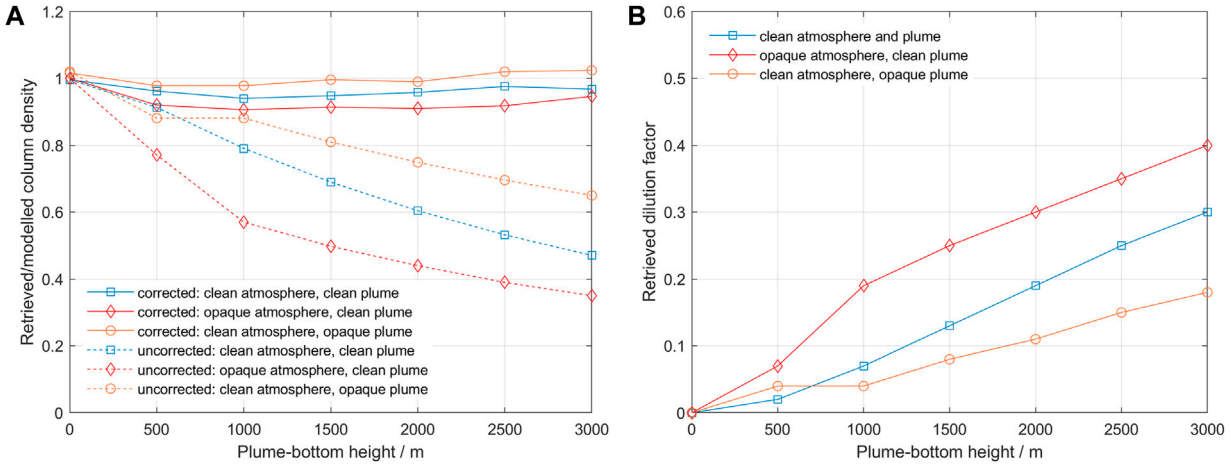

FIGURE 8
(A) Retrieved/modelled column density as a function of altitude for the three modelled cases. The results without correction are shown with dashed lines, and the results after the correction are shown with continuous lines. **(B)** Retrieved dilution factor as a function of altitude for the three modelled cases.

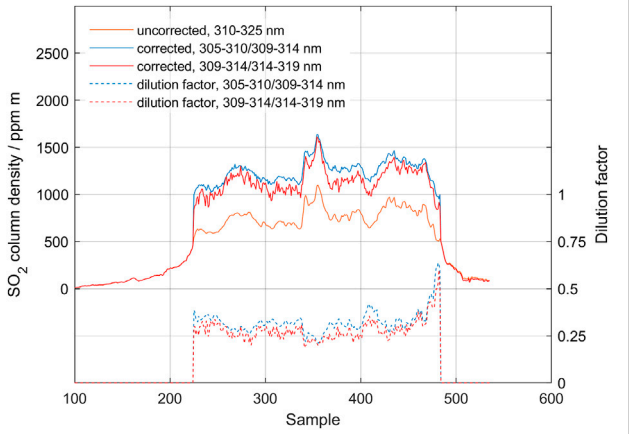

FIGURE 9
Traverse made in Fagradalsfjall on 27 April 2021. Standard evaluation (black) is compared to scattering corrected data using the lower bands (blue) and higher bands (red). Also shown are the derived dilution factors due to atmospheric scattering.

different column densities and scattering conditions: Fagradalsfjall located on Reykanaes peninsula on south Island (low columns 800 ppm m, clean air), Manam located off the northeast coast of mainland Papua New Guinea (very high columns 5,000 ppm m, high scattering), and Holuhraun located in the inland of north east Island (moderate columns 1,000–2,000 ppm m, low scattering).

4.2.1 Fagradalsfjall 2021

In March 2021, a fissure eruption occurred in Fagradalsfjall on the Reykjanes peninsula west of Reykjavik in Iceland. Figure 9 shows a traverse made around solar noon on 27 April 2021. The plume was relatively transparent, and it was easy to see through. The bottom of the plume was at about 550 m height, as determined by triangulation, and the background air was clean, but the sky was very cloudy. The initial measurement made using the standard range 310–325 nm yielded SO_2 columns around 800 ppm m. Dilution correction was applied using both the short wavelength intervals (305–310/309–314) and long wavelength intervals (309–314/314–319). Each evaluation gives similar results with corrected SO_2 columns around 1,200 ppm m, and average dilution factors of about 27%. Our corrections therefore yielded SO_2 column densities equal to 150% of the results from the standard DOAS evaluation. Note that even though both evaluation procedures yield similar results, the shorter wavelength interval gives a less noise. This demonstrates that, for low column densities, the stronger absorption in the shorter wavelength absorption bands gives a better-defined difference between the analysis windows and thus a sharper focus in the iterative correction technique.

4.2.2 Manam 2019

In May 2019, a one-week international field campaign was conducted at Manam volcano in Papua New Guinea (Liu et al., 2020). The purposes of this campaign were twofold: to improve data on gas emission from this highly emitting, remotely located and little studied volcano and to demonstrate the use of drones in volcano monitoring at challenging volcanoes. These drone measurements offered unique possibilities to test our dilution correction algorithm by performing SO_2 column measurements with a MobileDOAS instrument from various altitudes below the plume (Galle et al., 2021).

On 27 May, we performed two almost simultaneous measurements (30 min apart) of the SO_2 emission rate from the volcano using two different MobileDOAS instruments, one located on the ground close to sea-level continuously pointing at zenith through the center of the plume and the other performing a drone traverse under the plume at 1 km altitude above ground. The crater is located about 1,800 m above ground and emitted a barely visible plume with a stable direction during the measurement period at an approximate altitude of 2,000 m above ground. The wind was slow,

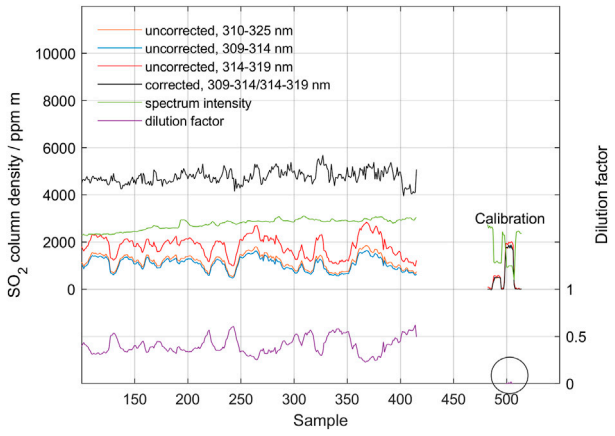

FIGURE 10
Measurement of the SO_2 vertical column at Manam on 27 May 2019, measured from a fixed position at ground. The results from measurements using the two bands 309–314 nm and 314–319 nm are shown as well as the initial and corrected columns. Also shown is the dilution factor and the spectral intensity (arbitrary units). At the end of the measurement, two cell measurements are shown with nominal values of 600 ppm m and 2,000 ppm m, respectively. Note the negligible dilution factor in this cell measurement marked with a circle. The spectrum from sample point 330 is inspected in the next figure, Figure 11.

and the sky was clear. Thus, this traverse measurement is expected to show less dilution than the ground-based instrument. It is also expected that both measurements, after dilution correction, should show similar maximum SO_2 columns.

Figure 10 below shows the result of the measurement from the ground for 30 min. Here, the two longer wavelength intervals (309–314.5 and 314.5–320 nm) are used as the final columns are relatively high and the more sensitive shorter interval will contain saturated absorption bands. The original standard DOAS evaluation (blue, 1,200 ppm m) is more than tripled to about 4,400 ppm m after the scattering correction (black). The dilution factor (orange) is about 0.4. Note that the main variation in the standard measurement seems to be linked to variations in the scattering dilution factor yielding a more constant overhead SO_2 column density after the scattering correction is applied. This short-term increase in dilution factor may be caused by increased scattering below the plume due to a change in atmospheric condition or plume height, or a decrease in the fraction of light that has passed the plume. The fact that the spectrum intensity (purple, arbitrary units) increases in correlation with increased dilution indicates that the most plausible cause of this variation in dilution factor is a change in atmospheric conditions below the plume. Finally, it should be noted that the 2,000 ppm m cell measurement at the end of the measurement yields negligible dilution (0.004). This is expected as there is no atmosphere between the cell and the instrument during these cell measurements. This confirms that the stray light level in the spectrometer was negligible in this case.

Both the final column values and the dilution factor is relatively high in the measurement shown in Figure 10. Thus, data from this measurement can be used to test the performance of the method under such conditions. Figure 11 shows the performance of the iterative search algorithm in sample point 330. Despite the large difference between the initial SO_2 column derived by standard DOAS analysis and the dilution-corrected column, the search algorithm finds a distinct cross-over, yielding an SO_2 column density of approximately 5,200 ppm m with a dilution factor of 0.45.

Figure 12 shows data from the MobileDOAS traverse made by drone at an altitude of 1 km above the ground. The drone traverses the plume at this altitude and then descends to 300 m altitude and starts to make a return traverse, which was not completed due to the need to land before losing power. The sampling period was set to 2 s. The maximum value of the corrected column reaches 5,000 ppm m, and the dilution factor is 0.08 at 1,000 m altitude and 0.30 at 300 m altitude (point 1,050, shown in circle). This is in good agreement with the measurements from the ground 30 min earlier, presented in Figure 10 (vertical column 5,200 ppm m, dilution factor 0.4) and confirms that the dilution caused by scattered light below the plume is the major process causing the spectroscopic imbalance between the two wavelength intervals.

4.2.3 Holuhraun 2014

The 31 August 2014–27 February 2015 volcanic eruption at Holuhraun in Iceland is the strongest source of sulfur dioxide in Europe over the past 230 years, with initial sustained emission rates exceeding 100,000 td^{-1} (Gíslason et al., 2015; Pfeffer et al., 2018). During the 6 month duration of the eruption, MobileDOAS as well as ScanningDOAS measurements were performed as part of the EU-project FUTUREVOLC. The measurements that were made close to the eruption site (5–10 km) were severely affected by atmospheric scattering, both in and around the gas plume, and showed SO_2 column densities up to 50,000 ppm m, causing severe evaluation problems. Additional measurements were conducted along the Ring Road following the Icelandic coast, at a distance 80–150 km from the eruption site. At these distances, the SO_2 columns had dropped to manageable values, and atmospheric scattering was significantly less than close to the eruption site. Figure 13 shows the results of a traverse made along the Ring Road, about 80 km north of the eruption site. Measurements were conducted around solar noon, and meteorological conditions were good with blue sky and a barely visible plume. The top of plume height was reported to be 1.6 km. A standard DOAS evaluation over the wavelength region 310–325 nm and a plume speed of 6 m s^{-1} yielded an SO_2 emission rate of 1,379 kg s^{-1}. Figure 13 shows the result after evaluation using the standard region, 310–325 nm (blue), as well as the result after applying the scattering correction (black) and the estimated dilution. The average correction in SO_2 column gave a 60% increase in emission rate with an average dilution factor of 0.2. It should be noted that this increased emission rate to 2,200 kg s^{-1} is even a bit higher than the underestimation due to dilution of up to 40% estimated in Pfeffer et al. (2018). Also, comparing with the radiative transfer modelling results (see Section 4.1), this dilution factor of 0.2 corresponds well with the modelled case of a clean atmosphere with a clean plume of 2,000 ppm m located at 2000 m altitude (Figure 8).

As the duration of this traverse was relatively long (45 min), we have also evaluated this traverse using the ozone correction procedure described above. This ozone correction, however, gave only a marginal change in the evaluation result: a 3% higher average column and an identical dilution factor. The small magnitude of this

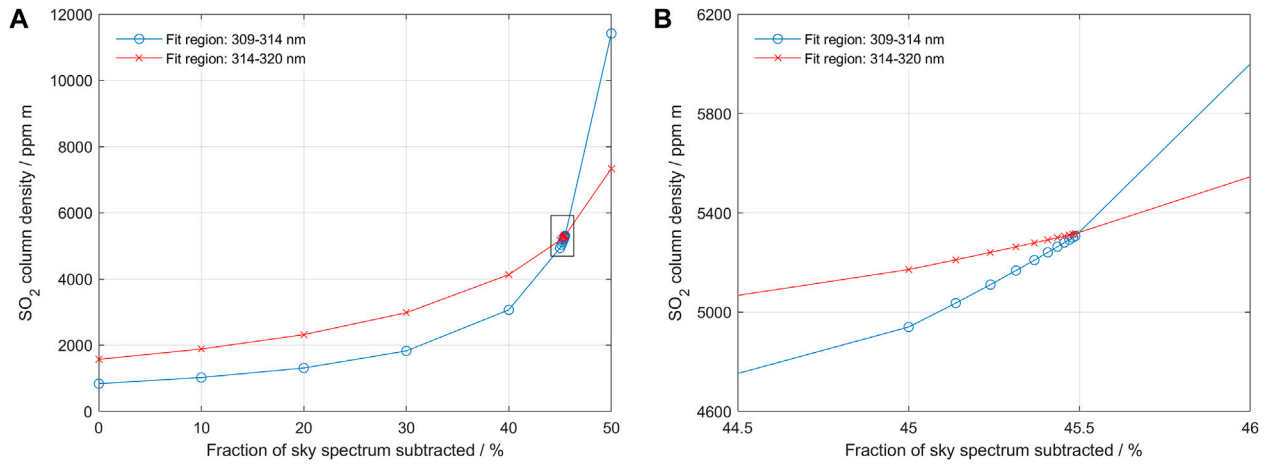

FIGURE 11
The iterative search process corresponding to data point 330 in Figure 10 above. The column value goes from 1,500 ppm m to 5,200 ppm m with a dilution factor of 0.45. Panel (**B**) shows a zoom-in of the region surrounded by a square in Panel **(A)**. Note that initially the search algorithm diverges and later converges towards the final cross-over, as predicted from modelling for high columns with high dilution.

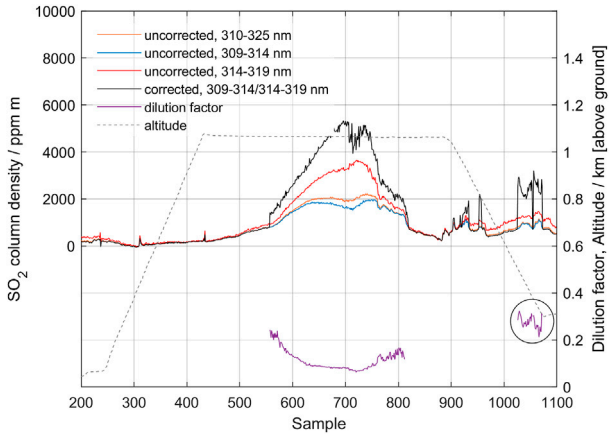

FIGURE 12
MobileDOAS measurement of the gas plume from Manam volcano, made using a drone on 27 May 2019. The drone passes under the plume at an altitude of 1 km above ground (dashed line). Results from using the two bands 309–314.5 nm and 314.5–319 nm as well as corrected column, dilution factor and altitude of the drone, as it traverses below the plume, are shown.

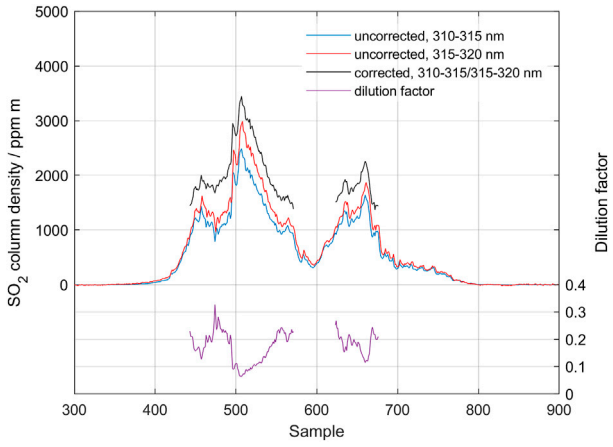

FIGURE 13
Traverse of the gas emission from Holuhraun fissure eruption in Iceland made on the Ring road on 21 September 2014.

effect is likely due to the fact that the traverse was made close to solar noon at 13:00 local time, so the solar zenith angle and total ozone column only changed slightly during the traverse.

5 Discussion and conclusion

This paper is a description of a novel approach to compensate for an atmospheric scattering effect that is known to significantly affect quantitative measurements of volcanic SO_2 emission rates. In its present form, the method is limited to situations when no significant multiple scattering occurs inside the volcanic plume itself, and when the absorption in the plume is strong enough to cause non-linear effects in the Beer-Lambert law (SO_2 optical depths greater than about 0.5; SO_2 column densities greater than about 400 ppm m).

Uncertainties exceeding 30% are still possible in situations where multiple scattering in optically thick volcanic plumes leads to pathlength extension (Kern et al., 2010). However, errors associated with light dilution effects which are especially pronounced when measuring a plume from distances greater than 2 km or in the presence of background aerosols or clouds and which are typically of a similar order of magnitude, are significantly reduced by our correction method. In situations where multiple scattering in the plume is not prevalent, the application of our method should eliminate atmospheric scattering as a dominant error source for SO_2 emission rate measurements, thus

reducing the total error which then stems only from imperfect spectroscopy, uncertainties in measurement geometry, and potential errors in wind speed (Galle et al., 2010, see Table 3). Typical errors in SO_2 emission rates measured in good to fair conditions would then be 20%–45%, depending on the accuracy of the aforementioned other factors.

Despite these limitations, the method is believed to be useful for a first-order correction of this major error source in many measurement situations. Of special importance is that the method only uses already existing spectral information in historical data and is relatively easy to implement in existing evaluation schemes. The approach is also very logical as it directly addresses the cause of the dilution effect; it iteratively subtracts the spectrum of light that has not passed through the plume.

Here we have exclusively discussed the method for the case of mobile traverses of volcanic SO_2 plumes. However, the same method can be applied to other gases, in other wavelength intervals, and for other measurement geometries, given that the conditions stated above are fulfilled.

In particular, the use of this method to correct for scattering effects in scanning DOAS measurements of volcanic SO_2 emissions is of high interest, but further modelling is required. During the past two decades, these instruments have been installed on many volcanoes, and thus large amounts of data are available, collected under varying atmospheric and volcanic conditions. For example, the NOVAC (Network for Observation of Volcanic and Atmospheric Change) [Galle et al., 2010; Arellano et al., 2021; www.novac-community.org] today has an archive containing gas measurements from more than 40 volcanoes collected since 2005. A re-processing of this archive, containing several millions of emission rate measurements, using the suggested algorithm is expected to give a detailed insight in the magnitude of this spectral dilution effect. This then opens the possibility to estimate the effect of dilution also in historical data made by COSPEC or DOAS instruments, where spectra are not available. As most estimates of volcanic emissions of species other than SO_2 are based on scaling X/SO_2 ratios to SO_2 emission rates, such a reprocessing would allow revision of emission estimates for these species as well. It should be noted, however, that the algorithm suggested here is based on the assumption that the clean air spectrum used in the iterative subtraction, and the true dilution spectrum caused by scattering below the plume, have similar shape over the two wavelength intervals used in the analysis. This condition is realistic for many cases when using MobileDOAS zenith looking measurements made close in time, while it may be less obvious for ScanDOAS measurements with varying looking directions between sky and plume measurements. Thus, a detailed analysis of the applicability of the suggested method for ScanDOAS measurements requires further investigation with modelling and measurements and is beyond the scope of this paper.

Data availability statement

The raw data and data presented in the figures are made available in the Supplementary Material.

Author contributions

BG and SA contributed to all parts of the paper. MJ wrote the program "Scatteringcorrection.exe" used to facilitate evaluation of the raw data according to the suggested method. CK and SA worked with the modelling of synthetic spectra and MP provided the data from Fagradalsfjall on Iceland. All authors contributed to the article and approved the submitted version.

Funding

The work at Chalmers University of Technology was funded by the FORMAS project "Development and Implementation of an Algorithm for Improved Volcanic Gas Emission Monitoring, Geophysical Research and Volcano Risk Assessment," the project "Aerial Observations of Volcanic Emissions from Unmanned Aerial Systems (UAS)" funded by the Alfred P. Sloan foundation, and a grant (149/18) from the Swedish National Space Agency.

Acknowledgments

We acknowledge the logistical and scientific support by Rabaul Volcanological Observatory (RVO), as well as the generous hospitality given by the Manam communities of Baliau and Manam during our field work in Papua New Guinea. The authors would like to thank Matt Varnam and the two journal reviewers for providing thoughtful comments on this manuscript. Any use of trade, product, or firm names is for descriptive purposes only and does not imply endorsement by the U.S. Government.

Conflict of interest

The authors declare that the research was conducted in the absence of any commercial or financial relationships that could be construed as a potential conflict of interest.

Publisher's note

Supplementary material

The Supplementary Material for this article can be found online at: https://www.frontiersin.org/articles/10.3389/feart.2023.1088768/full#supplementary-material

References

Aiuppa, A., Bitetto, M., Donne, D. D., Paolo, F., Monica, L., Tamburello, G., et al. (2021). Volcanic CO_2 tracks the incubation period of basaltic paroxysms. *Sci. Adv.* 7, eabh0191. doi:10.1126/sciadv.abh0191

Aiuppa, A., Moretti, R., Federico, C., Giudice, G., Gurrieri, S., Liuzzo, M., et al. (2007). Forecasting Etna eruptions by real-time observation of volcanic gas composition. *Geology* 35, 1115. doi:10.1130/G24149A.1

Arellano, S., Galle, B., Apaza, F., Avard, G., Barrington, C., Bobrowski, N., et al. (2021). Synoptic analysis of a decade of daily measurements of SO_2 emission in the troposphere from volcanoes of the global ground-based Network for Observation of Volcanic and Atmospheric Change. *Earth Syst. Sci. Data* 13, 1167–1188. doi:10.5194/essd-13-1167-2021

Bogumil, K., Orphal, J., Homann, T., Voigt, S., Spietz, P., Fleischmann, O., et al. (2003). Measurements of molecular absorption spectra with the SCIAMACHY pre-flight model: Instrument characterization and reference data for atmospheric remote-sensing in the 230–2380 nm region. *J. Photochem. Photobiol. Chem. A* 157, 167–184. doi:10.1016/S1010-6030(03)00062-5

Burton, M., Allard, P., Mure, F., and La Spina, A. (2007). Magmatic gas composition reveals the source depth of slug-driven strombolian explosive activity. *Science* 317, 227–230. doi:10.1126/science.1141900

Campion, R., Delgado Granados, H., and Mori, T. (2015). Image-based correction of the light dilution effect for SO_2 camera measurements. *J. Volcanol. Geotherm. Res.* 300, 48–57. doi:10.1016/j.jvolgeores.2015.01.004

de Moor, J. M., Aiuppa, A., Avard, G., Wehrmann, H., Dunbar, N., Muller, C., et al. (2016a). Turmoil at Turrialba Volcano (Costa Rica): Degassing and eruptive processes inferred from high-frequency gas monitoring. *J. Geophys. Res. Solid Earth* 121, 5761–5775. doi:10.1002/2016JB013150

de Moor, J. M., Aiuppa, A., Pacheco, J., Avard, G., Kern, C., Liuzzo, M., et al. (2016b). Short-period volcanic gas precursors to phreatic eruptions: Insights from Poás Volcano, Costa Rica. *Earth Planet. Sci. Lett.* 442, 218–227. doi:10.1016/j.epsl.2016.02.056

Deutschmann, T., Beirle, S., Frieß, U., Grzegorski, M., Kern, C., Kritten, L., et al. (2011). The Monte Carlo atmospheric radiative transfer model McArtim: Introduction and validation of jacobians and 3D features. *J. Quantitative Spectrosc. Radiat. Transf.* 112 (6), 1119–1137. doi:10.1016/j.jqsrt.2010.12.009

Deutschmann, T., Beirle, S., Frieß, U., Grzegorski, M., Kern, C., Kritten, L., et al. (2011). The Monte Carlo atmospheric radiative transfer model McArtim: Introduction and validation of jacobians and 3D features. *J. Quantitative Spectrosc. Radiat. Transf.* 112 (6), 1119–1137. doi:10.1016/j.jqsrt.2010.12.009

Edmonds, M., Herd, R. A., Galle, B., and Oppenheimer, C. (2003). Automated, high time resolution measurements of SO_2 flux at Soufrière Hills Volcano, Montserrat. *Bull. Volcanol.* 65 (8), 578–586. doi:10.1007/s00445-003-0286-x

Esse, B., Burton, M., Varnam, M., Kazahaya, R., and Salerno, G. (2020). iFit: A simple method for measuring volcanic SO_2 without a measured Fraunhofer reference spectrum. *J. Volcanol. Geotherm. Res.* 402, 107000. doi:10.1016/j.jvolgeores.2020.107000

Fickel, M., and Delgado Granados, H. (2017). On the use of different spectral windows in DOAS evaluations: Effects on the estimation of SO_2 emission rate and mixing ratios during strong emission of Popocatépetl volcano. *Chem. Geol.* 462, 67–73. doi:10.1016/j.chemgeo.2017.05.001

Galle, B., Arellano, S., Bobrowski, N., Conde, V., Fischer, T. P., Gerdes, G., et al. (2021). A multi-purpose, multi-rotor drone system for long-range and high-altitude volcanic gas plume measurements. *Atmos. Meas. Tech.* 14 (1–23), 4255–4277. doi:10.5194/amt-14-4255-2021

Galle, B., Johansson, M., Rivera, C., Zhang, Y., Kihlman, M., Kern, C., et al. (2010). Network for observation of volcanic and atmospheric change (NOVAC)—a global network for volcanic gas monitoring: Network layout and instrument description. *J. Geophys. Res.* 115, D05304. doi:10.1029/2009JD011823

Galle, B., Oppenheimer, C., Geyer, A., McGonigle, A., Edmonds, M., and Horrocks, L. (2003). A miniaturised ultraviolet spectrometer for remote sensing of SO_2 fluxes: A new tool for volcano surveillance. *J. Volcanol. Geotherm. Res.* 119, 241–254. doi:10.1016/S0377-0273(02)00356-6

Gerlach, T. M. (2004). Volcanic sources of tropospheric ozone-depleting trace gases. *Geochem. Geophys. Geosystems* 5, 1–16. doi:10.1029/2004GC000747

Giggenbach, W. F. (1996). "Chemical composition of volcanic gases," in *Monitoring and mitigation of volcano hazards*. Editors R. Scarpa and R. Tilling (Berlin, Heidelberg: Springer), 221–256. doi:10.1007/978-3-642-80087-0_7

Gíslason, S. R., Stefánsdóttir, G., Pfeffer, M. A., Barsotti, S., Jóhannsson, T., Galeczka, I., et al. (2015). Next article >> << Previous article Environmental pressure from the 2014–15 eruption of Bárðarbunga volcano, Iceland. *Geochem. Perspect. Lett.* 1, 84–93. doi:10.7185/geochemlet.1509

Johansson, M. (2009). *Application of passive DOAS for studies of megacity air pollution and volcanic gas emissions*. *PhD thesis*, Chalmers University of Technology, Gothenburg, 64.

Johansson, M., Galle, B., Yu, T., Tang, L., Chen, D., Li, H., et al. (2008). Quantification of total emission of air pollutants from Beijing using mobile mini-DOAS. *Atmos. Environ.* 42, 6926–6933. doi:10.1016/j.atmosenv.2008.05.025

Kern, C., Aiuppa, A., and de Moor, J. M. (2022). A golden era for volcanic gas geochemistry? *Bull. Volcanol.* 84, 43–11. doi:10.1007/s00445-022-01556-6

Kern, C., Deutschmann, T., Vogel, L., Wöhrbach, M., Wagner, T., and Platt, U. (2010). Radiative transfer corrections for accurate spectroscopic measurements of volcanic gas emissions. *Bull. Volcanol.* 72 (2), 233–247. doi:10.1007/s00445-009-0313-7

Kern, C., Deutschmann, T., Werner, C., Sutton, A. J., Elias, T., and Kelly, P. J. (2012). Improving the accuracy of SO_2 column densities and emission rates obtained from upward-looking UV-spectroscopic measurements of volcanic plumes by taking realistic radiative transfer into account. *J. Geophys. Res. Atmos.* 117 (D20), D20302. doi:10.1029/2012JD017936

Kern, C. (2019). *MatArtim: A matlab scripting interface for the McArtim radiative transfer model*. (unpublished) version 1.1.

Koschmieder, H. (1938). Luftlicht und Sichtweite. *Naturwissenschaften* 26, 521–528. doi:10.1007/BF01774261

Kunrat, S., Kern, C., Alfianti, H., and Lerner, A. H. (2022). Forecasting explosions at Sinabung Volcano, Indonesia, based on SO_2 emission rates. *Front. Earth Sci.* 10, 976928. doi:10.3389/feart.2022.976928

Liu, E. J., Aiuppa, A., Alan, A., Arellano, S., Bitetto, M., Bobrowski, N., et al. (2020). Aerial strategies advance volcanic gas measurements at inaccessible, strongly degassing volcanoes. *Sci. Adv.* 6 (44), eabb9103. doi:10.1126/sciadv.abb9103

Millàn, M. M. (1980). Remote sensing of air pollutants. A study of some atmospheric scattering effects. *Atmos. Environ.* 14 (11), 1241–1253. doi:10.1016/0004-6981(80)90226-7

Moffat, A. J., and Millàn, M. M. (1971). The applications of optical correlation techniques to the remote sensing of SO_2 plumes using sky light. *Atmos. Environ.*, 5 (8), 677–690. doi:10.1016/0004-6981(71)90125-9

Mori, T., Kazahaya, K., Ohwada, M., Hirabayashi, J., and Yoshikawa, S. (2006). Effect of UV scattering on SO_2 emission rate measurements. *Geophys. Res. Lett.* 33 (17), L17315. doi:10.1029/2006GL026285

Oppenheimer, C., Fischer, T. P., and Scaillet, B. (2014). "Volcanic degassing: Process and impact," in *Treatise on geochemistry*. Editors H. Holland and K. Turekian Second Edition (Elsevier), 111–179. doi:10.1016/B978-0-08-095975-7.00304-1

Pfeffer, M. A., Bergsson, B., Barsotti, S., Stefánsdóttir, G., Galle, B., Arellano, S., et al. (2018). Ground-based measurements of the 2014–2015 Holuhraun volcanic cloud (Iceland). *Geosciences* 8, 29. doi:10.3390/geosciences8010029

Platt, U., Lübcke, P., Kuhn, J., Bobrowski, N., Prata, F., Burton, M., et al. (2015). Quantitative imaging of volcanic plumes–Results, needs, and future trends. *J. Volcanol. Geotherm. Res.* 300, 7–21. doi:10.1016/j.jvolgeores.2014.10.006

Platt, U., and Stutz, J. (2008). Differential optical absorption spectroscopy principles and applications. in *Physics of Earth and Space environments*. Springer, 597. doi:10.1007/978-3-540-75776-4

Sparks, R. S. J., Biggs, J., and Neuberg, J. W. (2012). Monitoring volcanoes. *Science* 335, 1310–1311. doi:10.1126/science.1219485

Varnam, M., Burton, M., Esse, B., Kazahaya, R., Salerno, G., Caltabiano, T., et al. (2020). Quantifying light dilution in ultraviolet spectroscopic measurements of volcanic SO_2 using dual-band modeling. *Front. Earth Sci.* 8, 528753. doi:10.3389/feart.2020.528753

Vogel, L., Galle, B., Kern, C., Delgado Granados, H., Conde, V., Norman, P., et al. (2011). Early in-flight detection of SO_2 via differential optical absorption spectroscopy: A feasible aviation safety measure to prevent potential encounters with volcanic plumes. *Atmos. Meas. Tech.* 4, 1785–1804. doi:10.5194/amt-4-1785-2011

frontiers | Frontiers in Earth Science

TYPE Original Research
PUBLISHED 04 August 2023
DOI 10.3389/feart.2023.1022976

OPEN ACCESS

EDITED BY
Christoph Kern,
United States Geological Survey (USGS), United States

REVIEWED BY
Andre Butz,
Heidelberg University, Germany
Nicole Bobrowski,
Heidelberg University, Germany

*CORRESPONDENCE
Wolfgang Stremme,
stremme@atmosfera.unam.mx
Michel Grutter,
grutter@unam.mx

RECEIVED 19 August 2022
ACCEPTED 30 June 2023
PUBLISHED 04 August 2023

CITATION
Stremme W, Grutter M, Baylón J, Taquet N, Bezanilla A, Plaza-Medina E, Schiavo B, Rivera C, Blumenstock T and Hase F (2023), Direct solar FTIR measurements of CO_2 and HCl in the plume of Popocatépetl Volcano, Mexico. *Front. Earth Sci.* 11:1022976. doi: 10.3389/feart.2023.1022976

Direct solar FTIR measurements of CO_2 and HCl in the plume of Popocatépetl Volcano, Mexico

Wolfgang Stremme[1]*, Michel Grutter[1]*, Jorge Baylón[1], Noemie Taquet[1], Alejandro Bezanilla[1], Eddy Plaza-Medina[1], Benedetto Schiavo[1], Claudia Rivera[1], Thomas Blumenstock[2] and Frank Hase[2]

[1]Insituto de Ciencias de la Atmosfera y Cambio Climatico, Universidad Nacional Autonoma de Mexico, Mexico, Mexico, [2]Insitute for Meteorology y Climate Research, Karlsruhe Insitute of Technology, Karlsruhe, Germany

Volcanic CO_2 emissions inventories have great importance in the understanding of the geological carbon cycle. Volcanoes provide the primary pathway for solid-earth volatiles to reach the Earth's atmosphere and have the potential to significantly contribute to the carbon-climate feedback. Volcanic carbon emissions (both passive and eruptive degassing) included in inventories, largely stem from patchy surface measurements that suffer from difficulties in removing the atmospheric background. With a 27-year-long ongoing open-vent eruption, Popocatépetl ranks as one of the highest permanent volcanic CO_2 emitters worldwide and provides an excellent natural laboratory to design and experiment with new remote sensing methods for volcanic gas emission measurements. Since October 2012, infrared spectra at different spectral regions have been recorded with a solar occultation FTIR spectrometer. The near-infrared spectra allow for high precision measurements of CO_2 and HCl columns. Under favorable conditions, the continuous observations during sunrise allow the reconstruction of a plume cross-section of HCl and the estimation of the emission flux using wind data. Despite that the detection of CO_2 is more challenging, on April 26th, 2015 we captured a volcanic plume under favourable wind conditions which allowed us to reconstruct from this particular event a CO_2 emission rate of 116.10 $\pm$ 17.2 kg/s. The volcanic HCl emission on this event was the highest detected during the 2012-2016 period. An annual average CO_2 emission estimate of (41.2 $\pm$ 16.7) kg/s ((1.30 $\pm$ 0.53) Tg/yr) could be determined from a statistical treatment of the detected CO_2 and HCl columns in the IR spectra, and their corresponding molecular ratios, during this period. A total of 25 events were used to derive a mean CO_2/HCl molecule ratio of 11.4 $\pm$ 4.4 and an average HCl emission rate of (3.0 $\pm$ 0.3) kg/s could be determined. The CO_2 emissions of Popocatépetl were found to be around 0.32% of the total anthropogenic CO_2 emissions reported in the country and 3.6% of those corresponding to the Mexico City Metropolitan Area (MCMA). CO_2 emissions from the Popocatépetl volcano can be considered to play a negligible role in the global CO_2 budget, but should be taken into account.

KEYWORDS

CO_2, Popocatépetl, volcano, solar absorption, gas emissions, FTIR frontiers

1 Introduction

Located in Central Mexico and in the vicinity of highly populated urban centers, Popocatépetl is an active stratovolcano only 50 km SE from the Mexico City Metropolitan Area (MCMA) and 30 km SW from Puebla. Large pyroclastic flows have reached the MCMA in former epochs (Siebe et al., 1996) and after 70 years of dormancy the volcano reawakened in 1994, starting its current eruption. The current activity is characterized by permanent passive degassing, interrupted by periodic dacitic dome growth episodes accompanied by strombolian-type activity and Vulcanian explosions.

Popocatépetl is known to have one of the largest contributions of volcanic gas emissions worldwide (Gerlach, 1991), with a total SO_2-emission between 1993 and 2001 that is estimated to surpass the accumulated SO_2-emissions from the climatic 1991 eruption of Pinatubo (Delgado et al., 2001). In current years, Popocatépetl has been estimated to be among the top ten emitters, with around 2.8% of the total global volcanic SO_2 emissions (McLinden et al., 2016). The SO_2 plume of Popocatépetl has occasionally been detected by air quality monitoring stations in Mexico City (Raga et al., 1999; de Foy et al., 2009) and Puebla (Juarez et al., 2005) and, under certain meteorological conditions, it can impact regional air quality. Ash emissions from the volcano also affect local aviation.

Ground-based ultraviolet (UV) remote sensing techniques have shown to be effective in the measurement of SO_2 gas emissions from this active volcano from a safe distance Fickel and Delgado Granados, (2017); Platt et al. (2018); Galle et al. (2010); Delgado et al. (2001); Grutter et al. (2008); Campion et al. (2012); Campion et al. (2018); Schiavo et al. (2019). Additionally, other volcanic trace gases such as HCl, HF, SiF_4 have been detected in the Popocatépetl plume by passive infrared (IR) spectroscopy and give valuable information about this volcano (Love et al., 1998; 2000; Goff et al., 2001; Stremme et al., 2011; 2012; Taquet et al., 2017; 2019).

One of the most abundant volcanic gases, carbon dioxide (CO_2) is difficult to measure with remote sensing techniques because the high atmospheric CO_2 background concentration means that the relative contribution of volcanic plumes to the measured total atmospheric column is generally very small. On the other hand, *in situ* measurements are often associated with risk and are generally temporally sparse and spatially localized. Nevertheless, the CO_2 signal from the Popocatépetl plume was detected in the past by passive IR spectroscopy (Goff et al., 2001) during extraordinarily strong CO_2 emission episodes of 1998, for which the high CO_2/SO_2 ratios were interpreted to reflect a possible episodic assimilation of limestone during magma migration (Goff et al., 2001). These events were associated with very variable CO_2/SO_2 ratios and therefore the reported CO_2 emission rate is most likely not a representative mean value. Emission rates of up to 100 Gg/d (36.5 Tg/yr) were calculated during this exhalation (Goff et al., 2001).

Aiuppa et al. (2019) combined the estimated CO_2/SO_2 molecular ratio of 8.2 (Aiuppa et al., 2017), which was based on earlier successful measurements Goff et al. (2001), together with the satellite-based SO_2 flux estimate by McLinden et al. (2016) and Carn et al. (2017) in order to estimate an average CO_2 emission from Popocatépetl of 9.284 Gg/day, 3.4 Tg/yr or 107 kg/s. However, the assumed volcanic CO_2 emissions from earlier measurements of the CO_2/SO_2 ratio and the extrapolation to quiescent average out-gassing phases using more recent SO_2 emission estimates could overestimate the CO_2 contribution of Popocatépetl to the global carbon cycle Werner et al. (2019).

It is important to measurements (Goff et al., 2001), together CO_2 during various days in the typical and more frequent passive degassing state of the volcanic activity in order to obtain more statistically solid results and gain knowledge of the role these prolonged volcanic emissions play in the local, regional and global carbon budget. In recent years, the remote sensing technique using solar absorption high-resolution spectroscopy in the near-infrared has gained sufficient precision to detect enhancements of the CO_2 total column of less than one percent (Wunch et al., 2011). Instruments with lower spectral resolution (Gisi et al., 2012) using a similar measurement configuration have been successful in detecting CO_2 enhancements in the volcanic plume of Mount Etna (Butz et al., 2017) during field campaigns of short duration. In that study, the CO_2/HCl ratios and those of other molecular ratios showed high temporal variability.

In this work, we measured the volcanic gas composition from a fixed site during an extended time period using a high-resolution Fourier Transform Infrared (FTIR) spectrometer that has been used to document not only the atmospheric variability of CO_2 (Baylon et al., 2017), but also ozone (Plaza-Medina et al., 2017) and various gases of volcanic origin (Taquet et al., 2019). This station, the Altzomoni Atmospheric Observatory, forms part of the Network for Detection of Atmospheric Composition Change (NDACC) (De Mazière et al., 2018). In this paper we include information about the site, instrumentation (Section 1.1), and about our measurement strategy (Section 2). Further on, we describe how the volcanic gas emission rate is reconstructed from the given information (Section 3.1). For a particular day (26 April 2015), we present the retrieval strategy (Section 2.2) and how to deal with the airmass dependence (Section 2.2), how to improve the precision of the derived molecular ratio (Section 2.3) and calculate the cross-section (Section 3.2) and emission rate (Section 3.3). In that section, we also describe how we combine the CO_2/HCl molecular ratios and the HCl emission rates to obtain a statistically more significant estimation of the total CO_2 emission (Section 3.5), to provide then a discussion of the principal uncertainties (Section 3.4). The results are finally presented in Section 3.6, discussed in Section 4, and the conclusions are provided in Section 5.

1.1 Site, instrument, and measurements

Our measurements are taken from the Altzomoni Atmospheric Observatory (19.1187°N, 98.655°W, 3,985 m a.s.l.) using a high-resolution FTIR spectrometer from Bruker, model IFS HR120/5, that contributes to NDACC (De Mazière et al., 2018). The high-altitude station is located 11 km away from the crater of Popocatépetl, as can be seen in Figure 1. A solar tracker (Gisi et al., 2011) directs the radiation of the Sun to the interferometer, which

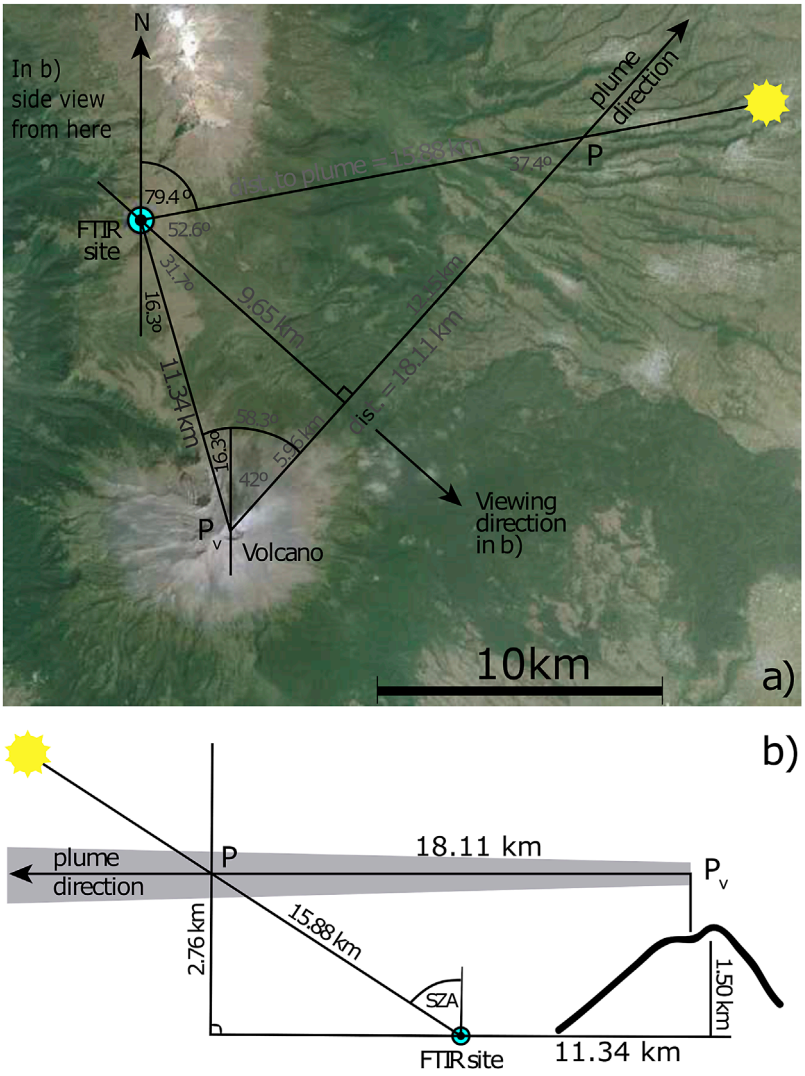

FIGURE 1
Observation geometry around the Popocatépetl volcano from two different perspectives at 06:45 LT on the morning of 26 April 2015: The top view in the upper panel **(A)** shows the plume propagation direction inferred from a wind direction = 222°. In the map, the FTIR site and the solar azimuth angle (79.4°) at that time are depicted, as well as the absolute distances from the measurement site to the plume position above the volcano (Pv) and at the point where the recorded solar radiation passed through the plume (P). **(B)** shows the side view with the observation site at the front looking perpendicularly towards the plume, while the instrument points to the rising sun. The side view illustrates how the solar beam reaching the instrument crossed the plume as the sun was rising. Again the absolute distances and heights are given for this particular event and are assumed constant while the sza decreased. A volcanic plume height of 2.76 km above the observation site was estimated from a plume distance at solar crossing point P of 15.88 km and a plume propagation direction towards 42.0° NE. The summit of Popocatépetl is located 1.5 km above the observation site.

measures spectra with a 0.02 cm^{-1} resolution (optical path difference = 45 cm), as commonly used in the Total Carbon Column Observing Network (TCCON) (Wunch et al., 2011). In the near-infrared spectral region (NIR), an aperture of 0.8 mm is chosen, which results together with the 418 mm focal length of the focusing and collimating mirror in an external and internal field of view of 2 mrad (approx 0.1°). Thus, the field of view diameter is less than 1/5 that of the Sun (the Sun has a size of approx 10 mrad or 0.5°.). The internal divergence and resulting self-apodization are not critical for the used spectral resolution. The remotely-operated FTIR instrument is started manually by an operator and then programmed to continuously measure a sequence of filters and detectors covering the range from 600 cm^{-1} (17 μm) to 10,000 cm^{-1} (1 μm). For these measurements in the NIR region, both CaF_2 and KBr beam splitters are utilized and an InGaAs detector records the signal of the interferograms (4,000 - 10,000 cm^{-1}). Unlike the MCT and InSb detectors used for the mid-infrared (MIR), the InGaAs detector is not cooled by liquid nitrogen (LN2). All applied detectors are able to record the interferograms in direct current mode making it possible to monitor the solar intensity variations and correct them before the Fourier transformation is performed (Keppel-Aleks et al., 2007). These intensity variations originate from thin clouds, or specifically in our case, from the volcanic plumes that move across the field of view during a single measurement (time of the forward and backward scan is 30–40 s). The correction, which removes smoothed intensity fluctuations of the interferogram

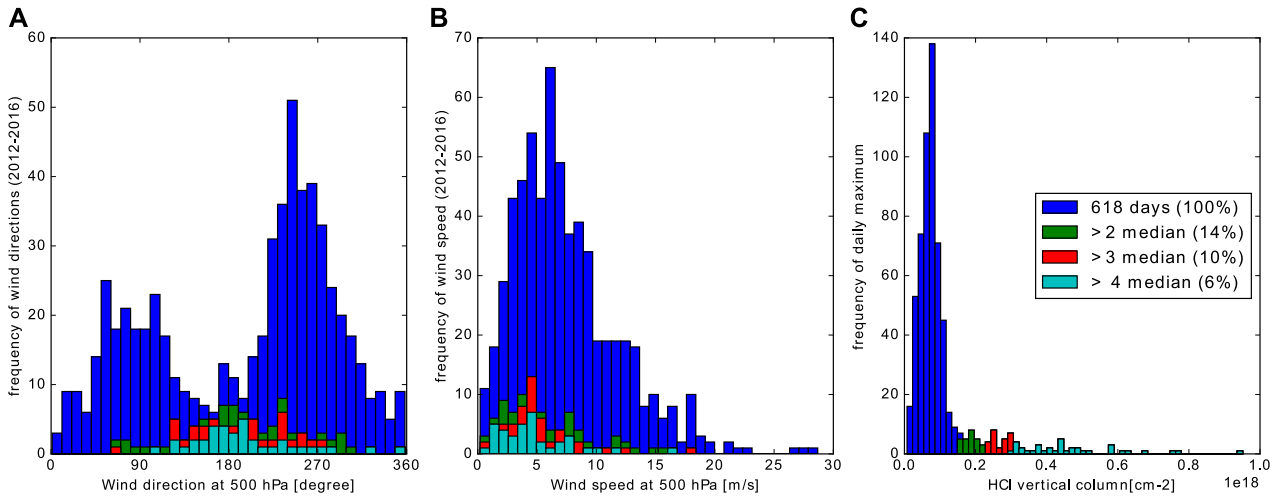

FIGURE 2
Frequency distribution of the meteorological Wind direction **(A)**, Wind speed **(B)**, and daily maximum of the vertical HCl columns **(C)**. The maximum HCl column retrievals are classified into subgroups based on the frequency of their occurrence **(C)**. The different colors represent measurement days for all measurements (blue), the highest 14% (green), highest 10% (red), or highest 6% (light blue). For these different sets of measurements, the histograms of the corresponding wind direction (WD) and windspeed (WS) are shown in panels **(A, B)**. The retrieval errors of the HCl product, retrieved in the NIR, is larger than the vertical HCl column density of the atmospheric background. The wind direction and wind speed used here were obtained from North American Regional Reanalysis (NARR) simulations for the 500 hPa pressure level as also described in the text. The most frequent wind direction for measurement with a significant HCl enhancement is towards the North. The two general most frequent wind directions however are towards the east (WD=270°)and west (WD=90°).

outside of the center burst, located at zero path difference, is realized in this work using routines from the "CALPY" software package (Kiel et al., 2016) and slightly improve the precision, Supplementary Section S2.

Measurements are possible almost every morning, but rising clouds typically prevent measurements in the afternoon. As shown in Figure 2, predominant wind directions at pressure level 500 hPa (around 6 km a.s.l.) are west to east and east to west. However for the detection of the plume, wind towards the north (WD=180°) is necessary. Figure 2 shows the wind speed and direction on all days with concurrent HCl measurements. The wind data (500 hPa) are taken for the time at which the highest by PROFFIT96 calculated HCl vertical column of the corresponding day was measured. Of all measurement days, 14% (approx once per week) show a maximum HCl column greater than 1.5E17 Molec/cm^2. This value is twice the median value μ (7.6E16 Molec/cm^2) and *ad hoc* chosen to classify days with a clear volcanic signal in the measurements. The corresponding wind direction frequency distribution for days on which a volcanic plume was detected shows a distribution around the wind directions towards North. Applying different, stricter criteria for the classifying of days with volcanic event detection, as 3 or 4 times of the median value results in a subset of 10% or only 6% of all days being chosen, but the relative distribution of wind directions shows a similar pattern and is valid for the subset of 25 measurement days with a HCl slant columns > 1E18 Molec/cm^2 which have been chosen for the analysis of the CO_2/HCl ratio Section 3.5. The PROFFIT96 output is the vertical column assuming a horizontal homogeneous atmosphere. Therefore it is simpler to classify the days using the vertical columns. However, the signal in the absorption spectrum is proportional to the slant column, which indicates whether we could expect to find volcanic CO_2 in the spectra of this day. Most plume intersections are actually recorded by high solar zenith angles (sza > 60°) and therefore the slant column is mostly greater than twice the vertical column, please see Supplementary Material.

2 Methodology

We present a new methodology to determine CO_2 emission rates from volcanoes using solar absorption IR spectral measurements taken from a fixed site. Solar IR spectra are continuously measured while the direct sunlight passes through the volcanic plume, allowing for an enhancement in the slant column density of CO_2 to be measured as a function of time. Accurate raytracing allowed for retrieving slant columns even for high (>80°) solar zenith angles during sunrise due to the location of the measurement site and the direction (Gisi et al., 2011). Simultaneous detection of other volcanic tracers such as HCl and HF from the same spectra proves that the measured ΔCO_2 anomaly is of volcanic origin.

2.1 Solar occultation measurements of gas plumes: vertical column, slant column, plume cross-section and emission rates

In solar-tracking FTIR measurements all detected photons take the same light path and the slant column is well defined by

the integration of the gas concentration along the line of sight. The vertical column is the vertical integral of the gas density independent from the observer geometry. The airmass factor is defined by the quotient of slant and vertical column and therefore approximately $\frac{1}{\cos(\mathrm{sza})}$ if the curvature of the light path can be neglected, and the atmospheric trace gas distribution is horizontally homogeneous (as is approximately true for background CO_2). Vertical columns describe the atmosphere independently of the observer viewing direction and are therefore useful for comparison, validation, bias corrections, or calculation of anomalies. The retrieval code PROFFIT9.6 therefore reports all retrieval results as vertical columns. If a volcanic plume is measured, however, horizontal homogeneity is not a valid assumption and the slant column itself is useful. We can formulate a potential enhancement of the slant column $\Delta col\,(sza)$ by gases in a volcanic plume in the framework of the output of the vertical columns by PROFFIT96.

$$\begin{aligned}\Delta col(sza) &= \frac{1}{\cos(\mathrm{sza})}\left(Vcol(sza) - Vcol_o\right)\\ &= \frac{1}{\cos(\mathrm{sza})}\int^{Top}\left(\rho(sza,z) - \rho_o(z)\right)dz\end{aligned} \tag{1}$$

According to the equation of continuity and the integrated form of the law of Gauss, the emission from a point source can be calculated by the integration of the flux through a closed surface around the point source. Typically we think in a cylinder or cone where only the sides contribute as the top is outside of the atmosphere.

$$\begin{aligned}E &= \int_A \left(d\vec{a}\cdot\vec{j}\right) = \oint_S \left(\int_o^\infty \left(\vec{ds}\times\vec{dz}\right)\cdot\vec{j}(z)\right)\\ &\approx \oint_S \left(\int_o^\infty \left(\vec{ds}\times\vec{dz}\right)\cdot\left(\rho(z)\,\vec{v(z)}\right)\right)\\ &= \oint_S \left(\vec{ds}\times\vec{e_z}\right)\left(\vec{v}\times\vec{e_z}\right)\underbrace{\left(\int_o^{Top}\frac{dz}{\cos(\phi)}\left(\rho_o(z)+\Delta\rho(z)\right)\right)}_{\text{slant column}}\\ &= \oint ds\cdot v_\perp\cdot\left(col(s)+\Delta col(s)\right)\end{aligned} \tag{2}$$

$$\begin{aligned}&\approx v_\perp \underbrace{\int ds\cdot\Delta col(s)}_{\text{i)plume cross-section-trajectories}}\\ &= v_\perp \underbrace{\cdot\int d\phi\cdot dist(\phi)\cdot\Delta col(\phi)}_{\text{ii)plume cross-section-MAXDOAS}}\end{aligned} \tag{3}$$

$$\begin{aligned}&\approx v_\perp \underbrace{dist\cdot\int\left(\frac{-dsza}{dt}\cdot dt\right)\cdot\Delta col(sza(t))}_{\text{iii)plume cross-section-solar absorption}}\\ &\approx v_\perp \underbrace{dist\cdot\sum_t\left(sza_t - sza_{t+1}\right)\cdot\frac{\Delta col_t + \Delta col_{t+1}}{2}}_{\text{iv)plume cross-section-this work}}\end{aligned} \tag{4}$$

Where E represents the emission rate in molecules per time, A represents the closed surface, ρ is the number density of the considered gas, $\vec{j}$ is the flux through the surface, $\vec{da}$ is the indefinite small area of the surface. The integration over the area is then divided by the integration along the viewing direction $(\vec{dz})$ of an instrument and perpendicular to the viewing direction $\vec{ds}$.

Platt and Stutz (2008); Galle et al. (2010); Platt et al. (2018) discuss in more detail different measurement geometries and measurement spectroscopic techniques using the photons scattered or emitted by the sky to calculate these integrals, plume cross-sections, and emission rates, as, for example, i) zenith sky DOAS from mobile platforms or ii) multi axis DOAS (MAXDOAS) using different viewing angles as done by the NOVAC network Galle et al. (2010). For solar absorption spectroscopy in the IR, our viewing angle has to follow the Sun and is identical to the solar zenith angle, and the plume cross-section is given by the integral iii) in Equation 4. It is calculated from the fixed site looking to the Sun and only under favorable conditions once a day. In contrast to the MAXDOAS, we are not able to choose a scanning geometry, but in principle, the plume cross-section is measured in principle the same way. Only a small area contributes to the integral of the closed surface so just this small part of the closed surface has to be measured. For gases with non-negligible atmospheric background concentration such as CO_2, the part of the slant column which represents the recently emitted gas is calculated by subtracting the background column. The vertical columns are subtracted and afterward the corresponding slant column anomaly of the target gas is calculated. Inside the retrieval code (PROFFIT9.6), the ray-tracing in the atmosphere is calculated with high precision as already mentioned, but the calculation of the slant column anomaly from vertical column anomaly is done in this work using the simplified airmass factor 1/cos (sza). The solar zenith angle (sza) is the apparent solar zenith angle, the angle at which the instrument is aimed to align the field of view to the center of the Sun and the angle of the line of sight in the lower atmosphere.

The slant columns (HCl) or slant column enhancements above background (CO_2) Δcol represent the integrated gas concentration (or gas concentration anomaly) along the line of sight. $v_\perp$ is the wind velocity component perpendicular to the viewing angle and to $\vec{ds}$, which corresponds to the connections of two points, each one represents the center of mass of the volcanic gas concentration along the two different lines of sight of consecutive measurements. As we measure the slant column as a function of the viewing and solar zenith angle $col\,(sza)$ we still have to estimate the distance from the instrument to the plume center to calculate ds ($ds = dist\cdot dsza$) between two consecutive measurements and, more specifically the components perpendicular to the line of sight and wind velocity. The wind velocity $\vec{v}$ might not be constant with altitude and along the line of sight, but we approximate the wind velocity by querying the NARR model at the altitude of the measured plume center.

Similarly, we estimate the distance between the instrument and the plume center $dist$. During several minutes required to measure the full plume cross-section, the distance changes slightly as a function of the sza and the spatial extent of the plume. The estimation of distance and height are not independent and a consistency check is possible. The spatial extent and geometrical form of the plume influence the estimation of ds (sza) and therefore the plume cross-section. However, if a constant distance is assumed to be valid for the whole plume cross-section, as is done here, knowledge about the geometrical form of the plume is not needed (Platt et al., 2018).

2.2 Spectral analysis and retrieval strategy

The retrieval strategies used in this work are adapted from Baylon et al. (2017), Taquet et al. (2019) and the standard NDACC and TCCON procedures, thus in this section we only detail the changes from the standard retrievals.

2.2.1 CO_2

The analysis of the spectra was performed with the retrieval code PROFFIT9.6 using the CO_2 band around 1.6 μm which is used by the Total Carbon Column Observing Network (TCCON) (Wunch et al., 2011), reaching precisions of 0.1% or better in the total CO_2 columns (Baylon et al., 2017).

There are some adjustments to the retrieval settings for the volcanic application to the common PROFFIT retrievals at the Altzomoni site. The *a priori* profile has a constant volume mixing ratio (VMR) of 400 ppm and the chosen constraint is a block Tikhonov type (Rodgers, 2000; Clarmann and Grabowski, 2007), similarly used for retrievals of carbon monoxide within the boundary layer of Mexico City (Stremme et al., 2009; Stremme et al., 2011) but with a free block for the altitudes 4–8 km. This approach ensures that the total column sensitivity, which is also called averaging kernel (AK) is around 1.0 in the lower troposphere and in the altitude of the volcanic plume. The strategy is similar to previous studies conducting either a plume model (Taquet et al., 2017) or scaling the profile of the troposphere (Butz et al., 2017).

2.2.2 O_2

In the TCCON and COCCON networks, the vertical O_2 column is retrieved from the same spectra as CO_2 and used to ensure the quality of the spectrum and to calculate the dry air mol fraction XCO_2. In Section 2.3 we describe how we use the O_2 column in a similar way to improve the estimation of the CO_2/HCl ratio. We slightly adapted the O_2 retrieval described by Baylon et al. (2017), in which tropospheric HF is not simulated in the spectra. However, HF is an important interference species and tropospheric HF should be fitted for volcanic application. A constructed HF profile which is constant from 4–7 km (possible altitudes for the volcanic plume) and zero above is scaled in the O_2 retrieval. Consequently the interference error between volcanic and tropospheric HF (first-overtone) and O_2 is small and irrelevant and no artificial correlation between O_2 with any volcanic trace gas (HCl, HF) can be observed.

2.2.3 HCl

HCl is the fourth most abundant volcanic gas emitted by Popocatépetl after H_2O, CO_2, and SO_2 (Love et al., 1998; Goff et al., 2001). Because HCl has a higher solubility in silicate melt than CO_2 and SO_2, HCl outgassing generally occurs at shallower depths/lower pressure (Aiuppa et al., 2009). In the mid-IR it is normally retrieved at around 2,800 cm^{-1} together with SO_2 at 2,500 cm^{-1} (Francis et al., 1998; Love et al., 1998; Stremme et al., 2011; Taquet et al., 2019), but can also be retrieved from its first overtone at 5,700 cm^{-1} (Butz et al., 2017). For this study, we retrieved HCl using the following three microwindows; 5,738.30–5,740.00 cm^{-1}, 5,767.00–5,767.75 cm^{-1} and 5,779.25–5,779.80 cm^{-1} with H_2O and CH_4 as interference gases and the HITRAN 2004, 2006, and 2012 spectral line lists, respectively. The line positions of HCl, H_2O, and CH_4 have been experimentally slightly adjusted to improve the fit. The HCl retrieval from the first-overtone results in slightly lower column amounts than when using the fundamental band. However, we restricted our analysis to the use of HCl results from retrievals in the NIR region in this work. As *a priori*, an average of HCl profiles, modeled with the Whole Atmospheric Community Climate Model (WACCM) is calculated and the constraint fixes the retrieved profile above 8 km a.s.l. to this apriori, but allows for free scaling of the lower part from 4 to 8 km. As a consequence, the averaging kernel for total column HCl is close to 1 around the plume height (6 km).

The most important PROFFIT retrieval settings of CO_2, O_2, and HCl are summarized in Table 1 and more details about the HCl retrieval strategy can be found in Taquet et al. (2019).

2.2.4 Airmass dependence of CO_2

It is known that a slightly incorrect simulation of the CO_2 line shape and errors in the spectroscopic parameters result in a small artificial airmass dependence of the retrieved CO_2 columns. This artifact is especially important and visible at high solar zenith angles (sza) (Wunch et al., 2010). If the chosen *a priori* CO_2 profile differs from the true background atmosphere, the airmass dependence of the sensitivity of CO_2 impacts the retrieval as well. Thus the dependence on the solar zenith angle can be eliminated by the use of a specially reconstructed *a priori* profile ρ_o (see Supplementary Material). Such correction was applied for the event of 26 April 2015, which is the most relevant CO_2 anomaly of our time series, so that it minimizes the air mass dependence and allows for better quantification of the anomaly. As shown in Figure 3, no significant sza-dependance was observed after applying the correction.

To analyze the CO_2/HCl ratios in all identified volcanic events, we did not reconstruct an *a priori* for each individual event. Instead, we fit and subtracted a polynomial of order 2, jointly with the time series of the volcanic tracer HCl and the O_2—anomaly and explain the CO_2 time series as the instrument viewing direction passes through the volcanic plume as a linear combination of different contributions (Section 3.5). For each measurement, the random and systematic errors in the CO_2 column are estimated by the internal error analysis of PROFFIT9.6 (i.e., Barthlott et al. (2015); Plaza-Medina et al. (2017); Baylon et al. (2017)).

2.3 Three strategies to quantify the volcanic CO_2 emissions and CO_2/HCl ratio

Three slightly different strategies for reconstruction of the CO_2 emission rate were applied to data recorded on 26 of April 2015, the day on which the strongest volcanic signal was measured. Strategy i), calculates the plume cross-section directly from the slant column anomalies of CO_2 and does not need the retrieval of another volcanic gas. This approach works for the quantification of the CO_2 emission even if the composition of the volcanic gas is variable as recently observed by Butz et al. (2017) for Etna volcano.

Strategy ii) assumes a constant molecular ratio between HCl and CO_2 in the volcanic gas plume. It calculates the emission flux for HCl, for which the atmospheric background can be neglected, and then multiplies the emission flux by the CO_2/HCl ratio. The ratio is obtained as the slope of the fitted straight line in a CO_2 HCl correlation plot.

TABLE 1 PROFFIT retrieval setting.

Target gas	Interference gases	Spectral windows	Remark	Reference
CO_2	H_2O CH_4	(6180.0,6260.0)	block Tihkonov	Baylon et al., 2017
		(6310.0,6380.0)	*a priori* 400 ppm	
HCl	H2O	(5738.0,5740)	tropospheric HCl	Taquet et al., 2019
		(5767.0,5767.8)	HITRAN 2008	
O_2	HF, H_2O, CO_2	(5779.2,5779.9)	with adjustments	Baylon et al., 2017
		(7765.0,8005.0)	tropospheric HF	

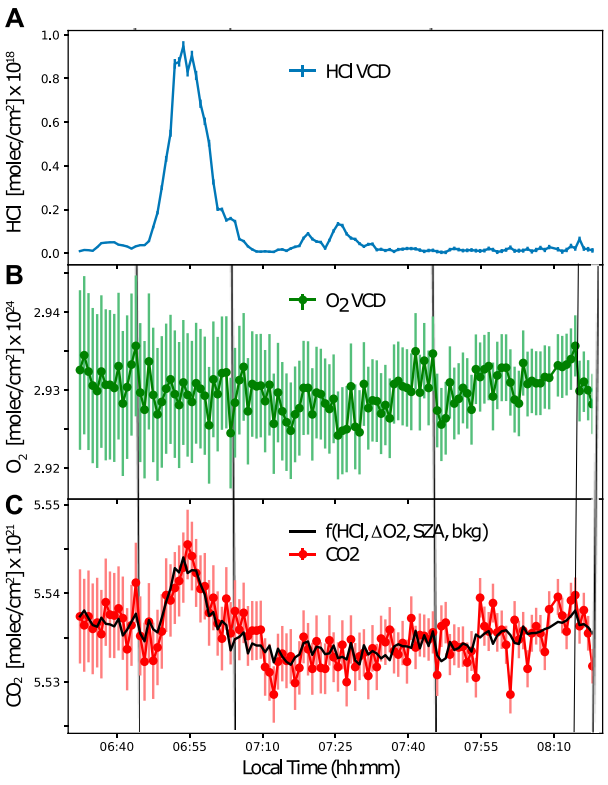

FIGURE 3
HCl **(A)** O_2 **(B)** and CO_2 **(C)** vertical columns measured on 26 April 2015 from the Altzomoni Atmospheric Observatory. The volcanic plume crossed the line-of-sight of the sun at around 06:55 LT. An enhancement in the columns of CO_2 and HCl can be clearly observed as the plume was crossed. The detected vertical CO_2 column anomaly, fitted by a function (black trace), follows the HCl volcanic enhancement but also the anomalies in the O_2 columns accounting for correlative errors (e.g., pointing error). In panel b in the middle, we see at 6:43, 7:00, 7:45, and 8:12 LT small variations of the O_2 column which can be seen also in the CO_2-time series. Subtraction of the sza-dependence (airmass, fitted with a second order polynomial) and the background CO_2 value works as a high pass filter.

Strategy i) and ii) work only if the CO_2 atmospheric background is constant in time. This assumption is rather likely for the remote site Altzomoni and the duration of only a few minutes in which the spectra with a volcanic plume are recorded. Unfortunately, there is a solar zenith angle-dependent bias observed, which is also called air mass dependence (Wunch et al., 2011) as already mentioned above. This solar zenith angle-dependent bias in the CO_2 measurements, if not corrected, would affect both strategies (i and ii) as it complicates the determination of the constant atmospheric background of CO_2 in strategy (i). This is the reason why an HCl-CO_2 scatter plot does not show a very nice and simple linear correlation, which is however needed for strategy (ii).

Knowing the total vertical column of CO_2 before and after the field of view intersects the plume allows us to determine the airmass dependence and correct it in the first step. Afterward, in a second step, either the plume cross-section can be calculated from the continuously observed slant columns (strategy i), or the assumed constant CO_2/HCl ratio is determined from the CO_2 vs HCl scatter plot (strategy ii).

However, the analysis in two steps required by these two strategies can increase the CO_2 emission uncertainties and the error propagation from the bias correction to the CO_2/HCl ratio is complicated.

Therefore strategy (iii), was designed to retrieve the CO_2/HCl ratios from all 25 plume intersections with slant column of HCl > 10^{18} molecules/cm^2. Therefore, the time series of the retrieved vertical CO_2 column of each plume intersect is modeled by a linear combination of different contributions from the atmosphere, volcanic plume as well as instrumental and spectroscopic limitations.

1) A atmospheric background CO_2 column
2) Solar zenith angle dependence
3) the contribution of the volcanic gas to the measured absorption
4) Differences between calculated and real atmospheric path length

The first two points are modeled by a polynomial. The background column might change either because of a growing mixing layer of Mexico City, which might reach the altitude of the site (Baumgardner et al., 2009; Garcia-Franco et al., 2018), or a different mass of background air might be observed due to the change in the solar angle. In addition, the apparent change in the background column rising from the airmass-dependent bias impacts the behavior of the retrieved background column. A polynomial of the second degree is used to reproduce the function of the solar zenith angle and works for all 25 analyzed events. The pointing error, which affects all gases with an atmospheric background in the same way, can be corrected with the retrieved O_2 column anomaly. The TCCON (Wunch et al., 2011) and COCCON (Hase et al., 2015; Alberti et al., 2022) analysis and in the recent work

of (Butz et al., 2017) XCO_2, the quotient of both columns (CO_2 and O_2), is calculated and therefore the pointing error is reduced. The retrieval of CO_2, O_2, and XCO_2 time series at Altzomoni and their independent and correlative errors have been studied and described by Baylon et al. (2017). Adding a new parameter (in this case O_2 columns) also adds a new error source (Baylon et al., 2017), so that unfortunately a contribution in the error in the XCO_2-product arises from the noise in the independent O_2 retrieval. Because the cam tracker (Gisi et al., 2011) used at the Altzomoni site is quite accurate, the pointing error is sometimes almost negligible and the use of the retrieved O_2 column might sometimes increase the statistical error. An erroneous estimation of the optical path length of the sunlight through the atmosphere affects the retrieved vertical columns of all gases in the same way. Any error in the line of sight results in the anomaly δO_2 in the retrieved vertical O_2 column, which is expected to be constant in time. This anomaly related to the optical path can be converted to an anomaly δCO_2 in the vertical column of CO_2 using the factor 400 ppm/21% based on the background concentration of both gases, Eq. 5. We can then subtract the estimated δCO_2 vertical column anomaly calculated from the δO_2, either completely or also partly (weighting with the parameter α ($0 < \alpha < 1$). There are plenty of reasons why the pointing error and the measurement noise error vary on some of the 25 events, for example, The impact of the pointing error increases with the solar zenith angle in general, and the signal-to-noise ratio varies depending on the instrument's optical configuration (KBr or CaF_2-beamsplitter), the presence of thin clouds or the volcanic plume might affect the signal to noise ratio. The solar tracking might be degraded through dust and dirt on the optics of the solar tracker and even some transient effects such as oscillations of the solar tracker around the Sun have been observed occasionally. The relative precision in the XCO_2 retrieval product might be worse than the CO_2 vertical column if the tracker works perfectly, but if the solar tracking is one relevant error source and O_2 could be retrieved from spectra with a high signal-to-noise ratio, it is possible to correct for the error in the line of sight successfully. Each short time series of a volcanic event has, according to the different error contributions, one optimal weighting factor α, which will optimize the statistical error in the anomaly of CO_2 during the short time that the field of view passes through the volcanic plume.

$$\tilde{CO}_2 = CO_2 - \alpha \cdot \frac{400ppm}{21\%} \cdot \delta O_2 \tag{5}$$

$$\sigma_{CO2} = \sqrt{\left(\sigma^2_{CO2-independent} + (1-\alpha)^2\sigma^2_{corr} + \alpha^2\left(\frac{400ppm}{21\%}\right)^2 \cdot \sigma^2_{O2-independent}\right)} \tag{6}$$

In Eq. 6 σ_{CO2} is the error in the finalized, optimized and corrected CO_2 column, $\sigma_{CO2-independent}$ refers to the statistical error in the retrieved vertical CO_2 column, which does not correlate with the retrieved vertical O_2 column. $\sigma_{O2-independent}$ is the error in the retrieved O_2 column which does not correlate with the CO_2 column.

Therefore, we adjust the factor α to minimize the error in the CO_2 column anomalies for both higher sza or lower signal-to-noise ratio, which is theoretically given as a function of the correlated error between CO_2 and O_2 and the independent error of the O_2 column. The mean values of the correlative and independent errors have be estimated either by PROFFIT9.6 or the analysis of consecutive measurements in large ensembles (Baylon et al., 2017), but are not known specifically for the measurements of different days and intervals with the volcanic plume measurements.

$$\alpha = \frac{\sigma^2_{corr}}{\sigma^2_{corr} + \left(\frac{400ppm}{21\%}\right)^2 \cdot \sigma^2_{O2-independent}} \tag{7}$$

Figure 3 presents the CO_2, O_2, and HCl vertical columns, with corresponding error bars calculated with PROFFIT9.6, for the volcanic plume intersection detected on 26 April 2015. The CO_2/HCl-molecular ratio was retrieved simultaneously by adjusting of the O_2-column anomaly and the sza-dependence as shown in Figure 3. The error in the CO_2/HCl-molecular ratio is estimated from the resulting residual as usually done for the measurement noise error in least-squares fitting.

The linear combination of different contributions should approximate the observed time series. The set of factors are the coordinates of the vector $\mathbf{x}$ and we describe this linear combination as matrix multiplication of the matrix K and the vector $\mathbf{x}$. The calculated vector $\mathbf{x}$ minimizes the cost function $[CO_2(t) - K \cdot x]^2$.

$$K = \begin{pmatrix} 1 & \Delta sza_0 & (\Delta sza(t_0))^2 & HCl(t_0) & \delta O_2(t_0) \cdot \frac{400ppm}{21\%} \\ \vdots & \vdots & \vdots & \vdots & \vdots \\ 1 & \Delta sza(t_{n-1}) & (\Delta sza(t_{n-1}))^2 & HCl(t_{n-1}) & \delta O_2(t_{n-1}) \cdot \frac{400ppm}{21\%} \end{pmatrix} \tag{8}$$

The weighting functions (the columns of the matrix K correspond to the background, linear and squared airmass dependence, the proxy for volcanic plume and the proxy for a pointing error in the last column in Eq. 8.

$$\mathbf{x} = \begin{pmatrix} const_{bkg} \\ airmass_1 \\ airmass_2 \\ CO_2/HCl_{molec.Ratio} \\ \alpha \end{pmatrix} = \underbrace{(K^T \cdot K)^{-1} \cdot K^T}_{=G} \cdot \mathbf{CO_2(t)} \tag{9}$$

The fourth coordinate from above is the CO_2/HCl ratio. With the definition of the Gain-matrix, we can easily calculate the measurement noise error in this ratio as shown in (Eq. 12).

$$rms = \frac{1}{n}\sum_{i=0}^{n-1}[\mathbf{CO_2(t_i)} - \mathbf{y_{fit}(t_i)}]^2 \tag{10}$$

$$S_{err} = rms^2 \cdot G \cdot G^T \tag{11}$$

$$error_{CO2HCl} = \pm\sqrt{S_{err}(4,4)} \tag{12}$$

The error in the ratio (Eq. 12) is calculated from the linear regression and helps to weight the events with different strong volcanic signals and quality of measurements.

The CO_2 background column can be calculated using the following equation.

$$\mathbf{y_{fit}} = K \cdot \mathbf{x} \tag{13}$$

$$\mathbf{CO2_{bkg}}: = K \cdot \begin{pmatrix} const_{bkg} \\ airmass_1 \\ airmass_2 \\ 0 \\ \alpha \end{pmatrix} \tag{14}$$

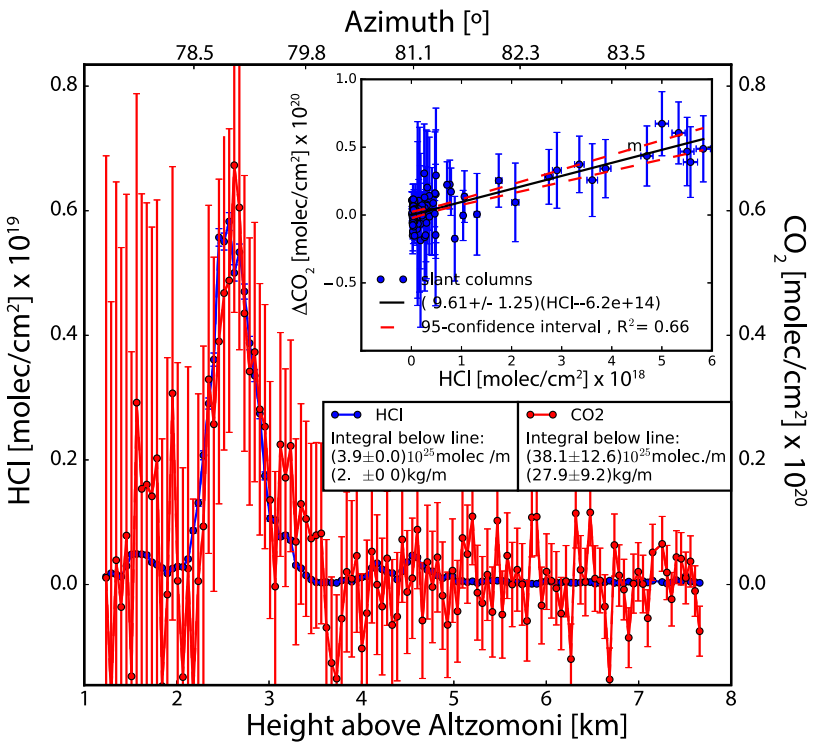

FIGURE 4
Measured slant column densities (SCD) of HCl and CO_2 anomaly *versus* reconstructed height (h=dist Cos(SZA); dist = 15.88 km) above the observation site (lower axis) and sza (upper axis). The CO_2 anomaly in the slant column is corrected for airmass dependence and improved by reducing the correlating error using the retrieved O_2 anomaly as shown in Fig.3. The inset is the scatter plot of HCl and CO_2 SCD's showing a strong correlation indicating that the detected CO_2 anomaly is of volcanic origin, and a valid and representative CO_2/HCl molecular ratio of 9.6 ± 1.3 has been calculated for the event.

Subtracting this background column from the CO_2 time series measured on 26 April 2015, we isolate the volcanic CO_2 as shown in Figure 4.

3 Results

3.1 The event on 26 April 2015

On the early morning of 26 April 2015, just after sunrise, Popocatépetl was passively degassing as it most frequently does and the sky was clear of clouds. The wind conditions at altitudes between 5,500 and 6,800 m a.s.l. were fairly constant as can be observed from the images captured every minute with the camera at the station pointing towards the volcano (see Supplementary Material). The plume was propagating towards the NE (wind direction = 222°) at a speed of approximately 8.2 m/s according to the radiosonde, launched daily at 06 LT from Mexico City. Continuous measurements of solar absorption spectra resulted in a full cross-section of the volcanic plume at around 06:44 LT, that together with the wind parameters, allowed for the emission flux of volcanic CO_2 and HCl to be determined. A schematic of the measurement geometry for this particular day is presented in Figure 1.

3.2 Plume cross-section

As already stated, on the early morning of 26 April 2015, consecutive solar absorption spectra were recorded just after sunrise starting at 06:30 LT. Each measurement had a duration of 37 s. At sunrise, the change in sza is rather fast and a complete cross-section through the volcanic plume was realized in about 15 min. The cross-section is directly given as a set of slant columns for which the time and the sza are known (see Figure 4). The plume cross-section can be converted to a function of height, as shown in Figure 4), since the distance from the observation site to the volcanic plume could be determined based on the known solar azimuth angle, the average wind direction, and the known distance between Popocatépetl's crater and the observation site (Figure 1).

With the above constraints, we have calculated a distance to the plume of 15.88 km, assuming that the height of the plume is 2.76 km above the observation site and 1.26 km above the crater. That the plume which propagated 18.11 km during about half an hour to reach the instrument line-of-sight, was rising to a height corresponding to its potential temperature (altitude of 6.75 km a.s.l). This propagation can be confirmed by a set of images taken from the Altzomoni Site (See animation in Supplementary Material).

TABLE 2 Errors considered in the CO_2 emission estimation for 26 April 2015 using the CO_2/HCl ratio.

Parameter	FTIR	Distance	WS	WD	Emission
HCl cross	3.9e25m^{-1}	15.88 km	8.2 m/s	222 °N	4.21 Tg/yr
CO_2/HCl	9.84	(WD ± 5°)	(sonde-NARR)	(altitudes)	—
$\sigma_{parameter}$	1.26	2.6 km	1.4 m/s	5°	—
$\sigma_{parameter}\{\%\}$	12.8%	17%	17%	13%	—
contrib.err	4.9e25 m^{-1}	6.5e25m^{-1}	0.85 m/s	0.65 m/s	—
Error %	12.8%	17%	17%	11.8%	29.7%
Error	0.54 Tg/yr	0.72 Tg/yr	0.72 Tg/yr	0.50 Tg/yr	1.25 Tg/yr

Alternatively, data from the North American Regional Reanalysis Data (NARR) (Mesinger et al., 2006) were used for the determination of wind velocity, plume height, and plume distance, leading to slightly different results (Table 2). This difference is used later to estimate the error associated with wind speed and direction uncertainties. However, the plume was observed at different times and the time intervals between our observation and the last available daily radiosonde observation could be quite large on some days. Instead, we decided to use the NARR data, which are available every 3 h and also assimilate the information of the radiosonde measurements. The statistical analysis that we present is therefore based on the combination of the FTIR cross-section measurements and wind information from model reanalysis data.

3.3 CO_2 emission rate calculation

For the calculation of the flux, or the instantaneous emission rate for a particular event, the wind velocity perpendicular to the plume cross-section is needed. This perpendicular component of the wind vector is estimated from the geometry as shown in Figure 1 and based on the radiosonde and/or the NARR model data. For the 26 April 2015 case study, the wind speed and direction used for the calculation are 8.2 m/s and 222°, respectively, leading to an angle between the measurement line-of-sight and the direction in which the plume propagates of 37.4°. The velocity component perpendicular to the cross-section is 8.2/sin (37.4°) = 4.98 m/s. The amount of molecules in the plume slice measured as the Sun increased its elevation angle across the plume is obtained by integrating the SCD over height. The instantaneous emission rate is then calculated by multiplying these two values, thus E_{CO2} = 36.7×10^{25} Molec/m × 4.98 m/s = 3.0 kMol/s, or in terms of mass, E_{CO2} = 134 kg/s (116 kg/s using NARR).

3.4 Errors and uncertainties

3.4.1 Gas ratios *versus* direct CO_2 emissions

The main uncertainty is given by the precision in the total CO_2 slant column measurement. The volcanic anomaly in the slant column of CO_2 is less than 1% of the atmospheric background (vertical column) and the precision of the measurement determined as the random error is around 0.2% of the total slant column, which results in a relative error greater than 20% in each slant column measurement. Figure 4 shows the retrieved slant column anomaly $\Delta CO_2(t) = \frac{1}{\cos(sza(t))} \cdot \left(VCO_2(t) - VCO_{2bkg}(t)\right)$. The errors in this slant column anomaly after background correction and subtraction are estimated as the propagation of the random error (err^{ST}_{CO2}) of the vertical column of CO_2 into the slant column anomaly:

$$error_{\Delta CO_2} = \frac{1}{cos\,(sza\,(t))} \cdot err^{ST}_{CO2} \tag{15}$$

The statistical error in the retrieval err^{ST}_{CO2} is analytically calculated by PROFFIT9.6, and the estimated uncertainty in the input parameters and the contributions of different error sources are described in more detail by Baylon et al. (2017). For the full CO_2 cross-section the weighted Gaussian sum of all errors in the individual column measurements results in an error of 35%. This large uncertainty can be minimized if we assume that the CO_2/HCl ratio is constant during the measurement of a single cross-section. Thus, we can independently calculate the HCl cross-section, which has a better signal-to-noise ratio, and determine a value of CO_2/HCl for that measurement sequence. As the atmospheric background of HCl is lower than the detection limit, the HCl slant column amount and the resulting cross-section can be determined with a far smaller uncertainty, and the main contributing error source will thus arise from the molecular ratio. In the slope fitted for the case study, shown in Figure 4 (inset), a relative error of 13% = 1.25/9.61 can be calculated from the 95% confidence interval. The same analysis could be done with HF instead of HCl.

3.4.2 Wind data

The uncertainty in the wind direction affects the emission rate in two different ways: a) The wind direction is an essential ingredient for reconstructing the measurement geometry, as in Figure 1, and impacts the calculation of the distance between the observation site and the plume cross-section. b) The wind direction is used to calculate the component of the wind velocity perpendicular to the plume cross-section as it is needed for the application of Gauss's Law. In a) the average wind direction of the plume is required, while in b) the wind direction just during the measurement of the plume cross-section is needed.

We assume both the mean and the final wind direction to be 222°, but we count them as two independent components for the calculation of the emission rate. The error in both the mean

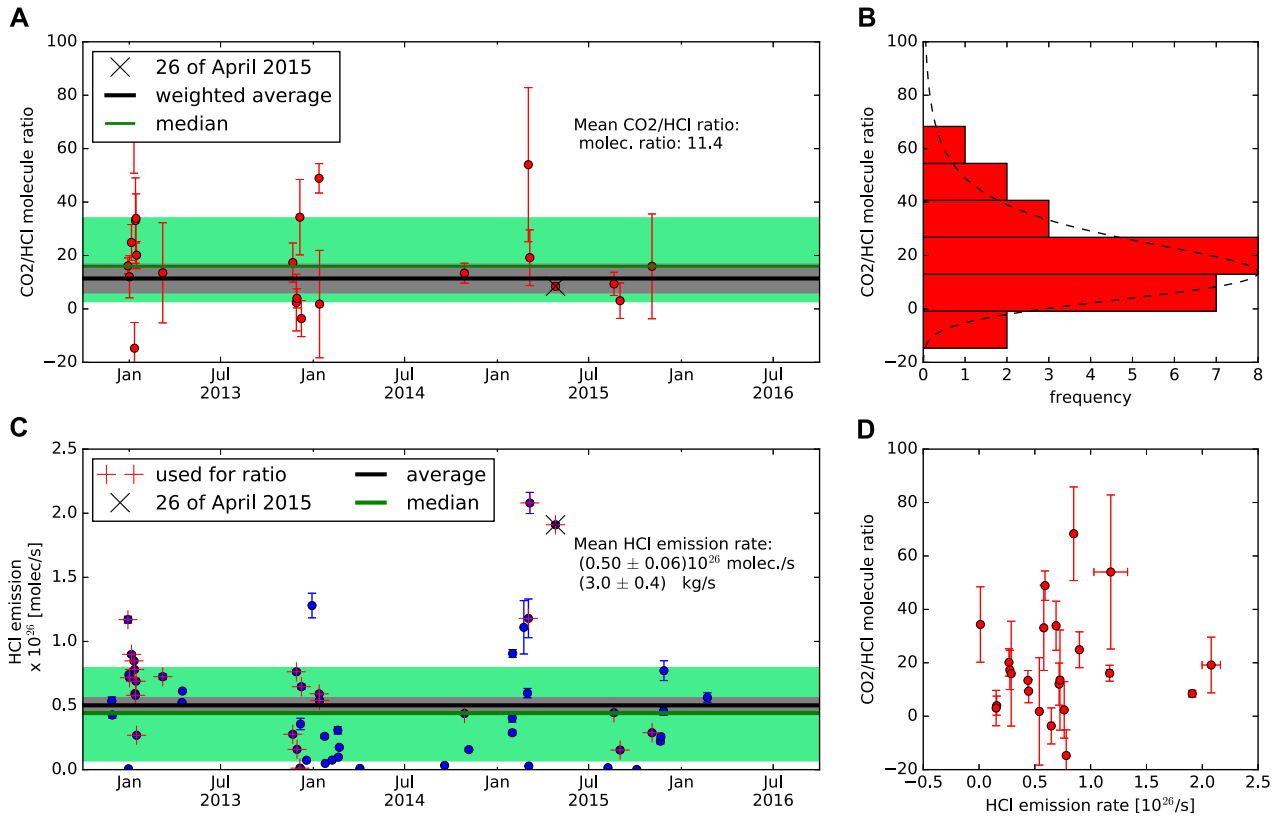

FIGURE 5
(A) The 25 events for which CO_2/HCl ratios were determined, shown as time series **(A)** and in a histogram **(B)**. **(A)** The green area marks the central region which contains 68% of the measured ratios, the black line and grey region represent the average and its standard error (uncertainty of type A). **(B)** The histogram of the measured CO_2/HCl ratios shows an asymmetrical distribution as expected for a positive quantity with natural variability and also negative values as a result of measurement errors. The dashed line models a distribution $\left(\int_o^\infty dx' \, exp(-ln(x'/10)^2 \cdot exp(-(\frac{x-x'}{10})^2))\right)$ obtained from the convolution of a log normal distribution (median μ^*=10, σ^*=1/$\sqrt{2}$) with a Gaussian distribution (measurement error σ = 10/$\sqrt{2}$). The line is not fitted but might help for qualitative discussion of the frequency distribution. Please note that the weighted averages of the CO_2/HCl molecular ratio of 11.4 ± 4.4 is slightly different from an average, without weighting the measurements by their errors (Supplementary Table S1). **(C)** HCl emission rate from Popocatépetl determined for 54 events by solar absorption IR measurements. The green area marks the region which contains 68% of the measured emission rates. The red dots with pluses (+) depict the measurements that have been analyzed also to determine the CO_2/HCl ratios and the case study (26 April 2015) is marked with a cross (X). Right **(D)**: No correlation between CO_2/HCl ratio and HCl flux (R=0.0) could be found. However, the large errorbars in the CO_2/HCl ratio indicate that no conclusion about a correlation between the molecular ratio and flux is possible from these measurements. The errorbars in the individual HCl-flux estimations (panels c and d) correspond to the error related to the column-integrated plume cross-section and are very variable. The errors should be considered as relative and are here only shown to distinguish measurements with different qualities, especially as the frequency of measurements varies depending on the different measurement modes and cycles. For 26 April 2015 the total error in the HCl flux is estimated to be around 25% (see Table 2).

and the final wind direction is estimated to be ±5°. This *ad hoc* estimated uncertainty in the wind direction corresponds to the median of the deviations of the two wind directions at 500 hPa and at 450 hPa pressure level of the NARR-reanalysis data. The +5° and −5° error propagates to an error of around +2.9 km or −2.3 km, respectively, resulting in an average of 17% for the reconstructed distance between the measurement site and the plume cross-section. The +5° or −5° error in the final wind direction results in an error in the wind component perpendicular to the cross-section of −11.8% and +11.0%.

Wind speed is critical for the flux calculation. In our case study, the wind speed measured by the radiosonde was almost constant 8.2 m/s over the various altitudes around the plume height (Table.2). The wind speed from the NARR model can be obtained from both its meridional (v) and zonal (u) components as WS = $\sqrt{u^2 + v^2}$ and was found to be slightly lower, 6.8 m/s. This discrepancy of 1.4 m/s was used to estimate the error in the wind speed. For the 26 April 2015 event, a more confident result is expected from using the velocity from the radiosonde since it was taken in the same hour. The total error in the emission rate is thus estimated to be around 30%. These values are summarized in Table 2.

3.5 Time series: HCl emission rates and CO_2/HCl ratios

In total, we analyzed 25 occurrences during which our instrument field of view intersected the volcanic plume and during which HCl and CO_2 could be simultaneously detected. All of these plume intersections have HCl slant columns greater than 1.0E18

TABLE 3 Comparison of molecular ratios and emissions of HCl, SO_2 and CO_2 from Popocatépetl.

Time	Molecular ratios			Emissions (kg/s)			Source and strategy (wind data)
	$\frac{CO2}{HCl}$	$\frac{HCl}{SO2}$	$\frac{CO2}{SO2}$	HCl	SO_2	CO_2	
2012–2016	11.42[a]	0.15[b]	1.7	2.99	35.2	41.2	This study (NARR)
26 April2015	CO_2 cross-section[c]			—	—	133	(Radiosonde) and (i)
26 April2015	9.61	straight line[d]		10.5	—	122	(Radiosonde) and (ii)
26 April2015	8.46	joint fit[e]		11.5	—	117	(NARR) and (iii)
2006–2017	—	—	—	—	≈25	—	Arellano et al. (2021)
2012–2017	—	0.11	—	—	-	—	Taquet et al. (2019)
Feb-Apr 2018	—	—	—	—	5–20.0	—	Theys et al. (2019)
2005–2018	—	—	—	—	9.51–38.05	—	Fioletov et al. (2016)
2005–2014	—	—	—	—	18.4	—	McLinden et al. (2016)
2012–2014	—	—	—	—	31.65	—	McLinden et al. (2016)
2005–2015	—	—	—	—	19.2	—	Carn et al. (2017)
2012–2015	—	—	—	—	31.2 ± 2.4	—	Carn et al. (2017)
2007	—	—	—	—	1.97–7.18	-	McCormick et al. (2013)
2005–2015	—	—	8.2	—	—	—	Aiuppa et al. (2017)
2005–2015	—	—	—	—	-	107	Aiuppa et al. (2019)
29 November2013	—	—	—	—	35	—	Campion et al. (2015)
1–4 March 2011	—	—	—	—	4–14.3	—	Lübcke et al. (2013)
8 November 2008	—	—	—	—	11.6	—	Krueger et al. (2013)
2007,2008	—	0.05, 0.15	—	—	—	—	Stremme et al. (2011)
March 2006	—	—	—	—	28.4	—	Grutter et al. (2008)
1995–1997	—	—	1.5–12	—	—	—	Roberge et al. (2009)
1994–1998	—	0.12–0.37	3–200	1–31 (2–20)	12–150	440–1157	Goff et al. (2001)
1993–1994	—	—	—	8.6	347–579	—	Goff et al. (1998)
1994–2002	—	—	—	—	81	—	Witter et al. (2005)
1994	—	—	—	—	17–145	—	Delgado et al. (2001)

[a]By error weighted mean, please see Supplementary Material.
[b]Correlation from consecutive measurements of the HCl-overtone (NIR) and SO_2 measurements, see Supplementary Material.
[c]The CO_2 emission is calculated without assuming correlation with another volcanic gas. (Strategy (i)).
[d]CO_2/HCL, ratio is obtained from the slope in a correlation plot of the vertical columns. (Strategy (ii)).
[e]The CO_2 time series is explained by a linear combination of HCl, the anomaly δO_2 and a polynomial. (Strategy (iii)).

Molec/cm^2 but volcanic CO_2 anomalies close to their detection limit. Applying strategy (iii) (see Section 2.3) and using scaling factor applied to the HCl time series yields the CO_2/HCl molecular ratio and its standard error for each event.

Figures 5A, B show the variability of the CO_2/HCl ratio for each plume intersect in the time series. The correlation of each molecular ratio with the HCl emission rate is shown in Figure 5D). The time series does not show a significant pattern or trend. The histogram of the derived ratios might be explained by a log-normal distribution convolved by a normal distribution, since all ratios should be positive, but are determined by relatively large measurement errors (Figure 5D). The weighted average CO_2/HCl ratio is found to be 11.4 ± 4.4 Molec. ratio and the correlation plot (inset d)) shows no significant correlation between the emission strength and the Molec. ratios (R^2=0.03).

The Figure 5C shows the time series of the 54 events for which the mean emission rate of HCl could be calculated. The HCl flux is rather variable ranges from 0.007 kg/s to 12.6 kg/s, with a median of 2.7 kg/s and an average and standard deviation of (3.0 ± 3.5) kg/s. From those, the 25 events which were also chosen for the estimation of the mean CO_2/HCl molecular ratio are plotted in red and marked with a plus in the same figure.

The use of O_2 anomalies for the determination of the volcanic CO_2 is not crucial for the case study (26 April 2015), but useful for the other 25 volcanic events, which are used to determine a mean CO_2/HCl molecular ratio of 11.4 ± 4.4 and have rather large

errorbars. Figure 3B shows scattering in the vertical O_2 column of around 0.2%, which is a similar magnitude as the volcanic anomaly in the CO_2 column. Interestingly, the CO_2/HCl molecular ratio determined for the above average emission rate on 26 April 2015 (8.46–9.6) is similar to the average ratio obtained from the full time series (11.4 ± 4.4, see Table 3).

As can be noticed from Figures 5A, B, despite the larger emission on 26 April 2015 (Figure 5C), the molecular ratio of the event lies very close to the mean value.

3.6 Total emissions

The CO_2 signature was only found strong enough to calculate the CO_2 plume cross-section with a reliable error (35%) during a single plume intersect, occurring during passive degassing. The maximal slant column anomaly of CO_2 reached a value of 1.6% above the vertical background column, which is clearly larger than the detection limit and precision. In general, the CO_2/HCl ratio is variable from day to day (Figure 5) and initially, it was not clear whether this single measurement occurred through an extraordinary enhancement of the CO_2/HCl ratio as found by (Goff et al., 2001) or due to an enhancement of the overall gas emission. On the event of 26 April 2015 the volcanic emissions reflected a typical behavior of passive degassing, during a dome destruction period (photos, Supplementary Figure S1).

Overall, we found that the CO_2/HCl ratio on 26 April 2015 was similar to the mean ratio of CO_2/HCl for the entire 2012–2016 measurement period. This hypothesis is supported by the analysis of 25 of 54 volcanic events, for which we found an average CO_2/HCl molecular ratio of 11.42 ± 4.44. Thus the CO_2/HCl ratio of 9.84 ± 1.26 measured on 26 April 2015 seems to be a typical ratio.

The CO_2 annual emission rate for the 2012 to 2016 period is estimated from the average CO_2/HCl molecular ratio (11.42 ± 4.44) and the HCl emission flux (3.0 ± 0.3 kg/s) and found to be (41.2±16.7) kg/s.

Using the HCl-product from this work and the SO_2 column retrieval from spectra recorded with the NDACC-filter 3 and 6 and detectors InSb and MCT, (Taquet et al., 2019), but measured within a 5 min coincidence criteria, an average molecule ratio SO_2/HCl of 6.6 was determined for the time period of this work (Supplementary Section S4). This ratio allows us a comparison with SO_2 emission data taken from the literature. Recent studies reporting SO_2 emissions of Popocatepetl based on different techniques are summarized in Table.3. Among these studies are UV-cam measurements (of 29 November 2013 (Campion et al., 2015) and 27 days between November and December 2016 (Schiavo et al., 2019), a former study using data of 1 month from various techniques during the MILAGRO field campaign in March 2006 (Grutter et al., 2008), results from the NOVAC-project (Arellano et al., 2021) and with the space-based SO_2 emission estimation covering the period 2007–2014 (McLinden et al., 2016). These studies cover a similar period as ours and help us to validate our new method to calculate volcanic gas emissions. The average emission rates of HCl, SO_2, and CO_2 in the period from October 2012 to June 2016 yield to (3.0 ±0.3) kg/s, (35.7 ±4.2) kg/s, and (41.2 ±16.7) kg/s respectively (corresponding to the annual emission rates of (0.094± 0.011) Tg/yr, (1.13± 0.12)Tg/yr and (1.30 ± 0.53) Tg/yr).

4 Discussion

The linear combination of a CO_2 background column, sza-dependence, pointing error, and volcanic anomaly successfully, gives us the confidence to apply this correction to the 25 plume intersections (days) where the highest HCl-slant columns have been measured and the slant HCl columns were greater than 10^{18} Molec/cm^2. The indirect estimate of the CO_2 emission, based on the CO_2/HCl ratio (11.4 ± 4.4 molecular ratio) and the HCl flux, avoids statistical bias since even events with CO_2 anomalies below the detection limit are taken into account in the determination of the emission rate.

4.1 Comparison of volcanic gas flux measurements with other methods

For the comparison of the volcanic gas flux from Popocatépetl with other measurements, in general, only SO_2 flux measurements are available from the literature, thus a comparison has to estimate the average molecular ratio of SO_2/HCl during passive degassing of the Popocatépetl which is around 6.6 ±0.3 for the period 2012 to 2016 and using the HCl retrieval from the first overtone. The slight difference in the SO_2/HCl molecular ratio values reported by Stremme et al. (2011); Taquet et al. (2019) (6.8 and 9.1) are due to the spectroscopic inconsistency and differences in the time period. Since SO_2 can be readily measured with conventional volcano monitoring techniques (e.g., Mobile DOAS, Scanning DOAS and SO_2 camera (Grutter et al., 2008; Campion et al., 2018; Platt et al., 2018; Schiavo et al., 2019; Arellano et al., 2021), it is common practice to determine the emission rate with the X/SO_2 ratio, where X represents CO2, HCl, etc. To apply this method we need to calculate the CO_2/SO_2 ratio which we do by measuring the HCl/SO_2 ratio and scaling this with the previously determined CO_2/HCl ratio. The resulting CO_2/SO_2 molecular ratio is 2.06 ± 0.7. The uncertainty of 33% in the average ratio is dominated by the uncertainty in the CO_2/HCl ratio and takes both into account i) the natural variability of the ratios and ii) the measurement errors. While the derived average CO_2/SO_2 ratio is in the range reported by Roberge et al. (2009), it is smaller than the estimation for the average ratio by (Aiuppa et al., 2019), as shown in Table 3 and on the lower range from the values of Goff et al. (2001).

In order to validate our method with previous studies, such as the study by Grutter et al. (2008) that combines various methods using thermal emission and UV-based techniques, or the studies by (Krueger et al., 2013), (Lübcke et al., 2013) and (Campion et al., 2015) using 2D visualisation methods with either a thermal emission spectrometer or a UV camera on particular days and (McLinden et al., 2016) or (Carn et al., 2017) basing their studies on long term satellite measurements, we have converted our HCl-flux results to SO_2 fluxes. HCl and SO_2 are both volcanic gases with low tropospheric background, however, SO_2 is also emitted by anthropogenic sources (de Foy et al., 2009). HCl, on the other hand, is less abundant in volcanic plumes, can only be measured effectively by IR spectroscopy and has not yet been measured by imaging techniques. The HCl-flux in this work multiplied by an average molecular SO_2/HCl ratio of 6.6 and corrected for the different molecular weights of SO2 and HCl correspond to

a SO_2 flux of (35.7 ± 4.2) kg/s which can be compared to different measurements and estimations reported in the literature and summarized in Table 3. These reported SO_2 emissions range from 5 kg/s to 579 kg/s in different periods. Especially if we consider the activity of the Popocatepetl during the period 2012–2014 (McLinden et al., 2016; Carn et al., 2017; Boulesteix et al., 2022), we find values corresponding to the 35.7 kg/s obtained from this work. The methodology presented here benefits from the location of both the Altzomoni Atmospheric Observatory and the volcano, and from the typical wind direction during the early morning driving the plume in the line of sight of the instrument and allowing a large number of solar absorption plume measurements. Our HCl-fluxes time series did not capture plumes from any strombolian phases associated with dome growth episodes or Vulcanian explosive activity accompanying dome destruction. In the long-term record both of these episodes are relatively rare compared to passive degassing and excluding these episodes of Strombolian and Vulcanian-style eruptions will bias the estimation only slightly. In and after the explosions a larger amount of gas is released and therefore a positive anomaly is expected, but prior to these explosions a decrease in gas emissions is typically observed. Somehow gas is retained until the explosions and the negative anomaly in the emission just before this explosion compensates for the positive anomaly due to the explosion (Love et al., 2000; Taquet et al., 2017). Our SO_2 flux of (36 ± 4) kg/s agrees well with the 31.2 ± 2.4 kg/s average reported for the 2012–2015 period Supplementary Material of Carn et al. (2017) and Boulesteix et al. (2022) and supports the assumption that quiescent emissions dominate the overall emissions from Popocatépetl.

4.2 Quantification of volcanic CO_2/HCl ratio by a linear joint fit

Measuring the CO_2 flux and the CO_2/HCl ratios is challenging because the volcanic part of the slant column of CO_2 is in the subpercentage region. The high CO_2 background and the sza-dependence for measurements with low solar elevation angles are much larger than the volcanic contribution to the total column as described before. However, a joint fit of different proxies for different contributions can explain the measuredtime series of CO_2. Here the HCl time series is used as proxy for the volcanic plume, the columnar O_2 anomalies ($\alpha\frac{400\text{ppm}}{21\%}\delta O_2$) as proxy for the pointing error, which refers to an error in the optical pathlength in the atmosphere and a polynomial covers the remaining contributions as a linear sza and squared solar zenith angle dependence and the background CO_2 column. This strategy of fitting and subtracting the O_2 anomaly instead of using the XCO_2 product is based on the recent work by Baylon et al. (2017), in which the error budget is separated into correlated and independent errors. Calculating the quotient XCO_2 is similar to a subtraction using alpha=1.0, as $\frac{CO_2}{O_2+\delta O_2} \approx \frac{CO_2}{O_2} - \frac{CO_2-(400ppm/21\%)\delta O_2}{O_2}$. We cannot explicitly explain why α is around 0.25 on the presented case study of 26 of April 2015, and varies between 0 and 0.6. But there are various aspects that impact the retrieved value of α: i) the ratio between the noise error in O_2 and the O_2-CO_2-correlative error, ii) the systematic parts between the O_2-CO_2-correlative error, iii) differences in the strength of the O_2-CO_2-correlative error, as maybe raytracing in the 7,800 cm^{-1} is slightly different from the 6,300 cm^{-1} spectral region, thus differently sensitive to pointing errors produced by the presence of a volcanic plume and other effects.

During decompression of magma rising from depth towards the surface, CO_2 first partitions to the vapor phase, only later followed by sulfur and chlorine (Edmonds et al., 2022). We, therefore, expect that deep magmatic recharge could lead to an increase in the CO_2/HCl ratio in the gases emitted from the top of the volcano. On the other hand, efficient release of chlorine from the magma can only occur as it reaches very shallow depths or even atmospheric pressure (Edmonds et al., 2001). Therefore, the HCl flux will primarily be driven by the availability of fresh magma at the surface.

Our measurements provide some limited information on magma migration in Popocatepetl's plumbing system. For one, the variability of the HCl flux is significant and exceeds the errors associated with each individual measurement. This variability is likely related to very shallow processes, in particular, the volume of chlorine-rich magma at or very close to the surface at the time of measurement. The variability of the measured CO_2/HCl ratio, on the other hand, is mostly smaller than the measurement uncertainty. We therefore cannot interpret individual measurements with regard to their underlying magmatic processes. We can, however, establish a baseline for the CO_2/HCl ratio to which future measurements can be compared. Based on the range of values we detected (see Figures 5A, B), any future measurements of CO_2/HCl significantly higher than 100 (after accounting for measurement accuracy and precision) should be considered anomalous and could be an indicator of deep magmatic recharge at Popocatépetl. Thus, our measurement techniques may provide valuable information on magma migration and possible future eruptive episodes.

The CO_2/HCl (11.42) molecular ratio might be converted to a $CO_2/SO_2 \approx 1.7$ using the SO_2/HCl ratio of 6.6. Our average CO_2/SO_2 ratio is consistent with that measured by Roberge et al. (2009) in a melt inclusion (i.e.,: ≈1 Molec. ratio for an inclusion captured at 400 MPa (15 km) representative of primary magma). The CO_2/SO_2 molecular ratio of around 2 is however in general lower than those obtained in studies carried out in 1993 and 1994 using remote sensing (Goff et al., 2001). Since we also see a large variability in our results and a distribution with a larger tail towards positive anomalies (Figure 5B), this ratio might have significantly higher values during some periods of short duration. However, in this work the number of measurements of the ratio is limited and the precision of the retrieved ratio does not allow to determine the variability, just the overall background value of the CO_2/HCl ratio in the plume of Popocatépetl.

5 Conclusion

In this contribution, we determine the average CO_2 and HCl emission rates of the active Popocatépetl stratovolcano by near-infrared solar absorption spectroscopy from a fixed site. Our measurements indicate that Popocatépetl has emitted in recent years an average of 1.3 Tg of CO_2 and 95 kt of HCl per year. The CO_2/HCl molecular ratio is on average around 11.42 but shows a large variability. No significant correlation between the HCl flux and the CO_2/HCl ratio was found. A particular case study is presented for a measurement recorded during the early morning of 26 April

2015. An anomaly in the CO_2 column on this day was visualized and the emission rate of Popocatépetl could be calculated directly from the CO_2 column measurements. Three different strategies for CO_2 and HCl flux analysis have been compared and cross validated. For the estimation of a representative mean emission rate for HCl and CO_2 during the period between 2012 and 2016, only one of these strategies were followed since the CO_2 signal was not always strong enough for a direct estimation. During 54 days in the measurement period, a cross-section of the volcanic plume was measured and the HCl emission rate was determined. The CO_2/HCl ratio could be measured in about half of these events and a mean emission rate of CO_2 could be calculated using this ratio and the HCl-flux.

Assuming a SO_2/HCl molecular ratio of 6.6, the average HCl emission during 2012–2016 obtained in this study corresponds to an annual emission rate of (36 ± 4) kg/s (3.1 ± 0.4) kt/d or (1.14 ± 0.13) Tg/yr) of SO_2. This result is completely independent of other methods used so far and is in agreement with other reported SO_2 emission rates. The CO_2/SO_2 molecular ratio of 1.7 is in accordance with some ratios measured by Roberge et al. (2009). However, the 41.2 kg/s average CO_2 emissions obtained in this study (equivalent to 1.3 ± 0.5 Tg/yr) is significantly lower than what has been estimated and assumed in former studies (Delgado et al., 2001; Goff et al., 2001; Witter et al., 2005; Aiuppa et al., 2017). According to these new results, the total CO_2 emissions of Popocatépetl contribute only with about 1% and 3.4% of the estimated anthropogenic CO_2 emissions in the Mexican territory (130 Tg/yr) and in the Mexico City Metropolitan Area (44 Tg/yr). Nevertheless, these CO_2 emissions from volcanic origin can be as strong as a coal-fired power plant and should be considered in regional carbon cycle studies and also included in global volcanic emission inventories.

Data availability statement

The original contributions presented in the study are included in the article/Supplementary Material, further inquiries can be directed to the corresponding authors.

Author contributions

WS coordinated the work and carried out the early morning. MG contributed in the reconstruction of the volcanic emission rate from solar absorption measurements, combining perpendicular cross-section, the geometry and writing of the manuscript. JB retrieved the CO_2 and O_2 columns from the NIR spectra. TB leads the German-Mexican collaboration for long-term operation as part of NDACC. FH has helped in the design and setup of the spectrometer and solar tracker and has developed the retrieval code PROFFIT. NT is responsible for the volcanological aspects and interpretation of the gas composition, reviewing the retrievals and the results. She has contributed to the analysis and writing parts of the paper. AB is responsible for the data acquisition, managing and processing of the spectra, as well as in the operation of the spectrometer. BS reviewed the emission of Popocatepetl and calculated the SO_2 emissions. EP-M helped to set up the spectrometer and carried out most of the solar FTIR measurements in Altzomoni. She contributed to the analysis, interpretation and writing of the paper. CR helped with the estimation of the SO_2 flux from Popcatepetl. CR has contributed to the analysis, interpretation and writing. All authors contributed to the article and approved the submitted version.

Funding

We acknowledge the financial support of DGAPA-UNAM PAPIIT (IN107417, IN111521, IA101620) and CONACYT (275239, 290589).

Acknowledgments

WS thanks DGAPA PASPA for supporting this research during the sabbatical 2019/2020 and The IMK-KIT for hospitality. CONACYT is acknowledged for the studentship of JB. We are grateful for the technical assistance provided by Alfredo Rodriguez, Miguel Robles, Delibes Flores, Omar López, and the Insituto de Ciencias de la Atmósfera and Cambio Climatico (UNAM) for the institutional support to carry out this study. Especially we thank Dr. Thomas Boulesteix for his help at the Altzomoni site, his fruitful discussions, and his motivation. We thank both reviewers for their constructive critics and helpful comments. Especially we thank Nicole Bobrowski (reviewer 2) for her good ideas and very careful revisions which have improved the manuscript substantially.

Conflict of interest

The authors declare that the research was conducted in the absence of any commercial or financial relationships that could be construed as a potential conflict of interest.

The reviewer AB declared a past co-authorship with the authors FH, TB to the handling editor.

Publisher's note

Supplementary material

The Supplementary Material for this article can be found online at: https://www.frontiersin.org/articles/10.3389/feart.2023.1022976/full#supplementary-material

References

Aiuppa, A., Baker, D., and Webster, J. (2009). Halogens in volcanic systems. *Chem. Geol.* 263, 1–18. doi:10.1016/j.chemgeo.2008.10.005

Aiuppa, A., Fischer, T., Plank, T., and Bani, P. (2019). Co 2 flux emissions from the earth's most actively degassing volcanoes, 2005–2015. *Sci. Rep.* 9, 5442. doi:10.1038/s41598-019-41901-y

Aiuppa, A., Fischer, T., Plank, T., Robidoux, P., and Di Napoli, R. (2017). Along-arc, inter-arc and arc-to-arc variations in volcanic gas co $2/s_t$ ratios reveal dual source of carbon in arc volcanism. *Earth-Science Rev.* 168, 24–47. doi:10.1016/j.earscirev.2017.03.005

Alberti, C., Hase, F., Frey, M., Dubravica, D., Blumenstock, T., Dehn, A., et al. (2022). Improved calibration procedures for the em27/sun spectrometers of the collaborative carbon column observing network (coccon). *Atmos. Meas. Tech.* 15, 2433–2463. doi:10.5194/amt-15-2433-2022

Arellano, S., Galle, B., Apaza, F., Avard, G., Barrington, C., Bobrowski, N., et al. (2021). Synoptic analysis of a decade of daily measurements of so_2 emission in the troposphere from volcanoes of the global ground-based network for observation of volcanic and atmospheric change. *Earth Syst. Sci. Data* 13, 1167–1188. doi:10.5194/essd-13-1167-2021

Barthlott, S., Schneider, M., Hase, F., Wiegele, A., Christner, E., González, Y., et al. (2015). Using xco_2 retrievals for assessing the long-term consistency of ndacc/ftir data sets. *Atmos. Meas. Tech.* 8, 1555–1573. doi:10.5194/amt-8-1555-2015

Baumgardner, D., Grutter, M., Allan, J. D., Ochoa, C., Rappenglück, B., Russell, L., et al. (2009). Physical and chemical properties of the regional mixed layer of Mexico's megapolis. *Atmos. Chem. Phys.* 9, 5711–5727. doi:10.5194/acp-9-5711-2009

Baylon, J. L., Stremme, W., Grutter, M., Hase, F., and Blumenstock, T. (2017). Background co_2 levels and error analysis from ground-based solar absorption ir measurements in central Mexico. *Atmos. Meas. Tech. Discuss.*, 1–18. doi:10.5194/amt-2016-418

Boulesteix, T., Legrand, D., Taquet, N., Coppola, D., Laiolo, M., Valade, S., et al. (2022). Modulation of popocatépetl's activity by regional and worldwide earthquakes. *Bull. Volcanol.* 84, 80. doi:10.1007/s00445-022-01584-2

Butz, A., Dinger, A. S., Bobrowski, N., Kostinek, J., Fieber, L., Fischerkeller, C., et al. (2017). Remote sensing of volcanic CO_2, HF, HCl, SO_2, and BrO in the downwind plume of Mt. Etna. *Atmos. Meas. Tech.* 10, 1–14. doi:10.5194/amt-10-1-2017

Campion, R., Delgado-Granados, H., Legrand, D., Taquet, N., Boulesteix, T., Pedraza-Espitía, S., et al. (2018). Breathing and coughing: The extraordinarily high degassing of popocatépetl volcano investigated with an so2 camera. *Front. Earth Sci.* 6, 163. doi:10.3389/feart.2018.00163

Campion, R., Delgado-Granados, H., and Mori, T. (2015). Image-based correction of the light dilution effect for SO 2 camera measurements. *J. Volcanol. Geotherm. Res.* 300, 48–57. doi:10.1016/j.jvolgeores.2015.01.004

Campion, R., Martinez-Cruz, M., Lecocq, T., Caudron, C., Pacheco, J., Pinardi, G., et al. (2012). Space- and ground-based measurements of sulphur dioxide emissions from Turrialba Volcano (Costa Rica). *Bull. Volcanol.* 74, 1757–1770. doi:10.1007/s00445-012-0631-z

Carn, S., Fioletov, V., Mclinden, C., Li, C., and Krotkov, N. (2017). A decade of global volcanic so2 emissions measured from space. *Sci. Rep.* 7, 44095. doi:10.1038/srep44095

Clarmann, T. v., and Grabowski, U. (2007). Elimination of hidden a priori information from remotely sensed profile data. *Atmos. Chem. Phys.* 7, 397–408. doi:10.5194/acp-7-397-2007

de Foy, B., Krotkov, N. A., Bei, N., Herndon, S. C., Huey, L. G., Martínez, A.-P., et al. (2009). Hit from both sides: Tracking industrial and volcanic plumes in Mexico city with surface measurements and omi so_2 retrievals during the milagro field campaign. *Atmos. Chem. Phys.* 9, 9599–9617. doi:10.5194/acp-9-9599-2009

De Mazière, M., Thompson, A. M., Kurylo, M. J., Wild, J. D., Bernhard, G., Blumenstock, T., et al. (2018). The network for the detection of atmospheric composition change (ndacc): History, status and perspectives. *Atmos. Chem. Phys.* 18, 4935–4964. doi:10.5194/acp-18-4935-2018

Delgado, H., Cardenas Gonzalez, L., and Piedad Sanchez, N. (2001). Sulfur dioxide emissions from Popocatépetl volcano (Mexico): Case study of a high-emission rate, passively degassing erupting volcano. *J. Volcanol. Geotherm. Res.* 108, 107–120. doi:10.1016/S0377-0273(00)00280-8

Edmonds, M., Liu, E., and Cashman, K. (2022). Open-vent volcanoes fuelled by depth-integrated magma degassing. *Bull. Volcanol.* 84, 28. doi:10.1007/s00445-021-01522-8

Edmonds, M., Pyle, D., and Oppenheimer, C. (2001). A model for degassing at the Soufriere hills volcano, Montserrat, west indies, based on geochemical data. *Earth Planet. Sci. Lett.* 186, 159–173. doi:10.1016/s0012-821x(01)00242-4

Espinoza, M. A. M., Garcia, T. M., Sahagun, A. M., and Torres, D. G. (2018). Inventario de Emisiones de de la CDMX 2014: Contaminantes criterio, toxicos y de efecto invernadero. Tech. rep., Secretaria del Medio Ambiente del Gobierno de la Ciudad de México.

Fickel, M., and Delgado Granados, H. (2017). On the use of different spectral windows in doas evaluations: Effects on the estimation of so2 emission rate and mixing ratios during strong emission of popocatépetl volcano. *Chem. Geol.* 462, 67–73. doi:10.1016/j.chemgeo.2017.05.001

Fioletov, V. E., McLinden, C. A., Krotkov, N., Li, C., Joiner, J., Theys, N., et al. (2016). A global catalogue of large so_2 sources and emissions derived from the ozone monitoring instrument. *Atmos. Chem. Phys.* 16, 11497–11519. doi:10.5194/acp-16-11497-2016

Francis, P., Burton, M. R., and Oppenheimer, C. (1998). Remote measurements of volcanic gas compositions by solar occultation spectroscopy. *Nature* 396, 567–570. doi:10.1038/25115

Galle, B., Johansson, M., Rivera, C., Zhang, Y., Kihlman, M., Kern, C., et al. (2010). Network for observation of volcanic and atmospheric change (novac)—A global network for volcanic gas monitoring: Network layout and instrument description. *J. Geophys. Res. Atmos.* 115, D05304. doi:10.1029/2009JD011823

Garcia-Franco, J., Stremme, W., Bezanilla, A., Ruiz-Angulo, A., and Grutter, M. (2018). Variability of the mixed-layer height over Mexico city. *Boundary-Layer Meteorol.* 167, 493–507. doi:10.1007/s10546-018-0334-x

Gerlach, T. M. (1991). Present-day CO2 emissions from volcanos. *Eos, Trans. Am. Geophys. Union* 72, 249–255.

Gisi, M., Hase, F., Dohe, S., and Blumenstock, T. (2011). Camtracker: A new camera controlled high precision solar tracker system for ftir-spectrometers. *Atmos. Meas. Tech.* 4, 47–54. doi:10.5194/amt-4-47-2011

Gisi, M., Hase, F., Dohe, S., Blumenstock, T., Simon, A., and Keens, A. (2012). XCO₂-measurements with a tabletop FTS using solar absorption spectroscopy. *Atmos. Meas. Tech.* 5, 2969–2980. doi:10.5194/amt-5-2969-2012

Goff, F., Janik, C. J., Delgado, H., Werner, C., Counce, D., Stimac, J. A., et al. (1998). Geochemical surveillance of magmatic volatiles at popocatépetl volcano, Mexico. *Geol. Soc. Am. Bull.* 110, 695–710.

Goff, F., Love, S. P., Warren, R., Counce, D., Obenholzner, J., Siebe, C., et al. (2001). Passive infrared remote sensing evidence for large, intermittent CO2 emissions at Popocatépetl volcano, Mexico. *Chem. Geol.* 177, 133–156. doi:10.1016/S0009-2541(00)00387-9

Grutter, M., Basaldud, R., Rivera, C., Harig, R., Junkerman, W., Caetano, E., et al. (2008). SO_2 emissions from Popocatépetl volcano: Emission rates and plume imaging using optical remote sensing techniques. *Atmos. Chem. Phys.* 8, 6655–6663. doi:10.5194/acp-8-6655-2008

Hase, F., Frey, M., Blumenstock, T., Groß, J., Kiel, M., Kohlhepp, R., et al. (2015). Application of portable ftir spectrometers for detecting greenhouse gas emissions of the major city berlin. *Atmos. Meas. Tech.* 8, 3059–3068. doi:10.5194/amt-8-3059-2015

Instituto Nacional de Ecología y Cambio Climático (INECC) (2018). Mexico: Inventario nacional de Emisiones de Gases y compuestos de Efecto invernadero 1990-2015 (version revisado). Tech. rep., Secretaría de Medio Ambiente y Recursos Naturales (SMARNAT).

Juarez, A., Gay, C., and Flores, Y. (2005). Impact of the Popocatepetl's volcanic activity on the air quality of Puebla City, Mexico. *Atmosfera* 18, 57–69.

Keppel-Aleks, G., Toon, G. C., Wennberg, P. O., and Deutscher, N. M. (2007). Reducing the impact of source brightness fluctuations on spectra obtained by Fourier-transform spectrometry. *Appl. Opt.* 46, 4774–4779. doi:10.1364/AO.46.004774

Kiel, M., Wunch, D., Wennberg, P. O., Toon, G. C., Hase, F., and Blumenstock, T. (2016). Improved retrieval of gas abundances from near-infrared solar ftir spectra measured at the Karlsruhe tccon station. *Atmos. Meas. Tech.* 9, 669–682. doi:10.5194/amt-9-669-2016

Krueger, A., Stremme, W., Harig, R., and Grutter, M. (2013). Volcanic SO_2 and SiF_4 visualization using 2-D thermal emission spectroscopy - Part 2: Wind propagation and emission rates. *Atmos. Meas. Tech.* 6, 47–61. doi:10.5194/amt-6-47-2013

Love, S. P., Goff, F., Counce, D., Siebe, C., and Delgado, H. (1998). Passive infrared spectroscopy of the eruption plume at Popocatépetl volcano, Mexico. *Nature* 396, 563–567. doi:10.1038/25109

Love, S. P., Goff, F., Schmidt, S. C., Counce, D., Pettit, D., Christenson, B. W., et al. (2000). *Passive infrared spectroscopic remote sensing of volcanic gases: Ground-based studies at White Island and Ruapehu, New Zealand, and Popocatépetl, Mexico*, 116. Washington DC American Geophysical Union Geophysical Monograph Series, 117–138. doi:10.1029/GM116p0117

Lübcke, P., Bobrowski, N., Illing, S., Kern, C., Alvarez Nieves, J. M., Vogel, L., et al. (2013). On the absolute calibration of so_2 cameras. *Atmos. Meas. Tech.* 6, 677–696. doi:10.5194/amt-6-677-2013

McCormick, B. T., Edmonds, M., Mather, T. A., Campion, R., Hayer, C. S. L., Thomas, H. E., et al. (2013). Volcano monitoring applications of the ozone monitoring instrument. *Geol. Soc. Lond. Spec. Publ.* 380, 259–291. doi:10.1144/SP380.11

McLinden, C. A., Fioletov, V., Shephard, M. W., Krotkov, N., Li, C., Martin, R. V., et al. (2016). Space-based detection of missing sulfur dioxide sources of global air pollution. *Nat. Geosci.* 9, 496–500. doi:10.1038/ngeo2724

Mesinger, F., DeMago, G., Kalnay, E., Mitchell, K., Shafran, P., Ebisuzake, W., et al. (2006). North American regional reanalysis. *North Am. regional reanalysis. BAMS* 87, 343–360. BAMS-87-3-343. doi:10.1175/bams-87-3-343

Platt, U., Bobrowski, N., and Butz, A. (2018). Ground-based remote sensing and imaging of volcanic gases and quantitative determination of multi-species emission fluxes. *Geosciences* 8, 44. doi:10.3390/geosciences8020044

Platt, U., and Stutz, J. (2008). *Physics of Earth and space environments*. Springer Berlin Heidelberg.Differential optical absorption spectroscopy: Principles and applications

Plaza-Medina, E. F., Stremme, W., Bezanilla, A., Grutter, M., Schneider, M., Hase, F., et al. (2017). Ground-based remote sensing of o_3 by high- and medium-resolution ftir spectrometers over the Mexico city basin. *Atmos. Meas. Tech.* 10, 2703–2725. doi:10.5194/amt-10-2703-2017

Raga, G. B., Kok, G. L., Baumgardner, D., Báez, A., and Rosas, I. (1999). Evidence for volcanic influence on Mexico city aerosols. *Geophys. Res. Lett.* 26, 1149–1152. doi:10.1029/1999GL900154

Roberge, J., Delgado-Granados, H., and Wallace, P. J. (2009). Mafic magma recharge supplies high co2 and so2 gas fluxes from popocatépetl volcano, Mexico. *Geology* 37, 107–110. doi:10.1130/G25242A.1

Rodgers, C. D. (2000). "Inverse methods for atmospheric sounding - theory and practice," in *Inverse methods for atmospheric sounding - theory and practice. Series: Series on atmospheric oceanic and planetary physics*. Editor D. R. Clive (World Scientific Publishing Co. Pte. Ltd.). doi:10.1142/9789812813718

Schiavo, B., Stremme, W., Grutter, M., Campion, R., Guarin, C. A., Rivera, C., et al. (2019). Characterization of a uv camera system for so2 measurements from popocatépetl volcano. *J. Volcanol. Geotherm. Res.* 370, 82–94. doi:10.1016/j.jvolgeores.2018.09.001

Siebe, C., Abrams, M., Macias, J. L., and Obenholzner, J. (1996). Repeated volcanic disasters in Prehispanic time at Popocatépetl, central Mexico: Past key to the future?*Geology* 24, 399. doi:10.1130/0091-7613(1996)024⟨0399;RVDIPT⟩2.3.CO;2

Stremme, W., Krueger, A., Harig, R., and Grutter, M. (2012). Volcanic SO_2 and SiF_4 visualization using 2-D thermal emission spectroscopy - Part 1: Slant-columns and their ratios. *Atmos. Meas. Tech.* 5, 275–288. doi:10.5194/amt-5-275-2012

Stremme, W., Ortega, I., and Grutter, M. (2009). Using ground-based solar and lunar infrared spectroscopy to study the diurnal trend of carbon monoxide in the Mexico city boundary layer. *Atmos. Chem. Phys.* 9, 8061–8078. doi:10.5194/acp-9-8061-2009

Stremme, W., Ortega, I., Siebe, C., and Grutter, M. (2011). Gas composition of Popocatépetl volcano between 2007 and 2008: FTIR spectroscopic measurements of an explosive event and during quiescent degassing. *Earth Planet. Sci. Lett.* 301, 502–510. doi:10.1016/j.epsl.2010.11.032

Taquet, N., Hernández, I. M., Stremme, W., Bezanilla, A., Grutter, M., Campion, R., et al. (2017). Continuous measurements of sif4 and so2 by thermal emission spectroscopy: Insight from a 6-month survey at the popocatépetl volcano. *J. Volcanol. Geotherm. Res.* 341, 255–268. doi:10.1016/j.jvolgeores.2017.05.009

Taquet, N., Stremme, W., Baylon, J., Bezanilla, A., Schiavo, B., Rivera, C., et al. (2019). Variability in the gas composition of the popocatepetl volcanic plume. *Front. Earth Sci.* 7, 114. doi:10.3389/feart.2019.00114

Theys, N., Hedelt, P., De Smedt, I., Lerot, C., Yu, H., Vlietinck, J., et al. (2019). Global monitoring of volcanic so2 degassing with unprecedented resolution from tropomi onboard sentinel-5 precursor. *Sci. Rep.* 9, 2643. doi:10.1038/s41598-019-39279-y

Werner, C., Fischer, T. P., Aiuppa, A., Edmonds, M., Cardellini, C., Carn, S., et al. (2019). "Carbon dioxide emissions from subaerial volcanic regions," in *Deep carbon past to present* (Cambridge University Press).

Witter, J. B., Kress, V. C., and Newhall, C. G. (2005). Volcan popocatepetl, Mexico. petrology, magma mixing, and immediate sources of volatiles for the 1994–present eruption. *J. Petrology* 46, 2337–2366. doi:10.1093/petrology/egi058

Wunch, D., Toon, G. C., Blavier, J.-F. L., Washenfelder, R. A., Notholt, J., Connor, B. J., et al. (2011). The total carbon column observing network. *Philosophical Trans. R. Soc. Lond. A Math. Phys. Eng. Sci.* 369, 2087–2112. doi:10.1098/rsta.2010.0240

Wunch, D., Toon, G. C., Wennberg, P. O., Wofsy, S. C., Stephens, B. B., Fischer, M. L., et al. (2010). Calibration of the total carbon column observing network using aircraft profile data. *Atmos. Meas. Tech.* 3, 1351–1362. doi:10.5194/amt-3-1351-2010

Frontiers in Earth Science

Investigates the processes operating within the major spheres of our planet

Advances our understanding across the earth sciences, providing a theoretical background for better use of our planet's resources and equipping us to face major environmental challenges.

Discover the latest Research Topics

See more →

Frontiers

Avenue du Tribunal-Fédéral 34
1005 Lausanne, Switzerland
frontiersin.org

Contact us

+41 (0)21 510 17 00
frontiersin.org/about/contact